# Geologic and geochemical vectors to mineralisation at the Resolution porphyry Cu-Mo deposit, Arizona

by

**Joshua James Phillips**

**BSc. (hons), M.Econ Geol.**

Submitted in fulfilment of the requirements for the degree of

Doctor of Philosophy

July 2019


UNIVERSITY OF TASMANIA

CODES

TMVC

TRANSFORMING THE MINING VALUE CHAIN

## Declaration of Originality

This thesis contains no material which has been accepted for a degree or diploma by the University or any other institution, except by way of background information and duly acknowledged in the thesis, and to the best of my knowledge and belief no material previously published or written by another person except where due acknowledgement is made in the text of the thesis, nor does the thesis contain any material that infringes copyright.

Joshua J. Phillips

Date: 10th August 2019

## Authority of Access

This thesis is not to be made available for loan or copying for eighteen months following the date this statement was signed. Following that time the thesis may be made available for loan and limited copying and communication in accordance with the Copyright Act 1968.

Joshua J. Phillips

Date: 10th August 2019

*blank page*

# Abstract

The Resolution porphyry Cu-Mo deposit, located within the Superior mining district, Arizona, has a resource of 1,787 Mt at 1.54% Cu and 0.035% Mo. It formed during the Late Cretaceous to Paleocene Laramide Orogeny and is one of the largest and highest grade porphyry Cu deposits in North America. Since that time, Tertiary gravels and volcanic rocks related to Basin and Range extension buried the deposit under approximately 1.5 km of cover. This deep cover prevented the discovery of Resolution until the 1990s, despite historical mining of the nearby Magma and Silver King epithermal deposits since 1875.

A significant component of the pre-mineralisation sequence in the Superior district are the Proterozoic basaltic lava flows and dolerite sills of the Mesoproterozoic Apache Group. The dolerite sills intruded between ca. 1,110 and 1,075 Ma, coeval with Midcontinent rift magmatism. They can be geochemically subdivided into four discrete suites using immobile element geochemistry, due to the different degrees of crustal contamination and fractionation. Generally, the dolerites have a slightly more enriched mantle signature than the older Apache Basalt. This is interpreted to reflect the distal influence of a mantle plume-head responsible for Midcontinent rift magmatism. The dolerite sills are derived from an enriched, shallow mantle source, similar to the Nipigon and Pigeon River suites of the Midcontinent rift. Two suites show evidence for significant contamination by the lower crust. One of these contaminated dolerite suites also retained significantly elevated levels of PGEs (~20 ppb combined Pt + Pd) compared to the other sills (Pt and Pd below detection limit).

The intrusion of Mesoproterozoic dolerite sills into the water-rich, salt-bearing Apache Group stratigraphy caused mobilisation of significant volumes of evaporite-derived hypersaline brine. Widespread K-feldspar - chlorite alteration of Apache Basalt occurred at this time, part of a previously undocumented phase of significant Mesoproterozoic potassium metasomatism within the Proterozoic volcanic rocks, centred on E-striking faults. This metasomatic event produced several protolith-controlled alteration assemblages in the Proterozoic rocks of the Superior district, including calc-silicate skarn assemblages within the Pinal Schist, patchy hematite - quartz alteration in sandstones, magnesian and magnetite skarn alteration of dolomitic rocks, epidote – calcite – chlorite alteration of the basaltic rocks, and widespread actinolite – chlorite – biotite – albite alteration in the dolerite sills. U-Pb dating of hydrothermal apatite in four epidote – calcite – chlorite-altered Apache Basalt samples returned ages ranging from 1,247 ± 52 Ma to 1,113 ± 55 Ma, implicating the intrusion of the dolerite sills as a major driver for Proterozoic hydrothermal activity in the Superior district. The apatite ages also correlate with uraninite and galena ages of uranium mineralisation from elsewhere in the region, suggesting that this was a basin-wide phenomenon.

A laser ablation inductively coupled plasma mass spectrometry (LA-ICP-MS) epidote U-Pb geochronology

method was developed as part of the current study in conjunction with apatite U-Pb geochronology. When applied to epidote in the Proterozoic basalts, the epidote U-Pb method provides similar precision to apatite (~5%), although initial results show a 10% offset in final age between apatite (e.g., 1,151 ± 48 Ma ) and epidote (e.g., 1,266 ± 57 Ma) due to the lack of a matrix matched epidote standard. The incorporation of $^{206}Pb$ and $^{207}Pb$ into routine LA-ICP-MS trace element analysis methods for epidote has enabled collection of geochronological and corresponding trace element data, although the uncertainties are larger (~10%). Using the routine trace element method, a composite age for all Proterozoic epidote analyses yielded an age of 1,183 Ma ± 23 Ma. This age confirms that there was a Proterozoic episode of epidote alteration in the district, broadly coeval with the intrusion of the dolerite sills.

Argon-Ar geochronology conducted on muscovite-altered samples from Silver King (75.70 ± 0.12 Ma and 74.31 ± 0.11 Ma) and the Magma vein (68.22 ± 0.11 Ma and 67.39 ± 0.29 Ma) indicate a temporal distinction between those Laramide epithermal deposits and the ca. 65 Ma Resolution porphyry deposit. This result confirms that alteration around the Silver King stock is significantly older than the main mineralising event in the district, and supports a possible genetic distinction between Resolution and Magma, as suggested by previous authors.

Epidote and chlorite LA-ICP-MS analyses from throughout the district were classified using supervised machine learning techniques including random forests and discriminant projection analysis, in order to discriminant the geochemical signatures of each generation of epidote and chlorite alteration associated with the multiple hydrothermal systems in the district. Proterozoic epidote is enriched in U, B, and HREEs and Proterozoic chlorite is depleted in Zn and Mn. These Proterozoic epidote and chlorite compositions represent mineral chemistry background for exploration in the region. Resolution-related epidote and chlorite were recognised in altered Apache Basalt as exposed in the Superior range front. The distal geochemical signature of Resolution is defined by elevated Pb and Sr in epidote, and Zn and Mn in chlorite. Epidotes related to Silver King were generally characterised by higher Sr, while those from Magma tended to show higher Ni, Cr, and V, when compared to epidote from Resolution. Chlorite from Silver King typically has higher Ti, Al and Ba, while chlorite from Magma is characterised by higher Ni and V values, compared to Resolution. The mineral chemistry footprint of Resolution defines an 4.2 km radius geochemical footprint around the deposit, and this alteration halo is partly exposed in the range front.

Results from carbon and oxygen isotope analyses of samples taken along epithermal veins that crop out in the range front west of Resolution range from -9.5‰ to 0.8‰ ($\delta^{13}C$) and and 10.5‰ to 23.7‰ ($\delta^{18}O$) relative to VPDB and VSMOW respectively, revealing significant exchange of magmatic fluids with country rocks. The carbon isotopic system has been disturbed by the diverse sources of carbon in the Apache Group (including Proterozoic kerogens), whereas the oxygen isotopic signature is interpreted to preserve a distal cooling trend away from primary magmatic compositions close to Resolution. Over

successive paragenetic stages, decreasing $\delta^{18}O$ compositions suggest increased degrees of mixing with meteoric fluids that had partially equilibrated with carbonate country rocks. At the district scale, the $\delta^{18}O$ values of main stage calcite define a 2.3 km depletion halo around Resolution.

Sulfur isotope analysis of sulfides from Resolution ($\delta^{34}S$ -9.6 ‰ to 4.4 ‰) support fluid evolution under predominantly oxidising sulfate-stable conditions, with magmatic sulfur as the dominant sulfur source. Locally within the Mescal Limestone, there is evidence that some evaporitic sulfur may have been incorporated in the fluids ($\delta^{34}S$ 4.4 ‰ and 0.59 ‰). Directly above the main mineralized zone at Resolution, sulfur isotopic compositions become increasingly negative with successive alteration stages (potassic average: -1.8 ‰, phyllic: -3.6 ‰, early advanced argillic: -3.8 ‰, late advanced argillic: -4.4 ‰), whereas laterally, sulfur isotopic compositions tended to increase due to exchange with more reduced country rocks under low temperature conditions (0.1 to 0.5 ‰). The zonation patterns defined by sulfur isotopes indicate that Resolution was the fluid source with outflow along major structures. There is also a westerly zonation toward more negative values (-5.0 to 1.5 ‰) along the Magma vein, implying the possibility of a second magmatic-hydrothermal fluid source to the west. A $\delta^{34}S$ value of -5.9 ‰ 2 km east of Resolution (termed Resolution East) may indicate a seperate oxidised magmatic-hydrothermal fluid source between Resolution and Superior East.

The Pb isotopic compositions of sulfides in the Superior district are particularly non-radiogenic, in accord with the rest of the southwest US, and support increasing lower crustal involvement in melts and/or metal contributions over time. At the deposit scale, early stages of alteration and mineralisation have slightly more radiogenic Pb isotopic compositions, indicating magmatic metal contributions were mixed with some metals scavenged from the Proterozoic wallrocks. The less radiogenic Pb isotopic compositions of sulfides with time at Resolution imply decreasing amounts of wallrock Pb incorporation. The least radiogenic magmatic Pb isotopic composition of sulfide samples define a 0.75 - 1 km halo around Resolution. This extends out to approximately 2 km based on the Pb isotopic composition of epidote. At the district scale, Pb isotopic compositions of sulfides and epidote tend to get more radiogenic with greater distance from the main Resolution hydrothermal centre, as fluids exchanged with the radiogenic Proterozoic country rocks. Magma ores have a more radiogenic Pb isotopic composition than Resolution.

The integration of mineral chemistry, isotopic and dating techniques has proven to be a powerful tool to discriminant propylitic alteration around giant porphyry deposits from other hydrothermal events that may have affected a district. This approach also shows potential for vectoring toward high temperature oxidised magmatic-hydrothermal fluid sources associated with porphyry mineralisation and has highlighted exploration targets in the Superior district that should be tested to assess the validity of this integrated geologic and geochemical approach.

# Acknowledgements

This thesis is the result of great vision, insight and ongoing support from many individuals, all of whom I am privileged to call colleagues. I have been fortunate to have been part of such a collegiate and innovative CODES and Earth Sciences family.

Firstly, I would like to thank my supervisors Prof. David Cooke, Assoc. Prof. Sebastien Meffre, and Dr Mike Baker for all your patience, help and support on this PhD journey. Special thanks to Dave for backing me when projects and scholarships fell through, for relentless enthusiasm, support and encouragement in those moments of critical self-doubt, and the unremitting red pen that has so dramatically improved the final product. Thank you, Sebastien, for patiently relaying the finer points of Pb isotopes and geochronology, you have been a cornerstone of this research. I am thankful to Mike for bringing me up to speed with mineral chemistry and reviewing chapters so quickly.

The Resolution project would not have been possible without the enthusiasm and support of Paul Agnew and Debora Araujo of Rio Tinto. Their support and encouragement have been invaluable in maintaining focus and bringing the project to a timely conclusion. I am also extremely grateful to Hamish Martin, Bill Hart and Carl Hehnke at Resolution Copper for welcoming me to site and providing me access and support to work on (?around) such a world-class orebody. Thanks to Tyler Barril and Kelsey Sherrad for providing a spare room and friendship during my field time in the Superior, as well as geologists Genelle Hicks, Scott Mcfadden, Rob Isaachson, Michael Bierwagen, Anthony Henager and Sydney Freitag for help in the field. Sincere thanks also to Don Hammer, former geologist at Magma and later consultant to Newmont, for sharing his wealth of knowledge on the geology of the Superior district, personalised field tours, fourwheel driving expertise and tips on getting a 2wd hire car up the range front - a true gentleman geologist.

I wish to thank all the AMIRA P1153 sponsor representatives, especially Tim Ireland, Mike Whitbread, Simon Gatehouse, Mary Harris, Andrew Wurst, David First, Trevor Shaw, and Rodney Allen for their insightful discussion and feedback, and for fostering such a cooperative research atmosphere. My fellow AMIRA students, Amos Garay, Ayesha Ahmed, Jen Thompson and office-mates Yi Sun and Emily Smyk, with whom I have weathered many 'dry-runs' and other PhD-related trials and tribulations, I would like to thank for your solidarity and friendship – often in the wake the red pen! Noel White, as

part of the research group, has been an enormous source of knowledge and experience, which he has shared freely and generously, often over a good red.

It has been a fantastic experience to be part of the wider world-class research group at CODES and Earth Sciences. I would also like to thank all those whose doors I have knocked at along the way including, Lejun Zhang, Jay Thompson, Paul Olin, Matt Cracknell, Evan Orovan, Leonid Danyushevsky and Ron Berry. A huge thanks to Al Cuison and Michelle Chapple-Smith for getting such great results on often particularly challenging lapidary submissions, and to Karsten Goemann and Sandrin Feig at the CSL for their help and advice running the SEM. I would also like to acknowledge all the support staff who have contributed to my time at CODES, in particular Jane Higgins, Deborah Macklin, Helen Scott, Karen Huizing and Troy Finearty, without whom the department would not function.

I am honoured to join the ranks of CODES graduates, and I have been fortunate to share my PhD years with some of the best. Thank you, Nathan Steeves, Shawn Hood, Joe Knight, Chris Leslie, Tom Ostersen (Osty) and Adam Abersteiner for all the tea-room banter, balcony beers and Weldborough fossicking trips along the way. Also to my non-geology friends, Tom and Abby (Tabby), and Tom and Pip (Tip), whose camping trips will become the stuff of legends, thank you for keeping me sane. To my family, in particular Lesley Phillips, thank you for all you have sacrificed and your undying support and belief in such a recalcitrant son!

Finally, to my partner Angela Escolme, an extraordinary geoscientist who blazed the PhD trail, and made it look easy. Thank you Ange for all your help, patience, humour and unwavering love and support over the years, I couldn't have done it without you.

# Table of Contents

# List of Figures

# List of Tables

# List of Appendices

*blank page*

# Chapter 1: Introduction

## 1.1 Preamble

Porphyry deposits are among the largest repositories of Cu in the world, containing about 60 percent of the known resources (John et al., 2010). Their large size and long mine lives combine to make these deposits valuable exploration targets for the mining industry. The economic importance and early exploitation of porphyry and associated epithermal deposits in the American Southwest underpinned much of the development in the region. Consequently, the SW US porphyry province was the crucible of early research regarding the characterisation and origin of this deposit class (e.g., Lowell and Guilbert, 1970; Gustafson and Hunt, 1975; Titley, 1982) and they are now well understood in regards to many aspects of their genesis (Richards, 2003; Cooke et al., 2005; Seedorff et al., 2005; Sillitoe, 2010).

Porphyry Cu deposits are genetically, temporally and spatially associated with porphyritic intrusive complexes that are emplaced in the upper crust (rarely deeper than 6 km; Seedorff et al., 2005). These multi-phase intrusive complexes include stocks, dikes and breccia pipes, that are most commonly derived from medium-K calc-alkaline melts of felsic to intermediate composition from depths of 5 to 15 km (Sillitoe, 2010). Multiple stages of intrusion can introduce volatiles and fluids before, during and after mineralization and/or alteration events. Research has shown that typically the Cu potential (fertility) of a system tends to relate to the degree to which a melt has retained its water and volatiles (e.g., Richards, 2003). This is primarily achieved by preventing of volatile escape to surface, through the action of compressional stress in the crust (Sillitoe, 1998; Cooke et al., 2005). Upon eventual overpressuring, these fluids exolve and escape, metasomatising the surrounding country rock, forming lateral and vertical alteration zonation patterns that are centred on the composite porphyry complex (Lowell and Guilbert 1970). The alteration assemblages commonly encountered around porphyry systems include sodic, calc-sodic, potassic, propylitic, phyllic, intermediate argillic and advanced argillic assemblages (c.f. Sillitoe, 2010). Hydrothermal alteration can define footprints that extend several kilometres from the causative intrusive complex and their spatial distribution can be used in to help vector towards the high temperature mineralised core of the porphyry system (Lowell and Guilbert, 1970). Detailed reviews of porphyry Cu deposit alteration characteristics provided by Sillitoe (1997, 2010), Hedenquist

and Richards (1998), Cooke et al. (2005), Seedorff et al. (2005) and Holliday and Cooke (2007) have provided in -depth appraisals of the genesis and exploration significance of the hydrothermal alteration features in porphyry systems.

### 1.1.1 Effect of basement geology on porphyry districts

At the district scale, porphyry Cu systems tend to occur in clusters (Sillitoe, 2010) or, particularly in the case of the south western US, along lineaments (Leveille and Stegen, 2012). Their spatial distribution is interpreted to reflect a combination of the extent of the parental pluton at depth, and the structural architecture that localised intrusive and hydrothermal activity (Sillitoe and Gappe, 1984; Sillitoe, 2010). However, some authors argue that the importance of basement architecture is exaggerated and that present-day trends and alignments are merely the result of Cenozoic extension (e.g. Favorito and Seedorff, 2017, 2018).

Mineralisation within a given porphyry district typically manifests as a diversity of deposit types depending on local conditions, including skarn, carbonate-replacement and superjacent high- and intermediate-sulfidation epithermal deposits. This diversity is in part due to localised structural and/or chemical variability in the country rocks and protracted, dynamic magmatic-hydrothermal evolution during the metallogenic event. However this variability can also be strongly influenced by the many millions of years of preceding and subsequent geologic evolution, such as at Bingham, USA (Babcock et al., 1995), Potrerillos, Chile (Olson, 1984; Marsh et al., 1997), Cadia, Australia (Wilson, 2003; Wilson et al., 2007), Batu Hijau, Indonesia (Garwin, 2000, Garwin, 2002) and the Baguio district, Philippines (Cooke and Bloom, 1990; Cooke et al., 2011).

An increasingly important facet of porphyry-related research has focussed on the spatial, temporal, structural and geochemical relationships between peripheral epithermal and skarn type deposits and central domains of porphyry-type mineralisation within a given district (e.g., Yerington, USA ,Dilles, 1987; Dilles and Einaudi, 1992; Dilles and Proffett, 1995; Butte, USA, Houston, 2001, 2014; Chile, Masterman et al., 2004, 2005; Collahuasi, Ireland, 2010) . The outcomes of this type of research have important exploration implications where epithermal deposits have been discovered but the porphyry mineralisation is yet to be revealed.

The past producing deposits of the Superior district are herein classified as epithermal rather than ‘mesothermal’ as they display textures and features consistent with epithermal deposits, as defined by White and Hedenquist (1995) as well as the many examples of other district-scale studies provided above. The term ‘mesothermal’ has historically been used to separate epithermal deposits of magmatic-hydrothermal origin from orogenic (formerly mesothermal) deposits of metamorphic origin.

### 1.1.2 Application of micro-analytical techniques to understanding porphyry districts

Recent advances in analytical techniques, such as laser-ablation-ICP-MS, now allow the detailed

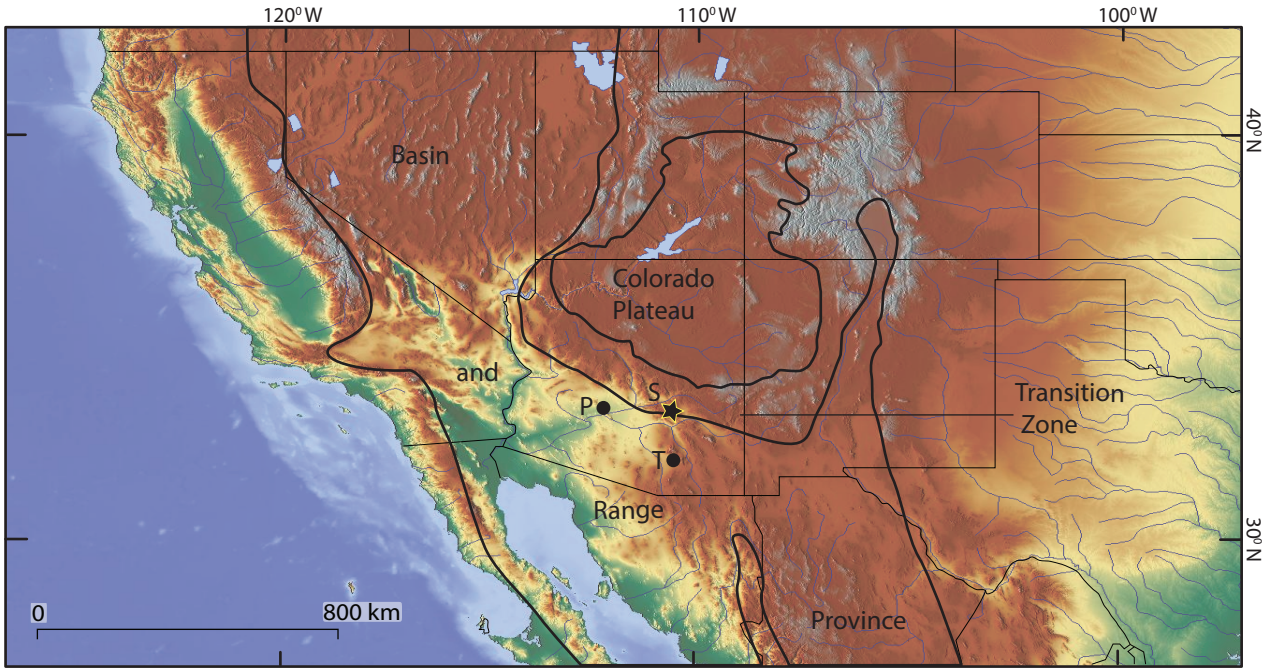


Figure 1.1 Location of the Superior district, on the edge of the Transition Zone between the Colorado Plateau and the highly extended Basin and Range Province. Abbreviations; S - Superior, P - Phoenix, T - Tucson.

chemical analysis of trace elements in alteration minerals. This has allowed the geochemical fingerprint of distal hydrothermal alteration to be detected at considerable distances from ore zones by analysing low-level trace element compositions of alteration minerals such as epidote and chlorite. This approach of niche sampling hydrothermal alteration features, rather than bulk sampling of rocks significantly increases the signal to noise and extends geochemical anomalies far beyond that of conventional whole-rock geochemistry (e.g., Wilkinson et al., 2015; Pacey, 2016). This can therefore facilitate vectoring and fertility assessment from a single, distal alteration domain (Cooke et al., 2014, 2017; Wilkinson et al., 2015, 2016). Within the broader geochemical halo defined by micro-analytical techniques, there is evidence for systematic changes in trace element concentrations (Cooke et al., 2014; Wilkinson et al., 2015, 2016). This suggests that processes controlling the relative mobility of trace elements show some consistency between multiple deposits and districts. Therefore the application of this techniques is not limited to select districts but could be applied worldwide. Application of targeted analysis of individual mineral phases from different parts of the same or multiple hydrothermal systems should provide insight into the relative position within a hydrothermal system and/or relationship of alteration features, whose origins and significance are unknown.

## 1.2 Aims and Objectives

This PhD thesis aims to provide a district-scale appraisal of the alteration and mineralisation features of the Superior district, Arizona, USA (Figure 1.1). The principal objective is to better characterise the far-field geochemical footprint of the buried giant Resolution porphyry Cu-Mo deposit but also to establish potential relationships between Resolution and the other deposits and mineralisation occurrences in the

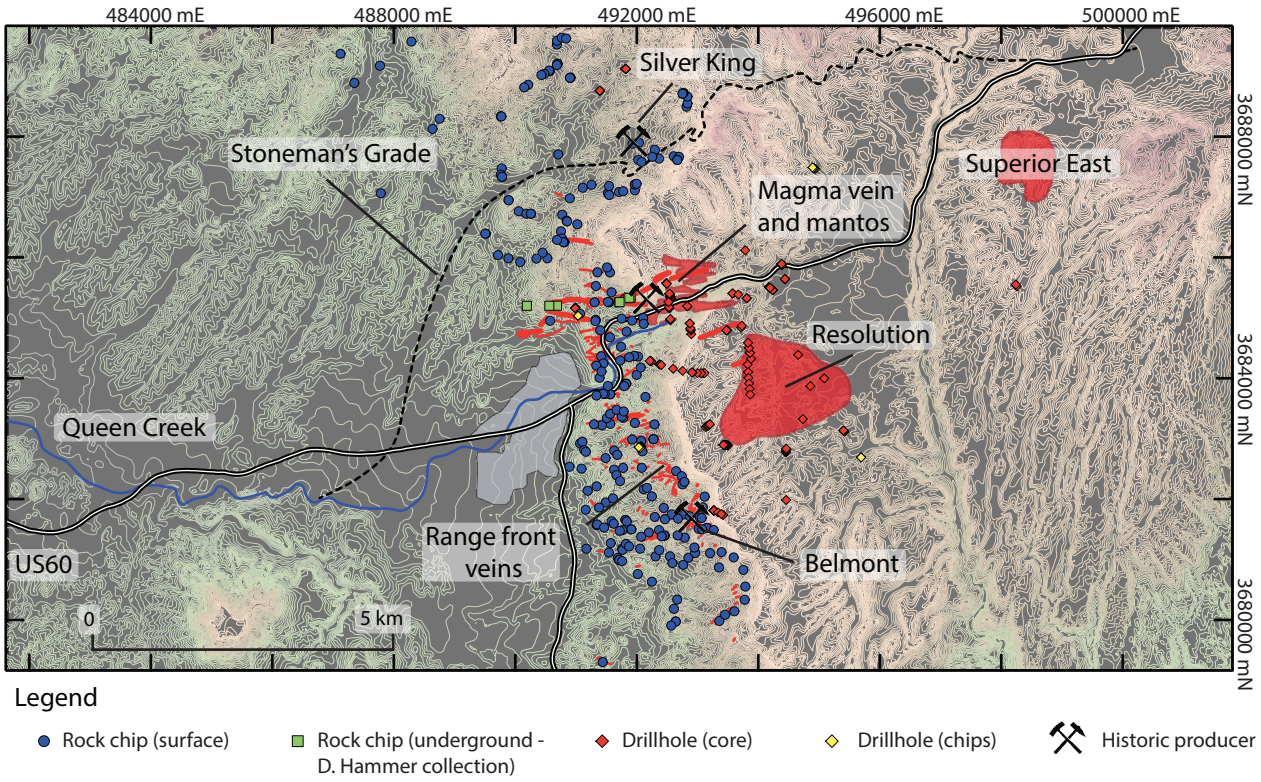


Figure 1.2 Sketch map of the Superior district showing the location of historic producers, undeveloped ore bodies, major infrastructure, topography and sample locations from the current study. Sample details provided in Appendix 1A.

district. This includes characterising and understanding the timing and significance of hydrothermal alteration features observable at surface throughout the district, and determining their origin. Therefore, the objectives of this study are to

1. Delineate and characterise the far field geochemical footprint of the Resolution porphyry Cu-Mo deposit and discriminant it from other hydrothermal events that have affected the Superior district

2. Characterise surficial hydrothermal alteration features in the Superior district and understand how the basement geology influenced mineralisation and alteration within the Superior district
3. Evaluate the temporal, chemical and genetic relationships between Laramide mineralisation types within the Superior district, particularly between the Resolution porphyry and Magma vein
4. Synthesise results into a set of exploration-focussed criteria that aid in the evaluation and screening of prospects and the discovery of large blind deposits in the region and elsewhere.


Figure 1.3 Photographs of different environments from around the Superior district. A. Prominent west-facing Apache Leap-escarpment at the head of the range front, dissected by steep east-west canyons. B. Steep rocky slopes of the range front with saguaro cacti. view looking northwest. C. Rolling grassy hills of the northern Superior district. View looking south, Picketpost Mountain in the far distance. D. Rugged Apache Leap plateau occupying the east of the district. View looking north, taken from above the Resolution ore body, Kings Crown Peak in the distance. E. View across the low-lying Tertiary basin to the west of the district. View looking west with Picketpost Mountain in the background.

## 1.3 Location and access

The Superior district is located in the Pinal County of Arizona, USA. It is situated approximately 70 km east of the capital city of Phoenix and 120 north of Tucson Figure 1.1) in the physiographic Transition Zone, between the highly extended domain of the Basin and Range province and the stable Colorado Plateau (Figure 1.1). Just 25 km northeast of Superior is Globe-Miami, servicing the porphyry Cu

district of the same name. Fifteen kilometres to the southeast of Resolution is the Ray mine, another giant porphyry-Cu deposit

Superior has a hot, semi-arid climate with temperatures ranging from 24 to 37°C in summer and 6 to 16°C in winter, and with an average annual rainfall of ~ 450 mm per year. The town of Superior has a land area of 5 $km^2$ and a population of 2837. The prominent north-trending Apache Leap escarpment dominates the landscape (Figure 1.2) and is the northern most part of the Dripping Springs Mountains. The Apache Leap escarpment is dissected and deeply incised by the ephemeral Queen Creek, which flows westwards into the Phoenix basin (Figure 1.2).

Landscape varies somewhat across the district. Along the west-facing range front, slopes are steep and rocky with the Apache Leap escarpment dominating the skyline (Figure 1.3 A-B). Vegetation can be limited on the exposed ridges, but becomes denser in the canyons. Mesquite, Agave and Saguaro, Barrel and Cholla cacti are the dominant species. Saguaro and Barrel cacti are present at lower elevations. In the north of the district, rolling grassy hills dominate (Figure 1.3C). The east of the district is dominated by the Apache Leap plateau, a rugged environment with difficult access except along ephemeral creeks (Figure 1.3D). In contrast, the west of the district is covered by low-lying gravel deposits. A Tertiary volcanic flow-dome complex, Picketpost Mountain, dominates the western skyline (Figure 1.3E).

## 1.4 Exploration history of the Superior district

The Superior district has a particularly colourful exploration history, beginning in the time of settlement of the American southwest by Europeans, who were engaged in bitter conflict with the indigenous Apache. The following review is summarised from Blake (1883), Hammer (2001) and Paul and Manske (2005).

Exploration began following the accidental discovery of native silver nuggets by a soldier, Sullivan, who was engaged in building the Stoneman's Grade road up to the Apache Leap Plateau in 1873 to enable retaliation to Apache raids. Some years later, after discharge from service, Sullivan worked on a ranch near the Salt River before suddenly disappearing, presumed killed by Apache in an attempt to relocate the outcropping silver ore. The rancher, Charles Mason, whom Sullivan had confided the discovery of the nuggets but not the actual location, lead numerous prospecting parties into the Pinal Mountains east of the Gila and Salt River Plains over a number of years. In 1874 claims were pegged over the Globe Mine and the Silver Queen (later Magma). In 1875, Mason and four others took a mule train to the Globe district to extract ore. On their way back, in March 1875, they were ambushed by Apache and one of their party was killed. After burying their comrade at the summit of Stoneman's Grade, they made camp at the base of the trail. One of the survivors was then sent out to inspect a prominent outcrop and return some of the material to the camp. The prospector came hurrying back into camp shouting with great excitement and passing around the long sought silver ore. The men were in no condition to remain and explore the area, instead making out across the desert that night for the town of Florence

to gather supplies, before hastily returning to their discovery the following day. On the 22nd of March 1875, standing on the highest point of the blue and green stained outcrop, the location they named Silver King, the first named location within the new 'Pioneer district'. Although the four survivors initially split ownership of the mine equally, through a series of transactions only one of the discovery party retained 50% ownership by January 1877. In May that year, the Silver King Mining Company was incorporated under the laws of California. It soon became the most successful and important silver mine in the United States. In 1881 an elderly man came to the now thriving town of Picketpost, close to the mine, taking great interest in the mill and processing of the ore. Eventually, he announced himself as Sullivan to the manager of the mine and humbly asked for work. Although very few of his acquaintances survived, he was positively identified and was taken into the employment of the company that day. Though long considered dead, he had left Mason's ranch, travelling across the deserts of NW Arizona and across the Colorado River to seek work in California, working as a farm hand. He had one day hoped to obtain sufficient means to return to Arizona a secure the benefits of his discovery. When he heard of the discovery of a rich silver deposit by Mason, he was convinced he had lost his opportunity to make the discovery for himself, but could not resist the desire to see the opening of the mine for himself. The first mining lease was granted over the Silver Queen claim in March 1875 and the first shaft sunk by 1882, to a depth of 400 ft. In 1893 the mine closed due to falling silver prices and little work was conducted again until 1910. The nearby Lake Superior and Arizona mine (formerly the Golden Eagle mine) was worked for a small amount of gold, and some oxidised copper ore was stoped. In 1910, the Silver Queen Mine was acquired by William Boyce Thompson and George Gunn who established the Magma Copper Company. Shortly afterwards, Thompson retired from the New York Stock exchange and founded Newmont Mining in 1916, which assumed control of most of his mining interests, including 23 % of the Magma Copper Company. The deepening of the Queen shaft to 800 ft in 1910-1915, demonstrated that the poddy, discontinuous, chalcocite mineralisation encountered at higher levels became more continuous at depth, prompting a major program of shaft sinking and development. By 1924, Superior had rail links with Florence and its own smelter. In 1943, following recommendations from Dr J. Gustafson, drilling was underway in search of the offset portion of the vein, the other side of the NS-5W fault. Instead of locating the Magma vein, the East Replacement vein and manto-type massive sulfides near the base of the Martin formation, later called A-bed, were found. High temperatures, wall instability and old hoist and ventilation equipment encouraged a shift in production focus to these new manto-type ores in 1953 and by 1966, the Magma vein had been abandoned, despite the continuity of high grades (~4% Cu).

In 1959, while developing the lower Martin replacement orebody (A-bed), a drive penetrated a previously unknown, major east striking fault, filled with weakly mineralised rock flour and dacite porphyry. This fault separated the familiar stratigraphy of the Magma mine to the north from a previously unknown, uncorrelated body of brecciated rocks that became known as 'the breccia'. Striking and underground fires

forced the closure of the mine in 1959-1960 and 1960-1961 respectively, but limited drilling and drive development was conducted in 1964 to further test the breccia block, even though no ore was found. Further drilling in 1965 aimed to fully delineate the north boundary of the breccia block. This program discovered another thin but high grade manto deposit in the upper Martin Formation (later B-bed). Encouraged by this discovery, further drilling rapidly discovered the remaining replacement deposits in the base and top of the Mississippian (C- and D-beds respectively) and in the Pennsylvanian (E-bed). These major discoveries, along with the observation that the mantos appear to have been fed by the through-going North Boundary and East Replacement Veins, led to more drilling of 'the breccia'. By 1966, the north and part of the west boundaries of 'the breccia' had been tested. The results of this drilling lead to the understanding of the breccia body occupied a down-dropped graben, probably bounded to the east by the Devils Canyon Fault and to the south by the Belmont vein. The graben was filled with volcano-sedimentary material of unknown thickness, but of strikingly similar appearance to Cretaceous rocks exposed close to the Christmas mine. In 1967 D. Hammer submitted a report outlining possible modes of formation along with exploration targets including, vein deposits along boundary faults, Palaeozoic-hosted replacement deposits preserved below the breccia and large masses of low grade disseminated material within the breccia. Ground holdings were expanded, though ground east of the Devils Canyon was considered too far by Magma management. In 1968, the Magma mine commenced a significant modernisation and expansion program, underwritten by the new 10 Mt manto discoveries. Shortly afterwards in 1969, Magma became a wholly-owned subsidiary of Newmont Mining Corporation. The following year, ASARCO acquired the ground east of Devils Canyon and discovered the 900 Mt Superior East deposit by drilling through 980m of Tertiary cover.

Towards the end of the modernisation program in 1971, a drill hole collared from a newly excavated hoisting station at the Number 9 shaft intersected an ore-grade vein (First South) in the interior of the breccia. This was quickly followed by the discovery of a second vein, (Second South), highlighting mineralisation potential within the breccia. A concurrent review of the exposed Belmont vein system led to recommendations by Don Hammer to pursue similar vein and manto targets to those discovered in the Magma mine, east of the outcropping Belmont veins, under the Apache Leap Plateau. Drilling on these recommendations took place between 1974 and 1981, but neither the Mesozoic rocks, the South Boundary fault nor the new replacement deposits were located. In 1982, low copper prices once again forced the closure of the Magma mine and in 1986 the pumps were stopped and the mine was flooded. In 1987 Newmont merged all of its Arizona assets with the Magma Copper Company and distributed its equity to its shareholders, rendering Magma a standalone company with new management.

In 1991, a renewed effort was made to locate the South Boundary fault, and with it massive sulfide replacement ores, which were still considered the most likely and profitable remaining ores in the Superior district. The first of these holes was completed in 1992 and although unsuccessful in its endeavour,

did intersect sericite-pyrite altered Cretaceous rocks with minor chalcocite and supergene oxides. Importantly, this was recognised by Magma geologists Alex Paul and Scott Mankse as an indication of proximity to porphyry style mineralisation. Between 1994 and 1996, nine low angle holes were drilled from the most southerly underground workings in the mine to test the continuity of alteration. Three of these holes intersected mineralisation sufficient to constitute the discovery of the Magma porphyry, over a century after the first discovery of native silver nuggets by Sullivan. In 1996 BHP bought and closed the Magma mine. In 2001 Rio Tinto negotiated an earn-in agreement with BHP, renaming the deposit Resolution and forming the Resolution Copper Company joint venture of which it currently owns 55%. The current global resource stands at 1.79 Gt @ 1.45 % Cu, and 0.035 % Mo (Rio Tinto 2017). Resource definition remains ongoing.

## 1.5 Previous research in the Superior district

As for exploration, geological research has a long history in the Superior District. It has been conducted largely with an economic focus, most commonly in the form of internal company reports. Blake (1883) was the first and only author to record the geology of the then operating Silver King Mine, while Ettlinger constructed the first geologic map of the Magma mine in 1912, which remained unpublished until inclusion in the first published account of the Magma Mine by Ransome (1914) and later by others (Short and Ettlinger, 1926; Short and Wilson 1938). The first published account of the geology of the wider Superior district was provided by Short et al. (1943), with sub-areas such as Silver King, Belmont-Queen Creek and Potts Canyon studied as PhD or MSc projects by Galbraith (1935) and Puckett (1970), Harshman (1939), and Wardwell (1941) respectively. The early descriptions provided by Short et al. (1943), are invaluable and have been used in this study to correlate observations made at Superior with regional mapping results (Globe, Ransome, 1903; Bisbee, Ransome, 1904; Superior, Ransome, 1914; Ray and Miami, Ransome, 1919). Valuable mapping and paragenetic work was completed by Gustafson (1961) allowing an updated appraisal of the geology of the Superior district and genesis of the Magma vein to be provided by Peterson (1962) and Hammer and Peterson (1968) respectively. Over the next two decades, significant contributions to the understanding of the Resolution graben were principally made by Don Hammer, mostly as internal reports to the Magma Copper Company. At the same time, key studies regarding the overall geologic evolution of SE Arizona and the wider southwestern United States were also being published (e.g., Shride, 1967; Titley, 1982; Dickinson, 1989). Although these did not directly study the rocks of the Superior district, the observations and interpretations presented in these studies were key to understanding the geology of Superior in a regional context. This important era in SW USA geological research helped define and understand the major periods in the evolution of the region, including Paleoproterozoic accretionary evolution (DePaolo, 1981; Condie, 1982; Condie and De Malas 1985; Copeland and Condie 1986; Bennet and DePaolo, 1987; Karlstrom and Bowring 1988), Mesoproterozoic sedimentation (Shride, 1967), and mafic magmatism (Wrucke, 1966; Hammond,

1983, 1986, 1990), Laramide orogenesis and mineralisation (Lowell and Guilbert, 1970; Dickinson and Snyder, 1978; Davis, 1979; Drewes, 1981; Heidrick and Titley 1982), and Tertiary extension and volcanism (Stewart, 1971; Crittenden et al., 1980; Frost and Martin, 1982). Though many of these studies have been superceded by later publications that have benefitted from more data and improved analytical techniques, the early studies laid the groundwork for understanding this complicated package of rocks.

A masters thesis documenting the First and Second South Veins was completed by Schott (1994) It provides some of the first descriptions of the sedimentary rocks in the lower part of the Cretaceous sequence. A description and exploration history of the Superior East deposit was provided by Sell (1995). Friehauf (1998) completed a thesis documenting aspects of the C Bed manto ore body, while Pareja (1998) documented the auriferous jasperoids of the Lake Superior and Arizona mine, considered to be the distal manifestations of manto-style mineralisation at surface. They also published papers together on the stable isotope systematics of the manto deposits of the Magma mine (Friehauf and Pareja, 1998). Since 2000, there has been a series of theses and publications regarding various aspects of the Resolution porphyry and Magma epithermal systems. Troutman (2001) documented the advanced argillic alteration present above the porphyry deposit. Mankse and Paul (2002) published the first fundamental account of the Resolution porphyry system, which was updated by Ballantyne et al. (2003). Harrison (2007) completed a masters thesis regarding the evolution of alteration and mineralisation within the Resolution porphyry system. This was followed by a fundamental review of the facies and geochronology of the Cretaceous volcano-sedimentary rocks from with the Resolution graben (Zulliger, 2007). Four masters theses documented the early dolerite-hosted potassic alteration, later phyllic and advanced argillic assemblages, and Paleozoic-hosted skarn mineralisation respectively (Schwarz, 2010; Winant, 2010; Troutman, 2001, McCarrel, 2012). The most recent geological update of the Resolution system was published by Hehnke et al. (2012). Recently characterisation of the magmatic-hydrothermal, phreato-magmatic and tectonic hydrothermal breccias within the Resolution porphyry system was provided by Keyahov et al. (2015). A brief review the Superior East deposit was completed by Sillitoe (2013).

## 1.6 Methods

This PhD study included two field seasons, totalling 13 weeks (April – May 2015; March – May 2016). Fieldwork initially focussed on graphic logging of selected intervals of drill core from the periphery of the Resolution deposit to aid in familiarisation. This was followed by district scale outcrop and core sampling from Resolution, Magma and Silver King. The principle objective of the field work was to collect sufficient and appropriate samples for the diverse array of geochemical techniques that were planned as part of this study. This included a representative suite of least-altered rocks for whole-rock geochemistry and a representative suite of altered and mineralised rocks from the district as well as a suite of altered samples from the range front (Figure 1.2).

Extensive laboratory work has been conducted in order to characterise the mineralisation and alteration styles present in the Superior district. Textural analysis of ground and polished rock slabs was conducted alongside acid etching and staining for potassium feldspar at CODES, University of Tasmania. A subset of samples were analysed with SWIR spectroscopy to aid in mineral identification, both on site at the Resolution Copper core processing facility, and at CODES.

A field split of each sample was submitted for whole-rock geochemical analysis at ALS in Perth, Australia, by Rio Tinto Exploration. In 2015, all samples other than those destined for propylitic mineral chemistry by LA-ICP-MS were submitted for four acid digest, ICP-MS (ME-MS61; ALS fees and services schedule, 2015), while the samples destined for mineral chemistry were analysed using a complete characterisation package (CCP-PKG), including major elements by XRF, trace elements by ICP-MS, and total carbon and sulfur by Leco furnace. In 2016, all elements were analysed using the complete characterisation method.

Geochronological studies were undertaken to constrain the hydrothermal alteration history of the Superior district. Uranium-lead dating of apatite and epidote was conducted by laser-ablation inductively coupled plasma mass spectrometry (LA-ICP-MS) at CODES, University of Tasmania, with a limited number of epidote duplicates sent to Dr Roland Maas at the University of Melbourne for isotope dilution multi collector ICP-MS (ID-MC-ICP-MS). Samples for Ar-Ar were submitted to Prof. Anthony Koppers at Oregon State University.

Trace element and radiogenic isotope analysis of epidote and chlorite were completed using LA-ICP-MS with the assistance of Mr Jay Thompson, Mr Paul Olin and Dr Sebastien Meffre at CODES. Multivariate statistical treatment and classification of mineral chemistry data was completed in collaboration with Dr Matt Cracknell at CODES. Stable isotope (S, C and O) analyses were performed at the Central Science Laboratory (CSL), University of Tasmania, by Christine Cook (S) and Dr Christian Dietz (C-O).

## 1.7 Thesis organisation

This thesis comprises ten chapters, organised as follows:

**Chapter 2** - Regional geology and metallogeny provides a review and synthesis of the regional geologic evolution of the Southwest United States porphyry-Cu province through time. This review provides a basis for much of the discussion presented in following chapters

**Chapter 3** - District geology, geochronology and structural architecture provides a brief review the geology of the Superior district, including observations from the author's own field work. It summarises the lithological findings and previous geochronology studies and relates observations made in the Superior district to more regional interpretations of the regional stratigraphic sequences, fault architecture and timing of Laramide igneous activity.

**Chapter 4** - Proterozoic igneous geochemistry presents new whole-rock geochemical data for the Mesoproterozoic Apache Group basalts and dolerite sills. These results are compared to results from previous studies and are evaluated in terms of tectonic setting and provide constraints on likely emplacement processes, and implications for Proterozoic PGE mineralisation in the district.

**Chapter 5** - Hydrothermal geochronology presents new U-Pb LA-ICP-MS data from hydrothermal apatite and titanite from in the Superior district. It presents a newly devised LA-ICP-MS method developed during the current study that allows routine U-Pb dating of epidote and applies it to provide district-wide temporal constraints on the timing of epidote crystallisation. Radiogenic Ar-Ar data collected from white mica from two Laramide ore systems as well as one potassium feldspar from altered basalts in the range front are also presented and interrogated in this chapter.

**Chapter 6** - Proterozoic alteration geochemistry describes the alteration facies and textures of altered Proterozoic mafic igneous rocks, and assesses their alteration geochemistry using an array of lithogeochemical techniques. Mass balance calculations are also used to assess metal mobility within these alteration assemblages.

**Chapter 7** - Laramide alteration and mineralisation documents the variety of Laramide aged alteration and mineralisation styles in the Superior district, based on reviews from previous workers and observations made during the author's field work. This chapter investigates the genetic relationships between the various systems and sets the scene for analysis of distal alteration minerals and geochemical methods in Chapter 8.

**Chapter 8** - Propylitic mineral chemistry presents over 1700 new LA-ICP-MS analyses from epidote and chlorite from around the Superior district and presents a multivariate classification workflow to discriminant epidote and chlorite related to the Resolution porphyry deposit. The trace element chemistry of these samples is then interrogated further to characterise the Resolution geochemical footprint in more detail.

**Chapter 9** - Stable and radiogenic isotopes presents and discusses C and O isotope data generated from epithermal veins exposed in the range front in order to constrain fluid sources and depositional processes. Sulfur and Pb isotope analyses from paragenetically constrained sulfide phases, and Pb isotopic analyses of epidote from Resolution, Magma and around Silver King are also presented in order to evaluate their genetic relationships and exploration signatures.

**Chapter 10** - Conclusions; presents a synthesis and major results of the thesis and discusses their implications for exploration for porphyry Cu deposits in the Southwest US. It concludes with recommendations for further research.

# Chapter 2: Regional Geologic Setting of Southwestern North America

## 2.1 Introduction

At its full extent, the southwestern North America porphyry copper province stretches from southeastern-most Utah to Sonora and the Sinaloa and Chihuahua border region of northwestern Mexico. It is centred on southeast Arizona. This area, located at the southwestern edge of the North American continental block, is underlain by a complex zone impacted by Proterozoic accretion and crustal suturing. The basement geology has been argued by some (e.g., Heidrick and Titley, 1982; Titley, 1982; Krantz, 1989; Bowring and Karlstrom, 1990; Sillitoe et al., 2014) to have profoundly influenced the Laramide belt of porphyry copper deposits, especially in light of the recent recognition of porphyry Cu-Mo mineralisation of Proterozoic age (Sillitoe et al., 2014). Various authors (e.g., Karlstrom and Bowring, 1988; Bowring and Karlstrom, 1990, Wooden and Miller, 1990; Eisele and Isachsen, 2001; Magnani et al., 2004; Whitmeyer and Karlstrom, 2007; Amato et al., 2008; Holland et al., 2015) have attempted to rationalise and constrain spatial and temporal aspects of the Proterozoic tectonics and metallogeny in this region. This chapter provides a brief review of the key aspects of the geologic evolution of the southwestern North America porphyry copper province in order to provide context for the geological, geochemical and geochronological results for the Superior district that are presented in subsequent chapters.

## 2.2 Proterozoic crustal architecture of Arizona

The Proterozoic orogenic belt that underlays south-western North America is fundamentally different from most Proterozoic orogens that surround Archean cratons in North America. Although largely undercover, the belt is large, stretching 1,300 km from the Cheyenne Belt in southern Wyoming to Sonora, Mexico (e.g., Karlstrom and Bowring 1988, Figure 2.1). Condie (1982; 1986) and Anderson (1986) proposed that North America grew southward through the progressive accretion of continental arc and continental margin basin rocks. Karlstrom and Bowring (1988) contradicted this model, showing instead that a series of juvenile terranes had been accreted from a south-easterly direction throughout the Proterozoic (Figure 2.1). This significant accretion event is thought to have occurred relatively rapidly

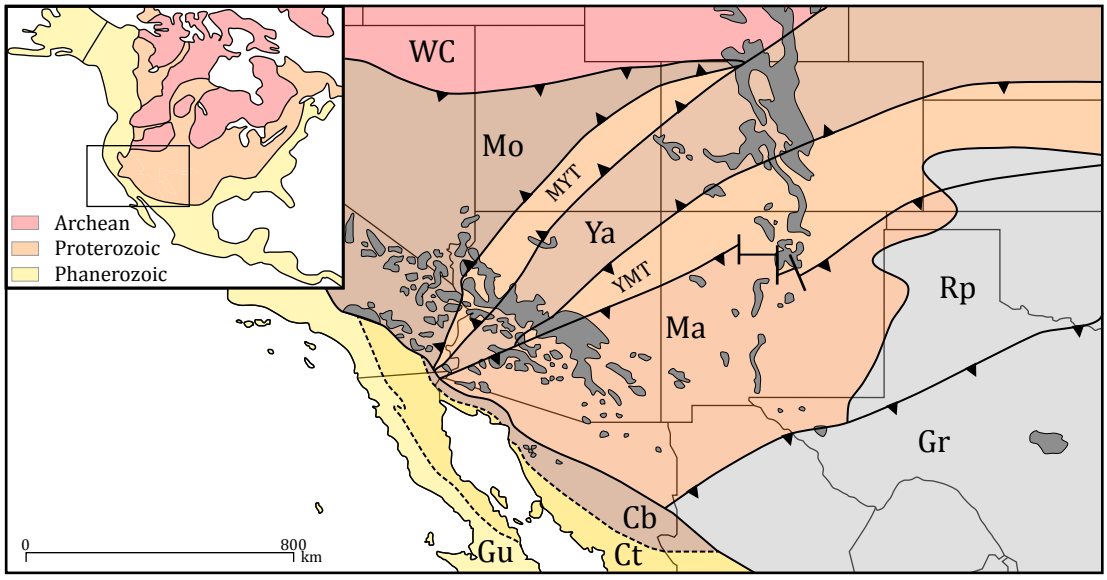


Figure 2.1 Basement provinces of southwestern North America, and the wider North American continent (inset). WC - Wyoming Craton; Mo – Mojave; MYT – Mojave-Yavapai Transition; Ya – Yavapai; YMT – Yavapai-Mazatzal Transition; Ma – Mazatzal; Rp – Rhyolite Province; Gr – Grenville Orogen; Cb – Caborca Block; Ct – Cortez Block; Gu – Guerrero Terrane. Compiled from Karlstrom et al. (2004); Amato et al. (2009); Amato et al. (2008); Holland et al. (2015).

(1,700 – 1,630 Ma; Karlstrom and Bowring 1988; Bowring and Karlstrom, 1990 Eisele and Isachsen, 2001; Magnani et al., 2004; Holland et al., 2015).

The Proterozoic crust in south-western North America area includes a number of major provinces (Figure 2.1) that in turn consist of discrete tectonic blocks. The Mojave Province is the oldest and northwestern-most of these, with the Yavapai and Mazatzal provinces located to the southeast. These are bound to the southwest to the Mojave derived-Caborca and Cortez terranes (Farmer et al. 2005; Stewart et al. 1990) and to the southwest by the Grenvillian orogenic belt (Figure 2.1). The Mojave, Yavapai and Mazatzal crustal provinces are interpreted to have been assembled during two main periods of convergent tectonism, the 1,780 – 1,680 Ma Yavapai and 1,650 – 1,630 Ma Mazatzal orogenies (Eisele and Isachsen, 2001; Whitmeyer and Karlstrom, 2007; Table 2.1).

### 2.2.1 Mojave Province

The Mojave Province is characterized by upper amphibolite to granulite facies Paleoproterozoic (1,780 – 1,350 Ma) gneisses (Karlstrom and Bowring, 1988; Bowring and Karlstrom 1990; Magnani et al., 2004). The gneisses preserve evolved radiogenic isotopic signatures reflecting an Archean crustal component (Holland et al., 2015). No Archean rocks have been found, and hence the origin and significance of this Archean component remains unclear. The oldest dated crustal rocks are granitoids that range from 1,780 Ma (Barth et al., 2000) to 1,760 Ma (Wooden and Miller, 1990; Duebendorfer et al., 2001). Some zircons in metasedimentary gneisses are as old as 2,600 – 2,830 Ma (Wooden et al., 1994; Duebendorfer et al., 2006), providing evidence for Archean source rocks.

Although originally interpreted as part of the Yavapai arc system by Karlstrom and Bowring (1988), it seems more likely that the Mojave Province represents a distinct microplate (e.g., Whitmeyer and Karlstrom, 2007). The nature of the boundary between the Mojave and Yavapai crustal provinces remains uncertain. It is interpreted as a 75-km-wide mixed Mojave-Yavapai Transition zone (MYT; Magnani et al., 2004; Amato et al., 2008; Holland et al., 2015; Figure 2.2) bound to the east and west by the west block-up Crystal Shear Zone (Ilg et al., 1996) and Gneiss Canyon Shear Zone, respectively (Holland et al, 2015). The MYT, originally described as the Hualapai-Bagdad block by Karlstrom and Bowring (1988), is composed of interleaved bimodal volcanics (ca. 1,709 Ma) that was intruded locally by 1,720 – 1,696 Ma granites and deformed from 1,706 to 1,696 Ma (Karlstrom and Bowring, 1988). The favoured interpretation of this transitional zone is of tectonic mixing of Mojave and Yavapai provinces (Whitmeyer and Karlstrom, 2007). Most of the Mojave province is interpreted to have been an Archean fragment, with the 1,840 Ma Elves chasm arc and later 1,800-1,700 Ma arcs (e.g., 1,780 – 1,760 Ma Transverse Ranges) accreted to it prior to the main Yavapai orogenic peak at approximately 1,680 Ma (Whitmeyer and Karlstrom, 2007; Figure 2.3; Table 2.1)

The Crystal Shear Zone marks a sharp surface boundary between the Mojave and Yavapai crustal provinces (Figure 2.2; Holland et al., 2015). However, the ultimate geometry of the transition is interpreted to reflect a ~200-km-wide middle-crustal duplex system in which the 1,750 Ma Vishnu Schist was deposited across both Mojave and Yavapai crust and later imbricated in an accretionary complex (Figure 2.2; Holland et al., 2015).

### 2.2.2 Yavapai Province

The Yavapai province is made up of a series of tectonic blocks. It is thought to be the product of the accretion of dominantly juvenile arc crust (Karlstrom and Bowring, 1988; Eisele and Isachsen, 2001), forming from 1,800 to 1,700 Ma, including probable out-board development and collisions of arcs from 1,780 to 1,720 Ma (Figure 2.3). An orogenic peak ca. 1,720 –1,680 Ma resulted in a progressive amalgamation of Yavapai crust to the Mojave province (Eisele and Isachsen, 2001; Magnani, et al., 2004, Whitmeyer and Karlstrom, 2007). The oldest rocks include 1,800 – 1,750 Ma granite-greenstone associations consisting of metavolcanic and associated metasedimentary rock that have been intruded by calc-alkaline plutons (Karlstrom and Bowring 1988). Although some evidence of older components exists (e.g., Bennett and DePaolo, 1987; Wooden et al., 1987; Selverstone et al., 2000; Hill and Bickford, 2001), the amount of Archean and pre–1,800 Ma Paleoproterozoic material incorporated into the Yavapai province is interpreted to be small (Whitmeyer and Karlstrom, 2007). This is supported by Nd isotopes from New Mexico that indicate differentiation from a depleted mantle source ca. 1,800 Ma (DePaolo, 1981), and also by Pb isotope studies that also indicate a juvenile origin (Aleinikoff et al., 1993). Arc rocks of the Yavapai province include the 1,760 – 1,730 Ma Ash Creek Block consisting of ca. 1,760 Ma basement and supracrustal sequence of intermediate volcanics that host a Precambrian VHMS

camp at Jerome (Karlstrom and Bowring, 1988; Lindberg, 1989). The basement has been intruded by the ca. 1,730 Ma Payson ophiolite (Dann, 1997). The entire sequence was cut by the 1,740 – 1,720 Ma Cherry batholith (Karlstrom and Bowring, 1988). The Green Gulch Block is also composed of series of supracrustal rocks (the Green Gulch volcanics) intruded by a ca. 1,740 Ma granodiorite (Karlstrom and Bowring, 1988). Conversely, the Big Bug Block is composed of ca. 1,750 Ma bimodal volcanics intruded by 1,750-1,735 Ma granodiorites that were in turn intruded by the syn-deformational Crazy Basin quartz monzonite (ca. 1,700 Ma). The lack of known basement and younger dates could imply that the Big Bug Block formed as part of a back-arc system to the Ash Creek Block during part of the Yavapai orogeny (Karlstrom and Bowring 1988; Bowring and Karlstrom, 1990). However, the original distribution, geometry and orientation of juvenile arcs and hence subduction polarity of the juvenile Paleoproterozoic arcs, remain poorly understood. This is due largely to intense northwest shortening near the end of the 1,680 Ma Yavapai orogenic peak (Whitmeyer and Karlstrom, 2007).

There was extensive deformation between 1,780 and 1,680 Ga within the Yavapai province (Karlstrom and Bowring, 1988; Table 2.1) The volcanic and granitoid batholith ages range from 1,800 to 1,750 Ma and are interpreted to record juvenile arc development and outboard collisions to form the 1,800 –1,750 Ma arcs (Whitmeyer and Karlstrom, 2007). The major period of accretionary welding of Yavapai arc terranes to North America is interpreted to have been a progressive deformation from ca. 1,710 to 1,680 Ga; defined as the Yavapai Orogenic Peak (Whitmeyer and Karlstrom, 2007)

### 2.2.3 Mazatzal Province

The Mazatzal province comprises ca. 1,680 – 1,600 Ma crust that is interpreted to have formed in continental volcanic arcs with associated back- arc related supracrustal successions and consists of at least four tectonic blocks (Karlstrom and Bowring, 1988; Bowring and Karlstrom, 1990; Eisele and Isachsen, 2001; Amato et al., 2008). The oldest rocks in the Mazatzal province are 1,680 – 1,650 Ma volcanogenic greenstone successions that are considered to have an oceanic origin (Karlstrom et al., 2004). The Mazatzal orogeny was a protracted period of deformation ca. 1,650 to 1,600 Ma that affected the 1,670 – 1,600 Ma rocks of the Mazatzal province and propagated northward into the previously assembled Yavapai basement, in a similar way to that envisioned during the Yavapai orogeny. The suture zone bounding the Mazatzal and the Yavapai provinces has been proposed along the Jemez lineament (Holbrook Line of Titley, 1982) in northern New Mexico (Figure 2.2; Magnani et al., 2004). Deep seismic reflection show oppositely dipping zones in the deep crust, converging in the region of the Jemez lineament, interpreted as a bivergent orogen and inter-wedging of crustal blocks (Magnani et al., 2004; Whitmeyer and Karlstrom, 2007). This Yavapai-Mazatzal Transition zone widens to the NE (Figure 2.1), resulting in a transition zone similar to that between Mojave and Yavapai provinces and may support the apparent diachroneity in timing of deformation in Arizona and New Mexico.

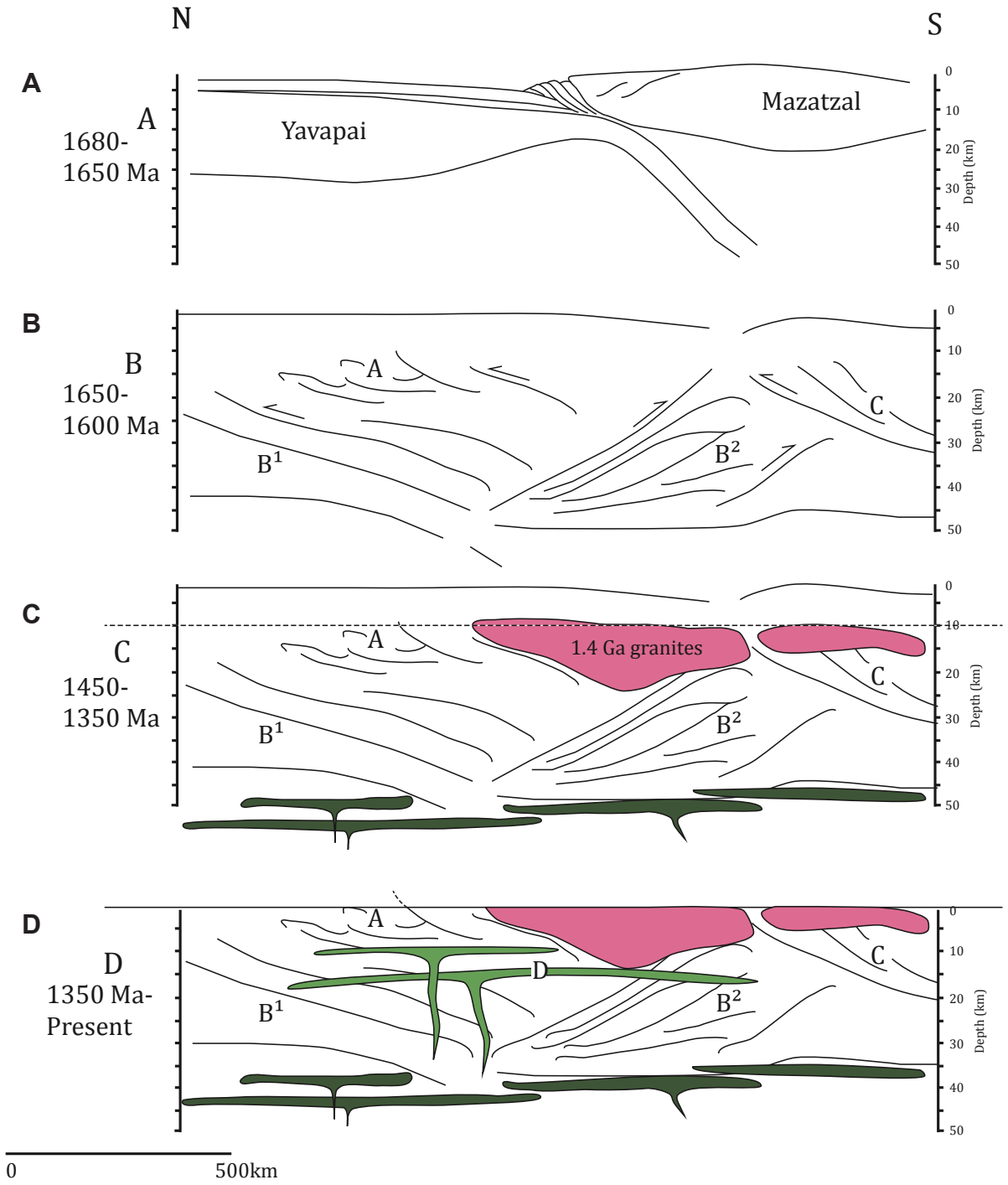


Figure 2.2 Interpreted tectonic evolution of the YMT zone based on depth-migrated CD-ROM seismic profile. (A) 1.70 Ga, Subduction of Yavapai crust generates the Mazatzal arc with sediments deposited over Yavapai basement. (B) 1.68–1.65 Ga, Mazatzal arc collides with the Yavapai margin, and as deformation progresses, bivergent structures nucleate. (C) 1.4 Ga, regional anorogenic magmatic event, producing 10 km of uplift, subsequent denudation and the emplacement of granitic and basaltic magma. (D) 1.1 Ga Mafic sills intrude the cratonic lithosphere, possibly exploiting the presence of the pre-existent Proterozoic suture. Reflectors: A – Proterozoic supracrustal rocks; B1 and B2 – bivergent Paleoproterozoic suture zone with opposing dips; C – Manzano thrust belt; D – Proterozoic mafic sills (modified after Magnani et al., 2004).

#### 2.2.3.1 Mazatzal Block/YMT

The Yavapai-Mazatzal Transition (Mazatzal block of Karlstrom and Bowring, 1988) has a relatively well constrained stratigraphy (Cox et al., 2002). The supracrustal rocks progress up section from Yavapai-aged

ophiolitic basement of the Payson ophiolite and East Verde River Turbidites, to the Mazatzal-aged mixed metavolcanic and metasedimentary rocks of the Alder Group (locally hosting small VHMS deposits), representing arc-related marine sedimentation (Karlstrom and Bowring, 1988; Dann, 1997;). Overlying this are rhyolites of the Red Rock group, representing caldera-style volcanism (Cox et al., 2002), and the Mazatzal Group quartzite. The passive margin sediments temporally overlapped with caldera style volcanism (Karlstrom and Bowring, 1988; Cox et al., 2002). Although the basal contact of the Mazatzal supracrustal rocks is not exposed, the ca. 1,738 Ma Gibson Creek batholith has been suggested to be Mazatzal basement (Karlsrom and Bowring 1988). The southern boundary of the Yavapai-Mazatzal Transition Zone, the sub-vertical Slate Creek shear zone is a several kilometre wide zone of tectonic mélange (Figure 2.2; Karlstrom and Bowring, 1988; Karlstrom et al., 2004).

#### 2.2.3.2 Sunflower Block

The Sunflower block is separated from the Yavapai-Mazatzal Transition Zone by the Slate Creek Shear Zone. It possesses a supracrustal package of rhyolites and arenites of uncertain age, but compositionally similar to those of the Red Rock and Mazatzal Groups of the Yavapai-Mazatzal Transition Zone (Karlstrom and Bowring, 1988). The rocks of the Sunflower group have significantly higher metamorphic grades than those of the adjacent Mazatzal block possibly due to the emplacement of a suite of 1,640 – 1,630 Ma granites south of the Slate Creek Shear Zone (Karlstrom and Bowring, 1988).

#### 2.2.3.3 Pinal Block

The boundary between the Sunflower and Pinal Blocks is obscured by ca 1,400 Ma granites, making the relationship of the two blocks ambiguous. The Pinal block has lower grade metapelitic rocks when compared to the high grade metamorphic rocks of the Sunflower block (Eisele and Isachsen, 2001). Formerly termed the Pinal Schist by Ransome (1903), the Pinal block includes not only the Pinal Schist but also widespread exposures of gneissic granitoids, meta-graywacke, quartzite, conglomerates, metavolcanics, cherts and carbonates (Eisele and Isachsen, 2001; Meijer, 2014). Early attempts at providing a geodynamic synthesis of the Pinal block were hindered because of the widely dispersed nature of the outcrops. Early workers (Condie and De Malas, 1985; Copeland and Condie, 1986) attempted assemblage-based subdivision of the Pinal block. There were named the Dos Cabezas and Pinal domains by Condie (1992). However, as Karlstrom and Bowring (1988) highlight, their boundary is oriented perpendicular to the regional foliation, fold axes and faults, suggesting that the subdivision of the Dos Cabezas and Pinal domains may represent something more akin to a facies change. The Pinal block has recently been reinterpreted in the context of a forearc subduction complex or accretionary prism, sourcing young continental arc material from the north (e.g., Eisele and Isachsen, 2001; Swift and Force, 2001; Meijer, 2014). If true, this requires a NW-dipping subduction zone between the Pinal and Cochise blocks.

#### 2.2.3.4 Cochise block

In southern Arizona, Eisele and Isachsen (2001) identified an accretionary boundary separating the 1,680 – 1,650 Ma rocks of the Pinal block from the 1,647 – 1,630 Ma rocks of the Cochise block. The latter is interpreted to be a juvenile volcano-sedimentary fault-bounded, allochthonous tectonic unit abutting the Pinal block to the south east (Eisele and Isachsen, 2001; Swift and Force, 2001). The suture between the Cochise and Pinal Blocks is constrained by the marked lithologic contrasts across the boundary, an increase in age of detrital zircons and a marked decrease of epsilon Nd(t), and has been interpreted as an intervening subduction complex (Swift and Force, 2001; Meijer, 2014).The Cochise block is interpreted as a juvenile volcanic arc, active predominantly from 1650 to 1630 Ma (Eisele and Isachsen, 2001). Sedimentation in the Cochise block was synchronous with volcanism and mafic rocks provide evidence of late-stage igneous activity at about 1,500 Ma (Eisele and Isachsen, 2001). Within the Cochise block, the time span from separation of material from a depleted upper mantle source to crystallization of evolved igneous rocks was rapid (50 to 100 m.y) and some felsic igneous rocks apparently intruded only slightly (~40 m.y) older basement. The time from crystallization to sedimentation was shorter than 35 m.y. for most of the Cochise block which supports a rapidly depositing system that was eroding juvenile arc material (Eisele and Isachsen, 2001; Swift and Force, 2001).

#### 2.2.3.5 Northern Mexico

Parts of northern and eastern Mexico are known to have Proterozoic basement. In both cases these are interpreted to be allochthonous blocks translated to their present position during the Phanerozoic (Dickinson and Lawton, 2002; Farmer et al., 2005; Centeno-Garcia et al., 2008). Northeastern Mexico is underlain by Grenvillian age basement, originally juxtaposed to the rest of the North American continent during the Mesoproterozoic Grenvillian Orogeny (Dickinson and Lawton, 2002). The 1,700 – 1,800 Ma Caborca block that underpins Northwestern Mexico is interpreted as originally part of the Mojave province, but was transported in a southeasterly direction along the Mojave – Sonora Megashear during the Jurassic (Silver and Anderson, 1974). Early work on the Mojave – Sonora Megashear, a structure first inferred by Silver and Anderson (1974), proposed that the Jurassic translation of the Caborca block was its first activation. It has more recently been interpreted to be related to a much older structure, the Proterozoic transform plate margin (Dickinson and Lawton, 2001). If this is the case, then what is now Northern Mexico was originally oceanic crust during the Paleoproterozoic accretionary development of southwestern North America.

## 2.3 Post-Accretionary Geologic Evolution

### 2.3.1 Proterozoic Intracratonic Basin Development

After an interval of erosion, shallow marine and coastal plain sedimentation took place across parts

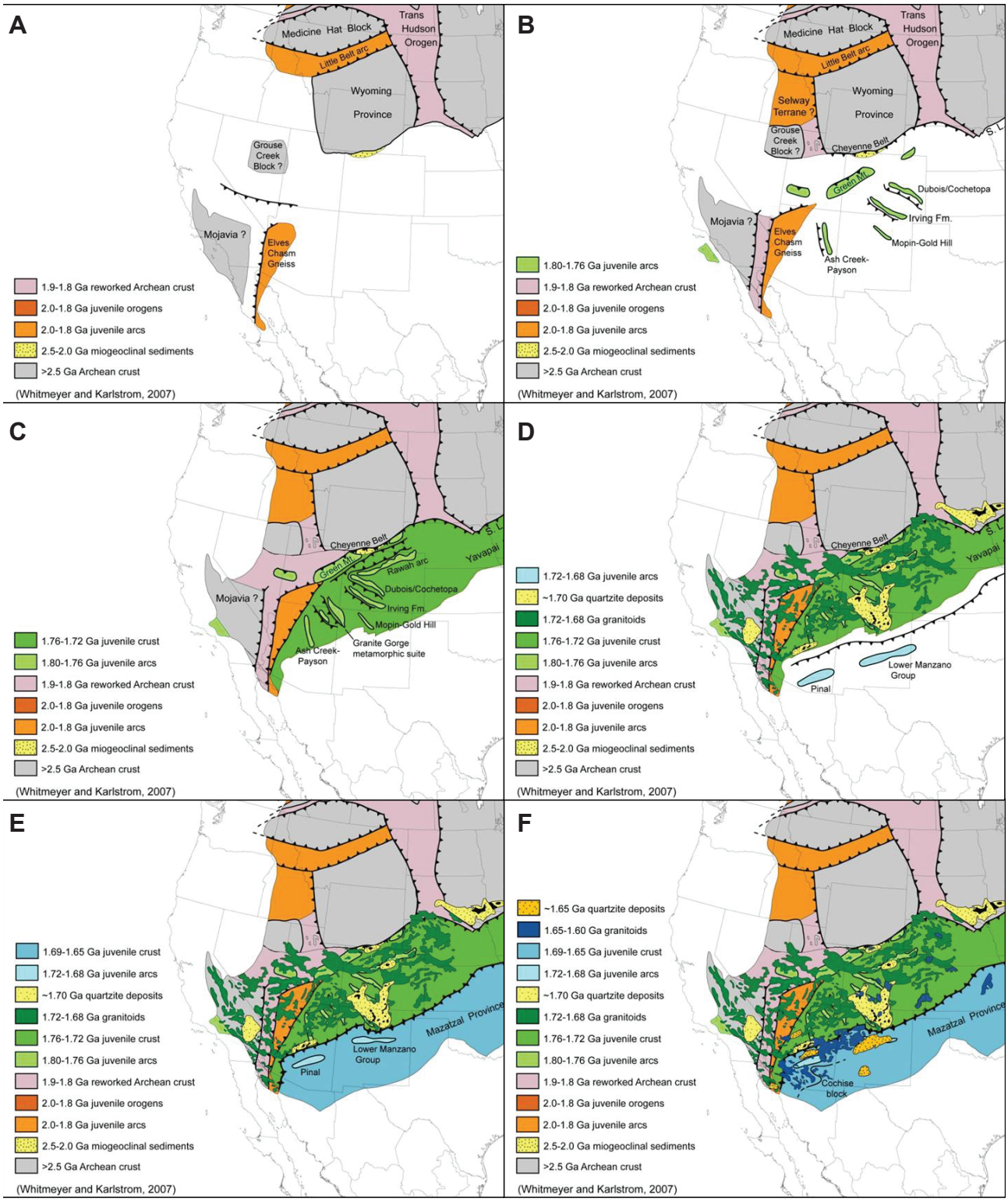


Figure 2.3 Geologic reconstruction matrix from 1,800 - 1,600 Ma, showing accretionary growth of southwest North America. Reproduced from Whitmayer and Karlstrom (2007).

of the continental block during the mid-Proterozoic, resulting in the deposition of the age-equivalent Unkar, Apache, Castner and Allamoore sequences (Timmons et al., 2005; Figure 2.4). Depositional sequences were up to 4.5 km thick locally, although ~850 m is more typical (Wrucke, 1989). This period of sedimentation produced two distinct units. The Apache Group consists of conglomerates, shales and

limestones and occurs mainly in a narrow belt through central Arizona. (Figure 2.4). The Apache Group was deposited between 1,420 and 1,100 Ma (Wrucke, 1989) with more restricted ages of 1,330 – 1,260 Ma reported by Timmons et al. (2005).

The Troy Quartzite overlies both the Apache Group and dolerite sills on a slight regional unconformity. The Troy Quartzite is a more spatially restricted unit that attains a maximum thickness of ~400 m in SE Arizona. It consists mostly of quartz-rich sediments (Wrucke, 1989), derived principally from the erosion of the Grenville Orogen, affecting the eastern edge of the North American continent (Mulder et al., 2017).

### 2.3.2 Dolerite Intrusion

During the Late Mesoproterozoic, the North American continent was subjected to a period of widespread mafic magmatism. In the southwestern U.S. this is manifested as extensive dolerite sills with subordinate dikes. Radiometric age determinations range from 1,140 Ma to 1,040 Ma (e.g., 1,100 ± 15 Ma; Wrucke, 1989 and references therein). U-Pb TIMS data from baddeleyite in dolerites from Arizona give ages of 1,080 ± 2 Ma, 1,080 ± 3 Ma, 1,088 ± 3 Ma and 1,094 ± 2 Ma (Bright et al., 2014). Similar ages obtained from dolerites in New Mexico indicate continuity of this large igneous province (Bright et al., 2014). Silicic igneous rocks of the same age have been interpreted to be crustally derived partial melts generated by heat from underplating of large volumes of mantle-derived mafic magma (Bright et al., 2014). These rocks form a large igneous province that extends for 1500 x 500 -1000 km (Figure 2.4). Magmatism occurred from 1,094 to 1,080 Ma, largely after the Grenville orogeny (Bright et al., 2014). Models for this event include (1) lithospheric delamination following the Grenville collision (Bright et al., 2014); and/or (2) arrival of a mantle plume beneath south-central Laurentia, with a northern portion responsible for the Mid Continent Rift - Keweenawan magmatism (Bright et al., 2014). A temporal relationship between the dolerites of the southwestern U.S. and the Keweenawan province has long been inferred (e.g., Helsley and Spall, 1972), and is supported by recent TIMS dating (Bright et al., 2014). However previous correlations with other large igneous provinces made by previous workers (Hanson, 2004; Ernst et al., 2008) are now under scrutiny (e.g., the 1,075 Ma Warakurna province in Australia is too young, and the 1,110 Ma Amazonian, Congo and Kalahari events are too old to be directly related; Bright et al., 2014). Instead though they might be diachronous products of similar processes.

The intercalated basalts and dolerite sills that intrude the Paleoproterozoic Apache Group imply a post-orogenic extensional regime and could be consistent with lithospheric delamination, or a slab break off model. Alternatively, a more complex tectonic regime such as an aulacogen, or failed triple point rift system (Dickinson, 1989) could account for mafic magmatism at this time. However, this seems less likely on the basis of geochronological correlation with the plume-related magmatism in the Mid Continent Rift and the lack of evidence for triple point style extensional tectonics in the southwest. What is clear is that by the late Proterozoic, Arizona was part of the stable continental interior of the

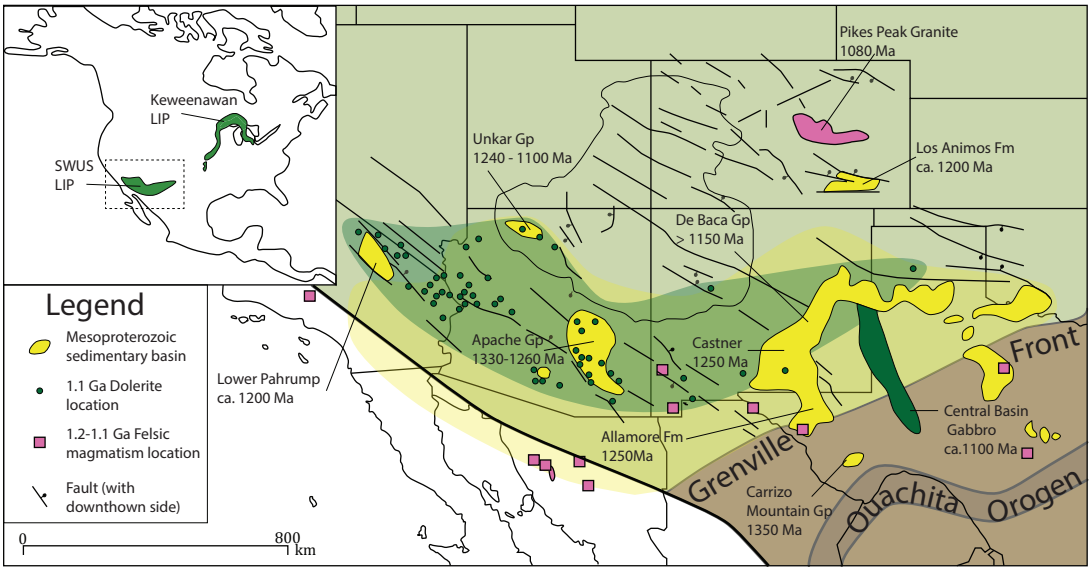


Figure 2.4 Map of the age and distribtion of Mesoproterozoic sedimentary basins and ca 1,100 Ma magmatic suite relative to the Grenville orogenic front. Modified after Timmons et al. (2005). SWUS LIP as proposed by Bright et al. (2014) relative to the Keweenawan LIP (inset).

Rodinia supercontinent (Dickinson, 1989).

### 2.3.3 Early – Mid Palaeozoic Platform Development

A hiatus of approximately 500 m.y. separated Proterozoic and Palaeozoic sedimentation in the southwestern U.S. Despite the length of this hiatus, there is only a slight angular discordance between the two sequences, suggesting that an exceptionally stable platform had developed by the early Palaeozoic (Dickinson, 1989). Paleozoic rifting was responsible for the development of the continental margin of North America, which then became the site of passive margin sedimentation over the next ~200 m.y. (Figure 2.5).

Early Palaeozoic sedimentary wedges thicken from the SW to NE toward the Palaeozoic landmass known as the Transcontinental Arch which underlays NE Arizona (Dickinson, 1989; Figure 2.5). Regular transgressions and regressions occurred during the Paleozoic, and the best recorded of these are in units at the base and top of the Palaeozoic sequence (Beus, 1989). Although initiation of sedimentation was diachronous across the state, the first major subsidence is recorded by the basal quartz-rich and minor arkosic sandstones of the Bolsa Quartzite in the south of Arizona, and its correlates the Tapeats and Coronado sandstones in the north and east of the state. The second major well-recorded event was a widespread inundation during Mississippian times (359 – 323 Ma; Beus 1989; Dickinson, 1989), resulting in the deposition of extensive regional carbonate sequences; the Redwall and Escabrosa limestones.

### 2.3.4 Late Paleozoic – Early Mesozoic Basins

During the Mid-Palaeozoic to Early Mesozoic, both the W and SE margins (Cordilleran and Ouachita,

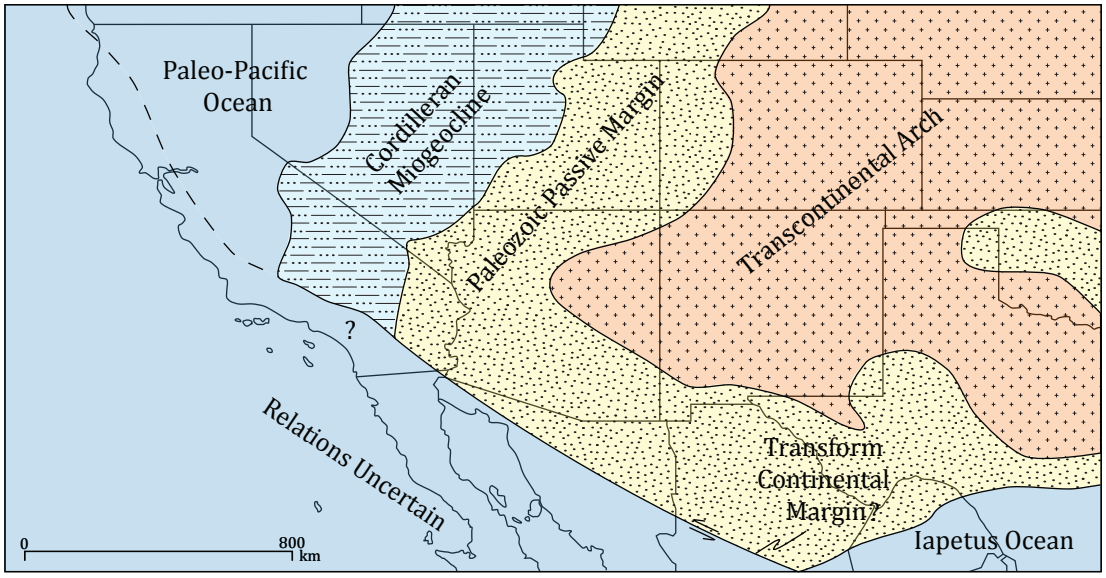


Figure 2.5 Early - mid Paleozoic geologic setting of the southwestern United States, showing passive margin sedimentation on the SW edge of Laurentia. Modified after Dickinson (1989).

respectively) of the North American continent were affected by orogenic activity, with platform sediments thrust across its edges (Figure 2.6). The orogens were not synchronous and had differing impacts on the southwest. The cordilleran Antler and Sonoma orogenies occurred during the Devonian-Mississippian and Permo-Triassic respectively while the Ouachita – Marathon orogeny occurred during Pennsylvanian-Permian time (Dickinson, 1989).

The Late Devonian Antler Orogeny appears to have had little effect on Arizona, as the large carbonate province represented by the Escabrosa limestone and its correlate, the Redwall limestone, apparently grew beyond the influence of detrital clastics of the orogenic belt, E and NE of the Roberts Mountain Thrust in Northern Nevada (Figure 2.6). No record of the Permo-Triassic Sonoma Orogeny is preserved in Arizona, as Permian strand lines and eolian deposits suggest area was still a stable margin setting (Dickinson, 1989).

The Ouachita deformation is well recorded in the rock record of Arizona. The Ouachita Orogeny was an extension of the Hercynian-Variscan orogenic system that sutured Laurentia and Gondwana, forming Pangea. The internal compressional stresses caused by collision with Gondwana caused the uplift of the Ancestral Rocky Mountains and created discrete depocentres mostly across NE Arizona (e.g., the Holbrook basin; Figure 2.6). SE Arizona was affected by down-flexure of the foreland in front of the Ouachita-Marathon thrust sheets, resulting in the formation of the Pedregrosa foreland basin (Dickinson 1989). The late Permian sequence is thicker and more continuous in the Pedregosa basin than NW Arizona and includes the thin but continuous subaerial 'Jelly Bean Conglomerate'. This unit is attributed to uplift and erosion of the fore-bulge adjacent to the belt of foreland basins (Figure 2.6; Dickinson, 1989). The Ouachita Orogeny first juxtaposed the Gondwanan Yucatán block of present-day Mexico against Laurentia (Dickinson and Lawton, 2001). Subsequent break up of Pangea saw partial rifting

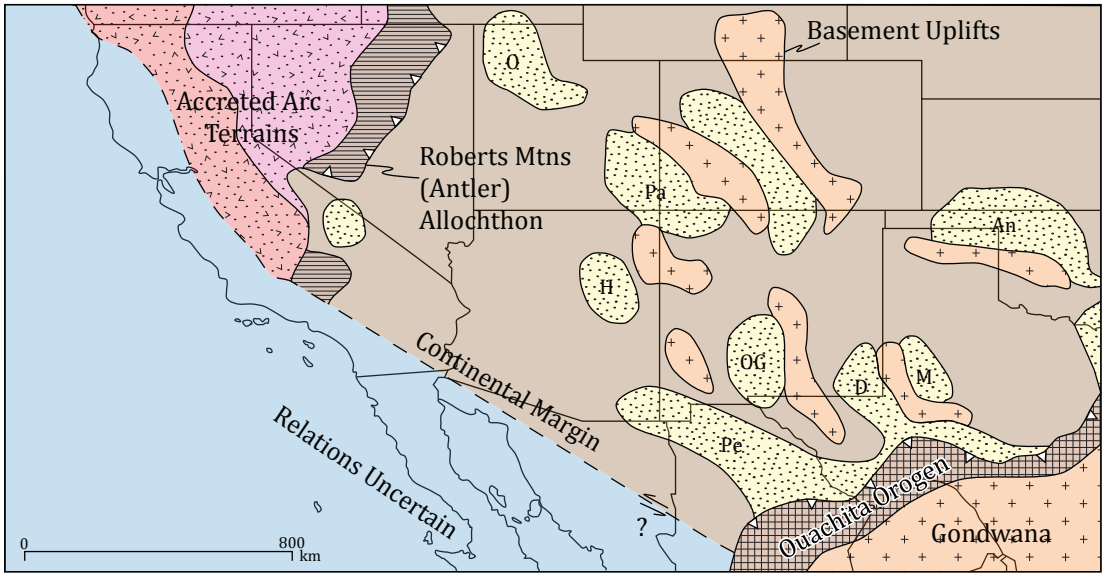


Figure 2.6 Late Paleozoic geologic setting of the southwestern United States showing the Ouchita and Antler orogens and the basements uplifts and associated basins of the ancestral Rocky Mountains. Modified after Dickinson (1989). Basins: An - Anadarko; Ar - Arkoma; D - Delaware; H - Holbrook; M - Midland; O - Oquirrh; OG - Oro Grande; Pa - Paradox; Pe - Pedregrosa.

and rotation of the Yucatán block during opening of the Gulf of Mexico during the Early Jurassic (ca. 175 Ma). Continental margin volcanic and intrusive rocks have been intersected by drilling and suggest this lithotectonic block was indeed built on older Gondwanan and Grenvillian crust (Dickinson and Lawton, 2001).

### 2.3.5 Mesozoic Magmatism

From the Late Triassic, a magmatic arc developed along the North American cordillera, presumably in response to fragmentation of Pangea and opening of the Atlantic Ocean to the east. This western arc straddled the Arizona – Sonora border but appears to have been truncated obliquely to the south by the transform margin of southern Laurentia (Figure 2.7). The transform margin is inferred to have stepped east to another east-dipping subduction zone that developed at the continental margin of the Yucatan block in western Mexico, which at this time was subducting the intervening Mezcalera Plate (Dickinson and Lawton 2001). Latest Triassic cratonic sedimentary units pass upward to Early Jurassic active arc sedimentary facies in the Sonoran Desert, constraining arc initiation to 205–175 Ma (Tosdal et al., 1989). Shortly after, or possibly during, arc initiation, the 1,780 Ma Caborca block was translated eastward from the Mojave province along a newly-formed sinistral shear zone (the Mojave-Sonora Megashear; Anderson and Silver, 1974), probably related in some way to the transform margin (Dickinson and Lawton, 2001). Subsequently, the Mezcalera Plate began oblique eastward subduction below the Caborca block (Dickinson and Lawton, 2001; Figure 2.7). At this time Baja California was situated well to the west of its current position, and is thought to have been part of an island arc, the Guerrero Terrane, located above a west-dipping subduction zone (Dickinson and Lawton, 2001; Figure

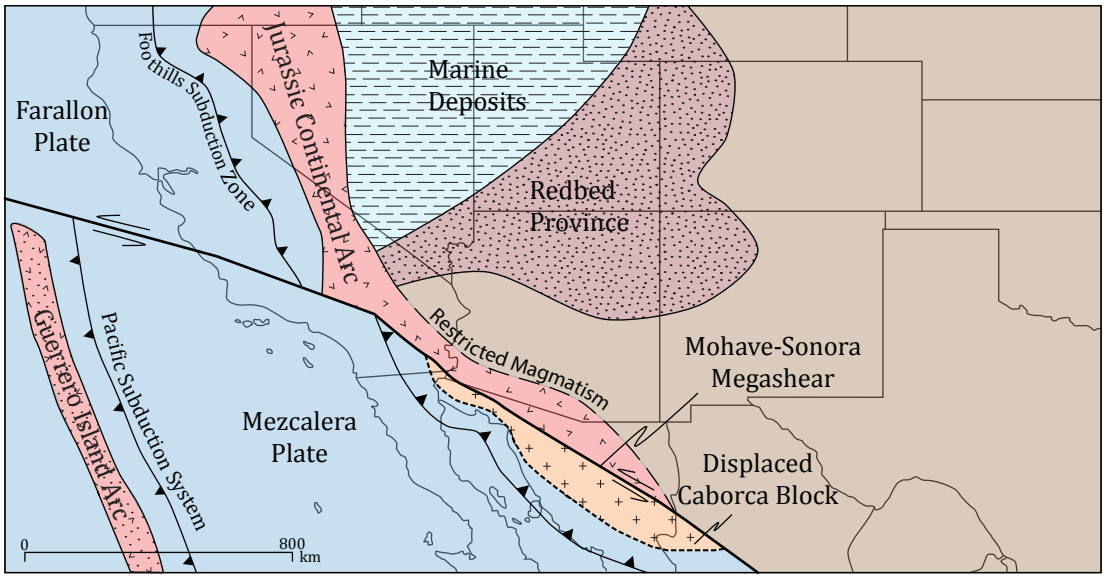


Figure 2.7 Mid Mesozoic geologic setting of the southwestern United States showing the trucation of the Jurassic continental arc and translation of the Caborca block along the transform Mojave-Sonora Megashear structure. Also shown are the back-arc sedimentary depocentres and the approaching Guerrero island arc terrane. Modified after Dickinson (1989).

2.7).

In Arizona, thick sequences of Early to Middle Jurassic arc volcanic rocks are associated with regionally extensive plutons in the southern third of the state (Dickinson, 1989). They are interpreted to have been emplaced during neutral to mildly extensional conditions related to normal subduction in the Cordilleran arc system (Dickinson and Lawton, 2001; Barton et al., 2011). Arc magmatism took place intermittently in a 200 km wide zone, extending approximately SE from present day northern Nevada to southern California and to a limited extent into northern Sonora (Dickinson, 1989; Tosdal et al., 1989; Barton et al., 2011; Figure 2.8). The margin south of the active arc is interpreted to still have been dominated by sinistral transform tectonics, accommodating minor eastward-directed subduction of the Mezcalera Plate under Mexico (Dickinson and Lawton, 2001; Centeno-Garcia et al., 2008).

Abundant Middle to early Late Jurassic magmatism (ca. 175–155 Ma) took place across a broad region, particularly north of Arizona. Igneous activity spread eastward across the central Great Basin into western Utah (Barton and Hanson, 1989). Middle Jurassic plutons were considerably more voluminous than their Early or Late Jurassic equivalents suggesting substantially higher magmatic fluxes to the mid-upper crust at this time (Barton et al., 2011), consistent with the interpretation of Dickinson and Lawton (2001; Figure 2.8). Late Jurassic to earliest Cretaceous magmatism (ca. 155–140 Ma) produced a relatively narrow belt closer to the continental margin and volcanic rocks of this age are sparse. The Late Jurassic – Early Cretaceous suite is compositionally diverse, with some alkalic intrusions in southern Arizona (Tosdal et al., 1989; Haxel et al., 2008). The apparent eastward arc migration during the Late Jurassic is interpreted to result from the switch in subduction polarity under the Guerrero arc following its accretion to the continent (Figure 2.9). Early Jurassic magmatism appears to have been considerably

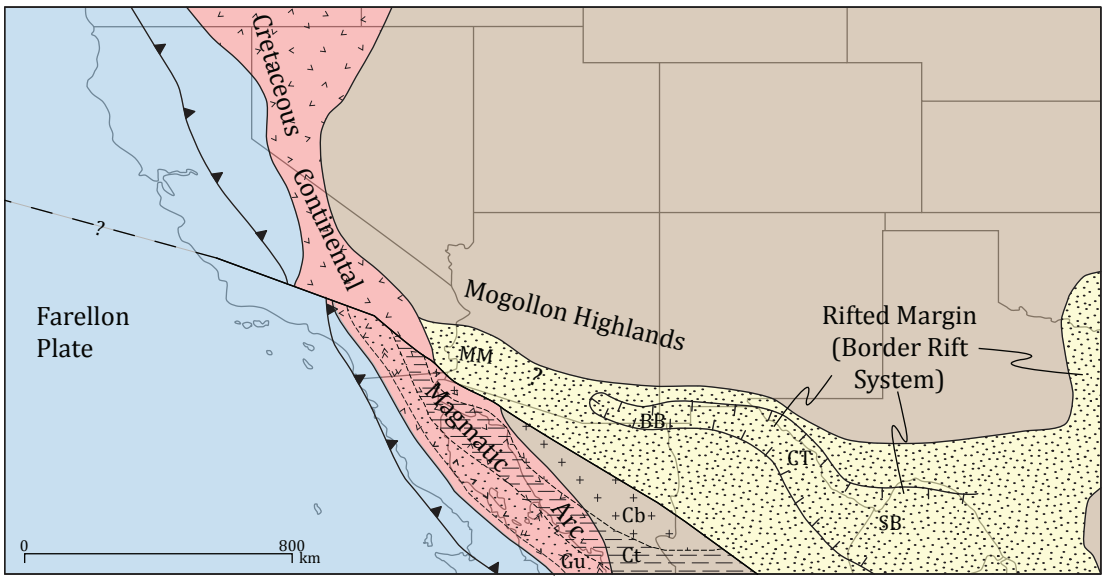


Figure 2.8 Late Mesozoic geologic setting of the southwestern United States, showing the composite Guerrero-Cortes-Caborca accretionary terrane and inboard border rift system as well as the position of the Cretaceous continental arc. Modified after Dickinson (1989).

smaller volume than the Middle and Late Jurassic events; interpreted by some (e.g., Barton et al., 2011) to indicate a slow initiation and development of the cordilleran arc, rather than rapid onset of arc magmatism. Dickinson and Lawton (2001) suggested that this increase in magmatism during the Early – Mid Jurassic is related to the foundering and roll back of the subducting plate as a response to the approach of the Guerrero arc (Figure 2.9).

As the Guerrero arc approached the continent during the Late Jurassic - Early Cretaceous, progressive consumption of the intervening oceanic Mezcalera Plate induced slab rollback beneath, and westward migration of, the Jurassic continental arc, temporarily halting arc magmatism in Mexico (Dickinson and Lawton 2001; Figure 2.9). This westward arc migration was accompanied by the development of major back arc basins, collectively referred to as the Border Rift System, including the McCoy, Bisbee and Chihuahua basins (Figure 2.12). Incipient extension was coincident in both space and time with the opening of the Gulf of Mexico during the Mid-Late Jurassic, and may have been a contributing factor to its formation (Dickinson and Lawton, 2001). The major period of Jurassic-Cretaceous subsidence in southern Arizona was broadly synchronous with westward arc migration. It may have been a back arc system forming in response to roll-back of the Mezcalera plate (Dickinson and Lawton, 2001). Alternatively, it could be interpreted as a retro-arc foreland basin related to the collision and accretion of the allochthonous island arc (Lasowski et al., 2013). Irrespective of the precise mechanism, subsidence was significant at this time. This is best demonstrated in the Bisbee basin in SE Arizona, where a 4 km thick marine and non-marine sedimentary sequence conformably overlies Jurassic volcanics (Dickinson, 1989). Across the Border Rift System, sedimentary fill was dominantly of marine origin, with terrigenous and volcanic input increasing to the NW, suggesting shallowing in that direction. The NW structural

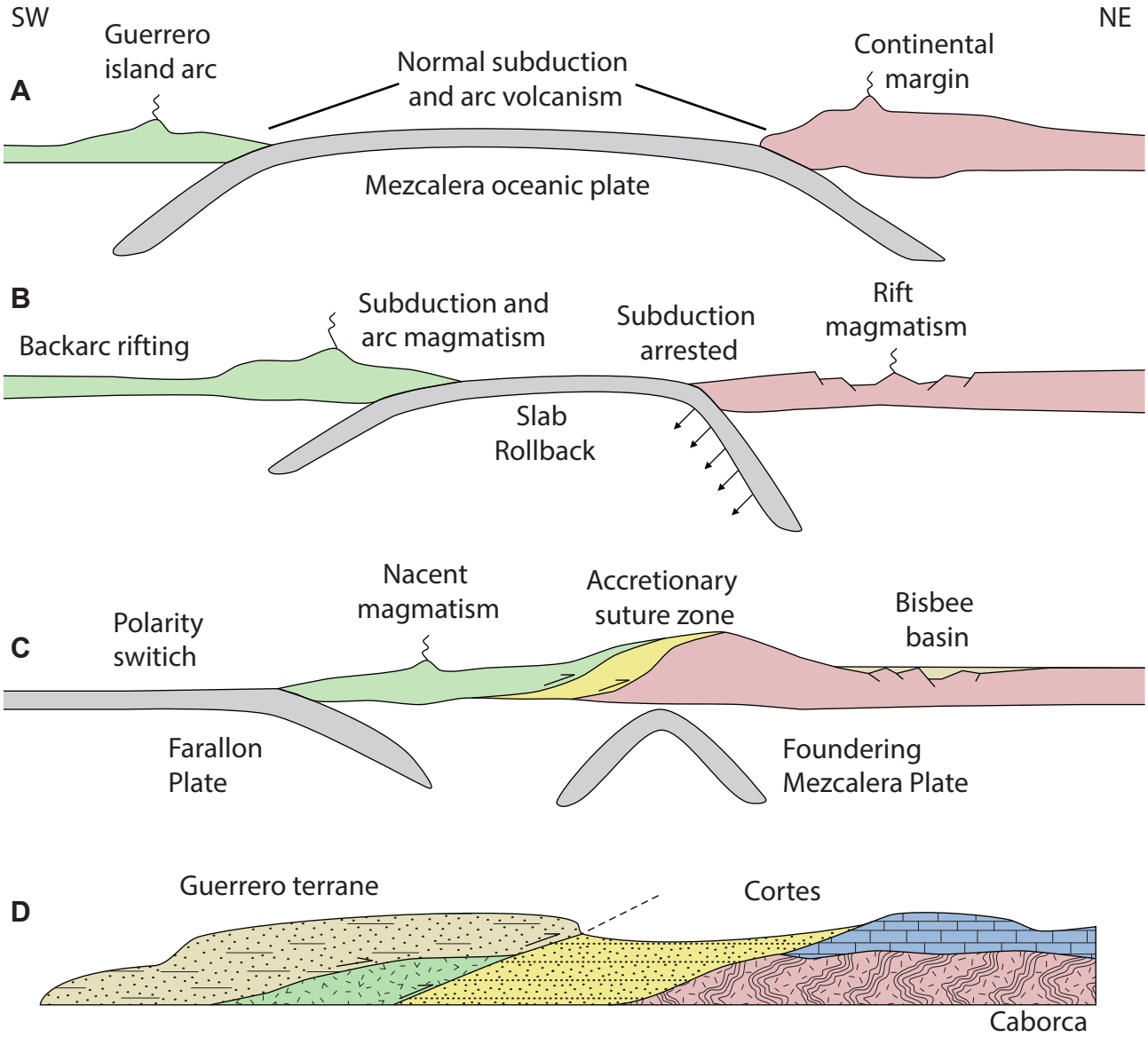


Figure 2.9 A-C Schematic time slice diagram showing the relationship between Guerrero accretion and development of the border rift system. Modified after Dickinson and Lawton (2001). D Schematic cross section through the Guerrero-Cortes-Caborca terrane. Modified after Centeno-Garcia et al (2008).

trend of this basinal system suggests a strong influence of basement architecture (Leveille and Stegen, 2012), most likely the Proterozoic transform margin.

Arc-continent collision and accretion occurred somewhere between the Early Jurassic (Centeno-Garcia et al., 2008) and Earliest-Mid Cretaceous (Dickinson and Lawton 2001), with the Paleozoic passive margin sediments of the Cortes Terrane and overthrust Guerrero arc now underpinning the majority of northwestern Mexico (Figure 2.9). Following arc collision and accretion, continuing subduction of the Farallon Plate under western Mexico resulted in a continental arc and associated back arc system contiguous with the cordilleran arc by the end of the Early Cretaceous (ca 100 Ma), The tectonic regime either remained compressional (Dickinson and Lawton, 2001) or was mildly extensional (Centeno-Garcia et al., 2008) during the Early – Mid Cretaceous. Magmatism was comparatively less varied, showing

progressive evolution over a 50 m.y. period from primarily quartz dioritic rocks in the Early Cretaceous to felsic meta-peraluminous compositions by the Late Cretaceous (Barton, 1996). Continuing subduction produced volcanic-plutonic arc assemblages on the mainland and in Baja California (Dickinson and Lawton, 2001; Centeno-Garcia et al., 2008), now contiguous with the mainland prior to the Neogene activity that opened the Gulf of California.

Mid-Mesozoic magmatism in the southwestern U.S. varied compositionally both in spatial and temporal contexts, spanning basaltic to rhyolitic, alkaline to strongly peraluminous compositions. Most of the Jurassic igneous rocks are sub-alkaline, oxidized hornblende-biotite granitoids or their volcanic equivalents, including the majority of Early to Middle Jurassic plutons in Arizona (Barton et al, 2011). They relate to the onset and continued development of a normally dipping subduction system on the western margin of Laurentia during the Late Triassic – Early Jurassic (Barton et al., 2011; Dickinson and Lawton, 2001; Figure 2.7; Figure 2.8). This Cordilleran arc, subducting the Farallon Plate, was truncated at the transform continental margin. The oceanic Guerrero arc is thought to have extended offshore in a SSE direction subducting the Mezcalera Plate. It was subsequently accreted to northern Mexico, creating a contiguous east-dipping subduction zone by the Early-Mid Cretaceous (Dickinson and Lawton, 2001; Centeno-Garcia et al., 2008); Figure 2.9). Accretion was preceded by the southeastward translation of the Caborca Block, a Proterozoic basement segment and associated Cortez terrane Paleozoic passive margin cover (Anderson and Silver, 1974; Farmer et al., 2005). This led to the creation of a major basinal system, the Border Rift System, and a pronounced westward shift in arc magmatism as subduction polarity switched under the accreted Guerrero Arc (Dickinson and Lawton, 2001; Centeno-Garcia et al., 2008).

#### 2.3.5.1 The Mojave-Sonora Mega-Shear.

The Mohave – Sonora Megashear of Silver and Anderson (1974) is an enigmatic component of the SW US basement architecture that juxtaposes the southwestern Laurentian margin against the 1.7-1.8 Ga Caborca Block (Anderson et al., 2005). Based on geological, geochemical and geochronological evidence, the basement of the Caborca block seems to have mostly originate from the Mojave province (Farmer et al., 2005). It was transported approximately 800 km to its present position via a 5 km wide mylonitic sinistral transfer zone, active mostly during the Early - Mid Mesozoic (e.g., Dickinson, 1989; Titley and Zurcher, 2008), and was probably related to the long lived transform continental margin (California-Coahuila Transform of Dickinson and Lawton, 2001). The onlapping Cortes Terrane is interpreted to relate to, and evolved at, the margin of the Caborca Terrane (Stewart et al., 1990; Centeno-Garcia et al., 2008; Figure 2.9). Broadly, it is made up of a thick succession of Paleozoic deep-marine turbidites that were thrust over Paleozoic platform limestone cover of the Caborca Terrane during Guerrero accretion (Stewart et al., 1990; Dickinson and Lawton, 2001). Centeno-Garcia et al., (2008) suggested that the presence of pre-accretion metamorphosed Paleozoic units at the base of the Guerrero terrane attest to a

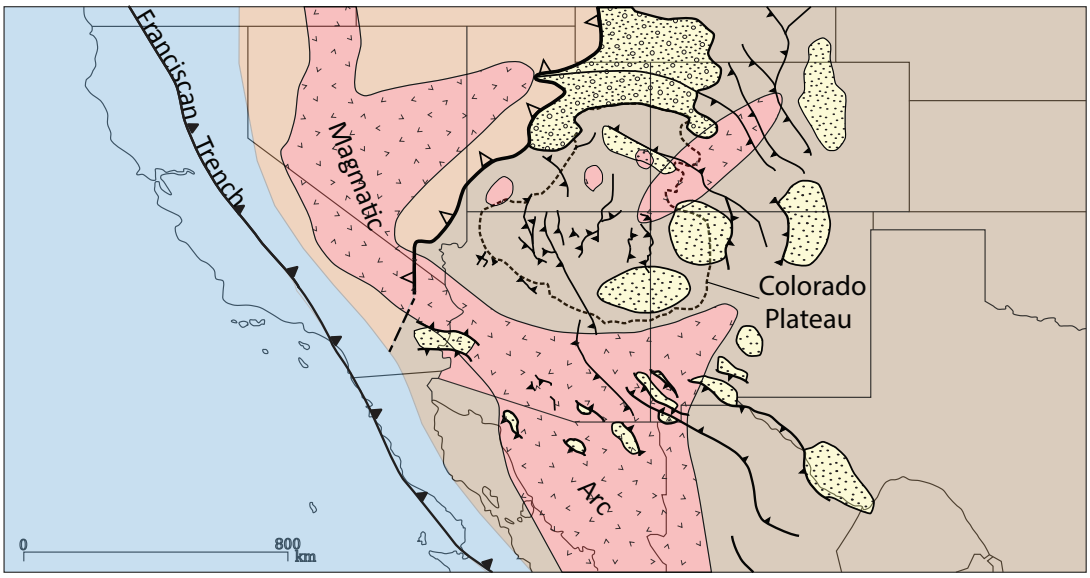


Figure 2.10 Sevier-Laramide geologic setting of the southwestern United States showing the Sevier thrust sheet. Eastward migration of the magmatic arc around the periphery of the Colorado Plateau crustal segment and inboard basment uplifts and associated sedimentary basins. Modified after Dickinson (1989), Krantz (1989) and Leveille and Stegen (2012).

more complex, multi-stage accretionary history.

Originally described by Silver and Anderson (1974), the 'Megashear Hypothesis' remains controversial, but their initial findings are consistent with the accepted Jurassic E-SE subduction direction of the Farallon Plate at this time. This timing relationship suggests association with the approach and/or accretion of the Guerrero island arc. Its spatial relationship to the SW margin of the border rift system may indicate some control on basin development and/or the localisation of minor Jurassic mineralisation. The exact location and relative timing of the structure has been hard to establish due to the subsequent Laramide compression and later Tertiary extensional effects on the area (e.g., Gray et al., 2008, Amato et al., 2009). Notwithstanding the continuing debate on the precise details of the structure, its relevance to geologic evolution, structural architecture and metallogeny appears profound.

### 2.3.6 Laramide Orogeny

#### 2.3.6.1 Introduction

The Laramide period, ca 80 – 45 Ma, saw the most intense orogenic event to affect the southwestern U.S. since the early Proterozoic. A hiatus of 25 to 30 m.y. occurred between the deposition of the Jurassic Bisbee group rocks and the oldest Cretaceous rocks, indicating a pronounced shift in the geologic evolution during this time (Dickinson, 1989). Laramide igneous centres produced the most important phases of porphyry copper mineralisation in the SW US porphyry Cu province (Figure 2.10). A profound change in geodynamics was caused by the flattening in subduction angle of the oceanic slab beneath the continental margin (e.g., Titley, 1982; Humphreys, 2009; Figure 2.12). This caused the magmatic arc to migrate as far east as New Mexico, western Texas and Chihuahua northeastern

Mexico during the peak of deformation, in the Mid Eocene (ca. 56 – 40 Ma; Leveille and Stegen, 2012). Arc migration was accompanied by substantial compressional deformation related to the increased friction with the sub-horizontal oceanic plate, driving significant crustal thickening. (e.g., Dickinson, 1989; Dumitru et al., 1991; Humphreys, 2009). The onset of Laramide deformation is recorded by syn-orogenic clastic sediments, deposited in down-faulted or down-folded blocks (Dickinson, 1989; Lehman, 1991; Gonzalez-Leon and Lawton 1995; Seager, 2004). Positive topographic features are likely to have been thrust-bounded basement cored uplifts (Davis, 1979; Dickinson 1989; Krantz, 1989). Crustal thickening in the south of the state induced regional uplift such that the Eocene landscape is thought to have been a widespread erosional surface (Titley and Zurcher, 2008).

The Laramide and Sevier Orogens have traditionally been described separately in the literature (Krantz, 1989) This is probably relates to the difference in character, with the Sevier Orogeny manifested as thin-skinned fold-thrust development and the Laramide characterised more by the development of basement cored uplifts, bound by high angle faults. However their proximity both in space (Figure 2.10) and time (Table 2.1) seems too much to be coincidental. Indeed, many authors (e.g., Livacarri et al., 1991; Humphreys, 2009) envision the Sevier orogeny, beginning as early as ca. 105 Ma (Livacarri et al., 1991), as a precursor to the main Laramide phase of deformation, with the transition attributed to relate to progressive thickening of the crust, related to the flattening of the Farallon Slab. Their differences in structural styles probably relate to their initial locations with respect to the continental margin (within the platform margin for the Sevier Orogeny; well inboard of the continental margin for the Laramide Orogeny; Krantz, 1989; Figure 2.10) and therefore affected by initial crustal thickness. It seems apparent that the two phases were controlled by the same geodynamic processes but merely represent crustal heterogeneity. They should therefore be described as the Sevier-Laramide Orogeny (e.g., Krantz, 1989; Livacarri et al., 1991; Humphreys, 2009).

Paleomagnetic results indicate that much of the northern cordillera, now occupying northwestern U.S. and western Canada, actually resided 1,300 km SSE of their current position prior to the Laramide. Hildebrand (2015) interprets this section of the crust to have been translated more than 1,000 km northward during the 80–45 Ma Laramide event. He proposed that by restoring the sinistral Texas Lineament, and Lewis and Clark transverse zone which is located about 1,300 kilometres to the north, along the Sevier thrust front, these paleomagnetic results can be rationalised in the context of a crustal scale northward translation of the northern cordillera during the Laramide Orogeny. The proposed restoration reunites two conspicuous belts of Late Cretaceous–Paleocene slab-failure plutons and porphyry copper deposits into a single zone extending continuously along western North America. Although the proposition of Hildebrand (2015) ties the Laramide and Sevier orogenies together, no field evidence has been found to support it. In addition, this interpretation is hard to reconcile with the clear evidence for intense compressional deformation that favours flat slab subduction (e.g., Humphries

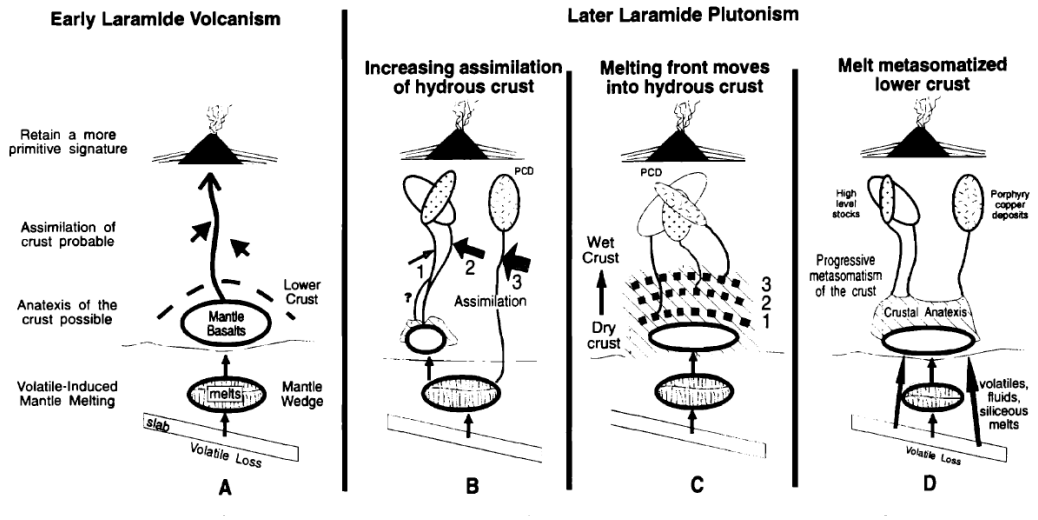


Figure 2.11 A. Melt generation during early Laramide volcanism. B-D Possible melting scenarios for porphyry Cu related Laramide plutonism. Reproduced from Lang and Titley (1998).

et al., 2009).

### 2.3.6.2 Laramide Magmatism

Magmatism in the Laramide arc began around 80 – 75 Ma (Late Cretaceous) and ended around 45 Ma (Middle Eocene; Dickinson, 1989; Bouse et al., 1999; Lang and Titley, 1998; Titley and Zurcher, 2008, Leveille and Stegen, 2012). It was responsible for voluminous plutonism and volcanism across Arizona (Figure 2.10). Relatively little is known of the original exposure, relief and volcanic rock distribution patterns during the Laramide. Subsequent widespread subaerial volcanism, erosion and extension have all served to obliterate or hide much of the Laramide rock record from this time. Interestingly, many areas where Laramide-age volcanic units are preserved are spatially associated with, or are host to, Laramide porphyry Cu deposits and/or their high level epithermal equivalents (e.g., Resolution, Mankse and Paul, 2002; Christmas, Koski and Cooke, 1982; Hillsboro, Dunn, 1982; Silver Bell, Richard and Courtright, 1966). Titley (1982) noted that the volcanic units from some of these porphyry Cu deposits that mostly have intermediate (andesitic) compositions and retain a primitive radiogenic isotopic signature (Lang and Titley, 1998). Volcanic breccias, locally with metre scale clasts, are common in many of these Laramide andesitic sequences (e.g., Titley, 1982 and references therein), indicating an explosive volcanic origin, and possibly plinian or ultra plinian eruption styles. However, they could also represent large-scale agglomerates or auto-breccias associated with lava flows (e.g. Nickerson and Seedorff, 2016).

Exposures of Laramide plutons are spatially restricted in Arizona. Where known from outcrop or drilling, they usually consist of composite centres ranging from intermediate granodiorite – monzonite compositions, typical of a continental arc setting to highly silicic granites (e.g., Schultze Granite, Creasey, 1980, 1984; Stavast, 2006). In some cases Laramide plutons have been shown to be sourced, at least in part, from lower crustal Proterozoic granites, suggesting large scale crustal recycling towards the end of the Laramide period (e.g., the Wilderness Suite and Oracle granites; Bouse et al., 1999; Lang and

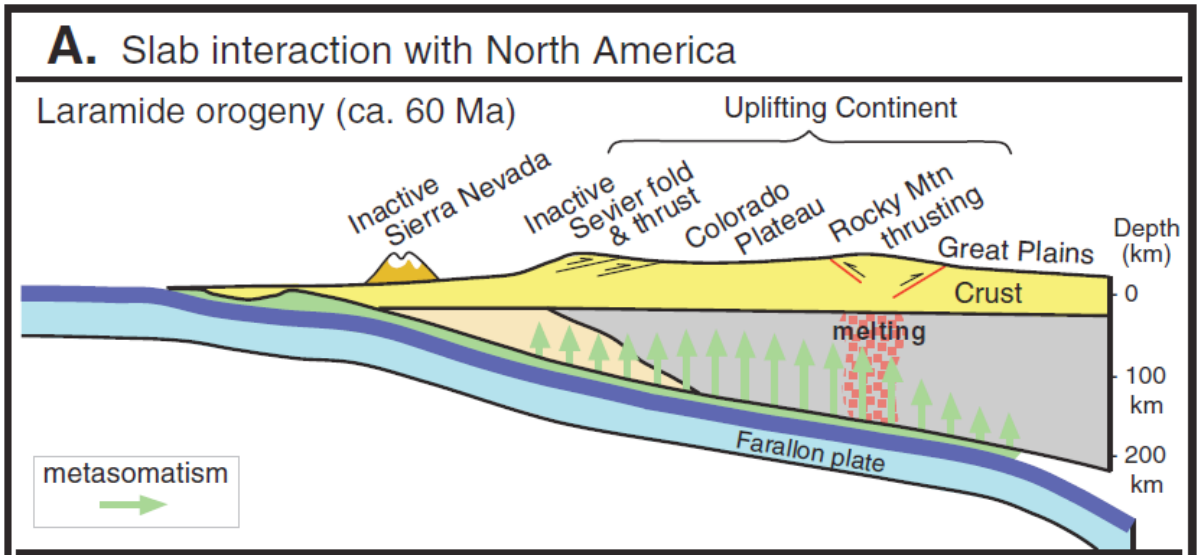


Figure 2.12 Schematic section through the Laramide continental margin showing the low subduction angle, thick-skinned deformation well inboard of the Jurassic arc, represented by the Sierra Nevada and Sevier thrust front. Reproduced from Humphries (2009).

Titley, 1998; Fornash et al., 2013). A number of both mineralised and barren Laramide magmatic suites have been shown to document consistent stages of evolution (Lang and Titley, 1998; Seedorff et al., 2005b; Leveille and Stegen, 2012). Over time there is generally an increase in $SiO_2$, changes in mafic mineral assemblages, increasing textural heterogeneity and a progression from barren to sub-productive to productive intrusions (Lang and Titley, 1998; Seedorff et al., 2005b; Leveille and Stegen, 2012). Additionally, younger intrusions show systematic changes in REE patterns that have been attributed to the involvement of amphibole, either in the source region or during fractionation, leading to a range of possible melting scenarios for later Laramide magmatism (Lang and Titley, 1998;Seedorff et al., 2005b; Leveille and Stegen, 2012; Figure 2.11). Intrusion shapes can vary from irregular to sub-circular, but some show a NW or NE elongation, suggesting a strong structural control on emplacement (Heidrick and Titley, 1982;). Many older Laramide plutons are crosscut by younger mineralised Laramide intrusions. Overall, igneous activity was confined mostly to south and west with most rocks having calc-alkaline andesite to rhyolite compositions (Titley, 1989; Lang and Titley, 1998 Seedorff et al., 2005b; Leveille and Stegen, 2012).

#### 2.3.6.3 Laramide Structures

The Laramide Orogeny produced a diverse array of structures and styles of deformation across the southwestern US. Some workers (e.g., Krantz, 1989, Haxel et al., 1984) have divided Arizona into several domains, based on the styles and magnitudes of deformation, specifically the Colorado Plateau, Transition Zone, SE Arizona and SW Arizona.

The Colorado Plateau is characterised by broad uplifts and adjacent basins, monoclines and small folds. Some of these structures, including NW-trending east-facing monoclines, were directly related

to Laramide reverse reactivation of high angle basement structures (e.g., Proterozoic Palisades fault and Palisades monocline – Reches 1978; Butte fault and East Kaibab monocline – Krantz, 1989). Other documented evidence of Proterozoic fault reactivation includes the Bright Angel Fault, which initially experienced 400 m of Proterozoic displacement followed by 76 m of Laramide reactivation with opposing sense of movement (Krantz, 1989). Davis (1978) asserted that monocline patterns across the Colorado Plateau mimic the Proterozoic basement architecture.

The Transition Zone is characterised by monoclines and uplifts, particularly in the Salt River Canyon area, where east-facing monoclines again indicate NE-SW shortening. Fault reactivation in this area is complex, with evidence for early exploitation of faults by 1,100 Ma dolerite sills (Silver, 1978).

The deformation in SE Arizona is complex, with an array of reverse/thrust faults, strike-slip faults, folds and penetrative tectonic fabrics. Low angle thrusts are common in this part of Arizona, and there are contrasting interpretations regarding their origin and timing in the context of the broader Laramide orogeny (e.g. Davis, 1979; Drewes, 1981; Titley, 1982), with the possibility that some may even be misinterpreted rotated Cenozoic normal faults. High angle NE trending strike slip faults offset and compartmentalised NW trending folds and reverse faults in the Tucson Mountains (Showalter, 1982). Titley and Heidrick (1982) showed that mineralised Laramide dikes, veins and faults in Arizona porphyry Cu deposits all strike reliably NE, suggesting that these arc-perpendicular structures controlled mineralisation during this period. Additionally the local presence of high strain zones and development of tectonites (Drewes, 1973) suggest that this part of Arizona experienced significantly more strain than areas to the north. The SW Arizona domain is generally less well understood from a structural perspective than the other three Laramide structural domains in Arizona. More Mesozoic volcanic and volcaniclastic rocks occurred here and the area was been affected by regional Laramide metamorphism and associated thrusting between 80 Ma and 58 Ma (Haxel et al., 1984), as well as significant post-Laramide extension.

#### 2.3.6.4 Laramide Geodynamics

The variations in Laramide structural styles in Arizona have led to contrasting models regarding the nature of the overall Laramide geodynamic setting. The overthrust model (e.g., Drewes 1973, 1976, 1981) proposes two large S-SW dipping thrust sheets in the south and southwest parts of the state. However many of the faults critical to this model are speculated to be located under cover, and/or have been shown to have little if any displacement by later workers (e.g. Titley, 1982). If the same level of fault inheritance and reactivation observed across the rest of Arizona has occurred in the south and southwest, then the pre-Laramide high angle faults make this style of thin skinned tectonics an unfavourable scenario (Titley, 1982). The uplift model of Davis (1979) proposed a large, NW trending basement cored uplift principally along reactivated Precambrian structures that formed in response to regional NE-SW shortening and crustal thickening. This model is supported by structural mapping and observations of Rehrig and Heidrick (1976) and Heidrick and Titley (1982), who revised the model to

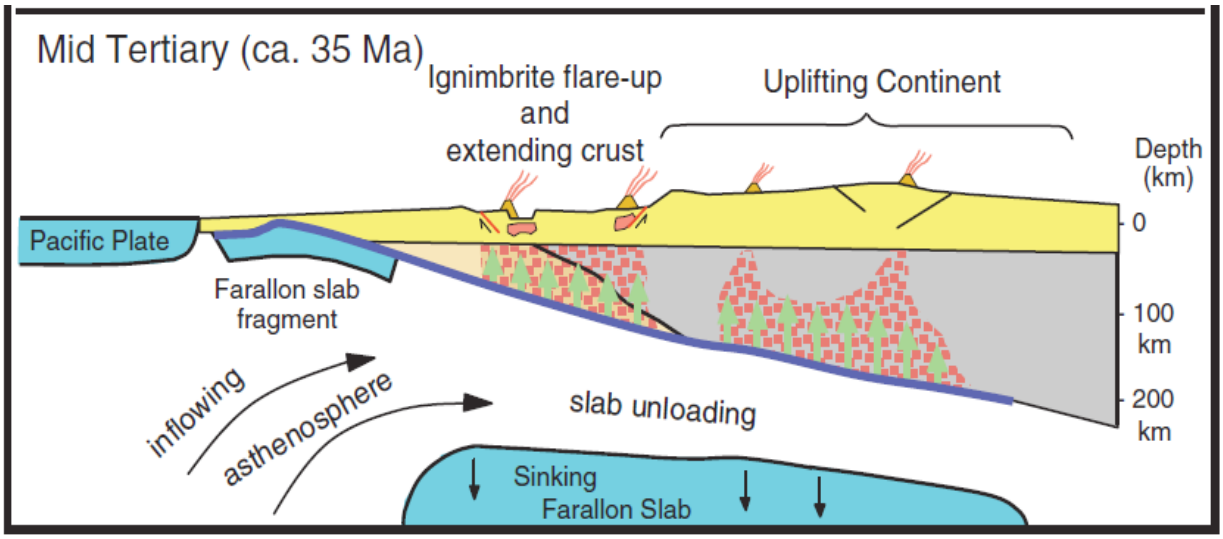


Figure 2.13 Schematic section through the mid Tertiary crust, showing the delamination of the Farrellon slab, associated uplift and extension of the continent in response to slab unloading and asthenospheric inflow-related silicic volcanism. Reproduced from Humphries (2009).

reflect a broader province of discrete uplifts.

Styles of Laramide structural evolution in Arizona can be compared in terms of style and magnitude. Though there is some disagreement about overall style (e.g., Davis, 1979; Drewes, 1981; Heidrick and Titley, 1982; most authors agree on NE directed compression. The Colorado Plateau, Transition Zone and SE Arizona are all characterised by fold-fault bounded uplifts, facilitated by pre-existing fault architecture and occurred in response to this NE directed compression (Reches, 1976; Davis 1979; Krantz, 1982; Showalter, 1982). Differences between the deformation styles in the three tectonic domains most likely relate to the magnitude of uplift, probably related to the degree of shortening, apparently increasing southwards (Titley, 1982). This may also relate to pre-Laramide crustal heterogeneity, with the schists of the SE domain able to accommodate more shortening that the thicker, crystalline accreted arcs of the northern Mazatzal and Yavapai terranes. While 30% crustal shortening has been calculated for SE Arizona, the Colorado Plateau experienced considerably less (on the order of several percent; Davis 1979).The local variations in orientation of axes of these uplifts was probably controlled by the orientations of the pre-Laramide faults rather than perturbations in the regional stress field (Davis, 1979; Titley, 1982).

SW Arizona sits in apparent discord to other tectonic domains in Arizona. Its penetrative tectonic fabrics and isolated exposures of complex thrust systems remain poorly understood. Although conjectural, the regional disparity could be interpreted in the context of crustal refrigeration, as proposed by Dumitru et al., (1991). In this model, the flat subducting slab displaced the hot asthenospheric wedge downwards, significantly reducing heat flow to the base of the crust. By this mechanism ductile deformation and metamorphism would have waned, transitioning to brittle deformation. The area would have occupied

a cooler fore-arc setting, allowing it to be affected by this thermal perturbation more-so than areas further to the north and east (Dumitri et al., 1991). However, because the domain is located closer to the continental margin, it may would not have seen much less relative change in thermal conductivity because it was already close to, or in contact with, the subducting slab. Alternatively, this area could be a southerly extension to the Sevier thrust system, and perhaps represents the transition from early Sevier-Laramide low angle thrusting to later Laramide metamorphism and high angle basement cored uplifts. What remains clear is the cause for the extremely widespread slab flattening event during the Sevier-Laramide period. Earlier authors (e.g., Ward ,1991) argue simply for an increased convergence rate, although more recent workers called on a combination of factors, such as plateau subduction beneath southern California, regional subduction dynamics associated with enhanced mantle-wedge suction and the decreasing age of subducted Farallon plate (Humphreys, 2009 and references therein).

### 2.3.7 Tertiary Magmatism and Extension.

The end of the Laramide Orogeny was diachronous across the North American Cordillera. In the northern part of the western U.S.A. the end of the Laramide Orogeny, around 48 Ma, coincided with the accretion of oceanic crust and associated westward arc migration (Humphreys, 2009). This created a tear, or window in the slab, separating the new, normally dipping subduction zone to the north and the continued flat slab subduction to the south of the inferred tear. Once created, this window propagated south, across the Great Basin progressively exposing hydrated lithosphere to upwelling asthenosphere and causing renewed magmatism, known as the Ignimbrite Flare Up (Figure 2.13; Humphreys, 2009). From 55 to 45 Ma south and western Arizona was intruded by voluminous peraluminous two-mica granites (Miller and Bradfish, 1980; Wright and Haxel, 1982; Arnold, 1986; Dickinson, 1989), suggesting crustal anatexis was still occurring at this time. This coincided with a short-lived, 10-30 m yr. lull in arc-style magmatism to the east. The subducting oceanic slab was thought to be still so shallow that it did not penetrate the asthenosphere and therefore did not promote large scale asthenospheric melting (Dickinson, 1989). The continued northeast-eastward migration of the slab's leading edge under the continent caused the peak interval of deformation in Rocky Mountains to the east and also contributed to the regional uplift and erosion across much of the southwest U.S. (Dickinson 1989). The earliest phase of extension, before rejuvenation of volcanism in the southern Basin and Range, represents a widespread erosional surface visible throughout much of the Southwest, and resulted in the deposition of the Whitetail conglomerate (Spencer and Reynolds, 1989; Leveille and Stegen, 2012; Figure 2.14).
By around 43 Ma, slab removal had begun in the south, with two progressive volcanic fronts advancing from the north and south, finally meeting in an area occupied by the Arizona-California-Nevada border (Humphries, 2009; Figure 2.14). Renewed Tertiary magmatism was accompanied by widespread extension in the western U.S. and Mexico, from the Oligocene (ca. 30 Ma; Dickinson 2002) to the Early Miocene (ca. 20 Ma). Large-scale W-SW-directed lithospheric extension was accommodated

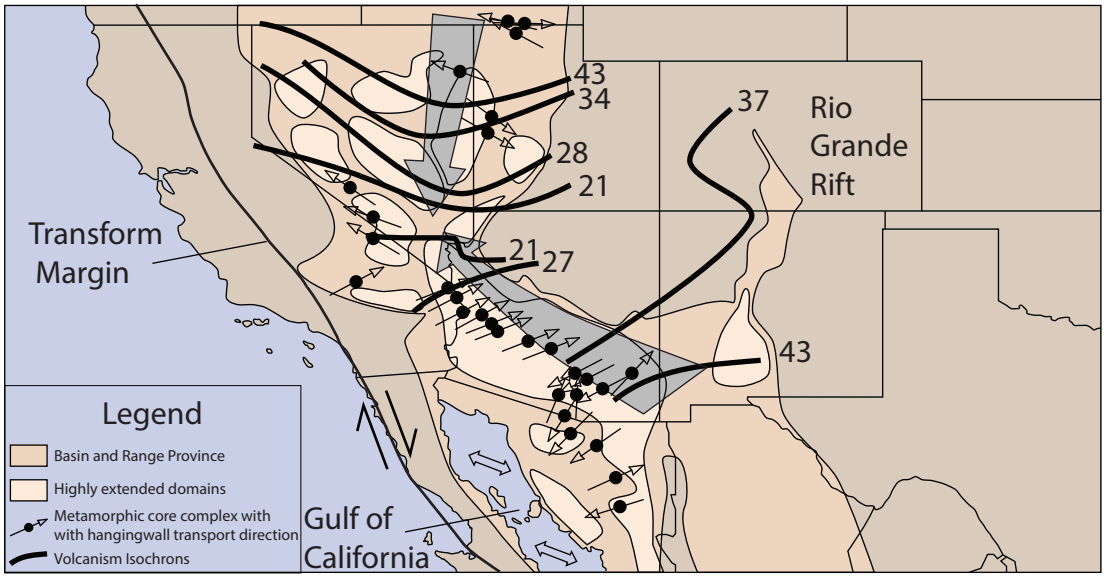


Figure 2.14 Map of Tertiary geologic setting of the southwestern United States, showing extended parts of the crust and location of metmorphic core complexes as well as the inward progression of volcanism, highlighting the diachronous nature of slab removal. Later reinitiation of transform tetonics also shown. Modified after Maher (2008) and Humphries (2009).

at upper crustal levels by movement along regional-scale low-angle detachment faults (Dickinson, 1991). Large displacement along these faults resulted in denudation and isostatic uplift of lower-plate mylonitic crystalline rocks that are now exposed in the centre of metamorphic core complexes (e.g., Catalina Mountains; Dickinson, 1998). Mylonitic fabrics produced by ductile shear along the down dip projections of detachment faults, and were then overprinted by brittle deformation and regional chlorite alteration (Spencer and Reynolds, 1898). The distribution of these features delineates the core of the modern Basin and Range province of western North America (Spencer and Reynolds 1989; Figure 2.14). The highest rates of extension were in the Early Miocene, broadly coeval with renewed and westward sweeping volcanism (Dickinson 1989; Spencer and Reynolds, 1989; Axen, 2008). An apparently non-magmatic corridor of rocks that avoided any significant extension located in NE Mojave, central Basin and Range, and under the Colorado Plateau. Reasons for this are poorly understood but may relate to crustal thickness (Axen, 2008), and was possibly a feature developed during Proterozoic accretion.

The profound geodynamic transition to widespread extension and renewed volcanism in the Mid-Tertiary is thought to be related to steepening, roll back and/or disintegration of the subducting Farallon Plate leading to introduction of new hot asthenosphere under the continental crust (Dickinson, 1989, 2002; Spencer and Reynolds, 1989; Spencer et al, 1995; Axen, 2008, Humphreys, 2009). Large scale lithospheric extension related to gravitational collapse of thinned crust with uplift occurring in response to slab unloading (Humphreys, 2009).

A transform plate margin began to evolve from the preceding subduction style margin as early as the Mid-Oligocene (~29 Ma; Axen, 2008). Extension occurring to the east of the Colorado Plateau in the Rio Grande Rift was essentially concurrent with the development of the San Andreas Fault zone along

Table 2.1 Summary of geodynamic events to have effected southwest North America.

| Event | | Crustal age (Ga) | Peak orogenesis Ga) | Deformation | Selected References |
|---|---|---|---|---|---|
| Paleoproterozoic accretion | Mojave assembly | Archean Core (?) 1.84 Elves Chasm and 1.8-1.7 Arcs | ? | Ductile accretion (?) | Wooden and Miller (1990); Barth et al. (2000); Coleman et al. (2001) |
| | Yavapai orogeny | 1.80 – 1.70 | 1.71 – 1.68 | Ductile | Karlstrom and Bowring (1988) Whitmeyer and Karlstrom (2007) |
| | Mazatzal orogeny | 1.70 – 1.60 | 1.65 – 1.60 | Ductile | Whitmeyer and Karlstrom (2007) |
| **Event** | | **Time Period (Ma)** | **Magmatism** | **Deformation** | **Selected References** |
| Mesoproterozoic Intracratonic Rifting | Basin development | 1330 – 1260 | Minor basaltic | Mild extension | Timmons et al. (2005) |
| | Dolerite intrusion | 1140 – 1040 | Major basaltic | NW directed compression, Post orogenic collapse and delamination | Bright et al. (2014) |
| Phanerozoic Margin Evolution | Paleozoic platform | ca ~540 – 250 | None | Transition from transform to rift margin | Dickinson (1989) |
| | Mesozoic arc development | ca. ~240 – 100 | Calc-alkaline, minor alkalic | initiation of E-dipping subduction zone, opening of Gulf of Mexico and border rift | Dickinson and Lawton (2001) |
| | Guerro accretion | ca ~200 – 100 | Calc-alkaline mafic-intermediate island arc | E-directed compression during accretion, possible influence on deeping of Border Rift System | Centeno-Garcia et al. (2008) |
| Sevier-Laramide Orogeny | Sevier phase | 85 – 75 | Calc-alkaline internediate - felsic continental arc | Thin skinned thrusting | Livacarri et al. (1991); Humphreys (2009) |
| | Laramide phase | 75 – 45 | | Basement core uplifts and monoclines | Humphries (2009) |
| Tertiary extension | Basin and Range | 55 – 21 | Slab removal and Asthenospehric upwelling | Gravitational collapse and extension | Spencer and Reynolds (1989) Humphreys (2009) |
| | Transform margin | 29 – present | Minor basaltic | Dextral transtension | Axen (2008) |

the west coast. The Mid-Miocene saw the continued development of the San Andreas fault and associated dextral faults, while rates of extension and core complex formation were slowing in the Basin and Range (Spencer and Reynolds, 1989; Axen, 2008; Humphreys, 2009). Towards the late Mid-Miocene, the extension direction rotated clockwise to the NW. By the latest Miocene, the San Andreas Fault Zone was well-established, dextral wrenching of the Gulf of California was underway and the Rio Grande Rift had opened (Dickinson, 2002; Axen, 2008, Humphreys, 2009).

### 2.3.8 Late Cenozoic Block Faulting and Subsidence

Volcanics and sedimentary rocks deposited between 12 and 5 Ma are not strongly tilted, but have been disrupted by late-stage, high angle faulting. This style of normal faulting is typically associated with cool, brittle crust, not necessarily expected in an area recently affected by hyper-extension and attenuation. Nevertheless, basin filling by deposition of the Gila conglomerate continued until the latest Miocene (Leveille and Stegen, 2012). Sporadic recent basaltic volcanism in Arizona (e.g., Axen, 2008) is associated more with upwelling through attenuated continental crust, rather than related to a subducting slab (Dickinson, 1989, Spencer and Reynolds, 1989; Axen, 2008). Fill thickness in many local terrigenous basins imply a structural relief of 2 – 4 km, with some of the deeper basin floors now 1 – 2 km below sea level. This Late Miocene structural regime is thought to have been curtailed by the transition to transform tectonics at the continental margin, due to a change in Pacific–North America Plate motion change from NNW to WNW at 8-7 Ma. This caused the Pacific Plate to move approximately parallel to the North America plate margin, inhibiting further extension (Humphreys, 2009).

## 2.4 Geodynamic Setting

The southwestern US was first brought together in an extended and chaotic period of crustal accretion from ca 1,700 – 1,600 Ma (Table 2.1). This was followed by a significant period of erosion before the deposition of the Apache Group sediments and minor related volcanics between 1,330 – 1,260 Ma. The region was then subjected to voluminous mafic magmatism at around 1,100 Ma, when dolerite sills intruded possibly in response to protracted Grenvillian orogenesis to the southeast.

During the Paleozoic, relatively stable passive margin conditions were established, with a number of marine transgressions in shelf carbonate sequences and minor terrestrial sedimentary rocks. During the Late Paleozoic to Early Mesozoic, a moderately east-dipping continental margin began to develop, most likely in response to the rifting of the Atlantic and break up of Pangaea. Around the time of arc initiation, the Caborca block, a segment of Proterozoic basement, is thought to have been translated along the enigmatic and contentious Mohave-Sonora Megashear (Silver and Anderson, 1979), or Coahuila-Tamaulipas Transform (Dickinson and Lawton, 2001), a large structure inboard of, but likely related to, the Proterozoic transform continental margin. This phase also included the accretion of the exotic Guerrero terrane, an intraoceanic island arc, which was welded to the continent during the Jurassic to

mid Cretaceous (Table 2.1).

By the mid Cretaceous the angle of subduction began to shallow and the arc transitioned into a state of compression, probably due to presence of a seamount or plateau on the downgoing Farrellon slab (Humphreys, 2009). Initially this was accommodated by the large scale thin-skinned thrusting of the Sevier Orogeny, with the Paleozoic passive margin sedimentary sequence thrust over the rigid crystalline basement (Table 2.1). This was succeeded around 80-75 Ma by thick-skinned basement cored uplifts and eastward arc migration of the Laramide Orogeny (Table 2.1). The flat slab subduction continued until approximately 50 Ma when progressive delamination and slab unloading began (Humphreys, 2009). This promoted voluminous asthenospheric upwelling and melting of the hydrated crust, leading to intense silicic volcanism (Spencer and Reynolds, 1989). Simultaneously the upper crust became hot and buoyant with the influx of mantle material, combined with the removal of the dense Farallon slab, so that the weaker parts began to extend and gravitationally collapse. This process lead to the formation of metamorphic core complexes and wider Basin and Range province (Dickinson, 1981). As the continental margin stabilised, dextral transpressional kinematics caused rifting of the gulf of California, and Rio Grande Rift, dynamics that continue to the present day (Table 2.1).

## 2.5 Metallogeny

### 2.5.1 Introduction

The Western US is one of the most intensely mineralised segments of the crust. Mineralisation types are varied and metallogenic events span a huge range in time and space. Three main mineralising time periods are broadly identified as having the most significant metallogenic potential in the western US, each of them with differing geodynamic controls.

### 2.5.2 Proterozoic metallogeny

Proterozoic mineralising processes in the Western US resulted in the formation of numerous deposit styles (Table 2.2). Towards the end of the Paleoproterozoic and prior to the onset of the main Yavapai Orogeny, volcanic-hosted massive sulfide (VHMS) deposits formed in a continental back-arc setting (Lindberg, 1989). This was followed by Paleoproterozoic porphyry Cu-Mo mineralisation (Sillitoe, 2014), presumably related to subduction and crustal assembly of the Yavapai Orogeny. During the Mesoproterozoic, the intrusion of dolerite sills at ca. 1,100 Ma is thought to be responsible for the emplacement of apparently small, but multi-commodity mineral occurences in the Apache Group basin (Wrucke et al., 1986).

#### 2.5.2.1 VHMS mineralisation

The Yavapai province hosts significant Precambrian mineralisation. These deposits are important

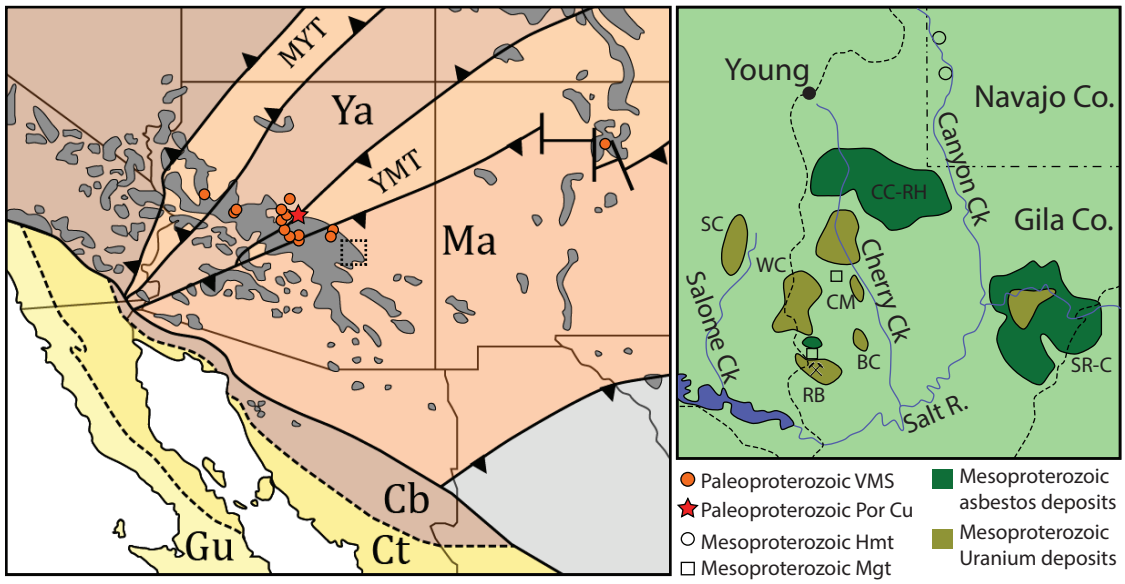


Figure 2.15 A. Paleoproterozoic ore deposits in southwest North America, shown relative to the distribution of Proterozoic outcrops. B. Mesoproterozoic U (Cu) - Fe - Asbestos deposits of the Apache Group in the Sierra Ancha region. Modfied after Wrucke et al. (1986).

both economically and with regard to the geodynamic development of Arizona. The mineralisation is dominantly of VHMS type. Paleoproterozoic porphyry Cu-Mo mineralisation was reported from Squaw Peak by Sillitoe et al. (2014). The most important Proterozoic VHMS districts in Arizona are the Cu-rich Verde district near Jerome, and the Pb-Zn-rich Big Bug and Old Dick districts, near Humboldt and Bagdad respectively (Figure 2.15). These districts account for >92% of all production from VHMS deposits in Arizona (Lindberg, 1989). The Jerome district produced 93% of all Cu mined from VHMS deposits in the southwestern US. Jerome was originally thought to be a replacement style deposit by early workers (e.g. Anderson and Creasey, 1958) but a volcanogenic model has been advocated in more recent appraisals (Lindberg 1989; Titley and Zürcher, 2008). The Big Bug (Humboldt) district near Bagdad includes numerous workings, the most significant of which are the Iron King and Boggs mines, which together produced 98% of the Pb and 62% of the Zn from this district. The deposits are hosted in Yavapai age rocks that are considered to represent an accreted intra-oceanic island arc (Lindberg, 1989). The ages of these deposits are around 1,700 Ma, making them part of a global family of stratabound, volcanogenic deposits (Titley and Zurcher, 2008). Ore controls are dominantly stratigraphic, with many deposits occurring at the interface between mafic-intermediate and felsic volcanics, commonly associated with exhalative iron cherts.

#### 2.5.2.2 Porphyry Cu-Mo mineralisation

The recently identified Proterozoic age for the Squaw Peak porphyry Cu-Mo prospect signals the recognition of a previously unknown porphyry-forming metallogenic event around 1735 Ma (Sillitoe et al., 2014). The apparent lack of other porphyries of this age in this region could be due to Mesozoic

Table 2.2 Summary of major Proterozoic districts and ore deposits in the southwest USA.

| District | | Significant Deposits | Deposit Style | Host Rocks | Production and ore grades | References |
|---|---|---|---|---|---|---|
| Jerome | | United Verde, UVX, Verde Central | VHMS | ~1,790 Ma Caldera-forming submarine rhyolite crystal tuff | 33.7 Mt @ 4.8% Cu, 0.0009% Pb, 0.13% Zn | Karlstrom and Conway (1986); Lindberg (1989); Titley and Zurcher (2008) |
| Humbolt | | Big Bug, Old Dick | VHMS SEDEX | Bimodal volcanics | 7 Mt @ 0.9% Cu, 1.8% Pb, 8% Zn | Anderson (1968); Gilmour and Still (1968); Lavery (1985); Lindberg (1989)' Titley and Zurcher (2008) |
| Camp Verde | | Squaw Peak | Porphyry Cu-Mo | ~1,740 Ma granodiorite, Cherry batholith | 40 Mt @ 0.31% Cu, 0.07% Mo, 2 g/t Ag | Sillitoe et al. (2014) |
| Sierra Ancha | Asbestos | Chrysotile-Salt River, Cherry Creek-Rock House, South Siera Ancha | Unclassified | Lower Member, Mescal Limestone | 75,000 t high grade spinning fibre | Bateman, (1923); Wilson, (1928); Stewart, (1955) |
| | Uranium | Workman Creek | | Grey and Red Units, Upper Dripping Springs Quartzite | 8.8 M lbs @ 0.11% $U_3O_8$ (reserve) 21,851 t @ 0.24% $U_3O_8$ (produced) | Granger and Raup (1964); Nutt, (1981) |
| | Iron | Fort Apache | | Precambrian karst altered Mescal Limestone | 14.4 Mt @ 20-67% Fe (Reserve) | Burchard (1931); Harrer, (1964) |
| | | Zimmerman Point | | | 15 Mt @ 26.5 % Fe (reserve) | |
| | | Centre Mountain | | | 6 Mt @ 40-60% Fe (reserve) | |
| | Hydro-carbons | N/A | | Black facies, Upper Dripping Springs Quartzite<br>Argillite Member, Mescal Limestone | 100-3500 ppm pyrolisable hydrocarbon (average) | Wrucke et al. (1986) |

– Tertiary cover, and/or the depth of erosion that has affected Proterozoic arc rocks. Either way, the small size of the Squaw Peak system and lack of similar aged deposits make the Proterozoic porphyry event insignificant compared to the Laramide. Still, it has been speculated that Proterozoic VHMS and porphyry mineralisation in Arizona could have preconditioned the mid-upper crust with copper, at least in this area of Proterozoic basement (Sillitoe, 2014).

#### 2.5.2.3 Magmatic Cu-Ni-PGE mineralisation

The 1100 Ma dolerite sills in the southwest US were emplaced coeval with the well-endowed Mid-Continent rift suite in north eastern North America. This raises the question as to whether there is possibility of magmatic Cu-Ni-PGE reserves associated with Proterozoic dolerite sills in Arizona.

#### 2.5.2.4 Ore deposits hosted by the Apache Group

***Asbestos***

Small asbestos occurrences in Arizona, typically exposed in steep canyon walls such the Salt River Canyon, were being reported as early as 1872 (Figure 2.15; Table 2.2). At that time, they were they the only known source of high quality spinning fibre on the American continent, which was in high demand for use as electrical cable coverings, especially on warships (Stewart, 1955). This meant despite the inaccessibility and high stripping ratio (1:30) approximately 35,000 tons was removed by the mid 1950s, after founding the town of Chrysotile. Unusually, the fibrous chrysotile occurs as discontinuous, sub-parallel veins in bands of serpentine, hosted within the Mescal Limestone (Wrucke et al., 1986). The serpetinised bands are stratigraphically controlled, occurring at the top of the Lower member, commonly exhibiting significant bedding parallel slip and dilation. Locally, chrysotile mineralisation can also be found in fault zones. A critical observation of these deposits is the presence of dolerite sills within 8-10m from this favourable stratigraphic horizon, leading early workers to interpret that these deposits were sourced from the dolerite sills (Bateman, 1923; Wilson, 1928, Wrucke et al., 1986). Previous interpretations of the origin of the chrysotile are wide ranging and typically vague, including metamorphic reaction of dolomite and chert (Wrucke et al., 1986) and precipitation from magnesium-rich fluids emanating from the diabase (Wilson, 1928, Shride, 1944, Stewart, 1955). The most likely ore-forming process remains the intrusion of the hot dolerite sills into water-saturated sediments with localised remobilisation of magnesium from the dolomitic Mescal Limestone into faults and fractures.

***Uranium***

Uranium first described in the early 1950s at the Red Bluff deposit, occurs throughout the upper member of the Dripping Springs quartzite of the Apache Group (Granger and Raup, 1969; Figure 2.15  Table 2.2). However, despite their broad extent, the limited size and tenor of the ~100 known deposits led the USGS to declare them uneconomic by 1956 and only limited work was conducted since that time. Uranium is concentrated in stylolite-like features as well as diffuse indeterminate 'vein' zones and lesser tabular or blanket deposits in and around fracture zones in the grey unit in the upper Dripping Springs quartzite. In both cases the mineralised zones are visually difficult to distinguish from the wall-rocks and have been determined almost exclusively by radioactivity measurements (Wrucke et al., 1986). Across one vein zone at small deposit in the Sierra Ancha region, elevated Fe, S, U, Pb, Cu, Ni, Co, Mo, Be

and REEs are reported, indicating that the hydrothermal fluid was enriched in these elements (Granger and Raup, 1969). Silver and Sn are also variably enriched. Typically these vein zones are very limited and extended no more than 100 m along strike and up to 1m wide. Primary ore minerals consist of uraninite, pyrrhotite, pyrite, chalcopyrite, galena and rare molybdenite, cubanite, and Fe-sphalerite. The most common gangue minerals reported are chlorite, calcite, ankerite and phlogopite with lesser fluorite. Weathering produces an array of secondary U and/or Cu species, including metatorbernite ($Cu(UO_2)_2(PO_4)2{\cdot}8(H_2O)$) as well as other secondary phosphate minerals, suggesting primary phosphorus bearing minerals are also present (Granger and Raup, 1969; Wrucke et al., 1986).

The competency and brittle fracturing observed in the grey unit is interpreted to have aided the focussing of oxidised fluids, while the chemically reducing agents of high organic carbon and diagenetic sulfide catalysed precipitation of the ore minerals (Wrucke et al., 1986). The presence and crystallinity of uraninite, molybdenite and Fe-sphalerite all suggest the ore deposition took place at relatively high temperatures. Uraninite bearing deposits are not recognised more than 100m from a dolerite sill and the size of the sill appears to have a bearing of the significance of the deposit (Granger and Raup, 1969), empirically suggesting a genetic association.

Uraniferous stylolites occur in the upper member of the Dripping Springs quartzite, and have been interpreted as products of diagenetic compaction and dissolution of the rock volume accompanied by concentration of U along stylolites (Granger and Raup, 1969). This is followed by remobilisation an re-precipitation in diffuse fracture networks in the coherent parts of the uraniferous grey unit, that relate to the pre-dolerite monocline development (Wrucke et al., 1986). Concentration of U was therefore a three stage process; (1) weathering and sedimentation of an anomalously uranogenic granite, (2) compaction, dissolution and development of stylolites and (3) hydrothermal remobilisation and structural focussing during dolerite emplacement. Some workers have interpreted the hydrothermal fluids, their constituent U and other metals, to be derived entirely from the differentiation of the dolerite, citing chemical evidence that the dolerite lost U during crystallisation (Neuerburg and Granger 1960). This particular study rests on a number of assumptions, most importantly, that the fluid itself originated from progressive dolerite differentiation, which seems unlikely. Despite this, a close spatial association between dolerite emplacement and U (+/- Cu Pb-Zn-Ag) deposits of the Dripping Springs is evident.

***Iron Ore***

Small quantities of iron ore (20-60 % Fe; Table 2.2), in the form of both hematite and magnetite, occur in the Mescal Limestone and to a lesser extent the Troy Quartzite. They are somewhat widespread throughout the northern part of the Apache Group, close to the Mogollon Rim, and in the southern Sierra Ancha region. The largest iron concentrations are hematitic, and occur in silicic and jaspilised portions of the karst-modified Mescal limestone, close to major dolerite intrusions. The most significant of these is the Fort Apache deposit, located in Canyon Creek (Burchard, 1931, Harrer, 1964; Table

2.2). The orebody ranges from soft, red, earthy hematite, to hard, grey and dense, with local specular hematite. Previous interpretations suggest that hematitic material, derived from lateritic weathering of the overlying basalt, accumulated in voids left by weathering of the Mescal limestone (Harrer, 1964; Wrucke et al., 1986). During the emplacement of the dolerite, hematite was partly or completely converted to magnetite (Harrer, 1964). None of these deposits have been developed as sources of ore.

***Hydrocarbons***

Kerogen has been found in unmetamorphosed rocks of the pyritic black facies and the argillite member of the upper Dripping Springs Quartzite (Desborough, 1984; Wrucke, et al., 1986). Average pyrolisable hydrocarbon values range from 100 – 3500 ppm (Desborough, 1984), although no significant accumulations are known. It remains unknown whether the source lithologies ever contained enough kerogen for hydrocarbon migration. Nevertheless, the presence of kerogen in these sediments not only has implications as a potential ligand for any subsequent hydrothermal system but also for the biotic evolution of the Apache Group basin and oil potential of Mesoproterozoic rocks world-wide (cf., Jackson et al., 1986; Dutkeiewicz et al., 1998).

***Copper***

Copper mineralisation of Proterozoic age was reported from steeply dipping mineralised faults in parts of the Grand Canyon area. Noble (1914) described two of the largest fault-veins from Copper Canyon. They consist of cuprite, chalcopyrite, bornite, chalcocite and argentiferous galena hosted in faults that display normal kinematics and cut basement Paleproterozoic schist and pegmatite as well and Mesoproterozoic Unkar group strata. The mineralised faults are truncated at the base of the Paleozoic sequence (Noble, 1914). These broad timing relationships suggest that mineralisation occurred coeval with a period of regional extension, after deposition of the Unkar group and intrusion of the dolerite sills. Hydrothermal activity related to intrusion of dolerite sills is tentatively suggested by Noble (1914), although he also recognised that some sills have been offset by the mineralised. It may be that these veins represent the Cu-rich end member of the Arizona U-Cu systems. Although these systems are currently considered small, they could have a broader regional extent than previously recognised.

***Hydrothermal alteration of dolerite sills***

Most of the previous interpretations regarding the mineral commodities of the Apache Group have related mineralisation in some way to intrusion of the dolerite sills, and some allude to alteration of the dolerite itself (e.g., Granger and Raup, 1969; Wrucke et al., 1986). This alteration has been identified in many petrogenetic studies of the dolerite (e.g. Shride, 1967; Smith, 1969, 1970; Nehru and Prinz, 1970; Fouts, 1974; Hammond, 1983). In all cases, alteration has been classified as ‘deuteric’, an out-dated term referring to an autochthonous, late-stage magmatic fluid and associated alteration, comparable to the formation of greisen in felsic rocks (Allaby, 1999).

Detailed examination of alteration in dolerite sills in the Death Valley region by Hammond (1983), revealed that the alteration could be defined using two end-member assemblages, 'greenschist' and 'amphibolite'. In the greenschist assemblage, clinopyroxene experienced only weak alteration, mainly to chlorite and epidote with or without actinolite, whereas plagioclase was thoroughly altered to a mixture of zoisite, epidote, sericite and albite (termed 'sausseritization' by Hammond, 1983). Hornblende is absent. In the amphibolite assemblage, plagioclase is largely intact whereas pyroxene has been almost completely replaced by hornblende and biotite, with rare or no chlorite and epidote. Intermediate alteration assemblages were also noted that show features pertaining to both assemblages (Hammond, 1983).

The preservation of olivine and the lower degrees of alteration distinguish the alteration of dolerites in Death Valley (Hammond, 1983) from the alteration observed in Arizona. In Arizona, the dolerites are less extensively altered and finer grained. Hammond (1983) interpreted the more intense alteration in Death Valley to relate to late magmatic fluids derived from differentiation of the sills, confined by impermeable overburden, thereby retaining heat and fluid and intensifying the effects of alteration. In contrast, the local observation of pegmatites and granophyric dikes in Arizona were interpreted by Hammond (1983) to represent rapid escape of these hydrothermal fluids and therefore lesser degrees of alteration in the dolerite sills.

Dolerite sills hosted in shallow, water-saturated sedimentary rocks are more altered that those emplaced in deeper crystalline basement (Hammond, 1983). There have been widespread observations of syn-emplacement soft sediment deformation in the upper parts of the host sedimentary package in the Death Valley region (Hammond, 1983), implying that interaction with surface waters was the major control on degree of alteration in the Proterozoic dolerites, rather than confinement of in-situ magmatic fluids derived from the dolerites. Some crustal water could have been incorporated at depth during assimilation of lower crustal material into the dolerite, however evidence for this process is only apparent in some of the dolerite sills and is therefore considered negligible (Hammond, 1983). Instead, it seems likely that the emplacement depth into a weakly consolidated, water-saturated sedimentary pile combined with groundwater depth, exerted the primary control on the amount of crustal fluid that interacted with the dolerite magma and therefore the degree of alteration (i.e., Death Valley dolerite sills were probably emplaced at shallower, more water saturated levels than those in Arizona). Initially however, the steep temperature gradient between the dolerite and the country rocks would have expelled water. Alteration of the dolerite is most likely to have occurred during retrograde cooling, when fluids could migrate into the intrusive complex. The 'greenschist-amphibolite' mineralogical spectrum suggested by Hammond (1983) for dolerite of California, therefore probably reflect differences in temperature as a result of numerous factors such as thickness of sill, cooling rate, distance from the intrusive margin and depth of emplacement.

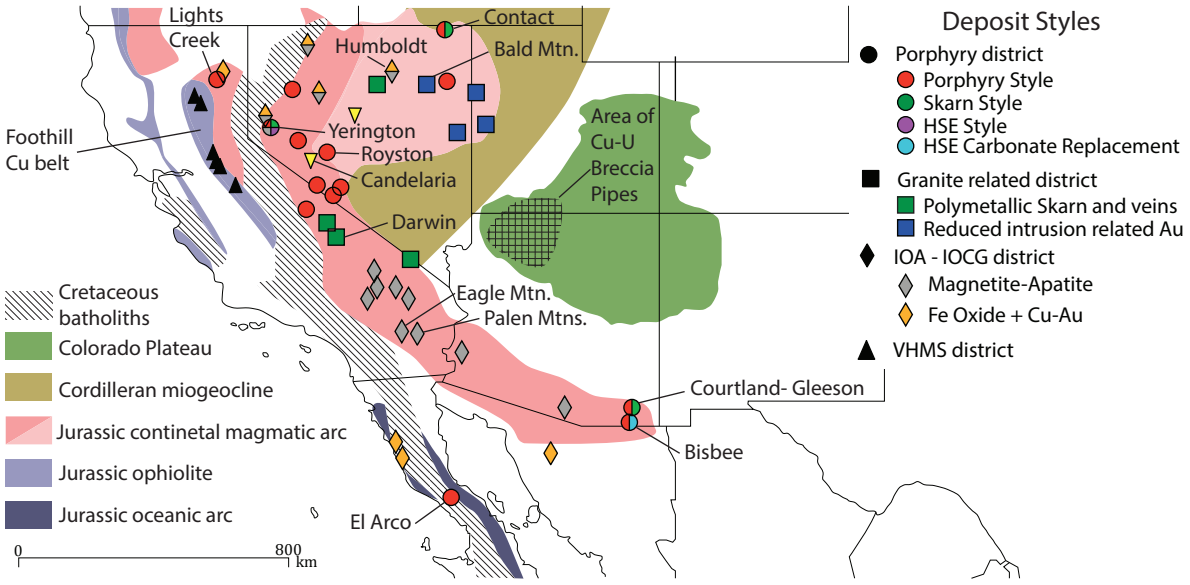


Figure 2.16 Map showing distribution and types of major mineral districts from the Early - Mid Mesozoic. Modified after Barton et al. (2001).

### 2.5.3 Early - Mid Mesozoic Metallogeny

#### 2.5.3.1 Introduction

The Mesozoic was the next major time period for mineralisation in Arizona and can be subdivided into two major styles. First, early in the Mesozoic, largely prior to the subduction initiation, basinal processes produced an MVT-style mineralisation in and around the Colorado plateau. Later, magmatic-hydrothermal deposits such as porphyry and IOCG formed in response to the establishment of the magmatic arc (Figure 2.16; Table 2.3).

#### 2.5.3.2 Cu-U breccia pipes

A peculiar, but important class of Mesozoic deposits are exposed in the walls of the Grand Canyon and throughout the Colorado plateau, inboard of the Mesozoic arc and back-arc domains (Figure 2.16). Copper-uranium mineralised breccia pipes developed in Paleozoic and younger rocks (Wenrich, 1985). The breccias are enriched in a wide range of elements but were primarily worked historically for U and to a lesser extent, Cu. The breccia pipes are mostly rooted in Mississippian Redwall Limestone (northern equivalent to the Escabrosa Limestone) and are interpreted to have formed as a result of solution collapse processes that occurred during karst development from the Mississippian to the Triassic (Wenrich, 1985). Mineralisation consists of uraninite associated with sphalerite, galena, chalcopyrite, tennantite, millerite, siegenite and molybdenite. Surficial encrustations of malachite also occur, locally associated with exceptional silver enrichment. Abundant pyrite and high organic carbon, including bitumen in some instances, acted as reductants for U precipitation (Wenrich, 1985). Mineralisation occurred over at least two time periods, ca. 260 Ma and 200 ± 20 Ma. The latter age is similar to the late Triassic stratabound uranium occurrences of the Colorado Plateau, including Promontory Butte, Arizona and

Mi Vida, Utah (Ludwig and Simmons 1992). The Triassic Chinle Formation contains felsic volcanic ash enriched in U, and leaching of U from this formation is inferred to have been the dominant source of U (Ludwig and Simmons, 1992). More broadly, the U/Pb ages link the deposits to the formation of the Midcontinent MVT districts (Wenrich and Titley, 2008). Fluid inclusions analysed from calcite, dolomite, quartz and sphalerite breccia cement have homogenisation temperatures of 80-140°C and salinities of >23 wt% NaCl, supporting an affinity to Mississippi Valley-type deposits and basinal brines (Wenrich and Titley, 2008). The Cordilleran passive margin to the west coupled with basement uplifts to the east are likely to have resulted in basin dewatering as a major mechanism for fluid flow (Wenrich and Titley, 2008). Mixing of oxidised groundwaters derived from overlying sandstones with reducing brines that had entered the pipes due to dewatering of the Mississippian limestones is considered as the main ore-forming mechanism for these deposits (Wenrich and Titley 2008). Mineralising fluids are thought to have interacted to a greater or lesser extent with Proterozoic basement along reactivated high angle faults. Lead isotope compositions in sulfides from uraniniferous pipes compared to those from the U-poor breccias suggest that the degree of interaction with Proterozoic basement was an important factor for the formation of the mineralised orebodies. Regardless of the reasons for these isotopic differences, their existence could readily be utilised for exploration.

#### 2.5.3.3 Porphyry, epithermal and IOCG mineralisation

Mineralisation was widespread along the Jurassic – Cretaceous magmatic arc of the western United States and extended into the central Great Basin (Barton et al., 2011), yet few deposits of Mesozoic age occur in Arizona (Table 2.3). Most known Jurassic mineralised centres are porphyry Cu or IOCG and are found in eastern California and northern Nevada with a few occurrences found in southern and Baja California (Barton et al., 2000; Staude and Barton, 2001). The best studied example in the western United States of Jurassic porphyry Cu (-Mo-Au) and related skarn deposits are in the Yerington district, Nevada (168–169 Ma; Dilles, 1987). This district is located in a back-arc position towards the northern end of the pre-Laramide Mesozoic arc and outside the traditional SW US porphyry Cu province. At Yerington, Sr isotope data unequivocally demonstrate the involvement of basinal fluids both in the porphyry centre and more distal IOCG-like deposits such as Pumpkin Hollow (Dilles et al., 1995). Other notable Jurassic deposits include Bisbee, Arizona (200 Ma; Lang et al., 2001) and El Arco, part of the exotic Guerrero Terrane in Baja California (165 Ma; Valencia et al., 2006; Figure 2.16). In these, as in other well-mineralized areas, multiple types of mineralisation are present. For instance, at Bisbee, massive sulfide-style carbonate-hosted high sulfidation replacement ores surround advanced argillic alteration in the upper part of a composite porphyry centre (Einaudi, 1982; Titley and Zürcher, 2008). Bisbee formed in a back-arc location (Bassett and Busby, 2005). The observation that both known continental Jurassic porphyry districts likely occupied an active back arc location and are generally small in comparison to later Laramide systems, suggests that the arc was probably subject to

Table 2.3 Summary of significant mineral districts and deposit styles of the Jurassic.

| District | Age (Ma) | Selected deposits | Mineralisation style | Resource estimates | References |
|---|---|---|---|---|---|
| Bisbee | 201 | Bisbee | Porphyry-Cu | 346 Mt @ 0.65% Cu | Bryant (1966), Einaudi (1982), Lang et al., (2000) |
| | | | HSE carbonate replacement | | Bryant (1966), Einaudi (1982), |
| Yerington | 168-169 | Yerington, Ann Mason | Porphyry Cu | 928 Mt @ 0.51% Cu, 495 Mt @ 0.4% Cu | Proffett and Dilles, 1995, Dilles et al., 2000 |
| | | Copper Casting, Mason Valley | Cu Skarn | 0.45 Mt @ 6% Cu; 1.5 Mt @ 3% Cu | Einaudi (1977) |
| | | Alunite Hill | HSE | Not reported | Lipske and Dilles, (2000) |
| | | Pumpkin Hollow, Buckskin | IOCG | 26 Mt @ 1.1% Cu; 0.2 Mt 1.5% Cu; | Proffett and Dilles, (1995); Dilles et al., (2000); Runyon et al., (2015a) |
| El Arco | 165 | El Arco | Porphyry-Cu | 1.02 Mt @ 0.51% Cu | Echavarri-Perez and Rangin (1978) |
| Lights Creek | 148 | Moonlight Creek | Porphyry Cu | 318 Mt @ 0.34% Cu | Storey (1978); Dilles and Stephenson (2010) |
| | 178 | Moonlight Valley, Engles and Superior | IOCG | | Storey (1978); Dilles and Stephenson (2010) |
| Bald Mountain | 159 | Bald Mountain | IRG skarn, polymetallic veins | 188.9 Mt @ 0.6 g/t Au | Nutt et al., (2007); Kinross Gold (2015) |
| Darwin | 155 | Darwin | Polymetallic skarn | 1.1 Mt @ 6% Pb, 6% Zn, 0.2% Cu, 170 g/t Ag | Newberry et al., (1991) |
| Candelaria | 192 | Candelaria | L-ISE | 4.5 Mt @ 137 g/t Ag, 0.2 g/t Au | Thompson et al., (1995) |
| Humboldt | 165-170 | Mineral Basin | IOA | 170 Mt @ 33% Fe | Johnson and Barton (2000) |
| | | Boyer, White rock | IOA | | Barton (2000) |
| Eagle-Palen | 165 | Eagle Mountain | IOA | 120 Mt @ 65% Fe | Dubois and Brummet, (1968); Mayo et al., (1998) |
| | | Palen Mountians | IOA | Not reported | Stone et al (1985), Fackler-Adams et al., (1997) |
| Foothills Cu belt | 160-165 | Penn | VMS | 0.88 Mt @ 4.24% Cu, 1.14% Zn, 2.3 g/t Au | Heyl (1948); Kemp (1982); Mattinen and Bennett (1986) |
| | | North Keystone | HSE | 0.21 Mt @ 2.2 % Cu | Clark and Lyndon (1962) |

Abbreviations; HSE = high sulfidation epithermal, IOCG = iron-oxide-copper-gold; IRG = intrusion-related gold; L-ISE = low- to intermediate sulfindation epithermal; IOA = iron-oxide-apatite; VMS = volcanogenic massive sulfide.

neutral to only weakly compressional tectonic regime at the time of formation (e.g., Leveille and Stegen, 2008) suggesting that flat slab style subduction was not occurring during the Jurassic (cf., Cooke et al., 2005). The lack of larger Jurassic porphyry systems could also relate to the deep level of erosion observed in rocks of this age (e.g. the widespread plutonic rocks of the Sierra Nevada; Figure 2.16)

The largest Mesozoic IOCG districts of the western United States, each of which contains multiple

deposits, are aligned along the main trend of the arc, and notably all are inboard of the Jurassic shoreline (Figure 2.16). Scattered IOCG prospects in western Baja California most likely belong to a separate belt in the Guerrero Terrane of Late Jurassic or Early Cretaceous age (Barton et al., 2011). The largest IOCG Cu resources are located north of the SW US porphyry province, mostly in the Yerington district (Figure 2.16). These deposits are formed by non-magmatic, (e.g., basinal or surface-derived) fluids during the Mesozoic, consistent with the progressive westward arc migration and associated back arc extension in the western United States during the Jurassic (Barton and Johnson, 1996).

Jurassic mineralisation can be split into two broad episodes, one at ~210 – 190 Ma and the other at ~155 – 170 Ma, which correspond to ill-defined pulses of magmatism (Barton et al., 2011). Early Jurassic mineralisation was fairly sparsely developed. It occurs mainly along the arc from southern Arizona, with porphyry Cu and associated carbonate replacement systems (e.g., Bisbee, Courtland-Gleeson; Lang et al., 2001) through eastern California - western Nevada (e.g., Candelaria, Thomson et al., 1995; Royston, Seedorff, 1991), and into northern California (Lights Creek, 178 Ma; Dilles and Stephens, 2010) where IOCG systems dominate. Few deposits are known to have formed between 190 and 170 Ma, coincidental with a lack of intrusions of this age (Barton et al., 2011). The second episode, to which most porphyry Cu and IOCG systems further north belong, correlates with a mid-Jurassic magmatic flare-up that affected areas in the Great Basin, seemingly much more so than the southwest (Barton, 2011).

This distribution of deposit types in space and time could reflect changing metallogenic and magma-forming controls northwards, related to the contrasting subduction styles in the southern part of the arc, compared with the north (section 2.3.5). It could also reflect a lack of preservation, demonstrated by the deep levels of erosion in Jurassic systems further south (Titley and Zürcher, 2008; Barton, 2011; Leveille and Stegen, 2012; Figure 2.16).

The lack of flat slab style tectonics in the western United States during the Mesozoic most likely hindered the development of large scale porphyry systems, such as those associated with the later Laramide period. Pre-Laramide magmatism was more diverse (e.g. alkali Ko Vaya suite in Southern Arizona; Tosdal et al., 1989; Haxel et al, 2008; Leveille and Stegen, 2012) suggesting that metallogenic controls were local, erratic and did not affect large areas of the crust coherently. Indeed, the three significant porphyry deposits of this period (Bisbee, El Arco and Yerington) all appear to have had entirely different first order controls on their emplacement (Table 2.3). Consequently, most of the economic Mesozoic deposits are composite in nature, i.e., they contain both porphyry-style high-temperature acid alteration, IOCG-style sodic-calcic alteration with sulfide-poor mineralisation, telescoped high sulfidation systems or combinations thereof (Table 2.3). Some districts contain hybrid alteration systems (e.g., porphyry and IOCG) with mixed fluid sources (e.g., Yerington; Dilles et al., 1995), others have undergone telescoping of a single fluid source (e.g., Bisbee; Titley and Zurcher, 2008). Others districts are composite systems

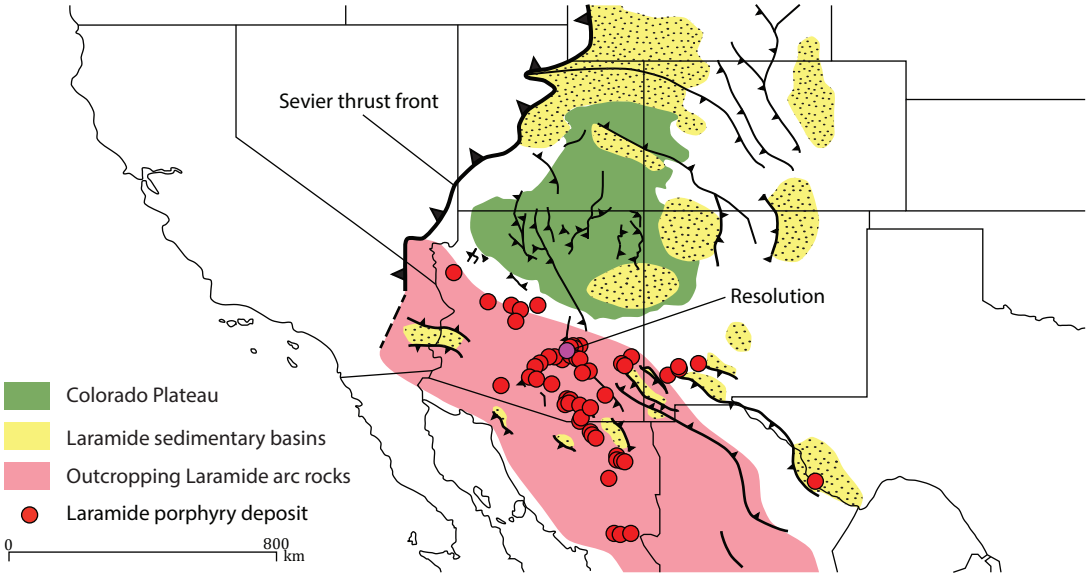


Figure 2.17 Laramide metallogenic map, showing distribution and types of major deposit overlain on Laramide outcrop and structural information. Modified after Leveille and Stegen (2012).

where temporally and compositionally distinct hydrothermal systems were superimposed (e.g., Lights Creek; Barton et al., 2011). Importantly though, most of the Mesozoic rocks have been eroded to plutonic levels, i.e. below the root zones of any pre-existing porphyry Cu deposit (Barton et al., 1988).

### 2.5.4 Laramide Metallogeny

The Laramide orogenic event occurred from 80 to 45 Ma (Leveille and Stegen, 2012). It was a time of regional compression and crustal thickening in western North America, related to the flattening of the Farallon slab and an attendant rise in crustal heat flow (Titley and Zurcher, 2008; Leveille and Stegen, 2012). Unusually for this style of tectonism, flat slab subduction was accompanied by extensive regional volcanism (c.f. Central Chile; Cooke et al. 2005; Hollings et al. 2005). Although later Tertiary erosion has removed as much as 2-3 km from the original tops of many Laramide volcanic systems, some remain deeply buried as a result of subsequent Basin and Range faulting (e.g., Resolution, Mankse and Paul, 2002).

Porphyry Cu-Mo (± Au) deposits and associated replacement style mineralisation are the major ore styles formed during this period, and represent the third largest accumulation of porphyry style Cu on Earth (Cooke et al., 2005). Epithermal base and precious-metal veins also formed in the region at this time but are generally related to the emplacement of porphyry systems (Figure 2.17; Table 2.3). Carbonate hosted, high temperature replacement systems, such as that noted earlier with regard to Bisbee, require some disambiguation. Although commonly grouped with skarn deposits in some metallogenic reviews as 'SKHTR' (SKarn, High Temperature Replacement) these deposits differ from traditional skarn deposits in that they do not exhibit either prograde or retrograde skarn mineralogy. Instead these deposits have alteration assemblages and ore mineralogies consistent with high sulfidation epithermal deposit styles.

Based on the available descriptions, these systems are inferred to be the product of shallow level high sulfidation mineralisation within a carbonate dominated stratigraphy, similar to the well-documented Peruvian systems of Colquijirca (Bendezu and Fontboté, 2009) and Cerro de Pasco (Baumgartner et al., 2008). In carbonate rocks, highly acidic magmatic-hydrothermal fluids are effectively neutralised and metals are concentrated within high grade accumulations, usually with a manto-type (sub horizontal, tabular) morphology. The carbonate hosted deposits of Arizona that have these characteristics will be referred to hereafter as high sulfidation epithermal (HSE) carbonate replacement deposits.

Laramide orogenic gold deposits are interpreted to have originated from deep metamorphism and possible dehydration of Proterozoic rocks (Goldfarb et al., 2005; Titley and Zürcher, 2008). They have been recognized in the relatively exhumed northwestern portion of Sonora and contiguous Arizona and California (Figure 2.17). In Mexico, available radiometric dates for these deposits suggest syn-orogenic Laramide mineralisation between 67 – 45 Ma (Iriondo and Atkinson 2000; Quintanar-Ruiz, 2008; Izaguirre et al., 2015). In the United States, ages of similar deposits remain poorly constrained. Some may in fact be Tertiary in age and related to detachment faults (Titley and Zürcher, 2008).

#### 2.5.4.1 Regional - district structural control

Laramide mineralised structures in Arizona are dominantly E-NE striking and dip at high angles (e.g., Rehrig and Heidrick, 1972; Heidrick and Titley, 1982). Mineralisation was localised around extensional areas in overall compressional setting. Structures that appear to have acted as first and second order controls include fault-fold bounded basement cored uplifts (BCUs) and associated sedimentary basins and WNW striking left lateral faults (e.g., those described by Krantz, 1989). It appears that these uplifted blocks were transported along reactivated faults and reflect a pre-existing basement architecture. The inherited fault architecture, coupled with the calculated principal stress direction ($75^0$ NE) during the Laramide, was largely responsible for the regional structural controls on emplacement of these deposits (Timmons et al., 2001; Titley and Zürcher, 2008, Leveille and Stegen, 2012). Even a brief appraisal of regional magnetic data (e.g., Leveille and Stegen, 2012) suggests that this part of the crust is highly segmented. Map patterns of the distributions of Laramide porphyry deposits draw attention to coincident long, linear laterally continuous magnetic features (Figure 2.17). The lineaments have been grouped broadly as the NE-striking Jemez Zone and NW-striking Texas Zone (e.g., Leveille and Stegen, 2012). The Texas Zone follows a structural grain developed during the final stages of the Grenvillian Orogeny in the Late Mesoproterozoic, recording a period of NE-directed extension (Timmons et al., 2001), but may have existed as early as the Yavapai Orogeny, acting as transform cross-arc structures. The Texas Zone lineament is followed closely by the Nacozari-Cananea-Sunnyside trend as well as the Jurassic Border Rift System and Laramide sedimentary basins (Figure 2.17). The NE-trending Jemez Zone is better known in the Colorado mineral belt 350 km to the north, but is also thought to follow a Proterozoic shear zone, in some way related to the boundary of the Yavapai and Mazatal crustal provinces

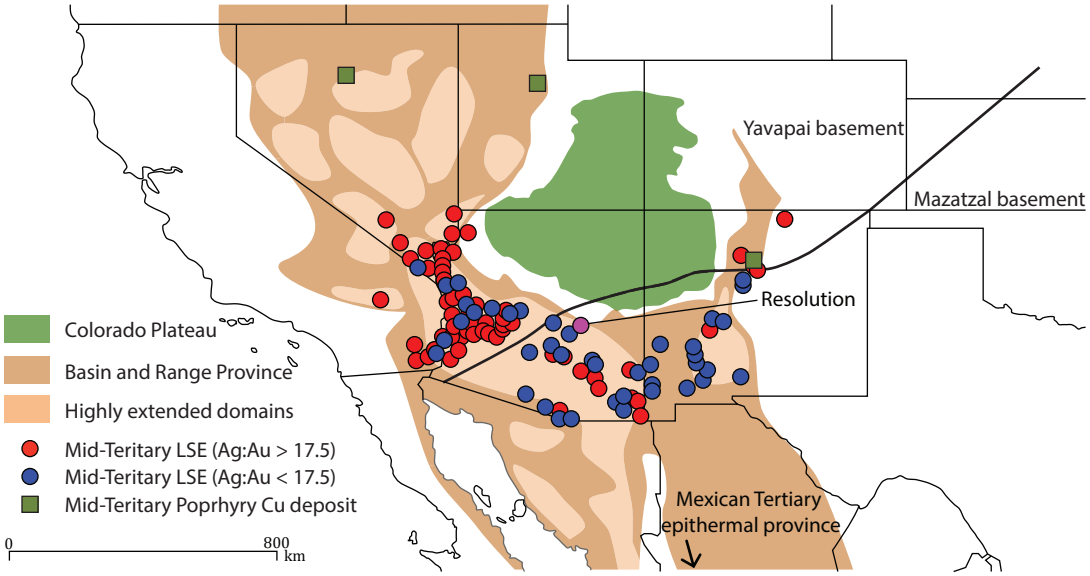


Figure 2.18 Tertiary metallogenic map showing the major districts and deposit styles fomred during the Tertiary. modified after Titley (2001).

(e.g., Holland et al., 2015). This has been referred to historically as the Holbrook Line in magnetic interpretations (e.g., Titley 1982). The Miami-Resolution-Florence-Ajo trend closely follows a segment of the Jemez Zone.

The nature and composition of the basement itself has been a first order control on the location of porphyry Cu deposits in the southwest (Titley 1982; Lang and Titley, 1998). Radiogenic isotope studies, showed that the Pinal and Cochise blocks of the Mazatzal Terrane, where most of the porphyry deposits are located (Figure 2.17), contributed significant amounts of material to productive magmas (Anthony, 1986; Bouse et al. 1999; Lang and Titley, 1998).

Another important feature of Laramide porphyry Cu deposits of south western North America is their apparent broad southward younging (Figure 2.17). This age relationship implies that whatever was driving the flattening of the Farallon slab, most likely an oceanic plateau (Humphreys, 2009), was being subducted obliquely to the continental margin.

### 2.5.5 Tertiary Metallogeny

In the Mid-Tertiary (ca. 45 – 25 Ma), there was a gradual change from compression to extension in response to unloading of the subducting slab. This coincided with voluminous magmatism in the Early Eocene which migrated progressively west, recorded by the widespread ignimbrites of this age (Titley and Zürcher, 2008; Leveille and Stegen, 2012). There is one documented post-45 Ma porphyry Cu deposit in the central southwest (Cerrillos, New Mexico; Maynard, 2005), several in southwestern Mexico (La Verde, San Isidro, Michoacan; Barton 1995) along with Bingham in Utah and Copper Canyon in Nevada, suggesting that porphyry Cu formation outlasted the compressional dynamics of the Laramide Orogeny.

In contrast to the Laramide, Eocene-Miocene magmatism was bimodal and evolved to more alkaline compositions with time. The magmas were more HFSE and HREE enriched, with strong negative Eu anomalies compared to Jurassic and Laramide igneous suites, indicative of less hydrous magmas and an increased degree of plagioclase fractionation than is observed in the Laramide melts (Leveille and Stegen, 2012). This implies that they were generated by asthenospheric upwelling, rather than subduction of a hydrous slab (Leveille and Stegen, 2012).

Tertiary mineralised centres occur in at least 180 districts throughout the southwest U.S.A and broadly fall into one of two styles; skarns or epithermal veins. They were summarized by Spencer and Welty (1989) for Arizona and by Camprubi et al. (2003) for Mexico, and have been compiled in Figure 2.18. Numerous, small porphyry Mo deposits, (37 Ma Cave peak, Texas; 35 Ma Victorio and 25 Ma Questra, New Mexico) also formed at this time, as well as scattered Sn-F-Be, W skarn and IOCG occurrences (Staude and Barton, 2001; Titley and Zürcher, 2008; Leveille and Stegen, 2012). The epithermal deposits are either gold-, silver- or base metal-rich, depending on which Proterozoic basement province they occur in, suggesting that mineralising fluids strongly reflect the basement composition and how it was affected by metallogenic events (Titley 1987, 2001). Most of the gold-rich veins formed in the Yavapai and Guerrero terranes, whereas silver- rich veins are more common in the Mazatzal terrane (Titley, 2001; Figure 2.18). These contrasting metal associations that change with space and time appear to relate to the evolving tectonic setting and associated intrusions. Titley (2001) provided compelling evidence that basement composition continued to affect metallogeny through the Tertiary in Arizona. Figure 2.18 shows the distinct metal associations in low (LSE) and intermediate (ISE) sulfidation epithermal veins. When plotted spatially, Ag/Au ratios of the epithermal deposits demonstrate a distinct change across the Jemez Zone (Holbrook Line) between the Yavapai and Mazatzal Proterozoic provinces. This Tertiary metallogenic association builds on similar observations in the Mesozoic and Laramide, where the more productive districts are located south of the Holbrook Line, the interpreted boundary between ~1,750 Ma thick felsic Yavapai and ~1,650 Ma thin variably schistose-mafic Mazatzal basement.

Tertiary mineral occurrences range from veins to modest replacement bodies, locally associated with small intrusive plugs and dikes. Volcanism peaked around 20 Ma, based on dating of numerous small stocks and dikes(Spencer and Welty, 1989; Titley, 2001). The Miocene volcanic succession increases in thickness from the southern part of Arizona into Mexico. Many of the epithermal vein districts in Mexico occur in the heart of the Sierra Madre Occidental province (Figure 2.18) and most are Oligocene in age and Pb-Zn-Ag dominant (i.e. Intermediate sulfidation epithermal; Ruiz, 1986).

### 2.5.6 Summary

Modest VHMS, small porphyry Cu-Mo, sediment-hosted U-Cu and hybrid Cu-U MVT-style systems are known from the Proterozoic to Mesozoic (Table 2.2, Table 2.3; Figure 2.15, Figure 2.16). However, the most economically important deposits in the southwest are porphyry Cu-Mo deposits that were

emplaced during the 80 – 45 Ma Laramide event. There were also three significant deposits formed in the Jurassic (Table 2.3, Figure 2.16, Figure 2.17) and one in the Oligocene (Leveille and Stegen, 2012). The entire Laramide porphyry province has been segmented by faults (Figure 2.17), probably reflecting an architecture first developed during Proterozoic accretion, that have assisted in localising and emplacing giant porphyry systems. Further, within that restricted time interval, 70% of contained Cu occurs within an area representing 10% of all known outcropping Laramide rocks. Where cut by Laramide intrusions, dolerites and carbonates host significant tonnages and above average grade of Cu. Laramide igneous rocks have geochemical and petrological characteristics of hydrous oxidised magmas (Leveille and Stegen, 2012), related to a potentially low angle subducting slab (Humphreys, 2009). Later Tertiary suites have more bimodal silica and a tendency towards more negative Eu anomalies, suggesting plagioclase fractionation and less hydrous conditions, interpreted as representing an upwelling asthenosphere (Leveille and Stegen, 2012).

Despite geochemical similarities between the Mesozoic and Laramide igneous rocks, the depth of erosion of the former suggests a reduced potential for porphyry Cu deposits, except in basins of the Border Rift System or the exotic Guerrero island arc. Additionally the western side of the Laramide arc is highly extended and eroded such that few deposits are known, and are unlikely to have survived erosion. The opposite problem is encountered in the Eocene-Oligocene arc where extensive volcanic cover rocks, especially in Mexico. Areas where plutonic and volcanic rocks are exposed together, are the most favourable for porphyry discovery. as they have the appropriate depth of erosion. Laramide porphyry systems continue to be the target of choice amongst most explorers in the southwest. These remain to be found buried under Tertiary and/or Quaternary overburden, such as was the case at Resolution (Mankse and Paul, 2002). These may also be variably rotated and dismembered if located within high-extension corridors in the Basin and Range province (Seedorff et al., 2005).

There is potential for discovery of orogenic gold deposits in highly exhumed and structurally favourable areas, such as those in the Sonoran Desert, close to the MSM. Similarly, the region is prospective for Middle Tertiary, H-ISE veins and replacement deposits associated with small stocks and dikes emplaced in carbonate dominated hosts, especially in areas such as the SMO. LSE Ag and Au-rich veins also seem to be an under-targeted resource in areas proximal to Tertiary caldera systems within Arizona (Figure 2.18). The next major discoveries in the province will most likely come from following up undrilled or poorly drilled extensions of known deposits laterally and at depth, including dismembered deposit fragments. Greenfields drill holes testing targets under post-mineral volcanic (SMO) and alluvial (BAR) cover are high risk but have the potential for new, large discoveries. Additionally Jurassic and Eocene-Oligocene deposits should not be discounted where permissive erosional level exists.

# Chapter 3: Geology, geochronology and structural architecture of the Superior district

## 3.1 Introduction

This chapter reviews the geology and structural architecture of the Superior district within the context of the broader region (Table 3.1, Figure 3.1). This literature review is supplemented with personal observations made during the course of this study, which focussed mainly on the Mesoproterozoic Apache Group sequence, associated dolerite sills and Laramide rocks. The Paleozoic carbonate section and post-mineral Tertiary cover is of lower importance to this study and is therefore only reviewed briefly here. The geology of the Superior district is largely consistent with the regional framework described by Ransome (1904). The Superior district has been studied and mapped extensively, most notably by Short et al. (1943), Hammer and Peterson (1968), Peterson (1969) and Schwarz (2007) and has been reviewed and revised by numerous authors (Manske and Paul, 2002; Ballantyne et al., 2003; Zulliger, 2007; Hehnke et al., 2012; Figure 3.2).

## 3.2 Previous Work

The extensive body of work on the geology of the Superior district is summarised in Table 3.1. Superior district mapping is compiled from Peterson (1969) and Spencer and Richards (1995), with the addition of major ore deposits and vein swarms (Figure 3.2). Figure 3.2 displays the schematic stratigraphic column, redrafted and modified after Hammer (1973).

## 3.3 Local Geology

### 3.3.1 Pinal Schist

The ca. 1,650 Ma Paleoproterozoic Pinal Schist forms the basement to the Superior district, as it does across much of SE Arizona (Figure 3.3). Despite the name 'schist', regionally this unit includes a range of lithologies, including carbonates as well as mafic, intermediate and felsic intrusive and volcanic rocks,

Figure 3.1 (opposite page) Simplified geology map of the Superior-Miami-Ray region. Selected faults; RF - Robles Fault; PF - Picketpost Fault; CF - Concentrator Fault; MF - Main Fault; CSF - Conley Springs Fault; SBF - Sleeping Beauty Fault; DCF - Devils Canyon Fault; MCF - Mineral Creek Fault; DSVF - Dripping Springs Valley Fault.

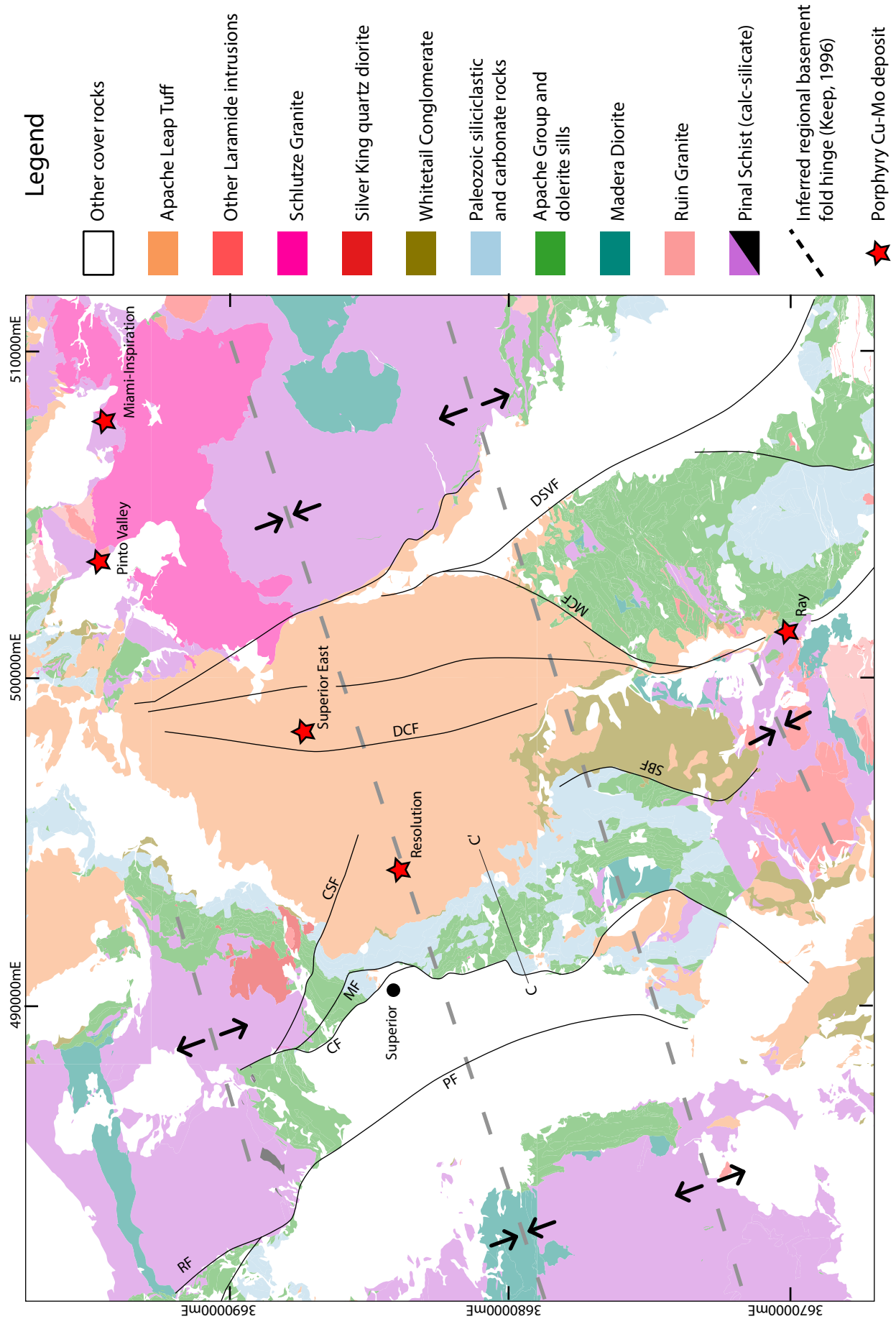
Legend
Other cover rocks
Apache Leap Tuff
Other Laramide intrusions
Schlutze Granite
Silver King quartz diorite
Whitetail Conglomerate
Paleozoic siliciclastic and carbonate rocks
Apache Group and dolerite sills
Madera Diorite
Ruin Granite
Pinal Schist (calc-silicate)
Inferred regional basement fold hinge (Keep, 1996)
Porphyry Cu-Mo deposit
510000mE
500000mE
490000mE
3690000mE
3680000mE
3670000mE
Miami-Inspiration
Pinto Valley
Superior East
Resolution
Superior
Ray
DSVF
MCF
DCF
SBF
CSF
MF
CF
PF
RF
C
C'

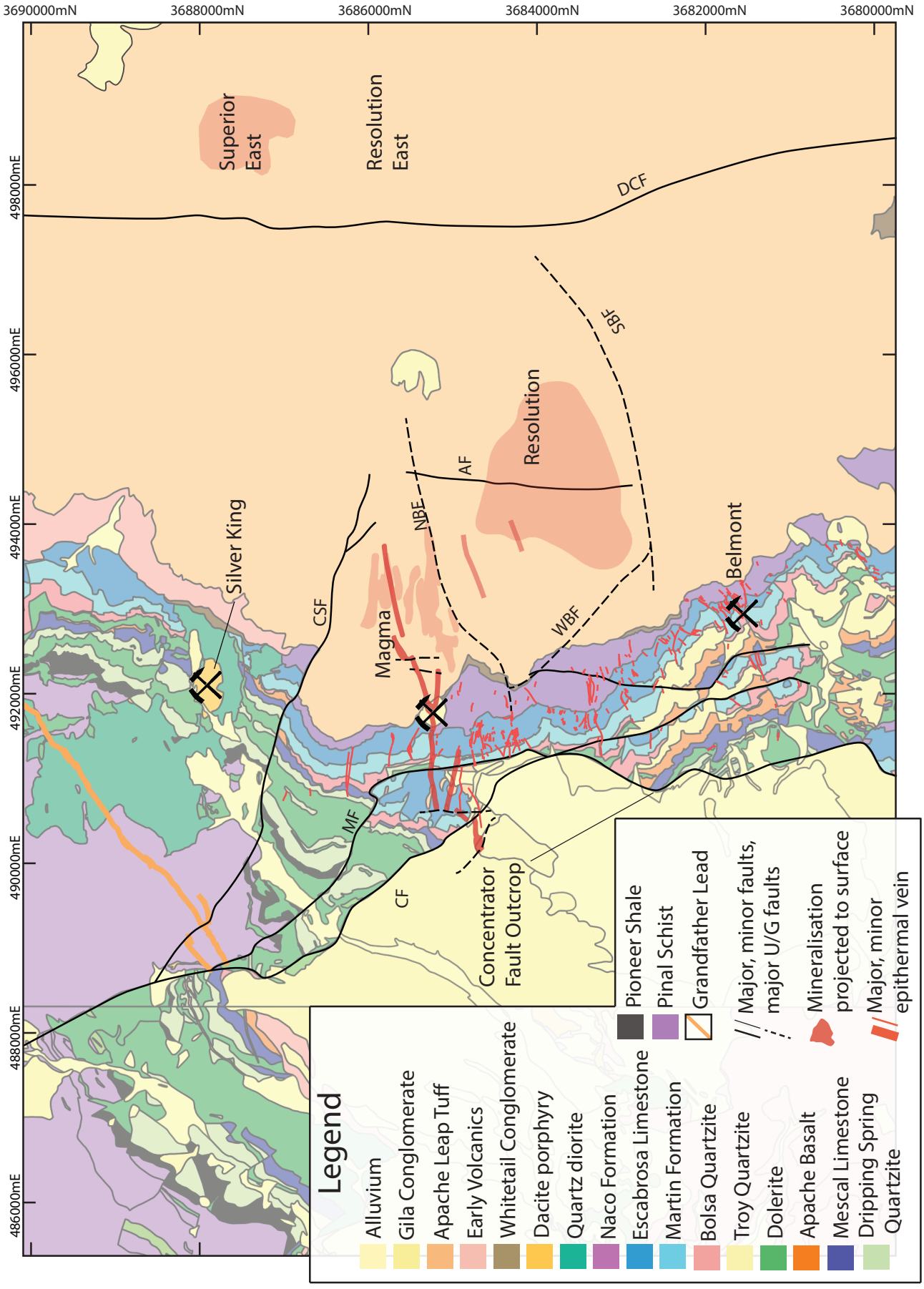
3690000mN
3688000mN
3686000mN
3684000mN
3682000mN
3680000mN
498000mE
496000mE
494000mE
492000mE
490000mE
488000mE
486000mE
Superior East
Resolution East
DCF
SBF
Resolution
AF
NBE
Silver King
CSF
Magma
WBF
Belmont
MF
CF
Concentrator Fault Outcrop
Legend
Alluvium
Gila Conglomerate
Apache Leap Tuff
Early Volcanics
Whitetail Conglomerate
Dacite porphyry
Quartz diorite
Naco Formation
Escabrosa Limestone
Martin Formation
Bolsa Quartzite
Troy Quartzite
Dolerite
Apache Basalt
Mescal Limestone
Dripping Spring Quartzite
Pioneer Shale
Pinal Schist
Grandfather Lead
Major, minor faults, major U/G faults
Mineralisation projected to surface
Major, minor epithermal vein

within the broader schistose meta-turbidite package (Eisele and Isachsen, 2001). In the Superior district, the Pinal Schist crops out in the NW of the map area (Figure 3.2). The dominant lithology at this location is medium-coarse grained quartz-muscovite schist (Figure 3.4 A) transitioning to a finer grained quartz-chlorite schist further to the west (Figure 3.4 B) with strong, penetrative NE-trending foliations. In the far northwest of the study area, the schist hosts andesitic dikes of probable Proterozoic age. Throughout the exposures of Pinal Schist in the north of the district and west into the adjacent map sheet, there are discontinuous calc-silicate lenses that consist of coarse grained andradite garnet, epidote, calcite and albite, with or without quartz (Figure 3.4 C).

Contorted veins and pods of milky quartz are locally abundant in the Pinal Schist, especially at the NW end of the Conley Springs Fault, where a prominent quartz knob occurs. Clasts of Pinal Schist are common in the overlying conglomeratic units of Proterozoic, Mesozoic and Tertiary age, suggesting that the schist was exposed repeatedly throughout the protracted history of sedimentation in the district (Figure 3.4 D).

***Regional Context and Interpretation***

Like much of the basement across the southwestern US, the Pinal schist has been researched extensively (De Melas, 1983; Condie and De Malas 1985; Copeland and Condie 1986; Karlstrom and Bowring, 1988; Condie, 1992; Eisele and Isachsen, 2001; Swift and Force, 2001). Various subdivisions, boundaries and nomenclature have been suggested (e.g., the western quartz wacke assemblage and the eastern volcanic assemblage of Copeland and Condie, 1986) in order to help understand the rocks of the Pinal Schist. Numerous interpretations have also been proposed for the depositional setting of the Pinal Schist, including an intra-arc basin (Copeland and Condie, 1986) or an intracratonic basin (Keep 1996; Eisele and Isachsen 2001). More recently, Meijer (2014) identified tectonic mélanges close to granitic rocks, and to oceanic and arc-like metavolcanic rocks, implying that the Pinal block formed as a forearc-subduction complex. This is inferred to have occurred above the NW-dipping subduction zone inferred from the Cochise block (Eisele and Isachsen, 2001; Swift and Force, 2001; Meijer 2014, Table 3.1). Eisele and Isachsen (2001) proposed that sedimentation in the Pinal block occurred later than 1,678 Ma and ended before 1,655 Ma, providing a 23 m.y. window for deposition.

A widespread calc-silicate assemblage, similar to that described above, was mapped by Spencer and Richards (1995) in the areas surrounding Superior. The broad distribution of the calc-silicate facies suggests formation via regional metamorphic processes. However, where observed close to the intrusive contact with the Laramide quartz diorite (Figure 3.1), O'Neal (2015) interpreted the calc-silicate rocks to be skarn related to the Laramide quartz diorite stock.

Figure 3.2 (opposite page) Geology of the Superior district, compiled from Peterson (1962) and Spencer and Richards (1995) Hehnke et al. (2012) with the addition of past producing mines and major undeveloped ore bodes. Selected faults: AF - Anxiety fault; CF - Concentrator fault; CSF - Conley Springs fault; DCF - Devils Canyon fault; MF - Main fault; NBF - North Boundary fault; SBF - South Boundary fault; WBF - West Boundary fault.

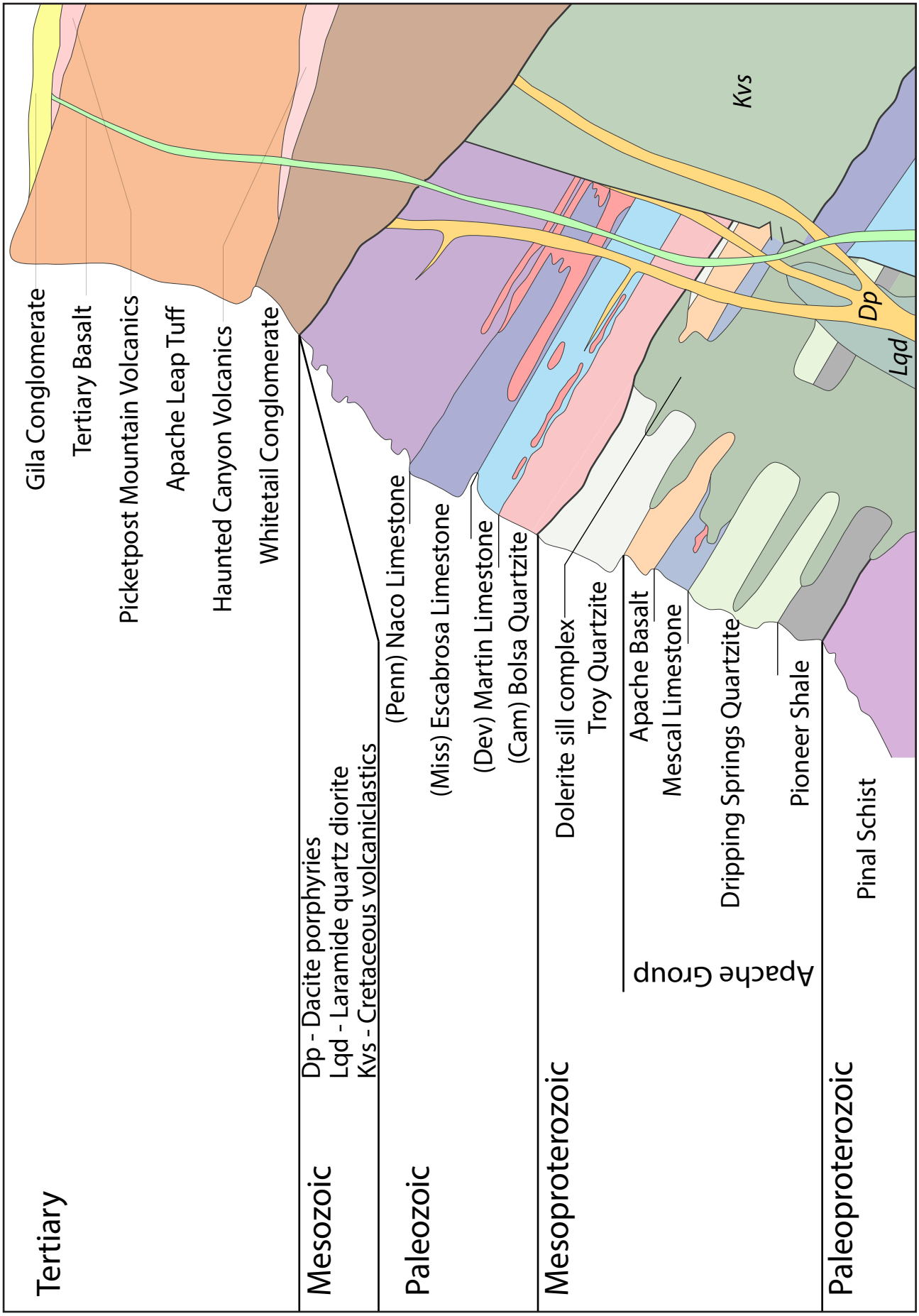


Figure 3.3 Schematic stratigraphic column of the Superior district. Modified after Hammer (1973).

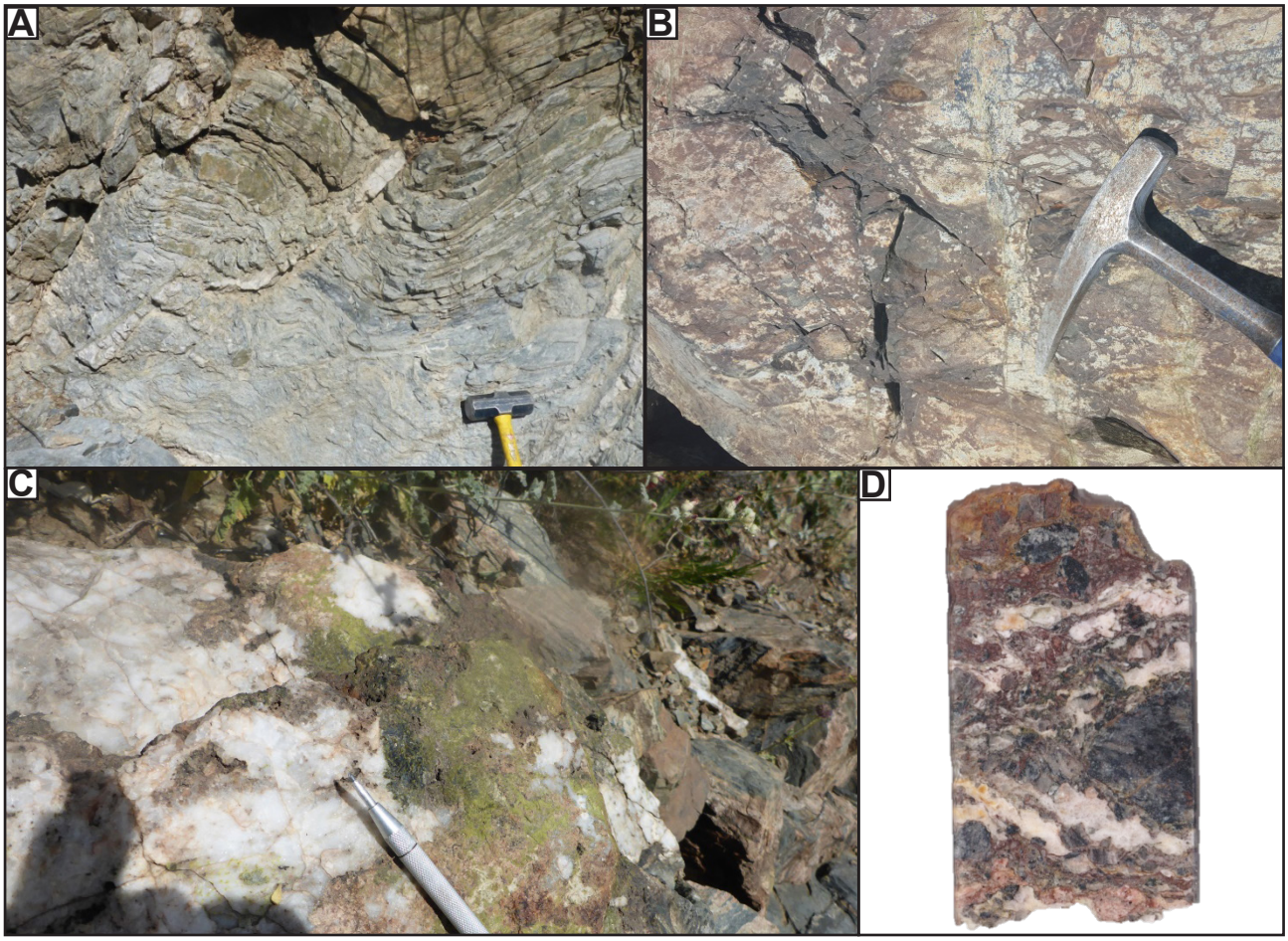


Figure 3.4 Examples of Pinal Schist from the Superior district. A. Thinnly bedded quartz-rich metasediment from the Conley Springs area. B. Fine grained chloritic schist. C. Calc-silicate altered facies D. RE15JP203 - Crenulated quartz-muscovite schist clast hosted in Tertiary conglomerate intersected in drilling.

### 3.3.2 Apache Group

Mesoproterozoic Apache Group rocks are widespread across SE Arizona, with the thickest and most complete section exposed north of the Salt River in the Sierra Ancha region, thinning towards the south (Ransome, 1904, 1916; Shride, 1967). Most units within the sequence are separated by a subtle unconformity, suggesting that there were repeated cycles of deposition and erosion due either to marine transgressions or uplift. The Apache Group is correlated with the Unkar Group of the Grand Canyon (Timmons et al., 2005). The group may have been deposited in one of a series of discrete intracratonic basins (Stewart, 1982) or as part of an interconnected foreland seaway related to Grenvillian orogenesis (Timmons et al., 2005).

#### 3.3.2.1 Pioneer Shale

Regionally, the Pioneer Shale consists of the basal Scanlan Conglomerate, overlain by a tuffaceous mudstone and intercalated arkose beds in the upper sections (Shride, 1967). The basal Scanlan Conglomerate is typically a well-rounded pebble-cobble conglomerate, but has also been observed as a thin layer of coarse gravel (Shride, 1967, Wrucke 1989). In rare occurrences well developed imbrication has been reported

| Era | Period | Group | Rock Unit | Units in Superior | Characterisitcs | Genetic Interpretation | Correlates |
|---|---|---|---|---|---|---|---|
| Cenozoic | Mid-Late Tertiary | Tertiary Cover | Gila Conglomerate | N/A | Fluvial deposits of pebble to boulder angular to subrounded clasts of all pre-existing lithologies in coarse poorly sorted arkosic matrix [2,6] | Synorogenic basin and range half-graben fill | |
| | | | Tertiary basalt | N/A | Small irregular bodies of grey aphanitic, locally vesicular basalt [2,6] | Not reviewed | |
| | | | Apache Leap Dacite | N/A | Welded glassy dacitic tuff [2,6] | Rapidly emplaced ignimbrite flows [6] | |
| | | | Haunted Canyon Volcanics | N/A | Rhyolitic tuffs and flows with perlite and obsidian at base [2,6] | | |
| | | | Whitetail Conglomerate | N/A | Eastward thickening unit of coarse conglomerate [2, 4, 6, 31] grading up into gypsum bearing lacustine mudstones and tuff horizons in the upper sections [31] | Synorogenic basin and range half-graben fill [31] | |
| Late Cretaceous - Early Tertiary | Laramide | Cretaceous Volcanics | Porphyry dikes (DP) | RDP<br>QLP | Narrow porphyritic dikes with quartz phyric phases appear to be cut by a feldspar phyric phase [4, 6, 31, 33, 35] | Ealry to syn mineral timing and related to Schultze Granite [33] | Rhyodacitic KVS [33] |
| | | | Cretaceous Volcanic Sandstone (KVS) | Rhyodacitic KVS | Series of intercallated lapilli and crystal rich tuffs [31, 33, 35] in south and east of Resoltuion block | Pyroclastic rocks [33] | Williamson Canyon Volcanics (Christmas) [4, 31] |
| | | | | Andesitic KVS | Thinnly bedded lithic greywacke interbeddded with andesistic tuff and breccias [31, 33, 35]; dominates the north and northwest sectors of the Resolution block [33] | Reworked laramide volcanics and detrital basment material during periods of volcanic quiescence [33] | Quartz diorite [33] |
| | | | Cretaceous Quartzose Sandstone (KQS) | N/A | Fine - medium grained well sorted medium - thickly bedded quartz arenite locally interbedded with siltstones. Characteristic matrix supported conglomerate near base [31, 33, 35] | Fluvio-deltaic environment, NW Bisbee basin [33] | Fort Crittenden Fm [33] |
| | | | Quartz Diorite | Fine grained, medium grained, porphyritic and aplitic | Irregular, medium-coarse grained hornblende-pyroxene phyric quartz diorite stock [1, 2, 4, 7] | Early Laramide phase of plutonism [34] | Andesitic KVS [33] |

| Era | Period | Group | Rock Unit | Units in Superior | Characterisitcs | Genetic Interpretation | Correlates |
|---|---|---|---|---|---|---|---|
| Paleozoic | Penn. | Paleozoic Cabonates | Naco Formation | Horquilla Formation | Cyclically interbedded fossiliferous limestones with subordinate terrigenous silstones [2, 20]; bryazoa common and increasing chert upwards [2, 4] | Repeated transgression and regression of carbonate seas [20] | N/A |
| | Miss. | | Escabrosa Limestone | Hachita Formation | Light grey crinoidal limestone (packstone-grainstone) [2, 4, 20] | Major marine transgression [19] | Redwall Limestone [20] |
| | Dev. | | Martin Formation | Jerome Member | Basal 'fetid dolomite' [2, 4, 6, 26, 27] Pale yellow fossiliferous limestone and yellow - purple calcareous shale [4, 6] | Shallow marine carbonate shelf - intertidal [19] | N/A |
| | | | | Beckers Butte Member | Thinly bedded gray frosted quartz sandstone with minor dolomite and red spots [2, 4, 19] | Fluvial-marginal marine [19] | N/A |
| | Cam | | Bolsa Quartzite | N/A | Ledge-forming quartz arenite with feldspar, grainsize and bedding thickness decreasing upwards; some shale interbeds and Skolithos fossils in upper parts [21] | Inter-subtidal [21] | Tapeats Sandstone [21] |
| Mesoproterozoic | Stenian | | Dolerite sills | N/A | Widespread in southwest US, medium-coarse grained ophitic-subophitic [2, 3, 8, 9, 10, 11, 12, 13, 16, 22, 23, 36] locally with feldspathic differentiates [2, 8, 9, 11] and/or retrograde alteration [1, 8, 9, 13]; mostly sill geometry, though subordinate dikes strike consistantly NW [36]; two major compositional types identified [10, 13, 16, 22, 23 36] | Sills formed by multiple intrusions [1, 2, 13, 22,] compositional types dervied from single magma [10, 13, 16, 22, 23] Differentiates result of late stage crustal contamination facilitated by surface water and high volatiles [8, 9, 11, 12] | Mid Continent Rift [36] |
| | Ectasian | | Troy Quartzite | Chediski and Quartzite members | Medium grained, well sorted, cross-bedded sparsely pebbly quartz arenite [1, 2, 22] | Shallow marine reworked fluvio-aeloian material of the Arkose member and Chediski member, not represented in Superior [1, 2, 22] | Nankoweap Formation [32] Dox Formation[38] |
| | | Apache Group | Apache Basalt | Four distinct flow units | Fine grained aphyric to plagioclase phyric basalt, locally vesicular with reddened autobreccia [1, 2, 22] | Subaerial extrusive lava, close to sea level [1,2] | Unkar Group [32] Crystal Springs Formation [38] |
| | | | Mescal Limestone | Argillite member | Basal breccia with intrafomrational clasts and chert and shale [22] | | |
| | | | | Algal member | Generally stromatilitic [22], though not observed in Superior [1 ,2] | Subtidal - intertidal [22] | |
| | | | | Lower member | Thinly bedded cherty dolomitic limestone [1, 2], with halite casts [22] | Coastal sabkah [22] | |

| | | | | | | | |
|---|---|---|---|---|---|---|---|
| MesoProterozoic | Ectasian | Apache Group | Dripping Springs Quartzite | Upper member | Finely laminated siltstone with high $K_2O$ (~10%) occurring as pure orthoclase; high organic carbon as well as diagenetic pyrite and uraniniferous stylolites [3, 5, 22] | Tidal flats [3, 5, 22] | Unkar Group [32] Crystal Springs Formation [38] |
| | | | | Middle member | Fine-medium grained, well sorted massive to thickly bedded arkosic sandstone [3, 22] strongly interuped by later dolerite | Shallow marine [3, 5, 22] | |
| | | | | Barnes Conglomerate | Rounded cobbles of grey-purplish grey quartzite, vein quartz with lesser jasper and volcanics in arkosic matrix [3, 22], clast supported; typically multiple conglomerate beds [1] | Fluvial-deltaic [3, 22] | |
| | | | Pioneer Shale | Upper Member | Dark purple-brown shale with pyrite-cored reduction spots [1,2] dominated by fine ash/ pyroclastic material [22] | Lacustrine [3, 22] | |
| | | | | Scanlan Conglomerate | Subrounded cobbles of vein quartz, dark grey quartzite, lesser schist and rhyolite [22] | Alluvial fan - braided river [3, 22] | |
| Paleoproterozoic | Statherian | Metamorphic Basement | Pinal Schist | N/A | Meta-turbidites represented by variable quartz-mica schists [14, 15, 17, 18, 24, 25, 28, 29,] interleaved with arc and oceanic meta-igneous rocks [28, 29] and tectonic melange [37] | Fore-arc subduction complex/ accretionary prism to the Mazatzal arc terrane [37] | Tyennan Schist, Western Tasmania [30] |

Table 3.1 Summary of the geology, interpreted environment of deposition and regional correlates of the Superior district. References: [1]Galbraith (1935); [2]Short et al. (1943); [3]Shride (1967); [4]Hammer and Peterson (1968); [5]Granger and Raup (1969); [6]Peterson (1969); [7]Puckett (1970); [8]Nehru and Prinz (1970); [9]Smith (1970); [10]Fouts (1974); [11]Smith and Silver (1975); [12]Schofield (1976); [13]Hammond (1983); [14]De Melas (1983); [15]Condie and De Melas (1985); [16]Hammond (1986); [17]Karlstrom and Bowring (1988); [18]Anderson (1989); [19]Beus (1989); [20]Blakey and Knepp (1989); [21]Middleton (1989); [22]Wrucke (1989); [23]Hammond (1990); [24]Condie (1992); [25]Keep (1996); [26]Friehauf (1998); [27]Pareja (1998); [28]Eisele and Isachson (2001); [29]Swift and Force (2001); [30]Burrett and Berry (2002); [31]Manske and Paul (2002); [32]Timmons et al. (2005); [33]Zulliger (2007); [34]Maher (2008); [35]Hehnke et al. (2013); [36]Bright et al. (2014); [37]Meijer (2014); [38]Mulder et al. (2016)

(Shride, 1967) although no consistent paleocurrent directions were recorded. Compositionally the conglomerate consists of granite and quartzite clasts closely packed within an arkosic sandy matrix. Where the Pioneer Shale overlies the Pinal Schist, schist fragments are common in the shale although angular feldspars still dominate the matrix. Overall composition of the Scanlan Conglomerate strongly reflects the local basement lithology, with granite- and quartzite-derived components most common (Shride, 1967). Thickness of the Scanlan Conglomerate, and the broader Pioneer Shale, varies dramatically with Pre-Apache relief. The tuffaceous mudstone that makes up most of the Pioneer section is composed of silt-sized angular feldspar and quartz grains and devitrified glass shards set in a clay matrix, (Shride, 1967). The mudstone has light brown reduction spots containing limonitic pyritic casts at their centres (Shride, 1967). Fine-medium grained hematitic arkose occurs mostly as interbeds with mudstone in the upper parts of the sequence. Despite thorough description by Shride (1967), lateral variations and recessive weathering in the Pioneer Shale can confuse its recognition locally.

In the Superior district, the Scalan Conglomerate is poorly represented. Short et al. (1943) reported two widely separated occurrences that were markedly different in character. The unit has not been reported from within the Magma mine, and was only encountered at one location in this study, approximately 100m north of the Conley Springs Fault (Figure 3.5 A). The Pioneer Shale is recessive and although present in the Superior district, the unit does not crop out well. However, just south of the Conley Springs Fault the Pioneer Shale occurs as light buff coloured highly fragmented fissile siltstone. Drilling by Resolution Copper intersected this lithology during underground development of the No.10 Shaft, where it occurs as a dark gray fine grained siltstone with diagnostic reduction spots (Figure 3.5 B).

***Regional Context and Interpretation***

The basal Scanlan Conglomerate of the Pioneer Shale was interpreted by Wrucke (1989) as having initially accumulated very locally derived material in pre Apache depressions. The fine feldspars and quartz grains and devitrified shards of the mudstone facies have been interpreted as suggesting significant contribution from distal, but potentially very large, volcanic centres that were deposited in the quiet waters of the early Apache basin (Shride, 1967; Wrucke, 1989). Arkoses in the upper section most likely represent times of more energetic sedimentation where supply of detrital material was higher. Overall, conditions in the basin are likely to have been reducing, based on the pyritic reduction spots.

#### 3.3.2.2 Dripping Springs Quartzite

The Dripping Springs Quartzite is regionally composed of three units, all of which occur in the Superior district, although no complete section is available due to extensive disruption by later dolerite intrusion. Short et al. (1943) noted that where present, the basal Barnes Conglomerate rests on a slight unconformity above the Pioneer Shale, suggesting some erosion took place between deposition of the two units. The Barnes Conglomerate grades up into the Lower Member, a massive to thickly bedded, locally cross

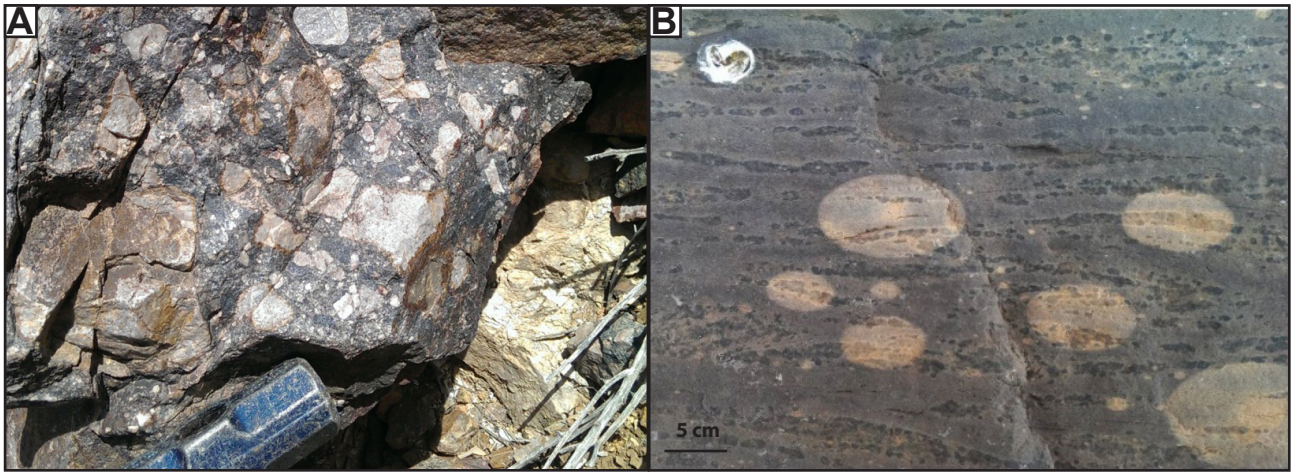


Figure 3.5 Examples of Pioneer shale in the Superior district. A. Outcropping Scanlan conglomerate, north of the Conley Springs fault. B. Resolution Copper Mining Ltd reference sample.

bedded arkosic sandstone (Figure 3.6 A). This is overlain by the Upper Member, an alternating sequence of fine grained feldspathic arenite and finely laminated, orthoclase rich siltstone (Figure 3.6 B). The high orthoclase content makes the Upper Member a prominent positive anomaly on radiometric surveys.

***Regional Context and Interpretation***

The basal Barnes Conglomerate was interpreted by Wrucke (1989) and references therein to represent an alluvial fan regionally transitioning south to a braided fluvial system. The Lower Member signals a switch to the massively bedded, well sorted arkose interpreted to be part of a transgressive sea reworking and redistributing sediments from distal locations, probably from the north (Ransome 1904, Wrucke 1989). The eventual regression, represented by the silty Upper Member (Figure 3.5 B), led to the deposition of extensive tidal flats manifested in alternating sandstone and siltstones, sourcing material from a hinterland rich in radiogenic elements (K/U/Th), which was probably unroofed granitic basement of the Mazatzal terrane (Ransome 1904; Shride, 1967; Wrucke 1989) or the Grenville Orogen (Timmons et al., 2005; Mulder et al., 2017).

#### 3.3.2.3 Mescal Limestone

The Mescal Limestone consists of up to four members; the Lower member, the Algal member, the Basalt member (local) and the Argillite member (Ransome, 1915). Although this units retains the name ‘limestone’, the original carbonate rocks are now thought to have been variably transformed to cherty dolomites (Wrucke, 1989). Where preserved, the Lower Member is described as consisting of a thinly bedded yellow-brown dolomite (Shride, 1967). Black chert occurs as discontinuous beds and laminae, differentiated from the later dissolution related chert breccias by its colour, although silicic altered collapse breccias are also noted (Shride, 1967; Wrucke, 1989). Regionally, the Algal member is characterised by a cliff-forming stromatolitic dolomite and upper slope forming, thinly bedded dolomite that rests conformably on the Lower member. This unit typically has a resistive nature due

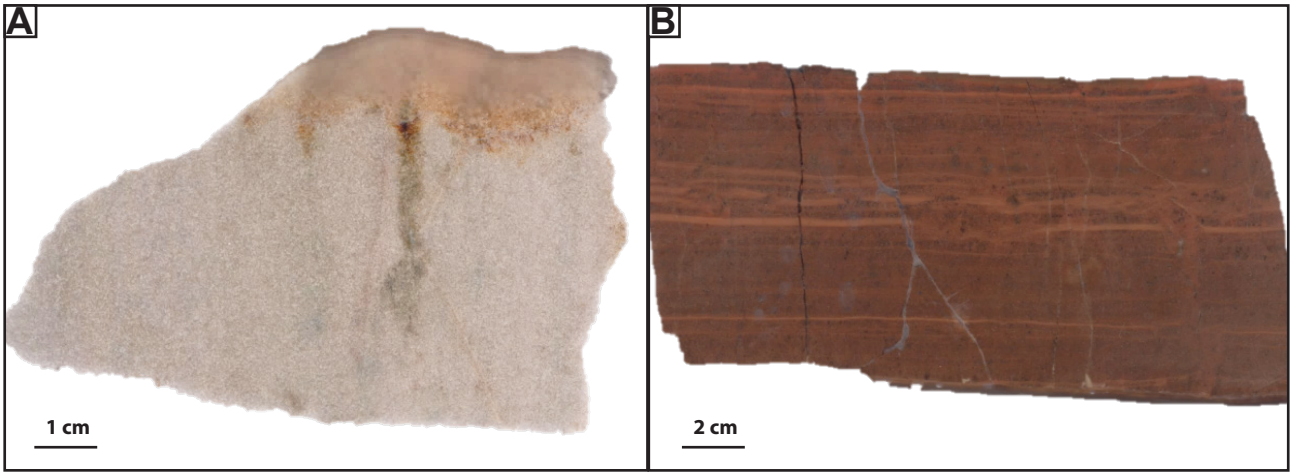


Figure 3.6 Examples of Dripping Spring Quartzite. A. RE15JP211 - Massive quartz-rich Lower Member of the Dripping Springs Quartzite. B. RE15JP210 - Finely laminated orthoclase-rich siltstone of the Upper Dripping Springs Quartzite.

to silicic alteration. Notably, the stromatalites are more laterally than vertically continuous (up to 60 km of constant thickness, McConnell, 1972, 1975; Wrucke, 1989). The Argillite member sits above a slight angular unconformity. It typically consists of a basal chert, intraformational chert breccia or chert conglomerate overlain by argillite or shale (Wrucke 1989). Up to 7% $K_2O$ has been reported by Desborough et al., (1984) suggesting similar tuffaceous origin as the upper Dripping Springs Quartzite. Minor basalt flows have been reported regionally between the Algal and Argillite members in the region - they closely resemble those of Apache Basalt.

Of the four units that comprise the Mescal Limestone regionally (Shride, 1967; Wrucke, 1989), only the Lower and Algal members are present in the Superior district. In the Superior district, the Lower member occurs as a thinly bedded light brown to off-white dolomite and limestone, well exposed in a strand of the Concentrator Fault on Highway 177 (Figure 3.7 A). Dark coloured irregular chert beds occur locally in the Lower Member. North of the Conley Springs fault, a poorly exposed, laterally discontinuous pyritic chert breccia was identified (Figure 3.7 B). Schwarz (2007) mapped a strongly silicified horizon at the base of the Mescal south of the Conley Springs fault, suggesting the silicic facies may be present at more than one location. Float matching this description was also encountered in the same area during the current study (Figure 3.7 C). Locally, small magnetite skarns have been replaced parts of the Lower Mescal Limestone near intrusive bodies. This is in agreement with observations made by Spencer and Richards (1995) in the adjoining quadrangle and Peterson's, (1969) report of seams of chrysotile at similar stratigraphic positions. Hydrothermal features within the Apache Group are discussed in more detail in Chapter 6.

The Algal member also occurs in the Superior district, but without the characteristic upper bedded dolomite unit that was described by Shride (1967). The lack of the upper two units in the Superior district suggests significant post-Algal member weathering and erosion in the area.

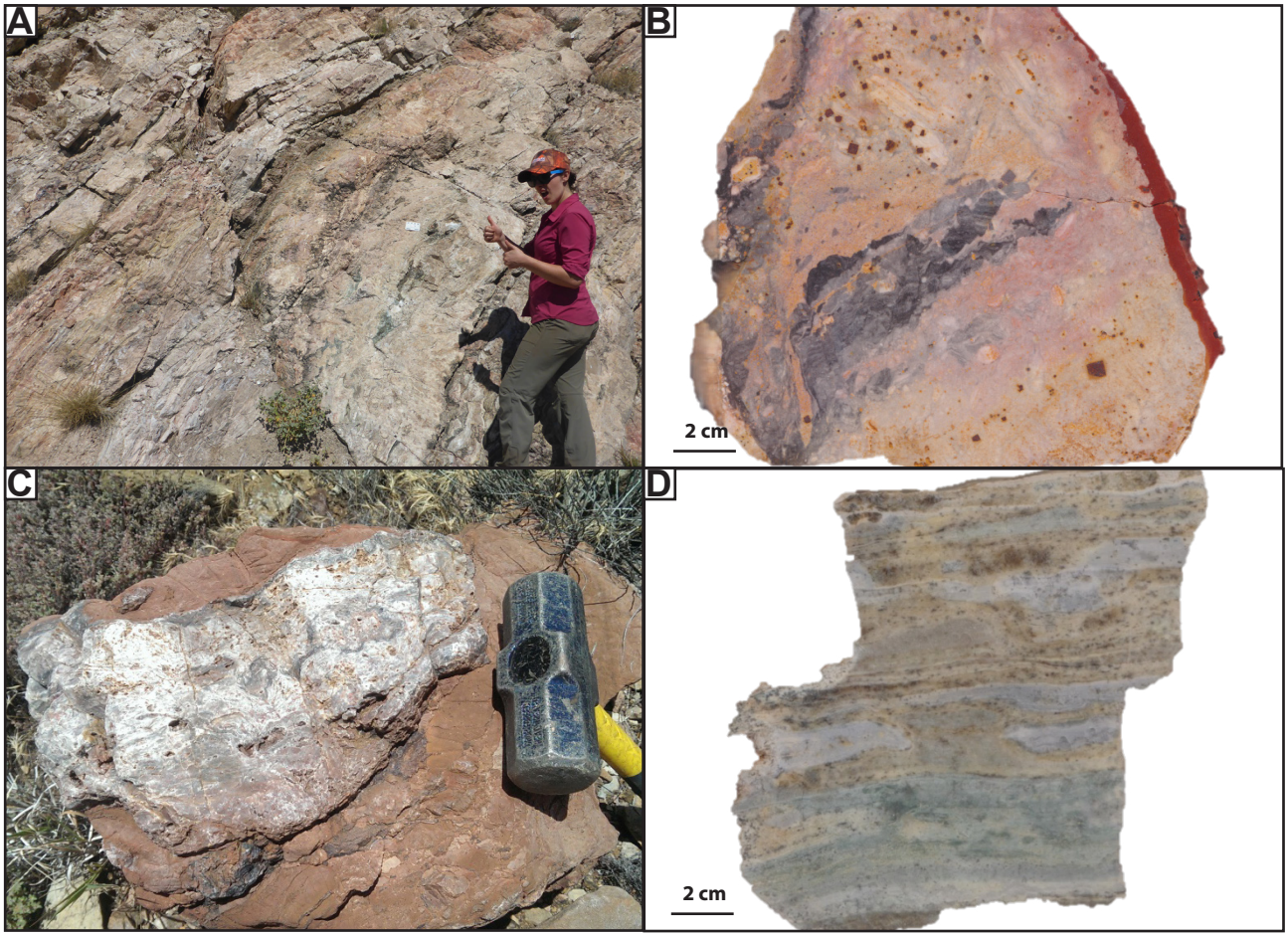


Figure 3.7 Examples of Mescal Limestone. A. Dolomitic Lower Member of the Mescal Limestone, exposed in a road cut on the HWY 177 south of Superior. B. Silicified pyritic siltstone and chert breccia from the north of the district. C. Silicifed chert breccia and hematitic silstone in float. D. RE15JP214 - Algal Member of the Mescal Limestone, exhibiting incipient serpentine alteration.

### *Regional Context and Interpretation*

The Lower member is thought to have formed in highly saline coastal sabkha environment based largely interpretation of salt dissolution features as rafts of halite in silica ooze (Wrucke 1989). The laterally persistent algal mats of the Algal member may have grown in protected sub-inter tidal mudflats, free from the scouring wave and current action that would disrupt lateral continuity (cf. columnar stromatolites of Shark Bay, WA; Wrucke, 1989). The volcanic nature of the upper part of the Mescal Limestone suggest the rejuvenation of distal volcanism, as well as eruption of mafic lavas nearby. The bimodal nature of this volcanism may have been the result of incipient intracratonic rifting.

The Mescal Limestone has a complicated depositional and erosional history. The argillite and basalt members are only present locally (Shride 1967, Wrucke 1989). After the deposition of the Algal member, extensive subaerial modification took place (Skotnicki and Knauth, 2007). Exposure to the atmosphere, either by uplift or regression, resulted in the development of widespread sinkholes and chert breccia formation related to solution collapse breccias and sporadic silicic alteration, presumably by silica-rich groundwaters (Skotnicki and Knauth, 2007). The originally dolomitic rocks were strongly leached of

magnesium during this period, possibly due to local silicic alteration (Shride 1967, Wrucke 1989). Parts of the Lower and Algal members of the Mescal Limestone that were not silicified during weathering, were altered locally by the intrusion of dolerite sills. This caused recrystallisation into a generally fine grained calc-silicate carbonate rock, locally associated with serpentine. Consequently, the Lower and Algal members are recognised in the field either as original cherty dolomite or fine grained garnet skarn.

#### 3.3.2.4 Apache Basalt

The Apache Basalt commonly overlies the Mescal Limestone in the Superior District (Figure 3.3). Short et al. (1943) identified four distinct flow units totalling approximately 65 m in thickness. Each flow is separated by a strongly vesicular (locally amygdaloidal) and locally reddened top (Figure 3.8 A). The uppermost flow is an exception, where vesicles are more common in the middle part, although this could relate to erosion of the upper part of a fifth flow (Short et al., 1943).

In the study area, volcanic autobreccia is common towards the top of individual flows (Figure 3.8 B). Autobreccia facies are locally welded and/or agglomeratic, as noted by Peterson (1969) and Schwarz (2007). These authors also noted that the basalt is highly amygdaloidal locally. In hand specimen, the amygdales contain chlorite, calcite, epidote and rarely quartz and can be stretched vertically in individual flow units (Figure 3.8 C). Though not previously described, rare breccias containing abundant fine grained bedded clasts were also encountered in the field area (Figure 3.8 D). Petrographic analyses by Short et al., (1943) revealed that the basalt flows of the Superior District are uniform in composition, being chiefly composed of plagioclase (60%) olivine (30%) and accessory quartz and magnetite (5% each).

The common red blotchy appearance observed through this unit was previously attributed to thermally oxidised hematite (e.g. Short et al., 1943; Peterson, 1969; Wrucke, 1989; Figure 3.7A), commonly observed in subaerial mafic volcanics worldwide. K-feldspar staining using sodium cobaltinitrate (Bailey and Stevens, 1960) conducted during this study has revealed that the red colouration in the Apache Basalt to be caused by hematite-dusted orthoclase alteration, an observation that is consistent with elevated $K_2O$ values in whole rock geochemistry obtained for the same samples. Hydrothermal alteration within the Apache Group stratigraphy is discussed in more detail in Chapter 6.

***Regional context and interpretation***

The regional distribution of the Apache Basalt is limited due to erosion during earlier Mescal times. Little documentation of this unit exists in the literature except to say that it occurs above the Mescal Limestone, is locally plagioclase-phyric, has a chlorite-altered groundmass and is associated with significant specular hematite (Wrucke, 1989). In some cases, specular hematite is abundant enough to warrant investigation as a source of iron ore, interpreted previously to have formed as a result of Precambrian weathering (Wrucke, 1989).

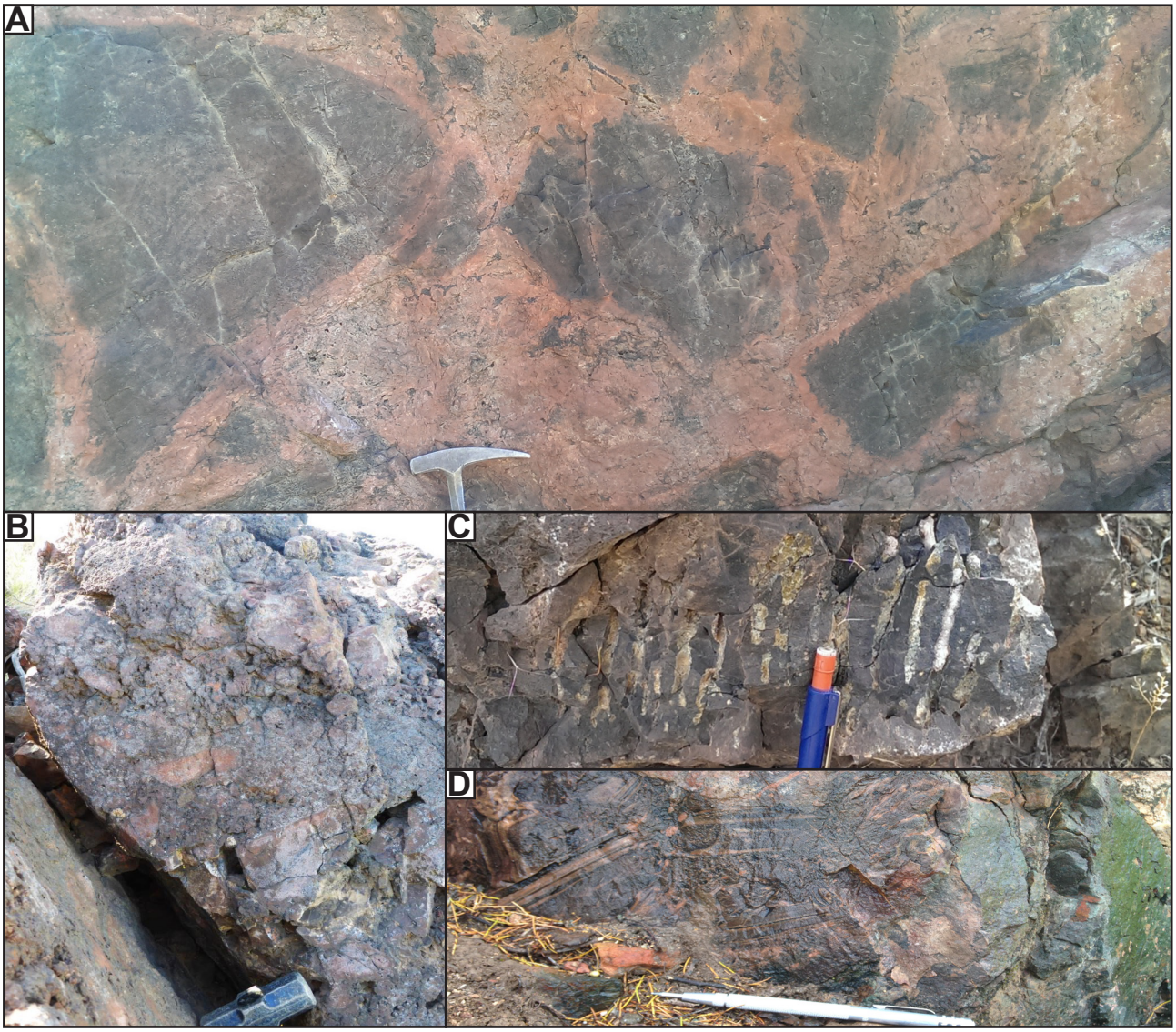


Figure 3.8 Apache basalt from the Superior district. A. Pseudobreccia developed wihtin a coherent basalt flow, defined by intense orthoclase - chlorite alteration. B. Autobreccia facies of the Apache basalt. C. Pipe vesicles, partially filled with calcite and epidote. D. Monomict xenolith rich breccia exposed on Apache Leap road. Clasts are finley laminated, orthoclase-rich siltstones.

Close inspection of a xenolith-rich breccia facies encountered in the study area reveals relict bedding in some mudstone clasts, defined by fine orthoclase grains (Figure 3.8 D). These clasts of country rock are interpreted be have been entrained during emplacement of the basalt. The fine laminations and high K-feldspar content make the most likely source of the sedimentary xenoliths the Upper Member of the Dripping Springs Quartzite. This suggests that although the majority of the more widespread pervasive-patchy orthoclase may be hydrothermal in origin, at least some orthoclase could have come from local assimilation of feldspathic country rock. Short et al. (1943) asserted that quartz observed petrographically in the Apache Basalt may relate to assimilation of quartz-rich country rocks.

#### 3.3.2.5 Troy Quartzite

The Troy Quartzite is the youngest Precambrian sedimentary rock unit regionally (Figure 3.3). The Troy

Quartzite has a basal Arkose member, which only occurs in the northern part of the Apache Group basin. This is overlain by the middle Chediski Sandstone Member, and the upper Quartzite Member which can be difficult to distinguish from one another (Wrucke, 1989). The Chediski Member is the most widespread member of the Troy Quartzite, thickening from north to south (Wrucke, 1989). It consists of friable, sparsely pebbly, massive to cross-bedded sandstone, which is typically conglomeratic at the base. The Quartzite member is strongly quartz-cemented and is characterised by thin to medium bedded cross stratified sandstone beds (Wrucke, 1989).

In the Superior district, the Troy Quartzite crops out only in the southernmost third of the map area, but is conspicuously absent within the Magma mine (Figure 3.1). A cross-bedded, strongly conglomeratic component, characteristic of the Chediski Member, has been observed through the lower half of the exposed sequence in the study area (Figure 3.9 A). This unit becomes more regularly bedded and uniform towards its top (Schwarz, 2007; Figure 3.9 B). Peterson (1969) reported convolute bedding, also characteristic of the Chediski Member, along with common liesegang banding. This suggests that the Troy Quartzite sequence in the Superior district is characterised by the Chediski Member, grading up in the Quartzite member. Cross bedding is characteristic of the Quartzite Member, but is absent in the Superior district, possibly due to lateral facies variation southwards from the type section to the north.

***Regional context and interpretation***

The basal Arkose Member is absent from the Superior district, but has been interpreted to have been deposited by early fluvial, and later aeolian processes, based on the presence of dune forms in its upper parts. The basal Arkose Member is spatially restricted to its type section in the Sierra Ancha region, north of the Salt River (Shride 1967, Wrucke 1989). The coarse grained, to conglomeratic material and thickly bedded nature of the Chediski Member is suggestive of rapidly deposited sand flows from readily available poorly consolidated material (Shride, 1967; Wrucke, 1989). South of the Salt River, the Chediski Sandstone Member can be difficult to distinguish from the overlying Quartzite Member.

#### 3.3.2.6 Dolerite

The Precambrian dolerite is an important constituent of the geology of the southwestern US. Sills up to tens of meters thick intruded a broad region from southern California and Nevada though Arizona and into southwestern New Mexico during the Mesoproterozoic. The dolerite has subjected to detailed study by Wrucke (1966), Smith (1969, 1970), Nehru and Prinz (1970), Wrucke and Shride (1972), Fouts (1974), Smith and Silver (1975), Schofield (1976), Hammond (1983 1986, 1990), Hammond and Wooden (1991), Howard (1991), Donaldini (2011), Donaldini et al. (2012) and Bright et al. (2014).

In central Arizona, the sills form prominent cliffs in the canyon exposures of the Sierra Ancha region (Figure 3.10 A). The sills locally inflated the Apache Group by up to 800m (Shride, 1967; Wrucke, 1989). Generally, fresh unaltered dolerite sills are medium to coarse grained with an ophitic to subophitic

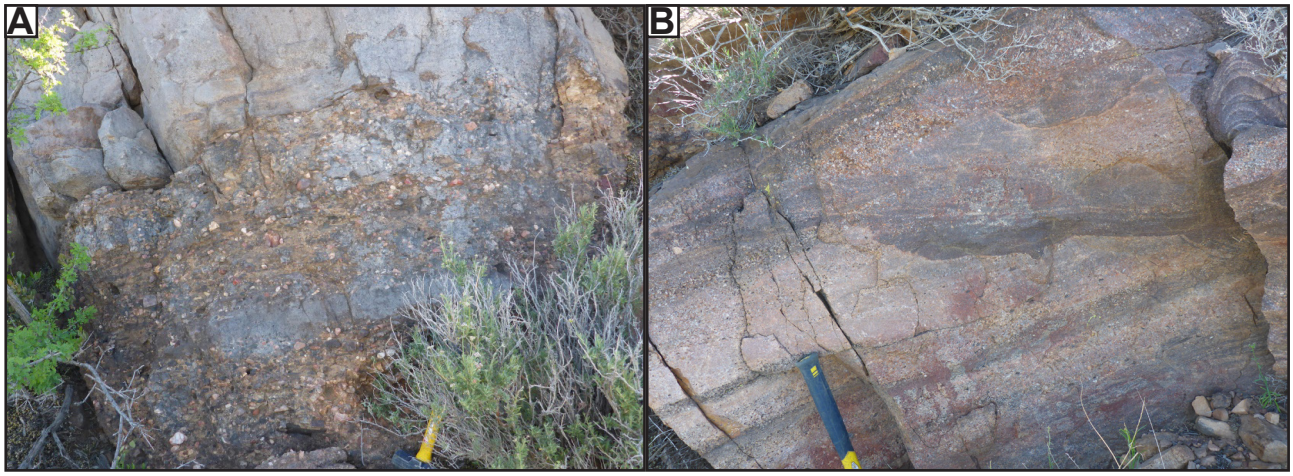


Figure 3.9 Troy quartzite from the Superior district. A. Basal conglomeratic facies above contact with Apache Basalt. B. Coarse gravel lenses in weakly cross-bedded quartzite, possibly Chediski member. Note also liesegang banding.

texture and composed principally of plagioclase (An35-An70) and clinopyroxene (augite) with lesser olivine and accessory titanite, Fe-Ti oxides, apatite and rarely pyrite (Shride, 1967; Smith 1970; Fouts, 1974; Hammond, 1983, Wrucke 1989; Bright et al., 2014). Previous studies have distinguished two general compositions of dolerite in the southwest US; an olivine tholeiite and quartz tholeiite. Olivine tholeiite appears to be the more widespread and better studied (Shride, 1967; Granger and Raup, 1969; Nehru and Prinz 1970; Smith, 1970, Smith and Silver, 1975), though Fouts (1974), Hammond (1983) and Bright et al, (2014) discuss both types. Most petrographic studies of the dolerite sills have identified the presence of hydrothermal alteration products, including but not limited to amphibole, chlorite, epidote and illite (e.g., Fouts, 1974; Hammond, 1983). This alteration has been observed in samples from central Arizona to California, suggesting that it was a regional scale event.

The dolerite sills include a sub-facies known as 'feldspathic differentiates' (e.g., Shride. 1967; Wrucke, 1989) or the 'syenite facies' (e.g., Granger and Raup, 1969). North of the Salt River, pegmatitic pods have been reported in the upper parts of sills, with up to 10 cm long plagioclase and 4 cm augite crystals occurring together with sparse pyrite. Granophyre containing sodic and potassic feldspar has also been reported locally with pegmatitic pods (e.g., Figure 3.10 B; Wrucke, 1989). This facies is commonly thoroughly weathered due to the presence of large amounts of pyrite. In some cases xenoliths of siltstone and arkose in various stages of digestion have been found near the base of the pegmatite pods (Smith and Silver, 1975). Potassic granophyre north of the Salt River was interpreted by Smith and Silver (1975) to be contaminated by the immediately surrounding country rock (Dripping Springs Quartzite). Quartz bearing and quartz-free aplites were the last phase of the dolerite to crystallise. The quartzose aplites occurs as irregular lenses, usually in contact with feldspathic hosts and contains very fine grained disseminated pyrite (Shride, 1967). The volumetrically less significant quartz-free aplite is composed mostly of pink feldspar (80-95%) and occurs as discontinuous, sharp-walled dikes within the larger dolerite sills.

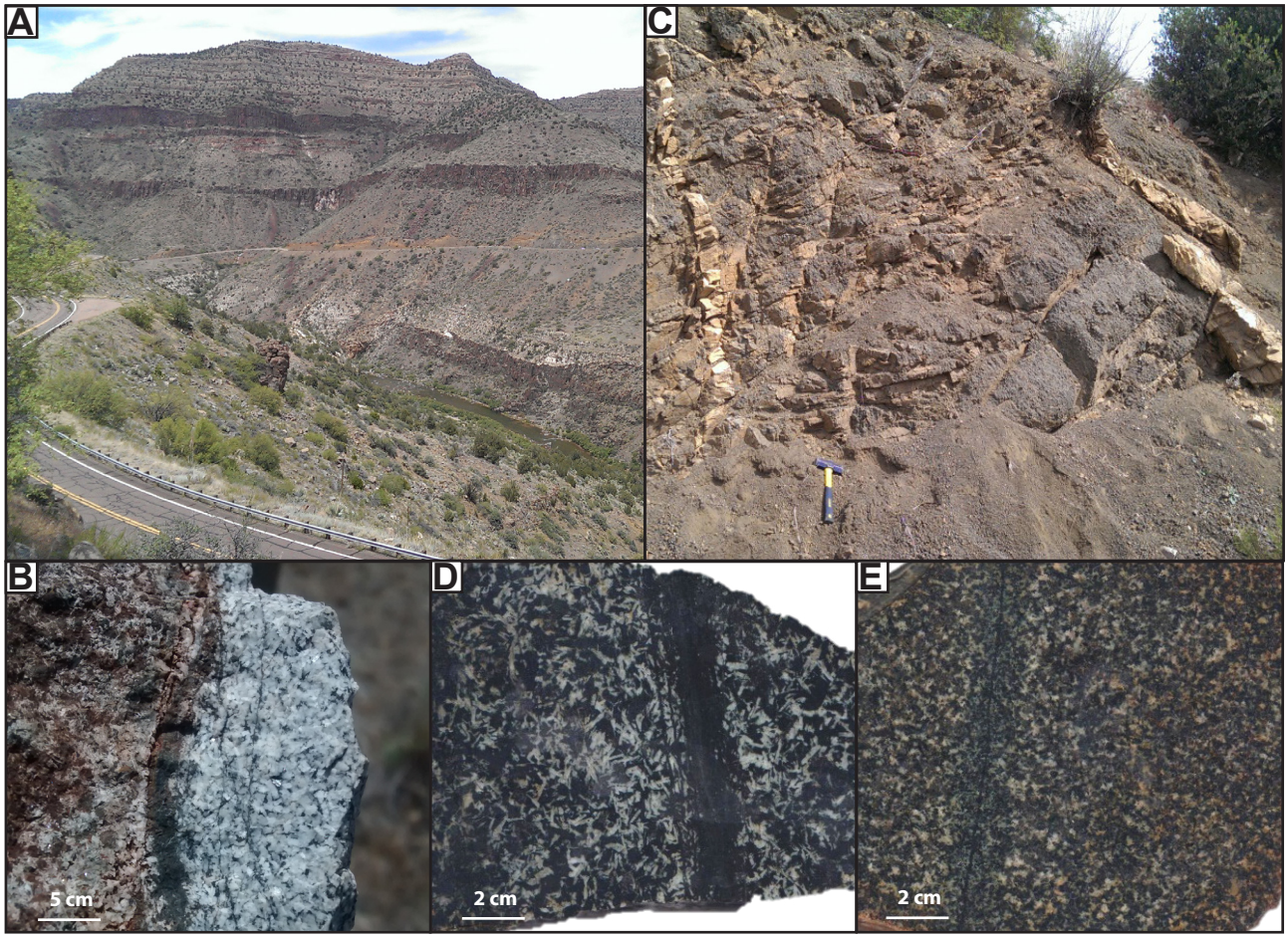


Figure 3.10 1100 Ma dolerite sills. A. Thick, cliff forming exposures of hard, dense dolerite in the Salt River Canyon. Note the exposures of the light coloured Mescal Limestone near the base of the canyon, and well bedded Paleozoic sequence at the top. B. Course grained plagioclase rich pod from the Salt River Canyon, part of the late stage differentiate facies. C. Weathered exposure, typical of the Superior district, cross cut by late dikes of Laramide age. D. RE15140 - Coarse grained ophitic textured dolerite with actinolite-chlorite vein. Groundmass also mostly altered to actinolite-chlorite. E. RE15JP200 - Fine grained dolerite with equigranular texture, together with an actinolite veinlet and earthy hematite staining.

Dolerite sills are an important component in the geology of the Superior district, where they preferentially intruded the geologic contacts of the Apache Group. They are best exposed in the northernmost and southernmost thirds of the map area where the lower half of the Apache Group is exposed (Figure 3.1). At almost all mapped locations in the Superior district, the dolerite is extensively weathered, forming crumbly recessive slopes (Figure 3.10 B). Large rafts of quartzite occur within dolerite sills but broadly retain their original structural attitude. The thickness of individual sills vary. Cumulatively the dolerite inflated the sedimentary package in the Magma mine by over 100% (Short et al., 1943). In historic workings of the Magma mine, dolerite sills occur in three stratigraphically consistent positions, the contact between the Pioneer Shale and Lower Member of the Dripping Springs Quartzite, the contact between the Lower and Upper Members of the Dripping Springs Quartzite and the contact between the Upper Member of the Dripping Springs Quartzite and the Mescal Limestone. The sills were previously referred to as the Lower, Middle and Upper sills and this nomenclature has been retained in more recent drilling by Resolution Copper. In the Superior district, the dolerite is comprised chiefly of plagioclase

and pyroxene with textures ranging from ophitic to sub ophitic to fine grained (Figure 3.9 D-E). Short et al. (1943) observed three types of dolerite petrographically in the Superior district; quartz-orthoclase dolerite, augite-hornblende dolerite that lacks quartz and orthoclase and with no discernible olivine, and an olivine dolerite that contains 10% olivine.

***Regional Context and Interpretation***

Chilled margins have been documented within individual dolerite sills suggesting that they formed from multiple intrusions (Shride, 1967; Smith, 1970; Hammond, 1983; Wrucke 1989). This composite sill-forming process is also responsible for the rafts of sandstone that occur within sills still with their primary orientation (Shride, 1967). The olivine and quartz tholeiite compositions have been interpreted by some authors to be related by fractional crystallisation processes (Hammond, 1983 1986, 1990), while the feldspathic facies have been interpreted to represent late-stage entrainment, assimilation and contamination by local country rocks (Smith and Silver, 1975).

Some authors have argued for emplacement depths of up to 15 km (Howard, 1991), despite the absence of ductile deformation or any other regional metamorphic features that might be expected to form at such depths. This is also at odds with other dolerite provinces worldwide. Dikes unaffected by later tectonism consistently strike northwest, defining a major swarm associated with the province (Bright et al., 2014), and providing insights into the stress regime controlling the feeder structures to the major sills. Timmons et al. (2005) argued for sill emplacement during NW-directed compression related to oblique collision during the Grenvillianorogeny.

The age of the dolerite sills was controversial until radiometric dating was introduced in the 1960s (e.g., Short et al., 1943). Since then there have been a large number of U-Pb dates of zircon and baddelyite published for the dolerite which have been summarised by Bright et al. (2014). New geochronology from Bright et al. (2014) was in agreement with previous ages and the generally accepted range for the dolerite sills in the region is therefore 1,110 to 1,075 Ma. Geochronology results have not been reported with corresponding mineralogy (i.e. olivine tholeiite or quartz tholeiite) precluding the evaluation of possible age differences between previously identified dolerite types.

### 3.3.3 Paleozoic Rocks

The Paleozoic sequences of the Superior district are not a focus of this thesis and are only reviewed cursorily here. They are an important host to replacement deposits in the Magma mine and were documented and studied in detail by Paul and Knight (1995), Friehauf (1998), Friehauf and Pareja (1998). Schwarz (2007) provided measured sections from the range front exposures.

#### 3.3.3.1 Bolsa Quartzite (Cambrian)

In the Superior district, the Bolsa Quartzite is a white to brown to red ledge-forming locally conglomeratic

arenite, consistent with the regional occurrences throughout southern Arizona described by Middleton (1989). Typically the unit comprises an upward fining sequence and coarse pebbly sandstones grading up to interbedded medium grained sandstone and interbedded silts and shales (Middleton, 1989). Regionally, the upward fining of grainsize is accompanied by a decrease in bedding thickness, an increase of cross stratification, mud cracks and the trace fossil Skolithos (Figure 3.11 A). In the Superior district, the lower Bolsa Quartzite is coarse grained and locally conglomeratic, with abrupt lateral and vertical facies changes. It grades upwards into finer grained and cross bedded quartzite (Short et al., 1943; Peterson, 1969; Schwarz, 2007) as it does regionally, though the mud cracks trace fossils are not well developed.

The variable thickness of the Bosal quartzite observed regionally is interpreted to result from infilling of Precambrian topography (Middleton, 1989). The Bolsa Quartzite of southern Arizona is correlated with the Tapeats sandstone of Northern Arizona, which is interpreted as an inter- to subtidal shallow marine deposit (Hereford, 1977).

#### 3.3.3.2 Martin Formation (Devonian)

The Martin Formation is well exposed in the Superior district. It has been described in detail by Peterson (1969), Friehauf (1998), Pareja (1998) and Schwarz (2007). The basal Beckers Butte Member is described as calcareous siltstone to argillaceous limestone (Pareja, 1998). The overlying 'fetid dolomite' marks the base of the more significant Jerome Member, which is widespread in the Superior district. The Jerome Member is distinguished by the characteristic basal dark grey fetid dolomitic mudstone, light grey aphanitic dolomite and an upper reddy-brown sandstone (Figure 3.11 B; Beus, 1989; Freihauf, 1998; Pareja, 1998)

The Martin Formation is the most widespread Devonian unit in Arizona. It is composed of a thin basal unit (Beckers Butte Member) and an upper thicker unit (Jerome Member; Beus, 1989). Collectively this sequence is interpreted to have been deposited in a fluvial-marginal marine setting deepening to a shallow marine carbonate shelf environment (Beus, 1989).

#### 3.3.3.3 Escabrosa Limestone (Mississippian)

In the Superior district, the Escabrosa Limestone crops out as a cliff forming, thickly bedded, light grey crinoidal limestone, with thin interbeds of shale and chert nodules (Figure 3.11 C; Peterson, 1969; Freihauf, 1998; Pareja, 1998; Schwarz, 2007).The Escabrosa Limestone spans Lower and Middle Mississippian times in southern Arizona (Beus, 1989). Regionally, it is characterised by a light grey thick bedded crinoidal grainstone. The Escabrosa Limestone of Southern Arizona is correlated with the Redwall Limestone in the north of the state and is interpreted to record a major marine transgression, depositing skeletal debris on a carbonate platform (Beus, 1989).

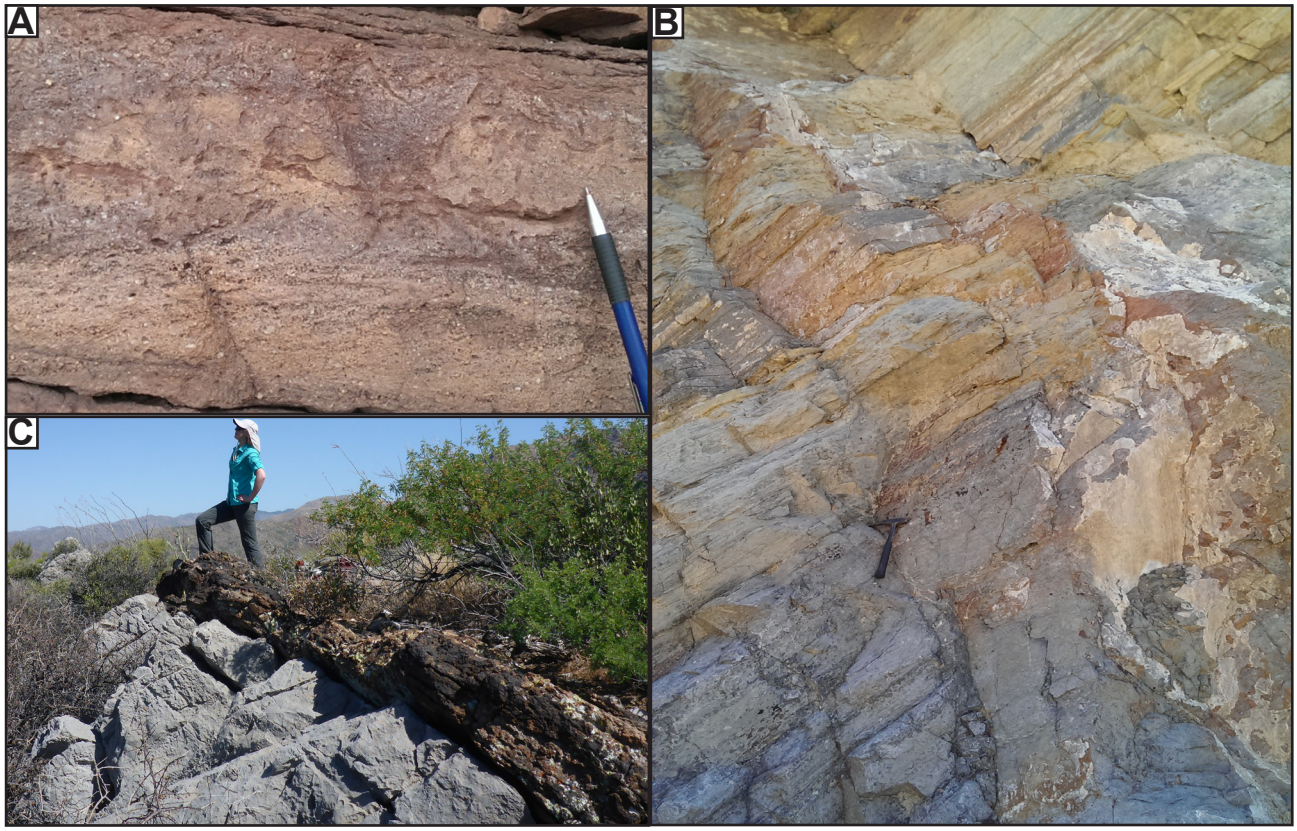


Figure 3.11 Paleozoic lithologies from the Superior district. A. Coarse grained bioturbated Bolsa Quartzite with weakly developed cross bedding. B. Transition from grey-buff coloured dolomite in the Martin Formation, exposed in the US60 road-cut, Superior. C. Characteristic prominent exposure of the crinoidal Escabrosa Limestone at the head of Donkey Canyon, Superior. Iron- and manganese -oxide stained siliceous manto also visible.

#### 3.3.3.4 Naco Formation (Pennsylvanian)

The base of the Naco formation is marked by a basal 'Maroon Shale'. The rest of the unit is composed of thinly bedded locally fossiliferous limestone with irregular cherty layers and interbedded shaley limestone (Schwarz 2007). Up-section the Naco Formation becomes more clastic (Peterson, 1969). The Naco Formation is well exposed in a road cut NE of Superior where it consists of alternating dark soft siltstone and light coloured calcareous sedimentary rocks (Figure 3.12). At this location, the Naco Formation contains a small tilted graben, possibly the upward extension of the important N-S5W fault, which is discussed in more detail later in this chapter

Regionally the Naco Formation comprises a lower, carbonate-dominant Horquilla Limestone and upper clastic-dominant Earp Formation. The Pennsylvanian rocks in the Superior district are correlated with the Horquilla Formation based on the abundance of carbonate. The gradational contact with the overlying Earp Formation is arbitrarily assigned where the clastic units become dominant over the carbonate beds, and are jointly interpreted as the result repeated cycles of transgression and regression of carbonate seas (Blakey and Knepp, 1989).The basal Maroon Shale is interpreted as a red-brown paleosol, demonstrating that at least minor post-Escabrosa erosion occurred prior to the deposition of the rest of the Naco Formation.

Figure 3.12 Exposure of rhythmically bedded Naco Formation, displaying normal offset. Possble candidate for surface expression of N-S5W fault known from underground mapping at the Magma mine. Width of view approximately 25-30m, looking north.

### 3.3.4 Mesozoic Rocks

Mesozoic rocks are largely absent from the Superior district. There are no Jurassic or Early Cretaceous rocks exposed in the area (Figures 3.2, 3.3). The most conspicuous Laramide unit exposed close to the Superior district is the 66-61 Ma Schultze Granite (Figure 3.1). Other Laramide units in the Superior district include the older (ca. 74 Ma) Silver King Quartz Diorite stock in the north of the study area (Figure 3.2). Intruding the Silver King Quartz Diorite is a smaller 500m wide stock of dacitic composition that is mineralogically similar to sporadic thin (generally less than 5m wide) dacite porphyry dikes that also occur throughout the Superior district.

A sequence of completely unexposed Cretaceous volcanic and volcaniclastic rocks, bounded by the North, South and West Boundary Faults, partially hosted the Resolution porphyry deposit and was first intersected during underground drilling south of the Magma mine in the 1960s (Figure 3.2). This Cretaceous graben is buried under up to 1.5 km of Tertiary cover (Manske and Paul, 2002). Zulliger (2007) conducted a detailed study of the Cretaceous volcanic and volcaniclastic package at Resolution, which provides the basis of much of the information synthesised below.

#### 3.3.4.1 Schultze Granite

Just outside of the Superior district, approximately 12 km to the north east, is the most significant Laramide intrusion in the region, the polyphase Schultze Granite (Figure 3.1). The Schultze Granite is

a large felsic pluton exposed in a structural horst between the Globe-Miami and Superior Districts. It has been studied extensively (e.g., Stavast, 2006; Loder, 2015) and is inferred to be the causative pluton for mineralisation in both the Superior and Globe-Miami districts (Seedorff et al., 2008). The Schultze Granite is polyphase (Figure 3.13 A-C), with up to 15 distinct facies previously identified (Creasey, 1984; Stavast, 2006). In general, the intrusive rocks of the Schultze Granite evolve from coarse-grained, locally megacrystic facies, to fine grained aplites and porphyry dikes. The Schultze Granite is unusually silicic for a mineralising pluton, with no hornblende phenochrysts and consistently reporting 70 – 72% $SiO_2$. Despite its textural heterogeneity, the pluton is chemically homogeneous (Stavast, 2006). It contains widespread basement xenoliths (Figure 3.13 D), consistent with interpretations that the pluton experienced significant crustal contamination. No evidence for underplating by mafic magma has been documented.

The Schultze Granite displays well developed hydrothermal features (Figure 3.13 E-F). At deeper levels observed in the pluton, alteration is characterised by barren quartz-K feldspar veins (Figure 3.13 E). At higher levels, greisen-style muscovite-clay veins are present (Figure 3.13 F), locally with chalcopyrite dominating over pyrite (Stavast, 2006). The orientations of each vein stage suggest that early quartz-feldspar veins were controlled by magmatic stress, whereas the emplacement of later muscovite veins was controlled by the regional stress regime (Stavast, 2006). Various phases of the granite have been dated using U-Pb on zircons that show a protracted cooling history between 66 and 61 Ma (Seedorff et al., 2005b; Table 3.2)

#### 3.3.4.2 Silver King Quartz Diorite

A small 2 x 3 km, irregular shaped stock intruded Precambrian and Paleozoic rocks in the north of the study area (Figure 3.1). It is composed of subhedral plagioclase with variable amounts of hornblende, pyroxene, biotite and interstitial quartz (Figure 3.14 A-B). Peterson (1969) described medium grained and fine grained phases, along with more mafic facies both with irregular coarse grained pegmatite pods. More detailed study by Puckett (1970) described an aplite facies and also a marginal porphyritic facies (Figure 3.14 C-D) which display both euhedral and partially resorbed hornblende phenochrysts (Figure 3.14 D). Where observed, the contacts of individual intrusive phases are typically irregular, though sharp contacts do exist (Figure 3.14 C). The western margin of the quartz diorite intruded Pinal Schist and is spatially coincident with strongly developed calc-silicate alteration in the schist, although this may have a more regional extent (Spencer and Richards, 1995).

Polymict hydrothermally cemented, sulfide-bearing breccias are exposed on the western edge of the stock (Figure 3.14 E-F). The breccias are localised between the contact of the quartz diorite, Pinal Schist and Grandfather Lead aplite dike (Figure 3.2). Limited outcrops at this location define a generally oblate dimension for the breccia body. Texturally the breccias vary from clast-supported with clast sizes of 5 – 20 cm and igneous and weak hydrothermal cement, to matrix-supported with fine grain pyrite and clast

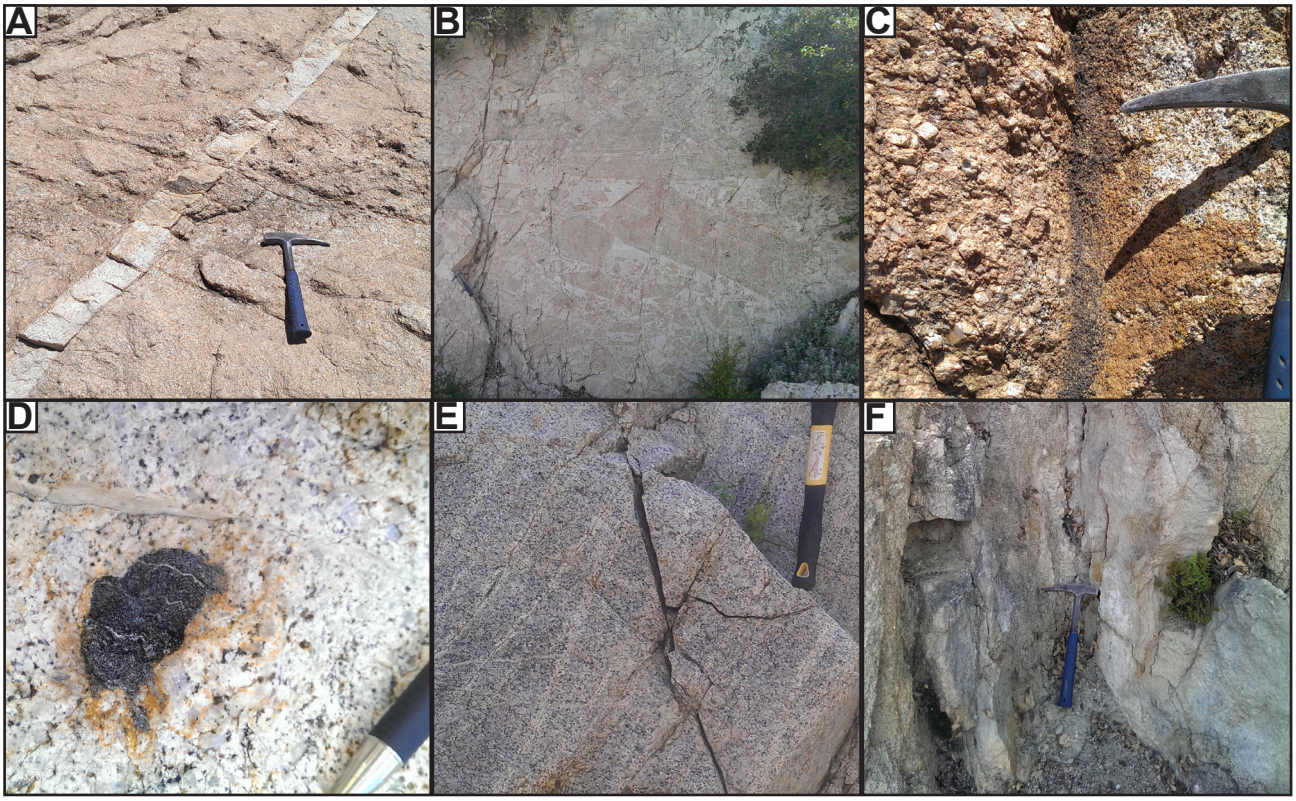


Figure 3.13 District exposure of the Schultze Granite, old US60. A. Equigranular granite cut by megacrystic dike, inturn cut by fine grained dike. B. Igneous cemented breccia, width of view approximately 4-5 m. C. Biotite schlieren at contact between equigranular granite and megacrystic dike. D. Partially digested crenulated biotite schist basment xenolith. E. Sheeted quartz K-feldspar veins at eastern end of the Pinto Valley bridge, US60. F. Recessive muscovite vein.

sizes of around 1 cm.

An Ar-Ar age determination of primary biotite returned a 74.8 ± 0.3 Ma age for the quartz diorite stock (Hehnke et al., 2013; Table 3.2). Late stage plagioclase rich and granitic dikes have also been dated using U-Pb on zircons at 73.5 ± 4.2 and 72.0 ± 2.0 Ma (O'Neal, 2015; Table 3.2).

***Interpretation***

The Silver King Quartz Diorite is a local example of early Laramide plutonism in the Superior district. Regionally, such intrusions typically have intermediate compositions and were less productive economically (Lang and Titley, 1998; Seedorff et al., 2005b). The quartz diorite stock in the Superior district has caused local magmatic-hydrothermal activity as indicated by the coarse grained pods reported by Peterson (1969), likely miarolitic cavities. Breccias at the margins of the stock are interpreted to have formed by attrition and abrasion in a magmatic-hydrothermal brecciation event, probably caused by catastrophic release of volatiles (e.g., Sillitoe, 1985).

#### 3.3.4.3 Dacite stock and associated porphyry dikes

A plug of dacite porphyry intruded the quartz diorite in the north of the study area and hosts the historically significant Silver King mine (Figure 3.2). The dacite at this location is intensely sericitised,

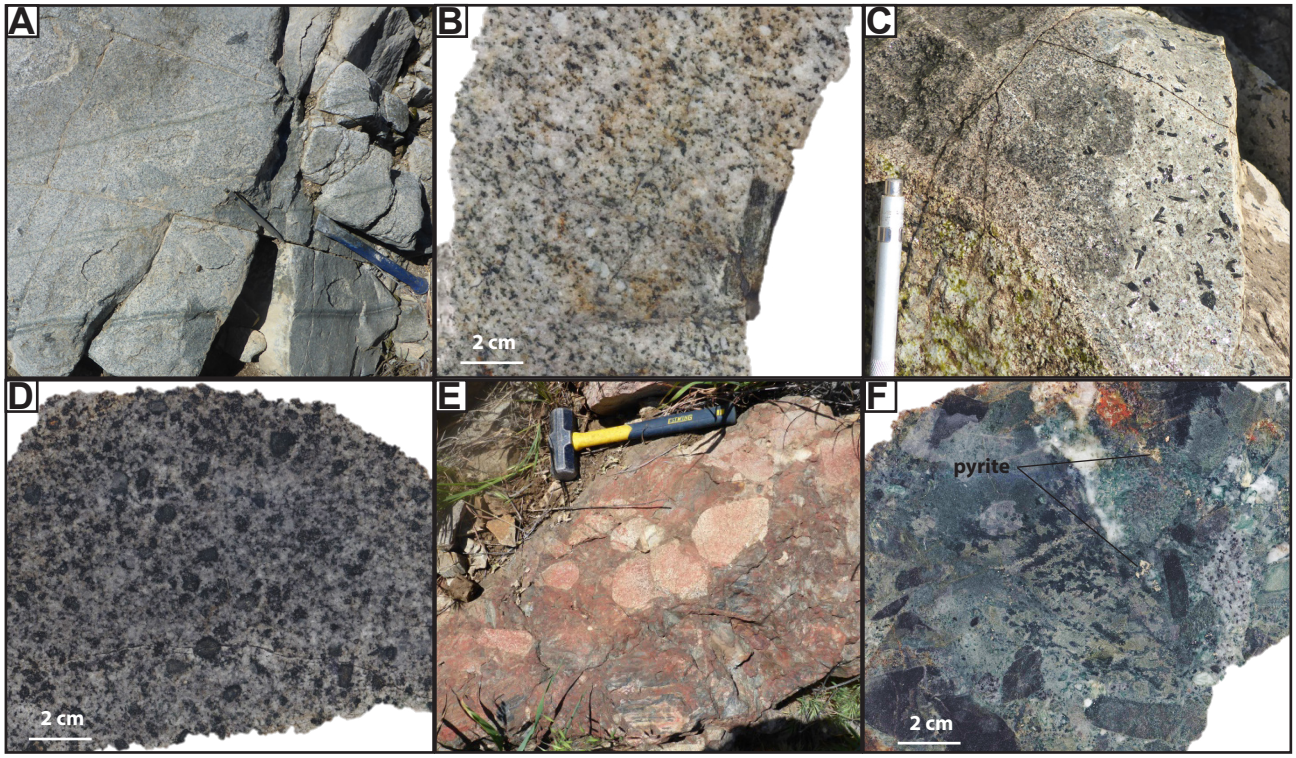


Figure 3.14 Textures of quartz diorite and associated lithologies from the Superior district. A. Fine to medium grained, equigranular quartz diorite with quartz-chlorite veins and basement xenoliths exposed in Silver King wash. B. RE16JP074 - Fine grained quartz diorite, with xenolith on right side. C. Late hornblende-phryic porphyry cutting fine grained equigranular quartz diorite. D. RE16JP075 - Hand specimen of a late porphyritic dike, showing partial resorption of hornblende phenocrysts. E. Outcropping polymict lithic breccia. F. RE16JP015 - Hand specimen of polymict lithic breccia, partially igneous cemeted, partially quartz cemented breccia. Pyrite in the centre-right of the photograph.

although original plagioclase phenocrysts can still be identified (Figure 3.15 A). Elsewhere in the district small irregular dacite dikes intrude faults and joints, as well as bedding planes, such as the 2-5 m wide fault-hosted dike at Magma (Figure 3.15B). Peterson (1969) reported a fine grained groundmass of plagioclase, K-feldspar hornblende and biotite for unaltered examples of the dacite dikes. These dikes are also commonly reported from the Magma mine and for Superior East, where they have been variably reported as quartz porphyry, quartz eye porphyry, quartz monzonite porphyry, dacite porphyry and granite porphyry (Figure 3.15 C-D; Sell, 1995; Manske and Paul, 2002; Ballantyne et al., 2003). In an attempt to standardise nomenclature, Resolution Copper have classified these dikes as either rhyodacite porphyry or quartz latite porphyry, depending of the abundance of quartz phenocrysts. Rhyodacite porphyries (KTqp; Manske and Paul, 2002; quartz eye and quartz monzonite porphyry; Ballantyne, 2003) are a series of felsic, quartz-rich intrusions. These generally have abundant rounded-subhedral quartz crystals in a fine plagioclase, K feldspar, biotite and amphibole groundmass (Figure 3.15C). Quartz-latite porphyries are less felsic, with only a few quartz eyes in a darker plagioclase, biotite, and amphibole groundmass (Figure 3.14D). In some cases they contain large orthoclase crystals, comparable to the Schultze Granite (Manske and Paul, 2002; Zulliger, 2007). The observed relative timing relationships from drilling at the Resolution deposit show rhyodacite with quartz-only veins have consistently been

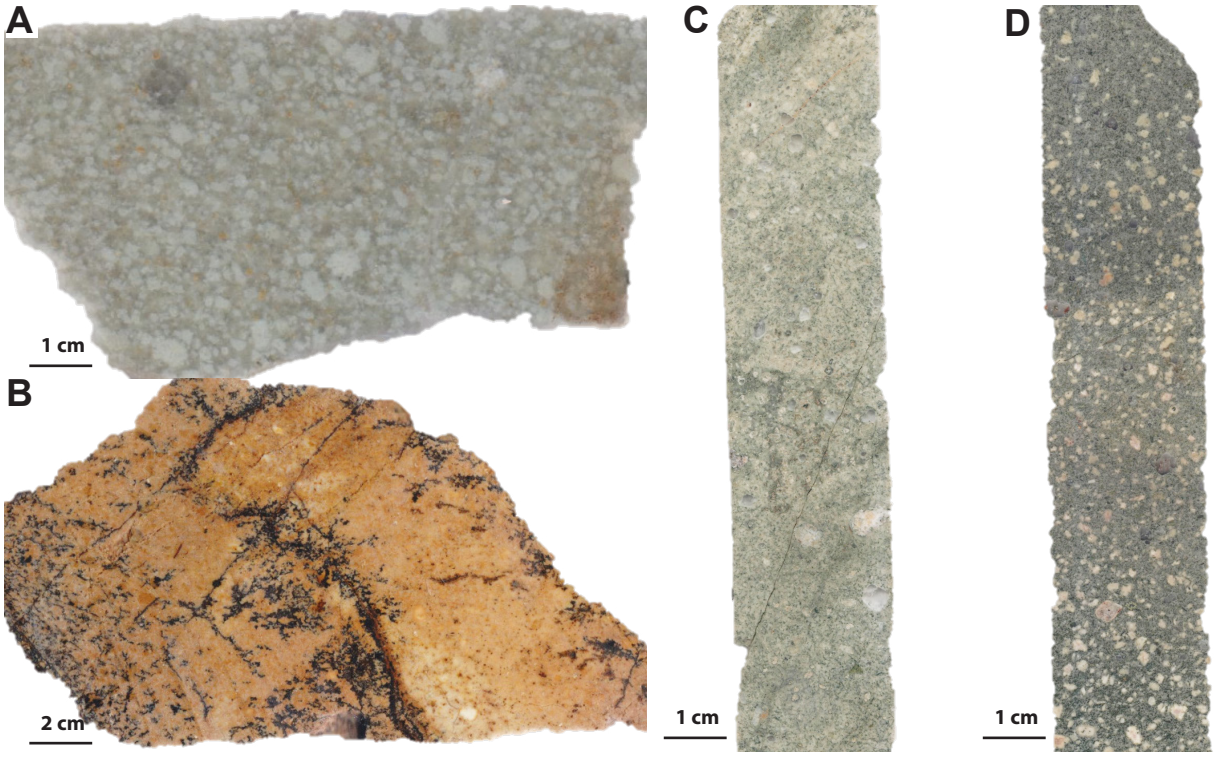


Figure 3.15 Porphyry dikes from the Superior district. A. RE16JP065 - Strongly illite-muscovite altered porphyry from the Silver King stock. B. Strongly manganese oxide stained dacite porphyry from the Magma discovery outcrop. C. RE16JP158 - Rhyodacitic dike. Note partially resorped K-feldspar megacrysts. D. RE16JP159 - Andesitic porphyry dike from the Magma mine.

truncated by quartz latite dikes (Zulliger, 2007). U-Pb zircon age dates for porphyry dikes around the district range from 69.3 ± 1.1 Ma to 63.8 ± 1.2 Ma (Seedorff et al., 2005b; Hehnke et al., 2013; Table 3.2). There is a general progression from older dikes at Silver King to younger dikes at Magma to and the youngest dikes at Resolution and Superior East (Table 3.2, Figure 3.19).

***Interpretation***

Mineralogical and textural characteristic of the porphyry dikes of the Superior district led some workers to interpret them as the final stages of crystallisation of the Schultze Granite (Mankse and Paul, 2002; Zulliger, 2007). Their porphyritic texture is consistent with a shallow crustal level of emplacement (John et al., 2010).

#### 3.3.4.4 Grandfather Lead Dike.

Locally known as the Grandfather Lead, a cream-pink coloured, strongly silicic altered, locally brecciated, NE striking, 5 m wide dike occurs in the NW of the map area (Figure 3.2). The dike has cut Proterozoic and Laramide lithologies suggesting a younger Laramide age, possibly coeval with the smaller porphyry dikes in the district. Additionally xenoliths are also common, similar in composition to those observed in the quartz diorite and Schultze Granite (Figure 3.15 A). Small relict equant feldspar phenocrysts are locally distinguishable, suggesting a dacitic to rhyodacitic composition. These have commonly been

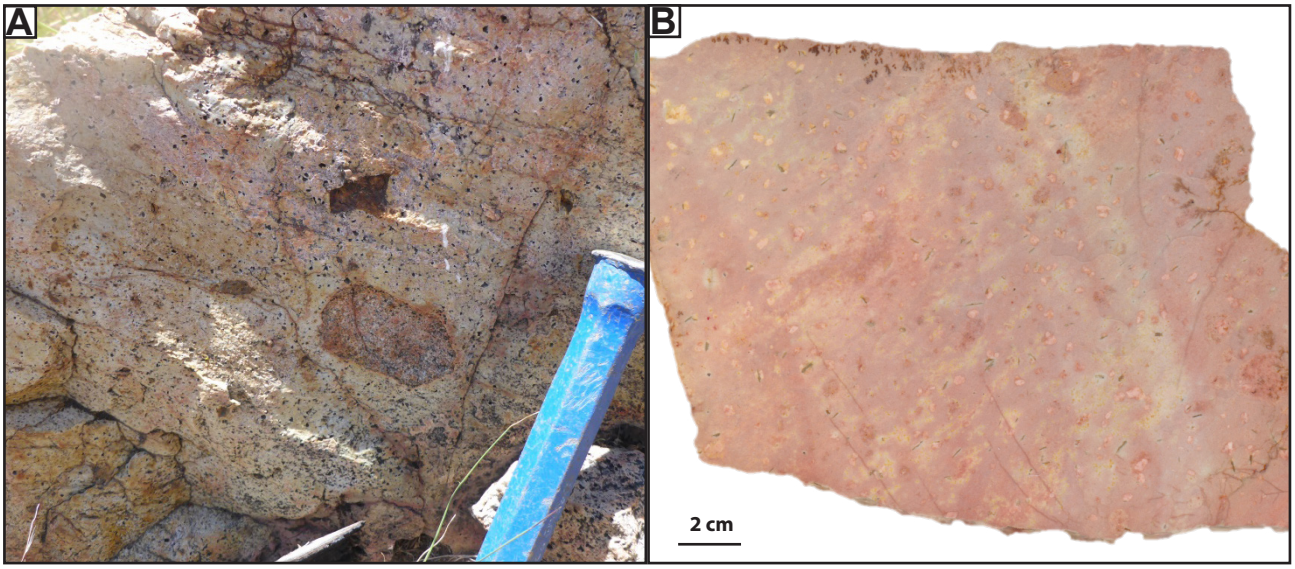


Figure 3.16 Grandfather Lead felsite dike. A. Typical exposure close to the southern edge of the quartz diorite, showing basment xenoliths, pocked surface from the weathering of altered felspars and strong silicification. B. RE16JP033 - Hand specimen of the Grandfather Lead dike with pink groundmass and selective illite-muscovite replacement of feldspars.

replaced by coarse sericite crystals, variably accompanied by pervasive silicic alteration (Figure 3.16 B).

***Interpretation***

The potential significance of the Grandfather Lead dike has been neglected by previous workers. The inferred late Laramide age, combined with strong silicic and sericitic alteration suggest that this unit warrants further investigation, given that is distal to known mineralisation (Figure 3.2)

### 3.3.4.5 Cretaceous volcanic and sedimentary rocks

Cretaceous volcanic and sedimentary rocks are confined to the buried half-graben under the Apache Leap plateau and are completely covered by later Tertiary rocks (Figure 3.2, 3.3). The graben has no surface expression in the district, although two of the three boundary faults are tentatively associated with a number of epithermal veins that crop out in the range front (Hammer, 1973). Inside the graben, the base of the Cretaceous stratigraphy is characterised by a dominantly siliciclastic sequence called the Cretaceous Quartzose Sandstone (Kqs). The Kqs is typically fine to medium grained, well to moderately well sorted, medium to thickly bedded (locally laminated) quartz arenite which is locally interbedded with cream-colored fine grained laminated arkoses and siltstones (Figure 3.17 A). A characteristic one to three metre thick matrix-clast supported conglomerate is present in its lower section (Figure 3.17 B), locally with monomict limestone sections containing corroded clasts (e.g. Figure 3.17 C). Thicknesses of individual beds can vary from a few tens of metres to <10 cm. This is probably likely to relate to growth faulting during graben development, differential erosion across fault blocks, pre deposition topography, or some combination thereof (Zulliger, 2007). Although the youngest detrital zircon ages cluster around 96.8 ± 2.2 Ma and constrain the maximum depositional age, other detrital zircons produced ages

ranging from Proterozoic (1700 and 1400 Ma) to Triassic (230 Ma), suggesting significant development of topography and exposure of basement geology during the time of deposition (Table 3.2; Figure 3.19; Zulliger, 2007). The Kqs is absent from the southern and eastern portions of the graben (Hehnke et al., 2012).

Overlying the Kqs is a Cretaceous sequence of volcanic and volcaniclastic rocks (Kvs). Although the Kvs typically presents as a polymict lithic breccia (Figure 3.17 D), two distinct lithological compositions are present. A broadly andesitic sequence occupies the north and west parts of the graben and is interbedded with sandstone units in the lower part of the section. The upper part of the section is dominated by andesitic – basaltic volcaniclastic rocks (Figure 3.16 E). Laramide U-Pb dates for the andesitic rocks suggest that this sequence is coeval with the quartz diorite (Table 3.2; Figure 3.19).

A sequence of rhyodacitic – dacitic volcaniclastics dominate the central, south and east sectors of the graben (Figure 3.17 F). In places they overlie a thinned Kqs, whereas elsewhere they directly overlie the Paleozoic section (Hehnke et al., 2012). Within this subunit of the Kvs, three lithofacies associations have been identified; rhyodacitic lapilli tuff (pyroclastic flows) crystal-rich tuff and a rhyodacitic lapilli tuff that cross cut the previous two facies and contains more deeply sourced schist clasts that are absent in the other facies. This breccia facies association has been interpreted as a diatreme complex (Zulliger, 2007). Detailed descriptions of these units can be found in Zulliger (2007) and Hehnke et al. (2012). Owing to the lack of understanding of the relationship to the andesitic and rhyodacitic units, a high degree of internal textural and compositional heterogeneity, and overprinting hydrothermal alteration, they share the Kvs label (Figure 3.16 D).

***Interpretation***

A tentative correlation between the Kqs and the poorly preserved, but regionally extensive Fort Crittenden Formation of the Bisbee group was made by Zulliger (2007). The Fort Crittenden Formation is interpreted to have been deposited in a fluvio-deltaic environment at the NW edge of the border rift system (Dickinson, 1989; Dickinson and Lawton, 2002).The temporal and compositional similarity between the quartz diorite and the andesitic Kvs suggest a genetic association. Hehnke et al. (2012) speculated that a volcanic centre was located above the quartz diorite and was the source of the andesitic Kvs. The rhyodacitic Kvs rocks are the extrusive equivalents of the coeval rhyodacite and quartz-latite porphyry intrusions within the graben, based on compositional and textural similarity as well as timing relationships (Table 3.2; Zulliger, 2007). They also share compositional and textural similarity with the Schultze Granite, which is the basis for the inferred genetic relationship between the granite, both porphyry types and all of the rhyodacitic facies of the Kvs (Zulliger, 2007; Hehnke et al., 2012).

### 3.3.5 Tertiary Rocks

The most significant and widespread Tertiary units in the Superior district are the Whitetail Conglomerate

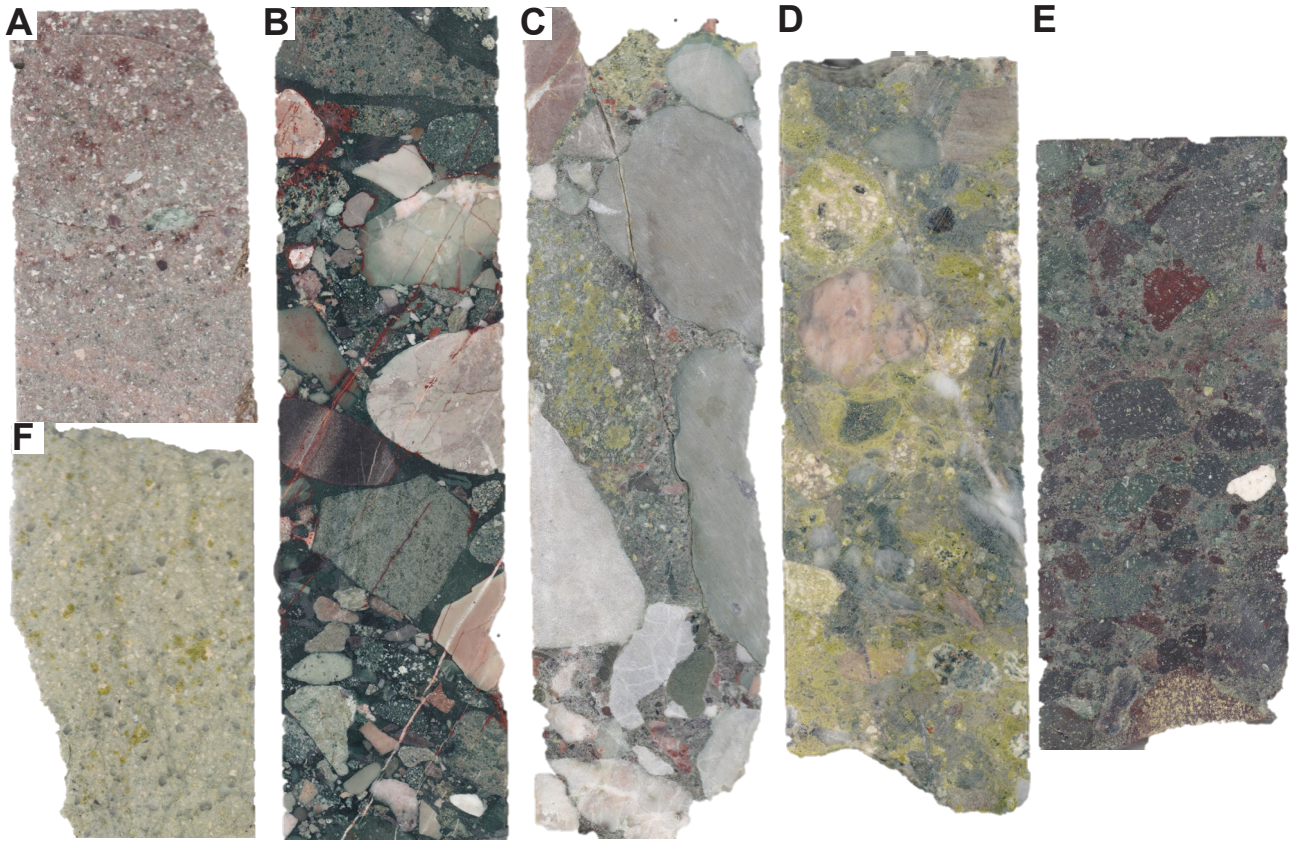


Figure 3.17 Facies of the graben-hosted Cretaceous sedimentary and volcanic rocks. All slabs are cut from HQ core (6.3 cm wide) A. RE15JP052 - medium-coarse grained lithic sandstone of the basal KQS. Note argillic alteration of some grains. B. RE15JP163 - Polymict clast supported conglomerate facies of the lower KVS, dominated by Proterozoic lithologies. C. RE16JP007 - Corroded limestone clast conglomerate, with volcaniclastic matrix material, suggesting entrainment in volcanic flow deposit. D. RE16JP096 - Typical polymict lithic volcaniclastic breccia, with clasts of all ages. Note strong epidote alteration around some clasts, difuse albite whisps and varible chlorite alteration of the matrix. E. RE16JP042 - Andesite clast-rich volcanic breccia, typical of the andesitic facies of the KVS. Note variable pervasive chlorite-hematite alteration. F. RE16JP048 - Coherent rhyodacitic volcanic rock, with selective epidote alteration.

and Apache Leap Tuff. Subordinate rocks include the Haunted Canyon Volcanics ('Early Volcanics'; Figure 3.3) that crop out in the far north of the range front, and the Picketpost Volcanics, Tertiary Basalt and Gila Conglomerates that are exposed throughout the Tertiary basin to the west of Superior (Figures 3.2, 3.3). These subordinate lithologies have limited exposure within the map area and were not encountered in this study (Figure 3.1). Consequently, they are not reviewed here. Detailed descriptions can be found in Short et al. (1943) and Peterson (1969).

#### 3.3.5.1 Whitetail Conglomerate

Paleozoic Naco group rocks and Cretaceous volcanic and volcaniclastic rocks are unconformably overlain by partially consolidated pebble to boulder size gravels and conglomerates of the Whitetail Conglomerate (Figure 3.3). Clasts comprise all local younger lithologies and the unit thickens markedly eastwards from areas where it is locally absent to sections 3 km east of the Apache Leap escarpment where it exceeds 1 km in thickness. The unit varies in character from volcanic-derived gravels (Figure 3.18 A) to coarse dolerite and Apache Group-derived conglomerate, locally with large boulders of schist, to poorly consolidated

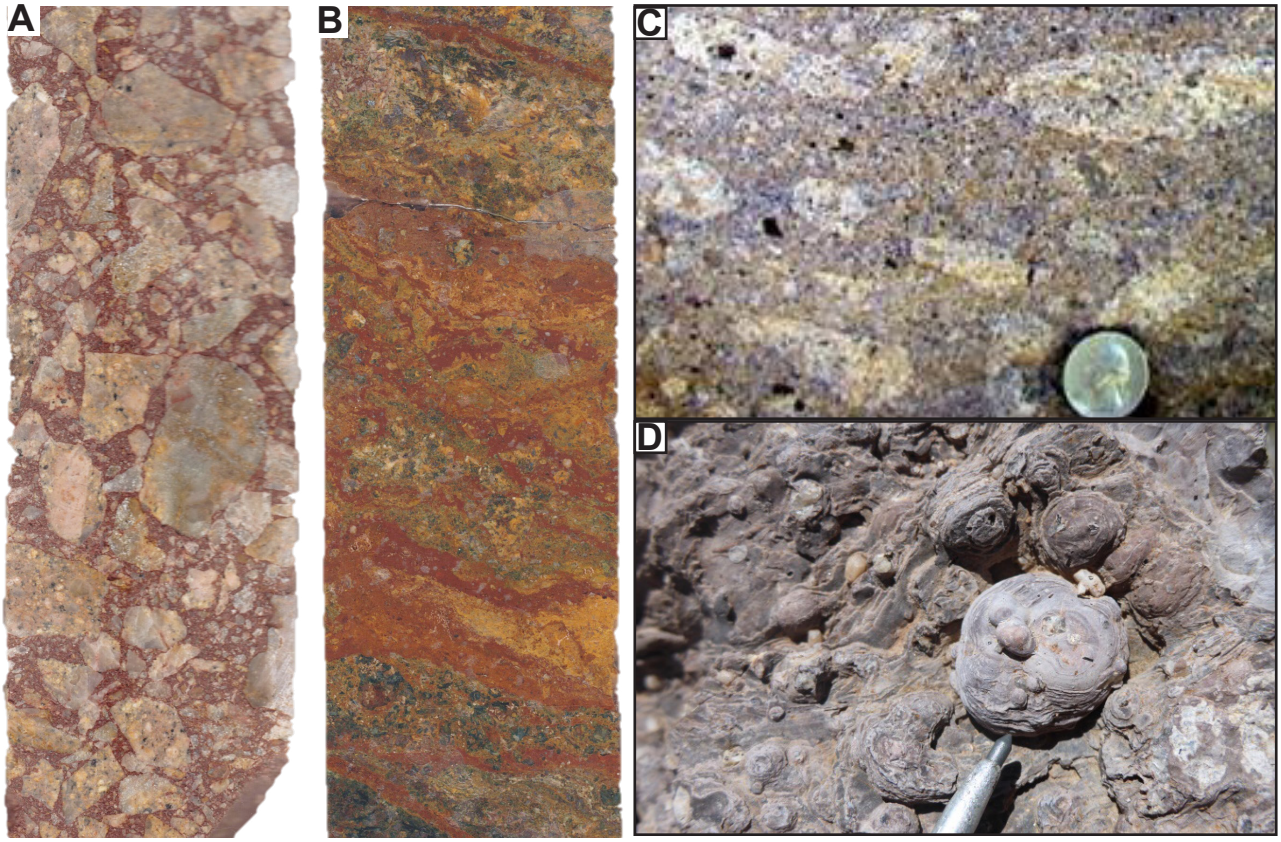


Figure 3.18 Tertitary lithologies encountered during this study. Slabs cut from HQ core (6.3 cm wide). A. RE15JP202 - Pebble conglomerate in the Tertiary Whitetail. Clasts are angular to sub-rounded highlighting the limited transport. B. RE15JP204 - Fine grained facies of the Whitetail conglomerate with strong iron-oxide staining and native copper. C. Typical exposure of the Apache Leap tuff, note the flattened pumice clasts (light coloured domains) Photo courtesy of Hamish Martin, Resolution Copper. D. Devitrified spherulite at the base of the Apache Leap

gypsum-bearing lacustrine sediments and marl near the top. The Whitetail Conglomerate has been subdivided by geologists at Resolution Copper into four readily distinguished lithofacies. Native copper is common in some parts of the Whitetail Conglomerate (Figure 3.18 B)

***Interpretation***

The structural geometry and confinement of the Whitetail Conglomerate is consistent with deposition synchronous with the onset of Tertiary extension and block rotation. The presence of large, outsized blocks of schist, termed slide blocks, are interpreted to have been eroded from the hangingwall of large reverse faults that were active during the Laramide Orogeny (e.g., proto-Concentrator Fault; Mankse and Paul, 2002; Figure 3.2).

#### 3.3.5.2 Apache Leap Tuff

The Apache Leap Tuff forms a prominent west-facing cliff above Superior (Figure 1.3 A). It covers a wide area south of Salt River, stretching from Superior in the west to the faulted contact with the Schultze granite well beyond the map area to the east (Figure 3.1). It is a biotite-phyric dacite and contains abundant flattened pumice clasts in a glassy groundmass, attesting to post-depositional welding (Figure

Table 3.2 Geochronology for the Superior district and Schultze Granite.

| Sample ID | Hole ID | From | To | UTM_E | UTM_N | Formation Name | Locality |
|---|---|---|---|---|---|---|---|
| BS05-845 | | | | | | Manitou Granite | Not Provided |
| DM04-655 | | | | | | Solitude Granite | Not Provided |
| | RES8A | 1824.68 | 1824.86 | | | Kqs | Resolution |
| | RES23 | 972.30 | 973.20 | | | Kvs (andesitic) | Resolution |
| | RES24 | 824.60 | 826.20 | | | Kvs (andesitic) | Resolution |
| | RES3 | 1205.04 | 1218.16 | | | Kvs (felsic) | Resolution |
| | RES1 | 988.20 | 1000.91 | | | Kvs (felsic) | Resolution |
| | RES2B | 1571.30 | 1584.45 | | | Kvs (felsic) | Resolution |
| | RES5D | 1443.49 | 1456.56 | | | Kvs (felsic) | Resolution |
| SK3 | | | | 491447 | 3687589 | Silver King Quartz Diorite | Silver King |
| #3 | | | | 490727 | 3688220 | Silver King Quartz Diorite (?) | Silver King |
| SK1 | | | | 492021 | 3687682 | Dacite porphry plug | Silver King |
| #1 | | | | 493538 | 3689156 | Silver King Quartz Diorite (?) | Silver King |
| #2 | | | | 491954 | 3689178 | Silver King Quartz Diorite (?) | Silver King |
| RES#3 | 3653A | | | | | Dacite porphyry dike | Magma |
| | RES5B | 2086.00 | 2131.50 | | | Rhyodacite porphyry | Resolution |
| | RES3 | 1133.26 | 1145.56 | | | Rhyodacite porphyry | Resolution |
| | S27 | 210.00 | 210.10 | | | Rhyodacite porphyry | Resolution |
| | RES2A | 2237.60 | 2238.70 | | | Rhyodacite porphyry | Resolution |
| | RES20 | 1177.00 | 1177.50 | | | Quartz-latite porphyry | Resolution |
| RES#5 | | | | 492016 | 3683628 | Quartz-latite porphyry | Resolution |
| | RES17F | 1687.00 | 1688.00 | | | Quartz-latite porphyry | Resolution |
| | A4 | 2017.00 | 2017.10 | | | Rhyodacite porphyry | Superior East |
| Pinto Valley | | | | | | Rhyodacite porphyry (?) | Pinto valley |
| BS03-108B | | | | | | Schultze Granite (Early) | Not Provided |
| 3-23-98-4 | | | | | | Schultze Granite (M-J) | Not Provided |
| DM03-710 | | | | | | Schultze Granite (M-J) | Not Provided |
| BS03-108A | | | | | | Schultze Granite (M-J) | Not Provided |
| DM04-670 | | | | | | Schultze Granite (Transitional) | Not Provided |
| DM04-669 | | | | | | Schultze Granite (porphyry) | Inspiration |
| DM04-560 | | | | | | Schultze Granite (C porphyry) | Not Provided |
| BS04-329 | | | | | | Schultze Granite (G porphyry) | Not Provided |
| | RES21 | 1789.80 | 1790.10 | | | Whitetail Conglomerate | Resolution |
| | RES20 | 757.00 | 758.00 | | | Whitetail Conglomerate | Resolution |
| | RES11 | 651.55 | 651.66 | | | Whitetail Conglomerate | Resolution |
| 6549 | | | | 3685040 | 492800 | Apache Leap Tuff | Superior |
| 6601 | | | | 3685565 | 494785 | Apache Leap Tuff | Superior |

Abbreviations; Kqs - Cretaceous quartzose sandstone, Kvs - Cretaceous volcaniclastic sandstone; ALC - Arizona Laserchron Centre; NMGRL - New Mexico Geochronology Research Laboratory; PCIGR - Pacific Centre for Isotope and Geochronology Research

| Description | Technique | Mineral | Age | Error (2 s) | Lab | Reference |
|---|---|---|---|---|---|---|
| Not provided | U-Pb | Zircon | 79.0 | 19.0 | ALC | Seedorff et al. (2005) |
| Not provided | U-Pb | Zircon | 70.0 | 10.0 | ALC | Seedorff et al. (2005) |
| Detrital zircons | U-Pb | Zircon | 96.8 | 2.2 | ALC | Zulliger 2007 |
| Zircon in andesitic lapilli tuff | U-Pb | Zircon | 74.1 | 2.4 | ALC | Hehnke et al. (2012) |
| Zircon in andesitic lapilli tuff | U-Pb | Zircon | 74.1 | 1.2 | ALC | Hehnke et al. (2012) |
| Zircon in lapilli crystal tuff | U-Pb | Zircon | 67.8 | 2.3 | ALC | Hehnke et al. (2012) |
| Zircon in lapilli tuff | U-Pb | Zircon | 67.6 | 1.3 | ALC | Hehnke et al. (2012) |
| Zircon in lapill crystal-lithic tuff | U-Pb | Zircon | 67.1 | 2.3 | ALC | Hehnke et al. (2012) |
| Zircon in lapill crystal-lithic tuff | U-Pb | Zircon | 66.4 | 1.1 | ALC | Hehnke et al. (2012) |
| Silver King Quartz Diorite stock | Ar/Ar | Biotite | 74.8 | 0.33 | NMGRL | Hehnke et al. (2012) |
| Granitic porphyry dike quartz diorite | U-Pb | Zircon | 73.5 | 4.2 | ALC | O'Neal (2015) |
| Sericitised dacite stock at Silver King | U-Pb | Zircon | 73.6 | 1.6 | ALC | Hehnke et al. (2012) |
| Plagioclase rich porphyry dike | U-Pb | Zircon | 72.0 | 2.0 | PCIGR | O'Neal (2015) |
| Plagioclase rich porphyry dike | U-Pb | Zircon | 69.0 | 4.0 | PCIGR | O'Neal (2015) |
| Pre-mineralisation dike in Magma vein | U-Pb | Zircon | 69.1 | 4.0 | ALC | Seedorff et al. (2005) |
| Eastern rhyodacite stock | U-Pb | Zircon | 69.3 | 1.1 | ALC | Hehnke et al. (2012) |
| rhyodacite with k-feldspar megacrysts | U-Pb | Zircon | 67.0 | 1.7 | ALC | Hehnke et al. (2012) |
| rhyodacite cutting Kvs | U-Pb | Zircon | 65.0 | 0.7 | ALC | Seedorff et al. (2005) |
| Course grained rhyodacite below Cu shell | U-Pb | Zircon | 64.1 | 1.9 | ALC | Seedorff et al. (2005) |
| Quartz-latite dike with quartz eyes | U-Pb | Zircon | 67.9 | 1.3 | ALC | Hehnke et al. (2012) |
| Dike cutting Naco Fm in Queen Creek | U-Pb | Zircon | 66.2 | 0.8 | ALC | Seedorff et al. (2005) |
| Quartz-latite dike with quartz eyes | U-Pb | Zircon | 66.0 | 0.6 | ALC | Hehnke et al. (2012) |
| Rhyodacite dike in Superior East | U-Pb | Zircon | 63.8 | 1.2 | ALC | Seedorff et al. (2005) |
| Not provided | U-Pb | Zircon | 63.6 | 1.9 | ALC | Seedorff et al. (2005) |
| Not provided | U-Pb | Zircon | 66.9 | 2.9 | ALC | Seedorff et al. (2005) |
| Not provided | U-Pb | Zircon | 64.0 | 0.6 | ALC | Seedorff et al. (2005) |
| Not provided | U-Pb | Zircon | 63.5 | 1.1 | ALC | Seedorff et al. (2005) |
| Not provided | U-Pb | Zircon | 62.9 | 1.3 | ALC | Seedorff et al. (2005) |
| Not provided | U-Pb | Zircon | 63.1 | 1.3 | ALC | Seedorff et al. (2005) |
| Not provided | U-Pb | Zircon | 63.7 | 1.6 | ALC | Seedorff et al. (2005) |
| Not provided | U-Pb | Zircon | 63.1 | 1.4 | ALC | Seedorff et al. (2005) |
| Not provided | U-Pb | Zircon | 61.3 | 1.4 | ALC | Seedorff et al. (2005) |
| Airfall tuff 80m above base of unit | Ar-Ar | Sanidine | 24.3 | 0.12 | NMGRL | Hehnke et al. (2012) |
| Airfall tuff 170m above base of unit | Ar-Ar | Sanidine | 22.0 | 0.06 | NMGRL | Hehnke et al. (2012) |
| Fine volcanic sediment 350m above base | Ar-Ar | Biotite | 21.8 | 0.32 | AIRIE | Hehnke et al. (2012) |
| Not provided | Ar-Ar | Sanidine | 18.6 | 0.05 | NMGRL | McIntosh and Fergusson (1998) |
| Not provided | Ar-Ar | Sanidine | 18.6 | 0.06 | NMGRL | McIntosh and Fergusson (1998) |

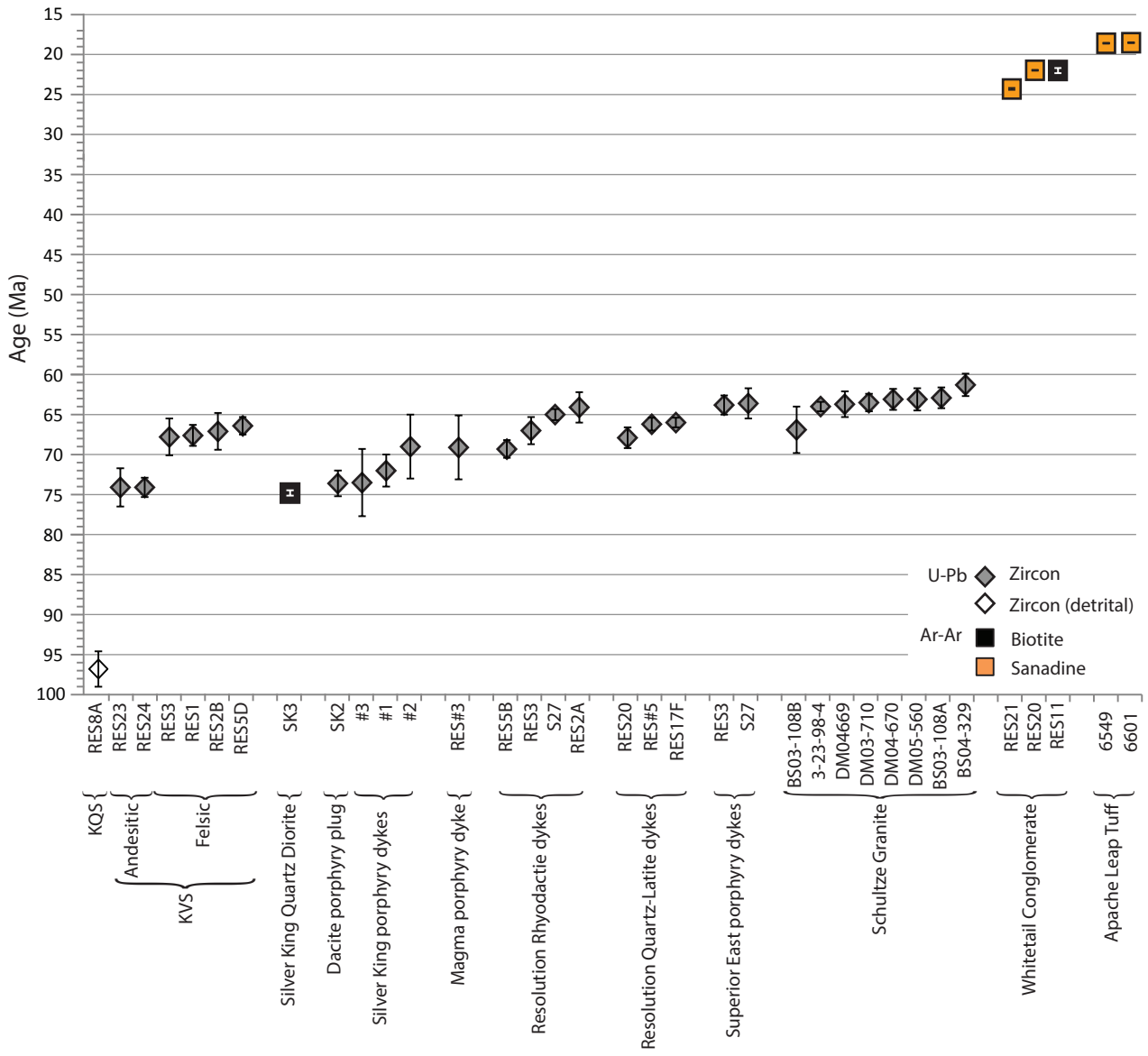


Figure 3.19 Geochronological evolution diagram for the Superior district, using data from Table 3.2

3.18 C). It is vitrophyric to spherolitic at its base, depending on the degree of local devitrification, and perlite is quarried from this unit locally (Figure 3.18 D). The degree of welding decreases upwards and is accompanied by an increase in devitrification and gradual colour change from dark brown to light grey.

***Interpretation***

The Apache Leap Tuff is interpreted to be a welded ash-flow or ignimbrite deposit (Hehnke et al., 2012). Eruption was likely from a large caldera located to the NW, probably around the Superstitions Mountains area (Ferguson and Trapp, 2001; Ferguson, 2005). Ar-Ar dating by McIntosh and Ferguson (1998) provides an age of 18.6 ± 0.06 Ma (Table 3.2).

## 3.4 Structural evolution

### 3.4.1 Introduction

This section presents observations regarding the structural development of the Superior district, presented in the context of the synthesis of regional deformation and geodynamic evolution presented in Chapter 2. A review of previous structural work is presented first to inform interpretations of new observations and measurements from the Superior district. New data include structural mapping of an exposed strand of the Concentrator fault, and a structural restoration of the Superior range front to demonstrate the limited effect of Tertiary extension on geochemical dispersion around Resolution. Although the structural architecture in the Superior district is today dominated by post-mineralisation Tertiary normal faulting, earlier events, including the formation of the enigmatic Resolution graben are vital components for the evolution of hydrothermal activity in the Superior district.

### 3.4.2 Structural evolution of the Superior district

#### 3.4.2.1 Paleoproterozoic metamorphism

Original Paleoproterozoic structural architecture in the Superior district is difficult to constrain, partly due to a lack of exposure but also because Paleoproterozoic tectonic features have been strongly overprinted, reactivated and/or obscured by later events. Mapping by Keep (1996) in the areas surrounding the Superior district demonstrated a consistent, steeply SE- or NW-dipping Paleoproterozoic metamorphic foliation and down-dip stretching lineations. Regional scale upright to recumbent folds were inferred based on stretching lineations and foliation attitude (Figure 3.1, 3.20). These folds, with generally SE dipping axial planes, were interpreted by Keep (1996) to represent reactivations along much older, syn-sedimentary faults during the Mazatzal metamorphic event (1,650-1,600 Ma; Whitmeyer and Karlstrom, 2007). Paleoproterozoic fold axes in the region were commonly sheared and/or intruded by ~1,400 Ma plutons such as the Ruin Granite, making them hard to identify in the field (Figure 3.1). One such fold is interpreted to sit beneath the centre of the Resolution deposit (Figure 3.1; Keep, 1996). During the current study, a NNW dipping reverse fault, hosting a boundinaged quartz vein was encountered near the Conley Springs Fault (Figure 3.4 A). Although a handful of other structures with this dip were also observed, few showed conclusive kinematic indicators and were rare above the Apache Group rocks. Faults with this attitude have no regional correlate except in the Paleo- and/or Mesoproterozoic.

#### 3.4.2.2 Mesoproterozoic basin formation

Although Mesoproterozoic growth faults are hard to identify in the Superior district as a result of overprinting by later structural events, inferences can be made about their possible orientations from regional observations. Timmons et al. (2001) demonstrated that the Unkar Group, regional correlate to the Apache Group (Shride, 1967), was deposited in basins controlled by NE-SW extension accommodated by

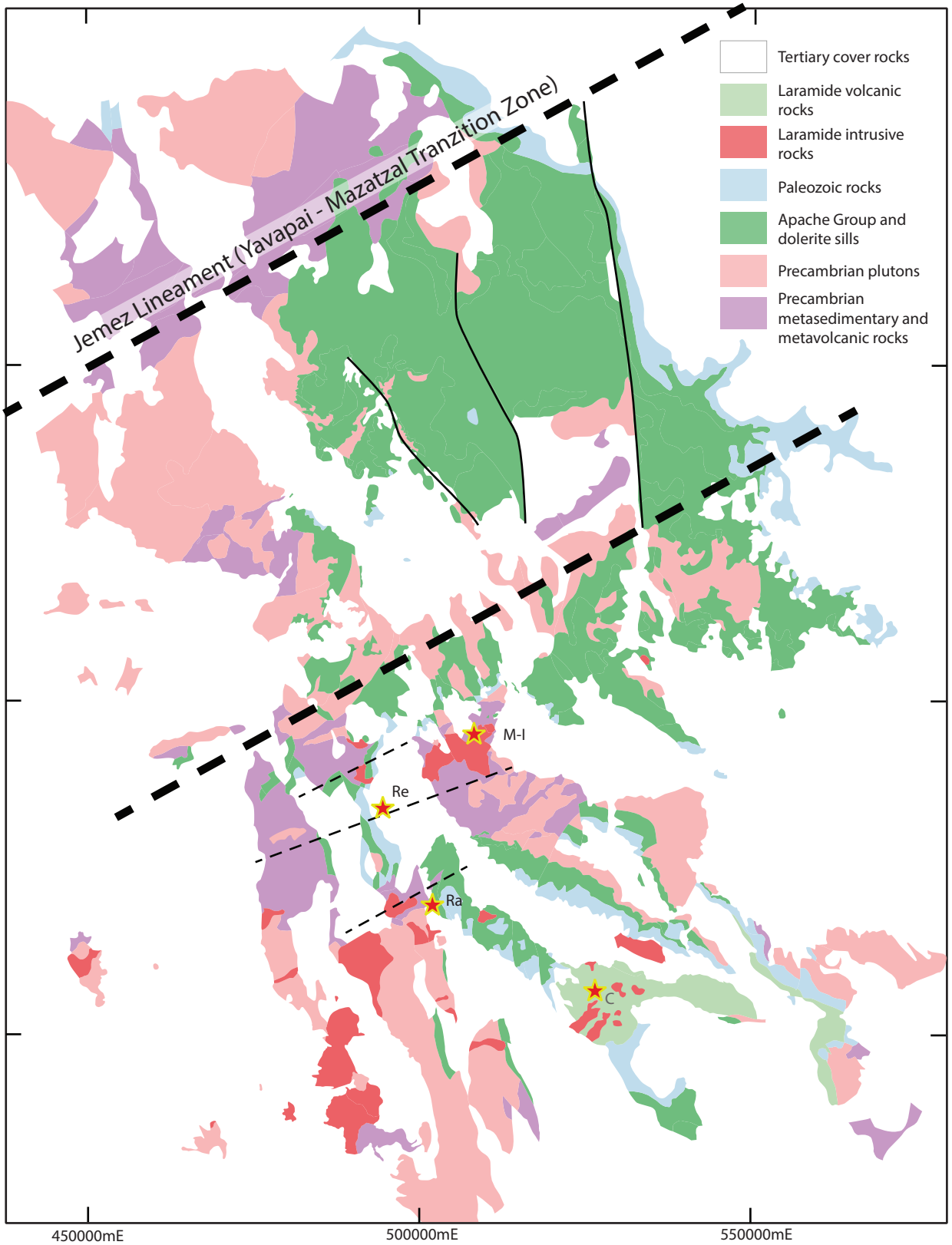


Figure 3.20 Regional extent and structural architecture of the Mesoproterozoic Apache Group basin in Arizona. Major crustal structures bound the main part of the basin to the north and south and correlate with regional scale folding mapped in the Pinal Schist, with internal distribution controlled by subsidary N-NNW striking faults, similar to those decribed for the Unkar Group in the Grand Canyon. Mapping after AGS 1:1,000,000 mapping (Richard et al., 2000). State fault data omitted for clarity (cf. Richard et al., 2000). For smaller scale Cenozoic fault mapping in southern half of map area, see Maher (2008). Selected porphyry Cu deposits; M-I - Miami-Inspiration; Re - Resolution; Ra - Ray; C - Christmas.

NW striking faults. This deposition was contemporaneous with periodic NW-SE Grenville contraction, which produced periods of syn-sedimentary compression evident in the Mesoproterozoic section of the Grand Canyon (Timmons et al., 2001).

Similar architecture can also be observed in the Apache Group (Figure 3.20). The larger part of the Apache Group basin is bounded to the north by the NE striking Jemez Lineament (Chapter 2) and to the south by a parallel structural zone that has been exploited by Precambrian plutons and now delineates a zone of more significant exhumation (Figure 3.20). This southern major structural zone also segments Tertiary extensional domains, suggesting that the main Apache Group basin is underlain by more coherent crustal material. The large structural zones mirror the orientation of the regional scale folds mapped by Keep (1996) suggesting they share a common Paleoproterozoic origin (Figure 3.20). Within the basin, the regional distribution of Apache Group rocks is strongly controlled by NW-NNW striking faults, similar to those described by Timmons et al. (2001, 2005). The similarity in structural architecture between the two Mesoproterozoic rock sequences supports the idea that the Apache Group rocks were deposited under a similar Grenvillian-dominated structural regime to their counterparts in the Grand Canyon. Transtension along NW striking Grenville faults also localised mafic magma responsible for the emplacement of the dolerite sills (Timmons et al. 2001, 2005; Bright et al., 2014). Although there is undoubtably a distinct Cenozoic structural overprint throughout this region, the localisation of both Laramide compressional and later Cenozoic extensional faulting is inextricably linked to the Proterozoic basement architecture.

In summary, reactivation along this Mazatzal-Yavapai accretionary boundary and subsidiary structures probably played an important role in Apache Group basin creation, with sedimentation localised in depocentres controlled by episodic extension principally along NNW striking faults during Grenville orogenesis (Timmons et al., 2005). Periods of uplift and erosion is also evident in the Mesoproterozoic sedimentary record, with angular unconformities separating all units within the Apache (Shride, 1967) and Unkar Groups (Timmons et al., 2005), suggesting the far-field stresses associated with the Grenvillian Orogeny were characterised by alternating transtensional and transpressional stresses. However it is also important to note that the location of the Apache Group rocks in the Superior district is at the westernmost limit of Apache Group exposure (Figure 3.20). Although this could relate to preservation, it remains possible that this represents a primary depositional limit and therefore could be subject to highly localised sedimentary and structural control.

#### 3.4.2.3 Neoproterozoic uplift

An unaddressed feature of the Proterozoic structural history of the Superior district is the exposure of dolerite sills at the uppermost Precambrian unconformity. In some cases dolerite sills are overlain directly by Bolsa Quartzite of Cambrian age (Figures 3.2, and 3.3). The Cardenas Lavas of the uppermost Unkar Group of the Grand Canyon have age determinations that suggest they are coeval with, and

therefore the eruptive product of, dolerite emplacement (Hendricks and Lucchitta, 1974). Despite the likely shallow level of emplacement of the dolerite sills, no such eruptive product has been identified south of the Grand Canyon. Therefore, a period of significant uplift and erosion must have occurred, at least in the Superior district, between sill emplacement at ca. 1,100-1,080 Ma and deposition of the middle Cambrian Bolsa Quartzite at ca. 540 Ma, in order for dolerite sills to be exposed at the Paleozoic unconformity. This period of erosion must have removed hundreds of meters, possibly kilometres of material and is likely related to the 'Grand Canyon Orogeny' or 'Neoproterozoic extensional episode', related to fragmentation of Rodina that tilted the rocks after the deposition of the ca. 750 Ma Chuar Group (e.g., Timmons et al., 2005). Indeed, the lack of Chuar group correlates in the Superior district is further suggestive of erosion or sedimentary hiatus due to uplift. The apparent conformity between the Proterozoic and Paleozoic sequences suggests that little to no tilting took place during the proposed period of uplift/exhumation.

#### 3.4.2.4 Paleozoic passive margin development

Steeply east-dipping faults were interpreted by Peterson (1969) throughout the range front to cut the lower parts of the Paleozoic section and terminate in either the Escabrosa Limestone or Naco Formation (Peterson, 1969). However faults of this age are not readily identifiable in the Superior district, suggesting that either they are not present or that they have been strongly reactivated by later events. Paleozoic growth faults were tentatively inferred in a consultant report by A. Kloppenburg (pers. comm., 2016).

#### 3.4.2.5 Laramide uplift and mineralisation

Though not as striking as the Tertiary events, evidence of compressional stresses of the Laramide Orogeny is readily apparent in the Superior district. Most notable is the Elm Canyon Thrust, an overturned fold exposed at the head of Elm Canyon on US60 (Figure 3.21 A), interpreted by many to be an overturned drag fold in the footwall of a major reverse fault – most likely the Concentrator Fault or a strand thereof. Near the base of the same canyon, incipient drag folding is exposed in a road cut (Figure 3.21 B). Similar observations were made by Maher (2008) identifying overturned rocks on an exposure of the Picketpost fault, north of Superior. Isoclinal folds are well exposed in a marble quarry, located stratigraphically above the Silver King Mine in the north of the district (Bill Hart, pers. comm., 2016; Figure 3.21 C). South of the study area, Keith (1976) mapped and interpreted major scale thrust faults in Apache Group rocks, although the larger part of the fault surface has been removed by erosion. Keith's (1976) mapping implies that at least in the south of the district, low angle thrusts may have truncated earlier high angle faults as compression during the Laramide Orogeny intensified.

Low angle reverse faults exposed underground between the Main and Concentrator Faults were also described by Short et al. (1943). They are interpreted here to represent a linkage/step-over zone typical in compressional settings, suggesting that Main Fault was also active as a reverse fault strand of the

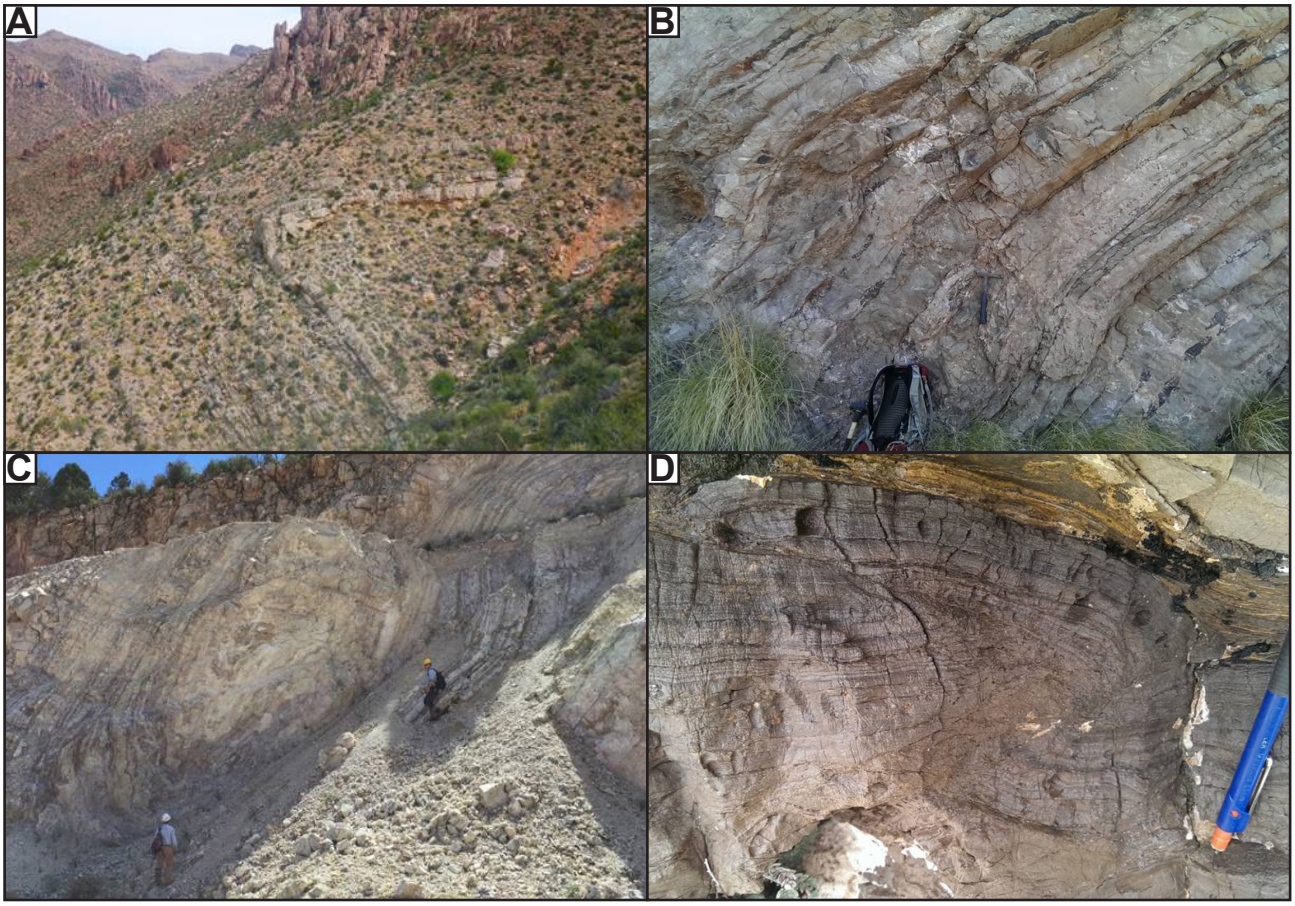


Figure 3.21 Laramide compressional features observed in the Superior district. A. Elm Canyon fold, looking NE B. Incipient drag folding exposed in Martin Formation along the US60 roadcut, Superior. C. Isoclinal folds exposed in the Omya marble quarry, north of Superior. Photograph courtesy of Bill Hart, Resolution Copper. D. Small scale uplift features observed in the Martin Formation in range front exposures east of Superior.

Concentrator during the Laramide Orogeny. Intraformational inward-dipping reverse faults in the Paleozoic carbonate rocks bound small scale uplifts (Figure 3.21 D).

Large slide blocks or boulders of Pinal Schist have been intersected in drilling of the Tertiary Whitetail Conglomerate, attesting to local exhumation of basement schist during the Tertiary, probably along large reverse faults such as the proto-Concentrator Fault during the Laramide Orogeny (e.g. Favorito and Seedorff, 2017).

#### 3.4.2.6 Resolution Graben

At Resolution, McCarrel (2012) proposed that the Anxiety Fault (Figure 3.1) when restored to its pre-Tertiary orientation, has a reverse sense of movement. This would plausibly explain the differential erosion experienced by the Paleozoic sequence across the graben. The reverse movement of the west-dipping proto-Concentrator Fault, as indicated by overturned Paleozoic limestones and apparent exhumation of basement rocks, together with reverse movement along the east-dipping Anxiety Fault, could plausibly have resulted in the formation of a small intramontane basin that, could have provided an early depocentre for the locally derived basal Kqs unit of the Cretaceous sequence, prior to the onset

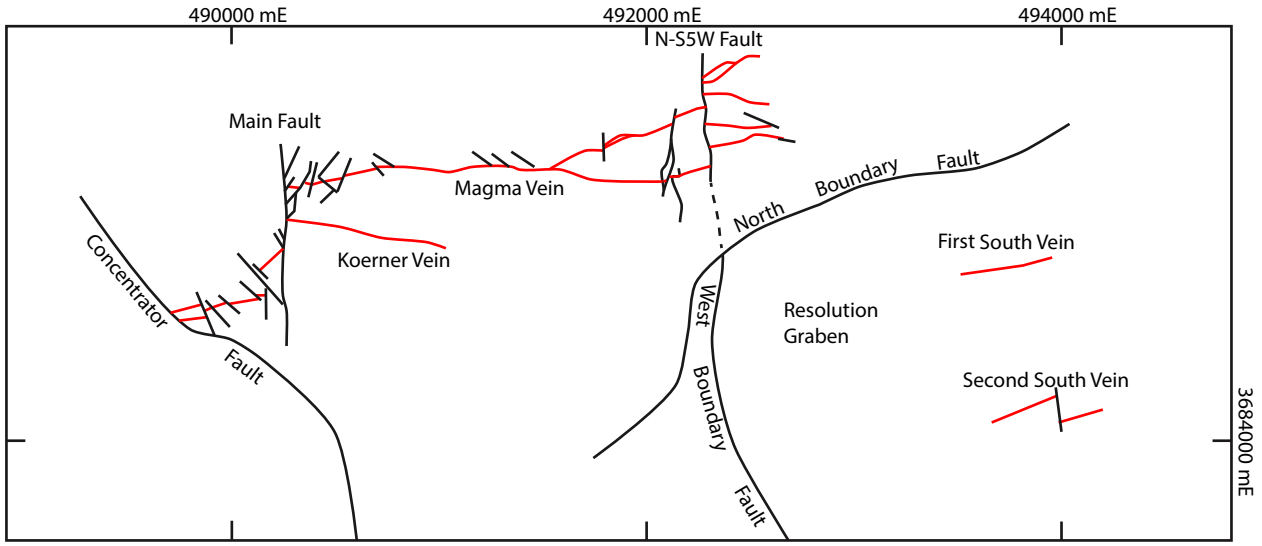


Figure 3.22 Sketch map showing the structural relationships around the Magma vein and Resolution graben. Modified after Schott (1994). Major and minor faults in black. Red lines are mineralised veins.

of volcanism in the area.

A major component of the Superior district's structural history is a phase of highly localised east-down normal movement, principally along the buried West Boundary Fault (Figure 3.2), which was probably a significant factor in the development of the greater part of the Resolution graben (Manske and Paul, 2002). However, the N-S5W Fault in the Magma Mine (Figure 3.22), initially mapped by Gustafson (1961) and later interpreted by Mankse and Paul (2002) to represent the continuation of the West Boundary Fault, shows principally sinistral strike-slip rather than normal movement, and has markedly less displacement. Figure 3.12 is thought to represent the surface expression of this fault in the US60 road cut, east of Superior. It is therefore proposed that the south-dipping North Boundary Fault strands, and to a lesser degree the Magma Fault (Figure 3.2) may have acted as relays to major east-down movement along the West Boundary Fault. The boundary faults therefore truncated the northward propagation of high magnitude displacement along the West Boundary Fault. Hammer and Peterson (1968) provided evidence for this history of movement in their description of early south-down movement along the Magma Fault. Short et al. (1943) highlighted a rotational component along the Magma fault with evidence for greater normal displacement at the western end of the mine than the east. Similarly, high magnitude east-down movement was apparently truncated by the South Boundary Fault zone. The Iron Cap fault, exposed south of the Belmont mine (Figure 3.2), is interpreted to be a strand of the South Boundary Fault and most likely truncated the West Boundary Fault. An isolated wedge of overturned Paleozoic rocks that is bounded on either side by right way-up oriented rocks, exists between strands of the South Boundary Fault (Hammer, 1973). This overturned sequence, similar to the Elm Canyon Thrust, probably originated in the hangingwall of the Concentrator Fault and was later down-faulted during graben formation (Hammer, 1973). This is good evidence that east-down movement followed major reverse movement along the Concentrator Fault in the Superior district. No regional analogue for

this phase of Laramide normal movement has yet been identified and the Resolution graben continues to be the most poorly understood aspect of the structural architecture at Superior.

The subsidence of the Resolution Graben appears to have been incremental, rather than a discrete event. The overlying Apache leap Tuff has been documented as having a constant inward dip above the centre of the deposit (Mankse and Paul, 2002; Hehnke et al., 2012). This may be the result of deposition within a paleovalley (e.g. Henry, 2008) or that the boundary faults continued to have been active, or at least discreetly reactivated, well into the Mid-Tertiary.

The lack of preferred orientations for both the porphyry dikes and the paragenetically early quartz-molybdenite veins may suggest a period of magmatically controlled neutral stress immediately prior to mineralisation. Paragenetically early and deep-seated quartz-K-feldspar alteration in the Schultze granite have been related a period of neutral stress during emplacement (Stavast, 2006), suggesting that pluton and or stock emplacement may have been the cause for this period of neutral stress (Schwarz, 2010). Major strike slip movement along ENE-oriented faults accompanied the emplacement of epithermal mineralisation along the range front as well as in the Resolution graben (Figure 3.2). Vein orientations in the Superior district, Resolution deposit and wider southwest US porphyry Cu province consistently strike ENE, demonstrating that the main mineralising phase is controlled by regional stress fields (Hammer and Peterson, 1968; Heidrick and Titley, 1982; Hehnke et al., 2013).

#### 3.4.2.7 Tertiary extension

Post-mineralisation Tertiary extensional faulting is of particular concern for the study of geochemical dispersion halos in the southwestern US porphyry Cu province. Hyper-extension, associated with metamorphic core-complex formation, affected areas of the southwest during the Mid-Tertiary. Locally, this process extended the upper crust by as much as 40 km and variably rotated fault blocks within the upper plate (e.g., Whipple Mountains core complex, Lister and Davis, 1989; Catalina Core Complex, Dickinson 1991). Later, more widespread high magnitude west-down normal faulting also occurred and was responsible for the half graben formation and block rotation characteristic of the Basin and Range Province.

Although there is no evidence for low angle core-complex related faults in the Superior district, high magnitude basin and range related normal faulting is evident. Significant normal faulting occurred following the deposition of the Apache Leap Tuff and substantial west-down offsets are documented along most of the north striking faults in the district, including the Devils Canyon, Picketpost, Robles, Concentrator and subsidiary Main and Lead Hill Faults in the range front (e.g., Maher, 2008; Figure 3.1). Barton et al. (2002, 2005) also note to possible presence of gently west-dipping faults that predate the main high angle normal faults, inferred to offset Resolution from Superior East. Normal faulting during the Mid-Tertiary is also responsible for the ubiquitous ~$30^0$ eastward dip in the district. Shallower dips observed north of the Conley Springs Fault suggest that this fault may have acted to some degree

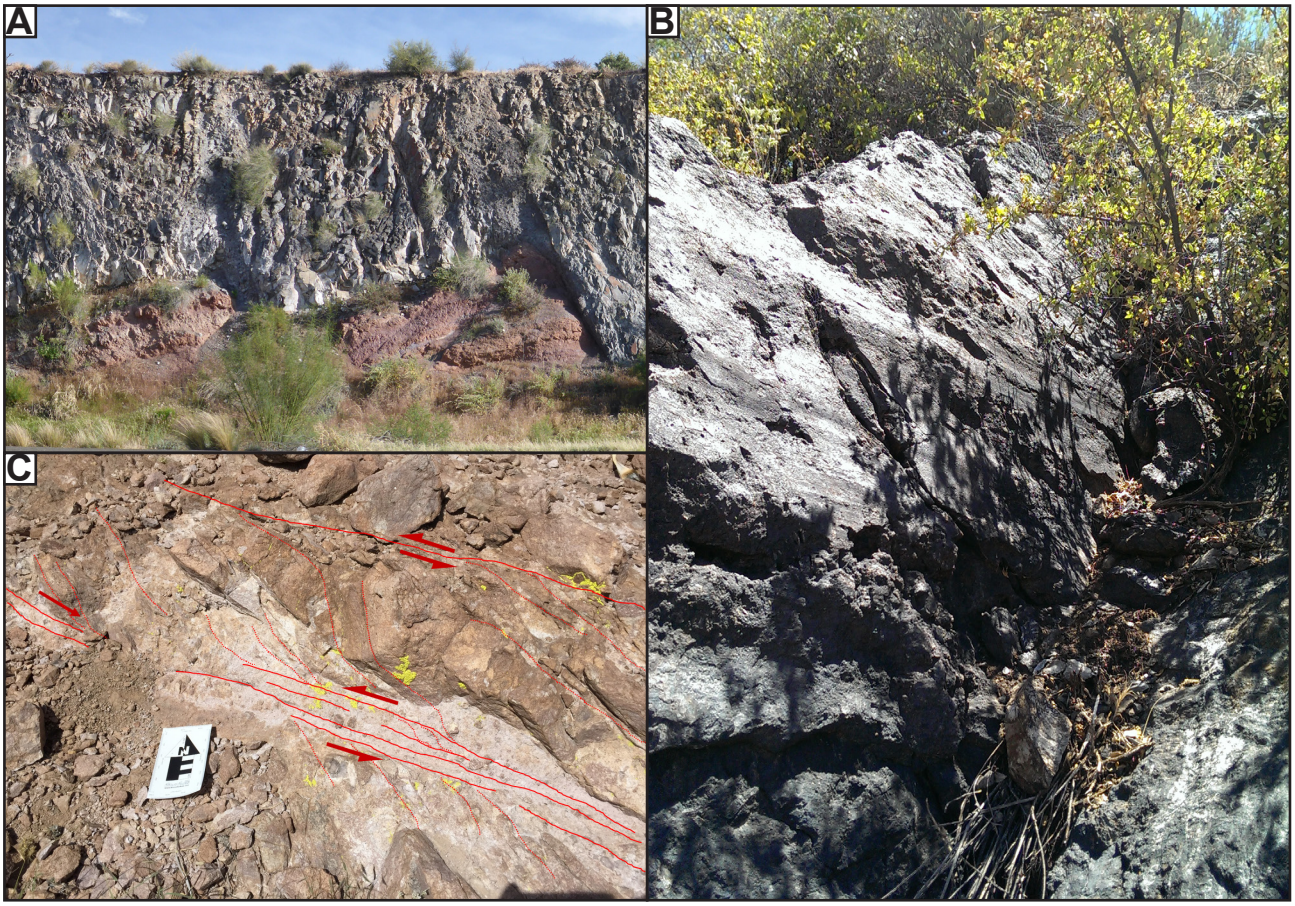


Figure 3.23 Tertiary structural features in the Superior district. A. View of normally faulting and rotated Tertiary basalt on US 60, west of Superior, looking south. Note basalt overlies Tertiary paleosol. B. Sub-horizontal grooves in truncated manganiferous epithermal vein above Queen Creek, looking southeast. C. Sinistral movement (timing unknown) observed in the Conley Springs fault. Image courtesy of Armelle Kloppenburg, (2016)

as a relay fault during Mid-Tertiary extensional faulting. West-down normal faulting in the Superior District continued beyond the eruption of Tertiary basalts (Figure 3.23 A)

#### 3.4.2.8 Late Tertiary strike-slip faulting

In the Magma mine, late sinistral movements have been noted along the north striking Main and NS-5W Faults. Although considered by Hammer and Peterson (1968) to be pre-mineralisation in timing, their sharp truncation of mineralisation combined with late sinistral kinematics observed along the Anxiety Fault (Mankse and Paul, 2002), Gant and Campground Faults (Figure 3.2; A. Kloppenburg, pers. comm., 2016) suggest there was at least a short period of post mineralisation sinistral faulting along north striking faults. This assertion is supported by sub-horizontal grooves observed in a fault surface truncating manganiferous epithermal veins in US 60 during this study (Figure 3.23 B). Sinistral faulting along north-striking faults may represent processes relating to far-field stress reorganisation immediately prior to the transition from extensional to the current transtensional plate margin conditions.

Other evidence for late stage dextral faulting is the offset observed in the Conley Springs Fault, which cuts Apache Leap Tuff (Figure 3.2, 3.23 C). Horizontal slickensides have been observed on the Conley

Springs Fault (B. Hart, pers. comm. 2016,) which may represent a phase of strike slip faulting related to the major dextral transtension described above. The Conley Springs also shows evidence for late stage sinistral faulting (Figure 3.22 D; A. Kloppenburg, pers. comm., 2016). Short et al., (1943) identified a phase of meter-scale strike-slip movement along the Magma vein-fault that post-dated Tertiary basalt emplacement, with kinematic evidence for both dextral and sinistral movements.

### 3.4.3 Concentrator Fault

***Mapping Results***

In an attempt to unravel some of the complex structural history of the Superior district, mapping of an exposed strand of the Concentrator fault was undertaken during the current study. The exposed fault plane, hosted in an exposure of the Lower Member of the Mescal Limestone on highway 177, is shown in Figure 3.24 with the field station location shown in Figure 3.2. All structures measured at this locality have curvilinear-irregular surfaces but cross cutting relationship can be clearly observed. The earliest faults are the least well developed and have no cross cutting relationships to help constrain relative timing but may appear to record syn-sedimentary growth faulting in the lower member of the Mescal limestone (Figure 3.24 A). The earliest faults are discontinuous and NW-dipping with an overall listric shape. They occur in the southern half of the exposure (Figure 3.24 A). The next set of early faults strike consistently NE, dip moderately – steeply SE and tend to show normal movement (Figure 3.20).

These SE dipping faults are cut first by a set of NW-dipping faults, which have reverse kinematics. In the centre of the exposure, this set of faults has a ramp-and-flat geometry with well-developed duplexing and breccia zones (Figure 3.24 A). Many of these faults appear to be bedding parallel and have similar dip directions to the earliest growth faults, suggesting there may have been some slip accommodated by bedding planes and/or growth fault reactivation. In some places along the reverse faults, small scale drag folding occurred, providing evidence for a phase of compressive stress that was accommodated by these structures (Figure 3.24 C-D). The small drag folds have a pre-Tertiary plunge and trend of approximately 100 ENE, suggesting the NW-dipping reverse faults observed in the Concentrator indicate a phase of roughly SE-directed compression.

The NW-dipping faults were in turn cut by a set of high angle, small-displacement faults (Figure 3.19). These structures have variable orientations but generally dip subvertically or steeply south and have low displacement, strike slip kinematics. In places they are weakly manganese oxide-stained.

All of the early-formed faults are cut by high angle normal faults. In places these seem to preserve relict compressional features (e.g., Figure 3.24 D), although their most recent movement is normal. They have similar, albeit steeper, attitude to the set of NW-dipping early reverse faults. Similar dip directions and relict compressive features suggests they may be a reactivated form of the early reverse faults. The dip of the green faults is generally perpendicular to the main extension direction (west) accommodated

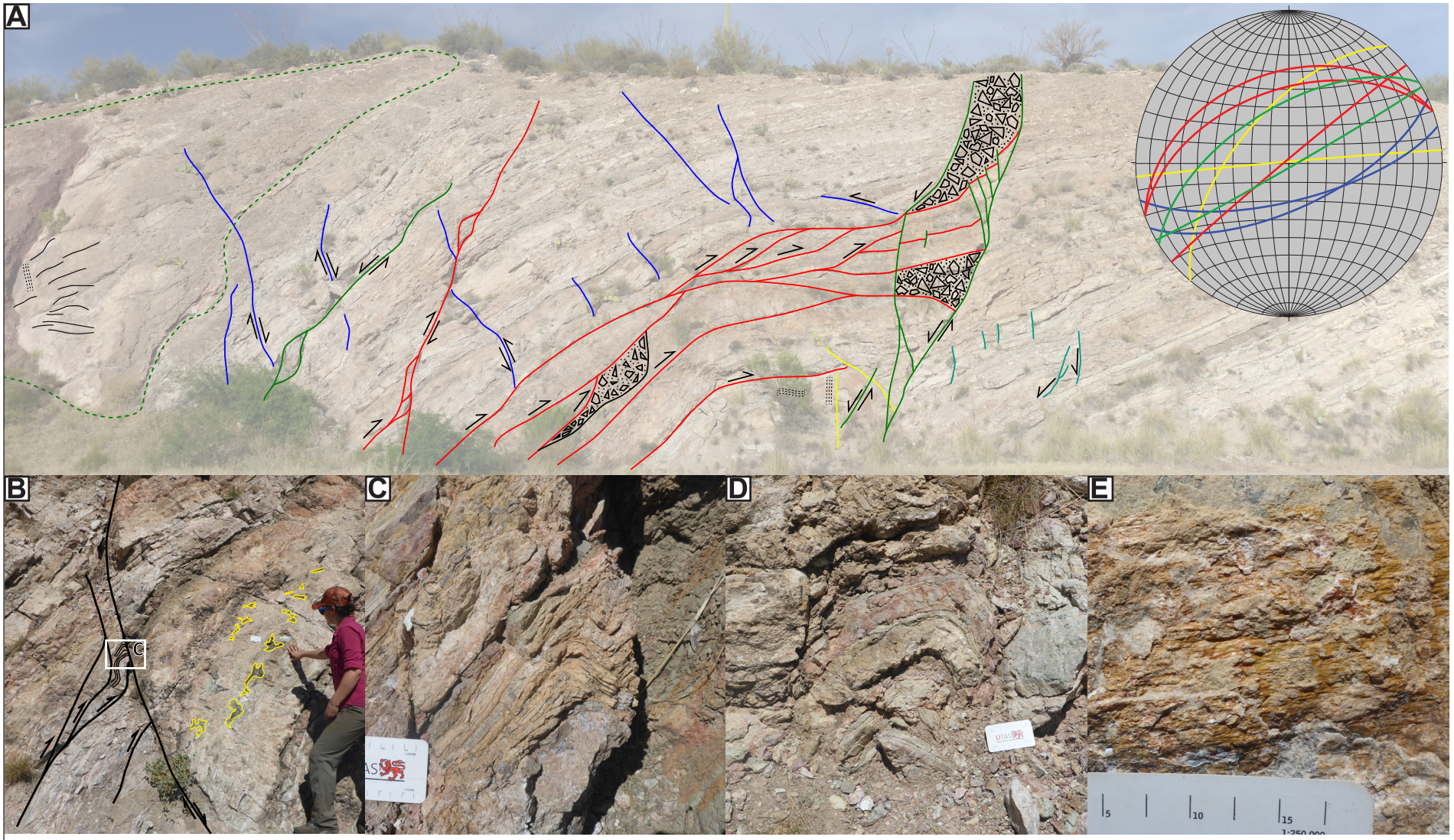


Figure 3.24 Structural mapping of the Concentrator Fault. A. Preliminary structural map of an exposed strand of the Concentrator fault, Hwy 177, south of Superior. See text for discussion. B. Close up fault strand and adjacent biotite alteration (yellow). C-D Drag folds exposed in faults that now show normal kinematics, suggesting reactivation of preexisting faults. E. Sub-horizontal slicken fibers, providing evidence for late stage strike slip movement along the Concentrator fault.

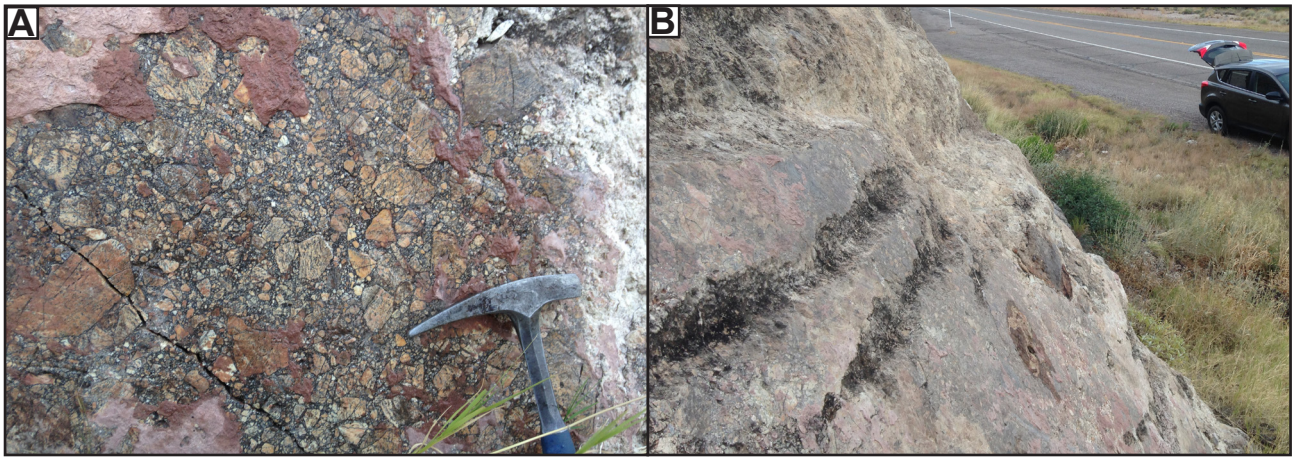


Figure 3.25 Features of the Concentrator Fault plane. A. Well developed fault breccias, with rounded clasts and milled matrix of manganiferous dacite porphyry, similar to Figure 3.15B surrounded by milled hematitic matrix. B. Large sub-horizontal grooves exposed in the same fault plane.

by the Concentrator Fault. At the north end of the exposure a major fault plane with well-developed fault breccia (Figure 3.25 A). Superimposed on the main Concentrator Fault plane is a set of large sub-horizontal grooves (Figure 3.25 B).

***Interpretation***

Although poorly developed, the discontinuous N-dipping faults in the south of the exposure are most likely intraformational syn-depositional faults, indicated by thickness changes above them (Figure 3.20 A). The SE-dipping faults have an unknown affinity with broader district or regional fault sets but may reflect the early NNE trending structural grain established by the Pinal Schist, which could have been reactivated during Apache Group deposition as subordinate relay structures to the main NNW-striking basin bounding faults.

It is possible that the NW-dipping reverse faults record the compressional stresses of the Laramide Orogeny accommodated along misoriented faults. However, their current attitude suggests probable origins either as Apache Group growth faults that were reactivated in response to far field Grenville related stresses as discussed by Timmons et al. (2001; 2005) The low displacement, high angle, strike-slip faults are most likely to be minor strike slip faults associated with larger scale NE-striking structures related to the Laramide Orogeny, which now host manganiferous epithermal mineralisation along the range front (Figure 3.2). Similar observations were made by Maher (2008). The large, well exposed west-dipping fault plane at the northern end of the exposure represents the major west-down extensional phase on the Concentrator Fault. The reactivation of NW-dipping reverse faults to extensional kinematics suggests a significant period of NW-directed extension (Figure 3.20 A), probably after major west-down movement. This is supported by sub-horizontal slickensides (Figure 3.23 E), and substantial sub-horizontal grooves (Figure 3.25 B) on the Concentrator fault plane, and on truncated epithermal veins (Figure 3.23 B).

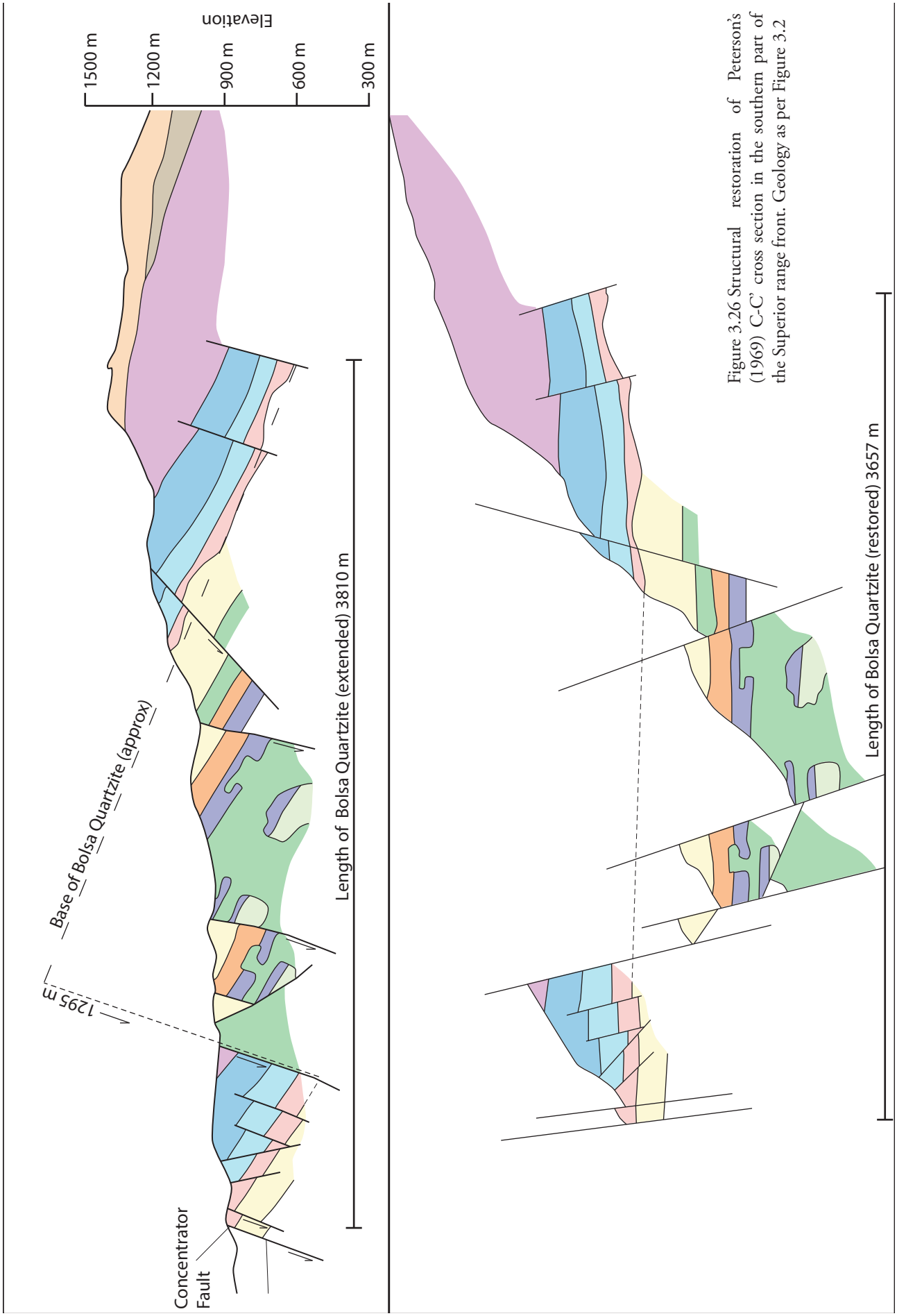


Figure 3.26 Structural restoration of Peterson's (1969) C-C' cross section in the southern part of the Superior range front. Geology as per Figure 3.2

### 3.4.4 Range front restoration

A structural restoration of fault blocks exposed in the range front of the Superior district was undertaken as part of the current study to constrain possible effects of post-mineralisation extension on the geochemical dispersion halo around Resolution. The section C-C' through the southern part of the Superior range front is taken from Peterson's (1969) map of the Superior Quadrangle and restored in Figure 3.26, using the base of the Paleozoic sequence. This section was chosen for its dissection of the southern, more structurally disrupted part of the Superior district range front. The results therefore indicate a maximum likely extension for the rest of the Superior district.

Results show that westward attenuation along range front faults in the south of the Superior district was limited to around 150 m (Figure 3.26). In contrast, the cumulative downward throw experienced by the westernmost fault block was in the order of 1,300 m (Figure 3.26). The limited lateral attenuation but large scale vertical displacement demonstrated by range front faults indicate an affinity with basin and range style deformation.

## 3.5 Summary of the geologic evolution of the Superior district

The local geology of the Superior district is, in many respects well-representative of South East Arizona. The Precambrian exposures are very similar to those described by Ransome (1916; Pinal Schist) and Shride (1967; Mesoproterozoic Apache Group, dolerite sills and Troy Quartzite) around the Sierra Ancha region. The schist package is interpreted as a meta-turbidite package originally deposited in the fore-arc of a NW-dipping subduction zone and subsequently metamorphosed during accretion of the arc to the rest of the continent around 1,650 - 1,600 Ma (Meijer, 2014). The Apache (and Unkar) Groups were deposited in a series of basins principally controlled by alternating transpressive and transtensive stresses associated with the Grenville Orogen. The NE striking structural grain evident in the Pinal Schist, along with a complimentary set of N-NW striking faults, control the regional scale structure observed in the basement, and many appear to have been reactivated during deposition of the Apache Group and during intrusion of the widespread dolerite sills. The Paleozoic sedimentary rocks have been well characterised by previous workers, notably Freihauf (1998) Freihauf and Pareja (1998) and Schwarz (2007), and correlate well with regional stratigraphy across the state (Middleton 1989; Beus, 1989; Blakey and Knepp, 1989). However, the structural control on the deposition of these units in Southern Arizona remains poorly constrained.

The Superior district records early Laramide magmatic and volcanic activity. Geochronology presented in Table 3.2 and Figure 3.19 highlight some key relationships between Laramide features of the Superior district. Firstly andesitic volcanic rocks deposited in the Resolution graben could be related to the emplacement of the quartz diorite, both compositionally and temporally. Secondly, there appears to be a systematic southward, then eastward progression in magmatism (Figure 3.19). Intrusive phases at

Resolution overlap with the felsic volcaniclastic Kvs, suggesting that they may also be coeval, correlating regionally with the emplacement of the Schultze Granite. The progression of magmatic ages, from Silver King, to Magma, Resolution, then to Superior East and Pinto Valley, suggest a relationship to the inwardly crystallising Schultze Granite.

Following Laramide uplift and magmatism, was a period of deposition in eastward-dipping half grabens associated with basin and range extensional faulting. Westward extension appears to have been limited to around 150 m, but vertical displacement was greater than 1 km. Extension was accompanied by extensive silicic volcanism, responsible for the deposition of the Apache Leap tuff at 18 Ma (Table 3.1).

The Superior district has been subjected to a series of traumatic deformation events spanning a time period from ~1,650 Ma to <20 Ma. Common to all regionally recognised events seems to be the continued reactivation of an early Proterozoic NW and NE striking fault architecture. Superior also provides evidence for other local structural events, not least the development of the Resolution graben, and with them an opportunity to refine details of its structural history.

# Chapter 4: Laramide alteration and mineralisation in the Superior district

## 4.1 Introduction

This chapter provides new observations of Laramide mineralisation and alteration from the Superior district (Figure 4.1; Table 4.1). These new data are combined with existing information to evaluate relationships between mineralised centres within the district, and sets the scene for appraisal of micro-analytical geochemical data presented in later chapters.

## 4.2 Resolution

### 4.2.1 Introduction

Since far-field vectors to mineralisation are the primary focus of this study, little work has been conducted within Resolution's main mineralised zone during this project. This section is therefore, based largely on previous reviews of Resolution (e.g., Troutman, 2001; Ballantyne et al., 2003; Manske and Paul, 2002; Harrison, 2007; Zulliger, 2007; Schwarz, 2010; McCarrel, 2012; Hehnke et al., 2012). It reviews the key features required for following chapters, which are concerned with vectoring towards mineralisation using mineral chemistry, stable and radiogenic isotopic studies. A comprehensive overview of the Resolution deposit was provided by Hehnke et al. (2012).

Although a porphyry target south of the Magma Vein was suggested as early as 1973 by Don Hammer (Hammer, 1973), Resolution was not discovered until 1995. It is now known as one of the largest and highest grade porphyry Cu-Mo deposits in North America (Hehnke et al., 2012). Given its setting, Resolution is surprisingly intact (Manske and Paul, 2002; Hehnke et al., 2012) - it is mostly undisrupted by the widespread Tertiary dismemberment the affected many other southwestern US porphyry Cu deposits (e.g., San Manuel - Kalamazoo; Lowell and Guilbert, 1970). The reasons for the late discovery of Resolution in the history of exploration of the Superior district are a combination of its considerable

Figure 4.1 (Opposite page) Geology of the Superior district, compiled from Peterson (1969), Spencer and Richards (1995) and Hehnke et al. (2012) with the addition of past producing mines and major undeveloped ore bodies. Selected faults: AF - Anxiety fault; CF - Concentrator fault; CSF - Conley Springs fault; DCF - Devils Canyon fault; MF - Main fault; NBF - North Boundary fault; SBF - South Boundary fault; WBF - West Boundary fault. Line of section shown in Figure 4.2 also shown.

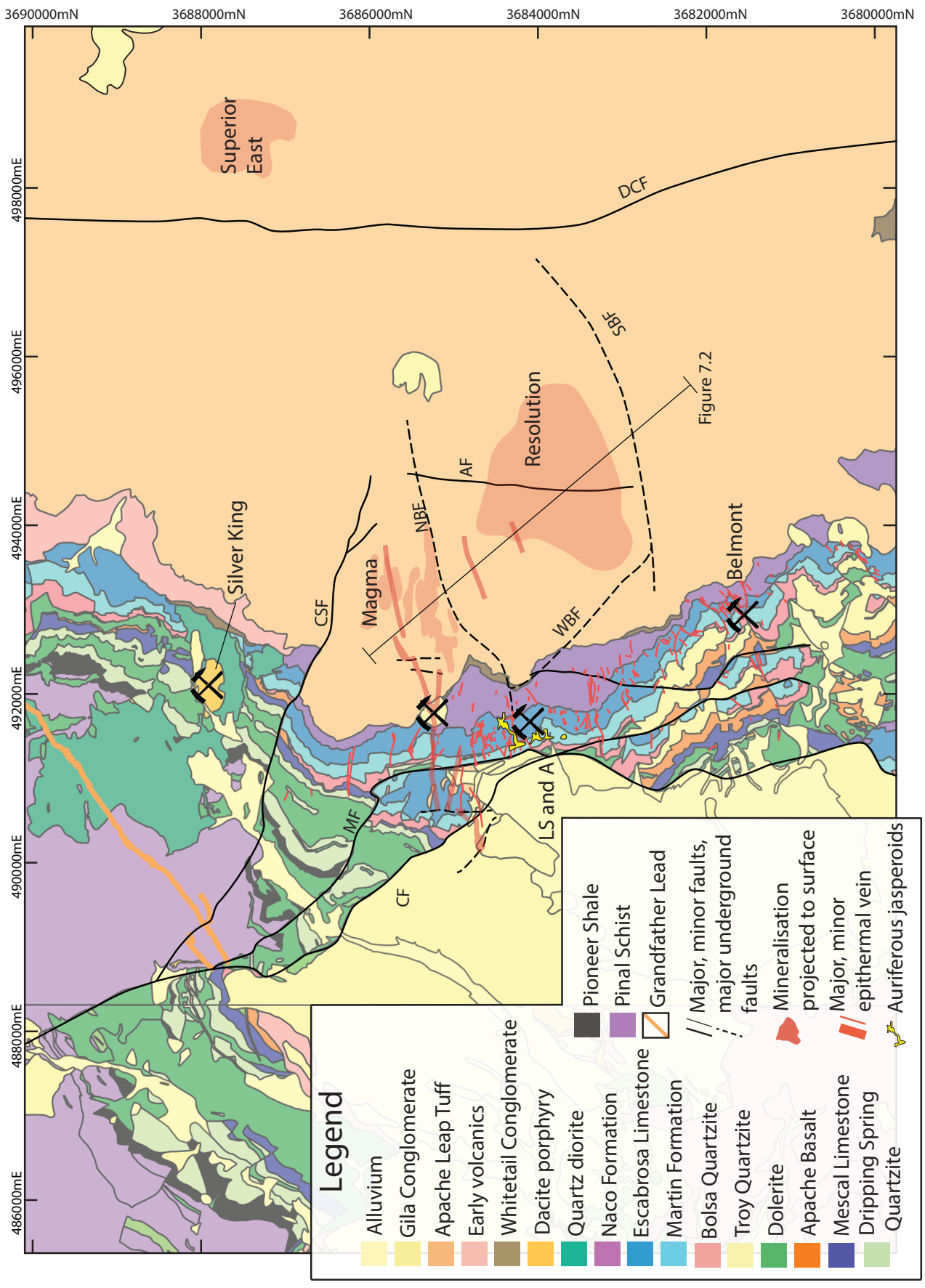
3690000mN
3688000mN
3686000mN
3684000mN
3682000mN
3680000mN
498000mE
496000mE
494000mE
492000mE
490000mE
488000mE
486000mE
Superior East
DCF
SBF
Figure 7.2
Resolution
AF
NBE
Magma
CSF
Silver King
WBF
Belmont
MF
CF
LS and A
Legend
Alluvium
Gila Conglomerate
Apache Leap Tuff
Early volcanics
Whitetail Conglomerate
Dacite porphyry
Quartz diorite
Naco Formation
Escabrosa Limestone
Martin Formation
Bolsa Quartzite
Troy Quartzite
Dolerite
Apache Basalt
Mescal Limestone
Dripping Spring Quartzite
Pioneer Shale
Pinal Schist
Grandfather Lead
Major, minor faults, major underground faults
Mineralisation projected to surface
Major, minor epithermal vein
Auriferous jasperoids

Table 4.1 Summary of Laramide age mineralised centres in the Superior District.

| Deposit | Deposit type | Pre mining resources | Orebody geometry | Host rocks | Structural control | Alteration facies |
|---|---|---|---|---|---|---|
| Resolution | Porphyry Cu-Mo | 1.7 Gt @ 1.6% Cu, 0.03% Mo | Saddle shapped vein stockwork and breccias | Proterozoic Apache Group; Paleozoic carbonates; Cretaceous volcanics; Laramide dikes | Hosted in blind graben, veins controlled by ENE Laramide strike-slip faults. | Potassic<br>Phyllic<br>Skarn<br>Advanced argillic<br>Intermediate argillic |
| Superior East | Porphyry Cu-Mo | 200 Mt @ 0.9% Cu | Shallow lens of veinlets and disseminations | Proterozoic Pinal Schist; Laramide dikes | Hosted in highly tectonised schist, high angle faults and sub-horizontal slickensides, east of DCF | Potassic<br>Phyllic<br>Advanced argillic |
| Magma | HS-IS Epithermal | 25 Mt @ 5% Cu | Skarns | Paleozoic carbonates | Hosted in ENE-striking vein system and favourable dolomitised carbonate beds | Low fluid:rock ratios<br>High fluid:rock ratios |
| | | | Tabular veins | Proterozoic Apache Group | Hosted in ENE-striking fault and associated branches | Phyllic<br>Propylitic |
| | | | Mantos | Paleozoic carbonate rocks | Hosted in favourable porous dolomitised carbonates (A-E beds) | Central<br>Intermediate<br>Marginal<br>Outer<br>Distal |
| 1st/2nd South Veins | IS epithermal | unknown | Structurally controlled discontinuous pods<br>Tabular veins | Cretaceous volcanics rocks | Hosted by ENE-striking faults | Phyllic<br>Propylitic |
| Belmont | IS epithermal | 21.6 Kt @ 0.8% Cu, 334 g/t Ag, 4.8 g/t Au | Tabular veins | Proterozoic Apache Group Paleozoic carbonate rocks | Hosted in ENE striking faults | unreported |
| Lakeshore and Arizona (LS&A) | IS epithermal -exotic | 90 Kt @ 15 g/t Au 27 g/t Ag and 0.4 % Cu | Nodular jasperoids | Devonian Martin Formation | A bed horizon | Proximal<br>Intermediate<br>Distal |

Abbreviations: bi = biotite; bn = bornite; cal = calcite; cc = chalcocite; chl = chlorite; cpy = chalcopyrite; dic = dickite; ep = epidote; FeOx = iron oxides; gnt = garnet; hm = hematite; ido = idocrase; kaol = kaolinite; mt = magnetite; MnOx =

| Alteration mineralogy | Alteration-mineralisation zonation | Supergene development | Hypogene ore mineralogy | Key references |
|---|---|---|---|---|
| Bi | Deep potassic is partially overprinted by phyllic, transitioning upwards into advanced argillic and outwards through intermediate argillic and into propylitic; skarn developed in carbonate strata | Strong chalcocite development below thick leached cap | Cpy > bn > cc ± en. | Troutman (2001) |
| Qz-ser-py | | | | Manske and Paul (2002) |
| Calcic and magnesian | | | | Harrison (2007) |
| Qz-kaol-dic ± top-py | | | | Schwartz (2010) |
| Ser - chl - ill/smec | | | | McCarrel (2012) |
| Bi | Weak potassic partially overprinted by white mica; transitions upwards into hypogene kaolinite | 200m thick leached cap with minor enrincment | Bn - cc at upper levels replacing Cpy-py at depth | Sell (1995) |
| Ser - py | | | | Sillitoe (2013) |
| Kaol | | | | |
| Tlc - sph - py - mt | Temporal zonation from gnt-py ± ido (high fluid:rock) to later tlc-sph-py-mt (low fliud:rock); all overprinted by ISE mineralogy (below) | N/A | gradient from high iron sph outwards to low iron sph, cut by gn, overgrown by cpy | Friehauf (1995) |
| Gnt - py ± ido | | | | |
| Ser ± py | Narrow phyllic halos to main veins and distal propylitic alteration in mafic rocks | Weak | Deep en - bn-py, to shallower ten-cpy, sph-gn in the uppermost levels | Gustafson (1961) |
| Ep - chl ± cal | | | | Hammer and Perterson (1968) |
| Py ± musc ± cc (zun - kaol - qz) | Outward gradation from proximal py ± musc ± cc (zun-kaol-qz) to distal hm-qz ± py (ser-chl) | Siliceous jasperiods, e.g., Lake Superior and Arizona. | Cpy - bn - py | Friehauf (1995) |
| Qz - ser ± chl ± cc | | | | |
| Py - qz - chl | | | Cpy - py | |
| Hm - qz ± py (ser - chl). | | | Hm ± cpy | |
| Bleached host rock | | | N/A | |
| Qz - ser - py | Zoned outwards from phyllic altered wallrock and cpy-bn-cc to propylitic altered wallrock and stringers of py-hm-qz | Weak | Cpy-bn-py with peripheral bn in high grade 'chimneys' | Schott (1994) |
| Chl - ep - cal - hm | | | | |
| unreported | unreported | Supergene resource | N/A | Hammer and Perterson (1968) |
| FeOx - MnOx | FeOx fragments cemented by late groundwater sourced quartz (+ Au) grading out into FeOx-MnOx with sharp contact | All quartz (+Au) from weathering processes; weak chalcocite at depth | Hm - py | Pareja (1998) |
| Cal (de-dolomitisation) | | | | |
| Tlc - cal | | | | |

manganese oxides; musc = muscovite; py = pyrite; qz = quartz; ser = sericite; smec = smectite; sph = sphalerite; tlc = talc; top = topaz; ten = tennantite.

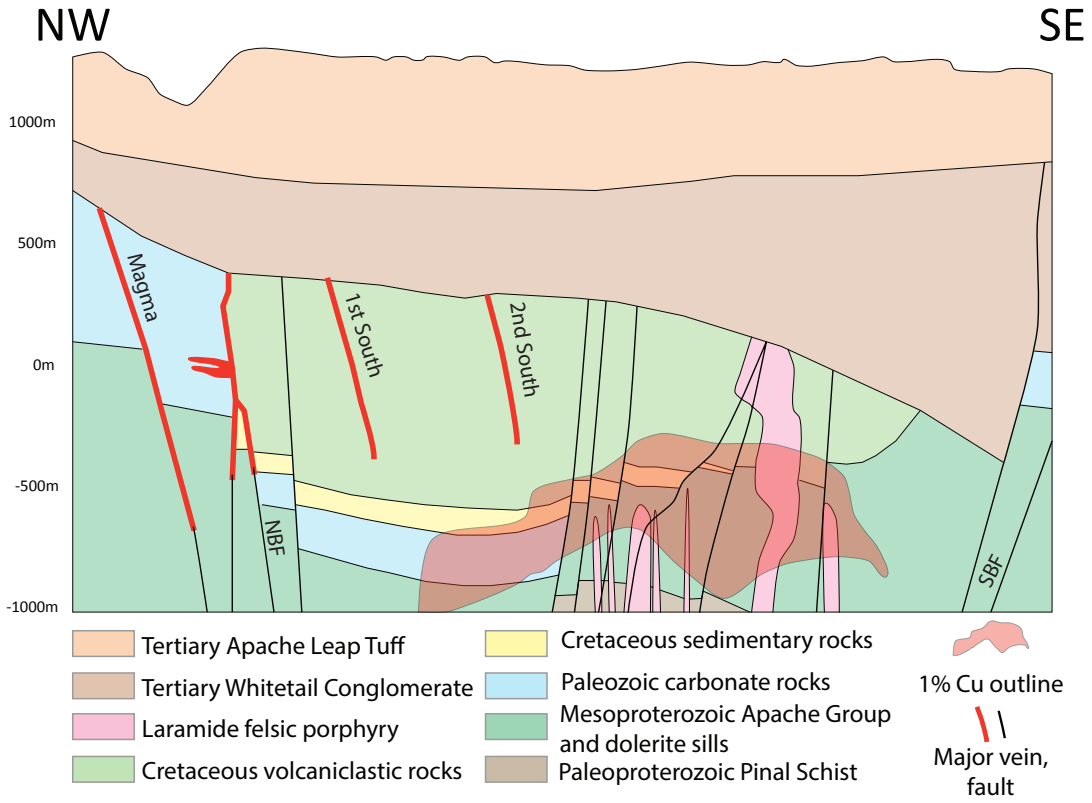


Figure 4.2 Simplified NW-SE cross section through the Resolution Graben showing relationships between major fault blocks and distribution of mineralisation. Abbreviations: NBF – North Boundary Fault; SBF – South Boundary Fault. Modified after Hehnke et al. (2012).

depth, post-mineralisation cover, lack of surface geophysical or whole-rock geochemical expression and complex graben-hosted structural setting. The geologic and structural setting of Resolution are therefore somewhat atypical compared to other deposits in the southwestern US porphyry Cu province.

### 4.2.2 Geology

The Proterozoic basement geology at Resolution is similar to that observed in the range front exposures of the Superior district (Chapter 3). Paleoproterozoic Pinal Schist underlies the Mesoproterozoic Apache Group, which is composed of a thin section of Pioneer Shale, Dripping Springs Quartzite, Mescal Limestone and minor basalt flows (Figure 4.3 A). However, the basalt is only preserved in the southwestern-most segment of the graben, and the overlying Troy Quartzite is absent from the graben (Figure 4.3 A).

The Paleozoic sequence inside the Resolution graben is significantly thinner than in the range front and is missing from the eastern part of the graben (Figure 4.2). The Paleozoic sequence in the graben has been pervasively altered to skarn.

Above the Paleozoic limestone sequence is an isolated remnant of Late Cretaceous – Early Tertiary volcano-sedimentary rocks, referred to at the mine as the Cretaceous quartzose sandstone (Kqs) and Cretaceous volcaniclastic rocks (Kvs; Chapter 3; Figure 4.2). The Kqs has been dated using U-Pb from

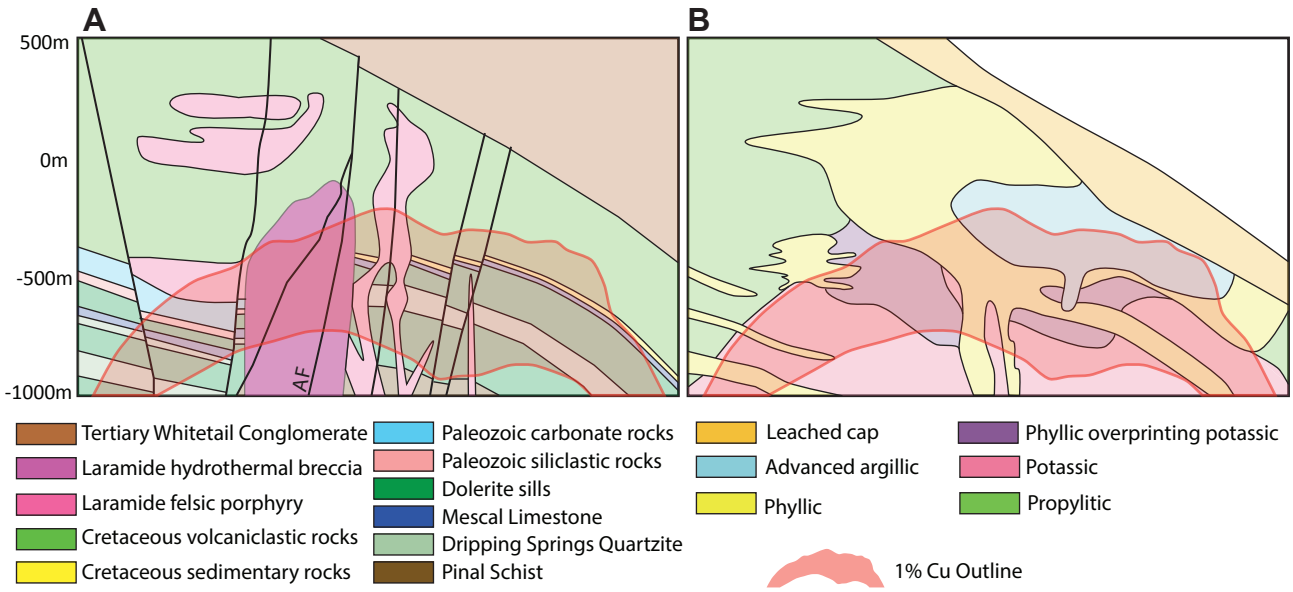


Figure 4.3 A East-west cross section through the Resolution deposit showing lithological and fault relationships with respect to the 1% Cu ore body. B Cross section through the Resolution deposit showing distribution and relationships of the major alteration domains. Modified after Hehnke et al. (2012). Line of section shown in Figure 4.1.

detrital zircons and provides a maximum depositional age of 96.8 ± 2.2 Ma (Table 3.2) These rocks are hosted in an unexposed Cretaceous graben, which preserves the Kqs and Kvs sequence to a thickness approaching 1 km, which are not exposed anywhere else in the district (Figure 4.1 and Figure 4.2). The graben is covered by the post-mineralisation Tertiary conglomerates and felsic volcanics (Figure 4.1 and Figure 4.2).

The andesitic facies of the Kvs, dated at around 74 Ma, is limited to the west and northwest of the graben while the 67 to 66 Ma felsic component occurs in the southern and eastern sectors, (Zulliger, 2007; Hehnke at al., 2012; Table 3.2). This sequence of Proterozoic basement, Apache Group and Cretaceous volcanics were intruded by a suite of 69 - 64 Ma rhyodacite and 67 - 66 Ma quartz-latite porphyry stocks and dikes of pre to early mineralisation timing (Figure 4.2, Figure 4.3 A; Mankse and Paul, 2002; Zulliger, 2007; Hehnke et al., 2012). The progenitor intrusion for mineralisation at Resolution has not yet been identified.

Breccias are common at Resolution (Figure 4.3 A). Three volumetrically significant magmatic-hydrothermal and phreatomagmatic breccias cut the sequence and are considered to be early to syn-mineralisation in timing, as demonstrated by the mutually discordant nature of both the breccia bodies and mineralisation (Hehnke et al., 2012; Keyahov et al., 2015). Quartz-phyric porphyry occurs as clasts within the breccias, and as dikes that cross-cut them, further bracketing their relative timing and suggesting a genetic relationship between the breccias and porphyries. A fourth tectonic-hydrothermal breccia type has also observed but is restricted to narrow structural zones that are considered to have been late stage conduits for high sulfidation mineralisation (Hehnke et al., 2012). Igneous-cemented breccias have also been documented, locally grading into coherent rhyodacitic porphyry, further suggesting

that the intrusion of these porphyry bodies is intimately associated with the widespread brecciation at Resolution (Hehnke et al., 2012; Keyahov et al., 2015).

Mineralised rocks at Resolution were overlain by the Whitetail Conglomerate during the Tertiary, as large scale eastward rotation of the district was accommodated along the Devils Canyon Fault, to the east of the main graben (Figure 4.1; Manske and Paul, 2002; Hehnke et al., 2012). The Whitetail Conglomerate is approximately 1.3 km thick directly above Resolution (Figure 4.2), and the unit thickens markedly to the east. Accompanying the overall eastward thickening and wedge-shaped geometry, is a gradual decrease in dip angle up section, indicating syn-extensional deposition. The Whitetail Conglomerate is overlain by 300 – 500m of Miocene Apache Leap Tuff. Above Resolution, the Apache Leap Tuff dips inwards towards the centre of the graben but elsewhere dips approximately $012^0$ to the NE suggesting that subsidence on the graben-bounding faults and the Devils Canyon Fault continued after the deposition of the Apache Leap Tuff (Hehnke et al., 2012).

### 4.2.3 Structural Setting

The structural architecture at Resolution is dominated by the host graben, which is arguably the single feature that sets it apart from other porphyry Cu deposits in the southwestern US (e.g., Seedorff et al., 2005; Figure 4.2). The geometry and structural controls on the graben have remained poorly understood since its discovery in 1959 (D. Hammer, pers. comm, 2016). The graben is bounded to the north and south by complex anastomosing fault zones, termed the North Boundary Fault and South Boundary Fault respectively (Hammer, 1973; Manske and Paul, 2002; Hehnke et al., 2012; Figure 4.1 and Figure 4.2). They are generally steeply dipping ENE-striking structural zones, each consisting of at least three sub parallel faults that have been variably intruded by Laramide aged porphyry dikes and are weakly mineralised. To the west, the graben is bounded by the West Boundary Fault, another complex structure that dips $85^0$ towards the southwest, although when restored to a pre-Tertiary orientation would probably dip ~$65^0$ NE (c.f., McCarrell, 2012). The eastern boundary of the graben is largely unknown, due to its depth as a result of later Tertiary westward extension and rotation. Although once thought to be bounded to the east by an intermediate structure somewhere between Resolution and the Devils Canyon Fault, drilling in this area has failed to conclusively recognise such a fault (Hehnke et al., 2012). The possibility remains that the Devils Canyon Fault bounds the graben to the east. Alternatively, it could be a strand of the Conley Springs Fault.

Contained within the graben are a set of steeply-west dipping faults, the largest of which is the Anxiety Fault (Figure 4.3 A). These faults separate the more deeply eroded eastern side of the graben from the western half, where Paleozoic rocks are at least partly preserved (Figure 4.3 A).The present-day attitude of the Anxiety and related faults suggest normal kinematics, although when restored to pre-Tertiary orientation they rotate through vertical and display evidence for east-dipping reverse movement, based on stratigraphic offset (Figure 4.2; McCarrell, 2012). These faults were probably responsible for the

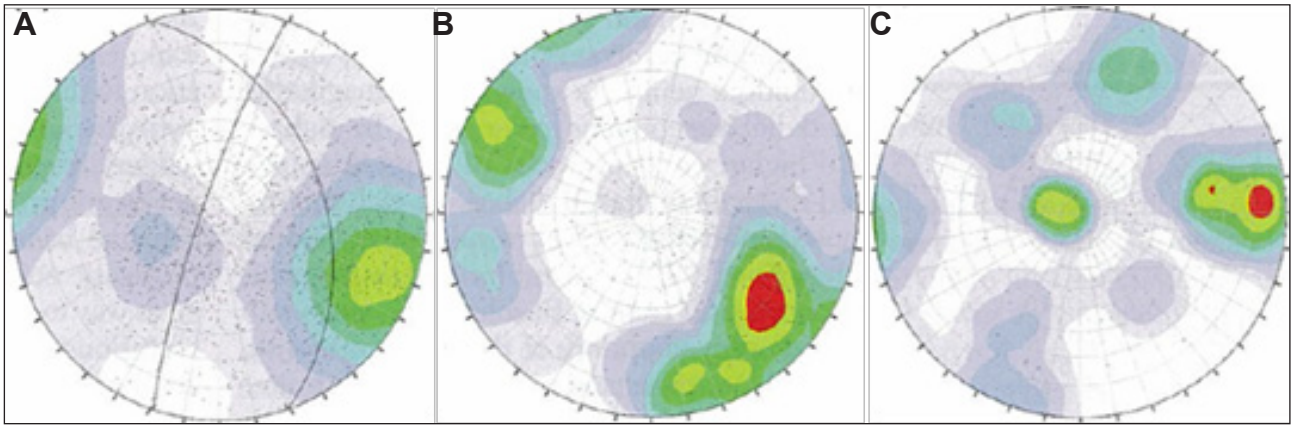


Figure 4.4 Lower hemisphere stereonets showing poles to A, slickensided shears, B chalcopyrite veins and C quartz-molybdenite veins reproduced from Hehnke et al. (2012). Note the correspondence between A and B but not C, suggestive of a change in stress regime at Resolution between the emplacement of the veins sets.

differential uplift and erosion that affected the graben and caused differential uplift of discrete structural blocks in the district. The Anxiety Fault crops out at surface (Figure 4.1; Kloppenburg, 2016) suggesting reactivation of these faults during the Tertiary. None of the graben-bounding faults conclusively crop out at surface, however a number of correlations have been made with range front veins (Hammer, 1973; Manske and Paul, 2002; Hehnke et al., 2012). The North and South Boundary faults are thought to be the along-strike continuations of the Monarch and Belmont epithermal veins respectively, which crop out in the range front (Figure 4.1; Hammer 1973). The West Boundary Fault has been correlated with the relatively low displacement NS-5W fault in the Magma Mine (Hammer, 1973; Manske and Paul, 2002, Hehnke et al., 2012; Figure 4.8) which may crop out on the US60 road cut (Figure 3.11). A normal fault that could be the upward projection of the West Boundary Fault was mapped by Hammer (unpublished 1:400 scale mapping) high in the range front exposures of the Naco Formation, just south of Queen Creek and US60.

The striking relationship between chalcopyrite-dominated veins and slickenside-lined shears that have been measured at Resolution (Figure 4.4 A-B) has also been observed at the Superior East deposit (Sillitoe, 2013). It suggests that most, if not all mineralisation was syn-tectonic in timing, and exploited E and NE-striking structures (Hehnke et al., 2012). This observation is consistent with the vein orientations observed in the Superior district range front, and broader region (e.g., Heidrick and Titley 1972).

Quartz – molybdenite veins have multiple preferred orientations, including a moderately dipping NW-striking set, steeply dipping N-striking set and possibly also a shallow dipping NE-striking set (Figure 4.4 C). Hehnke et al. (2012) suggested that this may represent a perturbation of the local stress regime prior to, and briefly during, the early stages of mineralisation, possibly tracking the progressive development of a radial fracture array during early emplacement of an intrusive body at depth. This idea was supported by Schwartz (2010), who mapped a large scale dome structure defined by the secondary biotite foliation in potassic-altered dolerite sills. The relationship between the Resolution hydrothermal system and the controls of the formation of the graben remain poorly understood.

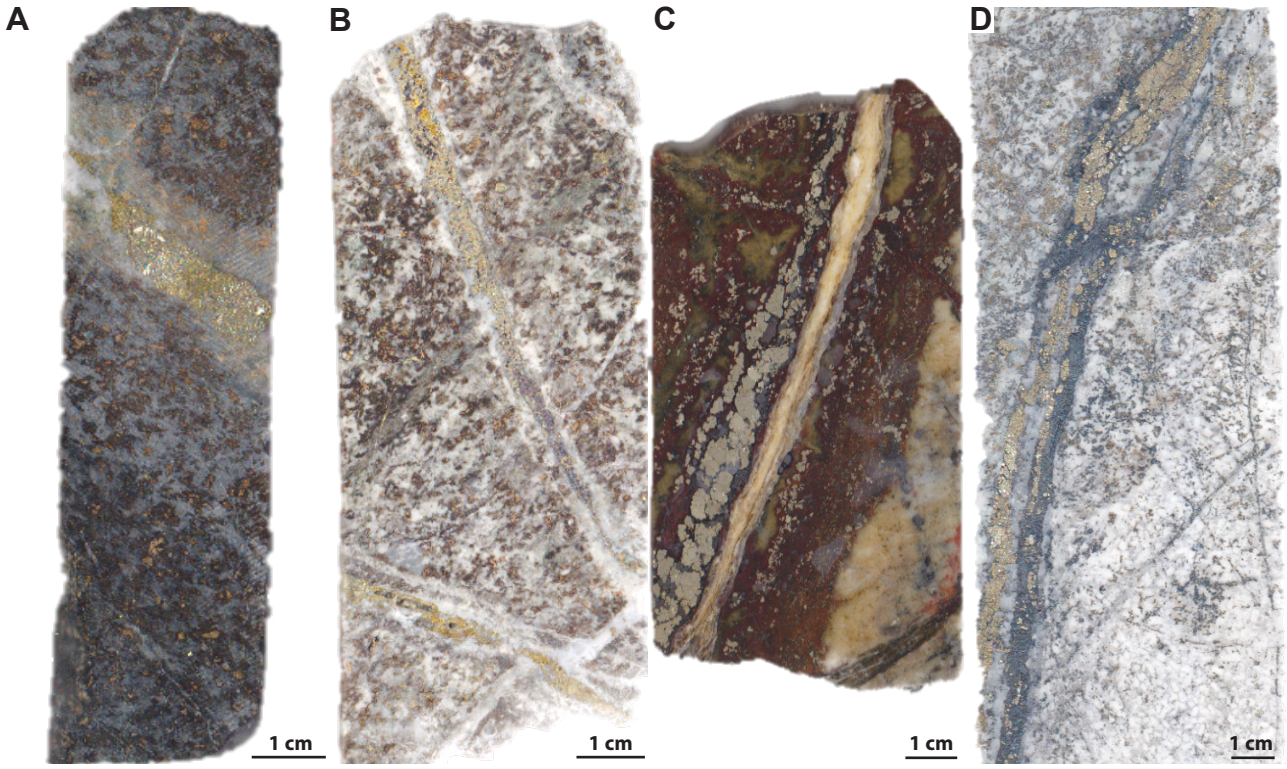


Figure 4.5 Examples of major selected alteration types encountered at Resolution. A RE16JP242, Early potassic alteration represented by intensely biotite altered dolerite displaying limited, pyrite dominant mineralisation. B RE16JP243, Phyllic stage sericite over printing earlier biotite alteration in dolerite, showing py-cpy ± bn stockwork veins. C RE15JP105, Intermediate argillic altered sandstone, dominated by strong pyrite-chlorite-sericite alteration around a calcite vein. D. RE16JP244, Kaolinite altered felsic porphyry with chalcocite replacing pyrite in veins.

### 4.2.4 Alteration

Resolution is a typical porphyry deposit in terms of it alteration assemblages and overprinting relationships (Figure 4.3 B; Hehnke et al., 2012). Potassic alteration at Resolution is dominated by intense biotite alteration in the host dolerite sills (Figure 4.5 A), with K-feldspar more common in felsic and siliciclastic sedimentary rocks. Anhydrite is a major alteration component at depth, while hydrothermal magnetite is restricted to the southern and north western flanks of the deposit, reflecting the distribution of mafic rock units (Hehnke et al., 2012).

Quartz - muscovite - pyrite alteration has strongly overprinted some potassic altered rocks, and also some propylitic assemblages (Figure 4.3 B, Figure 4.5 B). It affected all pre-mineralisation rocks to some degree, but is best developed in the uppermost Proterozoic rocks and Kvs (Figure 4.2B). Muscovite predominates over phengite and occurs as texturally destructive halos to quartz - pyrite ± copper sulfide veins (Hehnke et al., 2012). Muscovite is associated with minor fluorite, anhydrite and rutile. In places, muscovite has been variably replaced by kaolinite although diagnostic advanced argillic minerals are typically absent. In some peripheral locations, this is manifested by chlorite - illite - smectite ± pyrite alteration halos surrounding quartz-sulfide veins, defined as an intermediate argillic assemblage (Mankse and Paul, 2002; Figure 4.5 C)

Where present, advanced argillic alteration has overprinted quartz - muscovite - pyrite-altered rocks and

is confined to the uppermost parts of the deposit (Figure 4.3 B, Figure 4.5 D). The Kqs and Cambrian Bolsa Quartzite are the most preferentially altered units. Kaolinite and pyrite are the most abundant minerals within the advanced argillic assemblage with dickite the most diagnostic phase. Alunite, zunyite, topaz, woodhouseite and pyrophyllite have been reported in minor amounts (Troutman, 2001; Winant, 2010).

Propylitic alteration is well developed around Resolution. In Proterozoic rocks close to the South Boundary Fault, an early but minor phase of pyroxene and hornblende alteration to amphibole and magnetite has been reported (Hehnke et al., 2012). Based on the mineralogy observed and the location near a major NE striking structure, there remains a strong possibility that this alteration pertains to Proterozoic hydrothermal events that are documented in Chapters 6 and 7. A coherent inner propylitic subzone of actinolite-dominant alteration has not been delineated between the potassic and propylitic zones at Resolution (Hehnke et al., 2012). Epidote - chlorite - calcite - pyrite typifies the dominant propylitic assemblage at Resolution. It is particularly well developed in the andesitic Kvs (Figure 4.3 B; Figure 4.6 A-C) and to a lesser extent in the Proterozoic dolerite sills (Figure 4.6 D). Propylitic alteration from many porphyry deposits shows the continuation of epidote - chlorite alteration beyond the pyrite halo (Holliday and Cooke, 2007). This is also true at Resolution, where the outer limit of the Resolution pyrite halo is within the main propylitic epidote - chlorite zone, and pyrite abundance increases strongly inwards through the propylitic zone. In distal drillholes, epidote is absent, suggesting an outer chlorite ± calcite and hematite subzone (Figure 4.6 E-F). Abundant hydrothermal K-feldspar has also been observed within the propylitic assemblage, and has been reported to constitute up to 25% of the rock locally (Cooke et al., 2015). This unusual aspect of the propylitic assemblage of Resolution remains poorly understood. Inwards, the propylitic gives way to strong secondary biotite at depth and pervasive quartz - sericite - pyrite at higher elevations (Figure 4.3 B, Hehnke et al., 2012).

Skarn alteration of carbonate protoliths is strongly developed at Resolution, and is intense within the 1% mineralisation shell (McCarrell, 2012; Hehnke et al., 2012). Magnesian skarns have replaced dolomitic horizons within the sequence, notable in the Mescal Limestone and lower parts of the Martin Formation (McCarrel 2012; Hehnke et al., 2012). Early garnet-pyroxene bearing calcic skarns are overprinted by retrograde chlorite - epidote - calcite - hematite ± amphibole assemblages (Figure 4.7 A-D). Skarns that have been overprinted by phyllic, or 'skarn destructive' alteration present intense sericitisation of hydrous skarn assemblages. In these areas Ca and Mg have been leached to <1% (Hehnke et al., 2012).

### 4.2.5 Mineralisation

Grade, mineralogy and mineralisation style are strongly dependant on host rock and alteration type at Resolution. Mineralisation styles include porphyry-style stockwork, skarn, breccia cement and epithermal veins. Grades are generally higher in the carbonate rocks, dolerites, hydrothermal breccia and Kvs, and are lower in the siliciclastic rocks and felsic intrusions (Hehnke et al., 2012). Chalcopyrite

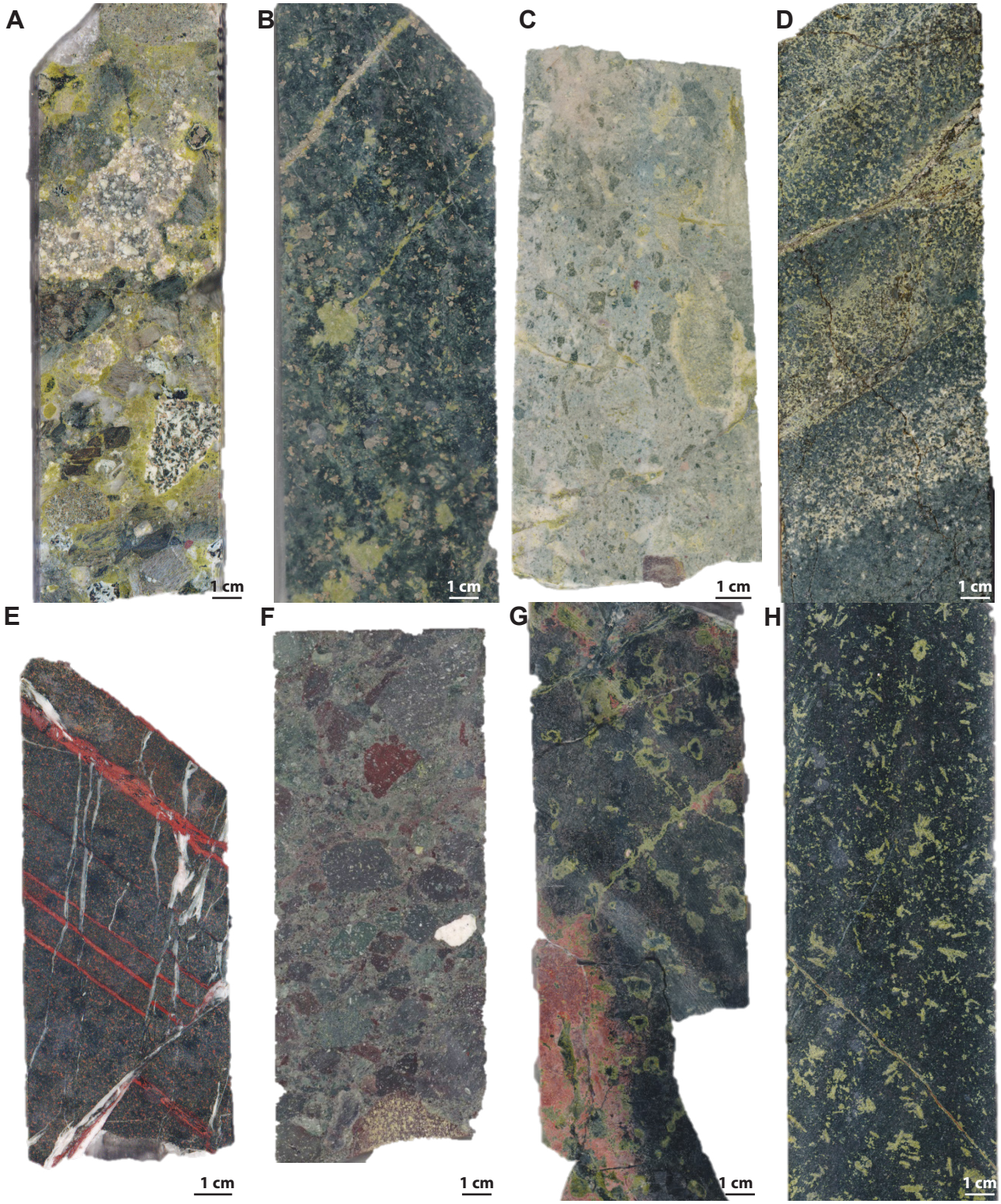


Figure 4.6 Examples of propylitic altered rocks from Resolution. A RE16JP092, Strongly epidote-chlorite ± pyrite altered KVS conglomerate - note preferential rimming of plagioclase-rich clasts. B RE16JP063, Strong selective epidote alteration of plagioclase, and chlorite alteration of the groundmass around a pyrite veinlet in dolerite. C RE16JP047, Epidote clots and sheeted veinlets in KVS andesitic crystal-rich volcaniclastic rock. D RE16JP041, Epidote-albite clots in intermediate andesitic volcanic rock. E RE15JP173, Strong chlorite alteration of the groundmass in basalt without epidote. Earthy hematite veins cross cut by late calcite veins also visible. F RE16JP042, Pervasive chlorite ± hematite alteration of clasts and matrix in andesitic Kvs breccia. G RE16JP081, and H RE16JP083, Orthoclase-chlorite-epidote alteration of the Apache Basalt adjacent to the 1% Cu ore body (U-Pb age = 1,773 ± 170 Ma; Chapter 6).

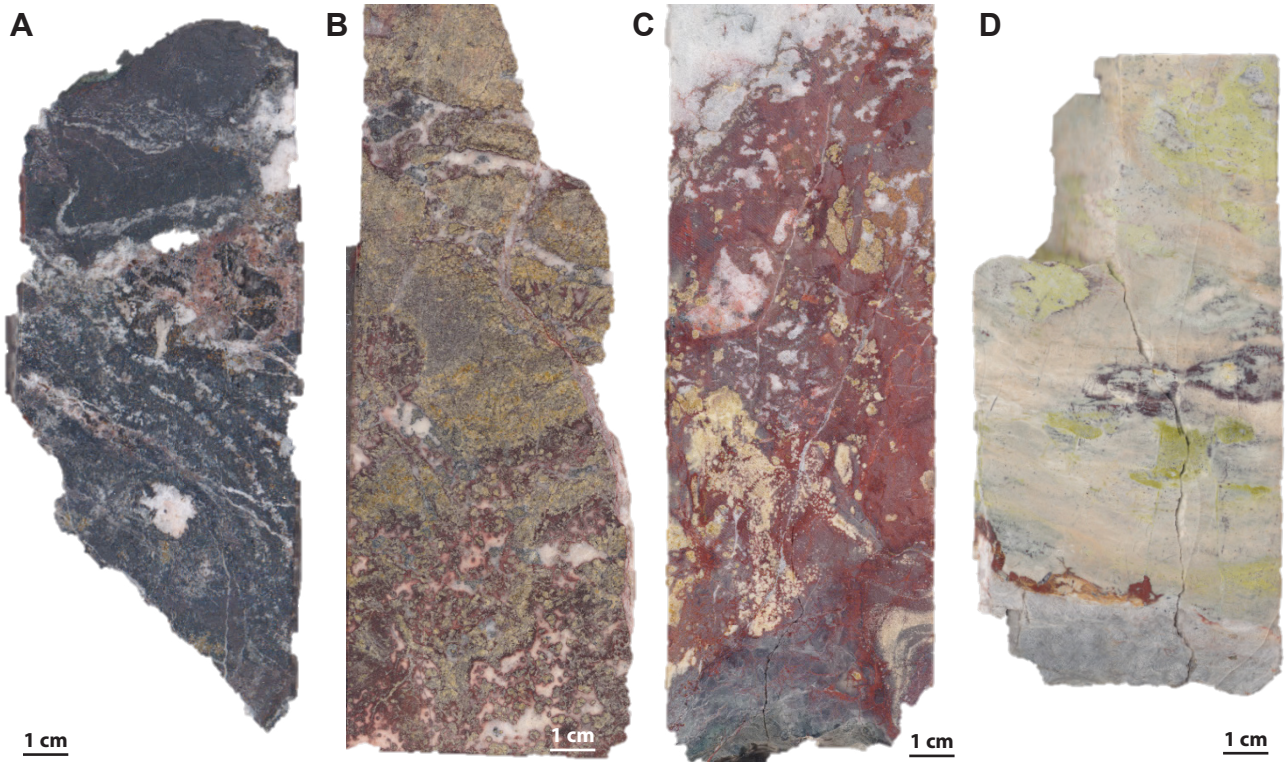


Figure 4.7 Examples of skarn altered rocks from within the Resolution graben. A RE15JP101, Massive magnetite skarn. B RE15JP099, Epidote-calcite-hematite ± chalcopyrite retrograde skarn. C RE15JP100, Garnet-hematite skarn adjacent to recrystallised marble D RE15JP205, Tremolite dominated skarn with fracture-fed epidote patches.

is the dominant ore mineral and typically the only ore mineral where rocks are only potassic altered (Figure 4.5 A). Where quartz - sericite - pyrite alteration overprinted potassic, grades are higher and there is a chalcopyrite - bornite assemblage suggesting significant hypogene upgrading took place during the phyllic stage at Resolution (Figure 4.5 B). A late high sulfidation assemblage of bornite - chalcocite - digenite and trace enargite is restricted to upper parts of the deposit and to narrow structurally-controlled zones where rocks are intermediate argillic or advanced argillic-altered (Figure 4.5 D). In the skarn zones, bornite is more common in magnesian skarns than calcic skarns. Where skarn destructive alteration occurs, grades are significantly higher, with assemblages of chalcopyrite - bornite - chalcocite - digenite, again suggesting that significant upgrading took place during phyllic alteration. Molybdenite is concentrated at the edges of early quartz veins that are considered to have formed at the transition between potassic and phyllic alteration stages (Hehnke et al., 2012). Although relatively minor, silver shows a good correlation with advanced argillic alteration, suggesting that silver substitutes into high sulfidation state Cu-sulfides (in this case chalcocite), a relationship also observed at Silver King (Blake, 1883; Galbraith, 1935).

Paragenetically, the evolution of fluids at Resolution seems to broadly conform to that observed at many calc-alkaline porphyry systems (e.g., Seedorff et al., 2005; Holliday and Cooke, 2007; Sillitoe, 2010; Cooke et al., 2014). Resolution is characterised by a temporal and spatial transition from deeper level, high temperature, high pH conditions to higher level, lower temperature acidic conditions (Figure 4.3

B). Schwarz (2010) documented a complicated but robust six-stage paragenetic sequence, which is summarised in Hehnke et al. (2012). Early potassic fluids are thought to have contributed somewhere between 20-45% of the Cu to the hydrothermal system while the majority was brought in later during the phyllic event, and subsequently upgraded again by high sulfidation state mineralisation.

There is a broadly tabular domain of chalcocite below the well-developed leached cap at Resolution. Petrography and unpublished Cu isotopic analysis suggests the chalcocite is of hypogene origin rather than the product of supergene enrichment processes (H. Martin pers. comm., 2016). The transitional oxide-sulfide zone is typically around 50 m thick, penetrating deeper along faults and fracture zones (Hehnke et al., 2012).

## 4.3 Superior East

### 4.3.1 Introduction

The modest size Superior East porphyry –Cu-Mo deposit (900 Mt @ 0.9% Cu; Table 4.1) is located 5 km northeast of Resolution (Figure 4.1). It was originally discovered by ASARCO in the 1970s following a well-planned and persistent exploration effort searching for mineralisation on the southwest flanks of the Schultze granite (Sell, 1995). It could be a separate, more deeply eroded system, based on its hydrothermal geochronology (presented in Chapter 6), although some authors consider it to be the disjointed eastern part of Resolution (e.g., Maher, 2008).

### 4.3.2 Geology

The Superior East deposit is also covered by over 600m of Apache Leap Tuff and ~1400m of Whitetail conglomerate (Sell 1995). The geology of this system was reviewed by Sillitoe (2013). The deposit is hosted in Pinal Schist, and was intruded by numerous quartz monzonite porphyry dikes on the east side of the Devils Canyon Fault. The numerous small dikes have been classified into four major types (Sillitoe, 2013). Volumetrically most abundant is the megacrystic biotite quartz monzonite (granite) porphyry with characteristic K-feldspar megacrysts. The second most abundant dikes are medium grained biotite quartz monzonite porphyry. There are also less abundant aplite porphyry and quartz-latite porphyry. The quartz-latite porphyry is unaltered, suggesting this was a later stage of intrusion (Sillitoe, 2013). The biotite quartz monzonites and aplite porphyries are cut by minor quartz veins but lack the larger (>0.5 cm) veins, suggesting they may have an inter-mineralisation timing.

### 4.3.3 Alteration

The alteration at Superior East is characterised by potassic alteration manifested as fine grained biotite, with K-feldspar only locally forming thin selvages around quartz veins (Sillitoe, 2013). This is overprinted at shallower levels by white mica which is also coincident with most of the copper mineralisation (Sillitoe,

2013). Muscovite alteration transitions upwards into hypogene kaolinite, suggesting that cooler, acidic fluids ascended to the shallowest levels of the deposit. Mutually cross-cutting relationships between faults and copper-bearing hydrothermal veins suggest that copper was introduced to the system during deformation (Sillitoe, 2013), similar to observations made at Resolution. Notwithstanding this timing relationship, the deposit itself does not appear to have been truncated by any post-mineralisation faults.

### 4.3.4 Mineralisation

Mineralisation at Superior East occurs as intergrown bornite - chalcopyrite veinlets and disseminations beneath a 200m thick leached cap. This transitions downwards into a lower grade domain of chalcopyrite - pyrite that is disseminated and in veins.

A genetic relationship between Superior East and the Magma epithermal vein was tentatively proposed by some workers (e.g., Sell, 1995) on the basis of similar mineralogies, and the along-strike position of Superior East (Figure 4.1). The abundance of supergene Cu mineralisation at Superior East could imply that high sulfidation mineralisation similar to Magma, could have been eroded from the top (Sillitoe, 2013). Alternatively this oxide material may have originated from leaching of the upper levels of Resolution with Cu-oxides reprecipitated in the deeper parts of the Whitetail basin, similar to the situation at Boyongan and Bayugo in the Phillippines (Braxton and Mathur, 2011).

## 4.4 Magma

### 4.4.1 Introduction

From soon after discovery of native silver at the base of a manganese oxide-stained outcrop in 1874, to mine closure in 1996, the Magma mine produced 25 Mt of ore, with an average grade of 5 % Cu (Paul and Manske, 2005). The fault-hosted intermediate to high sulfidation state epithermal vein system is one of many along the Apache Leap range front, but it is by far the richest in the district. While discovery and much of the early production was from the Magma vein itself, the mine consisted of a number of separate veins (Magma, Koerner, North Boundary and the First and Second South veins) as well as several limestone replacement ore zones, or mantos, which were discovered in 1948 (Paul and Manske, 2005).

### 4.4.2 Magma Vein

The geology of the south wall of the Magma vein is summarised in Table 4.1 and shown in Figure 4.8. Mineralisation is more continuous than the stoped areas suggest, because low grade mineralisation (<4.5% Cu) was not mined (Hammer and Peterson, 1968). The Magma vein is a tabular quartz - sulfide body that has replaced fault gouge and ranges in thickness from > 30 cm – 16 m with a maximum continually mineralised length of over 700 m. The vein walls are typically sharply bounded by wallrock,

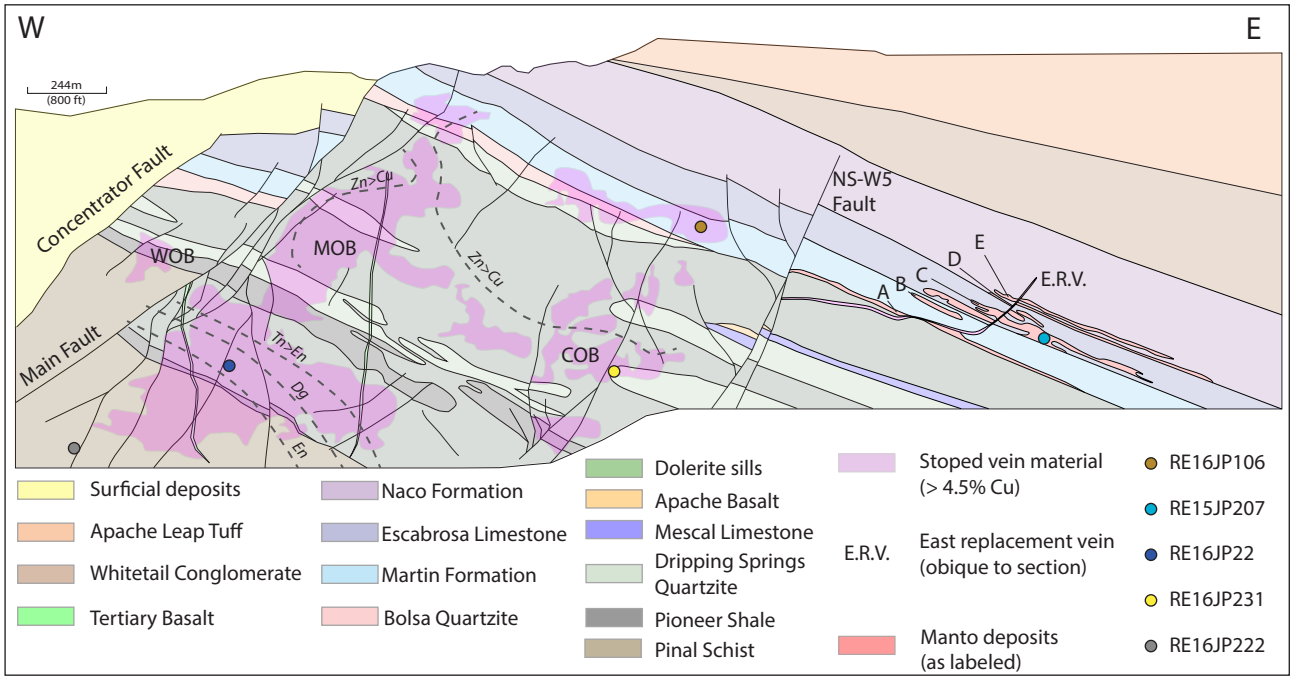


Figure 4.8 Projected long section showing the geology and mineralisation of the south wall of the Magma mine modified after Hammer (1973). Abbreviations: WOB = west ore body, MOB = main ore-body, COB = central ore bodies, En = enargite (delineates where enargite becomes the dominant ore mineral), Dg = digenite (delineates upper limit of digenite), Tn = tennentite. Sample IDs relate to Figure 4.10.

though some sections anastomose and branch out. This is most common at the junction between the Magma vein and the North and South branches.

The main ore body, which plunges steeply west parallel to the Main Fault, was the principal ore shoot and has seen the majority of mining activity (Figure 4.8). The west ore body is a smaller, offset part of the Magma vein on the west side of the Main Fault between 2000 and 2800 levels (Figure 4.8). The central ore bodies are a zone of discontinuous hematite-rich chalcopyrite mineralisation that is broadly parallel to the plunge of the main and west ore bodies (Figure 4.8).

The vein system occupies an ENE-striking fault zone and extends approximately 3 km along strike. The vein dips $65^0$ north and extends to a depth of 800 m, where it is reoriented and dips $78^0$ south (Hammer and Peterson, 1968). Owing to the difficulty in identifying pierce points along the fault, the net direction and amount of slip has not been determined accurately. However, best estimates from Short et al. (1943) are that faulting pre-dates mineralisation and caused approximately 162 m of dextral slip and 152 m of normal south-down movement, though the relative timing of these two movements is unknown. Hammer and Peterson (1968) identify three principal fault sets in the Magma mine, including one set with no surface expression:

1. An early ENE-striking system that hosts the Magma, Koerner, North Boundary and First/Second South veins. This is the most extensively mineralised fault set. It includes oblique WNW-ESE striking branches. The initial fault movement was probably normal (south down) and was then reactivated with a dextral strike slip sense during mineralisation

(Hammer and Peterson, 1968)

2. A strong NNW-striking and lesser NNE-striking fault system that has commonly offset the main veins. Weak mineralisation occurs along these secondary structures. The principal movements were dextral strike slip along NW-striking structures, and sinistral strike slip along NE-striking structures. The NE-striking structures have not been recognised at surface.
3. Well developed N-striking faults are late, west-dipping and experienced normal movement, locally with a significant sinistral component. The structural block between the Main and Concentrator faults has been strongly deformed by NW-trending faults and shears, most likely forming as linkage, or relay structures to the main faults during oblique compression. Many of these structures and their associated strands appear to show strong evidence for earlier compressional kinematics (e.g., Main fault; Figure 4.8; Hammer and Peterson, 1968).

Porphyry dikes intruded early ENE-striking faults and locally in NE-striking fault set. These NE-striking faults are only locally associated with mineralisation, suggesting that they are second-order oblique linkage structures that facilitated only minor leakage of fluids during mineralisation.

### 4.4.3 Alteration

Alteration is not a widespread, obvious phenomenon at Magma. Most of the strongly altered rocks are confined to an immediate halo around significant veins and do not extend more than 1 m into the wall rock (Hammer and Peterson, 1968). The less reactive schist and quartzite have undergone minor silicic and sericite alteration within 5-10 cm of individual veins. Alteration within the dolerite and dacite porphyry is better developed, with both of these lithologies strongly sericitised in or adjacent to the vein zone (Figure 4.9 A-C). Sericite alteration gives way outwards in the dolerite to selective replacement of feldspar phenocrysts by sericite, groundmass by chlorite and to pervasive sericite alteration in the dacite porphyry (Hammer and Peterson, 1968). Away from the major veins, subordinate sphalerite - galena veins are commonly bounded by a zone of epidote - calcite ± specular hematite alteration, especially where hosted by dolerite (Figure 4.9 D). This propylitic style alteration assemblage is locally associated with sheeted calcite veins, and pervasively developed locally where immediately adjacent to mineralisation.

### 4.4.4 Mineralisation

The hypogene ore mineralogy of the Magma vein system is summarised in Table 4.1 and Figure 4.10. The Magma vein is zoned, with galena and sphalerite restricted to shallower levels, and copper to deeper parts of the system (Figure 4.8; Figure 4.10). Copper minerals also define a zonation pattern, with higher sulfidation state phases (enargite-tennantite) confined to the deepest parts of the mine, and

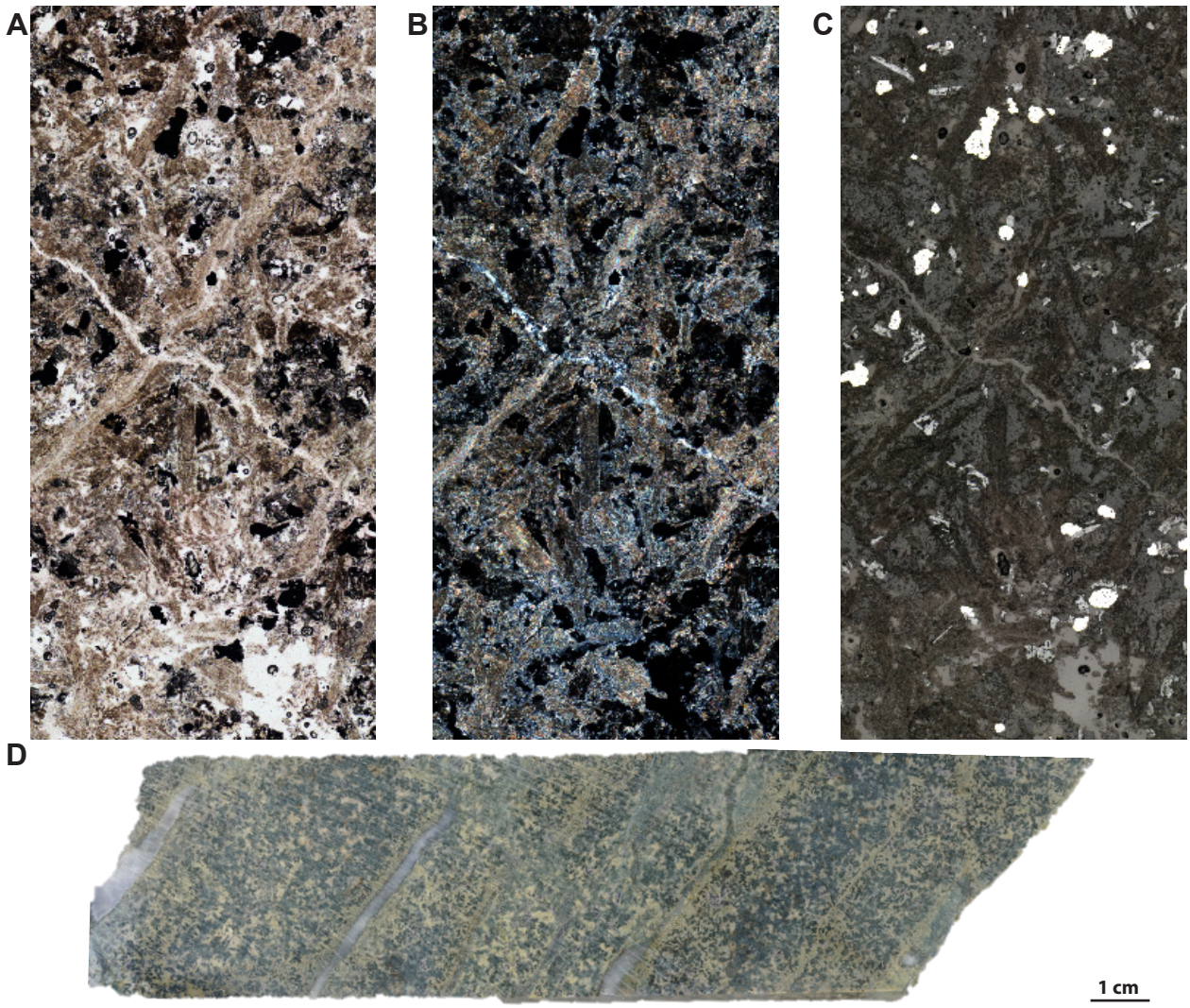


Figure 4.9 Photomicrographs of sericite altered wallrock immediately adjacent to the Magma vein (RE16JP086) showing (A) plain polarised light, (B) crossed polars and (C) reflected light images. Width of view is 5 mm. D RE16JP203, Strong epidote - chlorite alteration around calcite veins in dolerite adjacent to weak base metal sulfide veins from the Magma mine.

bornite, sometimes with significant chalcocite, constituting the dominant ore material in the central parts of the main ore body where high sulfidation state phases are absent (Figure 4.8, Figure 4.10 B-C). Chalcopyrite is the dominant ore mineral in the lower grade central ore bodies accompanied by significant specular hematite gangue (Figure 4.8, Figure 4.10 C; Gustafson, 1961). The manto deposits at Magma exhibit broadly similar copper mineralogy to the main vein, suggesting that they were emplaced contemporaneously or at least by similar fluids (Table 4.1, Figure 4.10). Importantly though, the high tenor phases of enargite, tennantite, and chalcocite are scarce and digenite is absent from the mantos, perhaps reflecting the strong buffering capacity of the carbonate wall-rocks reacting with the highly oxidised, acid fluids and producing this intermediate sulfidation mineralogy. The most significant gangue minerals in the vein are pyrite and quartz, with significantly less common carbonates and hematite, more common in the central ore bodies. At surface, the mineralogy of the vein is dominated by manganese oxides. Primary Mn-bearing phases such as rhodochrosite are not described by previous studies, but were

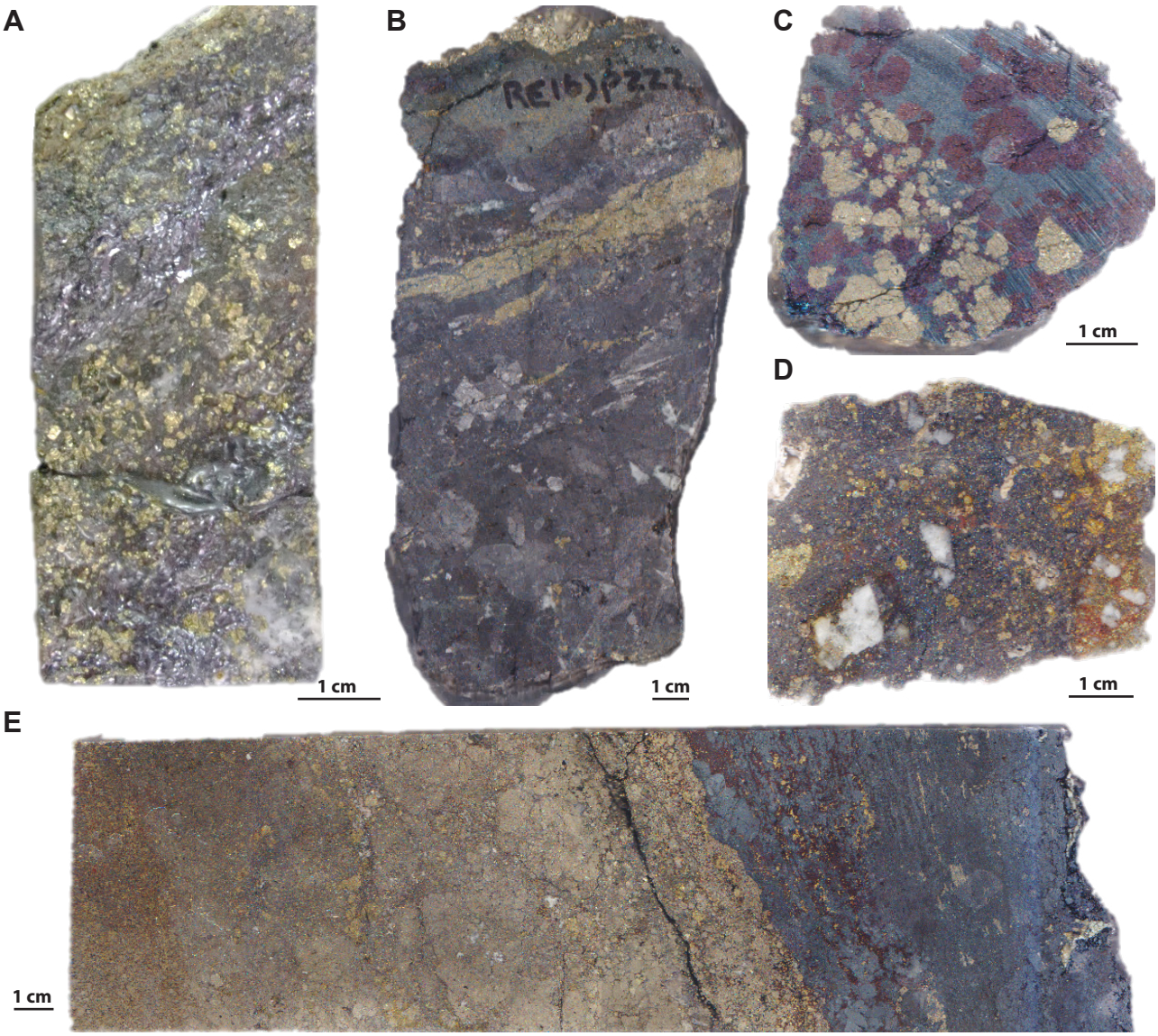


Figure 4.10 Ore samples from the Magma mine. A RE16JP106, Pyrite - galena ± sphalerite vein from high in the system. B RE16JP222, Massive enargite-pyrite vein from deep in the system. C RE16JP223, large pyrite and bornite aggregates overgrown by chalcocite, from the Main ore body. D RE16JP231, Specular hematite cemented breccia with clasts of pyrite-chalcopyrite and vein quartz. Some samples also contain clasts of wall rock lithologies.E RE15JP207, Massive sulfide from a manto lens, with characteristically sharp contact between pyrite ± chalcopyrite and massive chalcocite. See Figure 4.8 for sample locations.

encountered rarely during the current study.

Metal zonation patterns in the Magma vein are shown in Figure 4.8. Rather than being parallel with bedding and therefore implying a simple vertical zonation pattern, the metal zonation boundaries drawn on the Magma long section by Gustafson (1961) and Hammer and Peterson (1968) appear to dip slightly to the east (Figure 4.8). Assuming vein emplacement occurred before any major eastward tilting, this would suggest that after structural restoration, the fluid source would be located below and to the west of the main ore body (Maher 2008). This is an important interpretation that would suggest the hangingwall of the Concentrator Fault is prospective for both an along-strike extension of the Magma vein and a possible alternative porphyry-type fluid source to Resolution. However, Hammer (pers,

comm, 2016) argues against this hypothesis, citing the lateral zonation patterns around subvertical fluid pathways along the vein as more important.

Gustafson (1961) identified up to six paragenetic sequences for various ore types across the Magma mine, although deposit-wide correlation of these stages was not possible. Common to all of the ore types was the early deposition of pyrite, followed by the deposition of minerals with increasing Cu:Fe ratios that replaced pyrite. Where present, sphalerite preceded copper deposition.

There is evidence for a late stage mineralisation event, manifested by botryoidal crusts of chalcopyrite coating brecciated sulfides along open faults (Hammer and Peterson, 1968). Macroscopic corrosion of enargite at the deepest levels of the central ore body along with corrosion of chalcopyrite and bornite associated with deposition of rare native gold attest to a change in chemistry of the hydrothermal fluid as the system waned, or, the influx of a separately sourced fluid well after the Magma mineralising system had ceased (Hammer and Peterson, 1968). Gold deposition suggests a relationship to deep penetrating lateral supergene fluids associated with the formation of the auiferous Lake Superior and Arizona jasperoids (Section 4.8, Pareja, 1998).

Although the Magma vein system was discovered and initially exploited for supergene silver, in the wider context of mineralisation at Magma, supergene process were relatively unimportant (Hammer and Peterson, 1968). Nonetheless, material mined above the 900 level (approximately 274m below surface) was oxidised and/or weakly enriched via supergene processes, resulting in a wide variety of supergene minerals.

### 4.4.5 Carbonate replacement deposits (mantos)

At the eastern end of the Magma mine, replacement ores formed locally in reactive carbonate horizons, and are interbedded with unmineralised carbonate rocks. The mineralised horizons are referred to as the A-, B-, C-, D- and E-beds (Figure 4.8; Paul and Knight, 1995; McCarrel, 2012).

The economic manto deposits consist of large, tabular, massive sulfide bodies. Most of the production came from A and C beds (Paul and Knight, 1995). Although as thick as 30 m, they typically average 8 m thick and the longest continuously developed manto was approximately 300 m. The mantos have a distinct alteration zonation (Friehauf, 1995, Table 4.1). The mineral assemblages and their zonation pattern suggest that the principal control on metal deposition in carbonate rocks was acid neutralisation (Friehauf, 1998). The manto ores formed by initial replacement of carbonate host rocks by hematite - quartz assemblage which allowed later fluids to deposit Cu-Fe sulfides before being fully neutralised by the carbonate wallrocks. Sulfidation of hematite consumed sulfur and neutralised the ore fluid, resulting in a residual fluid that redeposited at the margins of the orebodies (Freihauf, 1998).

Although economic mantos are confined to the deeper parts of the Magma mine, distal expressions are manifest as sub-horizontal siliceous chert breccias that crop out along the range front (e.g., Lake Superior and Arizona Mine; Pareja 1998; Section 4.8). Close to manganiferous epithermal veins, the mantos host

pyrolusite as well as other manganese oxides, and in some cases, the mantos appear to emanate from the epithermal veins (e.g., the East Replacement Vein; Figure 4.8). This is consistent with underground observations (Hammer and Peterson 1968; Friehauf, 1998) and implies that the epithermal veins acted as feeders to the mantos.

### 4.4.6 Skarn Mineralisation

Although volumetrically minor compared to the veins and replacement ores at Magma, the occurrence of skarn is geologically important. The skarn-style mineralisation is structurally controlled, and cross-cutting relationships demonstrate that skarn formation predated massive sulfide replacement (Friehauf, 1998). Skarn is observed with each of the major veins, minor vein swarms and mantos. Skarn occurrences are restricted to the deep, southeastern parts of the Magma mine, closest to Resolution, and do not crop out at surface (Friehauf, 1998). Most skarns in the Magma mine are magnesian skarns, reflecting the dominant dolomitic protolith (Freihauf, 1998).

Skarns in the Magma mine share some similarities with classic zinc skarns, including the abundance of sphalerite, pyrite ± galena, a lack of copper sulfides, the occurrence of manganese-bearing phases (Einaudi, et al., 1981). However, based lower iron contents of sphalerite, skarns at Magma imply higher oxidation states than typical of zinc skarns (Table 4.1; Freihauf, 1998). The mineralogy and strong structural control at Superior suggest they are similar to skarns that form in the distal environment of porphyry copper systems (e.g., Yerington; Dillies and Einaudi, 1992; Einaudi, 2000).

The observed variation in skarn mineralogy from talc - sphalerite - magnetite - pyrite to garnet - pyrite - vesuvianite at Magma has been attributed to high and low fluid:rock ratios respectively (Table 4.1; Freihauf, 1998). The distribution of skarn at the deposit scale suggests a zoning toward greater fluid:rock ratios to the south and/or east, supporting a genetic relationship to either Resolution (Friehauf, 1998; McCarrell, 2012) or Superior East (Sell, 1995).

## 4.5 First and Second South Veins

The First and Second South veins are located south of the North Boundary Fault. They are hosted within the Kvs and have no surface expressions (Figure 4.1, Figure 4.2). They were discovered in 1971 and 1976 respectively, during southward exploration underground from the Magma mine. (Hammer, 2011). The First South Vein was poorly mapped and documented during mining, but was briefly characterised by Schott (1994). Both the First and Second South veins are hosted by the Kvs in ENE-trending structures, parallel to the Magma vein.

### 4.5.1 Alteration and Mineralisation

The Kvs wallrock immediately adjacent to the veins is strongly sericite altered, similar to the Magma vein. This transitions outwards to propylitic alteration with stringers of pyrite - hematite - quartz

(Table 4.1; Schott, 1994). Geometrically, the First South Vein produced a discontinuous zone of poddy mineralisation, whereas the Second South Vein was a discreet, planar and through-going (Schott, 1994), demonstrating an overall decrease in continuity of mineralisation between the two veins outwards from Resolution. Generally the ore mineralogy is similar to the Magma Vein. This includes the presence of Sn-bearing phases such as colusite ($Cu_{26}V_2[As,Sn,Sb]_6S_{32}$) and mawsonite ($Cu_6Fe_2SnS_8$) at Magma (Gustafson, 1961) and the First and Second South veins (Schott, 1994), which also contains stannite ($Cu_2FeSnS_4$; Schott, 1994). The paragenesis is similar to Magma in that there is (1) early Fe-oxide deposition, (2) pyrite (3) sphalerite-galena (4) main stage Cu sulfides, (5) late, weak base metals (Schott, 1994). The major difference between the First and Second South veins is that the Second South vein lacks any sulfosalt minerals, and contains lower quantities of sphalerite and galena (Schott, 1994).

## 4.6 Silver King

### 4.6.1 Introduction

Remarkably little is known of the Silver King Mine. Blake (1883) provided the only eyewitness account of the mining operation (Figure 4.1). The mine was worked from 1875 to 1896 exclusively for high grade silver, after a colourful discovery history (Blake, 1883). Details regarding the Silver King ore body are summarised in Table 4.1 (Short et al., 1943; Hammer, 2011). Unfortunately it was not possible to inspect the mine workings or any ore-grade material during this study, so emphasis was placed on characterising the alteration associated with the deposit within the context of the wider district. Due to its distance from Resolution (5 km NNW; Figure 4.1), the Silver King ore body is interpreted to be related to a separate hydrothermal system. Therefore, a synopsis of the alteration-mineralisation features observed in the immediate vicinity of the old mine is produced here with the aim of helping to delineate the footprint of the Silver King system and to help ascertain whether or not more significant porphyry style mineralisation could exist at its centre.

### 4.6.2 Geology

The Silver King ore body occurs as a quartz - sulfide stockwork vein and breccia body hosted in a strongly sericite altered dacite porphyry plug, similar in appearance to the sporadic porphyritic intrusions that crop out along the range front and in the Magma mine. The dacite porphyry intruded a larger quartz diorite stock, which in turn intruded the Proterozoic and the lowermost Paleozoic sequences (Figure 4.1). Both the quartz diorite and the dacite porphyry have been dated radiometrically and return early Laramide ages of 74.83 ± 0.33 Ma and 73.6 ± 1.6 Ma respectively (Table 3.2; Hehnke et al., 2012,). Seven different compositions of porphyry dikes (including the Grandfather Lead aplite) were documented by O'Neal (2015), although most of these were not encountered during this study. The vein - stockwork zone now plunges approximately $30^0$ west as a result of Tertiary extension, but there is no observable

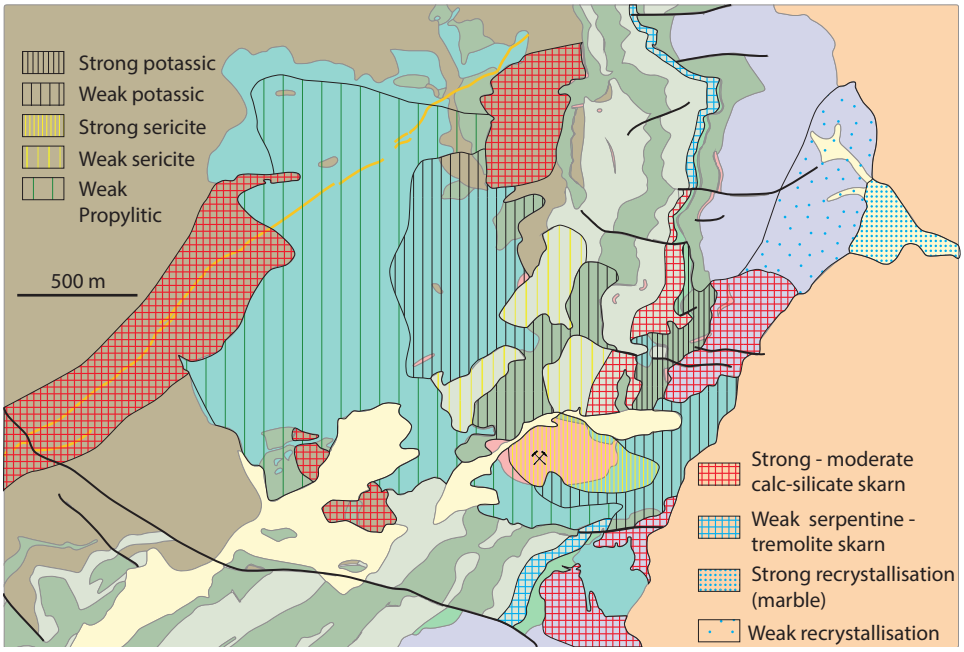


Figure 4.11 Alteration mapping around Silver King, modified after Hammer (2001) and O'Neal (2015). Simplified geology as per Figure 3.1

evidence for structural control on dacite stock emplacement or focussing of the breccia body.

### 4.6.3 Alteration

Detailed alteration mapping around the quartz diorite stock and Silver King ore body was conducted by O'Neal (2015; Figure 4.11). The Silver King host dacite porphyry is intensely sericite altered over an area of ~310 $m^2$ (initially mapped by Hammer, 2011), with alteration roughly centred on the Silver King open pit (Figure 4.11, Figure 4.12 A, Figure 4.13 A). Moderate to weak sericite alteration was mapped as continuing 4 km north along the range front, predominantly in siliciclastic units and to some degree, in the quartz diorite stock (O'Neal, 2015). During the current study, although not observed on the same scale as that reported by O'Neal (2015), quartz - sericite - pyrite alteration was observed in the quartz diorite immediately adjacent to the dacite porphyry (Figure 4.12 B,). Further away from the dacite contact, strong sericite alteration gives way to weak illite - chlorite alteration focussed around minor epithermal veins (Figure 4.12 C, Figure 4.13 B).

Weak potassic alteration was observed during the current study at a number of localities in the Silver King area (Figure 4.11). The quartz diorite has small clots and stockworks of magnetite-pyrite, typically associated with small cavities indicative of anhydrite dissolution (Figure 4.12 D). Strong potassic alteration was also observed in Apache Basalt directly east of the main quartz diorite exposure. In this case, the groundmass of the Apache Basalt is thoroughly altered to biotite and hosts veins of magnetite that also contain rare pyrite (Figure 4.13 C).

Propylitic-style alteration is subtle but extensive within the quartz diorite (Figure 4.11). It typically consists of small (<5 mm) veinlets of epidote and/or albite, usually with a thin albitic halo (Figure 4.13

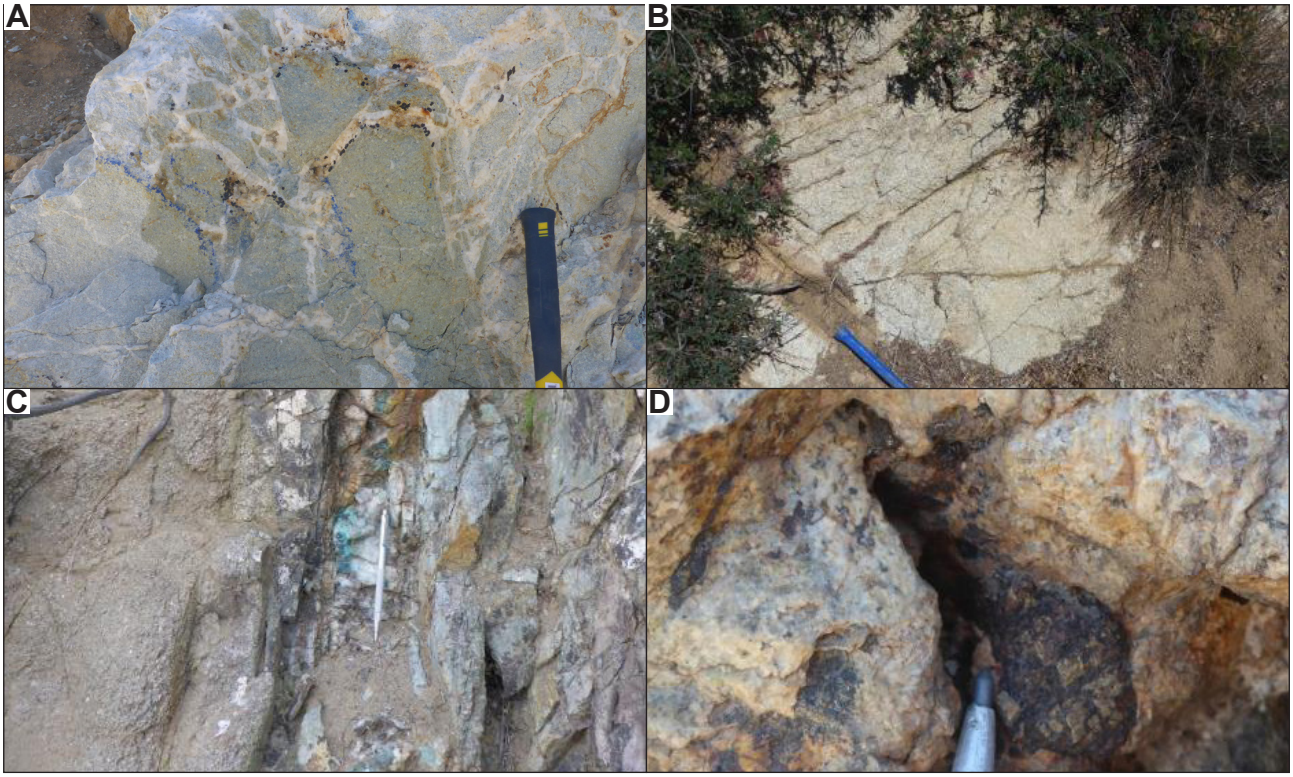


Figure 4.12 Field exposures of altered rocks from around the Silver King Mine. A. Quartz cemented, monomict, hydrothermal breccia from within the Silver King open pit, hosted by intensely sericitised dacite porphyry. Photo taken in the vicinity of 491922 mE, 3687868 mN. B. Recessive sericite alteration in the eastern lobe of the quartz diorite in the vicinity of 492289 mE, 3687769 mN. C. Illite-chlorite altered quartz diorite adjacent to weakly mineralised quartz vein close to the Grandfather Lead aplite dike in the vicinity of 490135 mE, 3688799 mN. D .Magnetite-pyrite clot in cavity of quartz diorite in the vicinity of 492247 mE, 3687653 mN.

D). Chlorite is variably present, typically occurring as partial replacements of large hornblende crystals in the porphyritic of the quartz diorite phase adjacent to epidote - albite veinlets.

Calc-silicate (skarn) alteration is also widespread at Silver King. It is contained within Paleoproterozoic Pinal Schist below the main intrusive complex, the Mescal Limestone and the Paleozoic carbonate sequence, adjacent to the quartz diorite. Small domains of red garnet, clots of magnetite and even small grains of chalcopyrite can also be seen (Figure 4.13 F). Above and below this, interflow basalts have been thoroughly magnetite altered. In the Paleozoic sequence, a skarn association with the intrusion of the quartz diorite is unequivocal. Both endoskarn and exoskarn have formed around the eastern apophasis of the quartz diorite (Figure 4.1). Typically, this is composed largely of pale beige tremolite and brown-red garnet with or without epidote veins and clots of specular hematite (Figure 4.13 G). Massive accumulations of specular hematite occur locally (Figure 4.13 H).

### 4.6.4 Mineralisation

Though mined predominantly for high grade supergene-enriched silver, the most abundant ore metals at Silver King were lead, copper and zinc (Short et al., 1943). Petrographic studies by Short et al. (1943) showed that pyrite and sphalerite were largely replaced by chalcopyrite and tetrahedrite and

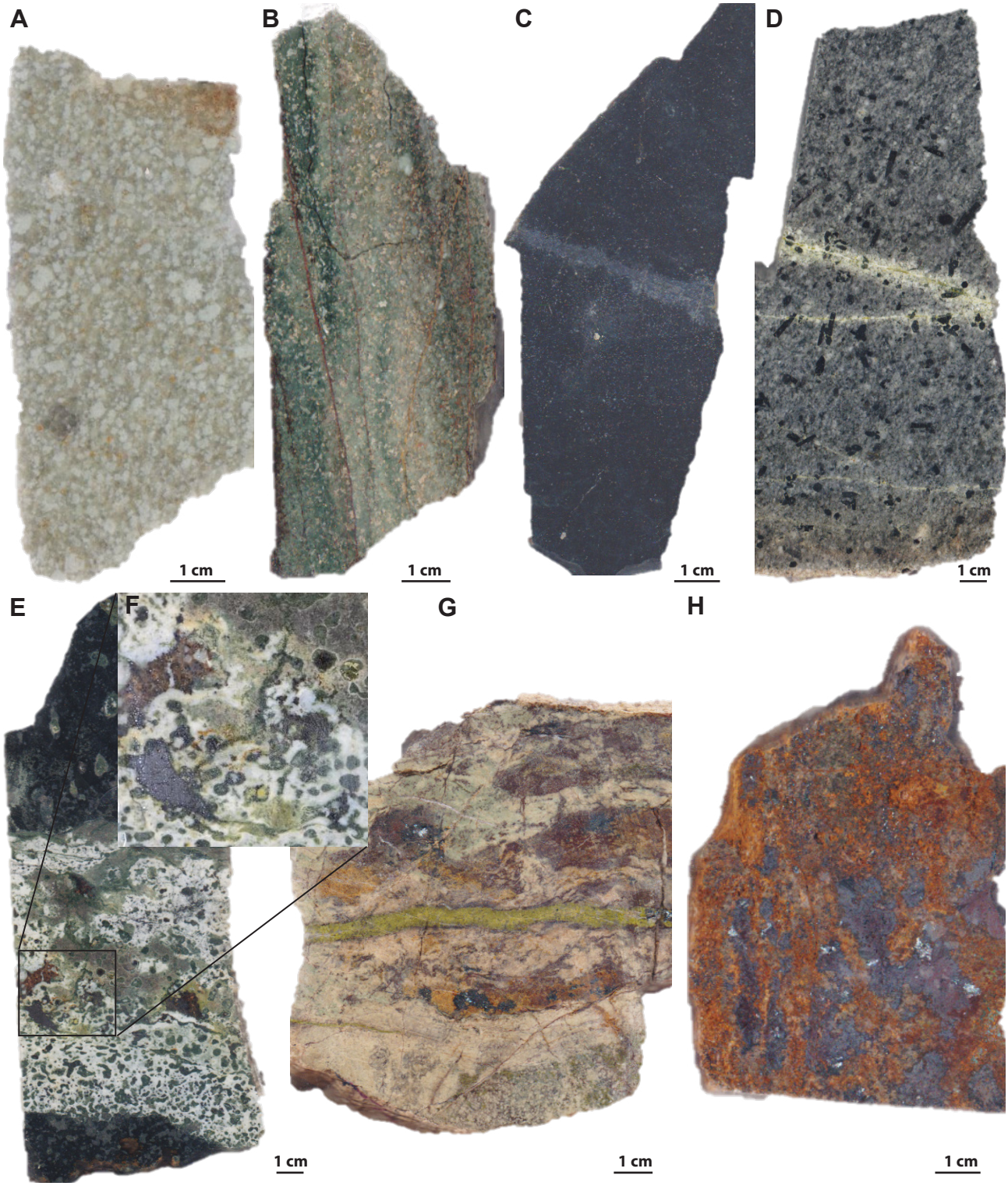


Figure 4.13 Hand specimens of altered rocks from around the Silver King area. A. RE16JP065, Bleached sericitised dacite porphyry from the Silver King open pit. B RE16JP019, Illite-chlorite altered wall rock from an adjacent to weakly mineralised vein. C. RE16JP026, Intensely biotite altered basalt with magnetite vein and disseminated pyrite from the range front east of Silver King. D. RE16JP077, Typical propylitic-style alteration in the porphyritic phase of the quartz diorite. E. RE16JP028, Intense tremolite-diopside skarn alteration of the Mescal limestone showing red garnet, magnetite pod and chalcopyrite (F, inset). G. RE16JP071, brown garnet-tremolite specular hematite skarn with through-going epidote vein. H. RE16JP079, Massive hematite-geothite hosted in Cambrian Bolsa Quartzite.

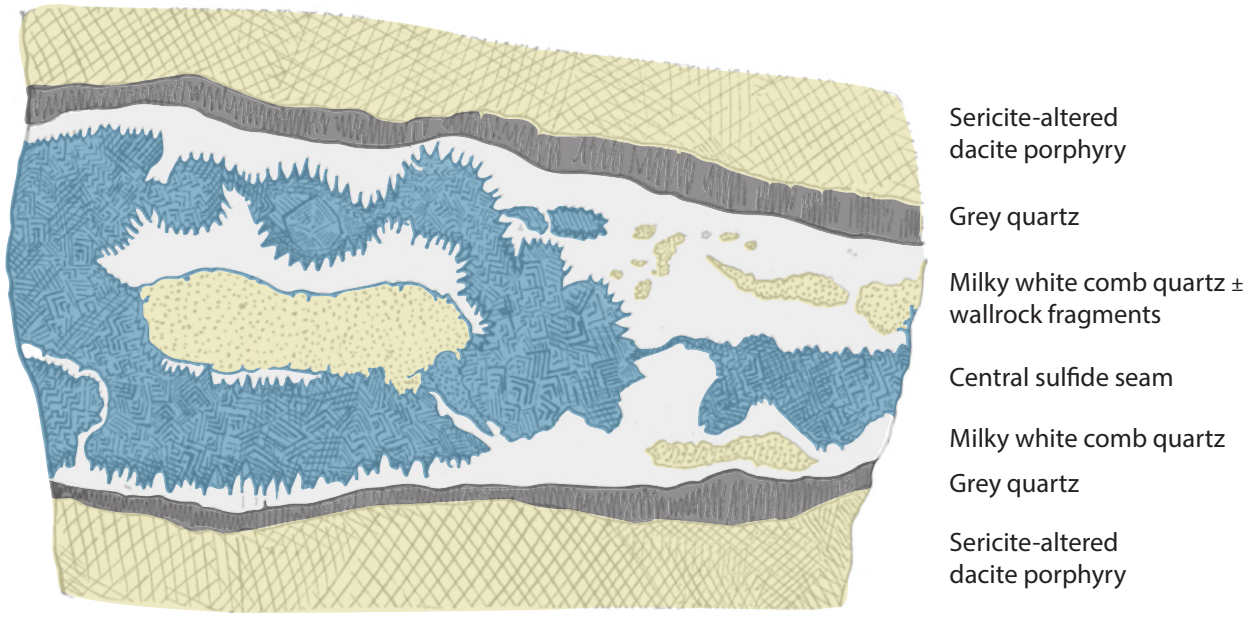


Figure 4.14 Sketch of an ore samples from the Silver King mine. Modified after Blake (1883).

then overgrown by bornite and galena respectively. Tetrahedrite contained weight percent silver, and is the only known hypogene Ag-bearing phase (Short et al., 1943). The sulfides occur as disseminations immediately adjacent to quartz veins and in the central seams of quartz veinlets (Blake, 1883; Hammer, 2011). The mineralised stockwork surrounds a central conduit of massive milky white crystalline quartz, exhibiting open space filling textures that are considered to pre-date ore deposition, along with minor amounts of barite gangue. Silver King was mined predominantly for supergene stromeyerite and native silver, which were the sources of the bonanza grades. Massive chalcocite was also common in the upper levels of the mine (Blake, 1883).

Although the dimensions of the stockwork zone reportedly to increased with depth, it was only ever mined to a depth of approximately 244 m below surface (800 ft level). Historical maps show further development down to 300 m below surface (985 ft level) towards the projected location of the orebody (Hammer, 2011). Since stoping did not continue, Hammer (2011) concluded that either (1) these developments were never actually excavated, (2) the mineralised stockwork was located but subeconomic or (3) mineralised stockwork was not found on the 985 level due to a fault offset or abrupt dip change on the controlling structure. Most historical reviews seem to favour the second hypothesis, suggesting that supergene enrichment bottomed out at the 800 level.

The character of Silver King is unique in the Superior District, being the only outcropping mineralised epithermal stockwork and breccia system. It is too far removed from Resolution to be derived from the porphyry (5 km distance; Figure 4.1) and is more likely to represent the distal expression of a nearer, as yet undiscovered magmatic-hydrothermal centre. It is likely to be part of a magmatic-hydrothermal system that produced other styles of alteration in the broader Silver King area (Figure 4.11). The high temperature potassic and skarn alteration assemblages that were observed during the current study

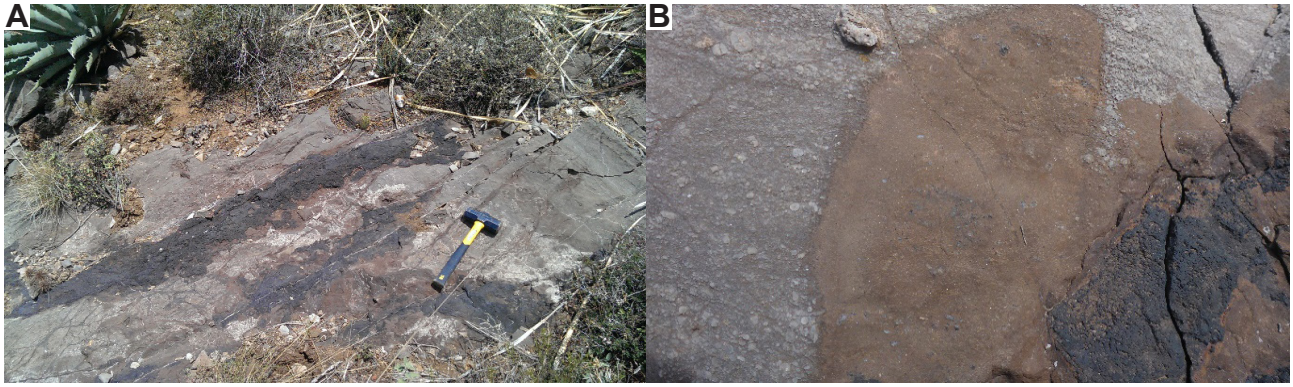


Figure 4.15 A. Typical exposure of manganiferous epithermal vein in the Superior district. Note the discontinuous nature and irregular wall geometry. B Typical alteration halo surrounding manganese oxide vein. Note the partial textural preservation of the crinoidal Escabrosa Limestone host.

indicate a centre approximately 1-2 km due east of the existing Silver King mine workings (Figure 4.11).

## 4.7 Epithermal veins and mantos

Many small outcrops of manganese and iron oxide-stained epithermal veins occur crop out at the base of Apache Leap (Figure 4.1). These are typically hosted in NE-striking fault that cut Paleozoic carbonate rocks (Figure 4.15 A). The walls of these smaller veins are generally highly irregular rather than planar (Figure 4.15). Apart from the Magma Vein, the Belmont Vein is the largest known epithermal vein in the range front (Figure 4.1). It is considered to be the westward extension of the South Boundary Fault (Hammer, 1973; Mankse and Paul, 2002; Hehnke et al., 2012). Belmont and many other veins in the region were explored and developed sporadically by small-scale miners during and after the First World War due to elevated metal prices, but the veins were never rich and/or consistent enough to consolidate land holdings and develop on a large scale, despite the presence of seemingly significant underground workings at Belmont. The extracted material consisted of mostly oxidised replacement ores with an estimated total endowment 21.6 Kt @ 0.8% Cu, 334 g/t Ag, and 4.8 g/t Au (Hammer and Peterson, 1968).

Alteration around Belmont and other veins is extremely restricted, consisting of a centimetre-scale, brown siderite halos that are variably texturally preserving (Figure 4.15 B). Beyond this siderite halo the wall rock contains weakly recrystallised calcite. Overall, visible alteration generally extends less that 1m from domains of semi-massive manganese oxides (Figure 4.15 A).

The veins vary in form and composition. Massive, crumbly, black oxide material that lacks internal textures or structures in the most common appearance observed in the Superior exposures, although locally the massive oxide material displays a network veinlet texture of apparently similar but more resistive mineralogy (Figure 4.16 A). Less commonly, competent veins have retained their internal texture, displaying complex cockade breccia textures of alternating metallic grey manganese oxides and pale iron carbonates with late calcite infill (Figure 4.16 B). Locally the manganese oxides and iron

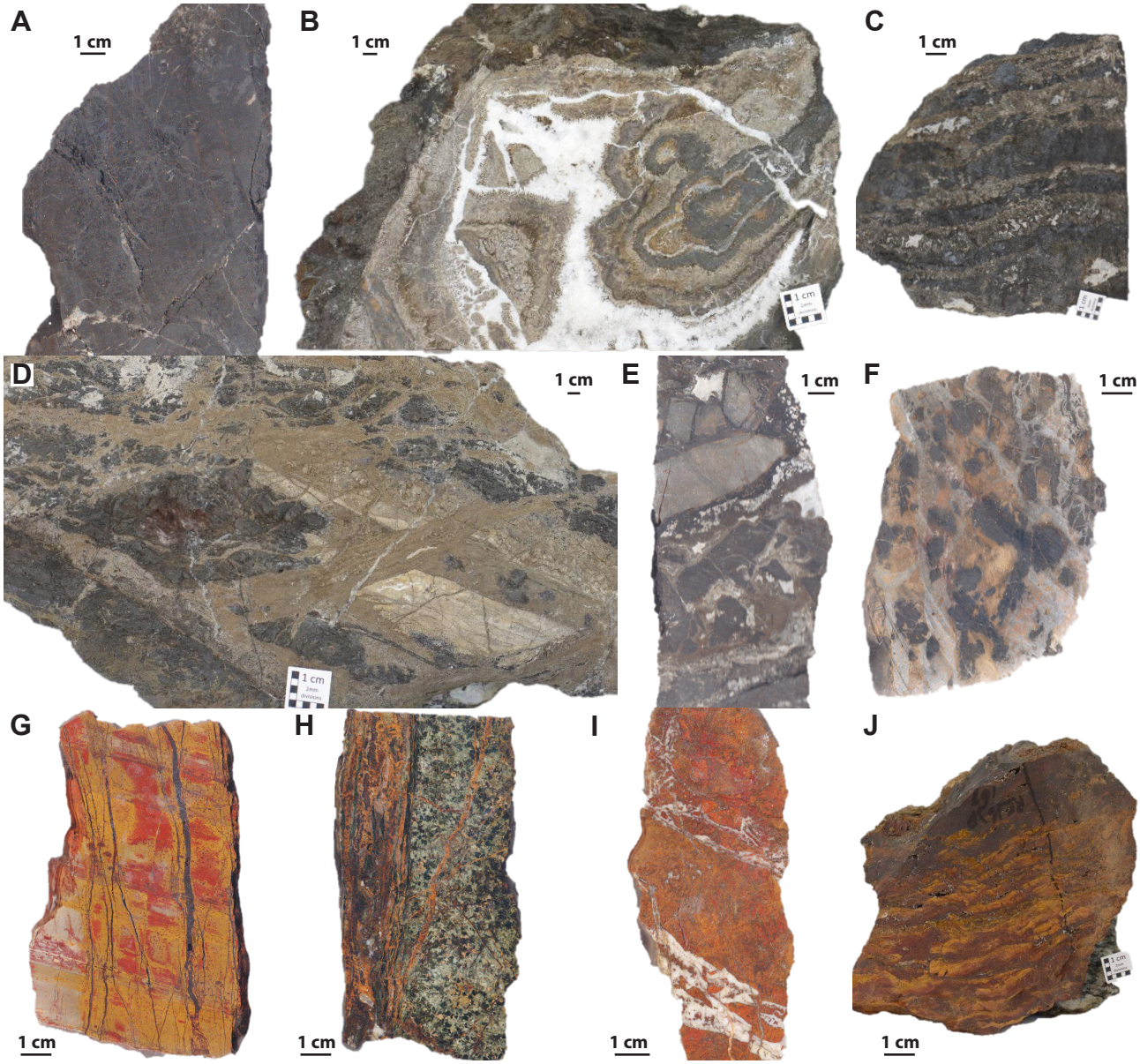


Figure 4.16 Hand specimens of Laramide epithermal vein textures from the Superior district. A RE16JP217, Typical massive manganese oxide. B, RE16JP172, Intricate cockade breccia texture found in the Monarch vein exposure along the US60 road cut. C RE16JP168 Bedded manganese oxide and siderite texture from the south of the district. D. RE16JP130, Paragenetic relationships shown in a vein from Cross Canyon. E. RE16JP179, Brecciated epithermal vein from US60. F RE16JP164, Poddy manganese oxide material. G RE15JP155, Sheeted goethite (after? pyrite) veins hosted in Upper Dripping Springs. H. RE15JP135, Manganocalcite-chlorite vein in weakly illite altered dolerite. I. RE15JP014, Ankerite vein with late calcite hosted in dolerite. J RE16JP167, Siliceous, japeroidal manto

carbonates present a banded texture that may preserve primary bedding, with a late calcite phase occurring as a central seam in the carbonate bands (Figure 4.16 C). There is a general progression from manganese oxides to later iron carbonates (Figure 4.16 B). Locally siderite veins cut manganese oxides that in turn are cut by weak calcite veinlets (Figure 4.16 D). Other vein textures include clasts within tectonic-hydrothermal breccia, with matrix material strongly stained by earthy hematite (Figure 4.16 E). Other veins are crop out as discontinuous tabular domains of poddy manganese oxide material with limited late carbonate, but surrounded in hematite stained quartz (Figure 4.16 F). Bladed calcite is a

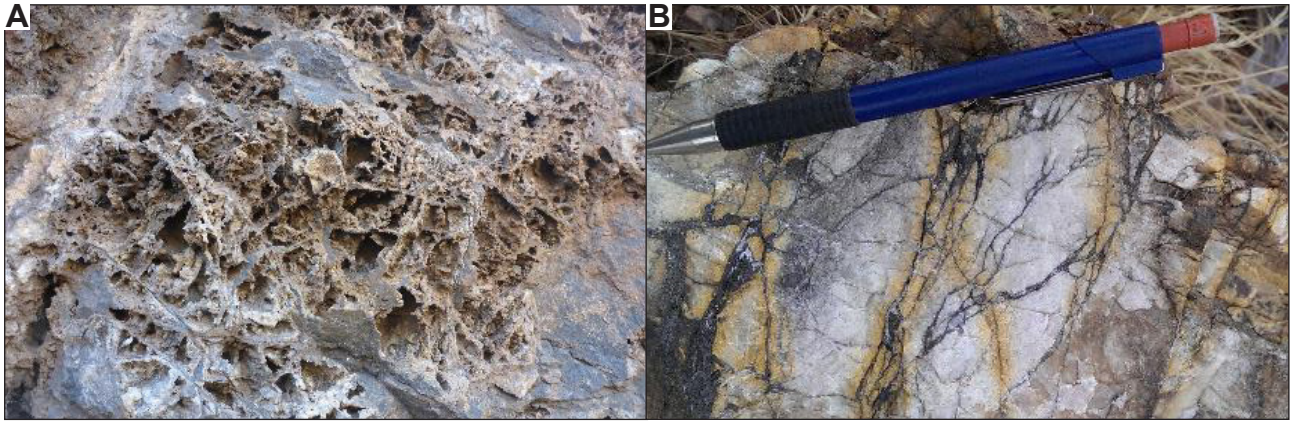


Figure 4.17 Field exposures of epithermal veins in the range front. A. Bladed calcite from the Belmont area (vicinity of 493011 mE, 3681519 mN. B. Oxidised epithermal veinlets comprising manganese oxides and calcite with yellow limonite halo hosted in Troy Quartzite in the vicinity of 494900 mE, 3681511 mN.

notable component at Belmont and adjacent veins (Figure 4.17 A). Bladed carbonate is indicative of shallow level boiling (Simmons and Christenson, 1994) and is linked to gold and silver mineralisation in low sulfidation epithermal deposits (White and Hedenquist, 1990). The observation of bladed calcite at the Belmont mine therefore provides evidence for boiling in epithermal veins at the southern end of the range front. This may in part explain the elevated gold grades and weaker copper mineralisation at Belmont compared to Magma (Hammer 1973).

Where the range front epithermal veins are not hosted by Paleozoic carbonate rocks, they become more mineralogically and texturally varied, but are generally much less volumetrically significant. Sandstone-hosted veins in the northern part of the range front consist of sheeted monomineralic goethite veinlets (presumably after pyrite) with strong red hematite staining (Figure 4.16 G). Weakly illite altered dolerite contains manganocalcite and chlorite veinlets (Figure 4.16 H). At the south end of the district is a single large ankerite vein (>1 m thick), also hosted by a dolerite sill (Figure 4.17 I). Where epithermal veins were observed in sandstone, they typically have the same manganese oxide ± late carbonate association, but have a yellow limonite halo rather than a brown siderite halo (Figure 4.17 B)

Where the veins cut favourable horizons in the limestones, mineralisation spread out laterally and produced minor mantos. These mantos typically have the same mineralogy as the vein proximal to the structure, but become highly siliceous and jasperoidal further away from the vein where they consist of hematitic microcrystalline quartz (Figure 4.16 J). Locally these siliceous mantos are variably enriched in gold (e.g., Lake Superior and Arizona, Table 4.1; Pareja, 1998).

## 4.8 Lake Superior and Arizona mine auiferous jasperoids

The Lake Superior and Arizona mine was a small operation located 1 km south of Magma. It was worked sporadically between 1885 and 1959 for gold-rich jasperiods along the up dip extension of the A- bed horizon, at the base of the Devonian Martin Formation (Table 4.1). As with the carbonate replacement deposits in the Magma mine, the jasperoids of Lake Superior and Arizona were concordant

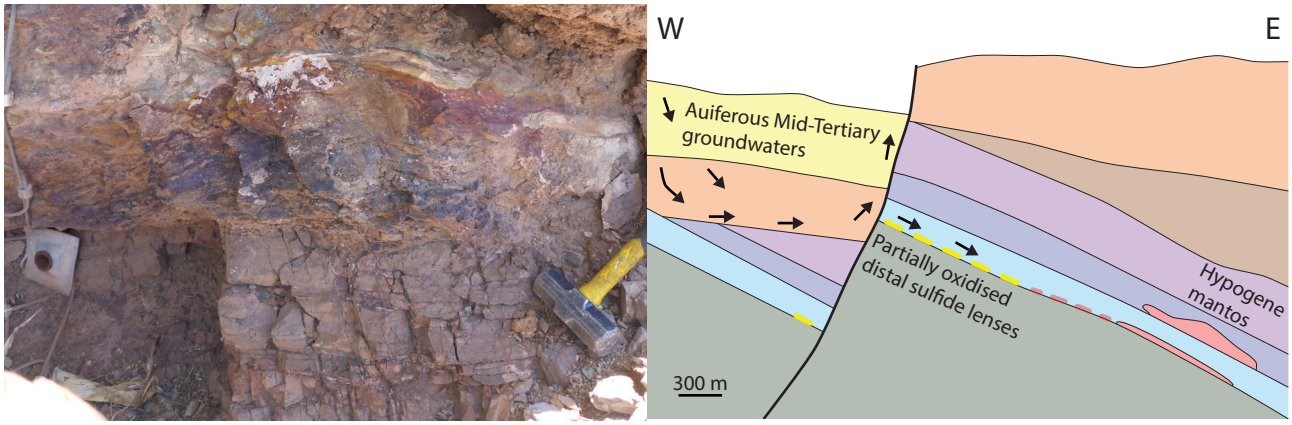


Figure 4.18 Auriferous jasperoids. A. Field exposure of hematitic jasperoidal nodule in the A-bed horizon of the Martin Formation, in the Superiod district range front in the vicinity of . B. Schematic cross section illustrating the mode of formation of the Au-bearing nodules and their relationship to the manto deposits of the Magma mine. Modified after Pareja (1998).

with bedding and attain their greatest thickness where an ENE-striking structure cut the favourable A bed stratigraphic horizon (Pareja, 1998). Generally jasperiods occur as 0.3 -1 m thick, 6-10 m wide and 12-30 m long (down dip), although they can be as large as 3 m thick and more than 100 m long. Two types of jasperiod characterise the district: iron oxide–rich (Au-bearing) and iron oxide–poor (barren) jasperoids (Pareja, 1998). Iron-oxide rich jasperoids are composed largely of brecciated iron oxides, essentially gossanous material, and are commonly leached, vuggy or exhibit a box-work texture with very fine grained paragenetically late quartz (Figure 4.18 A; Pareja, 1998). Although copper grades range from 0.03 – 0.3% there are no visibly discernible copper phases, except at the deepest levels of the mine where some supergene chalcocite was observed (Short et al., 1943). Small gold grains (~5 - 20 µm) can be found within the hematite fragments. Alteration is limited but summarised in Table 4.1. Average production grades are estimated at 15 g/t Au (Table 4.1, Pareja, 1998).

The Lake Superior and Arizona jasperiods are considered to be distal, discontinuous manifestations of the massive sulfide mantos from the Magma mine. Petrography, mass balance and fluid modelling results support formation by partial to complete oxidation of hypogene sulfides and the introduction of silica-saturated auriferous groundwaters during the mid-late Tertiary (Figure 4.18 B; Pareja, 1998).

## 4.9 Summary

The Superior district contains a range of magmatic-hydrothermal mineralisation styles that vary in geometry, grade, space and time. The most significant deposit is the Resolution porphyry Cu-Mo, deposit buried under ~1.5 km of volcanic cover and hosted in a structurally complex graben (Mankse and Paul, 2002; Hehnke et al., 2012; Figure 4.2). It has a resource of 1.7 Gt @ 1.6% Cu and 0.03% Mo. It is unusually high grade for a porphyry deposit and is one of the largest and deepest undeveloped Cu deposit in North America. It has a typical, well developed alteration zonation pattern but so far has not been demonstrated to extend to the surface.

The Superior East porphyry Cu-Mo deposit is also significant (900 Mt @ 0.9% Cu; Table 4.1). It has

been emplaced deeper in the stratigraphy and preserves fewer shallow level epithermal features, leading some to propose it represents a deeper dislocated part of the Resolution deposit (Maher, 2008). It too is deeply buried under ~2 km of post-mineralisation cover, making it uneconomic at this time (Figure 4.1).

The historically important Magma mine contains small but high grade, high to intermediate sulfidation style vein, manto and skarn mineralisation. Alteration is spatially restricted around the ore bodies and the relationship to Resolution is unknown, despite its proximity (Figure 4.1). The zonation of Zn - Pb ore at higher elevations and a progression of increasing sulfidation state Cu-sulfide minerals at depth and to the west have led some authors (e.g., Maher, 2008) to believe a porphyry source may exist at depth and/or in the hangingwall of the Concentrator Fault (Figure 4.8).

The First and Second south veins are hosted within the Kvs, occupying an intermediate position between Resolution and Magma (Figure 4.1). They share similar ore and alteration mineralogy but are within the propylitic envelope of Resolution and demonstrate a decrease in grade and continuity away from Resolution, implying a strong genetic link.

The Silver King deposit was discovered in 1875 and was historically one of the most important producers of high grade silver in the US. The ore occurs as a stockwork-breccia zone, with the sulfides occupying central seams of comb quartz veins and as minor disseminations in the sericite-altered dacite porphyry wall rock. Argentiferous tetrahedrite was the main hypogene ore mineral, upgraded to stromeyerite and native silver via supergene processes to produce the direct shipping ore. The alteration zonation around the epithermal Silver King deposit and occurence of Cu-sulfides at depth, suggests it is part of a separate magmatic-hydrothermal system to Resolution, and may have a distinct porphyry-style mineralised source. Although the host rocks have been dated (Chapter 3, Hehnke et al., 2012), the absolute age of the alteration and/or mineralisation remains unknown.

Oxidised epithermal veins (e.g., Belmont) and mantos (Lake Superior and Arizona) vary somewhat in geometry and grade but occur throughout the district (Figure 4.1). Their widespread occurence is potentially useful for geochemical vectoring to a porphyry source.

# Chapter 5: Proterozoic Igneous Geochemistry

## 5.1 Introduction

This chapter reports the results of whole-rock geochemical analyses of least-altered Proterozoic mafic igneous rocks from the Superior district, Arizona. A complete multi-element dataset is presented for dolerite and basalt samples from a single crustal terrane allowing the evaluation of source regions, and determination of what fractionation, crustal contamination, and/or shallow level assimilation processes were important for petrogenesis. The data are used to constrain igneous petrogenesis during the Mesoproterozoic and investigate likely tectonic drivers for the widespread mafic magmatism. This geochemical appraisal of the least-altered Proterozoic mafic rocks is required to help understand the host rocks to propylitic alteration and to provide context for interpretations made from mineral chemistry data presented in Chapter 8.

## 5.2 Previous work

Proterozoic dolerites and to a lesser extent the basaltic lavas and sills of the southwestern United States have been intensively studied petrographically (e.g., Wrucke, 1966, Shride, 1967; Nehru and Prinz, 1970; Smith, 1970), geochronologically (e.g., Bright et al., 2014 and references therein) and geochemically (e.g., Fouts, 1974; Smith and Silver 1975; Schofield, 1976; Pearce, 1980; Hammond, 1983, 1986, 1990; Hammond and Wooden, 1990; Bright et al., 2014). Numerous local studies contain geochemical data for individual sills, localities or districts (e.g., Smith and Silver, 1975; Schofield, 1976; Pearce, 1980; Hammond, 1983, 1986). Some regional-scale studies have provided whole-rock geochemical (e.g., Fouts, 1974; Hammond, 1990) and radiogenic isotope data (Hammond, 1991; Bright et al., 2014) for the wider province, highlighting the existence of two geochemically distinct compositions. Groupings in P/Zr data, provided by Hammond (1990), are also evident in Sm-Nd and Rb-Sr isotope systematics (Hammond and Wooden, 1990). Samples with low P/Zr data generally show lower $_{\varepsilon}$Nd values (+2.1 to -0.8) and a higher average initial Sr values (0.7045), whereas high P/Zr samples generally show a lower $_{\varepsilon}$Nd range (+3.5 to +4.5) and lower average initial Sr values (0.7035). These results were reproduced by Bright et al. (2014) with a smaller dataset. Although the whole-rock geochemical and Rb-Sr and Sm-Nd isotopic groups are not geographically distinct and coexist over a wide aerial extent, Pb isotopic data, also

collected by Hammond and Wooden (1990), show regionally coherent compositions. The variability in dolerite sills of the southwest US has therefore been interpreted as a function of olivine and plagioclase fractionation of two similar parental melts derived from a fairly homogeneous but regional extensive mantle source that retained provincial mantle Pb signatures, emplaced during a period of limited intra-plate extension (Hammond, 1990; Hammond and Wooden, 1990). Later studies demonstrated the coeval timing between mafic magmatism in the southwest US and the Keweenawan magmatism in Superior Province and that they might both be related to the same mantle plume event (Bright et al., 2014). Unfortunately, these previous studies did not present corresponding whole-rock and isotopic data and/or have limited trace element data, making it impossible to fully evaluate these interpretations. In this study, new geochemical data is presented to re-evaluate source material and the degree to which the dolerite magma has undergone fractionation, crustal contamination and/or assimilation.

## 5.3 Methods

Samples for whole-rock geochemical analysis were submitted to ALS in Perth, Australia, by Rio Tinto Exploration. In 2015, all samples other than those destined for propylitic mineral chemistry by LA- ICP-MS were submitted for four acid digest, an ICP-MS method that does not include $SiO_2$ (ME-MS61; ALS fees and services schedule, 2015), whereas the samples destined for mineral chemistry were analysed using a complete characterisation package (CCP-PKG), including major elements by XRF, trace elements by ICP-MS, and total carbon and sulfur by Leco furnace. In 2016, all elements were analysed using the complete characterisation method. Major elements were recalculated to 100% anhydrous. However, owing to a limited number of samples lacking $SiO_2$ data due to the aforementioned discrepancy in analytical method, some samples do not appear in plots with recalculated major element data.

Screening to determine the level of alteration in each sample was conducted by visually inspecting hand-samples and thin-sections, and was assisted by feldspar staining where appropriate. Thin sections were prepared at the Earth Sciences lapidary facility, University of Tasmania, Australia, and petrography was conducted using a Nikon Labophot-2 Pol standard polarizing microscope featuring an Olympus ColorView imaging system.

### 5.3.1 Hydrothermal alteration effects

Many samples collected during fieldwork for the current study were primarily collected for the purposes of assessing propylitic mineral chemistry. Consequently, all samples presented in this chapter show at least a weak degree of hydrothermal alteration. The effects of hydrothermal alteration on whole-rock geochemical compositions have therefore been assessed using a combination of petrography, bivariate and multivariate geochemical plots (Figure 5.1). Least-altered compositions are defined by a combination of visual observation, petrography and geochemical alteration indices presented in Figure 5.1.

Loss on ignition (LOI) can be used as a proxy for the degree of hydrothermal alteration (hydration

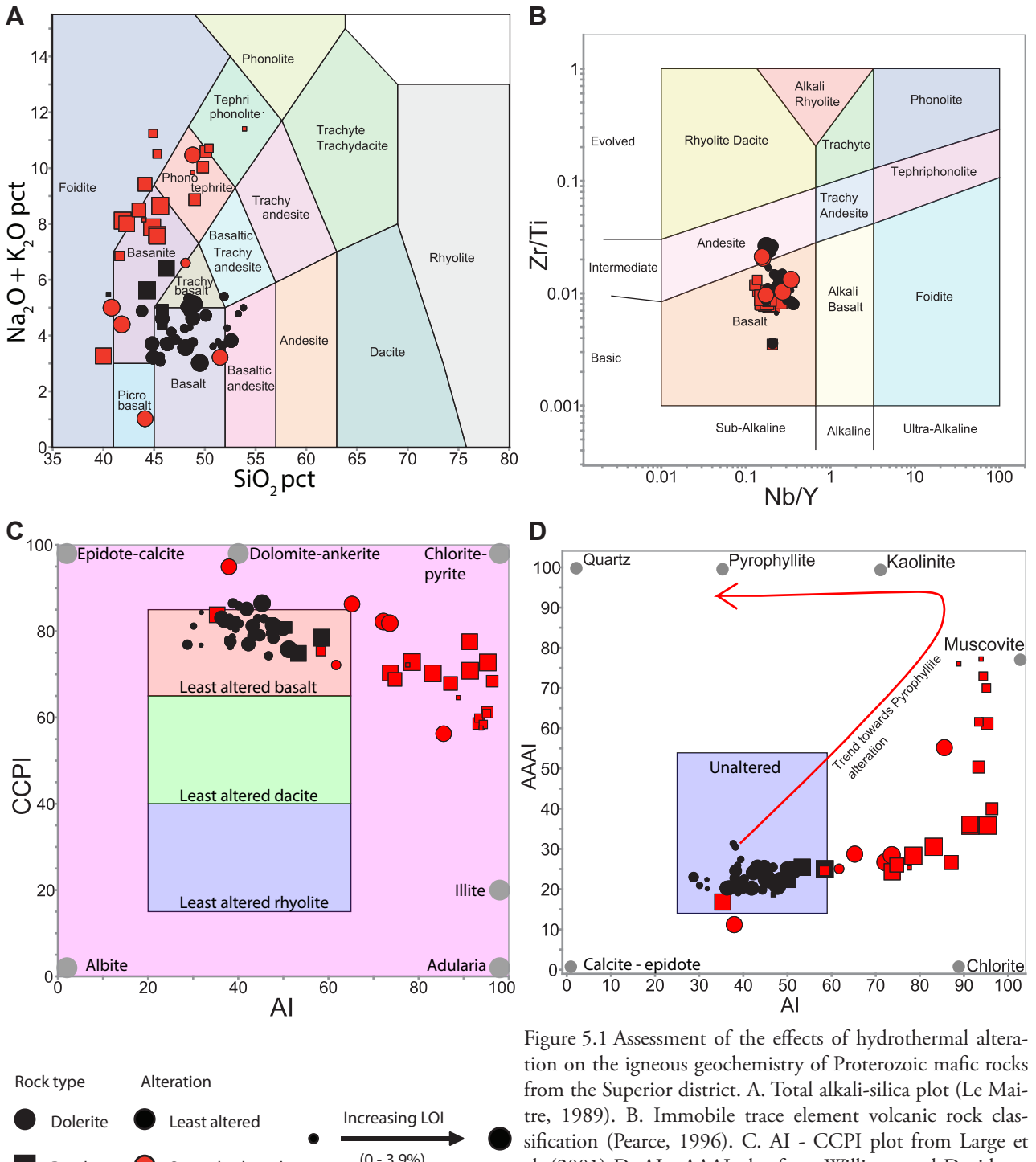


Figure 5.1 Assessment of the effects of hydrothermal alteration on the igneous geochemistry of Proterozoic mafic rocks from the Superior district. A. Total alkali-silica plot (Le Maitre, 1989). B. Immobile trace element volcanic rock classification (Pearce, 1996). C. Al - CCPI plot from Large et al. (2001) D. Al - AAAI plot from Williams and Davidson, (2004) showing the high LOI samples trending towards muscovite-illite fields. All data listed in Appendix 1A.

and/or carbonate alteration of mafic minerals) in a sample (Lechler and Desilets, 1987). In general, the higher the LOI, the stronger the effects of alteration and/or weathering. In order to screen samples for the effects of alteration, samples were plotted on a mobile-element total alkali–silica diagram (Le Maitre, 1989; Figure 5.1A) and an alteration box plot diagram (Large et al., 2001; Figure 5.1B) with symbol sizes scaled based on LOI. Dolerite samples tend to plot in the basalt field of Le Maitre (1989), however samples with high LOI (>4%) are scattered away from the centre of the least-altered (<4% LOI) cluster

Table 5.1 Average least-altered major element compositions for each dolerite lithotype and Apache Basalt. All data provided in Appendix 1B.

| Major oxide (%) | Type 1 | Type 1a | Type 2 | Type 2a | Apache Basalt |
|---|---|---|---|---|---|
| $SiO_2$ | 46.7 | 48.0 | 50.5 | 53.1 | 44.5 |
| $Al_2O_3$ | 15.4 | 12.2 | 13.8 | 12.5 | 15.3 |
| $Fe_2O_3$ | 13.7 | 15.3 | 11.0 | 14.7 | 15.3 |
| MgO | 6.04 | 4.79 | 6.29 | 3.77 | 6.58 |
| CaO | 7.56 | 8.19 | 9.00 | 6.12 | 5.97 |
| $Na_2O$ | 3.02 | 3.71 | 1.95 | 2.75 | 2.80 |
| $K_2O$ | 1.06 | 0.868 | 2.30 | 1.88 | 2.55 |
| $TiO_2$ | 2.14 | 3.83 | 1.01 | 1.75 | 2.30 |
| $P_2O_5$ | 0.404 | 0.565 | 0.138 | 0.223 | 0.316 |
| MnO | 0.213 | 0.243 | 0.260 | 0.200 | 0.236 |
| $Cr_2O_3$ | 0.0122 | 0.0138 | 0.0211 | 0.0083 | 0.0150 |
| LOI | 2.00 | 1.20 | 2.26 | 1.29 | 2.32 |
| C | 0.0469 | 0.0200 | 0.2822 | 0.0133 | 0.0460 |
| S | 0.0566 | 0.0425 | 0.0667 | 0.0150 | 0.0450 |
| Total | 98.5 | 99.0 | 98.5 | 98.3 | 98.3 |

and plot outside the least-altered field of Large et al. (2001). Basalt samples show a tendency to spread into the basanite field of Figure 5.1A, suggesting a mildly alkalic composition, with high LOI samples plotting >7% $N_2O$ + $K_2O$, indicating a strong association with LOI to alkali addition. There is also a noticeable natural break in the data points between altered and least-altered samples. Samples with > 4 wt.% LOI and/or plot outside the least-altered field of Large et al. (2001), have been excluded from investigation of primary igneous geochemistry. This approach is validated by plotting the samples on an immobile trace element rock classification (Pearce 1996; Figure 5.1B). The altered and least-altered rocks show identical trace element compositions and plot in the basalt field, suggesting that these basalts are not alkalic, but have undergone moderate alkali alteration, principally from the addition of K-feldspar, which is not a normally a major component of these rocks (Wrucke, 1966; Shride, 1967) unless in altered or fractionated examples (e.g., Smith and Silver, 1975). This observation is corroborated by the high abundance of K-feldspar that was revealed during feldspar staining (Figure 7.6 E-G).

## 5.4 Results

### 5.4.1 Major-element data

A total of 51 dolerite and 38 basalt samples were analysed for whole-rock geochemistry (Appendix 1A), 47 of these were excluded because of alteration (Figure 5.1). Distinct compositions are evident in the least-altered whole-rock geochemical data, especially in the trace element data. Table 5.1 and Table 5.2 provide average least-altered compositions of dolerite and basalt from the Superior district. A number of observations can be made regarding the average major-element compositions for the geochemically

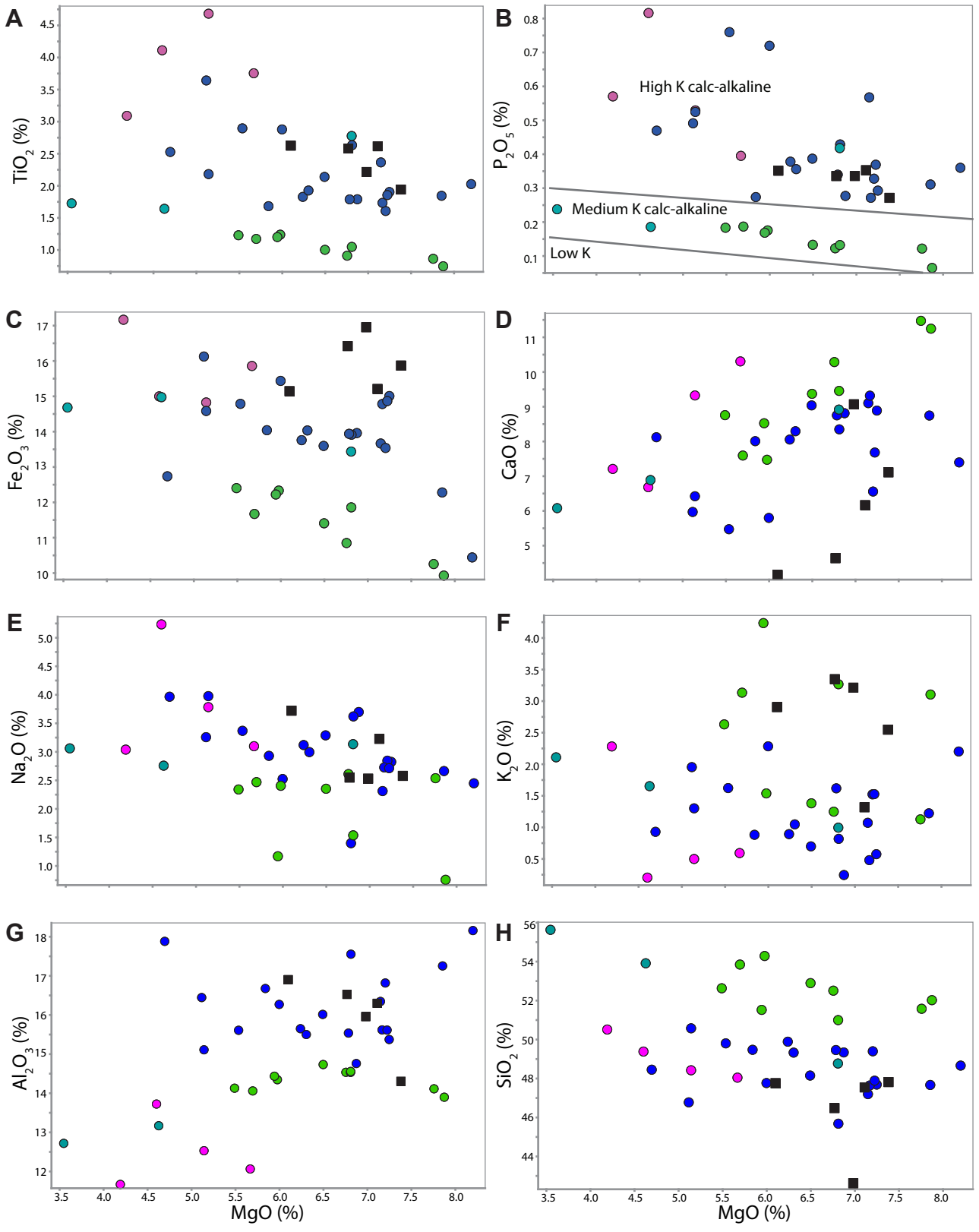


Figure 5.2 Major elements plotted against MgO for Superior district dolerite and basalt samples. Major elements recalculated to 100% anhydrous. Since some samples were not analysed for $SiO_2$, they could not be recalcuated and do not appear on the diagrams. All data listed in Appendix 1B.

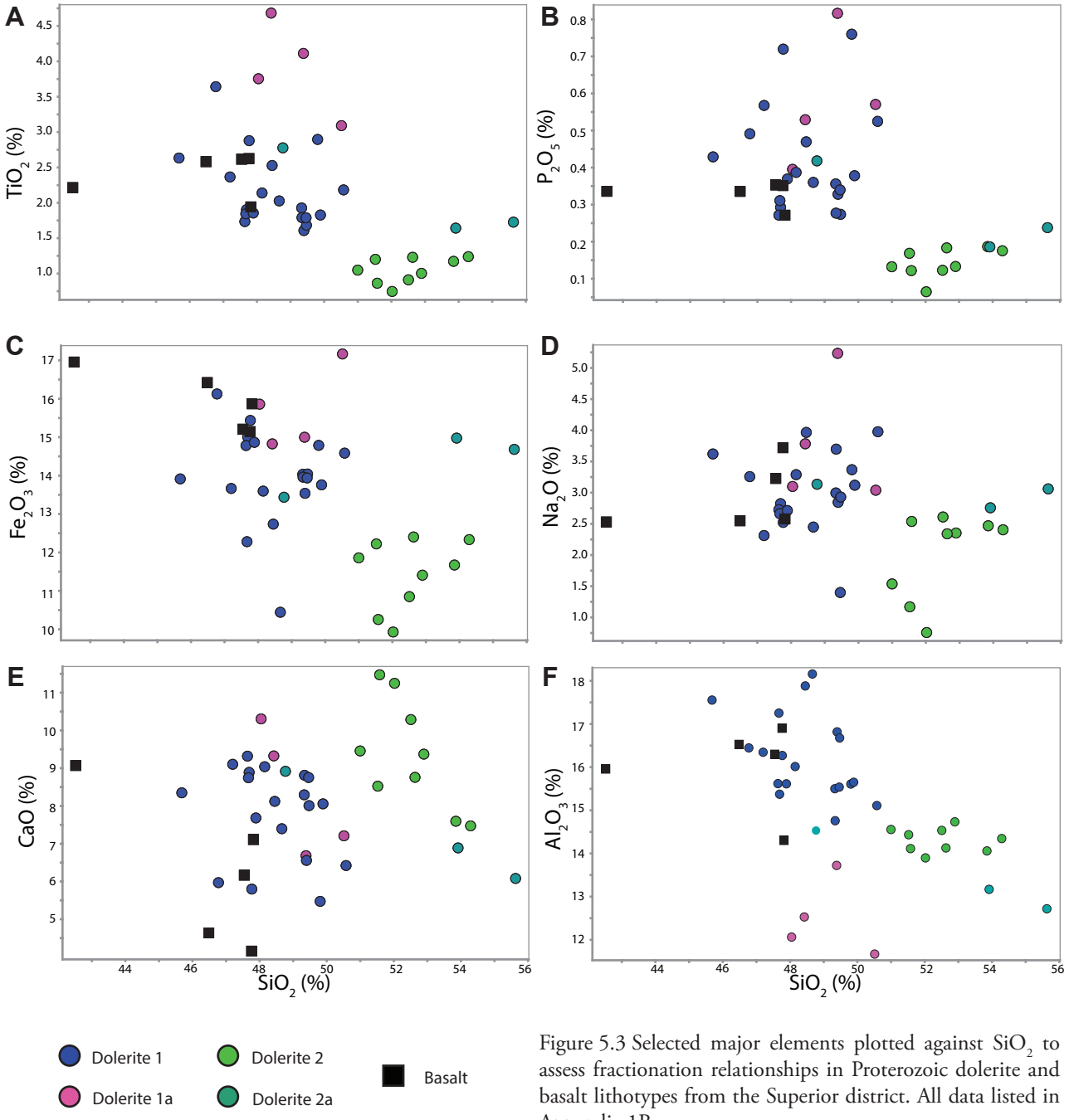


Figure 5.3 Selected major elements plotted against $SiO_2$ to assess fractionation relationships in Proterozoic dolerite and basalt lithotypes from the Superior district. All data listed in Appendix 1B.

derived lithotypes (Table 5.1).

Major element data distinguish two general compositional groups (Figure 5.2 and Figure 5.3). Figure 5.2 suggests the existence of a high Ti composition defined by dolerite 1 and 1a, and Apache basalt samples and low Ti composition defined by types 2 and 2a samples. The low Ti group also corresponds with a low $P_2O_5$, lower $Fe_2O_3$ and higher $SiO_2$ (Figure 5.2 B-CD). This compositional distinction is less clear in the alkali elements, but broadly the low $TiO_2$, $P_2O_5$, $Fe_2O_3$ and higher $SiO_2$ group tends to have higher CaO and lower $Na_2O$ and $Al_2O_3$ values than the high Ti group. The lack of correlation between the samples that plot in the high-K fields on the MgO vs $P_2O_5$ plot of Crawford et al. (2007) in Figure 5.2 B, the actual $K_2O$ values in Figure 5.2 F and the low Nb/Y values in Figure 5.1 B may suggest that

| Element (ppm) | Type 1 | Type 1a | Type 2 | Type 2a | Apache Basalt |
|---|---|---|---|---|---|
| Li | 23.2 | 17.5 | 15.6 | 22.9 | 54.0 |
| Rb | 28.2 | 18.5 | 71.7 | 71.7 | 49.9 |
| Sr | 405 | 297 | 207 | 214 | 286 |
| Ba | 416 | 376 | 412 | 445 | 467 |
| Cs | 1.71 | 0.730 | 1.65 | 1.71 | 1.99 |
| Sc | 23.7 | 42.8 | 36.1 | 34.3 | 24.2 |
| V | 247 | 444 | 251 | 385 | 224 |
| Co | 48.3 | 39.0 | 40.7 | 48.2 | 53.0 |
| Ni | 87.4 | 34.5 | 57.3 | 31.7 | 105 |
| Cu | 52.5 | 49.0 | 106.3 | 121.7 | 183.4 |
| Zn | 137 | 130 | 293 | 129 | 129 |
| Ge | 2.38 | 2.50 | 2.50 | 1.56 | 2.50 |
| As | 2.04 | 2.53 | 1.02 | 4.98 | 3.38 |
| Se | 0.679 | 0.750 | 0.444 | 1.060 | 0.600 |
| Cd | 0.271 | 0.250 | 0.928 | 0.228 | 0.250 |
| Hg | 2.40 | 5.88 | 1.95 | 2.20 | 4.10 |
| In | 0.0386 | 0.0380 | 0.0454 | 0.0602 | 0.0406 |
| Sn | 1.23 | 1.75 | 1.56 | 1.94 | 1.20 |
| Sb | 0.110 | 0.123 | 0.174 | 0.260 | 0.152 |
| Te | 0.0237 | 0.0250 | 0.139 | 0.0480 | 0.0960 |
| Tl | 0.214 | 0.250 | 0.196 | 0.246 | 0.226 |
| Pb | 26.2 | 18.5 | 33.7 | 17.2 | 6.4 |
| Bi | 0.0684 | 0.123 | 0.146 | 0.292 | 0.100 |
| Mo | 1.02 | 1.50 | 1.00 | 1.03 | 0.800 |
| W | 1.01 | 0.750 | 3.06 | 0.980 | 0.900 |
| Nb | 8.71 | 13.1 | 5.61 | 7.78 | 5.74 |
| Ta | 0.514 | 0.850 | 0.344 | 0.540 | 0.440 |
| Zr | 143 | 229 | 146 | 159 | 127 |
| Hf | 3.76 | 6.00 | 3.80 | 4.44 | 3.54 |
| Th | 1.48 | 2.27 | 3.39 | 5.74 | 0.730 |
| U | 0.379 | 0.793 | 0.969 | 1.35 | 0.522 |
| Y | 31.4 | 47.2 | 32.1 | 43.6 | 31.6 |
| La | 17.7 | 21.6 | 15.4 | 22.5 | 9.9 |
| Ce | 41.3 | 53.9 | 34.6 | 51.0 | 25.1 |
| Pr | 5.36 | 7.38 | 4.37 | 6.40 | 3.76 |
| Nd | 24.6 | 35.0 | 18.9 | 27.2 | 18.2 |
| Sm | 5.90 | 8.78 | 4.69 | 6.56 | 5.12 |
| Eu | 2.03 | 2.84 | 1.31 | 1.74 | 1.95 |
| Gd | 6.33 | 9.57 | 5.33 | 7.27 | 5.97 |
| Tb | 0.954 | 1.47 | 0.898 | 1.25 | 0.956 |
| Dy | 5.80 | 9.06 | 5.69 | 8.09 | 5.96 |
| Ho | 1.15 | 1.76 | 1.18 | 1.67 | 1.21 |
| Er | 3.27 | 5.03 | 3.46 | 4.74 | 3.49 |
| Tm | 0.463 | 0.713 | 0.526 | 0.697 | 0.498 |
| Yb | 2.93 | 4.74 | 3.34 | 4.52 | 3.16 |
| Lu | 0.442 | 0.708 | 0.531 | 0.700 | 0.486 |
| Ag | 0.253 | 0.250 | 0.311 | 0.272 | 0.250 |
| Au | 0.0008 | 0.0008 | 0.0042 | 0.0014 | 0.0026 |
| Pt | 0.0003 | 0.0003 | 0.0060 | 0.0003 | 0.0007 |
| Pd | 0.0006 | 0.0006 | 0.0077 | 0.0005 | 0.0017 |
| Re | 0.0009 | 0.0009 | 0.0009 | 0.0009 | 0.0010 |

Table 5.2 (opposite) Average least-altered trace element compositions for the different dolerite lithotypes and Apache Basalt. The complete dataset is provided in Appendix 1B.

the $K_2O$ - $P_2O_5$ relationship is different in this dataset to the arc magmas used in the creation of the field boundaries in Crawford et al. (2007). Generally, decreasing MgO values tend to correspond to increasing $TiO_2$, $P_2O_5$ and $Fe_2O_3$, $Na_2O$, $SiO_2$and decreasing CaO, although these trends are better developed in the low Ti types 2 and 2a. In general types 1a and 2a plot at lower MgO values than types 1 and 2 respectively perhaps suggesting they are slightly more fractionated equivalents. The general lack of any linear trend with MgO (Figure 5.2) and $SiO_2$ (Figure 5.3) for types 1, 1a and the Apache Basalt suggests that these suites have undergone limited fractionation. In contrast, low Ti types 2 and 2a show consistent trends of increasing $TiO_2$, $P_2O_5$, $Fe_2O_3$, $Na_2O$ and $K_2O$ and decreasing CaO and $Al_2O_3$ with increasing $SiO_2$ (Figure 5.3 A-G).

Significant deviation from the observed fractionation trends in Figure 5.3 D-E may support minor mobility of $Na_2O$ and CaO during later hydrothermal alteration. Comparatively, Apache Basalt samples and dolerite types 1 and 1a show very little correlation between major elements and $SiO_2$.

### 5.4.2 Trace element data

Trace element data from the Superior district is presented in Table 5.2 and Figure 5.4 to Figure 5.9. Trace- element data more effectively delineate distinct compositions within the dolerite, and better highlights additional sub-types 1a and 2a from the major lithotypes types 1 and 2. Average compositions for these groups are presented in Table 5.2. The low Ti groups also have low Ti/V, Ti/Nb, values (Figure 5.4), distinct MgO/Ni, MgO/Cr and Cu values and is enriched in Pt and Pd compared to other suites (Figure 5.5). The dolerite sub-types have significantly different Sc/Fe and Gd/Yb values compared to their corresponding major lithotype partner composition (Figure 5.6). Relative to primitive mantle compositions, low Ti group show significant enrichment in Th, depletion in Nb and strong negative Sr and Ti anomalies while types 2 and 2a show opposite Sr and Ti anomalies (Figure 5.7). Typically the Apache Basalt plots with the high Ti group, but shows a much flatter REE profile (Figure 5.7).

## 5.5 Discussion

Previous geochronology work conducted on the dolerite sills of the southwestern USA indicate that these rocks were emplaced between 1,110 and 1,075 Ma (Bright et al., 2014 and references therein). This observation has led some to correlate the major dolerite emplacement event in the southwestern US with the igneous suites of Midcontinent rift (Bright et al., 2014), which are widely interpreted as the result of mantle plume style magmatism (e.g., Hutchinson et al., 1990; Nicholson and Shirey, 1990). This section addresses how the dolerite samples from the Superior district fit into previous petrogenetic interpretations for the southwestern US, the petrogenetic relationship with earlier mafic magmatism (the Apache Basalt) and the degree to which their geochemistry reflects that of the Midcontinent rift,

and by association, a mantle plume-related source.

Generally, the two broad compositional groups are highlighted in the major element data that have been presented in previous studies of the southwestern US dolerite sills (e.g., Fouts, 1974; Hammond, 1983, 1990; Bright et al., 2014). There is additional complexity as demonstrated by the subtypes highlighted in the trace element data (Table 5.2, Figure 5.4, Figure 5.5 and Figure 5.6) that may indicate more fundamental differences in source type and that fractionation-contamination processes have affected these rocks more extensively than previously identified.

### 5.5.1 Redox and the role of water

The relationships between Ti and V and can be used to test for changes in redox because V becomes significantly less compatible under more oxidising conditions (Shervais, 1982, Pearce, 2014). The $TiO_2$/V relationship is distinct between the major lithotypes (i.e. types 1, 1a and 2, 2a) suggesting that processes affecting redox state may be important in producing the variable dolerite compositions of the Superior district (Figure 5.4 A). Generally, more oxidising conditions during mantle melting result from the addition of water (Pearce, 2008, 2014). Although this process is more common at subduction zones (Pearce, 2014) there is evidence that crystalline continental crust can contain significant quantities of water (Kozlovsky, 1984; Bailey, 1990; Wenzel and Sandmeier, 1992; Stevens, 1997). Although there remains a possibility that this water may be derived from the delaminated slab of the preceding Grenville Orogeny, the absence of any geologic evidence for emplacement of these dolerite sills at a continental margin suggests that dolerite types 2 and 2a interacted with or was contaminated by significant volumes of water-rich mid - lower crust or were partly sourced from partial melting such material. Indeed the crust of the Mazatzal Terrane is largely composed of juvenile island-, and subsequently continental arc material (Chapter 2) and would therefore provide a plausible explanation for a subduction-like signature from dolerite sills emplaced in continental crust.

### 5.5.2 Fractionation

Fractionation trends of inversely related $SiO_2$ and MgO are evident in the type 2 and 2a dolerite in major element chemistry (Figure 5.3) suggesting this major lithotype experienced some degree of fractionation whereas the absence of these trends in types 1, 1a and the Apache Basalt types suggest fractionation was limited in the latter lithotypes. The higher $SiO_2$ values associated with type 2a compared to type 2, suggest it may be a slightly more fractionated equivalent of type 2. This interpretation is supported by $TiO_2$/Nb ratios (Figure 5.4 B) which can also be also used to test for fractionation, and to some degree oxidation, by tracking the increasing substitution of less compatible Nb into Ti-bearing phases like rutile in more fractionated magmas (Green and Pearson, 1987; Schmidt et al., 2004). Higher overall Nb values can also be indicative of reduced magmas where rutile and ilmenite are readily available for Nb substitution, whereas lower Nb values may be more typical of more oxidised magmas where

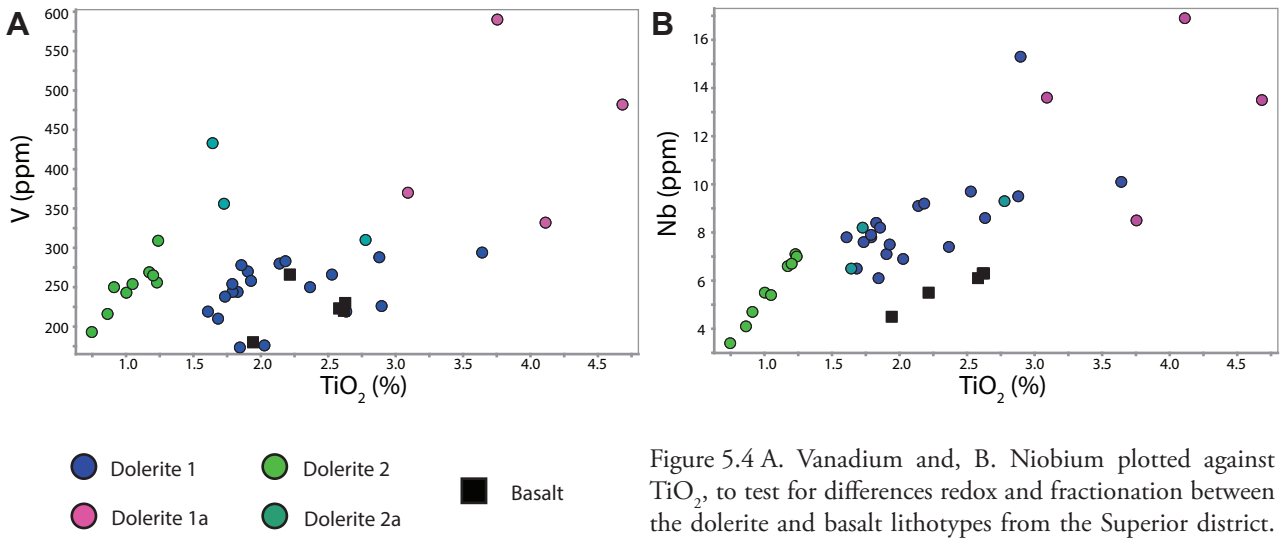


Figure 5.4 A. Vanadium and, B. Niobium plotted against $TiO_2$, to test for differences redox and fractionation between the dolerite and basalt lithotypes from the Superior district. All data listed in Appendix 1B.

there is less availability for substitution into ilmenite and rutile. This may therefore act as a corollary to interpretation of $TiO_2$/V ratios in Figure 5.4 A. The Apache Basalt samples show the highest $TiO_2$/Nb ratios (i.e. least fractionated), followed by a broad field containing types 1, 1a and 2a, with type 2 showing the lowest $TiO_2$/Nb ratio and therefore likely the most fractionated samples (Figure 5.4 B). Additionally Type 2 samples have generally lower Nb concentrations than other dolerite types (Figure 5.4 B), possibly supporting slightly more oxidising conditions as a result of interaction with water-rich crustal material as indicated by lower $TiO_2$/V ratios (Figure 5.4 A).

### 5.5.3 Metal budget and S saturation

Figure 5.5 compares the metal budgets of the basalt and dolerite lithotypes, plotted against MgO. Broadly MgO, Cr and Ni show a positive relationship probably related to Ni and Cr substitution for Mg in clinopyroxene and olivine, and subsequent fractional crystallisation (Mysen, 1979; Nabelek, 1980; Drake and Holloway, 1981; Figure 5.5). Types 2 and 2a define a higher MgO/Ni relationship than types 1 and 1a, probably related to either, lower Ni concentrations in the type 2 and 2a primary melt or substitution of Ni into another mineral, or a combination thereof. Apache Basalt samples tend to show high MgO and Ni values and span both groups (Figure 5.5 A). MgO/Cr appears indistinct between lithotypes (Figure 5.5 B). Types 2 and 2a tend, on average, to have higher Cu values than the remaining samples, and show a weak inverse relationship with MgO, possibly suggesting fractionation served to weakly concentrate Cu (Figure 5.5 C). The lower Cu values in types 1 and 1a may be the result of depletion, or simply a difference in initial Cu concentrations in the primary melt.

An intriguing aspect of the dolerite trace element geochemistry is the conspicuous enrichment in platinum and palladium in type 2 dolerites (Figure 5.5 D). Apache Basalt samples have concentrations of around 5 – 15 ppb Pt and Pd, which is considered a background level (Keays and Lightfoot, 2015) whereas dolerite types 1, 1a and 2a show below detection limit values for platinum group elements

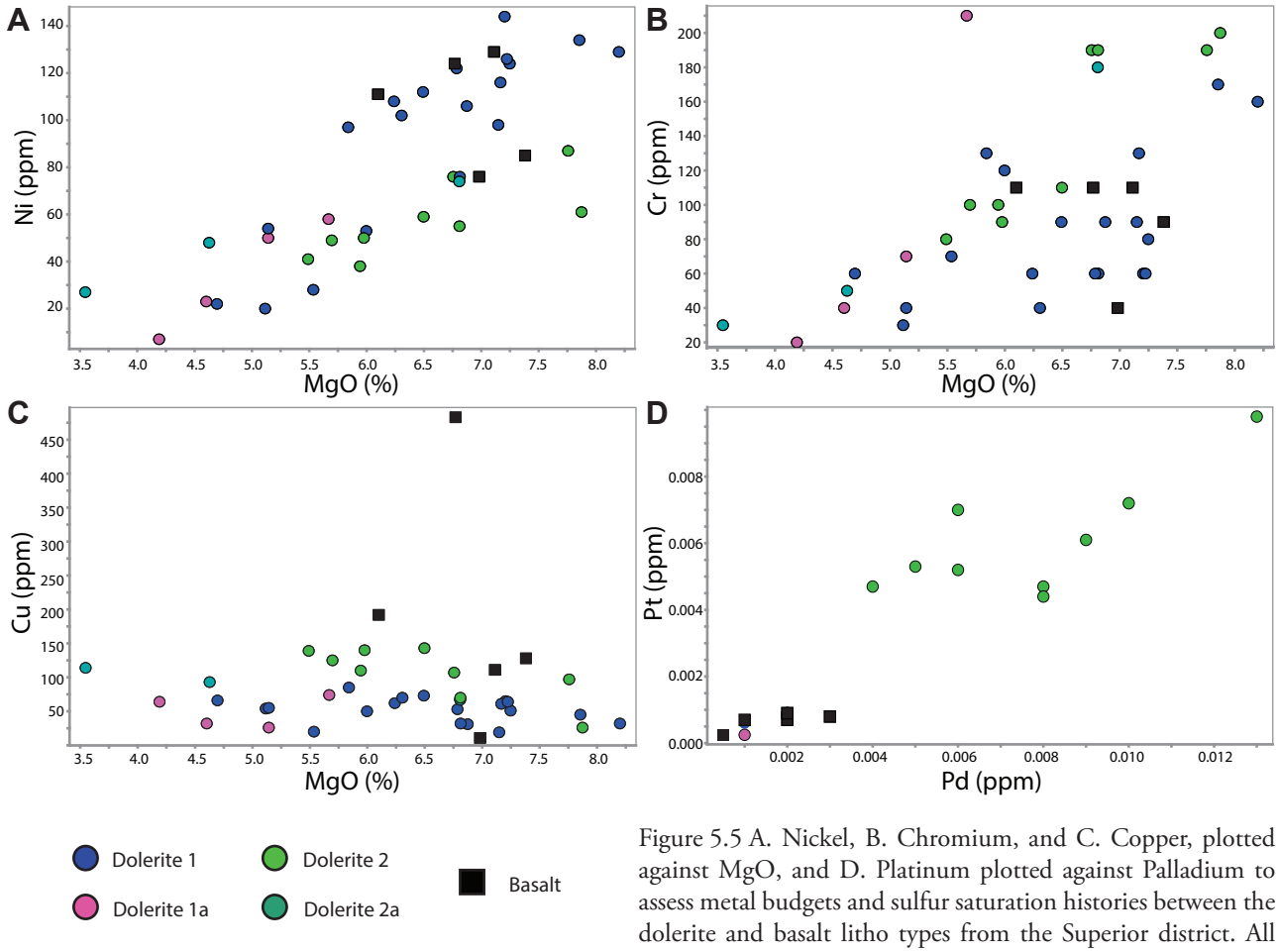


Figure 5.5 A. Nickel, B. Chromium, and C. Copper, plotted against MgO, and D. Platinum plotted against Palladium to assess metal budgets and sulfur saturation histories between the dolerite and basalt litho types from the Superior district. All data listed in Appendix 1B.

(PGEs), indicative of early S-saturation and removal of sulfide liquid. Type 2 dolerite shows anomalously high levels of Pt and Pd and at their upper limits return values over 20 ppb combined Pt + Pd (Figure 5.5 D). The PGE enrichment suggests that Type 2 dolerite did not undergo early-stage sulfur saturation and removal of immiscible sulfide, as indicated by type 1 and 1a. The sulfur saturation process can be inhibited by crustal contamination, which supresses the formation of an immiscible liquid (Ardnt et al., 2005). Not only is this petrogenetically significant but potentially highlights an exploration target, if this lithology interacted with local crustal sulfur to concentrate PGEs somewhere in the region.

### 5.5.4 Sources - the possible role of garnet

Scandium in type 2 dolerite shows significant departure from the otherwise systematic positive relationship with $Fe_2O_3$ (Figure 5.6 A) where Sc substitutes for Fe and Mg into silicates (Halley et al., 2016). This may suggest some involvement of garnet-bearing material with which Sc, and heavy rare earth elements (HREE), have a high partition coefficient (Arth, 1976; Irving and Frey, 1978). Since deep OIB-type mantle sources typically stabilise garnet and retain HREE during partial melting, Gd/Yb values have been used to evaluate the contribution of such a source, and therefore infer relative depth (e.g., Hollings et al., 2007, 2010). Figure 5.6 B shows Gd/Yb plotted against Sc/Fe, with high Gd/Yb

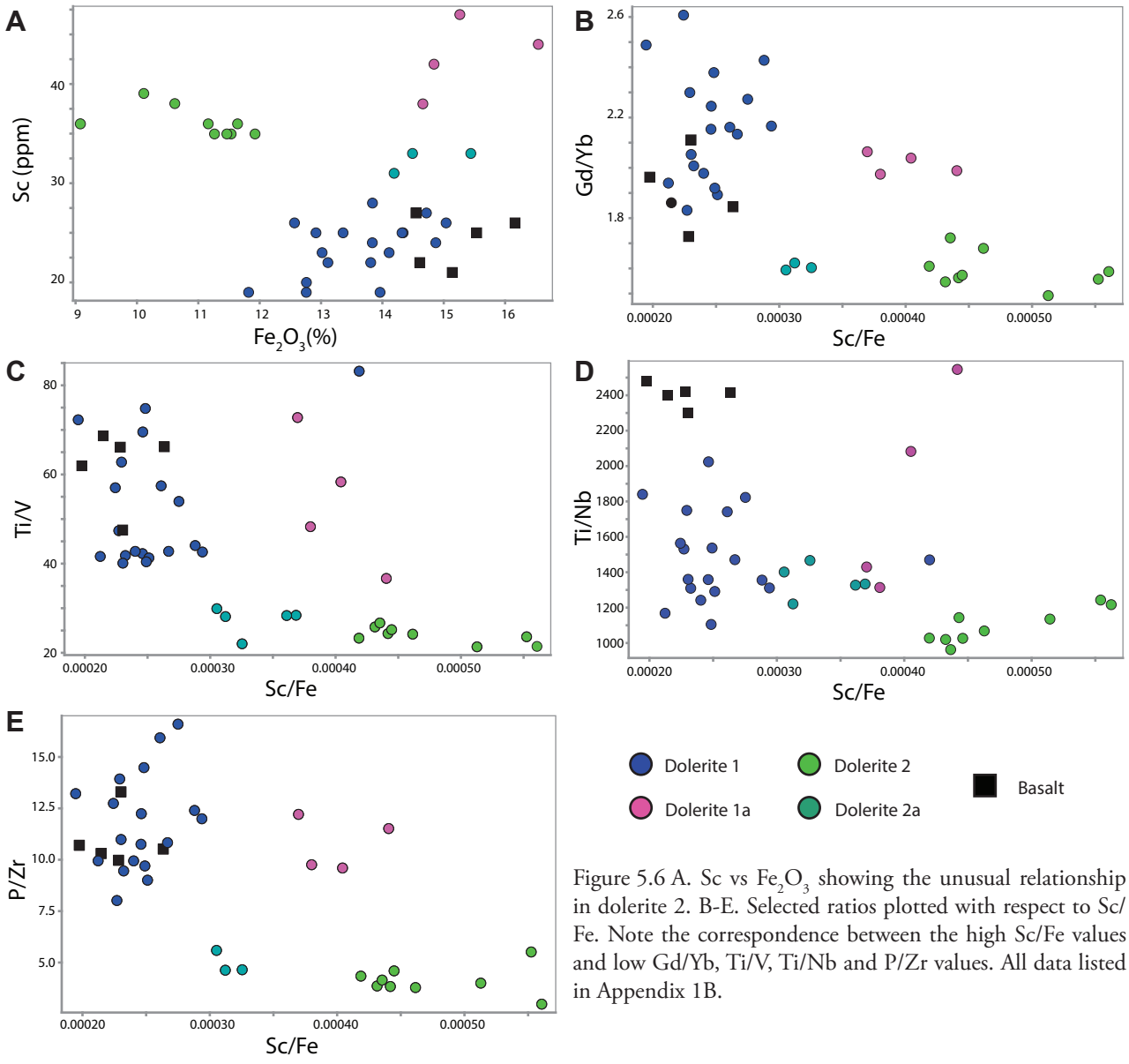


Figure 5.6 A. Sc vs $Fe_2O_3$ showing the unusual relationship in dolerite 2. B-E. Selected ratios plotted with respect to Sc/Fe. Note the correspondence between the high Sc/Fe values and low Gd/Yb, Ti/V, Ti/Nb and P/Zr values. All data listed in Appendix 1B.

values suggesting greater HREE depletion a therefore a slightly deeper source regions for types 1 and 1a, compared to 2 and 2a. Interestingly lower Gd/Yb values (higher HREE) correspond to high Sc/Fe values, suggesting that the type 2 source material or contaminant was slightly enriched in HREE and Sc. This higher HREE/MREE and high Sc/Fe could be interpreted as the signature for incorporation of crustal garnets, which have high partition coefficients for both HREE and Sc (Arth, 1976; Irving and Frey, 1978, in Rollinson, 1993). In the case of types 2 and 2a it seems more likely that the garnet-bearing material was assimilated after melt formation, in contrast to type 1 where the low HREE content suggests the garnets were retained during partial melting. Since the Pinal Schist forms the basement across a large area of the SWUS, it remains plausible that significant garnet occurs at mid- to lower crustal levels, and that this material was involved in the contamination of type 2 dolerite. Shallower and/or contaminated type 2 (high Sc/Fe, low Gd/Yb values; Figure 5.6 B) tend to also correspond to slightly higher oxidation, (lower $TiO_2$/V; Figure 5.6 C), and greater degrees of fractionation (lower

$TiO_2$/Nb values; Figure 5.6 D). Although cause and effect relationships are speculative, it is possible that contamination by metasedimentary, relatively water rich lower crustal material drove the type 2 melt to more oxidising conditions, and its higher $SiO_2$ content may have promoted, or been caused by, stalling and fractionation in the mid crust.

The correspondence of P/Zr values (Figure 5.6 E) to patterns in Gd/Yb, $TiO_2$/V and to some extent $TiO_2$/Nb suggest P/Zr values are also reflecting the same fractionation, contamination and redox processes and source signatures inferred from these ratios (Figure 5.6 B - D). Additionally, the two major compositional groupings are similar to those initially identified by Hammond (1990), though the actual ranges for each group are different (Hammonds 'Group A'; P/Zr = 0.006 - 0.010 and 'Group B'; P/Zr = 0.001 - 0.005) possibly due incomplete digestion of resistate minerals in the Hammond (1990) study.

### 5.5.5 Normalised trace element profiles

The median and upper and lower quartiles of compositional groups from the Superior district are plotted as a spider diagram, normalised to the primitive mantle values of McDonough and Sun (1995; Figure 5.7 A). Apache basalts have somewhat flat profiles, but show weakly negative Th and Nb-Ta anomalies with a weak positive Ti anomaly and a weakly listric heavy rare earth element (HREE) segment (Figure 4.7 A). Importantly however, Apache Basalt shows more subdued anomalies and a much flatter LREE segment (Figure 5.7 A).

All dolerite types present similar crustally contaminated (Nb-Ta and Zr-Hf depleted), but LREE enriched profiles, the latter typical of more E-MORB compositions (Sun and McDonough, 1989; McDonough and Sun, 1995). Dolerites from the Superior district lack the steep REE element profiles typical of OIB-type sources (Sun, 1980). Instead, subtle differences pertaining to the degree and type of fractionation and contamination of melts sourced from a LREE enriched mantle source intermediate in composition between MORB and OIB are evident (Figure 5.7 A).

Type 1a is distinct from type 1 demonstrated by strongly negative Sr and positive Ti anomalies not present in type 1 (Figure 5.7 A). Unusually, there is no negative Eu anomaly to accompany the negative Sr anomaly in type 1a, which would be more typical of plagioclase fractionation.

Type 2 and 2a dolerites exhibit stronger Th, Nb-Ta but weaker Zr-Hf anomalies than types 1 and 1a suggesting stronger degrees of crustal contamination (Figure 5.7 A). They also show pronounced negative Sr, Eu and Ti anomalies consistent with fractional crystallisation of plagioclase and titanomagnetite respectively, implying that types 2 and 2a spent significant time fractionating, probably in the mid crust (Pearce, 1983; Figure 5.7 A). Type 2 dolerite also has a flat to slightly upward trending HREE segment (Figure 5.7 A), again illustrating the likely role for high HREE-bearing material in the contaminant.

When plotted on a tectonic discriminantion diagram, three coherent clusters of data are evident (Figure 5.8; Pearce, 2014). Basalt samples plot in the MORB-OIB array transitional between N-MORB and

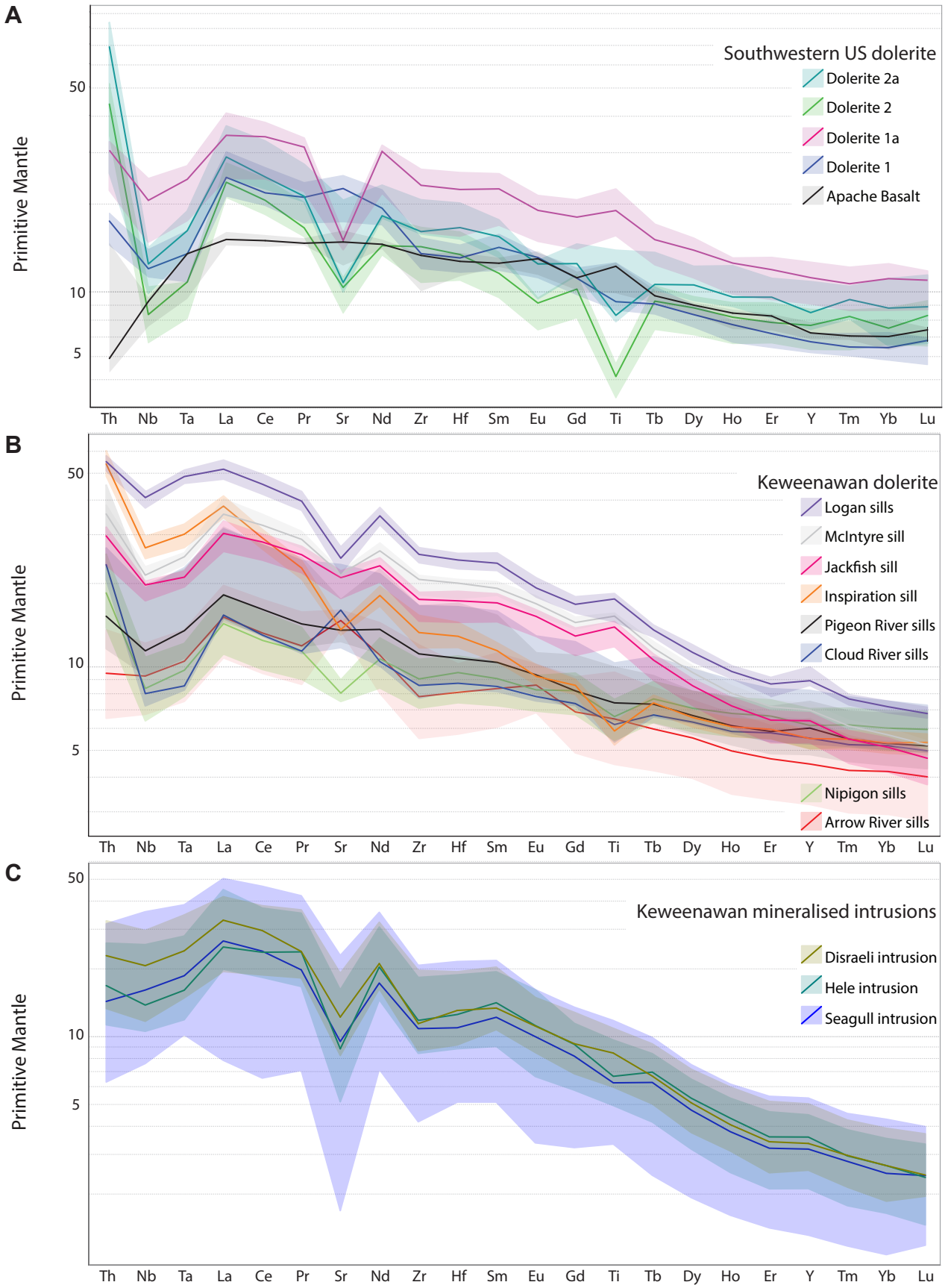


Figure 5.7 A. Normalised trace element profiles showing median compositions for, A. Superior district. B. Unmineralised dolerite sills and, C. mineralised ultramafic intrusions of the Midcontinent rift region. Shaded areas represent the upper and lower quartiles. All values are normalised to primitive mantle compositions of McDonough and Sun (1995). Data for Midcontinent rift from Cundari et al. (2013). Superior district data listed in Appendix 1B.

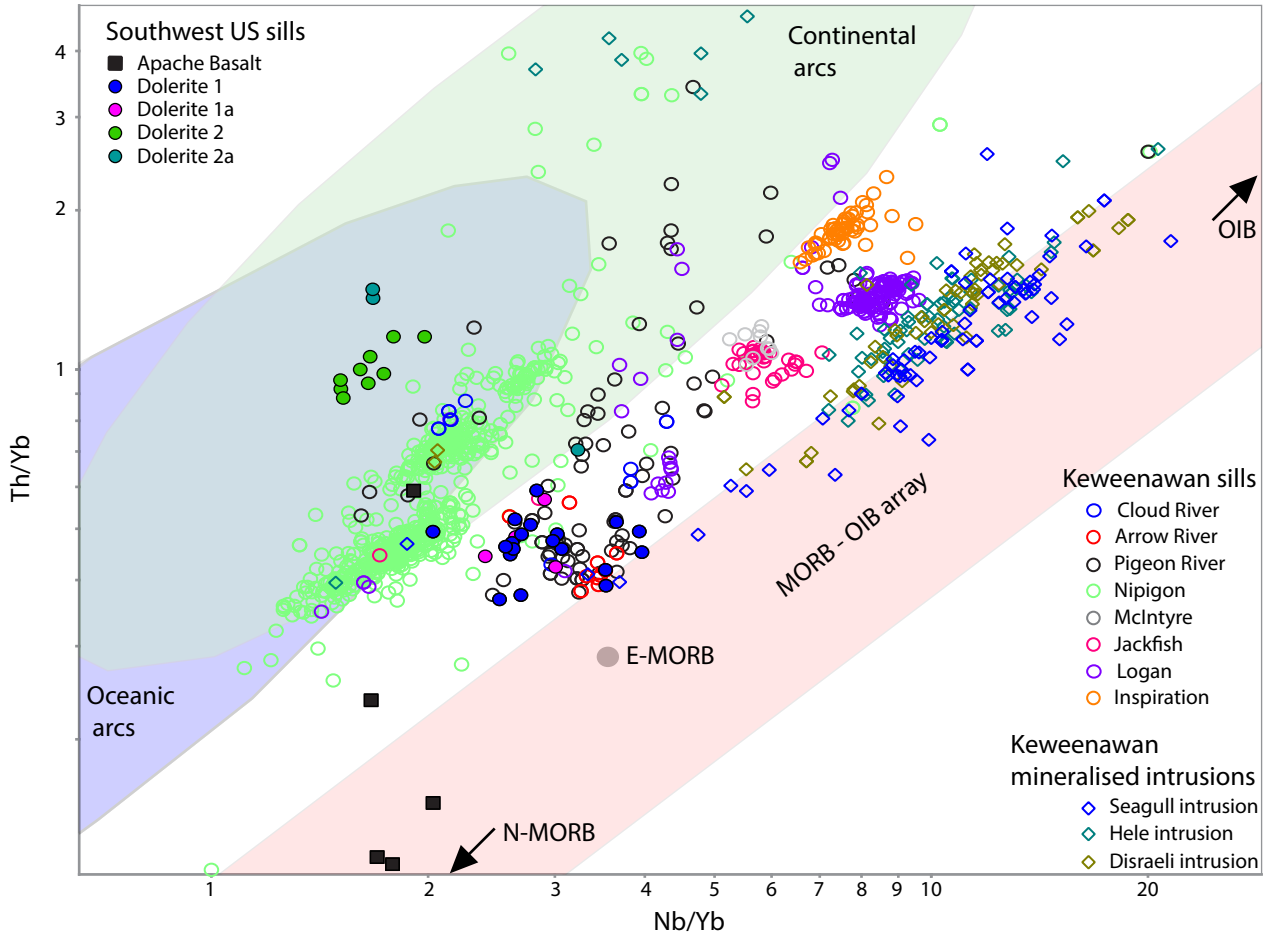


Figure 5.8 Tectonic descrimination diagram for mafic rocks of the Superior district and Midcontinent rift region. Types 1 and 1a plot close to E-MORB composition, along with the Arrow river, Pigeon river and Cloud river sill suites from the Mid-continent rift, but diplaced toward the continental arc fiel suggesting weak crustal contamination. Type 2 and 2a plot well into the contiental arc field, similar to the Nipigon sill suite from the Midcontinent rift, indicative of strong contamination. Data from Midcontinent rift from Cundari et al. (2013). Superior district data listed in Appendix 1B.

E-MORB, with a weak trend towards higher Th/Yb and lower Nb/Yb values, suggesting some parts of the basalt magma were weakly contaminated (Figure 5.8). Dolerite types 1 and 1a plot close to the MORB-OIB array, displaced from E-MORB toward a slightly higher Th/Yb ratio (Figure 5.8), supporting an enriched mantle source. Types 2 and 2a also plot close together in a field defined by overlapping continental oceanic arc domains, showing slightly higher Th/Yb and lower Nb/Yb ratios ratio compared to type 1 and 1a, that are supportive of an oxidised, strongly crustally contaminated component to these magmas (Pearce, 2014).

### 5.5.6 Comparison with the Midcontinent rift

Figure 5.7 shows the primitive mantle normalised values of dolerite sills from Superior, Arizona (Figure 5.7 A), compared to the unmineralised dolerite sills (Figure 5.7 B) and mineralised intrusive suites of the Midcontinent rift region (Figure 5.7 C; data from Cundari et al., 2013). Generally the SWUS dolerite sills are less LREE enriched, have deeper Nb-Ta anomalies and have a slightly shallower overall slope. Distinct but variable Sr and Ti anomalies are evident in both suites though rocks from the MCR

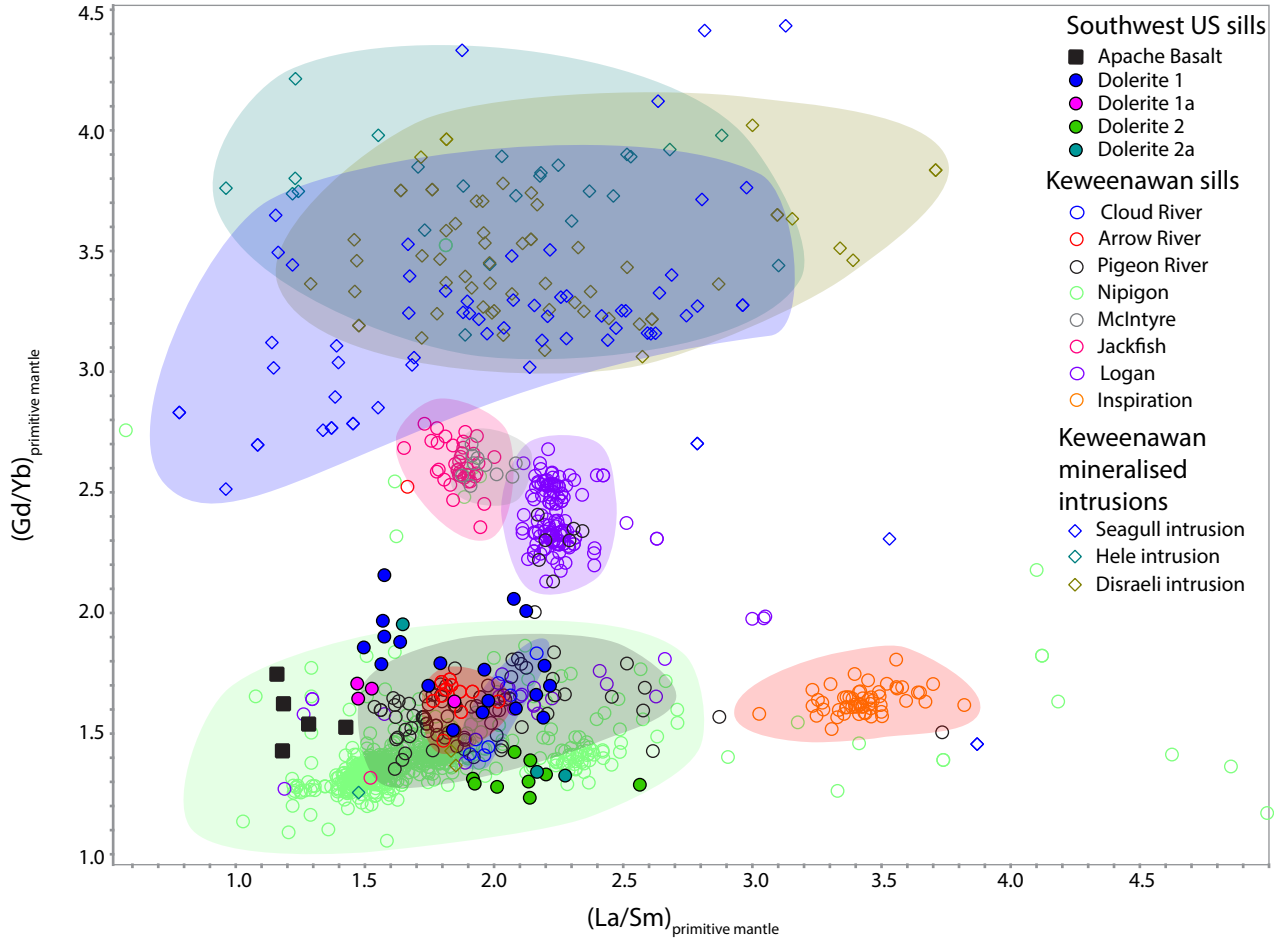


Figure 5.9 Rare earth ratio plot, normalised to primitive mantle values of McDonough and Sun (1995), showing the relative HREE depletion as a proxy for melting depth vs. and LREE enrichment as a proxy for enrichment from plume material for mafic rocks from the Superior district and suites form the Midcontinent rift region. Shaded fields highlight the main data cluster for each of the comparative Midcontinent suites. After Hollings et al. (2010). Data from Midcontinent rift from Cundari et al. (2013). Superior district data listed in Appendix 1B.

lack any significant Eu anomalies. The mineralised intrusions from the MCR are distinct in their limited evidence for any contamination, consistent and pronounced negative Sr anomaly and much more significant HREE depletion, usually interpreted as resulting from retention of HREE in a deep, garnet-stable source region (e.g., Hollings et al., 2007, 2010). Overall, Types 1 and 1a from the SWUS seem most similar to the Arrow River, Pigeon River and Cloud River suites from the MCR, while types 2 and 2a seem most similar to the Nipigon sills (Figure 5.7 Figure 5.8, Figure 5.9). This could support genetic links between the two igneous provinces.

The distinction in mineralised intrusions is further illustrated in significantly higher Nb/Yb values (OIB affinity; Figure 5.8) and higher Gd/Yb values (Figure 5.9), implying a greater garnet-stable component and therefore a greater depth of the source region. The large spread of points data from the mineralised intrusions between E-MORB and OIB suggests a mixed source region composed of both plume and upper mantle material. The unmineralised MCR dolerites are scattered but generally trend away from an intermediate OIB to E-MORB field towards the Continental arc fields, typical of crustally contaminated magmas (Figure 5.8). Interestingly Logon, Jackfish and McIntyre suites suggest intermediate source

depths consistent with their higher Nb/Yb ratios while Nipigon, Arrow River Pigeon River and Cloud River samples tend to plot at Gd/Yb and La/Sm values indicative of shallower source depths and weak LREE enrichment, along with dolerite sills and basalts from the Superior district (Figure 5.9). The Inspiration suite also appears to have sourced from relatively shallow levels, despite having a contaminated signatures but it also has much higher LREE enrichment than most other suites.

***E-MORB signature***

Although many samples plot around E-MORB compositions (Figure 5.8), there is no evidence that extension throughout the Laurentian crust progressed as far as an oceanic spreading centre or mid-ocean ridge during the Mesoproterozoic. Therefore the interpretation here is that MORB affinity in the southwestern US context really refers to subcontinental mantle. The general contamination signature is consistent with what might be expected in the early stages of continental rifting, but in the case of the Mesoproterozoic of North America, this rifting did not progress to plate separation. The enrichment signature, observed in the SWUS dolerites in particular, relates to the degree of interaction of the southwestern subcontinental mantle with the peripheral regions of the plume head that was active under the Keweenawan region. The argument for distal plume influence is based largely on the OIB affinity demonstrated by many of the suites in the MCR and the geochronological studies of the dolerite sills from the southwestern US, that indicate emplacement of these sills was contemporaneous with widespread emplacement of mafic magma in the Midcontinent rift (e.g., Bright et al., 2014 and references therein).

## 5.6 Summary of Proterozoic mafic rocks from the Superior district

This study confirms previous work that suggests there were two parental magmas that produced dolerite in the Superior district The Apache Basalt is part of a high $TiO_2$ group and shares some geochemical characteristics with type 1 dolerite in major and trace element geochemical data, including the general absence of MgO or $SiO_2$-related fractionation trends (Figure 5.2 and Figure 5.3). The Apache Basalt is the least fractionated (low $TiO_2$/Nb values, Figure 5.4 B; No Sr or Eu anomalies, Figure 5.7A), generally more reduced (High $TiO_2$/V, Figure 5.4 A), and sourced from a less LREE enriched source, intermediate in composition from 'N- to E-MORB' (subcontinental mantle) material (weak LREE enrichment; Figure 5.7 A; low Nb/Yb, Figure 5.8) at an intermediate to shallow depth (low to moderate Gd/Yb, Figure 5.9) compared to other suites. Apache Basalt samples underwent only minor crustal contamination during ascent (Low Sc/Fe, Figure 5.6; minor Nb anomaly, Figure 5.7 A; some high Th/Yb in Figure 5.8), and was probably undersaturated with respect to sulfur and therefore retained background levels of PGEs (Figure 5.5 D).

Type 1 dolerite, also part of a high $TiO_2$ group, shows evidence for moderate olivine and/or pyroxene fractionation (Figure 5.5) and ilmenite fractionation (high $TiO_2$/Nb, Figure 5.4). This lithotype is also

slightly more reduced (Figure 5.4) and sourced from enriched subcontinental mantle material (LREE enrichment, Figure 5.7; moderate Nb/Yb, Figure 5.8) from slightly greater depths than type 2 dolerite (higher Gd/Yb; Figure 5.9). Some crustal contamination is demonstrated in Figure 5.7 but low Sc/Fe suggest this contaminant was not unusually HREE rich (Figure 5.6).

Type 1a is compositionally similar to Type 1 in many respects (e.g., Figure 5.2, Figure 5.3 and Figure 5.5). However it appears to be slightly more fractionated (lower MgO values, Figure 5.2; higher $TiO_2$/Nb, Figure 5.4B; Sr anomaly, Figure 5.7 A), and contaminated (Nb-Ta, Figure 5.7 A) equivalent of the reduced, sulfur saturated, relatively deeply sourced type 1. The higher Sc/Fe ratio relative to type 1 suggests it may have interacted with some HREE and Sc rich, possibly garnet-rich contaminant.

Types 2 and 2a have distinctly different chemistry to the previous lithotypes and together define the low $TiO_2$ group that shows comparatively well-developed fractionation trends in Figure 5.2 and Figure 5.3. Type 2 dolerite is comparatively more oxidised (low $TiO_2$/V, Figure 5.4 A) more fractionated (high $SiO_2$, Figure 5.3; high $TiO_2$/Nb, Figure 5.4 B; strong Sr and Eu anomalies, Figure 5.7 A), more contaminated (strong Nb-Ta depletion, Figure 5.7 A; high Th/Yb, Figure 5.8) and more shallowly sourced (low Gd/Yb, Figure 5.9). Importantly, this lower $TiO_2$/V signature could implicate water, probably from lower crustally derived water. Together with an inferred shallower source region, this may provide evidence that dolerite 2 was partly sourced from partial melting of the lower crust in the presence of water, or that it interacted with significant volumes of that material during ascent. Perhaps most importantly, this lithotype shows a PGE enrichment of 10x background level (Figure 5.5 D), which is atypical for shallowly sourced melts (Keays and Lightfoot, 2015). This indicates the absence of early stage sulfur saturation, most likely due to the degree of contamination, which allowed PGEs to be retained. If parts of this lithotype did encounter sufficient crustal sulfur during late stages of emplacement, and the sulfide liquid was able to efficiently concentrate metals, the resulting deposit maybe high grade.

Type 2a dolerite shares many characteristics with type 2, but appears to be a more fractionated equivalent (lower MgO, higher $SiO_2$, Figure 5.2, Figure 5.3). It shares Nb-Ta contamination signatures (Figure 5.7 A), but presents lower Sc/Fe values than type 2 suggesting less of a garnet-rich contribution to contamination (Figure 5.5).

## 5.7 Exploration implications

The PGE-enriched type 2 dolerites in the Superior district were emplaced into relatively sulfur-rich country rocks, with evaporitic sulfates present in the Mescal Limestone and pyrite common in the Pioneer Shale and the Dripping Springs Quartzite (Shride, 1967; Chapter 3). Whether or not the type 2 dolerites were exposed to enough of this material to induce a late-stage sulfur saturation event that could have efficiently concentrated the PGEs remains unclear, but Wrucke (1989) reported sparse sulfides (pyrite and chalcopyrite) in some dolerite samples. The most prospective places to explore for PGE-enriched dolerites are likely to be depressions along intrusive contacts with the Mescal limestone. The

identification of a PGE-enriched dolerite is worthy of follow-up through more detailed framework studies that could spark exploration for this type of resource in the southwest. By-product PGEs were recovered from the historic Mission-Pima mine although no dolerite sills are reported from that area. There are also other, poorly documented reports of placer PGEs, commonly associated with Au, from seven other localities throughout Arizona (Peterson, 1993).

## 5.8 Conclusions

This study has provided insights into the magmatic evolution of the mafic rocks of the Superior district and enabled comparison to coeval suites of the Midcontinent rift. Two major compositional types, similar to high and low P/Zr groups identified by Hammond (1983), and two additional sub-types of dolerite identified from this geochemical dataset.

The Apache Basalt appears geochemically similar to type 1 dolerites but was derived from a slightly less enriched mantle source, possibly related to incipient interaction between upwelling plume material and typical subcontinental type mantle material below the continental crust of the SWUS.

The compositional types within the dolerite sills seem to have resulted from a fundamental difference in source depth and/or material that in turn affected the redox and fractionation processes, although cause and effect relationships cannot be determined unequivocally. Unusually the most shallowly sourced melt contains the highest background levels of PGE that may be worth investigating further as a source of mineralisation.

Although there is distinct variability in the samples from the SWUS, this variability is limited in comparison to that observed in suites from the Midcontinent rift. Here, mineralised intrusions have significantly different REE ratios and are likely to have had significant component of deep, garnet-stable OIB/plume type material in their sources. The dolerites form the SWUS are most similar to the shallow unmineralised Arrow River, Cloud River and Pigeon River suites (type 1), and Nipigon suites (type 2) and are sourced from variably enriched subcontinental mantle material. However subtle variations are visible in the SWUS dolerite data that suggest distinct sources that have undergone variable fractionation, contamination and oxidation to produce the different suites observed in the Superior district. An important possibility is that the lower volumes of magma emplaced in the SWUS, make them more susceptible to contamination by continental crust during ascent and may be the reason for a stronger contamination signature in the SWUS dolerites, compared to those from the MCR.

# Chapter 6: Hydrothermal Geochronology

## 6.1 Introduction

The southwestern US has a long and complicated metasomatic history. Recognised hydrothermal events range in age from ~1,650 to ~20 Ma (e.g., Karlstrom and Bowring, 1988; Spencer and Welty, 1989). In order to understand the history of hydrothermal alteration assemblages in the Superior district, new U-Pb geochronological data was obtained from hydrothermal apatite and titanite, and new Ar-Ar data was collected from muscovite- and K-feldspar-bearing samples. This chapter also outlines U-Pb dating results for epidote, using a new LA-ICP-MS method developed for the current study. These data are used collectively to constrain the ages of hydrothermal alteration from Silver King, Magma and district-scale alteration in the Superior region.

## 6.2 Previous Work

Previous hydrothermal geochronology results for the Superior district are summarised in Table 6.1. Magmatic U-Pb ages and Ar-Ar ages for intrusions were presented in Chapter 3 (Seedorff et al., 2005; Hehnke et al., 2012; Table 3.2). Previous geochronological studies by Hehnke et al. (2012) and Rio Tinto (unpublished) focussed on constraining the temporal evolution of magmatism, alteration and mineralisation of the Resolution and Superior East porphyry Cu-Mo deposits and showed that these systems formed around 65 - 63 Ma (Table 6.1).

## 6.3 Ar-Ar geochronology

### 6.3.1 Introduction

Samples of strongly illite-muscovite altered rocks from the Magma vein and the Silver King area were selected for Ar-Ar dating during the current study to constrain their ages of alteration and compare them to previous dating results from Resolution (Table 6.1). A strongly orthoclase-altered sample of Apache Basalt from the range front, inferred to be of Proterozoic, age was also submitted for dating (Figure 6.1). These data were acquired to inform temporal and genetic relationships between the mineralised centres across the district, and to help constrain the age of widespread hydrothermal alteration in the range

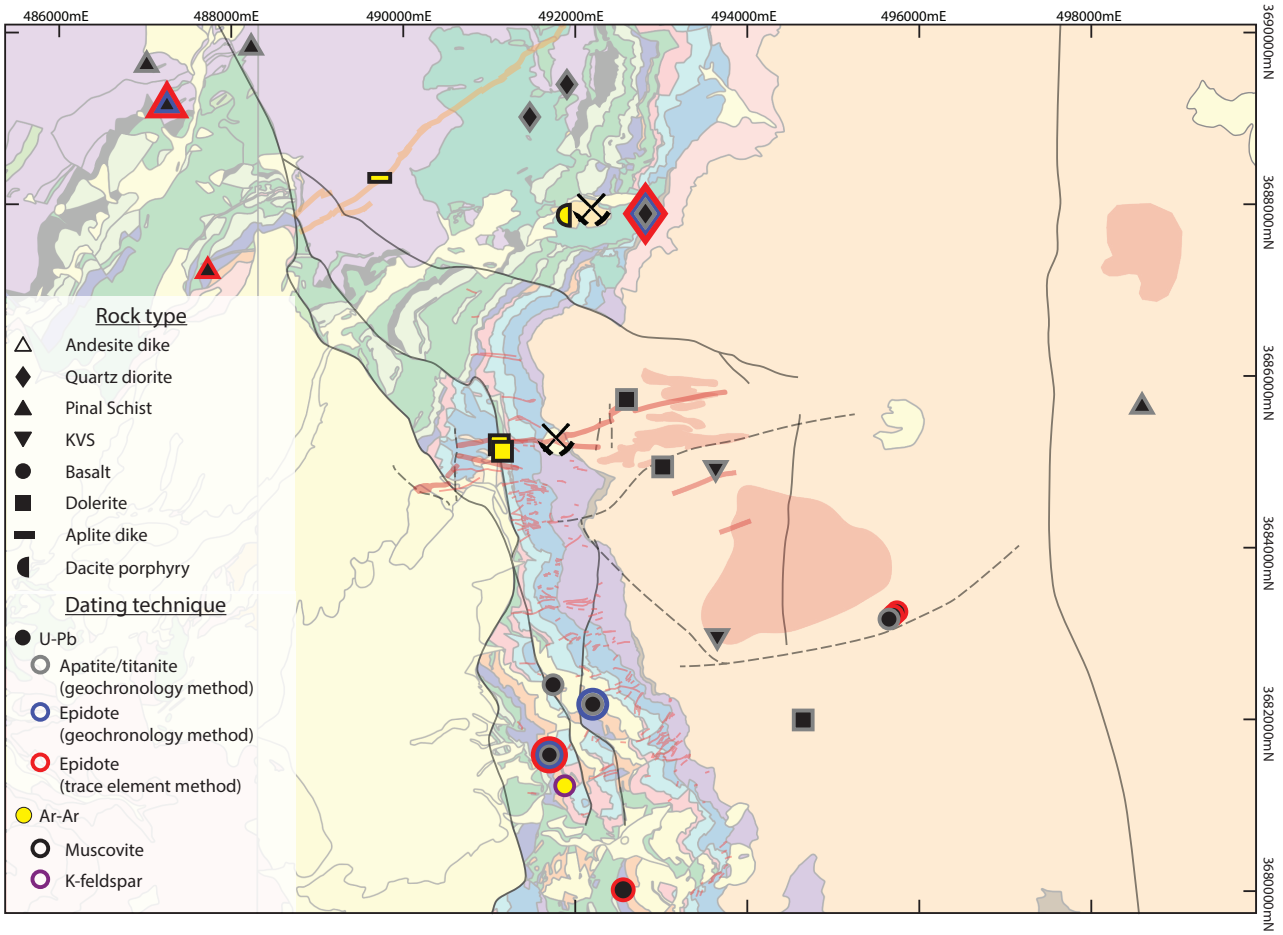


Figure 6.1 Map showing the locations of samples dated from the Superior district, Arizona. Geology legend as per Figure 3.2.

front, respectively.

### 6.3.2 Methods

Illite-muscovite altered samples were identified by visual inspection coupled with short wave infrared (SWIR) analysis. Samples were examined using transmitted light microscopy to confirm the presence of muscovite as the only significant potassium-bearing phase. Samples were submitted to the Argon Geochronology Lab at Oregon State University for sample preparation and analysis. Samples were coarse crushed and handpicked for the largest single crystals where available, or crystal aggregates.

$^{40}Ar/^{39}Ar$ ages were obtained by the incremental heating method using the ARGUS-VI mass spectrometer. The samples were irradiated in Irradiation 17-OSU-08 for 6 hours in the TRIGA CLICIT nuclear reactor at Oregon State University, along with the Fish Canyon Tuff (FCT-2-NM) sanidine Flux Monitor (28.201 ± 0.023 Ma; Kuiper et al., 2008). The $^{40}Ar/^{39}Ar$ incremental heating age determinations were performed on a multi-collector ARGUS-VI mass spectrometer at Oregon State University equipped with two Faraday collectors on mass $^{41}Ar$ and $^{40}Ar$, 1013 Ohm resistors on mass $^{39}Ar$, $^{38}Ar$, and $^{37}Ar$, and an ion-counting CuBe electron multiplier. This allowed simultaneous measurement of all argon isotopes, resulting in uncertainties (1σ) as low as 0.2-0.3%. This configuration provides the advantages of running in multi-collector mode while measuring the lowest peak ($^{36}Ar$) on the highly sensitive

Table 6.1 Prevous hydrothermal geochronology results from the Superior district.

| Hole/ Sample ID | From | To | Formation Name | Locality | Description | Tech-nique | Mineral | Age | Error (2σ) | Lab | Reference |
|---|---|---|---|---|---|---|---|---|---|---|---|
| Molybdenite mineralisation | | | | | | | | | | | |
| RES1B | 1825.6 | 1825.67 | Hydrothermal breccia | Resolution | Quartz-molybdenite vein cutting hydrothermal breccia | Re-Os | Molybdenite | 65.1 | 0.3 | AIRIE | Hehnke et al. (2012) |
| RES3B | 1551.5 | 1551.7 | Kvs | Resolution | Banded quartz-molybdenite vein cutting felsic Kvs | Re-Os | Molybdenite | 64.9 | 0.2 | AIRIE | Hehnke et al. (2012) |
| RES5B | 2082.1 | 2082.2 | Rhydacite porphyry | Resolution | Quartz-molybdenite vein in rhyodacite porphyry | Re-Os | Molybdenite | 63.9 | 0.2 | AIRIE | Hehnke et al. (2012) |
| DHRES -14 | 1033.0 | 1033.1 | Pinal Schist | Resolution East | Molybdenite vein in Pinal Schist associated with chloritic alteration | Re-Os | Molybdenite | 64.5 | 0.3 | DU | Rio Tinto (Unpublished data) |
| A-12 | 1351.18 | | Pinal Schist | Superior East | Not provided | Re-Os | Molybdenite | 63.8 | 0.3 | DU | Rio Tinto (Unpublished data) |
| A-16 | 1214.32 | | Pinal Schist | Superior East | Not provided | Re-Os | Molybdenite | 63.5 | 0.3 | DU | Rio Tinto (Unpublished data) |
| Potassic alteration | | | | | | | | | | | |
| RES7A | 2251 | 2251.1 | Dolerite | Resolution | Alteration in dolerite | Ar-Ar | Biotite | 63.5 | 0.38 | PCIGR | Hehnke et al. (2012) |
| RES1B | 1733.6 | 1733.7 | Hydrothermal breccia | Resolution | Matrix of hydrothermal breccia | Ar-Ar | Biotite | 63.2 | 0.39 | PCIGR | Hehnke et al. (2012) |
| RES2A | 2237.6 | 2238.7 | Rhyodacite porphyry | Resolution | Phenocrysts in coarse rhyodacite porphyry | Ar-Ar | Biotite | 63.1 | 0.11 | NMGRL | Hehnke et al. (2012) |
| HWY 177 | 490923 mE | 3682389 mN | Mescal Limestone | Concentrator Fault | Clots | Ar-Ar | Biotite | 62.3 | 0.15 | NMGRL | Hehnke et al. (2012) |
| RES5 | 1806.2 | 1806.3 | Hydrothermal breccia | Resolution | Matrix of hydrothermal breccia | Ar-Ar | Biotite | 62.1 | 0.34 | PCIGR | Hehnke et al. (2012) |
| Phyllic alteration | | | | | | | | | | | |
| RES5D | 1704 | 1704.1 | Rhyodacite porphyry | Resolution | Muscovite after biotite in phyllic altered porphyry | Ar-Ar | Muscovite | 63.3 | 0.46 | PCIGR | Hehnke et al. (2012) |
| RES2A | 2215.4 | | Rhyodacite porphyry | Resolution | Sericite in phyllic alteration overprinting potassic | Ar-Ar | Sericite | 62.9 | 0.3 | NMGRL | Hehnke et al. (2012) |

| Hole/ Sample ID | From | To | Formation Name | Locality | Description | Tech-nique | Mineral | Age | Error (2σ) | Lab | Reference |
|---|---|---|---|---|---|---|---|---|---|---|---|
| RES7B | 2051.1 | 2051.2 | Hydrothermal breccia | Resolution | Sericite in breccia | Ar-Ar | Sericite | 61.9 | 0.34 | PCIGR | Hehnke et al. (2012) |
| RES5B | 2103 | 2103.1 | Rhyodacite porphyry | Resolution | Sericite in advanced argillic alteration overprinting phyllic | Ar-Ar | Sericite | 61.9 | 0.34 | PCIGR | Hehnke et al. (2012) |
| A-09 | 1353.31 | | Quartz-latite porphyry | Superior East | Sericite from porphyry dike | Ar-Ar | Sericite | 62.4 | 0.11 | SGM | Rio Tinto (Unpublished) |
| Advanced argillic alteration | | | | | | | | | | | |
| RES3 | 1275.34 | | Kvs | Resolution | Alunite in Kvs | Ar-Ar | Alunite | 62.3 | 0.4 | PCIGR | Hehnke et al. (2012) |
| RES9J | 1378.3 | 1378.5 | Kvs | Resolution | Quartz - alunite - chalcocite - digenite veinlets in feldspathic Kvs | Ar-Ar | Alunite | 61.3 | 1.8 | NMGRL | Hehnke et al. (2012) |
| RES15A | 1601.8 | 1602 | Rhyodacite porphyry | Resolution | Fine grained alunite - dickite - kaolinite as breccia infil | Ar-Ar | Alunite | 60.4 | 0.2 | NMGRL | Hehnke et al. (2012) |
| RES5H | 1742.9 | 1730 | Rhyodacite porphyry | Resolution | Hypogene alunite in rhyodacite porphyry stock | Ar-Ar | Alunite | 51.7 | 0.29 | PCIGR | Hehnke et al. (2012) |
| RES13 | 1968.18 | | Rhyodacite porphyry | Resolution | Hypogene alunite in rhyodacite porphyry stock | Ar-Ar | Alunite | 49.5 | 0.57 | PCIGR | Hehnke et al. (2012) |
| Late pyrite | | | | | | | | | | | |
| RES9J | 1389 | 1389.1 | Kvs | Resolution | Massive pyrite vein with dickite infill in Kvs | Re-Os | Pyrite | 51.4 | 0.2 | AIRIE | Hehnke et al. (2012) |
| RES9J | 1394.1 | 1394.2 | Kvs | Resolution | Massive pyrite vein with dickite infill in Kvs | Re-Os | Pyrite | 22.9 | 0.1 | AIRIE | Hehnke et al. (2012) |

DU = Durham University; SGM = SERNAGEOMIN. All other Abbreviations as Table 3.2

electron multiplier. Irradiated samples were loaded into Cu-planchettes in an ultra-high vacuum sample chamber and incrementally heated by scanning a defocused 25 W $CO_2$ laser beam in preset patterns across the sample in order to release the argon evenly. After heating, reactive gases were cleaned up using an SAES Zr-Al ST101 getter operated at 400°C for ~10 minutes and two SAES Fe-V-Zr ST172 getters operated at 200°C and room temperature, respectively.

All ages were calculated using the corrected Steiger and Jäger (1977) decay constant of 5.530 ± 0.097 x $10^{-10}$ 1/yr (Min et al., 2000). For all other constants used in the age calculations, please refer to Table 2 in Koppers et al. (2003). Incremental heating plateau ages and isochron ages were calculated as weighted means with 1/σ2 as weighting factor (Taylor 1997) and as YORK2 least-square fits with correlated errors (York 1969) using the ArArCALC v2.6.2 software from Koppers (2002).

### 6.3.3 Results

New Ar-Ar geochronology results are summarised in Table 6.2 and presented on Figure 6.2, 6.3 and 6.4. Step heating of RE16JP021 yielded a robust plateau age of 74.31 ± 0.11 Ma (Table 6.2, Figure 6.2 A). Although there is some minor argon loss at low Ar-volume in early steps, the plateau comprises ~75% $^{39}$Ar and is stable to total fusion. Excluding these early steps the data yield an indistinguishable inverse isochron age of 74.42 ± 0.39 Ma (Table 6.2, Figure 6.2 B).

Step heating of RE16JP065 from the Silver King open pit produced significant excess argon but yielded a mini-plateau age (e.g., Piechocka et al., 2018) of 75.70 ± 0.12 that is indistinguishable from the inverse isochron age of 74.51 ± 1.60 Ma (Table 6.2, Figure 6.2 C-D). The inverse isochron demonstrates excess argon contamination from at least two sources. One trend of data points plot along a line that defines the composition of atmospheric argon which was probably incorporated during analytical procedures (Figure 6.2 D). However, many data points are anomalously radiogenic and plot back towards the Y axis at a consistent $^{36}$Ar/$^{40}$Ar of ~0.000015. This represents an unknown source of radiogenic argon.

The age spectrum from step heating of RE16JP086 is disturbed by the presence of excess argon (Figure 6.3 A). The inverse isochron demonstrates the limited atmospheric argon, accompanied by a significant radiogenic component (Figure 6.3 B). Despite this excess argon, the weighted mini-plateau age of 68.22 ± 0.11 Ma and inverse isochron age of 68.53 ± 0.45 Ma are consistent. Results from RE16JP086 within 0.5 m.y. of the more robust plateau age of 67.39± 0.29 Ma from RE16JP087 (Table 6.2, Figure 6.210 C-D).

Sample RE15JP034 also contains excess radiogenic argon (Figure 6.4). The lower temperature steps up to approximately 15-20% $^{39}$Ar, initially show a sharp decrease from ages ~ 1,000 Ma to ~ 200 Ma before gradually increasing to ca. 600 Ma (Figure 6.4 A). The lowest point on the age spectrum is interpreted as a minimum age, probably the result of resetting of older material. The inverse isochron age of 201.27 ± 35.71 Ma is somewhat older and significantly less precise that the weighted minimum step age of 186.63 ± 7.52 Ma, but the poor quality of the Ar spectrum makes this age of little use (Figure 6.4 B).

Table 6.2 Sample information and new Ar-Ar results for muscovite and K-feldspar altered samples in the Superior district. All data listed in Appendices 2A-E.

| Sample ID | Locality | UTM mE | UTM mN | Lithology | Alteration | Mineral | Whole-rock $K_2O$ (%) | Weighted plateau age | Error | %$^{39}$Ar | MSWD | Inverse isochron age | Error | MSWD |
|---|---|---|---|---|---|---|---|---|---|---|---|---|---|---|
| RE16JP021 | Grandfather Lead | 489759 | 3688318 | Aplite dike | Large platy muscovite crystals in pink groundmass | Muscovite | 4.48 | 74.31 | ± 0.11 | 74.8 | 1.05 | 74.72 | ± 0.39 | 1.09 |
| RE16JP065 | Silver King | 491923 | 3687869 | Dacite porphyry | Strong pervasive quartz - sericite | Illite-muscovite | 4.38 | 75.70 | ± 0.12 | 19.1 | 1.19 | 74.51 | ± 1.60 | 1.01 |
| RE16JP086 | Magma | 490981 | 3685167 | Dolerite | Strong replacement of plagioclase by sericite | Illite-muscovite | 5.1 | 68.22 | ± 0.11 | 8.2 | 2.09 | 68.53 | ± 0.45 | 1.77 |
| RE16JP087 | Magma | 490981 | 3685168 | Dolerite | Strong replacement of plagioclase by sericite | Illite-muscovite | 4.68 | 67.39 | ± 0.29 | 74.8 | 0.48 | 67.21 | ± 0.24 | 1.06 |
| RE15JP034 | Range front | 491864 | 3681229 | Basalt | Strong patchy-pervsive orthoclase - chlorite | Orthoclase | 9.25 | 186.63 | 7.52 | 7.2 | 0.88 | 201.27 | ± 35.71 | 0.88 |

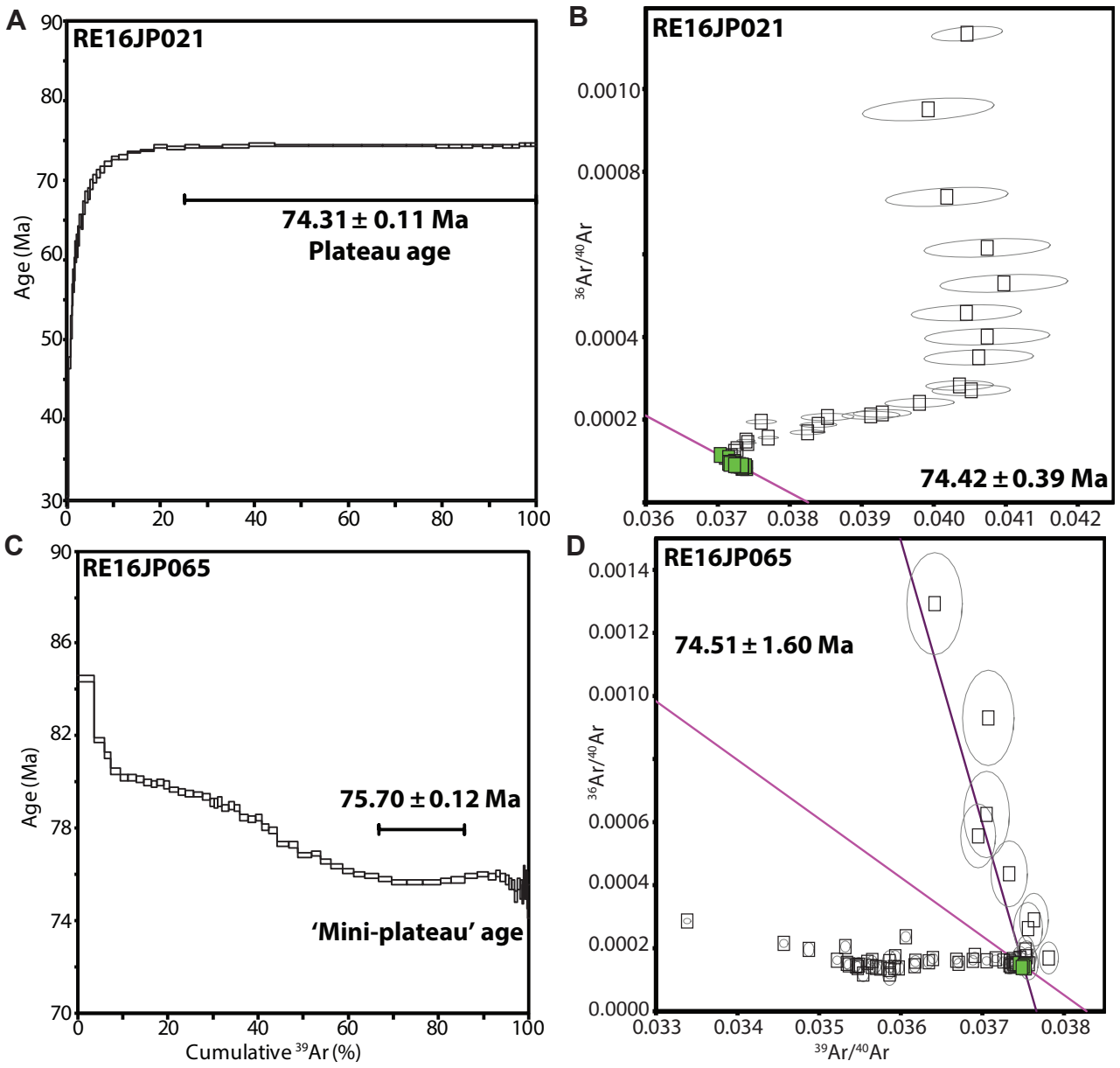


Figure 6.2 Step-heating plateau and inverse isochron plots for muscovite altered samples from the Silver King area. Filled squares are those steps used in the plateau ages. All data listed in Appendices 2A-B.

### 6.3.4 Discussion

The plateau ages produced from muscovite-altered samples in the Silver King area are similar to magmatic ages previously reported for both for the Silver King quartz diorite and the dacite porphyry stock (Table 6.2, Figure 6.5). Hydrothermal alteration in this area is therefore interpreted to have occurred contemporaneous with the emplacement of the exposed dacite porphyry plug.

Ar-Ar techniques can return ages that are somewhat younger than the crystallisation ages of the related intrusion (e.g., Cannell, 2004; Chiradia et al., 2012). As such, they can be considered a cooling age (i.e., when the muscovite grain cooled through the closure temperature of around 350$^0$C; Chiradia et al., 2012) rather than a crystallisation age. Since there is no discernible difference between the magmatic crystallisation ages and the hydrothermal muscovite ages from Silver King, it is proposed that there was

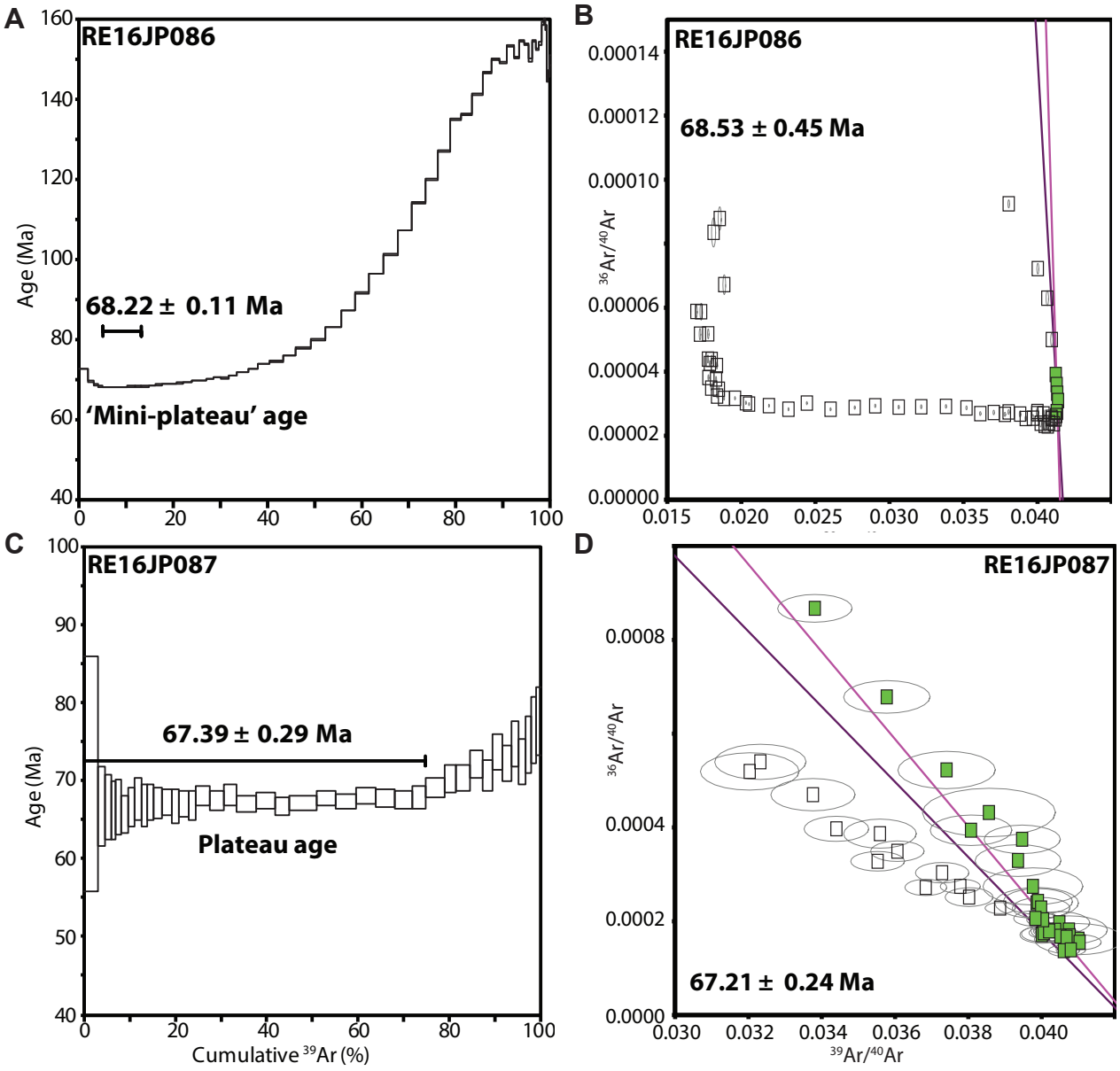


Figure 6.3 Step-heating plateau and inverse isochron plots for muscovite altered dolerite samples adjacent to the Magma vein. Filled squares are those steps used in the plateau ages. All data listed in Appendices 2C-D.

minimal heat transfer to the country rocks during stock emplacement, and that cooling and crystallisation of the stocks and associated muscovite alteration was rapid. This behaviour implies a shallow level of crustal emplacement for the dacite plug in the Silver King area, typical of porphyry systems (e.g., John et al., 2010; Sillitoe, 2010).

The new age determinations from muscovite-altered samples from adjacent to the Magma vein have provided the first radiometric constraints on its age. Results suggest the Magma vein may be older than Resolution (Figure 6.5), supporting speculations that the two deposits may be distinct hydrothermal systems (Seedorff et al., 2005b, Barton et al., 2005). One possibility for this age discrepancy is the progressive inward cooling of the Schultze Granite, inferred to occur below the Superior district, albeit at significant depth. Due to its low closure temperature, Ar ages can be zoned around large multi-

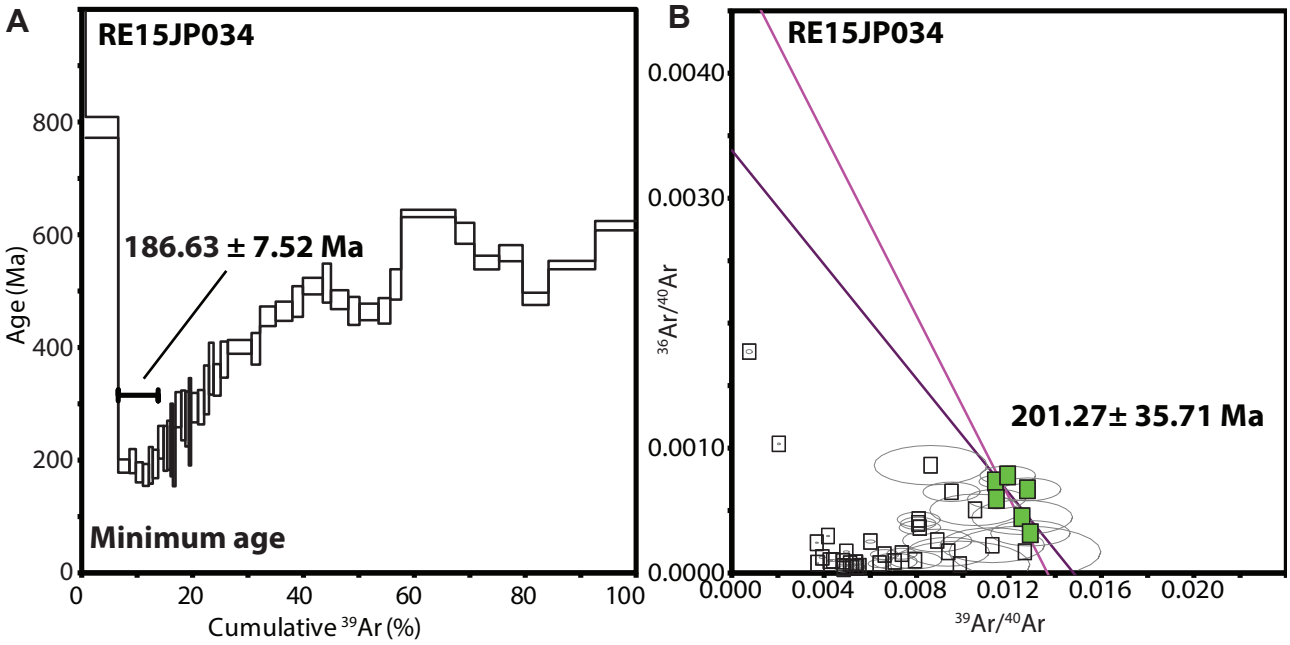


Figure 6.4 Step-heating plateau (A) and inverse isochron plot (B) for orthoclase altered basalt. Filled squares are those steps used in the minimum age. All data listed in Appendix 2E.

phase plutons (e.g., Cannell, 2004). It is possible that Magma, Resolution and Superior East all share, and occur above, a common magmatic source. If this were true, then due to its more distal location relative to the Schultze Granite, the muscovite at Magma may have cooled through 350$^0$C earlier than at Resolution and Superior East. Conversely, Superior East would have been the last part of the system to cool through 350$^0$C. However, the full extent of the Schultze Granite and the original position of the mineralised centres relative to it have been disrupted by Tertiary faulting, making inferences about paleothermal aureoles speculative. Furthermore, drilling at Resolution has yet to identify the causative pluton, despite reaching considerable depths below the mineralisation.

Uranium-lead dating of zircons from intrusions at Magma is limited to one sample, dated at 69.1 ± 4.0 Ma by Seedorff et al. (2005; Table 3.2; Figure 3.19). Unfortunately, due to its low precision, this age overlaps with U-Pb$_{zircon}$ ages from intrusions at Resolution, which range from 69.3 ± 1.1 Ma to 64.1 ± 1.9 Ma (Table 3.2; Figure 3.19), highlighting the possibility of Ar resetting by the younger intrusions at Resolution. However, the earliest onset of mineralisation at Resolution, as defined by the oldest Re-Os ages of molybdenite (65.1 ± 0.3 Ma, Table 6.1; Figure 6.5), provide a maximum likely age for muscovite crystallisation at Resolution after 65.4 Ma. It therefore remains permissible that alteration around the Magma vein occurred significantly earlier than at Resolution. This interpretation would be consistent with the general southward shift in the onset of magmatism from Silver King to Magma to Resolution then eastward to Superior East (Figure 6.12). Although there remains some possibility of staged cooling of muscovite at Resolution due to the prolonged nature of igneous activity, molybdenite ages constrain the maximum likely crystallisation age to post-65 Ma. While only limited data are available, the age difference between Magma and Resolution is interpreted to represent a discrete mineralising event in the

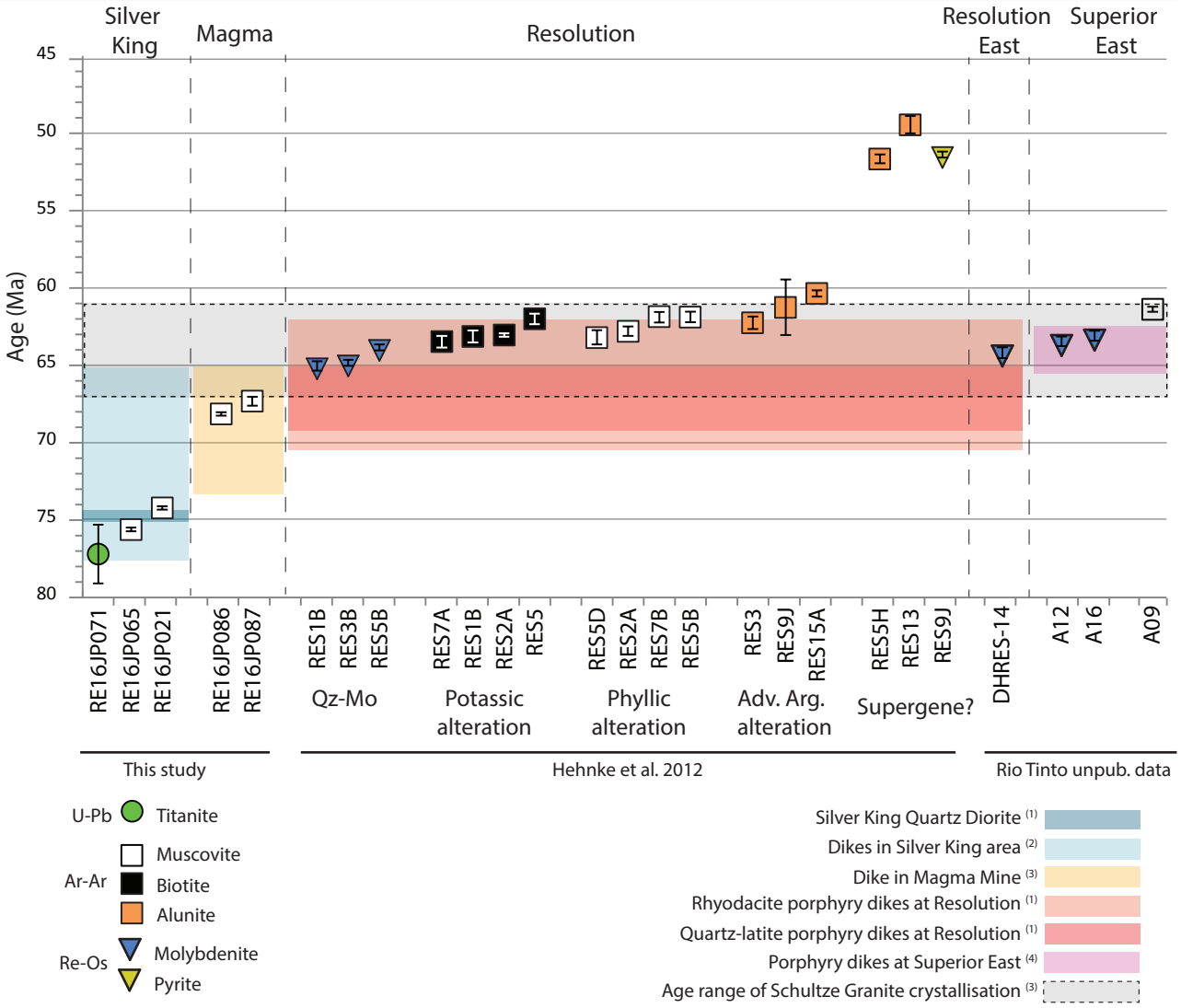


Figure 6.5 Laramide hydrothermal geochronological evolution of the Superior district, showing the southward, then eastward progression of magmatism and associated magmatic-hydrothermal activity, from Silver King south to Magma, then Resolution and finally bearing east toward Superior East. Data provided in Table 6.1, Table 6.6 and Table 6.2.

Superior district possibly related to an early phase of the Schultze Granite at considerable depth below the Superior district. More hydrothermal geochronology, either from muscovite-altered wall rocks, or directly applied to mineralisation at Magma, might provide more insight into the temporal relationship between Resolution and the Magma vein.

## 6.4 Apatite and titanite geochronology

### 6.4.1 Introduction

Apatite and titanite were chosen for geochronological investigation because the minerals can host significant U and they occur in a wide range of alteration types in the Superior district. Previous studies showed that these minerals can be effectively dated (e.g., Chew et al., 2011; Thompson et al,. 2016) and have closure temperatures estimated from both experimental and empirical studies that range from 425°C to 500°C (Chamberlain and Bowring, 2001) making them robust geochronometers.

### 6.4.2 Methods

#### 6.4.2.1 Analytical techniques

Samples from a range of rock types and alteration phases containing large (> 30 μm) apatite grains were reviewed using reflected light petrography. A subset of eighteen samples that contain a range of apatite textural types were selected as representative of a variety of alteration types and host rocks. These were analysed using in-situ laser ablation techniques to help constrain hydrothermal events throughout the Superior district (Table 6.4; Table 6.5).

Polished 25 mm rock mounts from eighteen samples containing apatite were characterised texturally to determine the apatite modes of occurrence (Figure 6.6). Apatite grains were classified into five groups; amygdaloidal, skarn, vein halo, matrix and detrital (Table 6.5). These samples were analysed by in-situ U-Pb LA-ICP-MS at CODES, University of Tasmania, using a laser ablation quadrupole ICP-MS system, employing the method described by Thompson et al. (2016) and Chew et al. (2011).

Calibration of U-Pb isotopic analyses was done using the OD306 apatite (Huang et al., 2015; Thompson et al., 2016), which was analysed throughout the analytical run using the same spot size and analytical conditions as the unknown samples. Calibration for Pb isotopes and trace elements was done using NIST610 glass measured at a 43 μm spot size measured repeatedly throughout the session to correct for any instrument drift. Lead isotope values for NIST610 were taken from Baker et al. (2004). USGS glasses BCR-2g and GSD-1g and internal standards Kovdor and McClure Mt (matrix matched apatite standard materials) were analysed as unknowns to assess the accuracy of the results. Titanite grains were analysed using the same instrument and analytical approaches as for apatite except, that U-Pb ratios were calibrated using the AUR100606 titanite standard (Best, 2012; Huang et al., 2015). Samples were analysed over two sessions, between July and October 2016. Isotopes analysed from both minerals included $^{204}$Pb $^{206}$Pb $^{207}$Pb, $^{208}$Pb $^{238}$U, $^{232}$Th, $^{31}$P, $^{56}$Fe and $^{140}$Ce. The second run also analysed for $^{89}$Y (Table 6.4).

#### 6.4.2.2 Instrumentation

Analyses were performed using an ASI Resolution S155 laser ablation system with a Coherent Compex Pro 110 ArF Excimer laser operating at 193 nm wavelength with a pulse width of ~20 ns. Ablation was conducted in an atmosphere of pure helium flowing at 0.35 l/min and the ablated particles were immediately mixed with argon after the ablation cell flowing at 1.05 l/min. Addition of $N_2$ at ~1.6 ml/min to the argon line was required for optimized Pb isotope collection. The mass spectrometer is an Agilent 7900 quadrupole ICP-MS, run in time resolved mode. Standards were analysed every 15-20 minutes throughout the run. Where apatite grains were smaller than 100 μm, titanite was analysed instead.

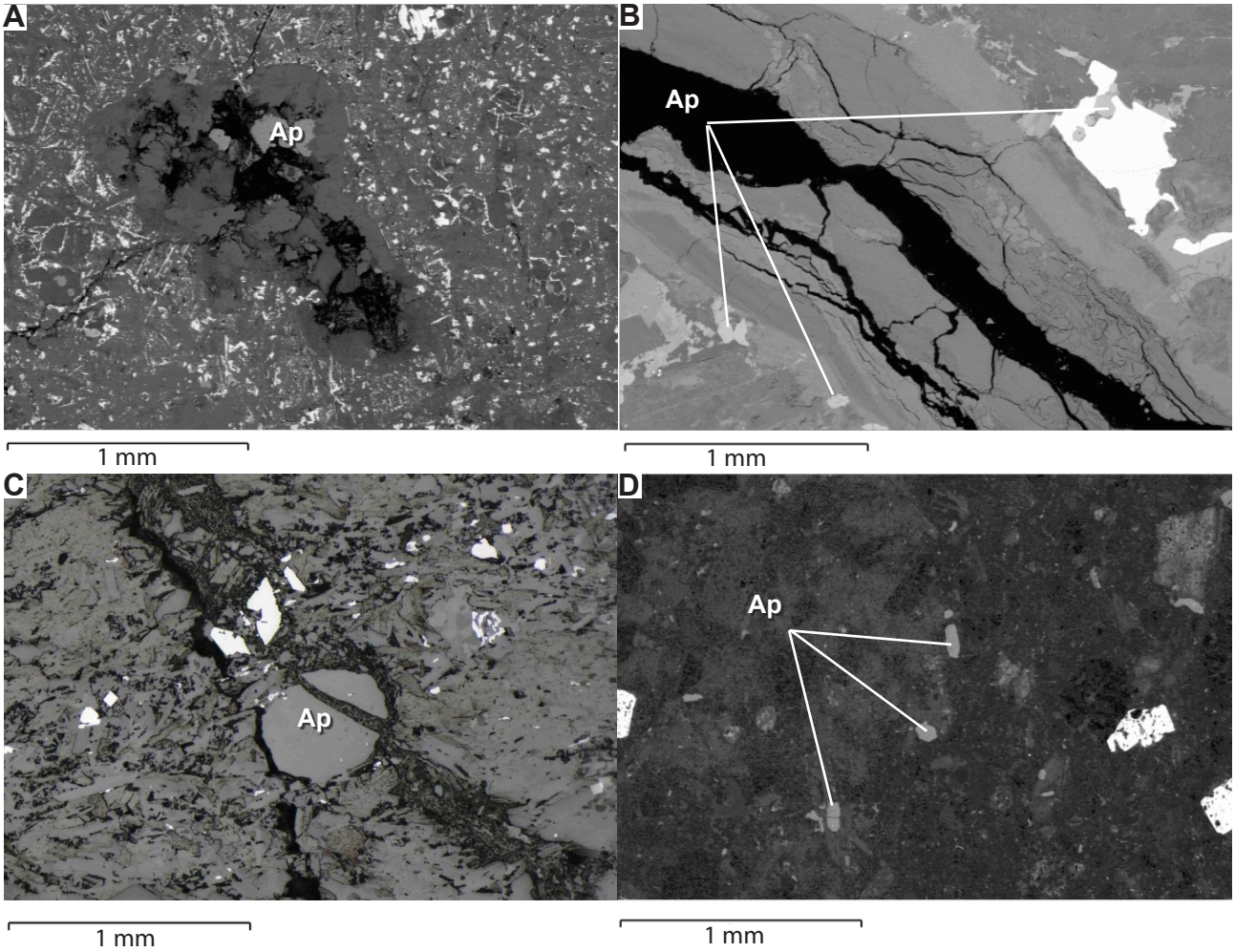


Figure 6.6 Textural classes of apatite in the Superior district. A. RE17JP085 - Amygdular apatite intergrown with chlorite. B. RE16JP060 - Vein halo apatite adjacent to an actinolite - chlorite vein in a dolerite. C. RE16JP059 - Detrital apatite in a quartz muscovite schist. D. RE15JP181 - Matrix apatite in a volcaniclastic rock.

#### 6.4.2.3 U-Pb age determinations and common Pb corrections

Uranium-lead geochronology of accessory phases such as apatite and titanite can be hampered by variable high abundances of common Pb. This problem can be overcome by calculating a common Pb correction and using it to anchor the Y-intercept of isochrons (e.g., Chew et al., 2011). There are a number of ways of calculating common Pb contents. Where there is a large spread of highly correlated data points that define a mixing array, between radiogenic and common Pb compositions, no assumptions need to be made about the latter. Where there is a poor spread of data along a mixing array the data can be anchored to a particular common Pb composition. The $^{204}$Pb, $^{207}$Pb and $^{208}$Pb correction techniques require an estimate of the Pb isotopic composition during the crystallisation of the mineral. In these instances the common Pb composition can be sought from external sources. Such sources can be a measured initial Pb value from a previous study of rocks from a similar age and region, or calculated from the global crustal Pb growth models (e.g., Stacey and Kramers, 1975). A thorough discussion and evaluation of these approaches is provided by Chew et al. (2011).

In the Superior district, the Pb isotopic composition of whole rocks and minerals have been shown to

diverge from global Pb models (Bouse et al., 1999). Whole rock Pb isotopic values were therefore collated from the literature to help with Pb corrections for U-Pb geochronology (Table 6.3). Whole-rock initial Pb values are available for the 1,700 Ma and 1,400 Ma plutonic rocks from the Yavapai terrane and for the 1,650 Ma Pinal Schist and 1,100 Ma dolerite sills of the Mazatzal terrane (Table 6.3). However, the measured isotopic values for these rocks vary enormously (e.g., 0.847 – 0.894 for $^{207}Pb/^{206}Pb$ for dolerite sills from central Arizona; Hammond and Wooden, 1991; Table 6.3), and are therefore considered somewhat unreliable. More precise values have been derived from hydrothermal galena from the 1,700 Ma Jerome VMS deposit, near Prescott (Wooden and Dewitt, 1991; Table 6.3). The Jerome deposit is considered to have a largely syngenetic origin with respect to the host rocks (Lindberg, 1989) and provides an initial $^{207}Pb/^{206}Pb$ ratio of 0.971 for the Jerome ores and Paleoproterozoic metavolcanic host rocks of the Ash Creek Group (Table 6.3). Since there is no high-precision Pb isotope data available from Proterozoic galena located in the Mazatzal terrane, the initial Pb value from the Jerome galena is used to anchor initial Pb composition in Proterozoic samples of the Superior district.

High precision initial Pb values are available for Laramide samples (Bouse et al., 1999). An initial $^{207}Pb/^{206}Pb$ value of 0.879 was published from the Magma vein by Bouse et al. (1999) implying significant inheritance and/or mixing of common Pb prior to, or during ore formation (c.f. Bouse et al., 1999; Lang and Titley, 1998; Table 6.3). Since the degree of common Pb inheritance/mixing is affected by the degree of crustal contamination of the ore-forming magma, initial Pb isotopic values may vary slightly from early to late Laramide systems, as crustal contamination of magmas increased over time during the Laramide (e.g., Titley, 1982, Bouse et al., 1999). However, since some crustal contamination of magmas is common to all Laramide systems to some degree, the initial Pb ratios from the Magma vein are considered more representative of the initial Pb composition of Laramide samples than estimates taken from Stacey and Kramers' (1975) average crustal growth model (0.879 and 0.839 respectively; Table 6.3).

Given the variability in, and inherent uncertainty associated with, whole-rock initial Pb values for the Pinal Schist (Wooden and Dewitt, 1991) and dolerite samples (Hammond and Wooden, 1991), combined with the lack of Proterozoic galena from the Mazatzal Province, coupled with the disparity between average crustal growth model (Stacey and Kramers, 1975), this study used Jerome galena values of Wooden and Dewitt, (1991) and Magma galena values of Bouse et al. (1999) to anchor Proterozoic samples and Laramide samples respectively. Isochrons and error calculations were generated using Isoplot v.4.15 (Figure 6.8; Appendix 2F. Ludwig, 2003).

#### 6.4.2.4 Matrix effects

Typically, matrix effects are caused by the unintended fractionation of two or more elements during analysis. This fractionation results in a discrepancy between measured and actual elemental concentrations in the sample. This can be particularly problematic in U-Pb age dating, where only a small change in

Table 6.3 Previously published Pb isotopic compositions for selected rocks and minerals from the southwestern USA.

| Dataset | $^{206}Pb/^{204}Pb$ | $^{207}Pb/^{204}Pb$ | $^{208}Pb/^{204}Pb$ | $^{207}Pb/^{206}Pb$ | Reference |
|---|---|---|---|---|---|
| Central Arizona | | | | | |
| 1.7 Ga plutonic rocks (Av.) | 21.442 | 15.871 | 38.930 | 0.740 | Wooden and DeWitt (1991) |
| Jerome galena | 15.72 | 15.27 | 35.344 | 0.971 | |
| Pinal Schist | | | | | |
| unknown sample ID | 19.01 | 15.635 | 38.710 | 0.822 | |
| unknown sample ID | 19.00 | 15.630 | 39.360 | 0.823 | |
| unknown sample ID | 18.82 | 15.599 | 39.011 | 0.829 | |
| unknown sample ID | 18.45 | 15.595 | 38.081 | 0.845 | Bouse et al. (1999) |
| unknown sample ID | 18.65 | 15.590 | 37.751 | 0.836 | |
| unknown sample ID | 18.21 | 15.550 | 38.182 | 0.854 | |
| Average composition | 18.690 | 15.600 | 38.512 | 0.835 | |
| Dolerite Sills | | | | | |
| GC1 | 17.594 | 15.507 | 37.162 | 0.881 | |
| GLB 1 | 18.265 | 15.558 | 38.145 | 0.852 | |
| LOM1 | 18.379 | 15.564 | 38.387 | 0.847 | |
| RVD | 17.950 | 15.462 | 37.914 | 0.861 | |
| SAP1 | 18.322 | 15.512 | 38.302 | 0.847 | |
| SAS1 | 17.298 | 15.472 | 37.016 | 0.894 | Hammond and Wooden (1990) |
| SCC1 | 17.489 | 15.486 | 37.216 | 0.885 | |
| SCC6 | 17.501 | 15.508 | 37.286 | 0.886 | |
| SCC9 | 17.716 | 15.510 | 37.497 | 0.875 | |
| 88SCM3 | 17.759 | 15.488 | 37.476 | 0.872 | |
| 88SCM5 | 17.822 | 15.481 | 37.562 | 0.869 | |
| Average composition | 17.827 | 15.504 | 37.633 | 0.870 | |
| Superior district | | | | | |
| Magma galena | 17.623 | 15.498 | 37.826 | 0.879 | Bouse et al. (1999) |
| Average crust | | | | | |
| 1,100 Ma | 16.891 | 15.491 | 36.566 | 0.917 | Stacey and Kramers (1975) |
| 60 Ma | 18.612 | 15.624 | 38.516 | 0.839 | |

the U/Pb ratio can result in a significant discrepancy in final age determinations. Elemental fraction can be caused by a range of factors, such as particle size distribution (e.g., Guillong and Gunther, 2002), radiation dose (e.g., Allen and Campbell, 2012) and ablation rate (e.g., Marillo-Sialer, 2014). Usually this is overcome by analysing standard reference materials that are as close as possible in composition and character as the unknown samples to be analysed, allowing corrections to be made for known sources of error. However, Thompson et al. (2016) conducted a detailed study on the causes of matrix effects in LA-

ICP-MS analysis of apatite, highlighting that even using the best matrix-matched standards available, there was still a 1-3% offset in LA-ICP-MS U-Pb ages. In apatite, this has been interpreted as related to a laser-induced elemental fraction (LIEF)-type process, where CaO deposited around the ablation site may scavenge U, probably because they have similar oxide boiling points ($2850^0$C for CaO and $2800^0$C for $UO_2$) while Pb (boiling point of PbO is $1535^0$C) remains mobile and may be transported to the plasma preferentially (Thompson et al., 2016).

### 6.4.3 Results

#### 6.4.3.1 Trace element compositions

Trace element analyses of apatite from the Superior district are shown in Table 6.4 and Figure 6.7. Geochronology results are presented in Table 6.5. Full trace element and Pb isotope dataset for all 246 spot analyses can be found in Appendix 2F.

For the apatites of the Superior district, a strong positive relationship is observed between Ce and Th over though a wide range of concentrations (<0.1 - >5000 ppm and <0.001 - >1000 ppm for Ce and Th respectively; Figure 6.7). The lowest Ce contents were measured largely in apatites hosted in Apache Basalt amygdales that have unambiguous hydrothermal textures (Table 6.5). The highest Ce concentrations predominantly come from apatite grains which occur in the matrix of dolerite sills or the quartz diorite stock (Table 6.5, Figure 6.1). The Pinal Schist contains multiple textural types of apatite, with data spread over a large range (Figure 6.7).

#### 6.4.3.2 U-Pb Ages

Geochronology results from 246 LA-ICP-MS spot analysis of 18 apatite-bearing samples are summarised in Table 6.5. Some of the apatite crystals analysed contained low U or Pb concentrations (<20 ppm) and/or were dominated by common Pb and could not be dated. Many of the apatites have sufficient radiogenic Pb to allow for age determinations. Some titanites were also dated.

Uranium-Pb geochronology results from apatite range from the Paleoprotozoic to the Cenozoic (Table 6.5). Both anchored and unanchored age results are presented in Table 6.5 as there is some uncertainty regarding the initial Pb composition on some, but not all, of the samples. Preferred ages highlighted in Table 6.5. The choice of preferred apatite ages vary from sample to sample, because the initial Pb anchor is not suitable for all samples, even within a given type (e.g., magmatic or hydrothermal; Table 6.5). This may be the result of using imperfect initial Pb anchors, but could also suggest that the Pb sources for these rocks were heterogeneous. Preferred ages in all but two of the samples (RE15JP088 and RE16JP157; Table 6.5) are those with a lower calculated uncertainty. For RE15JP088 and RE16JP157, the common Pb correction was chosen to provide consistent ages with similar samples. The preferred ages were used to construct the composite Concordia plots shown in Figure 6.8. Generally, the differences between

Table 6.4 Average major and minor element, and Pb isotope compositions for apatite analysed from the Superior district, Arizona. Locations in Table 6.5 The full dataset of 246 spot analyses can be found in Appendix 2F.

| Sample ID | Mineral | Rock type | P (%) | Fe (%) | Y (%) | Ce (%) | $^{204}$Pb (ppm) | $^{206}$Pb (ppm) | $^{207}$Pb (ppm) | $^{208}$Pb (ppm) | $^{232}$Th (ppm) | $^{238}$U (ppm) | $^{238}$U/ $^{232}$Th | $^{238}$U/ $^{208}$Pb | $^{238}$U/ $^{206}$Pb | error (1σ) | $^{207}$Pb/ $^{206}$Pb | error (1σ) |
|---|---|---|---|---|---|---|---|---|---|---|---|---|---|---|---|---|---|---|
| RE15JP073 | Apatite | Basalt | 20.1 | 0.392 | N/A | 0.0165 | 0.0222 | 0.346 | 0.267 | 0.625 | 0.584 | 0.128 | 0.416 | 0.530 | 0.786 | 3.45 | 0.779 | 0.164 |
| RE15JP085 | Apatite | Basalt | 20.7 | 1.02 | N/A | 0.0218 | 0.00301 | 0.217 | 0.0517 | 0.101 | 0.659 | 1.09 | 4.62 | 13.3 | 4.31 | 0.209 | 0.272 | 0.0174 |
| RE15JP088 | Apatite | Basalt | 21.9 | 0.306 | N/A | 0.0258 | 0.00574 | 0.181 | 0.0795 | 0.194 | 0.508 | 0.262 | 1.06 | 2.38 | 2.22 | 0.200 | 0.469 | 0.0400 |
| RE15JP181 | Apatite | Volcanics | 22.2 | 0.463 | N/A | 2.30 | 0.0422 | 0.775 | 0.773 | 1.60 | 29.2 | 6.46 | 0.224 | 5.408 | 8.77 | 0.502 | 0.805 | 0.0188 |
| RE15JP106 | Apatite | Dolerite | 22.8 | 2.34 | 1.39 | 2.77 | 0.0435 | 1.04 | 0.791 | 2.15 | 9.37 | 1.17 | 0.178 | 0.713 | 1.18 | 0.0391 | 0.746 | 0.0143 |
| RE15JP150 | Apatite | Dolerite | 23.1 | 0.173 | 1.38 | 2.37 | 0.0769 | 1.74 | 1.27 | 3.31 | 7.56 | 2.19 | 0.292 | 1.423 | 1.96 | 0.0611 | 0.606 | 0.0109 |
| RE15JP191 | Apatite | Skarn | 20.8 | 3.45 | 0.330 | 0.0709 | 0.153 | 2.86 | 2.40 | 5.82 | 0.657 | 0.546 | 0.917 | 0.193 | 0.170 | 0.0354 | 0.898 | 0.0191 |
| RE16JP019 | Apatite | Skarn | 20.1 | 3.27 | 1.28 | 0.383 | 0.0648 | 1.34 | 1.14 | 2.73 | 3.45 | 1.47 | 1.15 | 0.781 | 1.36 | 0.0363 | 0.847 | 0.0140 |
| RE16JP031 | Apatite | Andesite | 21.5 | 1.43 | 1.10 | 0.995 | 0.0514 | 1.06 | 0.846 | 2.07 | 6.49 | 1.66 | 1.11 | 3.09 | 2.59 | 0.557 | 0.678 | 0.0373 |
| RE16JP035 | Apatite | Schist | 14.7 | 11.1 | 0.174 | 0.0410 | 0.144 | 2.74 | 2.32 | 5.64 | 1.22 | 0.782 | 0.751 | 0.476 | 0.442 | 0.0652 | 0.803 | 0.0210 |
| RE16JP059 | Apatite | Schist | 23.6 | 0.130 | 1.17 | 0.249 | 0.181 | 3.50 | 2.74 | 6.75 | 14.6 | 24.2 | 10.7 | 3.70 | 5.18 | 0.225 | 0.790 | 0.00777 |
| RE16JP060 | Apatite | Dolerite | 22.9 | 1.06 | 1.55 | 2.32 | 0.0228 | 0.833 | 0.534 | 1.52 | 6.71 | 1.79 | 0.271 | 1.37 | 2.04 | 0.0604 | 0.616 | 0.0139 |
| RE16JP071 | Titanite | Quartz diorite | 0.0 | 1.00 | 1.14 | 1.49 | 0.00639 | 0.182 | 0.0968 | 0.351 | 37.3 | 7.16 | 1.19 | 26.5 | 32.7 | 0.992 | 0.553 | 0.0134 |
| RE16JP081 | Titanite | Basalt | 0.0 | 0.782 | 0.135 | 0.110 | 0.0169 | 1.12 | 0.326 | 0.712 | 1.44 | 4.82 | 44.9 | 12.9 | 3.52 | 0.0604 | 0.337 | 0.00552 |
| RE16JP150 | Apatite | Volcanics | 20.6 | 2.19 | 0.464 | 1.68 | 0.224 | 3.78 | 3.19 | 7.89 | 34.4 | 7.19 | 0.248 | 1.76 | 3.02 | 0.163 | 0.845 | 0.0211 |
| RE16JP157 | Apatite | Dolerite | 20.5 | 20.9 | 1.17 | 2.61 | 0.205 | 3.80 | 3.20 | 8.01 | 5.60 | 1.63 | 0.288 | 0.426 | 0.634 | 0.0316 | 0.681 | 0.0321 |
| RE16JP194 | Apatite | Dolerite | 23.3 | 1.82 | 0.819 | 1.12 | 0.0183 | 0.409 | 0.326 | 0.828 | 14.6 | 4.50 | 0.373 | 6.04 | 10.1 | 0.383 | 0.835 | 0.0231 |
| RE16JP200 | Apatite | Quartz diorite | 22.3 | 61.8 | 0.238 | 1.05 | 0.163 | 1.87 | 1.55 | 3.88 | 27.2 | 5.15 | 1.95 | 3.67 | 6.58 | 0.287 | 0.871 | 0.0234 |

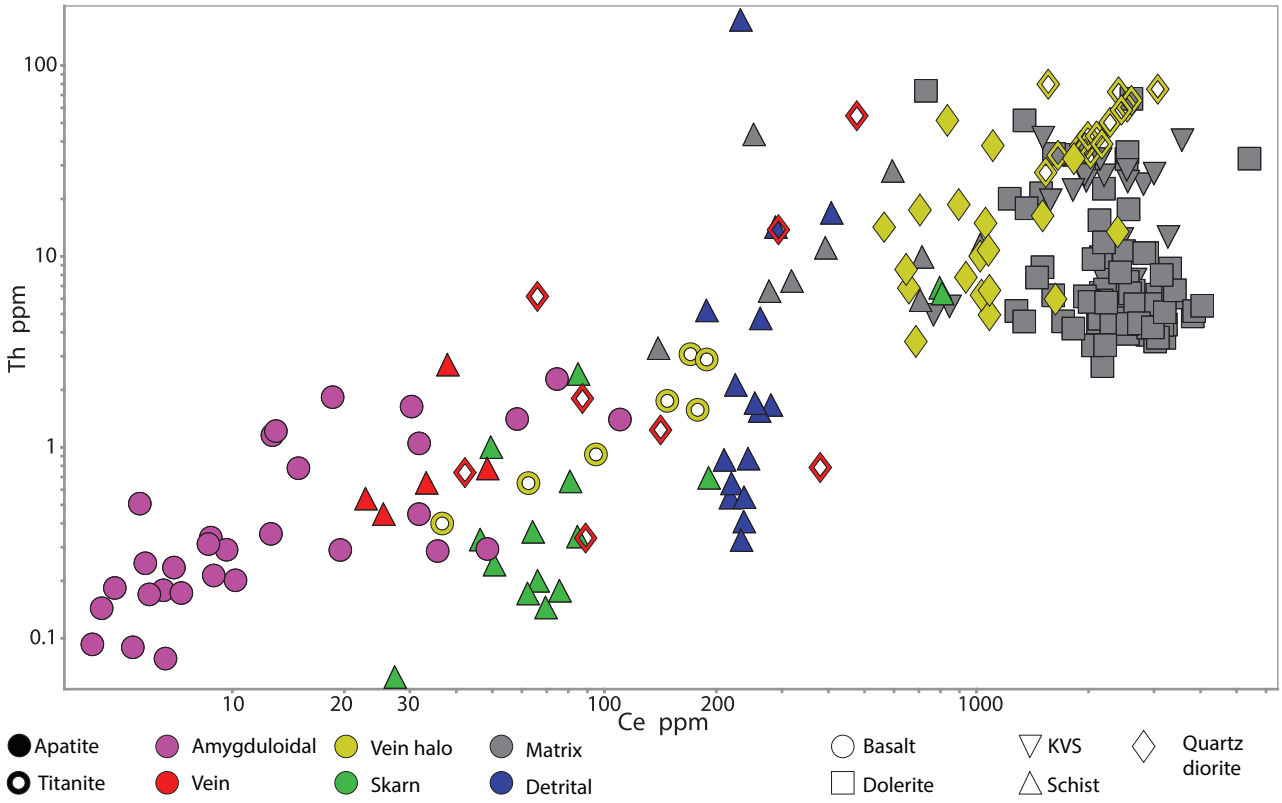


Figure 6.7 Bivariate Ce-Th diagram showing the relationship between apatite texture and trace element concentrations. Average compositions data listed in Table 6.4. All data listed in Appendix 2F.

anchored and unanchored ages are minor, and are well within error of each other.

### 6.4.4 Interpretation of trace element compositions and U-Pb ages

Trace element compositions can be used to help assess the origin of apatite crystals (Mao et al., 2016). Broadly, apatite with low concentrations of trace elements tend to be hydrothermal in origin. This is due to the low fluid partition coefficients for U, Th and REEs in hydrothermal environments relative to magmatic environments (Mao et al., 2016). Using a combination of host rock age, textures, apatite age and Ce-Th concentrations, inferences can be made regarding the origins of the apatites (i.e., whether they represent magmatic, hydrothermal, metamorphic or partially reset crystals). In some cases, (e.g., amygdular or vein hosted apatite) a hydrothermal origin can be determined unambiguously, corroborated by low Ce and Th concentrations (e.g., RE15JP073, RE15JP085 and RE15JP088; Table 6.5; Figure 6.7). For matrix or vein halo apatites, a metasomatic or magmatic origin remains unclear on textural grounds. In these cases, origin can be inferred from the absolute apatite age (by U-Pb geochronology) relative to its host rock and trace element composition. Where an apatite from matrix or vein halo returns an age similar to that of its igneous host rock, and it has high Ce values typical of magmatic apatites, a magmatic origin is inferred (e.g., RE16JP106, RE15JP150, RE15JP181, RE16JP060, RE16JP150 and RE16JP157; Table 6.5; Figure 6.7). Where apatite ages are younger than the host rock and Ce concentrations are intermediate between the high Ce-Th and low Ce-Th groups, the apatites are

Table 6.5 Comparison of U-Pb dating results using multiple common Pb anchors for apatite in the Superior district. Average Ce concentrations are derived from only the analyses used in the construction of the isochron.

| Sample ID | UTM mE | UTM mN | Mineral | Rock Type | Texture | Unanchored Age (Ma) | Error | MSWD | Common Pb anchor | Anchored Age (Ma) | Error | MSWD | Av. Ce (ppm) | Interpreted origin |
|---|---|---|---|---|---|---|---|---|---|---|---|---|---|---|
| RE15JP191 | 489769 | 3687321 | Apatite | Skarn | Vein halo | 1645 | ± 290 | 1.50 | 0.9714 | 1608 | ± 250 | 1.40 | 70.80 | Metamorphic |
| RE16JP035 | 487106 | 3689352 | Apatite | Schist | Matrix | 1601 | ± 270 | 0.69 | 0.9714 | 1771 | ± 530 | 2.50 | 41.00 | Metamorphic |
| RE15JP088 | 492104 | 3682171 | Apatite | Basalt | Amygdular | 1247 | ± 52 | 0.71 | 0.9714 | 1286 | ± 42 | 1.40 | 25.70 | Hydrothermal |
| RE15JP073 | 491610 | 3681604 | Apatite | Basalt | Amygdular | 1020 | ± 74 | 0.52 | 0.9714 | 1154 | ± 49 | 1.70 | 16.50 | Hydrothermal |
| RE15JP150 | 489876 | 3686937 | Apatite | Dolerite | Matrix | 1153 | ± 19 | 4.70 | 0.9714 | 1155 | ± 22 | 5.90 | 2363 | Magmatic |
| RE16JP081 | 495413 | 3683124 | Titanite | Basalt | Vein halo | 1138 | ± 62 | 5.90 | 0.9714 | 1153 | ± 56 | 6.90 | 110.2 | Hydrothermal |
| RE16JP060 | 494453 | 3681995 | Apatite | Dolerite | Matrix | 1122 | ± 66 | 1.40 | 0.9714 | 1152 | ± 36 | 1.40 | 2323 | Magmatic |
| RE15JP085 | 491655 | 3682404 | Apatite | Basalt | Amygdular | 1104 | ± 110 | 2.80 | 0.9714 | 1113 | ± 55 | 2.50 | 21.70 | Hydrothermal |
| RE16JP031 | 488275 | 3689553 | Apatite | Andesite | Matrix | 1131 | ± 330 | 0.43 | 0.879 | 1055 | ± 190 | 0.41 | 520.1 | Reset |
| RE15JP106 | 494937 | 3687453 | Apatite | Dolerite | Matrix | 1041 | ± 86 | 1.20 | 0.9714 | 1137 | ± 110 | 2.10 | 2769 | Magmatic |
| RE16JP157 | 490516 | 3685979 | Apatite | Dolerite | Matrix | 934 | ± 120 | 2.00 | 0.9714 | 1028 | ± 170 | 4.70 | 2613 | Magmatic |
| RE16JP019 | 490135 | 3688799 | Apatite | Skarn | Vein halo | 217 | ± 91 | 0.20 | N/A | N/A | N/A | N/A | 383.3 | Partially reset |
| RE16JP059 | 498240 | 3685548 | Apatite | Schist | Detrital | 78 | ± 17 | 2.50 | 0.879 | 82 | ± 19 | 3.20 | 249.4 | Reset |
| RE16JP071 | 492688 | 3687652 | Titanite | Quartz diorite | Skarn | 78.1 | ± 1.9 | 1.14 | 0.879 | 77.3 | ± 1.7 | 1.30 | 1490 | Hydrothermal |
| RE16JP150 | 493473 | 3684794 | Apatite | Volcanics | Matrix | 62 | ± 44 | 2.90 | 0.879 | 67 | ± 39 | 2.80 | 1675 | Magmatic |
| RE16JP200 | 491382 | 3688743 | Apatite | Quartz diorite | Vein halo | 63 | ± 15 | 0.00 | 0.879 | 38 | ± 390 | 5.00 | 1574 | Magmatic |
| RE15JP181 | 493491 | 3682895 | Apatite | Volcanics | Matrix | 53 | ± 20 | 1.11 | 0.879 | 61 | ± 15 | 1.14 | 2301 | Magmatic |
| RE16JP194 | 491809 | 3689102 | Apatite | Dolerite | Vein halo | 66.5 | ± 8.5 | 0.73 | 0.879 | 60.4 | ± 7.3 | 1.19 | 1117 | Reset |

interpreted to have been partially or totally reset by metasomatism. Sample RE16JP059 is a particularly good example of this phenomenon, where highly abraded and rounded apatites returned a Laramide age. Two other samples from the Pinal Schist (RE16JP019 and RE16JP031) also returned ages younger than that of their host rocks and have intermediate Ce, values suggestive of incomplete hydrothermal resetting (Table 6.5; Figure 6.7).

#### 6.4.4.1 Metamorphic apatite

The apatite analyses from RE16JP191 show the presence of three distinct Pb components in the full data set (Appendix 2F). The Proterozoic common Pb component has a $^{207}Pb/^{206}Pb$ weighted average of 0.925. The Cretaceous common Pb component has a $^{207}Pb/^{206}Pb$ weighted average of 0.848. A radiogenic Pb component has low $^{206}Pb/^{207}Pb$ and high $^{238}U/^{206}Pb$ ratios. A five point, low precision isochron using the high $^{207}Pb/^{206}Pb$ common Pb group and the radiogenic component intercepts concordia at 1,538 ± 290 (MSWD 2.5). Splitting the laser ablation profile data into eight individual segments (e.g., Petrus and Kamber, 2012; Kamenetsky et al., 2016) increases the number of points along the isochron towards radiogenic Pb and improves the MSWD but makes no differences to the uncertainty on the revised age determination of 1,645 ± 290 with an MSWD of 1.5 (Figure 6.8 A). RE16JP035 contains more radiogenic Pb than RE16JP191 and defines a coherent seven point isochron producing a similar Paleoproterozoic lower intercept age on Concordia of 1,601 ± 270 Ma.

#### 6.4.4.2 Hydrothermal apatite

Five of the samples analysed had textural and/or trace element (low REE) characteristics, consistent with crystal growth in a hydrothermal environment (RE15JP088, RE15JP085, RE15JP073, RE16JP071 RE16JP081; Table 6.5, Mao et al., 2016). Four of these returned Proterozoic ages (RE15JP088, RE15JP085, RE16JP081 and RE15JP073). These all plot on reasonably well constrained isochrons, with MSWDs ranging from 1.4 to 6.9 (Figure 6.8 B). Three of the Proterozoic samples define a tight range from 1,153 ± 45 Ma to 1,113 ± 55 Ma, while the fourth returns a considerably older age of 1,247 ± 52 Ma (RE15JP088; Figure 6.8 B). One sample returned a Late Cretaceous age of 77.0 ± 1.7 Ma (Table 6.5, Figure 6.8 D).

#### 6.4.4.3 Magmatic apatite

Six samples had textural and trace element characteristics indicating growth in a magmatic environment. Four of the samples have apatite ages that cluster between 1,153 ± 56 and 1,028 ± 170 Ma, a range overlapping with the hydrothermal apatite (Table 6.5, Figure 6.8 C). Three of the samples have much younger, low precision Cretaceous ages (67 ± 39 Ma, 61 ± 15 Ma and 63 ± 31 Ma; Table 6.5, Figure 6.8 E).

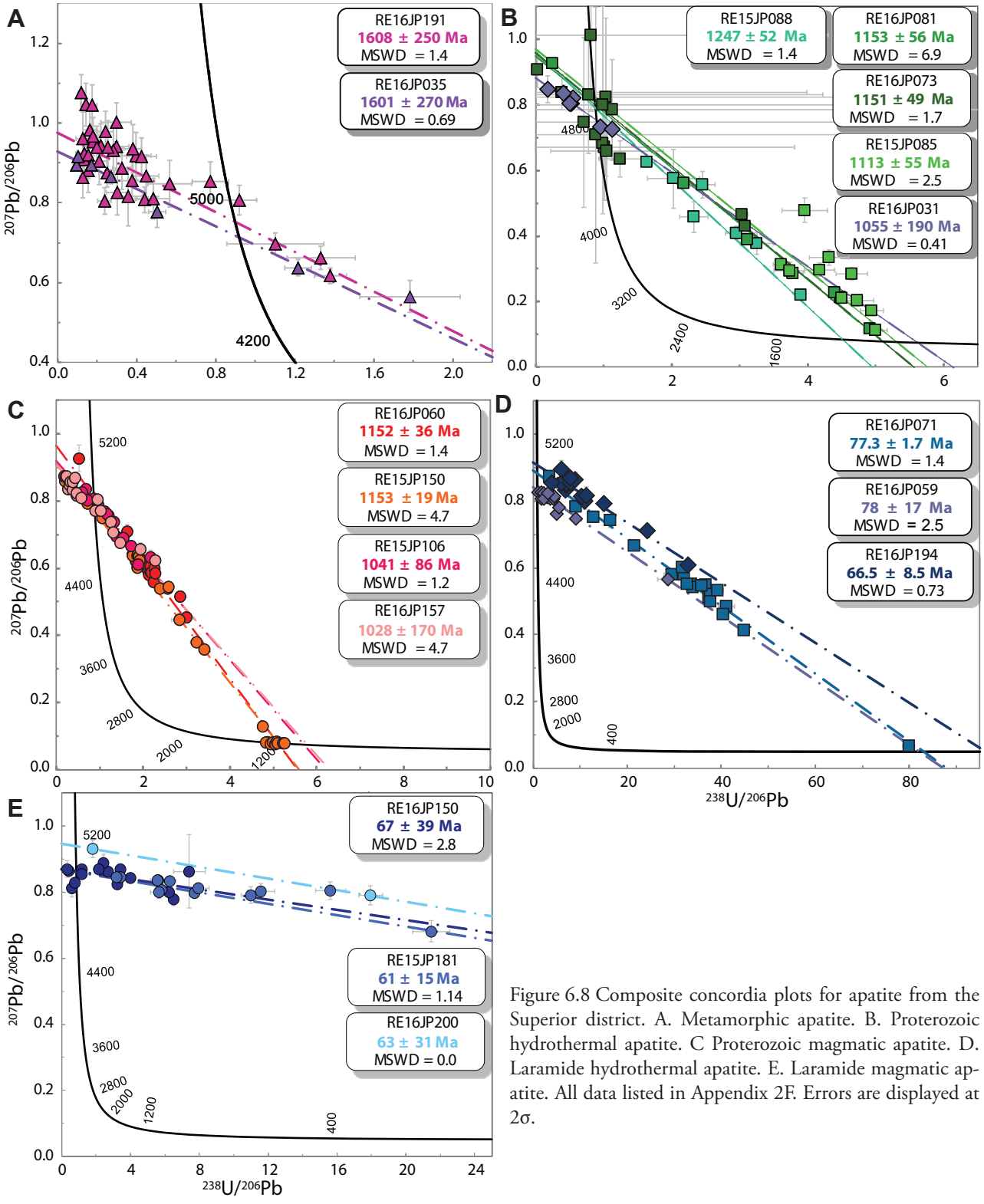


Figure 6.8 Composite concordia plots for apatite from the Superior district. A. Metamorphic apatite. B. Proterozoic hydrothermal apatite. C Proterozoic magmatic apatite. D. Laramide hydrothermal apatite. E. Laramide magmatic apatite. All data listed in Appendix 2F. Errors are displayed at 2σ.

#### 6.4.4.4 Reset apatite

Four samples have intermediate REE concentrations and are interpreted to have had their REE concentrations and U-Pb systematics either partially or totally reset (RE16JP019, RE16JP031, RE16JP59 and RE16JP197; Table 6.5). RE16JP019 returns an anomalous and isolated but reasonably precise age of 217 ± 19 Ma (Table 6.5).RE16JP031, RE16JP059 and RE16JP194 have intermediate Ce

concentrations and present younger apatite ages than their host rocks.

Apatite data from RE16JP031 return a preferred age of 1,055 ± 190 Ma, but is hosted in a Paleoproterozoic andesite dike from the Pinal schist. The apatite age is younger than its host rock and its Ce concentrations are lower than the magmatic apatites but higher than the hydrothermal apatite (Table 6.5). It is therefore interpreted that magmatic apatite crystals from this sample were reset by hydrothermal processes that postdate andesite emplacement.

Sample RE16JP194 is hosted in Mesoproterozoic dolerite but returned an age of 60.4 ± 7.3 Ma. It has a high Ce concentration (1,116 ppm; Table 6.5) suggesting apatite originally crystallised under magmatic conditions. This sample was collected proximal to the Laramide quartz diorite stock (Figure 6.1). The apatite is interpreted to have originally been Proterozoic in origin but the age was reset during Laramide magmatism.

Apatite U-Pb data from the Pinal Schist RE16JP059 illustrates perhaps the most compelling demonstration resetting of U-Pb composition in the Superior district. Apatites from this sample are texturally abraded (Figure 6.6 C), indicative of a detrital origin and incorporation into the ~1,650 Ma sandstone protolith of the Pinal Schist (Figure 6.6 C). However, U-Pb dating of this apatite yielded a Laramide age of 78 ± 17 Ma (Table 6.5). This result demonstrates emphatically that apatites from this sample have undergone complete U-Pb resetting accompanied by partial loss of REE, presumably due to heat from a nearby intrusion over 1,500 m.y. after initial deposition.

### 6.4.5 Discussion

The U/Pb data collected from apatites provides critical insight into major metasomatic and magmatic events that affected the Superior District. Magmatic ages returned from groundmass apatites of the 1,100 Ma dolerite sills, and matrix apatites from the 74-65 Ma volcaniclastic rocks are consistent with previously published conventional geochronology results for these rocks (c.f. dolerite - Bright et al., 2014; Cretaceous volcanic rocks - Zulliger, 2007; Table 3.2). Although the widely accepted age for sill emplacement is 1,100 Ma, a compilation of dates published by Bright et al. (2014) demonstrates that emplacement likely spans an age range of 1,110 – 1,070 Ma.

Several important observations can be made regarding the non-magmatic apatite ages. Firstly, although there is a wide range of ages (1,608 ± 250 to 60.4 ± 7.4 Ma), the clusters of ages around ~1,600 Ma, ~1,200 to 1,000 Ma and 77-60 Ma correlate with known events in the wider western US region.

The ~1,600 Ma ages from RE16JP191 and RE16JP035, albeit imprecise, are in broad agreement with ages reported previously for the period of crustal assembly and metamorphism (1,650 – 1,600 Ma Mazatzal Orogeny, Karlstrom and Bowring, 1988; Eisele and Isachson, 2001; Swift and Force 2001; Meijer, 2014; Figure 6.9), and the approximate age of the Madera Diorite that intrudes the schist in the Globe-Miami area (K-Ar and Rb-Sr ages ranging from 1,775 Ma to 1,578 Ma; Creasey, 1980). The presence of some Cretaceous common Pb in sample RE16JP191, suggests that this sample was partially

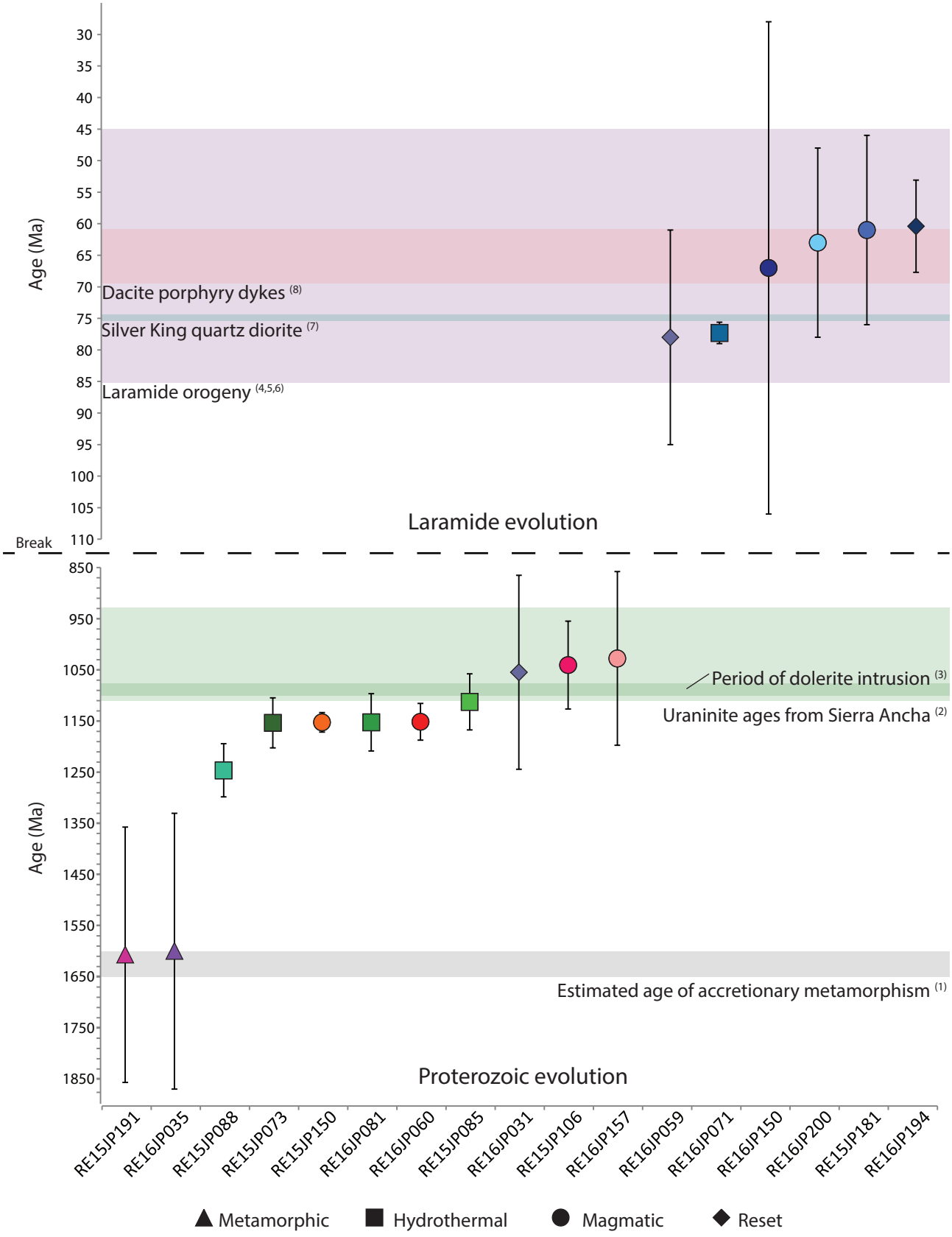


Figure 6.9 Geochronological evolution diagram showing apatite U-Pb age data plotted in context of known regional events. References - (1) Karlstrom and Bowring (1988); (2) Neuerburg and Granger (1960); (3) Bright et al. (2014) and references therein; (4) Dickinson (1989); (5) Titley and Zurcher (2008); (6) Leveille and Stegen (2012); (7) Hehnke et al. (2012); (8) Seedorff et al. (2005).

reset, presumably due to the emplacement of the nearby Cretaceous quartz diorite stock.

The 1,247 ± 52 to 1,113 ± 55 Ma U-Pb ages obtained from hydrothermal apatite from the amygdales in the Apache Basalt correlate well with magmatic crystallisation ages for the dolerite obtained by U-Pb analysis of magmatic apatite from this study (1,153 ± 19 to 1,028 ± 170 Ma) and from zircon and baddelyite from previous studies (ca. 1,110 to 1,075 Ma; Bright et al. 2014, Figure 6.9). These results demonstrate that hydrothermal alteration in the Apache Basalt and other Proterozoic rocks occurred during the late Meso- to early Neoproterozoic, most likely associated with the emplacement of the dolerite sills. This event reset Paleoproterozoic apatite (RE16JP031) to 1,055 ± 190 Ma (Table 6.5, Figure 6.8 B, Figure 6.9). The coincidence between age ranges defined by magmatic apatites from dolerite sills (1,153 ± 19 to 1,028 ± 170 Ma; Table 6.5) and hydrothermal apatites from the Apache basalts (1,247 ± 52 to 1,113 ± 55 Ma; Table 6.5) provides further support for this genetic relationship. Dolerite emplacement has previously been related to mineral occurrences in the Apache Group (Wrucke et al., 1986; Table 6.2). U-Pb age determinations obtained from uraninite and galena from some of these occurrences of the Sierra Ancha region were published by Neuerburg and Granger (1960), and define a similar period from 1,104 to 930 Ma, although no uncertainties were reported. Although there is no accompanying information for their data, they overlap in error with the hydrothermal apatites from the Superior district (Table 6.5). Similar Proterozoic basins elsewhere show similar alteration features. In northern Australia, world-class sediment-hosted base-metal style ores, such as HYC, McArthur River and Century are hosted in sedimentary sequences where oxidised brines have leached metals from the country rocks (e.g., Cooke et al., 1998, 2000; Davidson et al., 1998). The similarity in alteration style in the Superior district suggest potential for sediment-hosted base metal deposits in the Apache Group and its correlates.

The younger apatite ages (Figure 6.9) are clustered tightly between 77.0 ± 1.7 and 60.4 ± 7.3 Ma, and are defined by both magmatic and hydrothermal apatite (Figure 6.8). Laramide apatite ages were also obtained from Proterozoic rocks, suggesting significant resetting during Laramide magmatic-hydrothermal activity (e.g., RE16JP059 and RE16JP194; Table 6.5). The Laramide Orogeny caused widespread plutonism and magmatic-hydrothermal activity in the Superior district and elsewhere in southwest Arizona (Titley, 1982; Leveille and Stegen, 2012). Unfortunately, the precision of most of the apatite ages obtained in the current study cannot discriminant between early and later Laramide magmatic hydrothermal events. One quartz diorite hosted skarn sample (RE16JP071) returned a precise age of 77.0 ± 1.7 Ma (Table 6.5), allowing identification of an early Laramide hydrothermal event in the Superior district that predates the Resolution porphyry deposit (ca. 65 - 61 Ma; Hehnke et al., 2012; Table 6.5, Figure 6.8 D, Figure 6.9). The early Laramide age is in good agreement (within 2%) with the age of the causative stock (primary biotite $^{40}Ar/^{39}Ar$ age of 74.8 ± 0.33 Ma; Hehnke et al., 2012, Table 3.2). The small discrepancy in these two ages may be due to LA-ICP-MS matrix effects for the apatite analyses (e.g., Thompson et al., 2016).

## 6.5 Epidote Geochronology

### 6.5.1 Introduction

This study has attempted to use epidote as a geochronometer of hydrothermal activity in order constrain the origin of the widespread epidote alteration from the Superior district. This potentially allows epidote to be used as a geochemical screening tool to be used when acquiring routine trace element analyses. Cooke et al. (2014) and Wilkinson et al. (2015) demonstrated that the chemistry of epidote (and chlorite) changes systematically with distance from a porphyry centre. However, in ancient terranes that have protracted geologic histories and widespread, variable styles of epidote-bearing alteration, such as in the Superior district, a screening technique is required to isolate epidote of the appropriate age before attempting to vector towards mineralisation.

Results from apatite dating suggest that Mesoproterozoic hydrothermal fluids affected the rocks of the Superior district, a notion supported by previous studies (Wrucke et al., 1986). Mesoproterozoic epidote alteration most likely formed when connate fluids were heated and mobilised by the intrusion of dolerite sills, that efficiently transported U, Pb and a suite of other base-metals, which, under the right conditions could be incorporated into the A or M sites of epidote (c.f., Duncan and Maas, 2014). Given the U-bearing potential of epidote from the Superior district attempts were made to directly date epidote using the U-Pb method whilst collecting routine trace element data for mineral chemistry purposes. Apatite and titanite dating results were used to validate these epidote dating results.

### 6.5.2 Previous Work

Historically, epidote geochronology focussed on fission track techniques to date movement on faults, with some success (Naeser et al., 1970; Bar et al., 1974). Early attempts at epidote dating using U-Pb techniques were reported by Frei and Kamber (1995), Buick et al. (1999) and Cooke (2001). Direct dating of epidote has often proved difficult due to a number of factors such as low U concentrations, high common Pb, internal oscillatory/sector zoning as well as a lack of suitable reference materials (Duncan and Maas, 2014). More recently, Duncan and Maas (2014) attempted to date epidote directly using a stepwise leaching digestion method in order to eliminate unrelated Pb from fractures and/or micro inclusions, followed by multi-collector ICP-MS analysis. The stepwise method used progressively stronger acids to remove Pb from fractures and amorphous domains in early steps and retaining refractory micro-inclusions until the final HF dissolution step, thereby concentrating lattice bound Pb in the middle steps. However, results from Duncan and Maas (2014) showed that age determinations using this method were significantly older that the age of peak metamorphism and that Pb was probably inherited from the host rocks.

During the last decade, the application of U-Th-Pb geochronology of allanite (isomorphous with epidote) using LA-ICP-MS has received significant attention. Much of this work has been the development of

Table 6.6 Summary of LA-ICP-MS methods used in epidote U-Pb geochronology

| Laser parameter | Geochronology method | Trace element method |
|---|---|---|
| Mass List | $^{24}$Mg, $^{21}$P, $^{29}$K, $^{43}$Ca, $^{49}$Ti, $^{57}$Fe, $^{89}$Y, $^{140}$Ce, $^{202}$Hg, $^{204}$Pb, $^{206}$Pb, $^{207}$Pb, $^{208}$Pb, $^{238}$U, $^{235}$Th | $^{7}$Li, $^{11}$B, $^{23}$Na, $^{24}$Mg, $^{27}$Al, $^{29}$Si, $^{39}$K, $^{43}$Ca, $^{47}$Ti, $^{49}$Ti, $^{51}$V, $^{53}$Cr, $^{55}$Mn, $^{57}$Fe, $^{59}$Co, $^{60}$Ni, $^{65}$Cu, $^{66}$Zn, $^{75}$As, $^{88}$Sr, $^{89}$Y, $^{90}$Zr, $^{93}$Nb, $^{107}$Ag, $^{109}$Ag, $^{118}$Sn, $^{121}$Sb, $^{137}$Ba, $^{139}$La, $^{140}$Ce, $^{153}$Eu, $^{157}$Gd, $^{172}$Yb, $^{175}$Lu, $^{178}$Hf, $^{181}$Ta, $^{197}$Au, $^{205}$Tl, $^{206}$Pb, $^{207}$Pb, $^{208}$Pb, $^{209}$Bi, $^{232}$Th, $^{238}$U |
| Spot size | 110 μm | 30 μm |
| Laser fluence | 3.61 J/cm$^2$ | 3.56 J/cm$^2$ |
| Background length | 20 s | 30 s |
| Laser repetition rate | 10 Hz | 5 Hz |
| Analysis length | 90 s | 90 s |
| Effective sweep time | 164 ms | 933 ms |
| Pb isotope dwell time | 20 ms ($^{204}$Pb), 10 ms $^{206}$Pb, $^{207}$Pb, $^{208}$Pb | 20 ms |
| $N_2$ gas addition | Yes | No |

standard reference materials and LA-ICP-MS procedures (von Blackenburg, 1992; Gregory et al., 2007; Darling, 2012; Smye et al., 2014; McFarlane, 2016). However, owing to the similarity between allanite and other REE accessory phases such as monazite and xenotime and the general lack of allanite in common hydrothermal alteration assemblages, application of this method has primarily been directed towards dating metamorphic processes (Gregory et al., 2009; Boston et al., 2017).

### 6.5.3 Methods

#### 6.5.3.1 Laser ablation ICP-MS

Eighteen samples were chosen to span a range of rock and alteration types, including comparative samples that were dated using U-Pb on apatite and titanite. Two epidote geochronology methods were trialled in this study, both using the same instrumentation described in section 6.4.2 used for apatite and titanite analyses. The first of the two methods, identical to that used for apatite and titanite analysis (Table 6.5) is optimised for U-Pb geochronology so that only a few major and trace elements were analysed. The analysed isotopes are listed in Table 6.6. Samples that contained enough radiogenic Pb for U-Pb dating, plus some additional samples, were re-analysed using a second method optimised for trace element chemistry with 44 isotopes (Table 6.6), similar to that used by Cooke et al. (2014), but with the addition of $^{206}$Pb and $^{207}$Pb, counted for similar periods as the other trace elements. LA-ICP-MS ages derived from epidote are unanchored, allowing unbiased best fitting of the isochron. Matrix matched reference materials were not available for epidote, and so downhole fractionation was corrected using the 91500 zircon standard (Weidenbeck et al., 1995). To evaluate the accuracy and precision of both methods, the results have been compared to ages obtained from apatite from the same sample as well as data collected independently using the solution multi-collector ICPMS (Figure 6.11, Figure 6.12;

Appendices 2G and 2H).

#### 6.5.3.2 Isotope dilution multi-collector ICPMS

LA-ICP-MS geochronology data can be subject to matrix effects due to differential fractionation of U and Th from Pb when analysed in different minerals (Thompson et al., 2016, and references therein).The isotope dilution multi-collector ICPMS (ID-MC-ICPMS) offers a more precise technique free from the matrix effects related to ablating solid material. Therefore, three samples were sent for ID-MC-ICPMS analysis at the University of Melbourne.

Epidote grains were separated by the author at the University of Tasmania. Small quantities of whole rock material from each sample were coarsely crushed in a steel mortar and pestle and panned to remove fine grained particles. Three size fractions (coarse, medium, fine) were examined to establish the fraction that yielded the best epidote grains for separation. The epidote-dominant fraction was further concentrated by panning in a watch-glass and then dried at $50^0$C for 24 hours. The largest epidote grains were handpicked from the dried concentrate using a needle and binocular microscope. Samples were then sent to Dr Roland Maas for digestion and analysis at the University of Melbourne. Three to four fractions (0.7-16 mg) from each sample were cleaned and digested in dilute acid and then split to provide small aliquots for trace element analysis. Where appropriate, epidotes were equilibrated with $^{233}$U-$^{205}$Pb spikes. Isotope ratios were measured on a Nu Plasma MC-ICPMS equipped with 10-11 Ω Faraday detectors and a CETAC Aridus desolvating system. All data reduction was done using the EarthTime MS Excel spreadsheet of Schmitz and Schoene (2007).

To ensure that there were no issues with the dissolution, separation and analysis, five fractions of titanite from the well characterised monzonite at Mt Dromedary (SE Australia) were analysed as a secondary standard. They produced an age of 98.91 ± 0.29 Ma, consistent with high-precision biotite Ar-Ar (99.1 ± 0.1 Ma, Phillips et al., 2017) and zircon $^{206}$Pb/$^{238}$U zircon (99.12 ± 0.02 Ma, Schoene et al., 2006).

### 6.5.4 Results

#### 6.5.4.1 LA-ICP-MS epidote dating

***Geochronology method***

The full epidote U-Pb isotope dataset for all 203 spot analyses by the geochronology method and 117 analyses by the trace element method analyses are available in Appendix 2G. Of the eighteen samples analysed by the LA-ICP-MS method optimised for U-Pb geochronology, only four samples contained sufficient radiogenic Pb for dating (Table 6.7). The remaining samples are dominated by common Pb (Appendix 2G). The Pb isotopic compositions of these non-radiogenic samples is discussed in detail in Chapter 9.

Individual spot analyses were used to construct isochrons and the data have been compared to the apatite

Table 6.7 Comparative results of U-Pb dating of apatite and epidote using the same analytical method and between epidotes analysed using different methods, including ages determined from the trace element method without corresponding apatite or epidote ages determined using the optimised geochronology method.

| Sample ID | Rock Type | UTM mE | UTM mN | Apatite/Titanite (Geochronology method) | | | Epidote (Geochronology method) | | | Epidote (Trace element method) | | |
|---|---|---|---|---|---|---|---|---|---|---|---|---|
| | | | | Age (Ma) | Error | MSWD | Age (Ma) | Error | MSWD | Age (Ma) | Error | MSWD |
| RE15JP073 | Basalt | 491610 | 3681604 | 1,151 | ± 48 | 1.7 | 1,266 | ± 57 | 0.89 | 1,253 | ± 81.0 | 1.6 |
| RE15JP088 | Basalt | 492104 | 3682171 | 1,247 | ± 52 | 0.71 | 1,404 | ± 26 | 0.48 | Not analysed | | |
| RE16JP036 | Schist | 487333 | 3688871 | Not analysed | | | 1,230 | ± 160 | 2.7 | 1,048 | ± 180 | 0.29 |
| RE16JP071 | Quartz diorite | 492688 | 3687652 | 77.30 | ± 1.7 | 1.3 | 85.60 | ± 6.0 | 0.91 | 84 | ± 23.0 | 0.71 |
| RE16JP006 | Basalt | 492558 | 3679925 | Not analysed | | | | | | 1135 | ± 84 | 18 |
| RE16JP034 | Basalt | 487771 | 3687053 | | | | | | | 858 | ± 100 | 0.45 |
| RE16JP082 | Basalt | 495411 | 3683126 | | | | | | | 1084 | ± 66 | 0.99 |
| RE16JP082b | Basalt | 495411 | 3683126 | | | | | | | 1203 | ± 40 | 6.7 |
| RE16JP083 | Basalt | 495402 | 3683137 | | | | | | | 1173 | ± 170 | 2.0 |

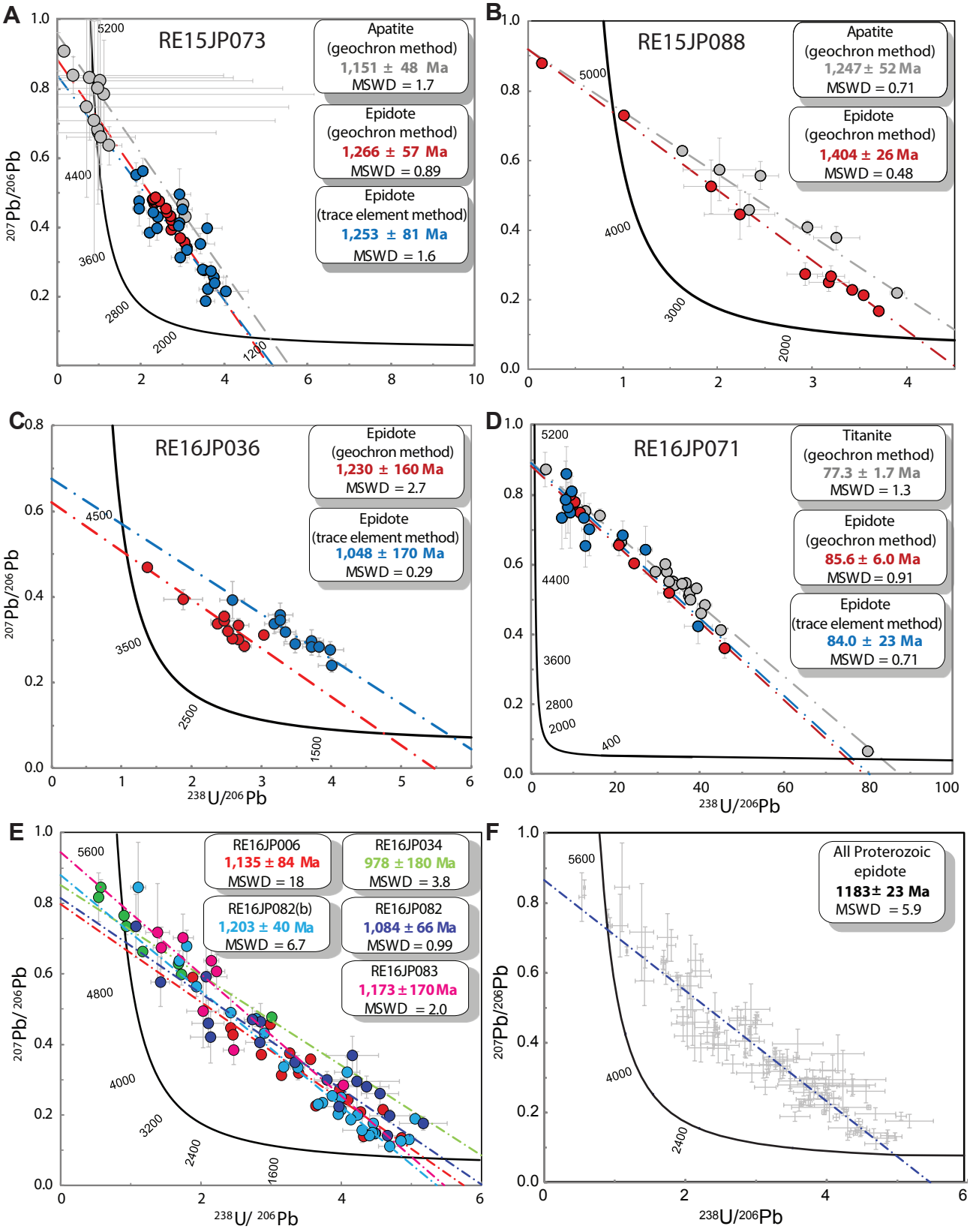


Figure 6.10 Concordia plots showing the comparison between geochronological results from apatite and epidote from the same using the same method and between geochronological results from epidote using different methods. A. RE15JP073. B. RE15JP088. C. RE16JP036 D. RE16JP071. E. All remaining results from epidote using the trace element method, without comparative results using the geochronology method. F All Proterozoic epidote analyses from the trace element method. Errors are given at 1σ. All data presented in Appendix 2F and 2G.

geochronology data from the same samples (Figure 6.10 A - D). Although there is broad agreement between epidote and apatite derived ages for the same samples, the ages returned by epidotes are typically 10-15% older than those from apatites (Table 6.7). Errors and MSWDs from the epidote analyses are significantly better than those from apatite (Table 6.7). Additionally, some samples show a significant increase in radiogenic Pb in epidote compared to that in apatite (RE15JP073 and RE15JP088; Figure 6.10) This initial trial suggests that under certain conditions epidote can host sufficient U to be dated using LA-ICP-MS.

***Trace element method***

The trace element method provided both epidote geochronological data and trace element concentrations for vectoring from the same samples. Results are presented in Table 6.7 and Figure 6.10, which compare epidote ages derived from the geochronology and trace element methods. The trace element method yielded ages that are comparable to the geochronology method for the same sample. Only one sample, RE16JP031, has ages that do not overlap in error (Table 6.7). Five additional samples that were analysed without comparative apatite or epidote ages from the geochronology method yield ages that span a range from 1,203 ± 40 to 978 ± 180 Ma (Figure 6.10 E). A combined isochron, derived from all samples analysed using the trace element method yielded an age of 1,183 ± 23 Ma (Figure 6.10 F).

### 6.5.4.2 Isotope dilution multi-collector ICP-MS

The full ID-MC-ICP-MS data set can be found in Appendix 2H. The results for each sample are summarised below.

***RE16JP071***

On the $^{238}U$-$^{206}Pb$ and $^{235}U$-$^{207}Pb$ isochron plots, epidote U-Pb dating results define linear arrays with apparent ages of 72.5 ± 8.9 Ma and 73 ± 15 Ma, respectively suggesting that the U-Pb systems are coeval and undisturbed (Figure 6.11 A-B). Using the Magma galena common Pb anchor (Table 6.3), the data on the Tera-Wasserburg Concordia diagram yield an intercept of 73.9 ± 3.1 Ma with MSWD of 6.6 (Figure 6.11 C).

***RE15JP073***

The U isotope dilution run for RE15JP073 failed and U/Pb ratios had to be calculated from trace element results, leading to a possible loss of precision of several percent. This may have been the reason for considerable amounts of scatter in the U-Pb isochron plots (Figure 6.11 E-F). Age regressions for the three data points thus have very large uncertainties ($^{238}U$-$^{206}Pb$ 1,032 ± 750 Ma $^{235}U$-$^{207}Pb$ 1,049 ± 600 Ma; Figure 6.11 D-E). More robust and precise ages were obtained using only the Pb isotopic compositions. On the $^{207}Pb/^{204}Pb$ vs $^{206}Pb/^{204}Pb$ and inverse $^{207}Pb/^{206}Pb$ vs $^{204}Pb/^{206}Pb$ isotope diagrams, the three data points form identical isochrons of 1,085 ± 52 Ma (MSWD 0.28) and 1,086 ± 57 Ma

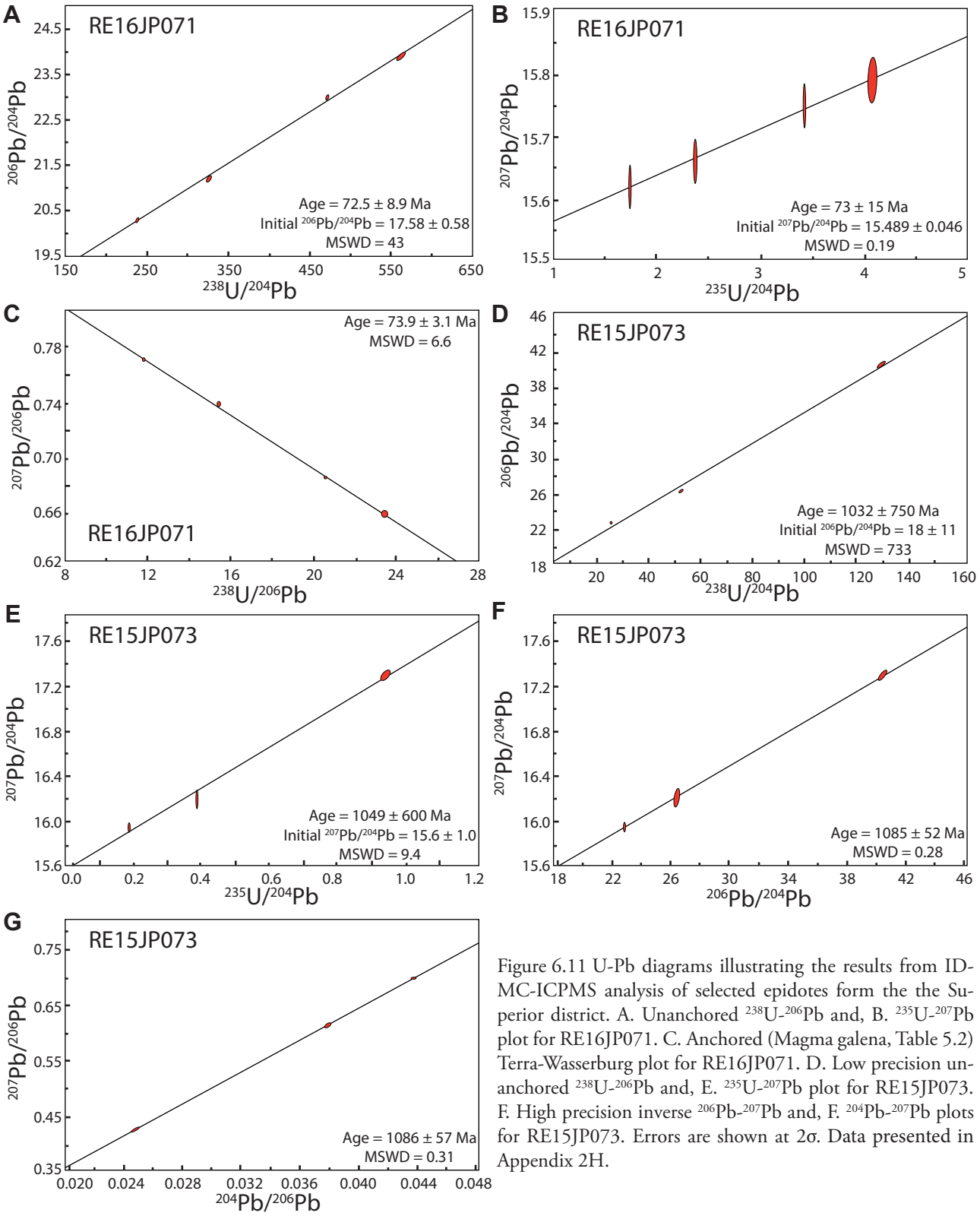


Figure 6.11 U-Pb diagrams illustrating the results from ID-MC-ICPMS analysis of selected epidotes form the the Superior district. A. Unanchored $^{238}U$-$^{206}Pb$ and, B. $^{235}U$-$^{207}Pb$ plot for RE16JP071. C. Anchored (Magma galena, Table 5.2) Terra-Wasserburg plot for RE16JP071. D. Low precision unanchored $^{238}U$-$^{206}Pb$ and, E. $^{235}U$-$^{207}Pb$ plot for RE15JP073. F. High precision inverse $^{206}Pb$-$^{207}Pb$ and, F. $^{204}Pb$-$^{207}Pb$ plots for RE15JP073. Errors are shown at 2σ. Data presented in Appendix 2H.

(MSWD 0.31), respectively (Figure 6.11 F-G). The reasonably large age uncertainties are the result of the limited range of isotopic compositions.

### *RE15JP181*

LA-ICP-MS data for epidote from this sample revealed very low U/Pb and is dominated by common Pb (Appendix 2H). This was identified initially from semi-quantitative solution-mode ICPMS scans of

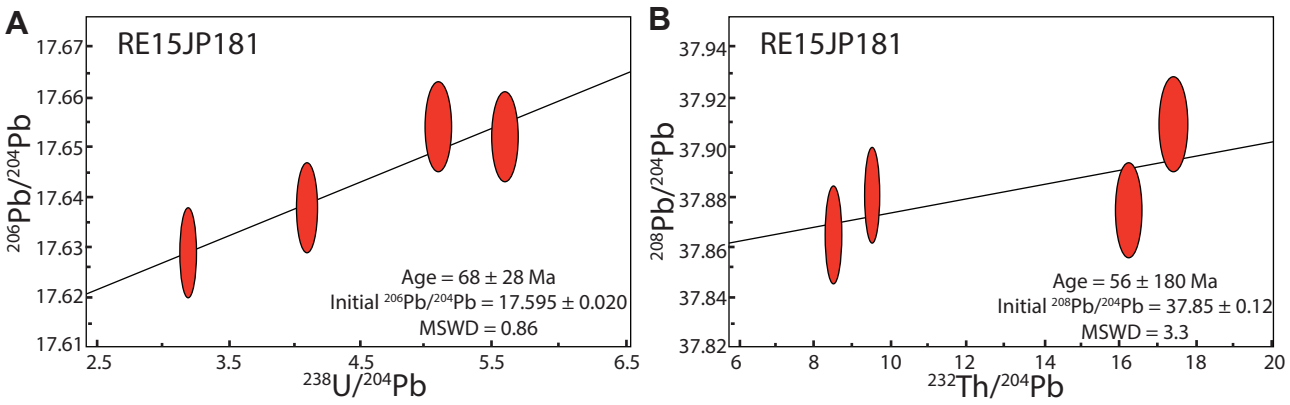


Figure 6.12 A. $^{238}U$-$^{206}Pb$ and B. $^{232}Th$-$^{208}Pb$ diagrams from ID-MC-ICPMS analysis of RE15JP181. Ages are low precision due to the presence of common Pb. Errors are shown at 2σ. Data presented in Appendix 2H

sample solutions prior to splitting the trace element aliquot. Because of these issues, the four fractions for RE15JP181 were not spiked. Despite the low U/Pb and Th/Pb and small range in Pb isotope ratios, the data form linear arrays on U-Pb and Th-Pb isochron diagrams ($^{238}U$-$^{206}Pb$; 68 ± 28 Ma, MSWD 0.86; $^{232}Th$-$^{208}Pb$; 56 ± 180 Ma, MSWD 3.3; Figure 6.12). Regressions were done assuming two sigma input errors of ± 2% for U/Pb and Th/Pb, and ± 0.05% for the $^{206}Pb/^{204}Pb$ and $^{208}Pb/^{204}Pb$. While imprecise, these ages support a Late Cretaceous age for epidote in RE15JP181. The initial Pb composition is similar to RE16JP071 (Appendix 2H).

### 6.5.5 Discussion

When comparing epidote and apatite ages from the same sample, determined using the same analytical parameters, there is a ~10% offset between the ages from the two minerals (Table 6.7). This consistent discrepancy is indicative of analytical matrix effects related to the lack of an epidote standard material (c.f., Thompson et al., 2016). Given the lack of epidote standard reference material, the matrix effects observed in the current study could relate to a wide range of factors, including variable ablation rate between epidote and the non-matrix matched standard reference material, and also the 1-3% uncertainty in corresponding apatite age calculations caused by LIEF-type processes described earlier. The lack of a matrix-matched epidote standard means that mass bias and down-hole corrections needed to be made using a zircon standard, and this probably contributed to the observed offset in ages between the apatite and epidote ages. The development of an epidote standard would significantly improve epidote dating results. Overall, the results of this study demonstrate that some epidote samples have significant quantities of U and can be used for directly dating hydrothermal events.

Comparing the results from both epidote U-Pb dating methods trialled here, there are significantly higher uncertainties associated with the simultaneous collection of trace element data and geochronology data. Nevertheless, the results are within analytical uncertainty in two of the samples (RE15JP073 and RE16JP071) and MSWDs remain similar across the dataset (Table 6.7).

Analysing additional extra Pb isotopes adds significant value to the mineral chemistry workflow of

Cooke et al. (2014). It provides a valid, first pass estimation of epidote age while collecting a routine trace element suite. It also highlights epidotes suitable for reanalysis using the geochronology method to obtain more precise ages if required. In areas where periods of epidote growth are separated by significant time intervals, such as in Arizona, the combination of geochronology and trace element collection represents a fit for purpose approach for distinguishing multiple epidote-forming events.

In the case of the Superior district, sample RE16JP071 returned a well-correlated isochron age for the ID-MC-ICPMS data (73.9 ± 3.1 Ma; Figure 6.11 C), which is within uncertainty of the LA-ICP-MS titanite age from this sample (77.3 ± 1.7 Ma; Figure 6.8 D). Despite the failure of the isotope dilution run for RE15JP073, a robust Pb-Pb age of 1,085 ± 52 Ma was calculated, which falls well inside the error window defined by apatite data for this sample (1,151 ± 48 Ma; Table 6.7). Similarly to RE16JP071, the ~10% offset in isotope dilution and LA-ICP-MS epidote ages relate to the lack of an appropriate epidote LA-ICP-MS standard.

## 6.6 Conclusions

New geochronological results for hydrothermal alteration and mineralisation in the Superior district have revealed the presence of a major Mesoproterozoic hydrothermal system, in addition to the Laramide intrusive related alteration systems. These results have significant implications for mineral exploration which are considered in detail in Chapters 7 and 8.

### 6.6.1 Ar-Ar dating

Ar-Ar geochronology of muscovite from the Silver King area (74.31 ± 0.11 and 75.70 ± 0.12 Ma; Table 6.2, Figure 6.5) demonstrates that hydrothermal alteration in this area is associated with early Laramide intrusive rocks currently exposed at the surface (quartz diorite, 74.8 ± 0.33 Ma, dacite plug, 73.6 ± 1.6 Ma; Hehnke et al., 2012). The muscovite-altered wall rocks to the Magma vein were altered around 68.22 ± 0.11 to 67.39 ± 0.29 Ma, 3-4 m.y. prior to the commencement of molybdenite mineralisation at Resolution (65.1 ± 0.3 Ma; Table 6.2, Figure 6.5). Ar-Ar geochronology of K-feldspar returned a minimum age of ca. 190-200 Ma, suggesting some degree of resetting of a Proterozoic age.

### 6.6.2 U-Pb apatite dating

Conventional U/Pb geochronology of accessory apatite and titanite demonstrates several episodes of varied metasomatism in the Superior district, extending from Paleoproterozoic and Mesoproterozoic to Laramide times. Coincidence in age of hydrothermal apatites hosted within amygdales of the Apache Basalt (1,247 ± 52 to 1,113 ± 55 Ma, Table 6.5, Figure 6.8 B) and the magmatic crystallisation age of the dolerite sills, determined from magmatic apatites in this study (1,153 ± 19  1,028 ± 170 Ma), U-Pb on zircon and baddelyite in previous studies (ca. 1,110 to 1,075 Ma; Bright et al., 2014) and uraninite ages from the Sierra Ancha uranium deposits (1,104 - 930 Ma; Neuerberg and Granger, 1960; Figure 6.9) suggests a genetic relationship between the emplacement of the sills, uranium (copper) deposits of

the central Arizona and apatite-bearing alteration of the Superior district (Figure 6.9). Apatite dating also indicates resetting of U-Pb systematics during dolerite intrusion and the later Laramide orogeny.

### 6.6.3 U-Pb epidote dating

Trial U-Pb dating of epidote suggests that under some circumstances, epidote contains sufficient U to be dated using LA-ICP-MS, demonstrating its potential as a geochronometer. Using an optimised geochronology method, epidote results were reproduced with the same precision as for apatite, but with a distinct matrix-related 10-15% offset in age determinations between epidote and apatite, as the result of using a zircon reference material to correct for laser-induced isotopic fractionation. The correlation of ages from epidote with those from apatite and titanite, confirm that both 1,183 ± 23 Ma Proterozoic and Laramide epidote alteration affected the Superior district. The U-Pb dating method allows discriminantion between Proterozoic and Laramide hydrothermal alteration in the Superior district and the wider southwest US porphyry Cu province. The development of a well characterised epidote standard reference material is required to ensure epidote's potential as a robust hydrothermal geochronometer.

# Chapter 7: Proterozoic metasomatism in the Superior district

## 7.1 Introduction

This chapter documents the products of hydrothermal alteration of the Proterozoic rocks in the Superior district and summarises previous observations from the wider Apache basin. A combination of field, petrographic, and geochemical evidence are presented to characterise the alteration mineralogy, timing relationships and to interpret the likely fluid sources responsible for alteration. It evaluates possible links between Proterozoic metasomatism and U-(Cu) mineralisation elsewhere in Arizona, and also Laramide mineralisation of the Superior district.

## 7.2 Previous Work

Mineralisation occurrences in Proterozoic rocks of the Southwest United States, in particular the Apache Group, have been sporadically studied since the 1950s, but have received little attention in recent years. Early studies focussed on the somewhat isolated mineral occurrences of the Sierra Ancha region, such as uranium (Granger and Raup, 1969; Nutt, 1984), asbestos (Bateman, 1923; Stewart, 1955), iron ore (Burchard, 1931; Harrer, 1964; Wrucke et al., 1986), often with reference to only a single host rock. Accordingly, hydrothermal alteration was in general, poorly documented or discussed, except by Granger and Raup (1969), or where observed petrographically in the studies of the dolerite sills (e.g., Shride, 1967; Smith, 1969, 1970; Nehru and Prinz, 1970; Fouts, 1974; Hammond, 1983). Actinolite - chlorite alteration of the Proterozoic dolerite was recognised and mapped by Force (1998) between Ray Cu-Mo porphyry system and the Superior district, although that study attributed the observed alteration to Laramide hydrothermal processes. Apart from Wrucke et al. (1986) there has been no systematic basin-wide study or mineral-systems review of the Apache Group of the Southwestern United States, despite the wide variety of mineral resources reported from this package of rocks.

In Arizona, hydrothermal alteration of the dolerite sills vary as a function of distance from the sill contact, with the intensity of alteration decreasing toward the centre of sills (Granger and Raup, 1969). Dolerite within 30 - 45 m of sill margins in the Sierra Ancha and Salt River areas are intensely altered, with pyroxenes altered to amphibole, chlorite, epidote, and serpentine; olivine to talc; and plagioclase to albite and/or sericite. Very close to the contact, biotite, and in some cases K-feldspar, is abundant.

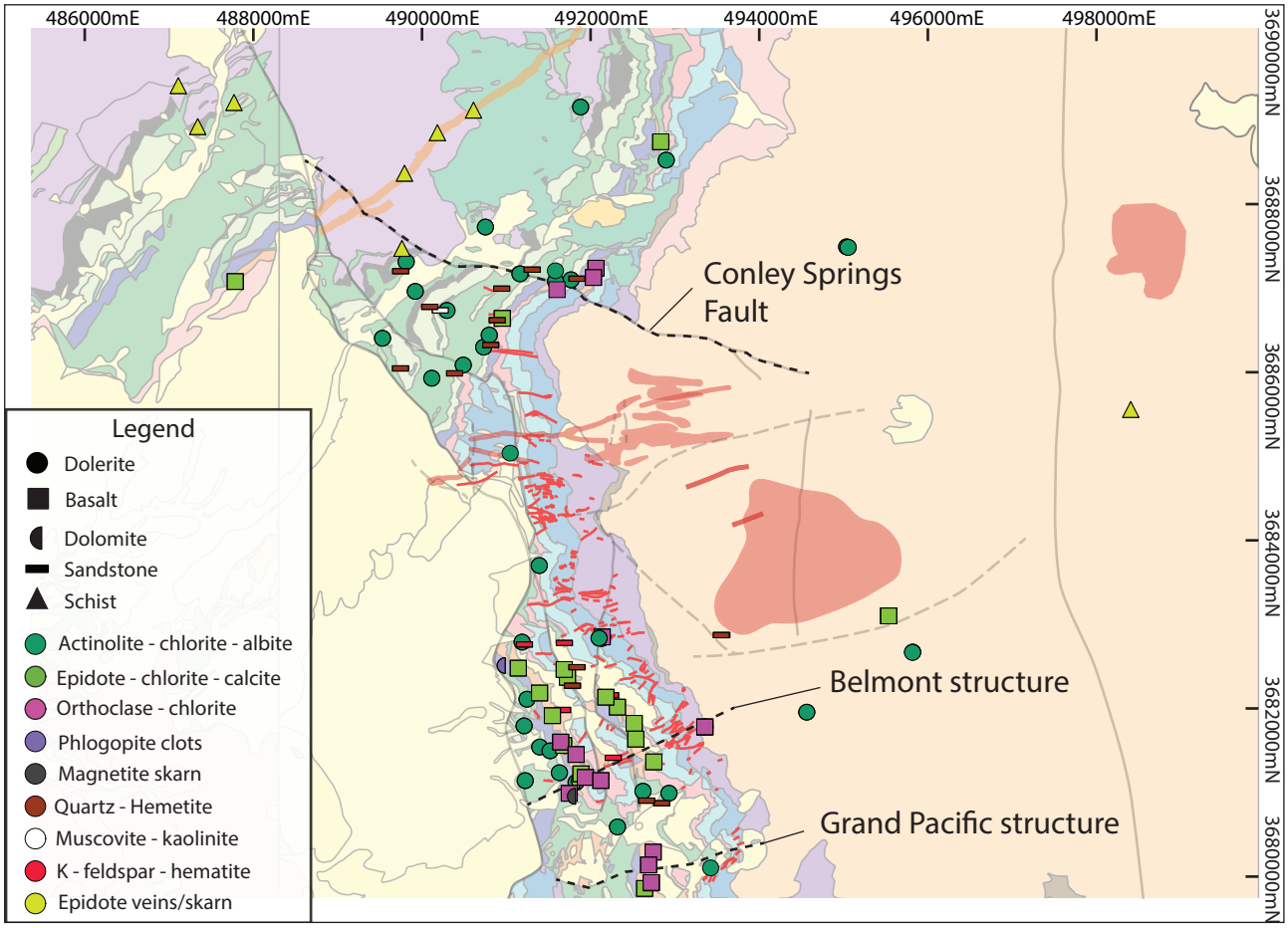


Figure 7.1 Map of the Superior district, showing the locations of Proterozoic alteration assemblages as determined from field and hand specimen observations. Geology and mineralisation as Figure 3.1.

Neuerburg and Granger (1960) and Granger and Raup (1969) documented 'black deuteric veins' composed of fibrous amphibole and biotite, partly replaced by chlorite, with small but widespread zircon crystals. Some of these veins have bleached selvages, suggesting leaching of adjacent mafic minerals in the wall rock. Zirconium is significantly enriched in these veinlets, several hundred times that observed in the dolerite itself (Neuerburg and Granger 1960; Granger and Raup, 1969). These iron-rich, silica-undersaturated veins were interpreted by previous authors to represent late stage magmatic fluids, derived from the final stages of differentiation of the dolerite magmatic body, which concentrated a range of elements including U and Cu.

## 7.3 Proterozoic alteration in the Superior District

Proterozoic alteration in the Superior district and wider Apache basin is strongly host-rock controlled (Figure 7.1). Direct geochronological evidence is limited to samples of the Apache Basalt and one sample of Pinal Schist (Chapter 5). Where possible, the relationships between various alteration phases have been established based on field and petrographic observations, and supported by observations from the literature. These alteration relationships are outlined in the following sections. Where relative timing or cross-cutting relationships between alteration assemblages are absent, some inferences have been made

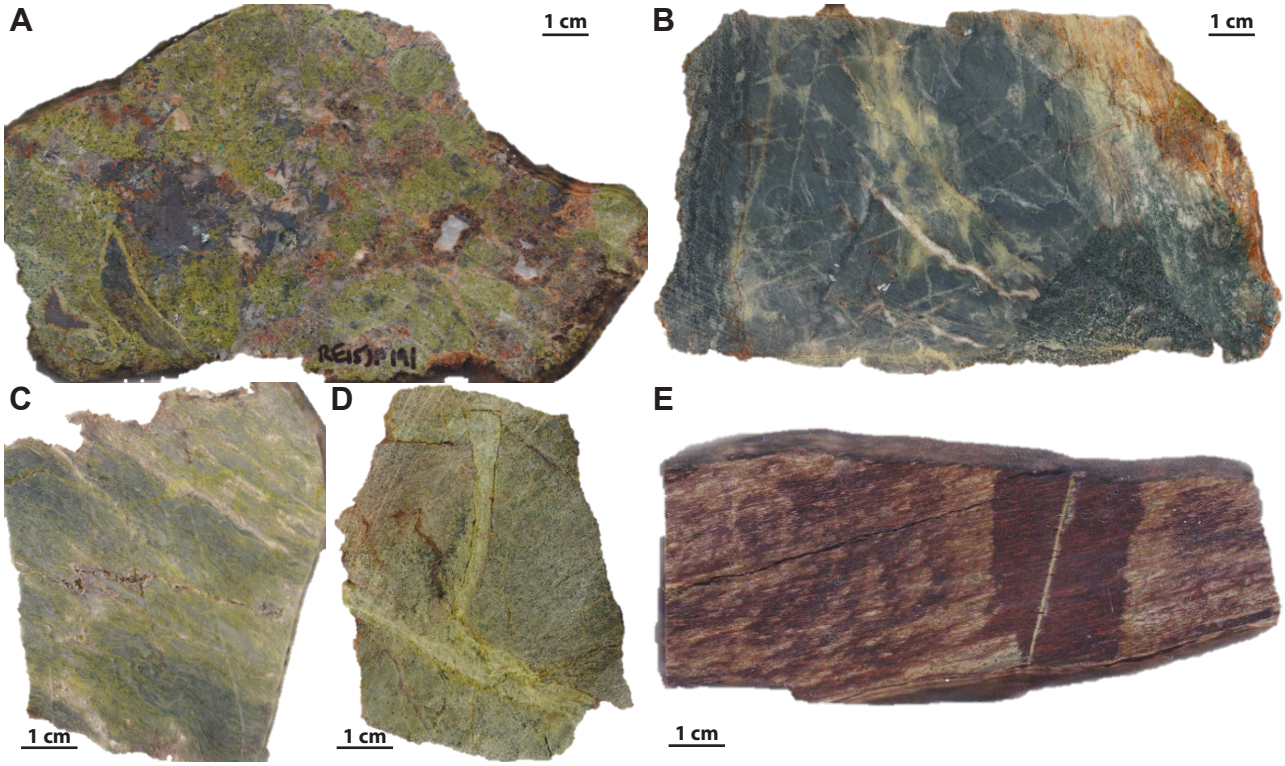


Figure 7.2 A. Massive epidote - calcite - garnet - mushketovite-altered Pinal Schist of the calc-silicate facies of Spencer and Richards (1995; RE15JP191) B. Wispy pervasive epidote and discontinuous quartz veinlets in a quartz-rich facies of the Pinal Schist (RE16JP014). C. Epidote exploiting cleavage in Pinal Schist (RE16JP020) . D Sharp-walled stockwork style veining and weak pervasive epidote in Pinal Schist (RE16JP035). E. Thin epidote veinlet with asymmetrical chlorite halo in chlorite-albite altered Pinal Schist (RE16JP036)

regarding whether specific alteration types are part of the Proterozoic alteration suite.

### 7.3.1 Calc-silicate skarn and epidote veins in the Pinal schist

Within the Paleoproterozoic basement, notably in the north of the study area, conspicuous calc-silicate skarn crops out on the hillsides and float material occupies drainages (Figure 7.1). Outcrops are patchy but broadly delineate a NE-striking zone within the schist package, sub parallel to the Grandfather Lead felsic dike and projecting into the contact zone with the quartz diorite (Figure 7.1). This skarn has previously been interpreted to be Laramide age (O'Neal, 2015). Mineralogically, the skarn consists of red-brown garnet intergrown with epidote, with later albite, quartz and calcite (Figure 7.2 A). Notably, these skarns locally contain mushketovite, a magnetite pseudomorph of bladed hematite (Figure 7.2 A). Epidote ± quartz ± albite veins are also locally present in the Pinal Schist but are somewhat variable in form. They occur as diffuse wispy veins in low metamorphic grade quartz-rich facies of the Pinal Schist (Figure 7.2 B), and as veins along cleavage planes in higher metamorphic grade rocks (Figure 7.2 C). Thick, sharp-walled epidote veins with multiple orientations also occur (Figure 7.2 D), however their relative timing is poorly constrained. Although these epidote occurrences have not been dated, their textures suggest a metamorphic origin (Figure 7.2 B-C). In chlorite-rich facies veins are typically smaller, post-date cleavage and locally exhibit chloritic selvages (Figure 7.2 E). The epidote in this sample has

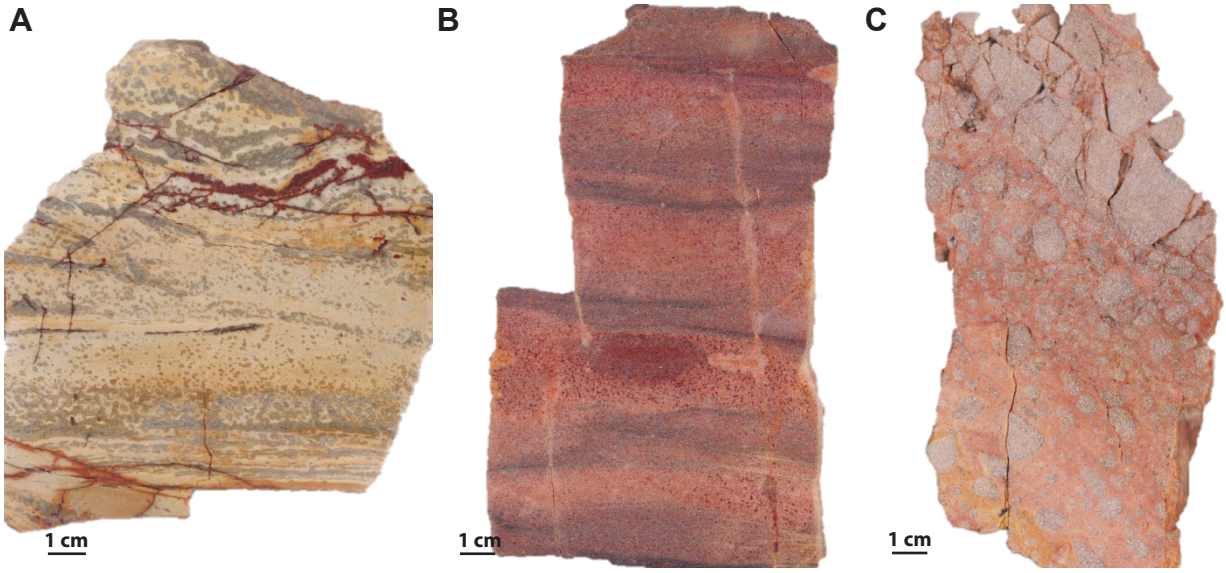


Figure 7.3 A. Muscovite - kaolinite altered Upper Dripping Springs Quartzite (RE15JP199). B Bedding parallel K-feldspar alteration in the Lower Dripping Springs Quartzite (RE15JP048). C. K-feldspar and quartz cemented fault breccia in Lower Dripping Springs Quartzite (RE15JP132).

been dated at 1,230 ± 160 Ma (Table 6.7; Figure 6.8).

### 7.3.2 Potassic alteration in quartzites

Between the Concentrator and Conley Springs Faults (Figure 7.1), an outcrop of thinly laminated Upper Dripping Springs Quartzite has a mottled appearance, quite different from its regional, least altered equivalent (Figure 7.3 A). Mineralogically, this outcrop is now composed of quartz, muscovite, kaolinite, with subordinate relict feldspar and some fracture-controlled hematite (Figure 7.3 A). Though somewhat texturally obscured, primary cross-bedding is still visible. The patchy, recrystallised textures within the muscovite-rich domains appear to be controlled by the primary composition of the individual layers, and may be equivalent to the 'spotted rocks' described by Neuerberg and Granger (1960). The Dripping Springs Quartzite has undergone potassic alteration, which produced locally selective replacements (Figure 7.3 B). In the Dripping Springs upper member, K-feldspar alteration is preferentially developed along coarser grained beds (Figure 7.3 B). In the lower member, K-feldspar cemented and partly replaced rock flour matrix in a monomict sandstone breccia (Figure 7.3 C). Sub-vertical K-feldspar veinlets have cross cut bedding and locally branch out laterally in the coarser grained beds, where they coincide with patches of hematite alteration (Figure 7.3 B).

Alteration textures evident in potassic-altered Dripping Springs Quartzite provide evidence for the permeability architecture during alteration. Sub-vertical fractures visible in hand specimen are interpreted to have acted as fluid pathways, with lateral flow evident along coarser layers (Figure 7.3 B). Some sub-vertical K-feldspar veinlets have patchy hematite alteration. A breccia with a fine grained monomict matrix and sub-rounded to rounded clasts grades out to an angular clast supported facies (RE15JP032; Figure 7.3 C). This is interpreted to be a tectonic-hydrothermal breccia, cemented by

K-feldspar and quartz. Pervasive alteration in the Dripping Springs Quartzite suggest that this unit was highly permeable, and may have been an aquifer for Proterozoic K-rich fluids (c.f., quartz sandstones in the McArthur Basin; Cooke et al., 1998, 2000).

### 7.3.3 Quartz - hematite alteration in quartzites

The thickly bedded, well sorted sandstones of the Superior district contain monomict quartz - hematite cemented breccias (Figure 7.4 A-E). The clasts range from sub-rounded (Figure 7.4 A, D) to sub-angular (Figure 7.4 B) to angular (Figure 7.4 C) and are composed of quartzite. The breccias are cemented by quartz and hematite. Hematite ranges in colour from brown (Figure 7.4 A, B) to red (Figure 7.4 C) to yellow (Figure 7.4 D, E), suggesting mixtures in the iron oxide species (goethite, hematite and limonite respectively). The quartz - hematite breccias occur as sub vertical, discontinuous tabular to lenticular domains, typically about a meter in width but many tens of meters in length. This geometry, coupled with the sub-rounded clasts observed in some examples suggest the breccias may be of tectonic origin, which have later been cemented by quartz and hematite.

Patchy quartz - hematite alteration also occurs in coherent sandstones (Figure 7.4 F-I). Similar to the breccias, patches vary in colour from red to brown and range in size from 0.5 – 10 cm (Figure 6.3 F-G). In some drillhole examples quartz-hematite alteration occurs as larger domains within the sandstone units (Figure 7.4 I), although the broader morphology of these occurrences in unknown. Alteration spots of similar mineralogy are reported by Granger and Raup (1969), although their examples are generally less than 1 cm. Therefore, the quartz - hematite patches encountered in the Superior district may be large-scale equivalents of those described by Granger and Raup (1969) from the Sierra Ancha regions. There are no timing constraints on this style of alteration, but since it is not evident in Paleozoic siliciclastic rocks such as the Bolsa Quartzite. Because the mineralogy is compatible with other alteration assemblages in the Apache Group rocks of the Superior district, it is tentatively included here in the Proterozoic alteration suite.

### 7.3.4 Fe-Mg skarn and asbestos in the Mescal Limestone

Prominent, though somewhat dissected, outcrops of Mescal Limestone are exposed along the base of Apache Leap. At numerous locations, irregular, sub-bedding parallel bodies of magnetite occur within the lower member of the Mescal Limestone (Figure 7.5 A). Magnetite occurs as discrete tabular bodies, and as a series of bands within the limestone, typically accompanied by tremolite. The thicknesses of individual bodies range from <1 cm bands (Figure 7.5 A) to ~15 cm domains (e.g., Figure 7.5 B).

Another interesting aspect of the Mescal Limestone is the presence of chert breccias. These occur sporadically around the Superior district and have been interpreted to relate to weathering and solution collapse phenomena (Skotnicki and Knauth, 2007). At some locations in the Superior district, the chert breccias contain goethitic pseudomorphs of pyrite (Figure 7.5 C), although no remnants of primary

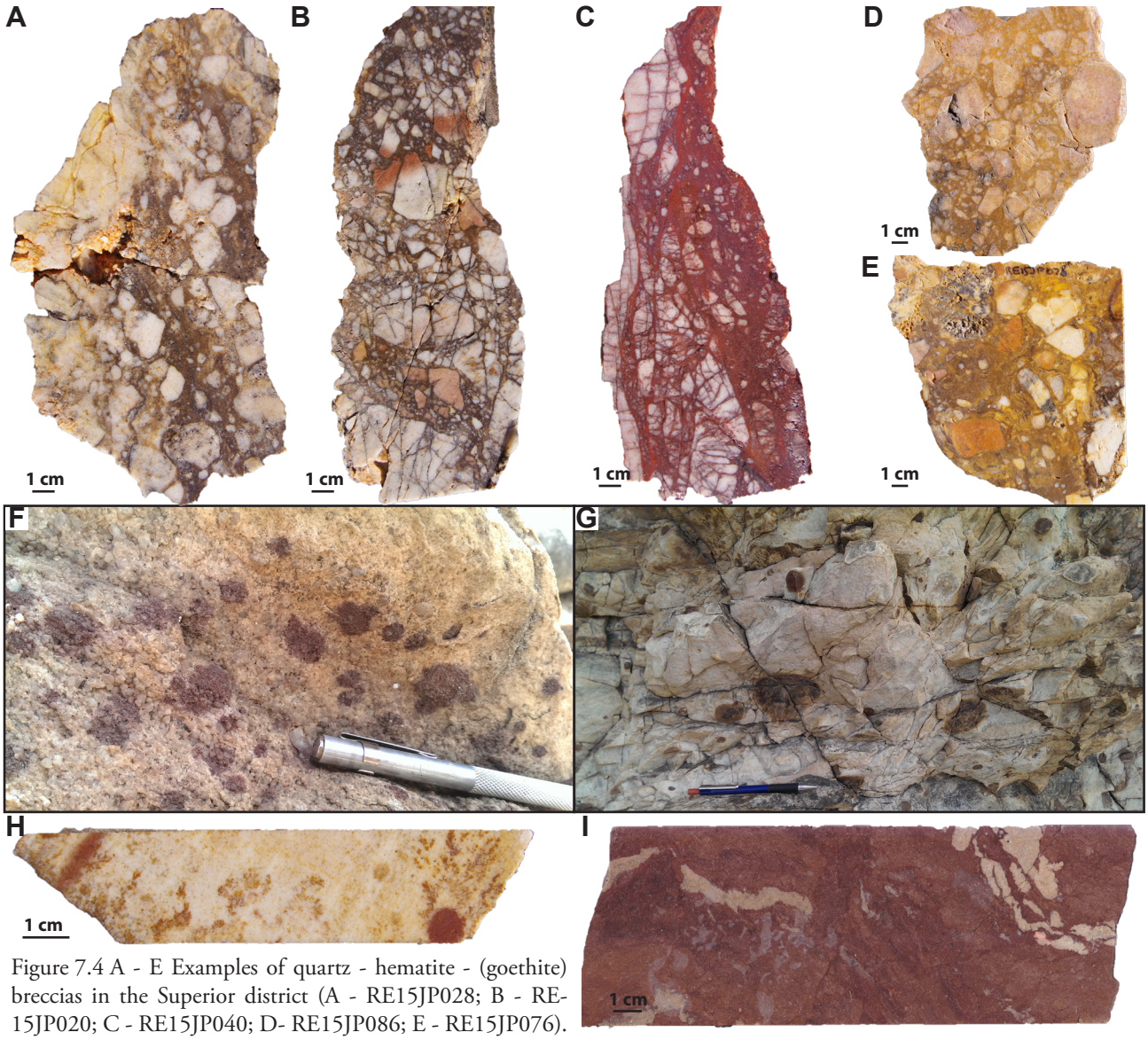


Figure 7.4 A - E Examples of quartz - hematite - (goethite) breccias in the Superior district (A - RE15JP028; B - RE-15JP020; C - RE15JP040; D- RE15JP086; E - RE15JP076). F - I examples of hematite patches in the Superior district (F - vicinity of 490000 mE, 3686000 mN; G - vicinity of 492000 mE, 3682000 mN; H - RE15JP078; I - RE15JP185)

pyrite were observed in the field. There are inclusions of cubic goethite within the microcrystalline quartz that cements the breccias (Figure 7.5 C). The goethite casts are conspicuously absent from domains of dark chert (Figure 7.5 C) and seem most abundant in the most disrupted parts of the samples.

Clots of coarse crystalline phlogopite within the lower member of the Mescal Limestone, are exposed on Highway 177, south of Superior (Figure 7.1). The clots occur as irregular bedding-parallel masses in an otherwise bleached lower member of the Mescal Limestone (Figure 7.5 D).

Regionally, bedding parallel chrysotile and serpentine characterise asbestos occurrences in the Mescal Limestone of the Sierra Ancha Region (Chapter 2). These asbestos workings are reported to have a strong stratigraphic control, occurring near the top of the highly dolomitic lower member and within 10 m of a dolerite sill, empirically linking them to the emplacement of dolerite sills (Bateman, 1923; Stewart, 1955). Examples encountered in the Salt River Canyon show typical tremolite alteration with subordinate serpentine and a strong silicic overprint (Figure 7.5 E).

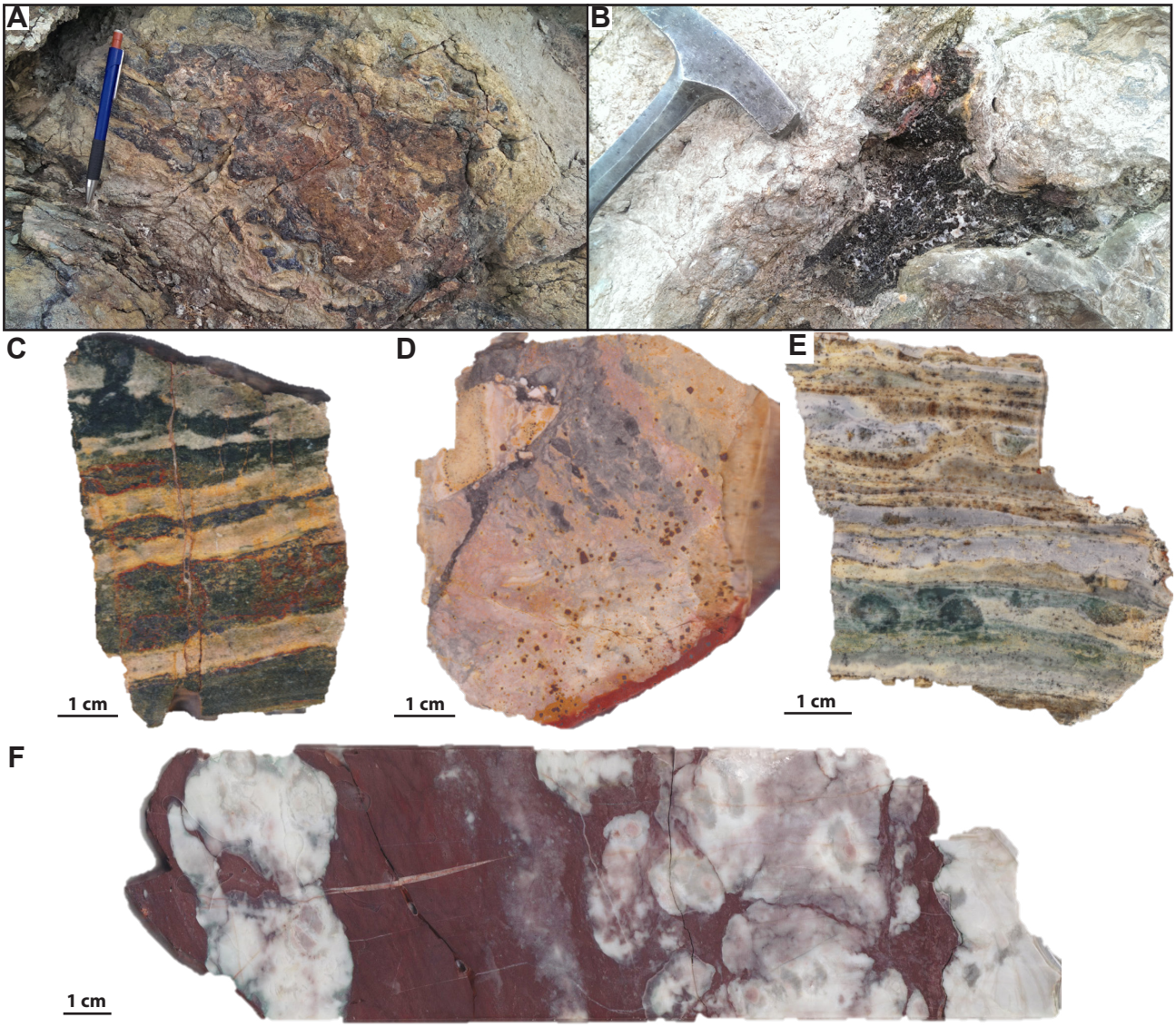


Figure 7.5 A. Massive-blebby magnetite skarn hosted in Mescal Limestone also along Apache Leap road (vicinity of 491500 mE, 3681000 mN). B. Irregular biotite clot in Lower Mescal Limestone exposed in the Concentrator Fault (vicinity of 491000 mE, 3684000 mN). C. Banded magnetite skarn from Mescal Limestone on Apache Leap Road (RE15JP017). D. Pyritic chert breccia from the Lower Mescal Limestone (RE15JP045). E Silicified diopside - serpentine altered Mescal Limestone from the Salt River Canyon, possibly altered stromatal facies of the Algal Member (RE15JP212). F Hematitic silt filling paleo-karst voids in the Mescal Limestone. Note the recrystallised textures, indicative of thermal metamorphism, but lack of magnetite in the iron-rich matrix (RE15JP103).

Some authors have interpreted the iron occurrences in the Mescal Limestone to be the result of the replacement of layers of Fe-rich material derived from the erosion of the overlying basalt (e.g., Wrucke et al., 1986). However, no void space or evidence of sedimentation is observable in the magnetite bodies of the Superior district. Furthermore, where Fe-rich material has been intersected in drilling, no such transformation is evident, despite high temperature recrystallisation of the limestone clasts (Figure 7.5 F).

Possible interpretations of the origins of the chert-hosted goethite (e.g., RE15JP045; Figure 6.3 C) include (1) a period of diagenetic pyrite formation prior to brecciation and cementation by microcrystalline quartz, (2) a period of early dark chert formation and subsequent hydrothermal brecciation resulting

in cementation by quartz-pyrite, (3) or hydrothermal fluids preferentially altering the light coloured domains in the chert after brecciation. Although the Mescal Limestone has been interpreted to have been deposited in a sabkah environment (c.f., Shride, 1967; Wrucke, 1989), which could explain the formation of diagenetic pyrite, sulfides are not reported from elsewhere in the Mescal Limestone. The pyrite casts Mescal Limestone of the Superior district is interpreted here to have a hydrothermal origin, and is tentatively included in the Proterozoic alteration suite.

Phlogopite (and biotite) are well-documented products of thermal metamorphism of the Mescal Limestone by the dolerite sills (Granger and Raup, 1969). However, some phlogopite occurrences in the lower member of the Mescal Limestone have been dated by Ar-Ar as Laramide (62.3 Ma ± 0.15; Hehnke et al., 2012). Given their location within the major Cenozoic Concentrator Fault, that shows contractional fabrics of probably Laramide age, it remains possible that the Ar systematics may have been reset during the Laramide Orogeny.

### 7.3.5 Intense orthoclase - chlorite ± hematite alteration of the Apache Basalt.

The most widespread alteration assemblage exposed in the Superior district is the intense orthoclase – chlorite assemblage that has affected the Apache Basalt (Figure 7.6). Since its initial observation and description (Short et al., 1943) the intense reddening of the basalt has been interpreted to be hematitic dusting through oxidation and weathering processes (Short et al., 1943; Shride et al., 1967; Wrucke et al., 1989). However, feldspar staining using the sodium cobaltinitrate method of Bailey and Stevens (1960) during this study has shown that this was a phase of intense potassium metasomatism (Figure 7.6 E-G). Intense orthoclase - chlorite - hematite alteration was texturally destructive, producing patchy to pervasive alteration of the basalt (Figure 7.6 A), although primary textures are variably preserved (Figure 7.6 B). Locally, quartz is abundant as irregular, randomly oriented veinlets, and stringers that in extreme examples have coalesced to form stockworks (Figure 7.6 C, Figure 7.7 A). There are incipiently developed crackle breccias, and quartz also occurs with chlorite in amygdales (Figure 7.7 A, B). Vesicular facies of the Apache Basalt are particularly striking, with chlorite- and locally quartz-filled amygdales and intense orthoclase halos grading out to orthoclase - chlorite altered groundmass (Figure 7.7 B). In places, notably along the base of Apache Leap, conspicuous breccias containing randomly oriented thinly laminated clasts with alternating black and red lamina are visible (Figure 7.6 E). Where alteration is most intense, the rock is composed almost solely of intergrowths of orthoclase and chlorite. Where textures are preserved, plagioclase phenocrysts are preferentially altered to orthoclase and the groundmass is variably pervasively altered to orthoclase - chlorite (Figure 7.6 F). In some cases, planar mono-mineralic specular hematite veins are associated with areas of intensely altered basalt (Figure 7.7 C).

Pervasive alteration of the brecciated basalt caused preferential replacement of finer grained matrix with the larger clasts armoured by chilled margins (Figure 7.6 B). This could also be a pseudo-breccia texture. There is a conspicuous lack of vein-hosted orthoclase-chlorite in the Apache Basalt, supporting low fluid

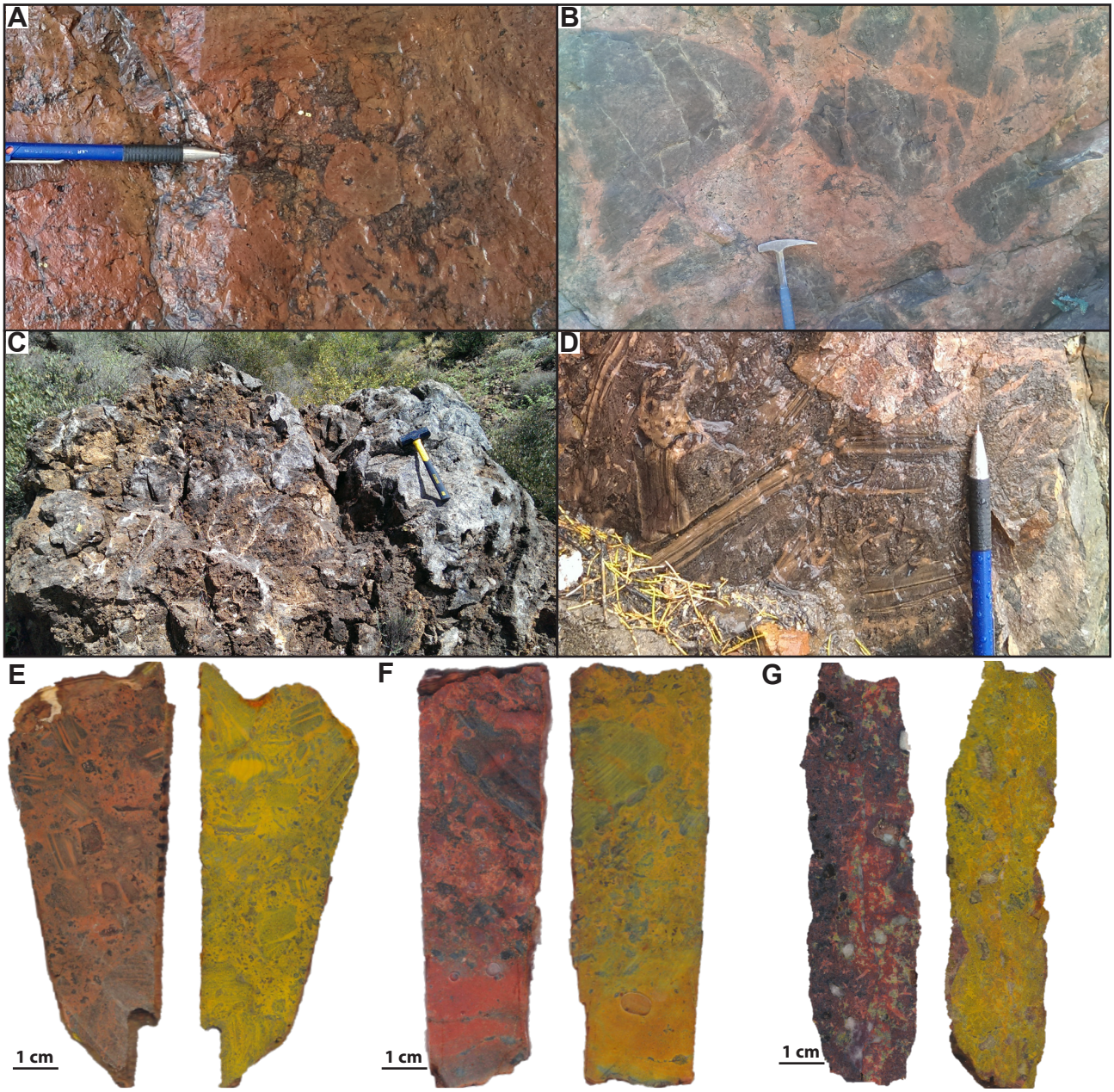


Figure 7.6 A. Field exposure of intense-pervasive orthoclase chlorite alteration in Apache Basalt (vicinity of 491500 mE, 3682500 m N). B Field exposure of intesely orthoclase –chlorite altered volcanic breccia ( vicinity of 492000 mE, 3681000 mN). C. Large boulder of irregular quartz stockworking in a drainage of the Superior range front (vicinity of 492500 mE, 3682000 mN). D. Exmaple of orthoclase altered xenolith breccia in Apache Basalt (vicinity of 491500 mE, 3680500 mN). E - G Three examples of Apache Basalt before and after sodium cobalt-nitrate straining for potassium feldspar (E - RE15JP016; F - RE15JP034. G - RE15JP049).

pressures and fluid migration controlled by horizons of high primary permeability in the Apache Group stratigraphy, such as coarse sandstone beds and vesicular or agglomeratic basaltic units.

Sedimentary clasts observed locally in the basalt (Figure 7.6 E) are strikingly similar to regional outcrops of the Upper Dripping Springs Quartzite, but may also represent parts of the now eroded Argillite Member of the upper Mescal Limestone. In polished hand specimens, orthoclase is concentrated in lamina within the siltstone xenoliths, suggesting that both assimilation of K-rich sediment and K-metasomatism occurred (Figure 7.6 E).

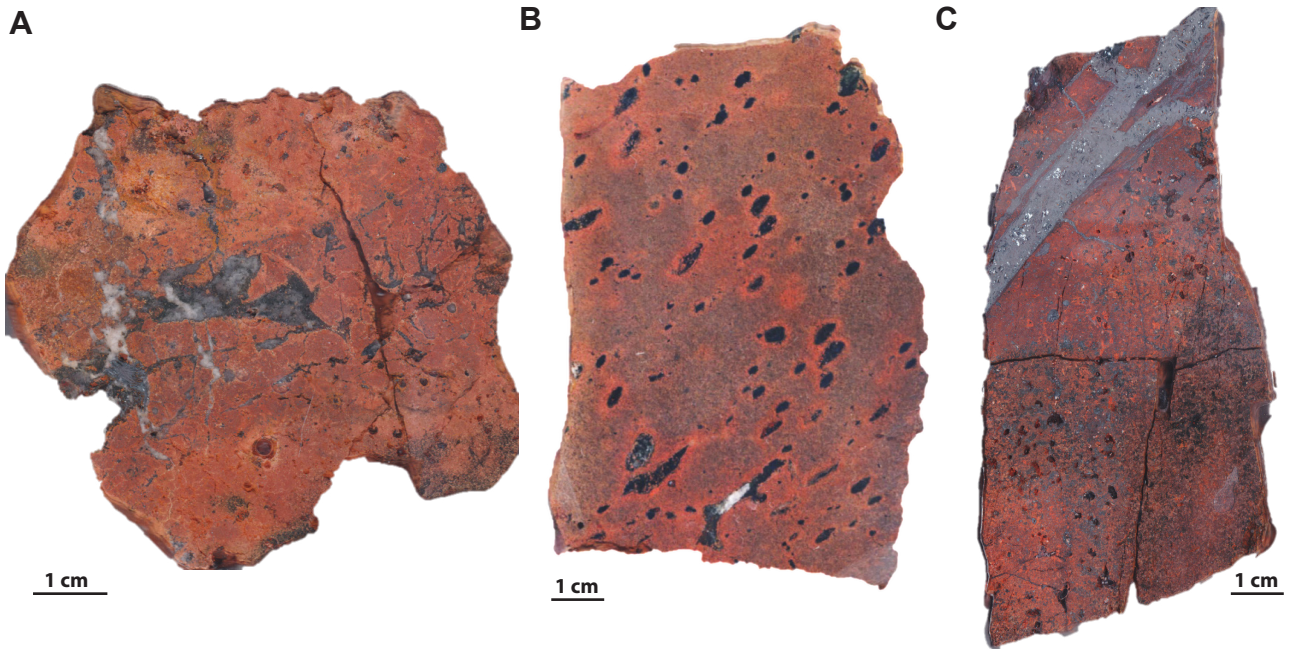


Figure 7.7 Examples of orthoclase - chlorite alteration textures in the Apache Basalt. A Intense, texturally destructive orthoclase alteration with incipient quartz and specular hematite cemented crackle breccia (RE15JP032). B Intense, texturally preserving orthoclase-chlorite alteration in a strongly vescicular facies of the Apache Basalt. Note the preference of chlorite (± quartz) for vesicles with strong orthoclase rim (RE16JP005). C Intensely orthoclase altered basalt, with mono-mineralic specular hematite vein (RE15JP072)

### 7.3.6 Epidote - chlorite - calcite alteration of the Apache Basalt

Zones of texturally preserving, epidote, chlorite, calcite and apatite alteration has overprinted orthoclase - chlorite - hematite alteration (Figure 7.8). Typically orthoclase is weakly developed to absent (e.g., Figure 7.8 A) with a fracture controlled (Figure 7.8 B) or patchy-pervasive texture (Figure 7.8 C-F). Epidote, chlorite, calcite and apatite are typically confined to amygdales (Figure 7.8 A,E). Epidote also occurs as small aggregates (Figure 7.8 B,) large patches (Figure 7.8 C), or irregular veins (Figure 7.8 D), although overall, epidote veins are rare. Selective epidote replacement of plagioclase, as well as replacement of the matrix of monomict basalt autobreccia were also rarely observed. Chlorite has generally pervaded the groundmass to varying degrees, in contrast to the chlorite amygdale-fill that characterises the orthoclase - chlorite - hematite alteration facies (Figure 7.8 B, E-G), although chlorite-filled amygdales were observed locally (Figure 7.8 G). Calcite occurs exclusively as intergrowths with epidote in the amygdales. Although specular hematite is rare in this assemblage, it typically occurs in subordinate amounts as small clots where orthoclase is present (Figure 7.8 B). Quartz is also uncommon in this assemblage, but has been locally observed in vesicles (Figure 7.6 G). Apatite occurs as short stubby prismatic crystals intergrown in amygdales with either epidote - chlorite - calcite or a combination thereof (Figure 7.9).

### 7.3.7 Actinolite – chlorite – albite ± biotite ± epidote alteration of dolerite sills

Alteration of the Proterozoic dolerite sills of the southwestern USA is discussed in detail by Neuerburg and Granger (1960), Smith, (1970), Nehru and Prinz, (1970), Fouts, (1975), Schofield, (1976), and

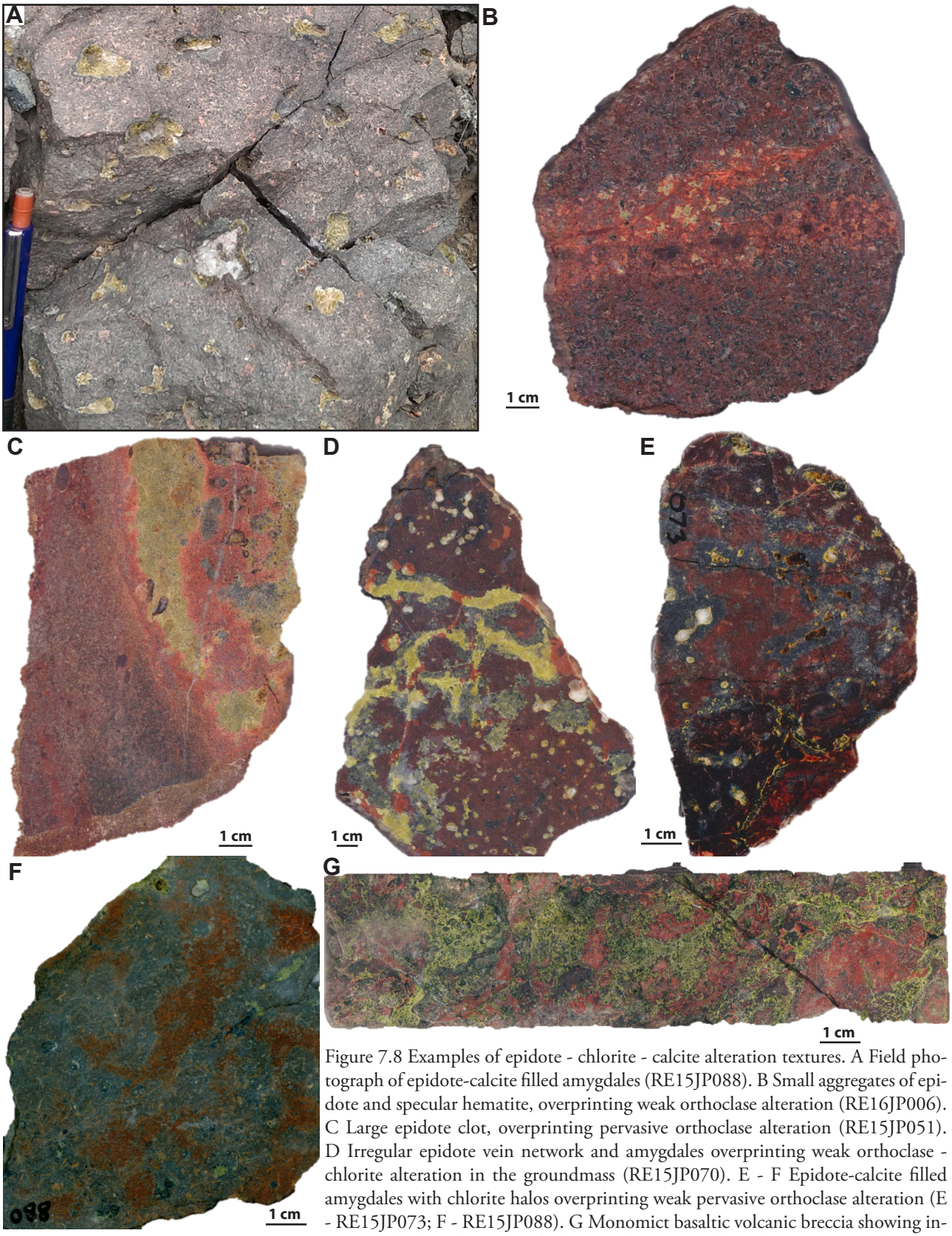


Figure 7.8 Examples of epidote - chlorite - calcite alteration textures. A Field photograph of epidote-calcite filled amygdales (RE15JP088). B Small aggregates of epidote and specular hematite, overprinting weak orthoclase alteration (RE16JP006). C Large epidote clot, overprinting pervasive orthoclase alteration (RE15JP051). D Irregular epidote vein network and amygdales overprinting weak orthoclase - chlorite alteration in the groundmass (RE15JP070). E - F Epidote-calcite filled amygdales with chlorite halos overprinting weak pervasive orthoclase alteration (E - RE15JP073; F - RE15JP088). G Monomict basaltic volcanic breccia showing intense orthoclase alteration of coherent clasts and well developed epidote alteration of the matrix, locally with clots of specular hematite (RE16JP080).

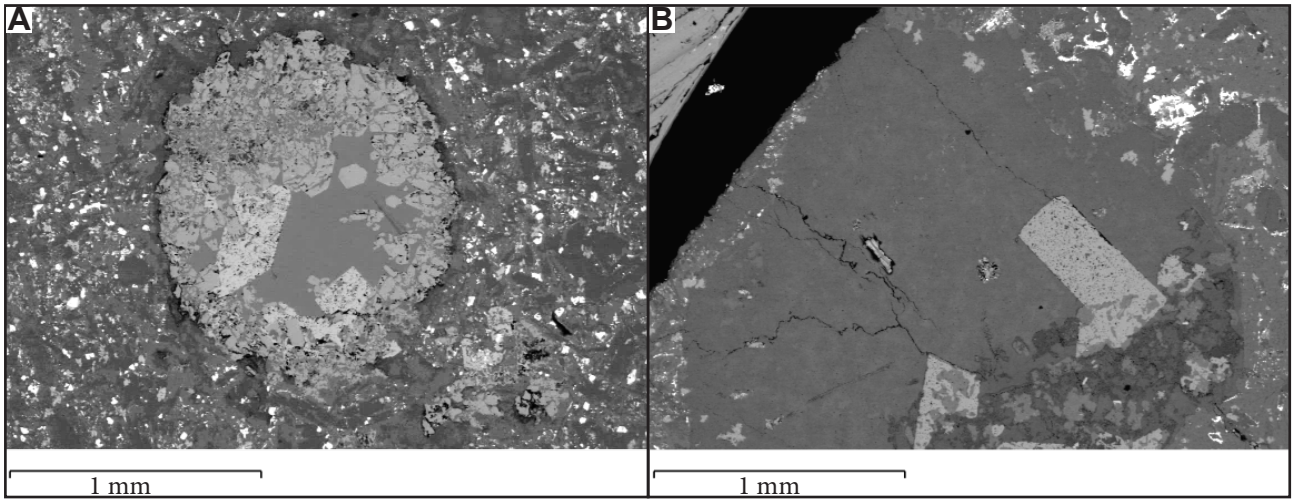


Figure 7.9 Euhedral apatite crystals intergrown with (A) epidote and calcite- and (B) chlorite-filled amygdale in the Apache Basalt. A. RE15JP073, dated at 1151 ± 49 Ma, B. RE15JP088, dated at 1247 ± 52 Ma (Table 6.5; Figure 6.8 B).

Hammond, (1983, 1986). Actinolite alteration of the dolerite sills in the Superior district is widespread, both pervasively and as veins, similar to that described by the aforementioned authors (Figure 7.10 A). Alteration varies between actinolite-dominant (Figure 7.10 B) and albite-dominant (Figure 7.10 C), with or without epidote (Figure 7.10 D) but most samples appear to have roughly equal proportions of both actinolite and albite (Figure 7.10 E).

Actinolite is commonly intergrown with albite and chlorite in the dolerite sills. Where alteration intensity is weaker and primary textures are preserved, actinolite has selectively replaced pyroxene (Figure 7.11 A). Albite is variably intergrown with K – feldspar and replaces plagioclase and chlorite has typically altered hornblende. Biotite is also present locally. Most commonly intense actinolite – albite - chlorite alteration pervasively developed and can be associated with actinolite veins (Figure 7.11 B-F and Figure 7.12). Primary textures have typically been destroyed. Actinolite – chlorite veins commonly lack albite, but albite occurs as part of the adjacent alteration halo (Figure 7.11 C). Albite is intimately intergrown with actinolite where chlorite is less prevalent (Figure 7.11 D-E) and also occurs interstitial to actinolite (Figure 7.11 F). In one sample, a biotite veinlet cross-cuts an actinolite – chlorite vein (Figure 7.12 A). Epidote is present locally in veins and clots (Figure 7.12 B). Small, euhedral apatite crystals and rare allanite crystals occur in actinolite - chlorite altered rocks locally (Figure 7.12 C). Quartz and/or calcite are present in small quantities, in the veins and also actinolite-altered rocks. K-feldspar alteration is less common in the dolerite than in the basalt. Only one dolerite sample collected in the current study shows well-developed K-feldspar, although it remains unclear whether this K-feldspar is a product of magmatic differentiation or hydrothermal alteration (Figure 7.12 D). The K-feldspar vein has been crosscut by an actinolite - quartz - calcite vein, providing evidence of the early timing for K-feldspar formation (Figure 7.12 D).

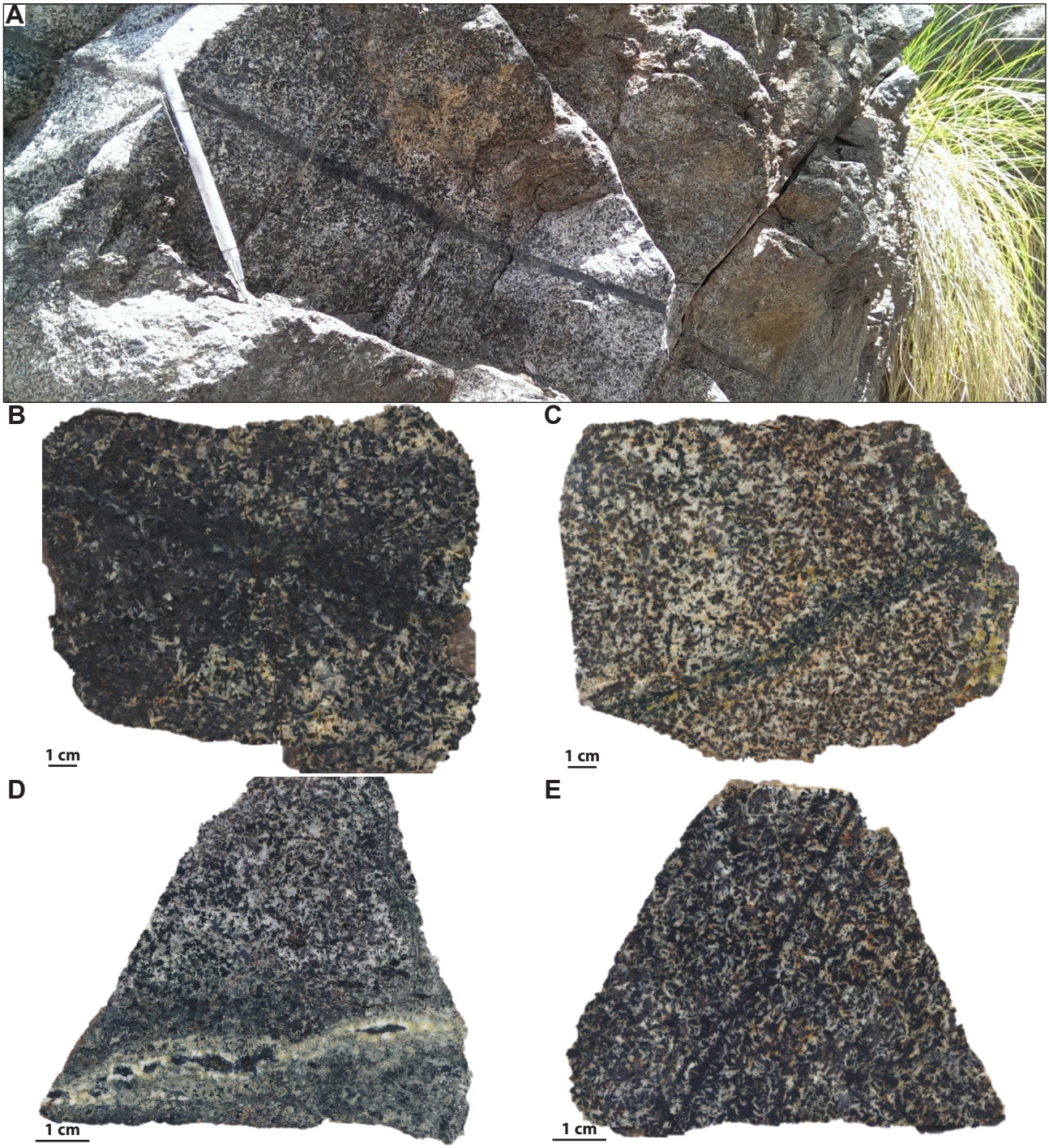


Figure 7.10 A. Field photograph of a thick, planar mono-mineralic actinolite vein with albite halo in dolerite close to the Conley Springs Fault (vicinity of 491000 mE, 3687000 mN). B Strong pervasive actinolite alteration with marginal domains of albite (RE15JP131). C Actinolite veinlet in pervasively ablite-altered dolerite, with weak epidote development (RE-15JP150). D Irregular actinolite - albite - epidote vein with weak actinolite halo grading out into a pervasivily albite-altered groundmass. (RE15JP216). E. Actinolite veinlet in pervasively actinolite - albite-altered dolerite (RE15JP133).

### 7.3.8 Illite - muscovite alteration in dolerite sills

Illite has weakly but pervasively altered plagioclase locally in the dolerite, preserving primary igneous textures (Figure 7.13 A). Illite has also been reported be previous authors as halos to actinolite veins, giving a bleached appearance (e.g., Neuerburg and Granger, 1960; Hammond, 1983). Since few dolerite

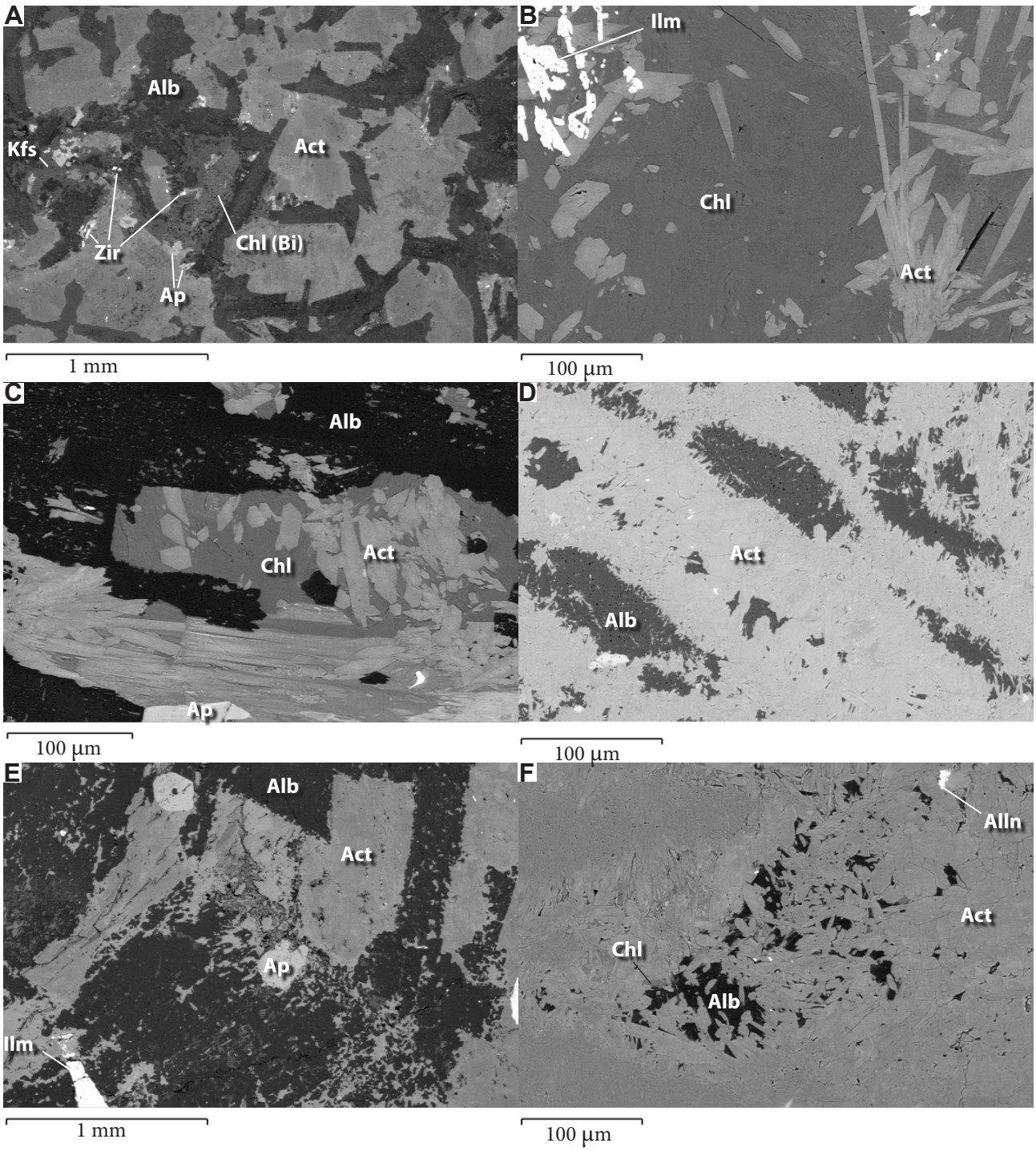


Figure 7.11 Examples of actinolite - albite - chlorite alteration textures viewed under SEM. A Albite intergrown with minor K-feldspar replacing plagioclase and actinolite ± chlorite alteration of pyroxene (RE15JP011). B - C Strongly developed, weakly texturally destructive actinolite - chlorite alteration, surrounded by albite (RE15JP156). D Intense, thoroughly texturally destructive actinolite - albite alteration (RE15JP194). E Actinolite alteration of phenocrysts, surrounded by pervasive intergrown albite - actinolite alteration of the groundmass, spatially associated with two euhedral apatite crystals (RE15JP131). F Massive actinolite with interstitial albite, chlorite and rarely, allanite (RE15JP141).

samples from this study contain illite alteration and no cross cutting timing relationships were observed little can be said regarding the association of illite alteration and other alteration assemblages in the dolerite. The K-feldspar and actinolite imply an alkaline to near-neutral conditions, whereas the illite provides evidence that the fluids became weakly acid locally (e.g., McArthur basin, Cooke et al., 2000).

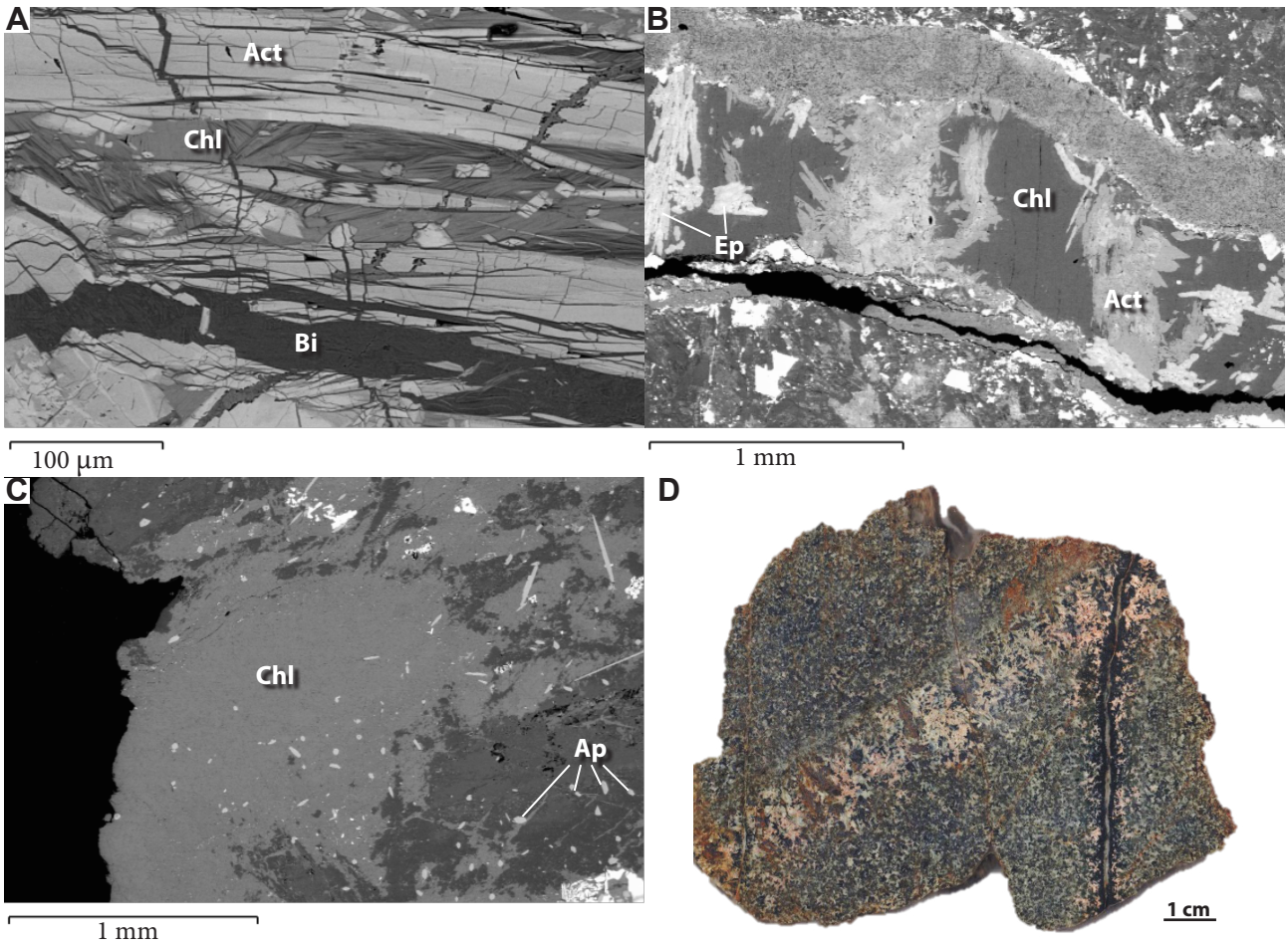


Figure 7.12 A. Mutually cross-cutting actinolite - chlorite and biotite veinlets (RE15JP032). B. Actinolite - chlorite - epidote vein (RE15JP139). C. pervasive chlorite alteration associated with significant quatities of apatite crystals (RE15JP111). D. Tabular domain of coarse K-feldspar with planar upper contact and diffuse lower contact, cross-cut by actinolite - chlorite vein with central seam of quartz - calcite and narrow halo of K-feldspar (RE15JP080).

## 7.4 Timing Constraints

### 7.4.1 Field relationships

Timing constraints on the Proterozoic alteration assemblages described in this chapter are subtle but unequivocal. The alteration facies described above are evident only in the Proterozoic rocks in the Superior district. The Paleozoic and Mesozoic rocks do not exhibit this style of alteration. A minor exception apart from illite-altered dolerite and orthoclase – chlorite-altered basalt clasts that can be observed within otherwise unaltered conglomeratic sections of the Kvs, bracketing this style of alteration to at least pre-Cretaceous times (Figure 7.13). These field relationships show that the orthoclase - chlorite - hematite and actinolite - albite - chlorite assemblages are unrelated to Laramide hydrothermal activity, in contrast to the interpretation of Force (1998). Timing relationships have been further constrained by Heidecker (1978), who reported clasts of altered basalt within the basal conglomerate of the Troy Quartzite in the Workman Creek area of the Sierra Ancha region, north of Superior, suggesting hydrothermal activity probably began prior to the deposition of the Troy Quartzite. An alternative interpretation of Heidecker's

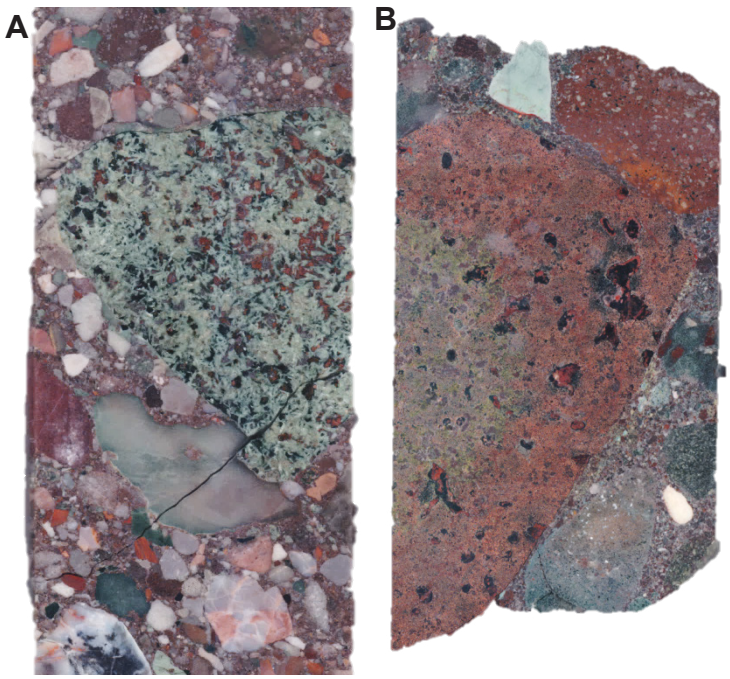


Figure 7.13 A. Illite-altered dolerite clast contained within relatively unaltered Kvs (RE15JP167). B Orthoclase - chlorite altered basalt clast contained within an otherwise unaltered section of the Kvs sequence (RE16JP038). Both samples are HQ drillcore.

(1978) observations is that reactive basalt clasts entrained within the Troy Quartzite, were preferentially altered relative to the quartz-rich sedimentary clasts during post-Troy Quartzite hydrothermal activity.

### 7.4.2 Geochronology

As demonstrated in Chapter 6, apatites from the Superior district record multiple hydrothermal events. Apatites from three amygdale-hosted epidote - chlorite - calcite samples, part of the epidote ± chlorite ± calcite assemblage (Section 7.3.6), yielded ages ranging from 1,247 ± 57 Ma to 1,113 Ma ± 55 (Section 5.3). These ages constrain the formation of the apatite–bearing epidote ± chlorite ± calcite assemblage (and by textural association, the strong orthoclase – chlorite assemblage) to the Late Mesoproterozoic. The U-Pb age dating results for apatites from this alteration assemblage overlap the ~1,100 Ma dolerite sill emplacement (Bright et al., 2014 and references therein).

## 7.5 Mafic alteration geochemistry

Alteration lithogeochemistry has been employed to geochemically and spatially domain alteration types in the Superior district. In contrast to Chapter 4, where immobile trace elements were primarily used to understand protolith geochemistry, here major elements are used to identify dominant alteration mineral assemblages. This section focuses on Proterozoic mafic rocks from the district as they provide the best spatial coverage of altered rocks. Mass balance calculations are also used to investigate fluid chemistry and speculate on fluid sources.

### 7.5.1 Previous work

Using changes in major element chemistry to map alteration throughout large parts of hydrothermal systems relies heavily on the systematic collection of high quality multi-element data. Accordingly, this method has only been developed relatively recently due to the increasingly widespread availability of commercial, low-cost, multi-element analyses (Halley et al., 2015, Halley et al, 2016, Escolme, 2016). Although geochemical discriminantion of alteration is gradually becoming a more widespread technique, (e.g., Escolme 2016) it has been applied primarily during active mineral exploration rather than academic research due to the large number of assumptions made concerning the meaning and relative significance of chemical trends or gradients. In mining and exploration applications this ambiguity is overcome, to some degree, by using large datasets (Halley et al., 2015, 2016; Escolme, 2016). In academic research, this ambiguity is overcome by detailed mineralogical and textural observations (e.g., Large et al., 2001, Williams and Davidson, 2004, Davis and Whitehead, 2006) which are not readily available, or practical, in large datasets. Halley (unpub) provided a comprehensive exploration geochemical appraisal of drillhole data of the Resolution porphyry Cu-Mo system. The current study applies this method to the altered surficial rocks of the wider Superior district.

### 7.5.2 Methods

By plotting geochemical data on major element geochemical discriminantion plots, populations of discrete alteration styles can be identified from whole rock geochemical data (e.g., Large et al., 2001; Williams and Davidson, 2004; Davies and Whitehead, 2006; Halley et al., 2015; Halley et al., 2016; Escolme, 2016). The methods applied here follow those outlined by Large et al. (2001; alteration index box plots), Williams and Davidson (2004), Davies and Whitehead (2006), Halley et al. (2015 and 2016), and Escolme (2016; alkali-alumina plot and Ca-K-Na ternary plot). Whole rock geochemical data used in this chapter are the same as those used in Chapter 4 and are tabulated in Appendix 1C. Data processing and manipulation was conducted using ioGAS software (version 6.3.1). Sample classification is based on natural populations and breaks inherent to the dataset, rather than fixed fields.

### 7.5.3 Results

#### 7.5.3.1 Major elements

Whole rock geochemical data from the altered rocks from the Superior district have been plotted on established carbonate - chlorite - pyrite index (CCPI) and advanced argillic alteration index (AAAI) box plots (Figure 7.14 A-B; Large et al., 2001, Williams and Davidson, 2004) and alkali-alumina plot (Figure 7.14 C; Davies and Whitehead, 2006). The samples define geochemical trends toward illite – muscovite-rich compositions (Figure 7.14 A-B), which would typically be associated with acid alteration. However, strong illite-muscovite alteration assemblages have not been observed in the hand specimens collected

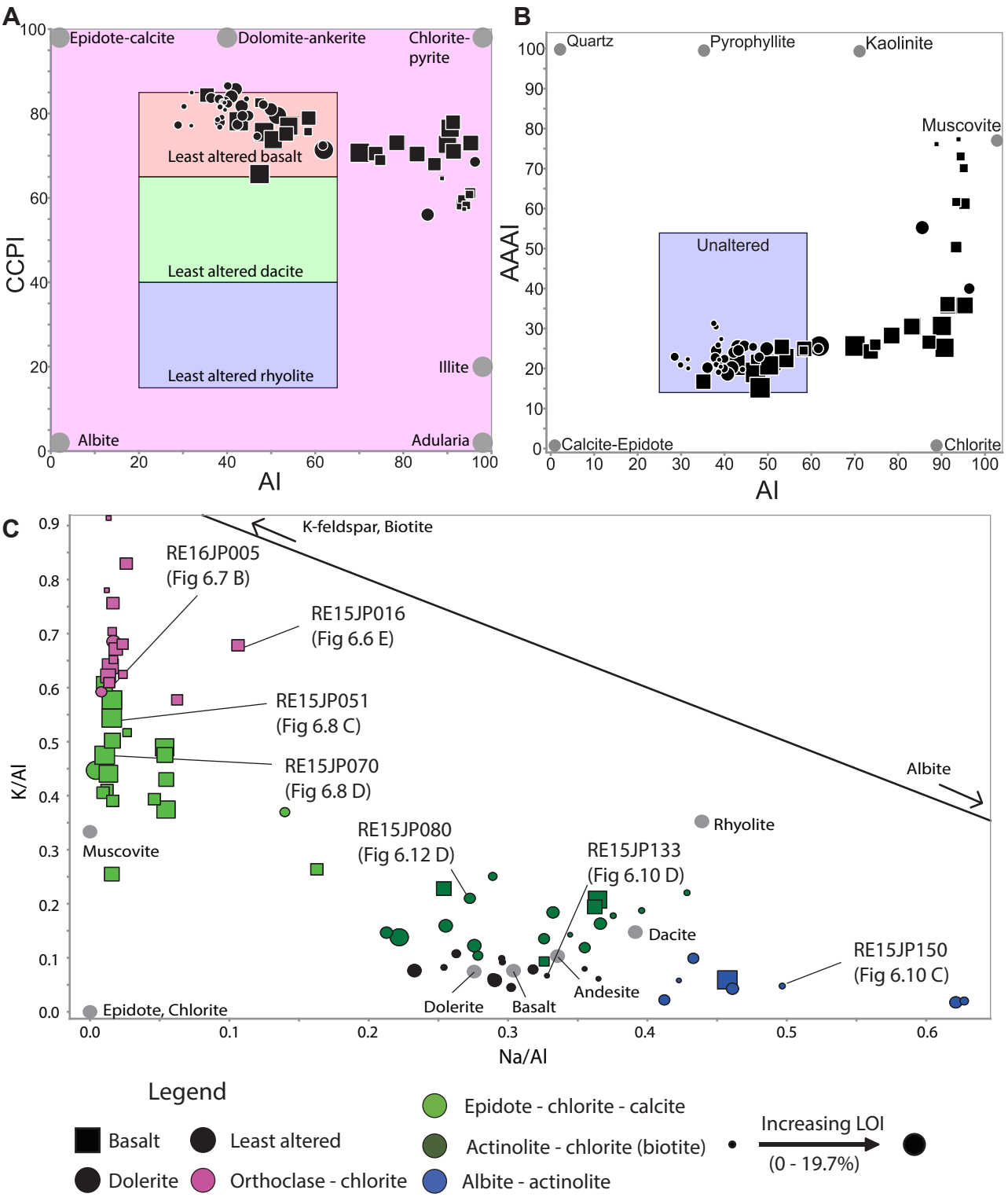


Figure 7.14 Geochemical data for Proterozoic altered mafic rocks of the Superior district. A. CCPI alteration box plot (Large et al., 2001) B. AAAI alteration box plot (Williams and Davidson, 2004). C. K/Al – Na/Al molar ratio plot adapted from Davies and Whitehead (2006) showing mafic igneous samples from the Superior district. Data listed in Appendix 1C.

in the current study.

Several geochemical groups can be delineated using a combination of mineralogical and textural observations, coupled with their geochemical properties (Figure 7.14 C). Data points from mafic rocks

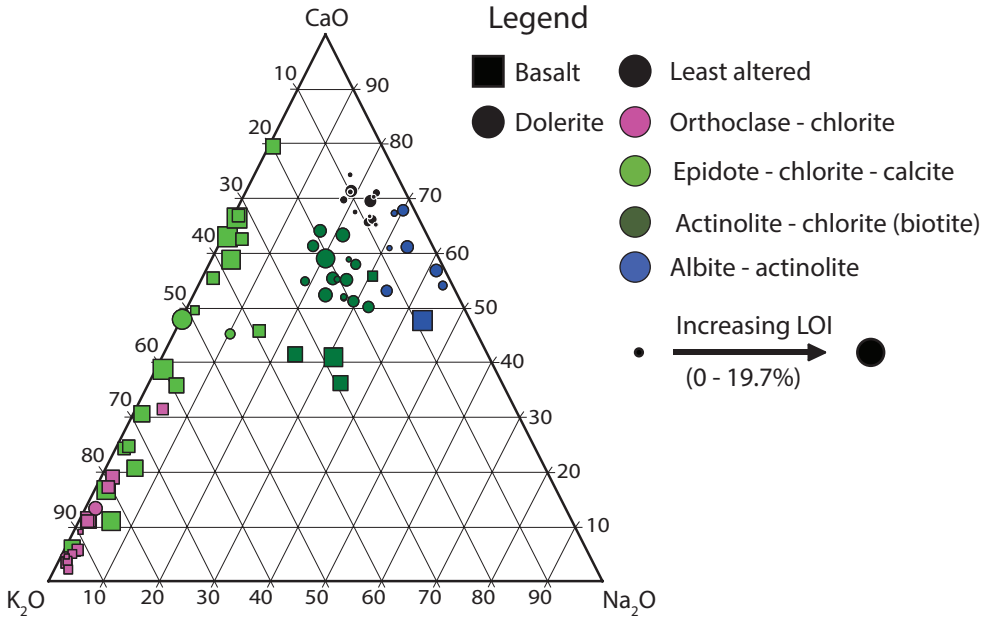


Figure 7.15 A. Ca-K-Na ternary diagram illustrating the sublte chemical changes associated with the biotite-actinolite alteration of the Proterozoic mafic rocks in the Superior district. All data listed in Appendix 1C.

of the Superior district have therefore been plotted on the alkali-alumina plot, sized by LOI and colour coded by the alteration types described in Section 7.3.1 – 7.3.8 based on their major element chemistry (Figure 7.14 C). The broad spread of points around the least altered composition of dolerite and basalt on Figure 7.14 C suggests many of these samples are not strongly altered or have largely undergone isochemical alteration. Subtle increases in K/Al values combined with variable increases in LOI, indicate that these rocks are weakly potassic altered, consistent with observations of secondary biotite and/or K-feldspar (Figure 7.12 A, D). Although samples with this alteration type appear strongly altered in hand specimen, actinolite alteration is challenging to identify geochemically using the alkali-alumina plot, except by the increased loss on ignition (LOI) caused by the hydrous nature of actinolite. Incipient biotite and/or K-feldspar alteration, though visually subordinate, is the most significant geochemical signal apparent using this plot. The distinction between actinolite - chlorite ± biotite ± K-feldspar altered and least altered samples is more obvious on the Ca-K-Na ternary diagram, where actinolite – chlorite ± biotite ± K-feldspar altered samples also show significant Ca depletion (Figure 7.15). Samples that plot with low K/Al values but high Na/Al values are indicative of albite-dominant alteration. Strong albite alteration in these samples is typically accompanied by abundant actinolite (e.g., RE15JP150; Figure 7.10 C) though for the aforementioned reasons, the geochemical signal is weak.

Points that plot with high K/Al but very low Na/Al (<0.1) values on the alkali molar ratio plot (Figure 7.14 C) are indicative of strong potassic alteration (e.g., Davies and Whithead, 2006). This is consistent with hand specimen observations of intense orthoclase – chlorite alteration (e.g., Sample RE15JP005; Figure 6.7 B). The K/Al values, are lower than might be expected due to the abundance of chlorite (K/Al = 0), which offsets the high K/Al values associated with orthoclase. Samples that plot at low Na/Al and K/Al values (<0.575; Figure 7.14 C), show strongly elevated loss on ignition (LOI) values.

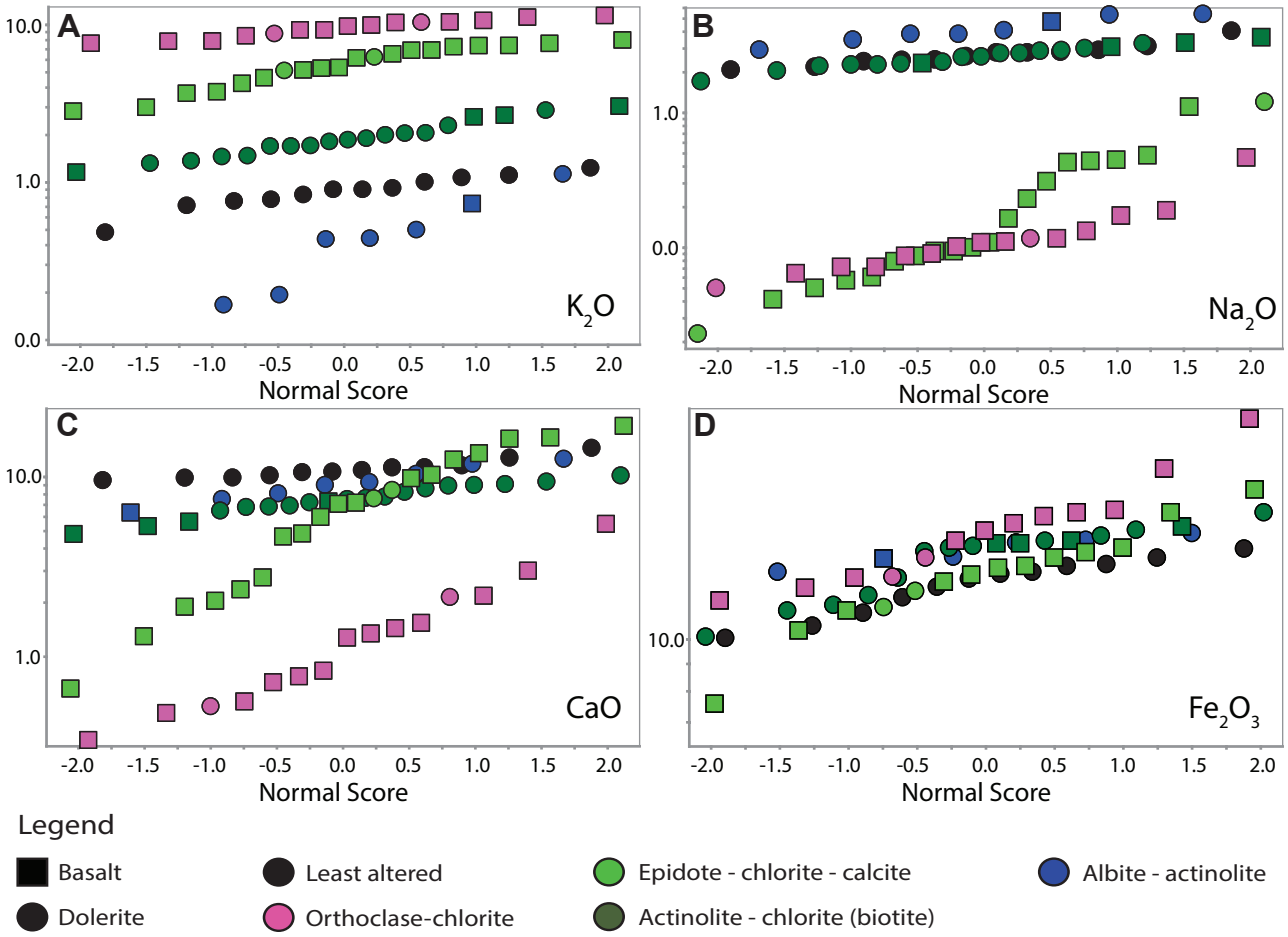


Figure 7.16 Relative enrichment and depletion diagrams for selected major elements for Proterozoic altered mafic rocks of the Superior district. A. Potassium. B. Sodium. C. Calcium. D. Iron. All data listed in Appendix 1C.

Without visual inspection of these samples, they would typically be interpreted geochemically as strongly muscovite (i.e., acid) altered as they plot close to the composition of end-member muscovite (Figure 7.14 A-C). Instead, these samples are epidote - chlorite - calcite and orthoclase - chlorite altered (Figure 6.8). Their positions on the alkali-alumina diagram (Figure 7.14 C) reflect the mixed chemical composition caused by alteration overprinting, which shifted the orthoclase - chlorite-altered samples towards lower K/Al compositions. However, because epidote - chlorite - calcite alteration was incomplete, and there is relict orthoclase alteration in these samples, whole rock K/Al compositions plot between orthoclase and epidote - chlorite, where strongly muscovite altered rocks would typically plot (Figure 7.14 A-B).

Relative enrichments or depletions of elements in any alteration type compared to a least-altered rock composition can be viewed using probability plots (Figure 7.16). Alteration facies that plot above the line defined by least altered samples can be considered enriched in that element, and depleted in elements that plot below the least altered samples. For the Superior district, potassium contents increase from actinolite - biotite through epidote - chlorite - calcite to orthoclase - chlorite assemblages, whereas the albite - actinolite assemblage is relatively depleted in K (Figure 7.16 A). The actinolite - biotite assemblage has similar Na contents to least-altered samples (Figure 7.16 B). Calcium has been largely depleted in all alteration types relative to least altered samples, except for a few epidote – chlorite – calcite altered rocks

(Figure 7.16 C). The orthoclase - chlorite and actinolite - biotite assemblages are enriched in Fe relative to least-altered rocks (Figure 6.13 D). Similarly, the orthoclase - chlorite assemblage, also shows evidence of Fe addition compared to least-altered samples, an observation that is consistent with the presence of specular hematite veins in hand specimen (Figure 7.16 D).

***Interpretation of major element geochemistry***

The major element geochemistry of the Proterozoic mafic rocks of the Superior district corroborates hand specimen and petrographic observations. Notably, the alkali alteration assemblages associated with Proterozoic metasomatism have mineralogical and geochemical equivalents that can be observed in porphyry Cu systems. In the context of porphyry Cu exploration, the discovery of high temperature, alkaline alteration can be highly significant (e.g., Sillitoe, 2010), especially where potassic-altered rocks host quartz stockworks, such as that observed in the range front (e.g., Figure 6.5 C). Where biotite occurs with actinolite (another a high temperature mineral; Cooke et al., 2014), the assemblage is often considered diagnostic of the inner propylitic subzone (Holliday and Cooke 2007). Epidote - chlorite - calcite alteration, is typical of distal porphyry-related propylitic alteration in volcanic rocks (Cooke et al., 2014). Consequently, without the hydrothermal geochronology results described in Chapter 6, the Proterozoic alteration assemblages observed in the Superior District could be confused with alteration zones around a Laramide porphyry Cu system.

#### 7.5.3.2 Trace elements

Figure 7.17 shows relative enrichments and depletions in trace elements for each of the Proterozoic alteration assemblages relative to least altered samples of the Apache Basalt and Proterozoic dolerite. Zinc and Mn are strongly depleted in the orthoclase – chlorite altered rocks, but moderately to strongly enriched in epidote – chlorite - calcite altered rocks (Figure 7.17 A-B). Arsenic and antimony are uniformly enriched across all alteration assemblages relative to least altered rocks (Figure 7.17 C-D). Copper shows depletion in most of the orthoclase – chlorite, epidote – chlorite – calcite and albite – actinolite samples, but shows minor enrichment in actinolite – biotite samples (Figure 7.17 E). Bismuth is enriched in epidote – chlorite – calcite and albite – actinolite altered rocks but not in the orthoclase - chlorite assemblage (Figure 7.17 F). Conversely, U is enriched in all assemblages relative to the least-altered rocks (Figure 7.17 G).

***Interpretation of trace element geochemistry***

Trace element compositions can help to distinguish Proterozoic metasomatism from Laramide hydrothermal alteration in the Superior district. Although the enrichment of Zn and Mn in the epidote – chlorite – calcite assemblage is similar to what might be from porphyry Cu deposits (Halley et al., 2015), the enrichment patterns of other distal elements such as As, Sb, and proximal elements such as

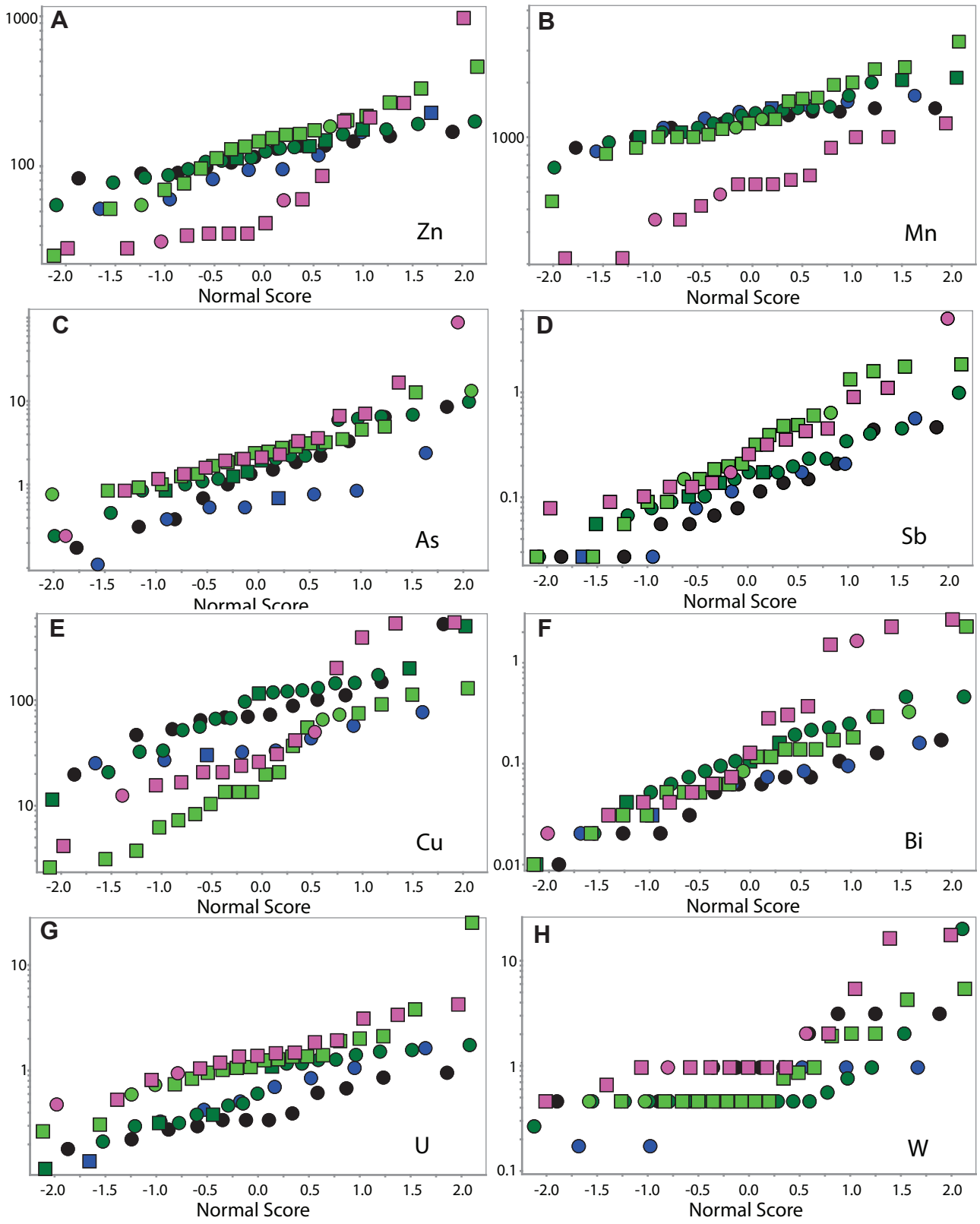


Figure 7.17 Relative enrichment and depletion diagrams for selected trace elements for Proterozoic altered mafic rocks of the Superior district. A. Zinc. B. Manganese. C. Arsenic D. Antimony. E. Copper. F. Bismuth. G. Uranium. H. Tungsten. All data provided in Appendix 1C

Cu, Bi, and U are notably at odds with propylitic alteration around porphyry Cu deposits. As for Zn and Mn, As and Sb are depleted in the core of a porphyry deposit, and elevated in peripheral propylitic zones

(Halley et al., 2015). In the range front, these path finder elements show enrichment across all alteration types and do not define spatial zonation patterns (Figure 7.17 C-D).

Enrichment and depletion of Cu, Bi, U and W (Figure 7.17 E-H) help to distinguish the different types of alteration in the Superior district. Copper is largely depleted in the Proterozoic orthoclase - chlorite alteration assemblage. Bismuth is mostly enriched in the epidote - chlorite and actinolite - biotite assemblages. Uranium is elevated in all Proterozoic alteration assemblages in the Superior district. The unusual behaviour of the critical elements argues against a magmatic, porphyry Cu-type origin for these fluids and instead suggests a highly oxidised brine, capable of leaching and transporting significant quantities of base metals and U (e.g., Cooke et al., 1998).

### 7.5.4 Spatial relationships

Figure 7.18 shows the spatial distribution of alteration types in the mafic rocks of the Superior district. Due to the limited number of albite - altered rocks in this dataset, little can be said regarding their distribution. Strongly orthoclase - chlorite-altered samples cluster in areas where the Apache Basalt is cut by NE-striking faults (e.g., Belmont and Grand Pacific structures) in the south of the district, and by the NW-striking Conley Springs Fault in the north of the district (Figure 7.18). The spatial distribution of the most strongly potassic-altered samples at the western end of the South Boundary-Belmont Fault coincides with outcropping magnetite skarns (Figure 7.5 A-B), providing evidence that Fe was transported by these fluids. Strong orthoclase - chlorite alteration transitions laterally into epidote - chlorite stable alteration in the Apache Basalt (Figure 7.18). Conversely, actinolite - chlorite ± biotite alteration of the dolerite do not define obvious zonation patterns

The coincidence of strongly orthoclase-chlorite altered basalt and magnetite skarn showings around NE striking faults imply that these faults were active during the Precambrian, and imparted a strong control on focussing Proterozoic hydrothermal fluids. These faults were reactivated in the Laramide, as they host epithermal veins arrays.

### 7.5.5 Mass balance calculations

#### 7.5.5.1 Methods

Mass balance calculations methods of Grant (1986) are used in this section to quantify geochemical changes related to Proterozoic alteration in the Superior district. Specifically, subsets of altered Apache Basalt are compared to equivalent least-altered samples of the same rock type (Tables 6.1 and 6.2). Apache Basalt samples were used in this study due to their homogeneity when compared to the dolerites, and also because the basalts have been altered by two major types of alteration, orthoclase – chlorite and epidote – chlorite – calcite, with texturally constrained relative timing relationships. Average compositions were generated for three least-altered samples (Least altered samples: RE15JP090,

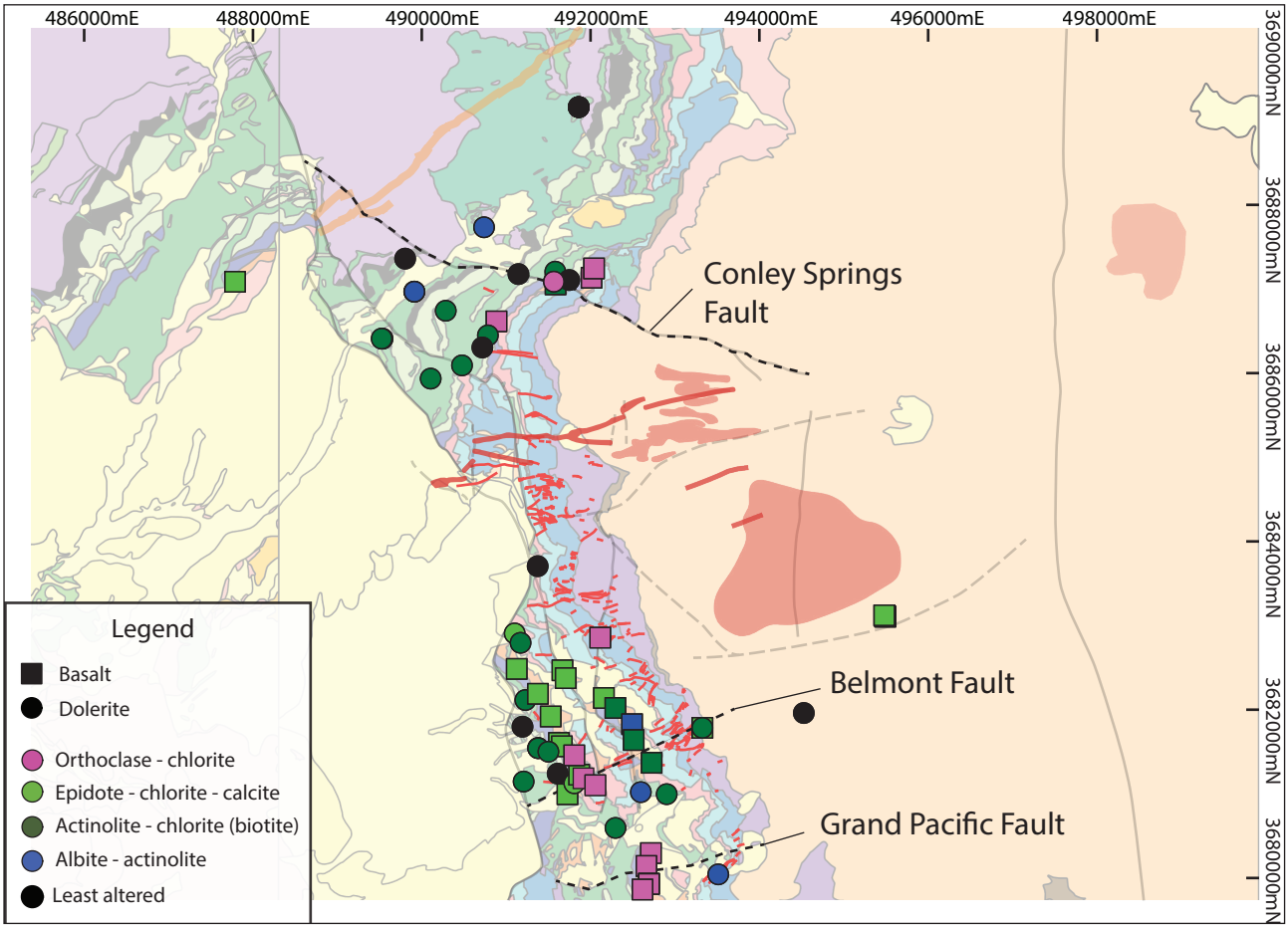


Figure 7.18 Geological map of the Superior district showing spatial distribution of Proterozoic alteration assemblages in the Proterozoic Apache Basalt and dolerite sills. Geology as in Figure 3.1. Geochemical data listed in Appendix 1C.

RE15JP120 and RE15JP139; Appendix 1C), 14 orthoclase - chlorite samples and 15 epidote – chlorite-altered samples. Gresens' equation, rearranged by Grant (1986) is:

$$C^A/C^O = (M^A/M^O)*(Ci^A/Ci^O)-1$$

Where $C^A/C^O$ is the final change in concentration between an altered and unaltered sample pair, $M^A/M^O$ is the isocon reference line calculated from changes in concentration between unaltered and altered sample pairs of immobile elements, and $Ci^A/Ci^O$ is the ratio between immobile elements in the altered and unaltered sample pair. $C^A/C^O$ values less than 1 indicate depletion and numbers greater than 1 indicate addition. $M^A/M^O$ values > 1 indicate overall mass addition and values < 1 indication overall mass removal.

To define the isocon, groups of immobile elements are first selected. Fitting the isocon by eye, as suggested by Grant (1986, 2005) is subjective, and is strongly influenced by the scaling of immobile trace elements (Baumgartner, 1995 and Olsen; Ague and van Haren 1996; Mukherjee, 2008). An alternative to viewing the ratio between elements (altered rock / least-altered rock) on a scatter diagram, as used by Grant (1986, 2005) is to plot ranked ratios on a bar graph (Janoušek et al., 2006), a variation of the histogram method presented by Ague and van Haren (1996). An unpublished macro-enabled Microsoft Excel spreadsheet created by David Doutch and Robert Scott at CODES, University of Tasmania is used here

to choose an isocon and to produce mass balance results.

Plotting the ranked ratios (Figure 7.19 A and Figure 7.20 A) allow qualitative comparison of elemental change between altered and least altered samples in order to select a group of immobile elements. Where a suite of elements define a plateau of 1:1 relationship between altered and least-altered rocks they can be considered immobile. The black solid lines represent the best-fit plateau defined by the least-mobile elements (Figure 7.19 A and Figure 7.20 A). Dashed lines (± 0.1), represent a domain of 10% uncertainty, where mobility is uncertain due to the inherent heterogeneity in the least altered compositions. In Figure 7.19, $Al_2O_3$, $TiO_2$, Nb, Sc, Y, Zr define an acceptable plateau and were selected as immobile. Although Fe and Si also fall within this window, textural observations have shown that these elements are mobile locally and therefore they were not used as immobile elements in the mass balance calculations. Analysis by this method has so far not been completed in the Superior district.

#### 7.5.5.2 Results

The results of the mass balance calculations are presented in terms of raw and relative mass changes for major elements (wt %) and trace elements (ppm) in Table 7.1 A (orthoclase – chlorite altered samples relative to least altered) and Table 7.1 B (epidote – chlorite – calcite-altered relative to least altered), respectively.

Relative mass change results for the altered Apache Basalts have been plotted graphically in Figure 7.19 B-C and Figure 7.20 B-C. In Figure 7.19 B-C, comparison of least altered to orthoclase-chlorite altered samples indicate significant addition of $K_2O$ (315%, Table 7.1 A) consistent with observations of intense orthoclase alteration (Section 6.3.4). There have also been significant additions of $P_2O_5$ (86%) and S (27%, Table 7.1 A). The immobile elements $TiO_2$ and $Al_2O_3$ show less than 5% change. MgO, MnO and CaO all show significant depletion with values of -44%, -62% and -71% respectively (Table 7.1 A). Sodium the most strongly depleted, -95%. Of the trace elements, the LILEs Th (906%), U (220%) Rb (96%) W (91%) and Ba (21%) are most significantly enriched, along with metals Sb (92%), Bi (84%), As (48%) and Sn (38%) as well as some Ag (19%) and minor Mo (11%, Table 7.1 A). Notably, the most significant depletions are observed in the base metal suite including Pb (-24%), Ni (-29%), Co (-31%), Cu (-36%), Cr (-39%) and Zn (-49%), also with significant depletion of Au (-31%) and Sr (-35%). Moderate depletions of La, Ce and V are also significant.

The immobility plateau for epidote – chlorite – calcite samples compared to least-altered samples is poorly defined (Figure 6.17A). Zirconium, Y, Sc, $Al_2O_3$ and $TiO_2$ define a plateau around 0.96, and were selected as immobile (Figure 7.20 A). $Na_2O$ was the most depleted major element (Table 7.1 B, Figure 7.20 B-C), whereas CaO MnO and MgO all showed modest enrichment in the epidote - chlorite - calcite altered rocks (29%, 10% and 11% respectively; Table 7.1 B, Figure 7.20 B-C).

Of the base metal suite Ni, Cu and Cr show losses of -23%, -33% and -45% respectively, whereas Co shows a small net gain of 5%. Zinc and Pb were enriched by 61% and 51% respectively in the epidote

Table 7.1 Mass balance data showing chemical difference between A. orthoclase - chlorite altered and least-altered samples and B. epidote - chlorite - calcite-altered and least-altered samples, arranged from greatest addition to greatest depletion for major and trace elements. Mass change is given in weight percent for major oxides and ppm for trace elements.

| A | | | | B | | | |
|---|---|---|---|---|---|---|---|
| **Elements** | **Ranked ratio** | **Mass change** | **Relative change** | **Elements** | **Ranked Ratio** | **Mass change** | **Relative change** |
| $K_2O$ | 4.08 | 6.83 | 315% | $K_2O$ | 2.95 | 4.75 | 219% |
| $P_2O_5$ | 1.83 | 0.267 | 86% | S | 2.52 | 0.121 | 173% |
| S | 1.25 | 0.0185 | 27% | LOI | 1.93 | 2.68 | 108% |
| $Fe_2O_3$ | 0.99 | 0.00989 | 0% | CaO | 1.20 | 1.64 | 29% |
| $SiO_2$ | 0.97 | -0.560 | -1% | MgO | 1.03 | 0.722 | 11% |
| $TiO_2$ | 0.96 | -0.0729 | -3% | MnO | 1.02 | 0.0204 | 10% |
| $Al_2O_3$ | 0.94 | -0.719 | -4% | $Al_2O_3$ | 1.01 | 1.34 | 9% |
| LOI | 0.86 | -0.326 | -13% | $SiO_2$ | 0.948 | 0.145 | 0% |
| MgO | 0.56 | -2.89 | -44% | $P_2O_5$ | 0.897 | -0.0122 | -3% |
| MnO | 0.37 | -0.132 | -62% | $Fe_2O_3$ | 0.789 | -0.755 | -5% |
| CaO | 0.29 | -3.96 | -71% | TiO2 | 0.868 | -0.176 | -7% |
| $Na_2O$ | 0.05 | -2.90 | -95% | $Na_2O$ | 0.121 | -2.67 | -87% |
| Th | 9.89 | 4.57 | 906% | U | 4.71 | 2.25 | 408% |
| U | 3.14 | 1.20 | 220% | Th | 4.02 | 1.69 | 334% |
| Rb | 1.92 | 49.69 | 96% | Bi | 3.86 | 0.30 | 317% |
| Sb | 1.89 | 0.110 | 92% | W | 2.46 | 1.66 | 166% |
| W | 1.88 | 0.908 | 91% | Sb | 2.08 | 0.151 | 124% |
| Bi | 1.81 | 0.0775 | 84% | As | 1.96 | 1.94 | 112% |
| As | 1.46 | 0.826 | 48% | Rb | 1.83 | 50.8 | 97% |
| Sn | 1.36 | 0.499 | 38% | Te | 1.72 | 0.134 | 85% |
| Ba | 1.19 | 96.4 | 21% | Tl | 1.58 | 0.186 | 71% |
| Ag | 1.17 | 0.0465 | 19% | Ag | 1.57 | 0.177 | 69% |
| Tl | 1.13 | 0.0392 | 15% | Zn | 1.49 | 70.5 | 61% |
| Zr | 1.09 | 13.6 | 11% | Pb | 1.40 | 3.74 | 51% |
| Mo | 1.09 | 0.0855 | 11% | Ba | 1.30 | 190.0 | 41% |
| Nb | 1.06 | 0.421 | 8% | Cd | 1.27 | 0.0861 | 38% |
| Te | 0.96 | -0.00324 | -2% | Mo | 1.16 | 0.211 | 25% |
| Y | 0.96 | -0.887 | -3% | Ga | 1.16 | 4.17 | 25% |
| Ga | 0.94 | -0.746 | -4% | Ge | 1.15 | 0.602 | 24% |
| Se | 0.92 | -0.0432 | -7% | Sr | 1.09 | 45.5 | 17% |
| Sc | 0.92 | -1.66 | -7% | Sc | 1.01 | 2.14 | 9% |
| Nd | 0.89 | -1.83 | -10% | Co | 0.971 | 2.44 | 5% |
| Ce | 0.88 | -2.75 | -10% | Sn | 0.930 | 0.0126 | 0% |
| V | 0.86 | -26.0 | -12% | V | 0.895 | -7.00 | -3% |
| La | 0.84 | -1.51 | -15% | Y | 0.889 | -1.25 | -4% |
| Cd | 0.83 | -0.0393 | -15% | Zr | 0.865 | -8.62 | -7% |
| Ge | 0.82 | -0.422 | -17% | Au | 0.855 | -0.0003 | -8% |
| Pb | 0.75 | -1.77 | -24% | Nb | 0.835 | -0.562 | -10% |
| Ni | 0.70 | -32.0 | -29% | Nd | 0.827 | -1.98 | -11% |
| Co | 0.68 | -15.7 | -31% | La | 0.817 | -1.20 | -12% |
| Au | 0.67 | -0.0011 | -31% | Ce | 0.808 | -3.31 | -13% |
| Sr | 0.64 | -92.6 | -35% | Se | 0.737 | -0.131 | -20% |
| Cu | 0.63 | -52.2 | -36% | Ni | 0.714 | -24.7 | -23% |
| Cr | 0.60 | -41.0 | -39% | Cu | 0.624 | -46.8 | -33% |
| Zn | 0.51 | -56.3 | -49% | Cr | 0.512 | -46.2 | -45% |

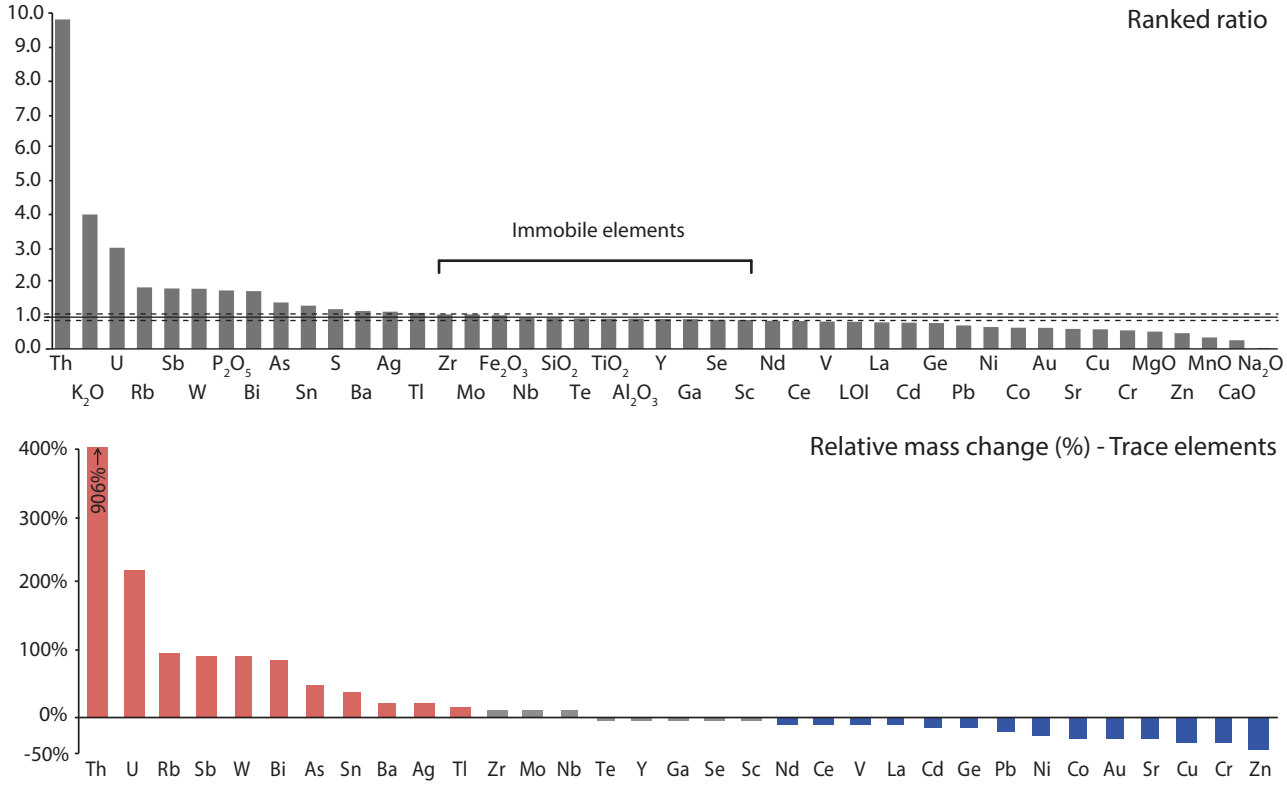


Figure 7.19 A. Isochon diagram showing the ratio of elements from orthoclase - chlorite-altered samples relative to least-altered samples. High field strength elements that plot at or close to a ranked ratio of 1 have been used for the mass balance calculation applied to the rest of the data. B Percentage mass change in trace elements between least-altered and orthoclase-chlorite altered samples. C. Percentage mass change in major elements between least-altered and orthoclase-chlorite altered samples. Plotted in macro-enable spreadsheet of Doutch and Scott (in prep), adapted from Grant (1986). Zr, Nb, Y, $TiO_2$, Sc and $Al_2O_3$ were considered immobile and mass balance caluations. Red = enriched; Grey = immobile; Blue = depleted. Data listed in Table 7.1 A.

– chlorite – calcite-altered rocks, compared with -49% and -24% depletion in the orthoclase - chlorite-altered rocks. The element suite of U, Th, W, Rb, Ba, Bi, Sb, As and Ag, which consists of the most strongly enriched elements in the orthoclase - chlorite-altered rocks, is also the most enriched element suite in the epidote - chlorite assemblage (Table 7.1 B, Figure 7.20 B-C)

## 7.6 Discussion

### 7.6.1 Mineralogical implications for fluid temperatures and pH

Alteration mineralogy can be influenced by a range of factors, including but not limited to, host-rock composition, permeability, pressure, temperature, redox, sulfur saturation, and salinity (Corbett and Leach, 1998; Cooke et al., 2000). Paleo-temperatures and pH conditions can therefore be estimated from alteration mineralogy (Figure 7.21; Hemley et al., 1980; Henley and Ellis, 1983; Reyes, 1990).

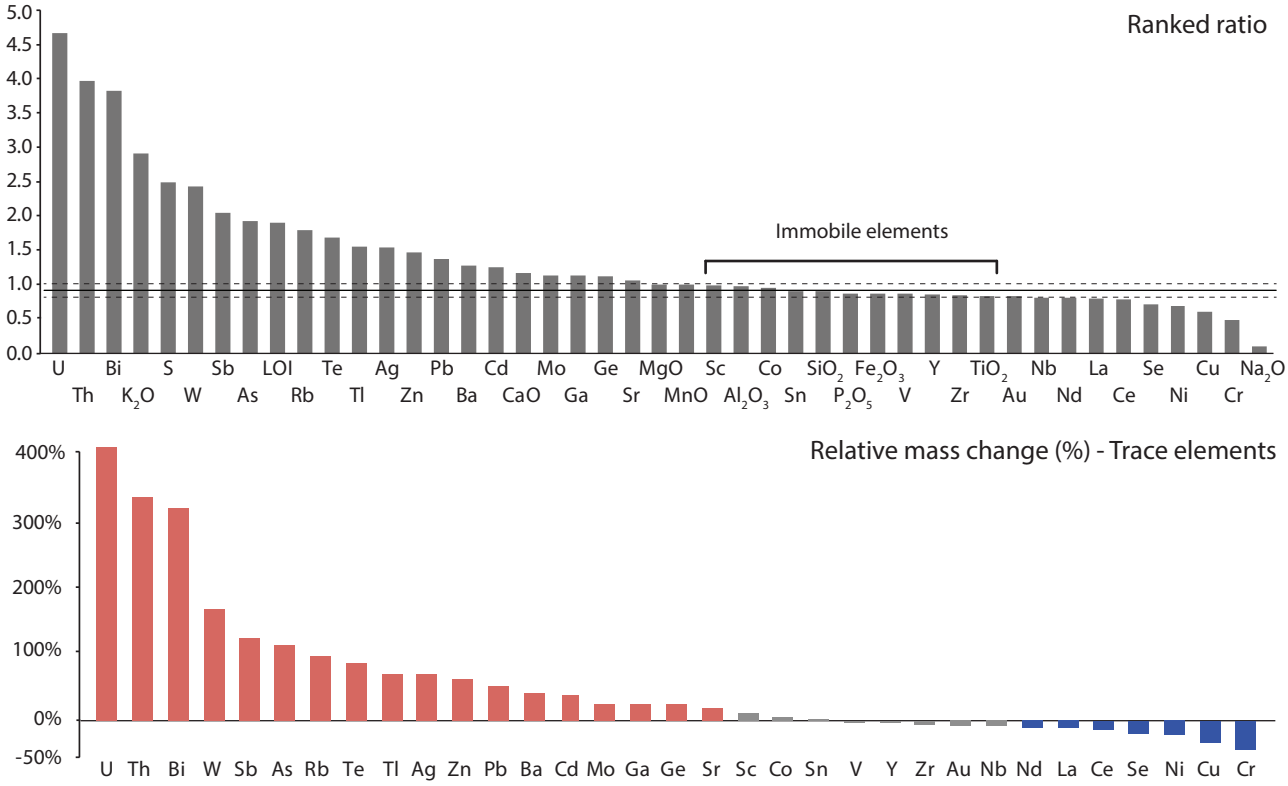


Figure 7.20 A. Isochon diagram showing the ratio of elements from epidote - chlorite - calcite-altered samples samples relative to least altered samples. High field strength elements that plot at or close to a ranked ratio of 1 are used for mass balance calculations applied to the rest of the data. B Percentage mass change in trace elements between least-altered and epidote - chlorite - calcite- altered samples. C. Percentage mass change in major elements between least-altered and orthoclase - chlorite altered samples. Plotted in macro-enable spreadsheet of Doutch and Scott (in prep), adapted from Grant (1986). Zr, Nb, Y, $TiO_2$, Sc and $Al_2O_3$ were considered immobile and have been used for mass balance caluations. Red = enriched; Grey = immobile; Blue = depleted. Data listed in Table 7.1 B.

Magnetite observed in skarn-altered Mescal Limestone and Pinal Schist is indicative of high temperatures. Where it occurs in the core of porphyry deposits, it is inferred to have crystallised at sub-magmatic temperatures between 500 – 400$^0$C, based on experimental studies (Figure 7.21, Simon et al., 2000). For magnetite skarns in the Superior district, a temperature estimate of > 400$^0$C is consistent with the general proximity of magnetite skarns in the Mescal Limestone and Pinal Schist to within 50 - 100 m of dolerite intrusions, and the quartz diorite respectively.

K feldspar and chlorite can be stable together between 200 and approximately 425$^0$C (Figure 7.21). The orthoclase - chlorite alteration in the Superior district probably precipitated at the upper end of this temperature range based on the association with actinolite alteration.

The epidote – chlorite – calcite assemblage has an estimated temperature range of > 200 – 425$^0$C (Figure 7.21). The epidote - chlorite - calcite assemblage overprints the orthoclase - chlorite assemblage and is therefore interpreted to be a somewhat lower temperature assemblage.

Quartz – hematite alteration in the sandstones of the Superior district cannot be constrained in terms of its temperature of formation due to the wide temperature range of stability for these minerals. The hematite implies oxidised (sulfate predominant) conditions (Cooke et al., 2000).

Actinolite - chlorite ± biotite alteration of the dolerite sills has a temperature stability range of > 350 – 425$^0$C indicating this is a relatively high temperature assemblage (Figure 7.21). Hammond (1983) described alteration in the dolerite sills of southern California and central Arizona as approaching two end member compositions, which she classified as greenschist and amphibolite assemblages. Her amphibolite assemblage caused pyroxene to be altered to actinolite, whereas biotite and plagioclase remained relatively intact. Her greenschist end-member assemblage had plagioclase altered to albite and epidote, and pyroxene altered to chlorite (Hammond, 1983). These assemblages are most likely metasomatic rather than reflective of metamorphic grade, and probably represents a transition from higher to lower temperature alteration as the Proterozoic basinal fluids entered the sills after a period of cooling subsequent to their emplacement, were reheated and finally cooled.

Generally, alteration assemblages in the Proterozoic rocks of the Superior district are consistent with weakly alkaline to near-neutral pH conditions (Figure 7.21; Corbett and Leach 1998). Muscovite-illite alteration in Dripping Springs Quartzite from the Sierra Ancha Region was described by Granger and Raup (1969), who interpreted it to relate to thermal metamorphism by the intrusion of dolerite sills. Instead, the minor, variable amounts of white mica in regional exposures of the dolerite sills (Shride, 1967; Smith, 1969, 1970; Nehru and Prinz, 1970; Fouts, 1974; Hammond, 1983) and in the Dripping Spring Quartzite in the Sierra Ancha (Granger and Raup, 1969) and the Superior district (Figure 7.3 A) are here inferred to indicate weakly acid hydrothermal conditions locally (c.f., Cooke et al., 2000).

### 7.6.2 Age and relationship of alteration assemblages

Hand specimen analysis and feldspar staining of Proterozoic rocks in the Superior district has revealed a previously undocumented period of intense K-metasomatism. Uranium-lead geochronology on basalt-hosted hydrothermal apatite and epidote (Chapter 6) indicates that metasomatism occurred during the emplacement of ca. 1,100 Ma dolerite sills. Three U occurrences from the Sierra Ancha also report ages ranging from 1,104 – 930 Ma (Neuerburg and Granger, 1960), suggesting a genetic link between U mineralisation in the Sierra Ancha, hydrothermal alteration in the Superior district and regional emplacement of dolerite sills. There have also been empirical links made previously between dolerite intrusion and other Apache Group-hosted mineral occurrences in the Sierra Ancha (e.g., chrysotile asbestos, Bateman, 1923; Stewart, 1955).

Actinolite alteration in the dolerite sills could not be dated during the current study. It is inferred to be linked to potassic alteration of the Apache Basalts by the variable presence of biotite and rarely K-feldspar (e.g., RE15JP080, Figure 7.12 D) and by its district scale distribution (Figure 7.1). Petrologic reports from previous workers (e.g., Hammond, 1983) suggest this style of dolerite alteration is a regional

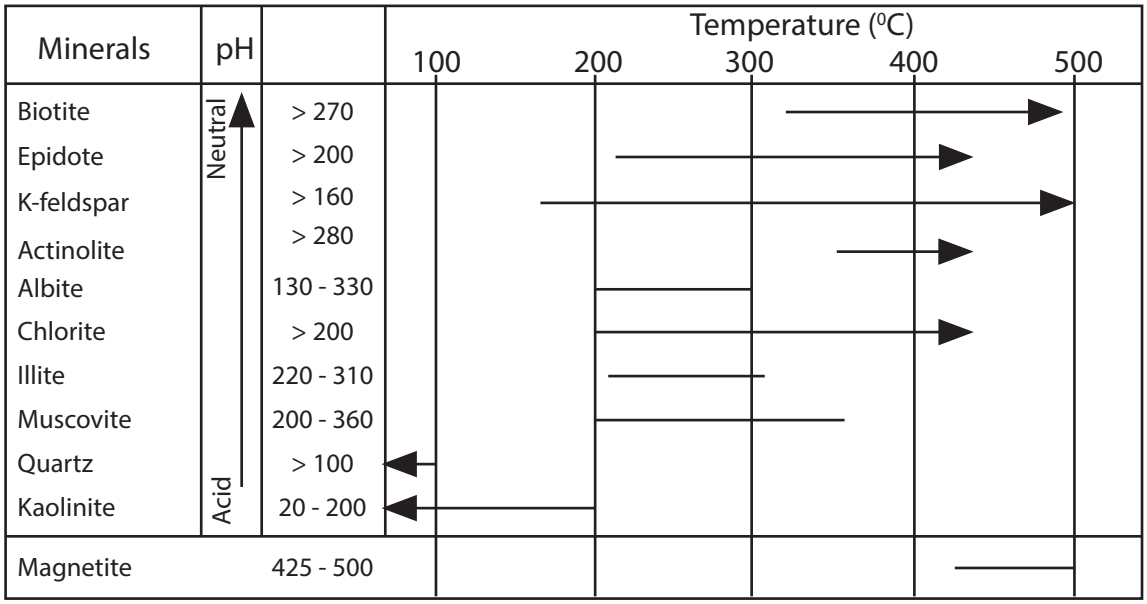


Figure 7.21 Common temperature stability ranges in geothermal systems for hydrothermal minerals observed in the Proterozoic mafic rocks of the Superior district. This data can be used as a guide for the mineral stability ranges in hydrothermal systems, however exceptions can occur due to extremes in fluid chemistry. Data deduced empirically from active geothermal systems, experimental modelling and fluid inclusion studies; Hemley et al. (1980); Henley and Ellis, (1983); Hedenquist and Houghton, (1987); Reyes, (1990). Minerals have been arranged by their stability with respect to pH. Sulfide and magnetite formation temperatures from experimental studies (Simon et al., 2004). Figure modified from Masterman (2003) and Pass (2010).

phenomenon and occurred coeval with or immediately after sill emplacement at ca. 1,100 Ma.

Determining relative timing relationships between alteration assemblages in the Apache Group has been hampered by the strong host rock-control on individual assemblages which limited the development of overprinting relationships. Textural observations have demonstrated that the epidote – chlorite – calcite assemblages post-date the strong orthoclase – chlorite assemblage within the basalt (Figure 7.8). Actinolite alteration within the dolerite, despite most likely being a high temperature assemblage, is thought to post-date, at least in part, the early orthoclase – chlorite alteration on account of the cross cutting relationships demonstrated in Figure 7.12 D. It may be that dolerite sills drove off pore water from the host rocks during emplacement driving migration of potassic brines through the Apache Group. As the sills crystallised and cooled, thermal collapse has allowed fluids to migrate into the dolerite sills. Although the dolerite would have crystallised, it would still have retained significant amounts of heat, especially in the centre of thicker sills, thereby producing higher temperature actinolite-stable assemblage during alteration.

There are several alteration types in the Superior district that are suspected to be Proterozoic in timing. Although no unequivocal timing constraints are available for chrysotile, serpentine and magnetite alteration of the Mescal Limestone, empirical observations have linked them to intrusion of dolerite sills (Bateman, 1923; Stewart, 1955) and therefore to this period of Proterozoic metasomatism. No timing constraints are available for quartz - hematite breccias or epidote alteration in the Pinal Schist. They do not show any consistent spatial association with dolerite sills. Their mineralogy is permissive of a

relationship to Proterozoic metasomatism, but their significance and relationships with the Proterozoic alteration assemblages remains unconstrained.

### 7.6.3 Mineralogical and lithogeochemical overlap with porphyry-style alteration

Four alteration assemblages were identified in the Proterozoic mafic rocks of the Superior district using major element chemistry and validated against hand specimen observations. Without hydrothermal geochronology and familiarity with the regional geologic context, the high to moderate temperature alkali alteration mineralogies of the Superior district could be mistaken for alteration assemblages that might be encountered peripheral to a porphyry Cu system (e.g., Seedorff et al., 2005; Sillitoe, 2010; Cooke et al., 2014). Mineralogically, there is no way to distinguish the dolerite-hosted actinolite-biotite alteration from inner propylitic assemblages that occur adjacent to porphyry system (e.g., Holliday and Cooke, 2007; Cooke et al., 2014), or Mesoproterozoic epidote – chlorite – calcite alteration in the Apache Basalt from propylitic alteration distal to a porphyry centre (Figure 7.8). However, this study has shown that using relative enrichment and depletions patterns of trace elements in the different Proterozoic alteration assemblages, they are demonstrably different to what might be expected in a typical porphyry Cu system. Additionally, the Proterozoic hydrothermal system was sulfur-poor, which contrasts with the relatively sulfur-rich propylitic and potassic alteration at Resolution.

### 7.6.4 Proterozoic sources of fluids and metals

Previous workers have argued that the dolerite sills were sources of fluids and metals for the various alteration assemblages and mineral occurrences of the Apache Group rocks in central Arizona (e.g., Neuerburg and Granger, 1960; Granger and Raup, 1969; Wrucke et al., 1986). In contrast, geological, mineralogical and geochemical evidence presented in this chapter indicates that the dolerite was not the dominant fluid or metal source for the Proterozoic metasomatism. For these elements to have been sourced from the dolerite, they would need to be efficiently concentrated and removed prior to completion of crystallisation in a late-stage hydrothermal fluid. The only observable features with which this mechanism of fluid exolution could be attributed are the actinolite veins. These Fe-rich and quartz undersaturated veins are unlikely products from the late-stage granophyric and aplitic pods that mark the final crystallisation of the dolerite sills. A hydrothermal fluid related to the cm - m scale late-stage granophyric crystallisation should be enriched in $SiO_2$, $K_2O$ and $Al_2O_3$, precipitate predominantly quartz, feldspar and phyllosilicate minerals, and should be volumetrically insignificant. The generally pyroxene-phyric dolerites are unlikely to have been capable of exolving any significant volumes of fluid. due to their anhydrous nature (c.f. Loucks, 2014).

Alteration of the dolerite by formation waters from the Dripping Springs Quartzite was first suggested by Smith and Silver (1970) and Hammond (1983). Intra-formational unconformities and paleo-karst observed in the Apache Group support shallow burial, periodic emergence and probable saturation by

surface waters at the time of dolerite emplacement (Shride, 1967; Beeunas and Knauth, 1985; Wrucke 1989; Skotnicki and Knauth, 2007). Primary porosity in oxidised sandstone aquifers such as the lower Dripping Springs Quartzite and paleo-karst cavities in the of the Mescal Limestone (Skotnicki and Knauth, 2007) could have held significant volumes of fluids. The intensely dolomitic nature of the Mescal Limestone, and previous reports of halite casts is consistent with a residual bitten brine.

Accounts of asbestos workings in the Mescal Limestone demonstrate a strong stratigraphic control on the mineral occurrences (Bateman, 1923; Stewart, 1955). Significant addition of K, U, Th, P and other LILEs to the altered basalts (Figure 7.19), suggest that these elements were most likely sourced from elsewhere in the Proterozoic stratigraphy. The most likely source is considered to be the upper member of the Dripping Springs Quartzite, which is anomalously potassic and uraniniferous (up to 7% $K_2O$ and 5 ppm U; Granger and Raup 1969; Nutt, 1981, 1984; Wrucke 1989). The Apache Basalt may assimilated some K-rich sediments, based on observations of xenoliths of laminated orthoclase-rich siltstone xenoliths from the Upper Dripping Springs member (Figure 7.6 E). Most of the K is hydrothermal in origin based on the textural observations of pervasive alteration. Copper and other base metals were leached from the Apache Basalts during K metasomatism (Table 7.1).

The lack of evidence of significant Fe enrichment in the mass balance calculations, combined with observations of specular hematite veins, suggest that the Fe required for these veins was probably sourced from the wallrocks, and may only have been mobile at the cm to m scale. Significant Fe must have been leached from either the basalt, the dolerite (post-crystallisation) or other Fe-rich units for it to be deposited in significant quantities in the magnetite skarns of the Mescal Limestone. No evidence was found in the current study for the lateritic concentrations of Fe produced by weathering of the basalt, and subsequent transformation of lateritic Fe into magnetite, as suggested by previous authors (e.g., Burchard, 1931; Harrer, 1964; Wrucke, 1986). Iron mobility requires high salinity fluids, as inferred for basin-related IOCG deposits worldwide (e.g., Barton and Johnson, 2000; Williams et al,. 2005; Chiaradia et al., 2006; Barton et al., 2014). Halite casts have been reported from the Mescal Limestone (Wrucke, 1989) providing evidence of a local evaporitic source of salt, a favourable indication for hypersaline brine formation. The modest S enrichment in the basalt that has been highlighted in mass balance calculations, which was probably evaporitic, sourced from sulfate-bearing horizons of the Mescal Limestone (Heidecker, 1978).

Mass balance calculations have shown that up to 36% of the Cu, and significant quantities of Pb, Zn, Ni and Cr, was leached from the basalt during K metasomatism. Some of this Cu, and to some extent other base metals, were redeposited in distal, lower temperature epidote – chlorite – calcite assemblages. Base metal leaching implies there is potential for sediment-hosted base-metal mineralisation (e.g., Cooke et al., 1998) in the reduced trap rocks of the Apache Group.

### 7.6.5 Genetic model for the Mesoproterozoic hydrothermal system

The alteration assemblages observed in Apache Group rocks from the Superior district suggest they were probably formed during two major phases of hydrothermal activity (Figure 7.22). The initial prograde stage was associated with dolerite intrusion into shallowly-buried sediments, which drove hydrothermal fluid flow through at least some parts of the Apache basin during the Mesoproterozoic (Figure 7.22 A). In dolomitic horizons of the Mescal Limestone, this caused formation of chrysotile asbestos and serpentine veins. Salt and sulfate derived from local evaporates produced a heated, hematite-stable hypersaline brine. It strongly leached the Mesoproterozoic sedimentary sequence, in particular the upper member of the Dripping Springs Quartzite and Apache Basalt, acquiring large quantities of K, U Th, P, other LILEs, base metals and possibly Fe. In locations proximal to the dolerite sills significant quantities of Fe were deposited as magnetite skarns in the Mescal Limestone (Figure 7.22 A). Specular hematite formed veins in the Apache Basalt and also earthy hematite patches in variably potassic-altered Dripping Springs Quartzite. Based on mapped alteration intensity in the range front, (Figure 7.18), the brines exploited major E-NE-striking faults. Fault breccias in brittle sandstone units strongly focussed oxidised fluids (Figure 7.4), although the timing of this alteration assemblage remains unconstrained. The intensity of alteration observed in the basalt, and to some extent sandstones, varied as a function of primary permeability, with vesicular and/or brecciated horizons in the basalt and coarser beds in the sandstones particularly susceptible for alteration (Figure 7.3 B, Figure 7.6). The general lack of veins or hydrothermal breccia in altered rocks except for the dolerite, is consistent with fluid flow in porous media. There was a strong protolith control on alteration assemblages, with epidote - chlorite - calcite assemblages particularly well developed in the basalt and locally in the Pinal Schist. Quartz sandstones were cemented by quartz and cut by quartz-hematite fault breccias. Alteration of the dolerite occurred during thermal collapse as the sills cooled (Figure 7.22 B). Fluids were then able to penetrate the sills, along cooling joints and cracks, leading to actinolite veining and widespread alteration of the dolerite.

## 7.7 Conclusions

A previously unidentified period of intense K-metasomatism affected rocks of the Superior district during the Mesoproterozoic, coeval with the emplacement of dolerite sills. Several alteration types are tentatively linked with this phase of hydrothermal activity, although cross cutting relationships are scarce. A moderate to high temperature, oxidised, hyper-saline brine sourced from the basin was mobilised by the emplacement of dolerite sills and focussed along E-NE striking faults and permeable horizons within the stratigraphy. Significant quantities of K, Th, U and LILEs, and base metals and Fe were leached from the upper Dripping Springs Quartzite and Apache Basalt respectively. Mineralogically, some Proterozoic alteration assemblages are indistinct from typical alteration assemblages around porphyry Cu deposits, making alteration mapping in the Superior district problematic.

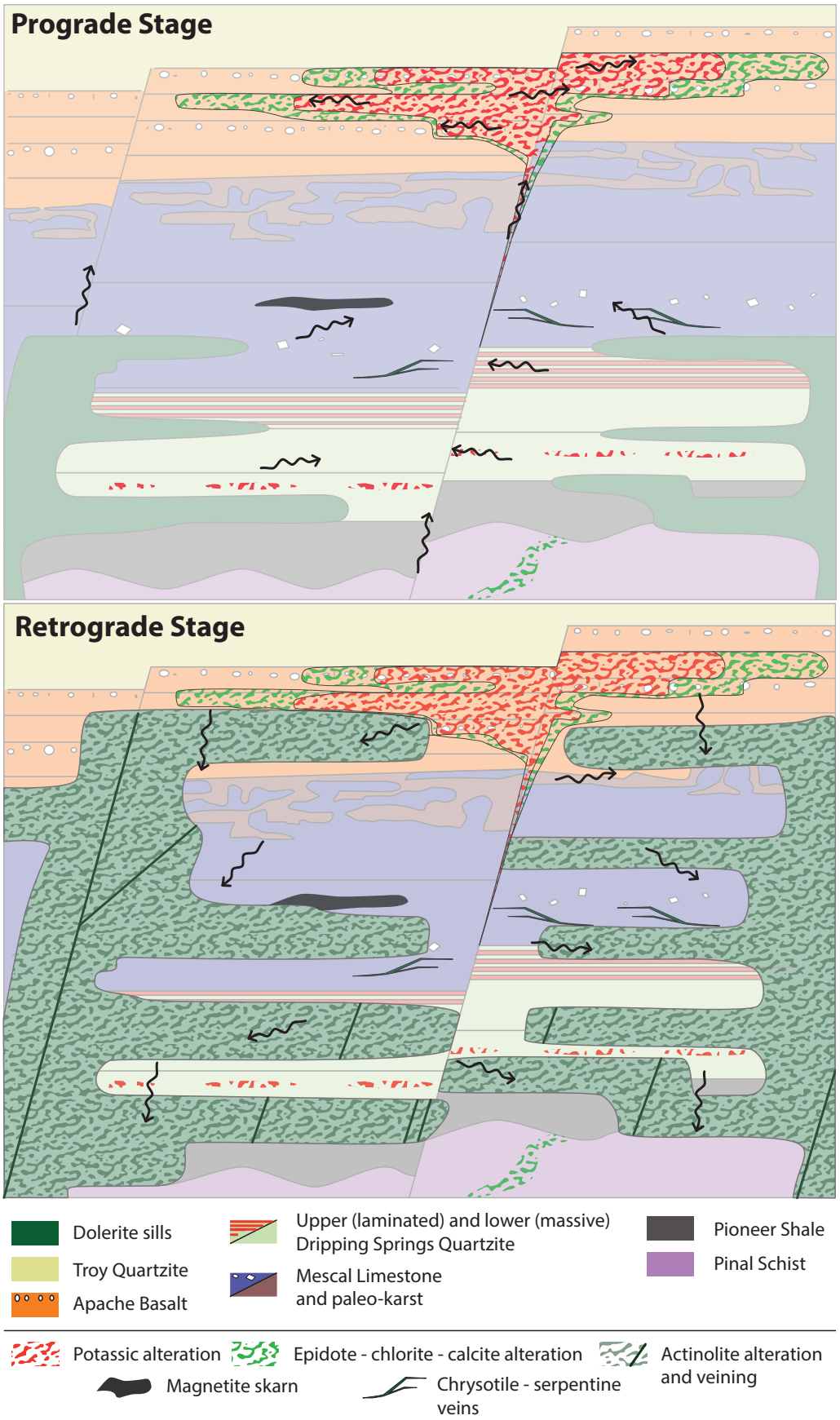


Figure 7.22 Schematic two-stage model for the formation of alteration assemblages observed in the Proterozoic rocks of the Superior district. A. Prograde phase, where emplacement of dolerite sills mobilised brines in the Apache Group, which where focussed along E- striking faults and permeable horizons. B Retrograde phase, where thermal collapse allows ingress of brines, causing strong actinolite - biotite - chlorite alteration in the dolerite sills

# Chapter 8: Epidote and chlorite chemistry

## 8.1 Introduction

Considerable efforts are currently being invested into the detection of low-level geochemical anomalies distal to porphyry deposits through the application of laser ablation inductively-coupled plasma mass spectrometry (LA-ICP-MS) analyses (e.g., Cooke, 2001; Cooke et al., 2014; Baker et al., 2015; Cooke et al., 2015; Wilkinson et al., 2015; Pacey; 2016; Baker et al., 2017; Cooke et al., 2017). This chapter presents new analyses of epidote and chlorite from the Superior district and demonstrates the use of supervised and unsupervised multivariate statistical techniques to overcome ambiguity in large geochemical datasets, and to help further discriminant Proterozoic and Laramide hydrothermal alteration in the district.

## 8.2 Previous Work

Pioneering investigations of the systematic chemical changes in spatially constrained samples of propylitic altered rocks around porphyry Cu deposits in the USA using wet chemical and microprobe techniques were conducted by Ballantyne (1981) and Norman et al. (1991), respectively. The development of LA-ICP-MS techniques in the late 1990s provided an alternative method for this work (e.g., Cooke, 2001) and resulted in developments in increased spatial resolution and throughput, allowing significant research efforts to be made around the development of mineral chemistry as an exploration tool for porphyry and related deposits (Cooke et al., 2014; Wilkinson et al., 2015). There a number of approaches that have been applied in this field of research that can be broadly classified into two fields: (1) porphyry indicator minerals (PIMs), which generally use the chemistry of detrital magmatic and/or reseistate hydrothermal minerals to identify the potential for porphyry-style mineralisation within a district; and (2) porphyry vectoring and fertility tools (PVFTs), which assesses the low-level trace element compositions of spatially constrained common hydrothermal minerals, such as epidote, chlorite, alunite and quartz, to predict the location and potential endowment of a deposit (Cooke et al., 2017). Significant work investigating the trace element concentrations in hydrothermal epidote and chlorite with respect to the location of porphyry copper deposits has been done at CODES, at the University of Tasmania, and Imperial College, London, among other institutions, through on-going industry co-funded AMIRA projects.

This has included both method development and real-world trials, and mostly remains unpublished. The basic premise was set out by Cooke et al. (2014) who presented spatially-constrained epidote chemical analyses that appear to show a systematic relationship with respect to known porphyry copper deposits. These authors demonstrated that the epidote-group minerals, common and widespread in distal hydrothermal alteration facies around porphyry copper deposits, locally contain measurable and significant concentrations of trace elements that were commonly thought to preferentially reside in other minerals, such as sulfides. Their work implies that the trace element composition of epidote group minerals vary spatially with respect to the centre of the magmatic-hydrothermal system. The epidote-group minerals were found to host anomalous concentrations of Cu, Au, Mo, Sn and Bi in high temperature, sulfide-stable alteration conditions proximal to the site of porphyry copper ore formation. In distal, lower-temperature, sulfide-poor settings the concentrations of these elements in epidote were found to be low, but concentrations of As, Sb, Pb, Mn and Sr are elevated (Cooke et al., 2014). These observations suggest that analysis of epidote via LA-ICP-MS may allow low-level distal anomalies to be detected in weakly altered rocks. There were also indications that greater metal enrichment in epidote occurred around the best mineralised deposit in this district, implying that epidote could be a fertility indicator (Cooke et al., 2014).

As part of the same research program, Wilkinson et al. (2015) showed that chlorite compositions varied systematically around the Batu Hijau porphyry Cu-Au, Indonesia. Chlorite was found to host a variety of elements associated with the distal alteration facies that occur around porphyry copper deposits. Wilkinson et al. (2015) showed that chlorite mineral chemistry extended the detectable geochemical footprint at Batu Hijau to a radius of 4.5 km from the deposit centre compared to a radius of 1.5 km defined by anomalies of Cu, Au and Mo detected by whole-rock analyses. Many of the trace element substitutions in chlorite were interpreted to be temperature-dependant, such that variations in concentrations of Ti, Mg, V, Li and Sr (among others) in chlorite recorded the paleothermal aureole imposed by the Batu Hijau hydrothermal system. Similar chemical gradients in chlorite were reported by Baker et al. (2015) from the Collahuasi district and by Baker et al. (2017) for El Teniente of northern and central Chile, respectively. In practical terms, this antithetic relationship of high- and low-temperature elements in chlorite allowed Wilkinson et al. (2015) to develop a 'proximitor' equation to predict the distance that a given hydrothermal chlorite sample is from the centre of the hydrothermal system. The result of the equation is a radius, expressed as an absolute distance, yielding a sphere of possible locations. Ideally, an array of distributed samples would yield a series of spheres, of different sizes depending on their position relative to the centre of the thermal anomaly. The location at which many such spheres intersect would then provide a target corresponding to the thermal centre.

Mineral chemistry vectoring was applied at Resolution (Cooke et al., 2015) and at North Parkes (Pacey, 2016) with surprising success. At Resolution a set of 12 samples with propylitic alteration assemblages were taken from drillholes in a section line that passed directly over Resolution. Chlorite vectoring

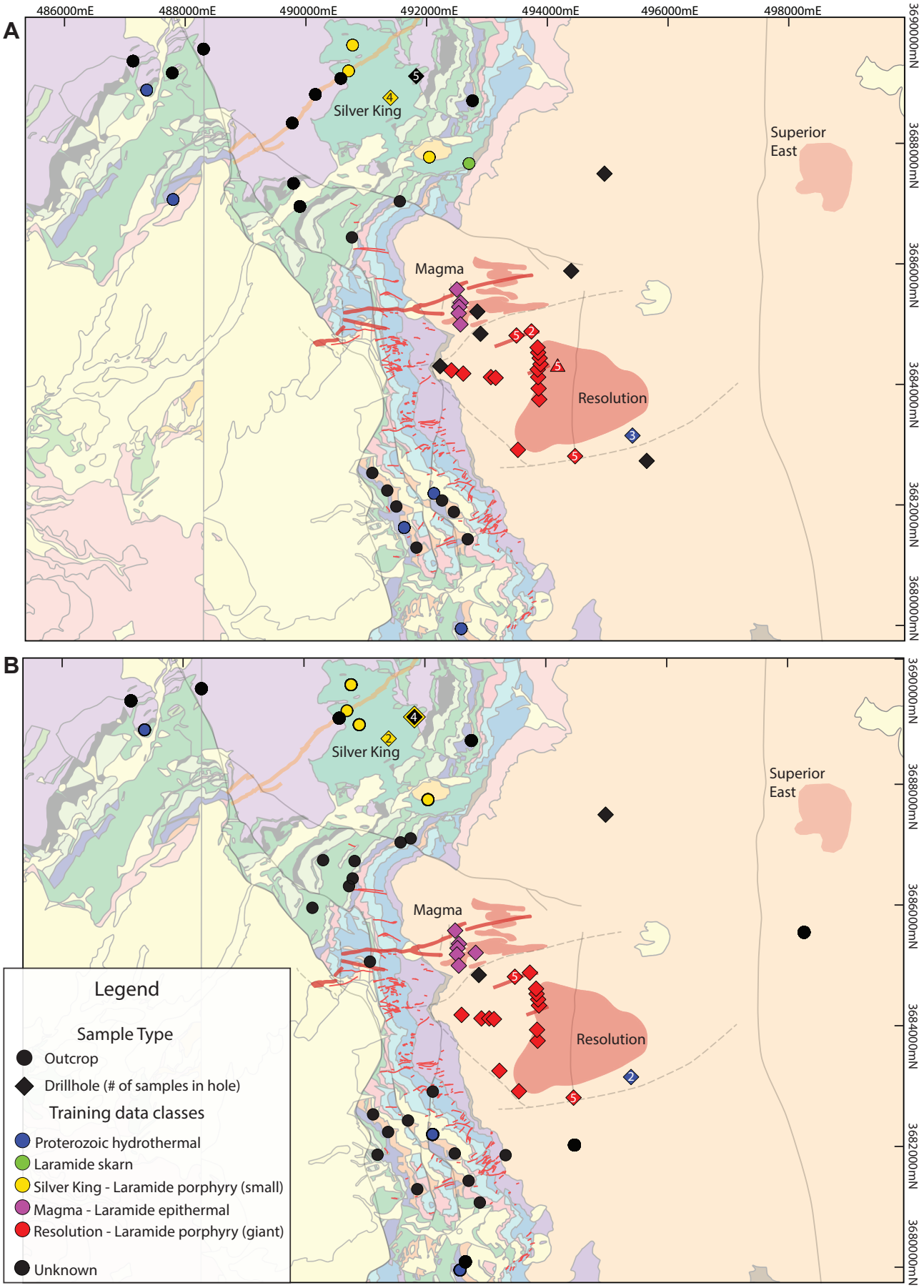


Figure 8.1 Sample maps for the Superior district showing the distribution of and type of samples used in the training dataset and unknown classification for (A) epidote and (B) chlorite. Geology as per Figure 3.2.

identified the centre of the deposit using the Ti/Sr proximitor equation calibrated with the Batu Hijau reference sample results published by Wilkinson et al. (2015). However, the epidote mineral chemistry in the same samples at Resolution provided a subdued fertility response compared to other deposits of comparable magnitude. Duplicate sampling and trace element analyses were conducted by Rio Tinto and Resolution Copper, confirming the results of the initial study but still resulting in subdued trace element anomalies in epidote. Understanding the causes of this apparent lack of strong epidote trace element anomalism, and a desire to define a more distal geochemical halo could be identified around Resolution in the Superior district were main motivating factors in initiating the current PhD research project.

## 8.3 Methods

### 8.3.1 Sample locations

Epidote and chlorite-altered samples were collected as widely across the district as outcrop and the occurrences of these minerals permitted (Figure 8.1). Every effort was made to achieve an even sample grid, but constrained by the geology in that the distribution of epidote in basement rocks was strongly controlled by the distribution of mafic to intermediate protoliths. Epidote is well developed in the Kvs within the Resolution graben, and in Proterozoic basalt flows and dolerite sills that are part of the pre-mineralisation sequence. Post-mineralisation cover accounts for more than 70% of the surface material in the study area, and these rocks lack epidote and chlorite, preventing their incorporation into the sample grid. Instead, drillcore samples were collected at 100 - 200 meter spacing down hole close to the Resolution orebody (Figure 8.1). Surface samples were collected at a spacing of approximately 300 m in the range front where possible (Figure 8.1).

### 8.3.2 Instrumentation

LA-ICP-MS analyses were conducted using an ASI Resolution S155 laser ablation system with a Coherent Complex Pro 110 ArF excimer laser operating at 193 nm wavelength with a pulse width of ~20 ns. This is coupled with an Agilent 7900 quadrupole ICP-MS, housed at the CODES LA-ICP-MS analytical facility, University of Tasmania. The laser ablation system is equipped with in-house sample chambers, capable of carrying 20 x 1 inch round mounts; comprising 18 samples and two standards. The aerosol and gas mixture was passed through a pulse-homogenizing device (Laurin Technic, Australia) prior to direct introduction to the torch, where the stream of ablated aerosol is split into 10 tubes with differing residence times before being recombined prior to entering the plasma. Each analysis was performed in time-resolved mode, which involves sequential peak-hopping through the mass spectrum.

### 8.3.3 Quantitative multi-element analysis

A total of 1,762 epidote spots and 1,139 chlorite spots were analysed using the method outlined by Cooke et al. (2014), including material from veins, altered wall rocks and skarns. Initially, 42 masses were analysed from each spot. This was expanded to 44 isotopes in order to include $^{206}$Pb and $^{207}$Pb as a result of the geochronology method development outlined in Chapter 6. Ablation took place in an atmosphere of pure helium flowing at 0.35 l/min and the ablated particles were immediately mixed with argon after the ablation cell flowing at 1.05 l/min immediately after the ablation chamber. The quantitative analyses of epidote and chlorite were performed by ablating spots 19 or 29 μm in size, with a laser repetition rate of 10 Hz. For the 193 nm laser, the beam fluence at the sample was ~3 J/cm$^2$. The analysis time for each sample was 90 s, with 30 s for measurement of the gas background with the laser off and a 60 s of signal analysis with laser on. Isotopes measured were $^{7}$Li, $^{11}$B, $^{23}$Na, $^{24}$Mg, $^{27}$Al, $^{29}$Si, $^{39}$K, $^{43}$Ca, $^{47}$Ti, $^{49}$Ti, $^{51}$V, $^{53}$Cr, $^{55}$Mn, $^{57}$Fe, $^{59}$Co, $^{60}$Ni, $^{65}$Cu, $^{66}$Zn, $^{75}$As, $^{88}$Sr, $^{89}$Y, $^{90}$Zr, $^{93}$Nb, $^{107}$Ag, $^{109}$Ag, $^{118}$Sn, $^{121}$Sb, $^{137}$Ba, $^{139}$La, $^{140}$Ce, $^{153}$Eu, $^{157}$Gd, $^{172}$ Yb, $^{175}$Lu, $^{178}$Hf, $^{181}$Ta, $^{197}$Au, $^{205}$Tl, $^{208}$Pb, $^{209}$Bi, $^{232}$Th and $^{238}$U. Acquisition time for each mass was set to 0.02 s, with a total sweep time to analyse all masses, around 0.65 s. The NIST-612 glass standard (NIST, USA) was used for calibration analyses with a 79 μm beam size and 10 Hz frequency. This standard was analysed at the beginning, then every 30 mins throughout each session, and at the end of the run to assess and correct for mass bias and drift. A secondary standard, GSD-1G, was run at the smaller spot size, and was used to detect and correct for plasma-loading effects. Typically 5-10 grains of epidote and 10-20 grains of chlorite were each analysed with 5-10 different spots, in order to average around 20 usable spot analyses per mineral per sample after QC checks and filtering. Data reduction was done according to the methods established by Longerich et al. (1996) and Danyushevsky et al. (2011) using Ca as the internal standard for epidote and Al as the internal standard for chlorite, both calculated stoichiometrically. Time intervals for data reduction were selected by visual inspection of each spectrum. Parts of a spectrum that were contaminated by mineral inclusions (indicated by spikes in trace element counts), and also parts where concentrations changed markedly between the commencement and conclusion of ablation were not integrated. In total, approximately 2400 LA-ICP-MS analyses were discarded due to poor-quality spectra. Generally, quality control (QC) of epidote resulted in rejection of 10-20% and QC of chlorite typically resulted in >50% rejection. For chlorite, this was typically due to excessive potassium concentrations, most likely due to partial replacement of biotite.

Chemical mapping of individual epidote grains was also undertaken with the aim to identify zonation and multiple stages of crystallisation within samples. This approach utilised the same instrumentation, but with the use of a 9 um spot size rastered as lines over individual grains.

### 8.3.4 Multivariate analytical techniques

Geochronological results presented in Chapter 5 suggest that there were multiple episodes of epidote

and chlorite deposition in the Superior district. Although dating results have constrained the origins of a select number of samples, there are also many other samples with poorly constrained origins. In order to screen out older alteration phases, so that only the Laramide epidote and chlorite related to Resolution are used in the vectoring approach of Cooke et al. (2014) and Wilkinson et al. (2015), discriminantion of Laramide and pre-Laramide alteration minerals was necessary. The following method describes the workflow applied to classify multi-element data from epidote and chlorite. The classification aims to distinguish between five epidote and four chlorite types associated with the various styles of mineralisation within the Superior district, specifically; Proterozoic hydrothermal alteration, Laramide unmineralised skarn (epidote only; Silver King), Laramide small porphyry (Silver King), Laramide epithermal (Magma) and Laramide giant porphyry (Resolution). This involved using a suite of samples constrained by geochronology as a training set. All data conditioning, processing and analysis was conducted using KNIME version 3.4.1. (Berthold et al., 2007) with embedded R programming language scripts using R version 3.0.3 (2014-03-06) (R Core Team, 2014), with the assistance of Dr Matthew Cracknell of the informatics and machine-learning TMVC research group, CODES, University of Tasmania.

#### 8.3.4.1 Data conditioning and pre-processing

Multivariate classification algorithms cannot process null, zero or text values, the latter most commonly representing concentrations below the analytical detection limit. In order to analyse the mineral chemistry data with multivariate statistical techniques, below detection limit needed to be imputed. Below detection limit (<DL) data in LA-ICP-MS datasets are inherently complicated because the detection limits for each mass are calculated for each spot analysis after integration and are therefore unique for each element on each spot. This leads to significant variability in detection limits for the same element. The <DL data was therefore imputed as half of the median DL for each element across the dataset. Additionally, variables that are inconsistently filled across the dataset (e.g., $^{206}$Pb and $^{207}$Pb), or contain greater than 30% below detection limit (e.g., Ag, Cu, Cr in epidote) were also removed, as they do not significantly affect class membership. The data were then log-10 transformed to derive a distribution closer to a normal distribution, which is a common preparatory step among classification algorithms for negatively skewed populations. Strongly correlated variables led to bias among the classification results. A correlation matrix for the log-transformed data was used to identify correlated element pairs and the subordinate, (i.e., less abundant or less commonly detected member of any correlated pair was removed from later processing. In this dataset, Ce, Gd, Lu, Hf and Ta were removed to ensure element independence. Furthermore, for both epidote and chlorite, several major elements were identified as having negligible influence on later classifications and were removed before further processing (i.e., Mg, Na and K for epidote, and Ca, Na and K for chlorite). A small number of samples collected more than 30 km away from the Resolution deposit were omitted completely as these are inferred to belong to different geologic environments. All elements were transformed to their base-10 logarithm prior to

Table 8.1 Number of samples and valid analyses in each training data class for epidote and chlorite in the Superior district

| Class | Distinguishing attributes | Epidote | | Chlorite | |
|---|---|---|---|---|---|
| | | Samples in class | Analyses in class | Samples in class | Analyses in class |
| Proterozoic hydrothermal | Direct U-Pb age dates from apatite and epidote (Chapter 6) | 7 | 196 | 3 | 88 |
| Early Laramide small porphyry (Silver King) | Hosted in ~74 Ma quartz diorite | 8 | 142 | 6 | 83 |
| Early Laramide unmineralised skarn (Silver King) | Hosted in Paleozoic sedimentry rock with calc-silicate mineralogy but lacks sulfides | 2 | 31 | 0 | 0 |
| Laramide epithermal (Magma) | Intense epidote alteration of dolerite adjacent to Magma epithermal vein | 9 | 170 | 9 | 155 |
| Laramide giant porphyry (Resolution) | Hosted in Cretaceous Kvs and located in graben-hosted propylitic halo to Resolution | 27 | 481 | 23 | 302 |
| Unknown | All Pre-Cretaceous host rocks with no other age or alteration-type constraints | 27 | 666 | 32 | 487 |

training and prediction.

#### 8.3.4.2 Multivariate classification

***Training data***

In order to classify epidote and chlorite of ambiguous origin, a training data set of analyses of these minerals from altered rocks of known origins were used to train the classification algorithm. Epidote data from the Superior district were subdivided into a series of groups based on existing information regarding the age, size of mineralising system and the types of alteration they represent (Table 8.1). Epidote with Proterozoic ages record the fluid chemistry of the Proterozoic hydrothermal event. Skarn epidote that yielded a Laramide crystallisation age is spatially associated with the ~74 Ma quartz diorite stock at the Silver King porphyry-epithermal system, and has been interpreted as a distinct early Laramide hydrothermal event related to, but distinct from, propylitic epidote hosted within this quartz diorite. Epidote hosted in the Kvs and occurring in the Resolution graben has been interpreted to belong to the giant Laramide Resolution porphyry deposit. In these previous examples, geochronology, host rock age, and spatial distribution relative to host rocks were the predominant factors guiding classification. Mineral texture was also used to classify epidote, irrespective of host rock age. For example, epidote adjacent to the Magma vein manifests as networks of epidote veins immediately adjacent to quartz-sulfide veins of epithermal style. This style of epidote veining and the association with unambiguous epithermal textures is not known elsewhere in the district and therefore this epidote was used as the training data for Laramide alteration related to epithermal veins. All other epidote samples were treated as 'unknown' (Table 8.1).

Chlorite has been subdivided and the training data selected in a similar way to epidote. Where chlorite is

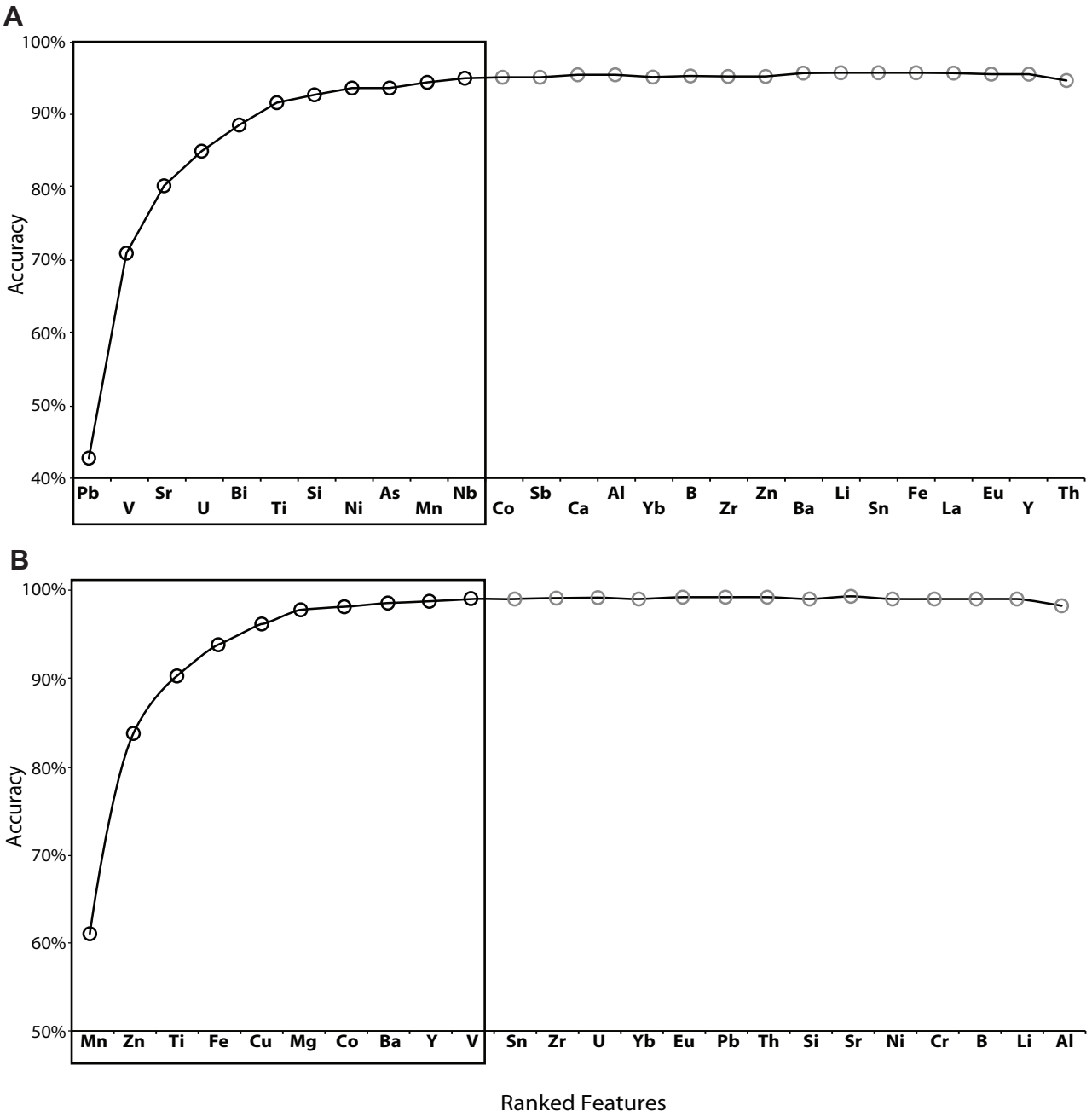


Figure 8.2 Results of backward feature elimination, showing elements ordered by their importance for the seperation of training data classes. A. Epidote. B. Chlorite. Box shows elements used in final classifications. All data listed in Appendices 3A(i) and 3B(i).

hosted in either Kvs or the quartz diorite, then they are considered to relate to Laramide giant porphyry (Resolution) of the early Laramide small porphyry (Silver King), respectively. Likewise, if the chlorite is intergrown with epidote in a sample that has a direct U-Pb epidote age, the two minerals are considered to be synchronous and the epidote geochronology results have been applied to the intergrown chlorite. Classification algorithms are most successful when all the classes are represented by similar numbers of members, that is, the classes are 'balanced'. In the presence of substantial differences in the number of members in each class, the output classification will be biased towards the major class. To reduce the effect of class imbalance in the training data, the major class (Laramide giant porphyry, Table 8.1) was

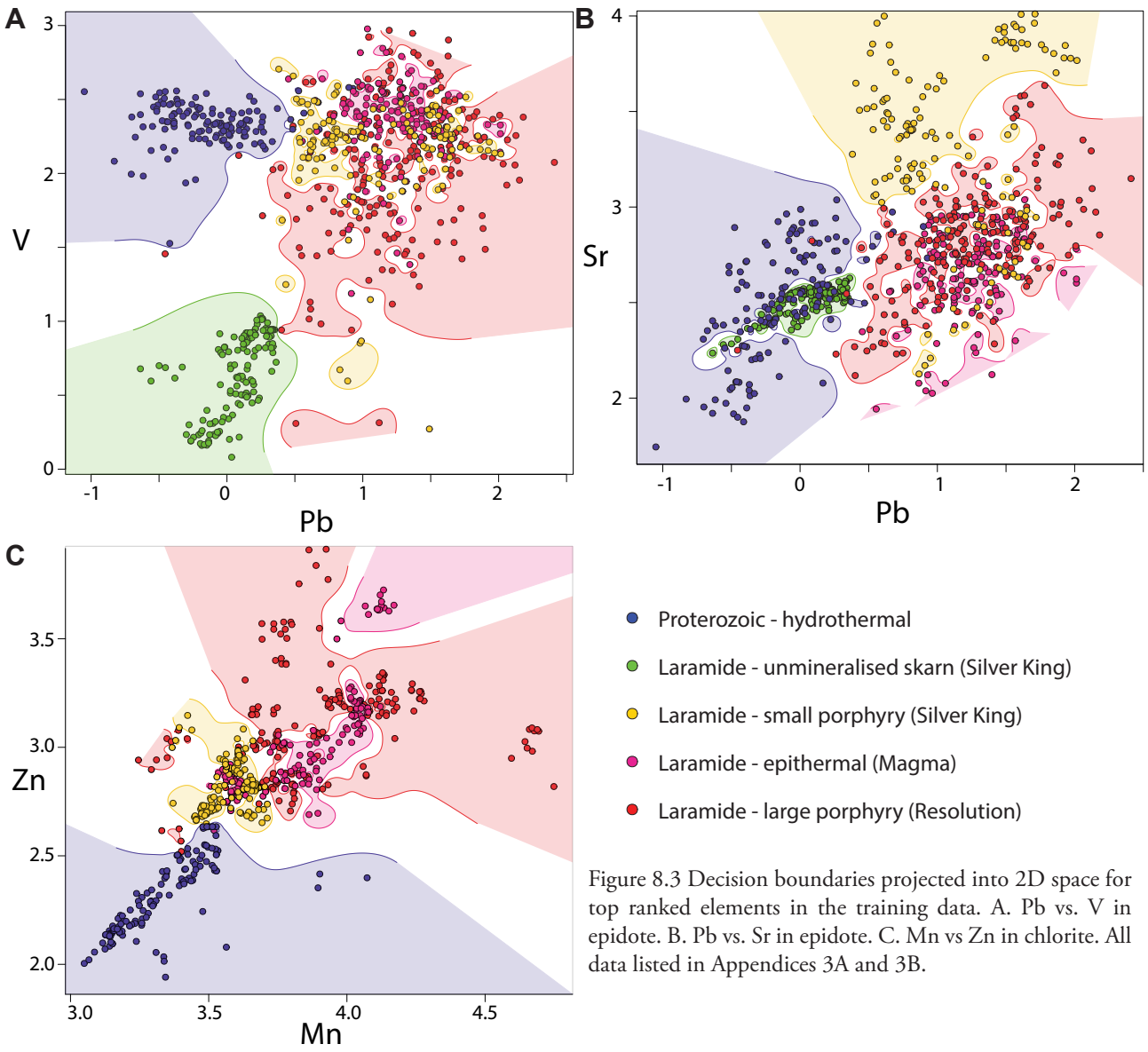


Figure 8.3 Decision boundaries projected into 2D space for top ranked elements in the training data. A. Pb vs. V in epidote. B. Pb vs. Sr in epidote. C. Mn vs Zn in chlorite. All data listed in Appendices 3A and 3B.

desampled to 30% of the original number of analyses using random sampling. In turn, the minority classes were oversampled by the Synthetic Minority Oversampling Technique (SMOTE; Chawla et al., 2002). SMOTE oversamples the minority class by creating synthetic values based on interpolation between real values of the target class and a number of nearest neighbours of the same class (in this case three neighbours). SMOTE then randomly samples a point along lines established between the target class and its neighbours in the data space and determines the value of the synthetic instance based on this randomly chosen point.

***Feature selection and prediction evaluation***

The most relevant features (elements) for the classification were selected using a backward feature elimination method, with embedded three-fold cross validation for sampling training and test data in every iteration. Top ranked features that generated 95% accuracy were selected for final classifier training and testing (Figure 8.2)

Decision boundaries were generated by interpolating class membership probabilities for a given class and projected in two-dimensional space for visualisation (Figure 8.3). Decision boundaries were plotted for the training data based on 0.67 class membership probability threshold among the top-ranked elements. For a given sample both the class membership proportions, and the mean class membership probability were calculated in order to evaluate the misclassification of unknowns, especially where there are limited analyses.

Discriminant projection analysis (DPA) or Linear Discriminant Analysis (LDA) is another classification algorithm that can determine the separation within and between a priori geochemical groups (in this case, the training data classes) using a function that describes the relative control of elements within and between groups (Fisher, 1936; Rao, 1948). The number of projections produced by the algorithm among 'n' classes is n-1. Projections can then be plotted in two or three dimensions to allow visualisation of element associations (structure coefficients) within and between groups. Here, this method is applied to the Superior district epidote and chlorite training data to identify relative elemental associations and their influence on individual groups to make broad inferences about differences in fluid chemistry of those groups (Table 8.2; Table 8.3). A Random Forests algorithm was then used to attribute the remaining unknown samples to the known compositional groups, thereby overcoming uncertainty of epidote origin where no other constraints exist.

***Final Classification***

Classification was executed using the Random Forests classifier (Breiman, 2001; Table 8.4; Table 8.5). The Random Forests classification algorithm was developed by Breiman (2001) as an extension to the decision trees method. Recent reviews and geoscience applications can be found in Cracknell et al. (2014), Cracknell and Reading (2014), and Kuhn et al. (2016). Random Forests classifications are based on a majority vote cast by multiple random decision trees. Randomness is introduced by randomly subsetting a predefined number of input features to split at each node of a decision tree and by 'bagging'. In this implementation of Random Forests, the Information Gain Ratio was employed to calculate the information purity of child nodes as compared to that of their parent node. The number of trees was set to 301 and the random number of input features parameter was set to the default (square root of the total number of input features).

## 8.4 Results

### 8.4.1 Training data

#### 8.4.1.1 Element importance for classification

Trace elements were ranked by importance for discriminanting epidote (Figure 8.2 A) and chlorite (Figure 8.2 B) training data groups. For the training data used in the epidote classification, Pb, V, Sr,

Table 8.2 Discriminant projection results for epidote training data

| DP1 | | DP2 | | DP3 | | DP4 | |
|---|---|---|---|---|---|---|---|
| U | 0.43 | Ni | 0.53 | Sr | 0.46 | B | 0.50 |
| B | 0.43 | V | 0.36 | V | 0.40 | As | 0.30 |
| Lu | 0.42 | Cr | 0.28 | Li | 0.35 | V | 0.23 |
| Yb | 0.42 | Co | 0.24 | Ti | 0.30 | Pb | 0.22 |
| Y | 0.40 | Si | 0.23 | Ba | 0.27 | Co | 0.22 |
| Eu | 0.40 | Mn | 0.20 | Mn | 0.16 | Sb | 0.19 |
| Co | 0.32 | Pb | 0.20 | Si | 0.14 | Sr | 0.16 |
| Ti | 0.28 | Bi | 0.16 | Al | 0.11 | Ca | 0.10 |
| Ni | 0.25 | Lu | 0.12 | Pb | 0.11 | Al | 0.077 |
| Cr | 0.21 | Yb | 0.11 | As | 0.10 | Ba | 0.0011 |
| V | 0.20 | Sb | 0.11 | Sb | 0.069 | Nb | -0.00047 |
| La | 0.20 | Cu | 0.076 | B | 0.063 | U | -0.0088 |
| Li | 0.17 | Y | 0.064 | Zn | 0.0077 | Yb | -0.013 |
| Sn | 0.13 | Fe | 0.063 | Nb | 0.0035 | Y | -0.019 |
| Fe | 0.10 | Zr | 0.024 | Co | -0.023 | Lu | -0.025 |
| Zr | 0.10 | Ti | 0.013 | Cr | -0.025 | Eu | -0.028 |
| Ca | 0.072 | Sn | -0.010 | Lu | -0.036 | Si | -0.050 |
| Cu | 0.042 | Zn | -0.058 | Cu | -0.041 | Fe | -0.078 |
| As | 0.013 | Eu | -0.069 | Eu | -0.047 | La | -0.078 |
| Th | -0.031 | B | -0.10 | Yb | -0.072 | Th | -0.083 |
| Al | -0.047 | Ca | -0.12 | Y | -0.13 | Zr | -0.10 |
| Bi | -0.049 | U | -0.13 | Fe | -0.13 | Li | -0.10 |
| Si | -0.079 | La | -0.16 | Bi | -0.14 | Sn | -0.12 |
| Ba | -0.11 | Th | -0.16 | Ni | -0.14 | Zn | -0.12 |
| Sb | -0.33 | Nb | -0.16 | Zr | -0.14 | Cr | -0.16 |
| Mn | -0.38 | As | -0.17 | Ca | -0.15 | Mn | -0.17 |
| Zn | -0.38 | Al | -0.19 | Th | -0.17 | Cu | -0.21 |
| Sr | -0.38 | Ba | -0.19 | Sn | -0.18 | Ni | -0.24 |
| Nb | -0.46 | Li | -0.24 | La | -0.28 | Ti | -0.29 |
| Pb | -0.81 | Sr | -0.38 | U | -0.40 | Bi | -0.35 |

DP = discriminant projection

U, Bi and Ti account for over 90 % of the variance between groups (Figure 8.2 A). For chlorite, Zn, Mn, Ti, Fe and Cu account for over 95% variability (Figure 8.2 B). Decision boundaries show how the relative abundances of top ranked elements vary between groups (Figure 8.3). For epidote, there are distinct regions in the diagram for each of the major classes (Figure 8.3 A). Most importantly, higher concentrations of Pb characterise the Laramide epidote types, whereas the Proterozoic hydrothermal epidotes contain relatively low Pb concentrations (Figure 8.3 A). Although the skarn sample from Silver King contains Pb at concentrations similar to those in Proterozoic epidote, it can be distinguished by its low V content (Figure 8.3 A. Epidote in the other Silver King samples typically has higher Sr than Resolution or Magma type epidote (Figure 8.3 B). The strongest separation of chlorite groups is

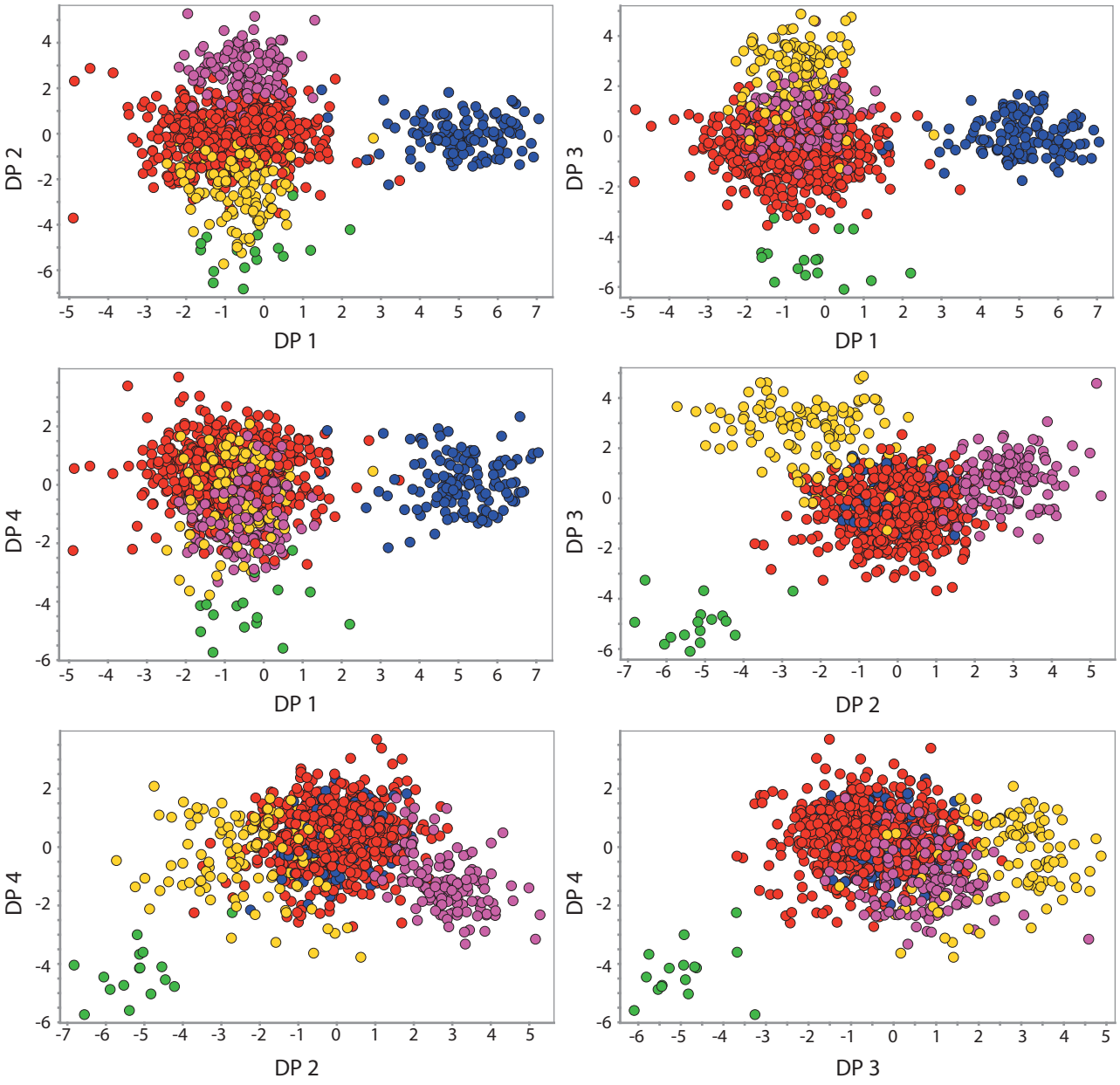


Figure 8.4 Discriminant projection matrix for epidote training data from the Superior district. Note projection 1 (DP1) seperates Laramide from Proterozoic, DP2 seperates Magma and to some extent Silver King from Resolution, DP3 seperates Silver King porphyry from Silver King Skarn from Magma and Resolution. Legend as per Figure 8.3. All data listed in Appendix 3A.

governed by Zn and Mn (Figure 8.3 C).

### 8.4.1.2 Discriminant projection of training data

Backward recursive feature elimination and Random Forests both use a stepwise approach to classification. This approach is effective but may mask associations *within* groups. Elemental associations within groups can be useful when characterising samples of unknown affinity since the association may constrain the fluid chemistry responsible for different generations of crystallisation, and/or aid the recognition of a limited group of elements amenable to niche sampling by more rapid, cost effective means (e.g., pXRF). Projections within the epidote data show that high values of discriminant projection 1 (DP1) distinguish

Table 8.3 Discriminant projection results for chlorite training data

| DP1 | | DP2 | | DP3 | |
|---|---|---|---|---|---|
| Zn | 0.68 | Ti | 0.44 | Ba | 0.43 |
| Mn | 0.58 | Pb | 0.40 | B | 0.31 |
| Sr | 0.39 | Fe | 0.37 | Al | 0.31 |
| Na | 0.27 | Sn | 0.26 | Li | 0.28 |
| Fe | 0.22 | Ba | 0.25 | Pb | 0.26 |
| Zr | 0.19 | Li | 0.23 | La | 0.24 |
| Pb | 0.19 | Th | 0.21 | Sr | 0.23 |
| U | 0.10 | Al | 0.20 | Na | 0.21 |
| Cr | 0.10 | U | 0.18 | Ce | 0.20 |
| Si | 0.094 | Sr | 0.16 | Sn | 0.20 |
| Ba | 0.079 | Ce | 0.15 | Mg | 0.15 |
| Ni | -0.022 | La | 0.13 | U | 0.14 |
| Sn | -0.025 | Zn | 0.088 | Eu | 0.12 |
| Yb | -0.027 | Yb | 0.088 | Y | 0.024 |
| Ce | -0.043 | Zr | 0.015 | Th | -0.012 |
| Al | -0.045 | Cu | -0.012 | Yb | -0.013 |
| Th | -0.059 | Na | -0.020 | Cr | -0.028 |
| Y | -0.060 | Eu | -0.039 | Cu | -0.053 |
| B | -0.074 | Y | -0.065 | Zr | -0.087 |
| Eu | -0.11 | V | -0.068 | Mn | -0.14 |
| La | -0.12 | Mn | -0.085 | Ti | -0.15 |
| V | -0.14 | Mg | -0.18 | Zn | -0.16 |
| Cu | -0.21 | B | -0.19 | Fe | -0.16 |
| Mg | -0.23 | Si | -0.19 | Co | -0.20 |
| Co | -0.26 | Co | -0.25 | Si | -0.21 |
| Ti | -0.31 | Cr | -0.37 | Ni | -0.25 |
| Li | -0.72 | Ni | -0.65 | V | -0.58 |

DP = discriminant projection

Proterozoic hydrothermal epidote from all other types (Figure 8.4 A-C). Table 8.2 demonstrates that high values in this projection are controlled by U, B, REEs, and Co, implying that the Proterozoic hydrothermal epidote is enriched in these elements. In contrast, the Laramide groups at the opposite end of this projection are characterised by a strong enrichment in Pb, Sr, Zn, Mn, Sb and Nb (Table 8.2, Figure 8.4 A-C). Projection 2 splits the Laramide epidote training classes (Figure 8.4 A, D-E). This projection is controlled at high values by Ni, V, Cr, Co and by Sr, Li and Ba at low values (Table 8.2). Projections 3 and 4 show limited distinction between the four major epidote groups but show strong separation of skarn-type epidote from Silver King (Figure 8.4 B-F), suggesting that this epidote is enriched in U, La, Sn (DP3) and Bi, Ti, Ni and Cu (DP4).

Chlorite training data were classified into four groups and therefore only three projections (Figure 8.5). As for epidote, DP1 discriminants Laramide from Proterozoic hydrothermal epidote (Figure 8.5 A-B).

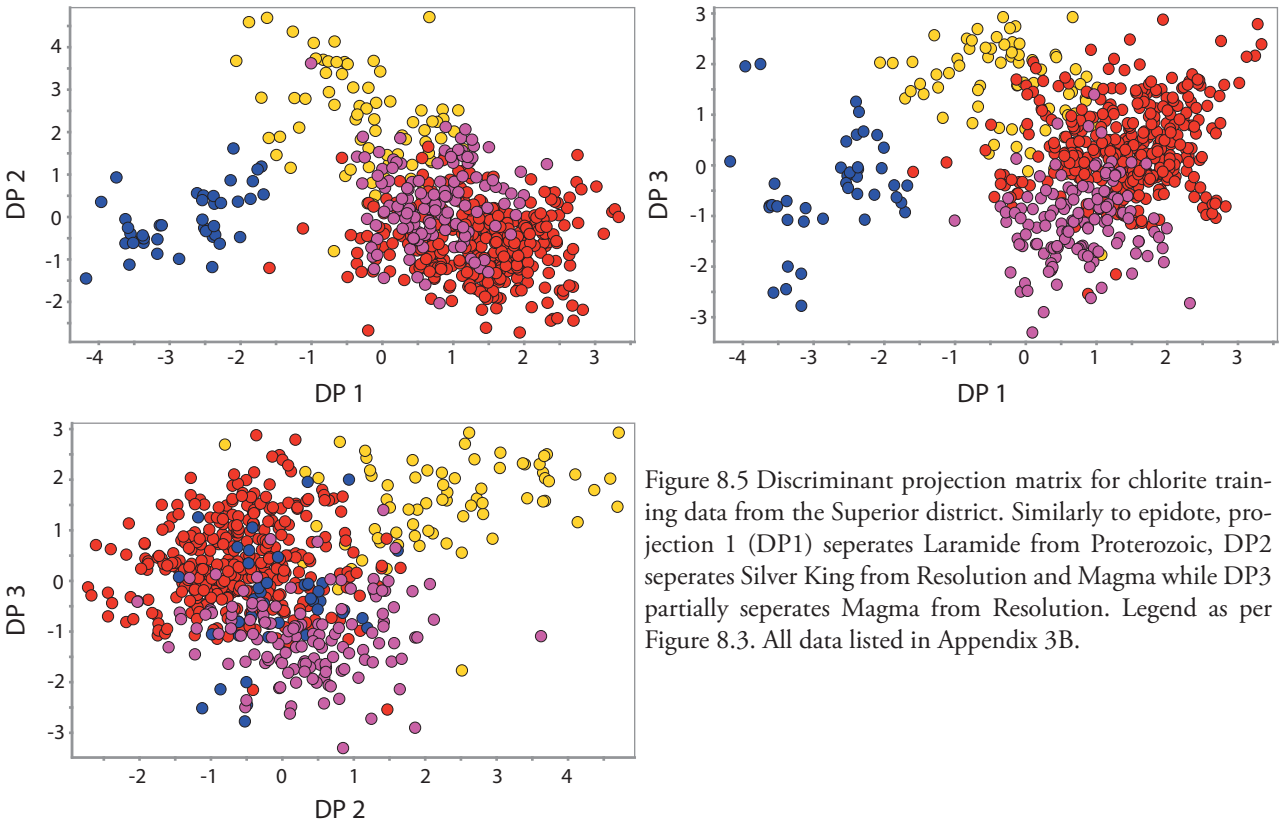


Figure 8.5 Discriminant projection matrix for chlorite training data from the Superior district. Similarly to epidote, projection 1 (DP1) seperates Laramide from Proterozoic, DP2 seperates Silver King from Resolution and Magma while DP3 partially seperates Magma from Resolution. Legend as per Figure 8.3. All data listed in Appendix 3B.

However the chlorite from Silver King has slightly lower DP1 values than other Laramide samples, so this division is imperfect. The major controls on DP1 are Zn, Mn and Sr and Fe at high values and Li, Ti, Co and Mg at low values, suggesting Laramide and Proterozoic chlorite have these element associations, respectively (Table 8.3). Projection 2 shows that some of the Silver King chlorites is enriched in Ti, Pb and Fe (Figure 8.5 B-C; Table 8.3) whereas DP3 indicates that Magma-type chlorite is enriched in V, Ni, Si, and Co relative to the other Laramide suites (Figure 8.5 B-C; Table 8.3).

Overall, there is good distinction between the chemistry of Laramide and Proterozoic epidote and chlorite, although there appears to be some overlap between the various Laramide training data groups.

### 8.4.2 Classification results

#### 8.4.2.1 Epidote

Results of the final classification of unknown epidote are presented in terms of proportional class membership by sample and average probability of epidote membership to a given class (Table 8.4). Many of the unknown samples (34/40) samples have epidote compositions from two or more classes (Table 8.4, Figure 8.6 A) while the remainder had epidotes from only a single class (Table 8.4, Figure 8.6 A). To understand this heterogeneity, it is important to note that the results in Figure 8.6 are presented in terms of proportion of epidote analyses (from a given sample) predicted as a given class (A*), and as an average probability for all analyses of from that sample belonging to that class (B*). The difference

Table 8.4 Results of Random Forests classification of unknown epidote from the Superior district.

| Sample ID | Random Forests majority prediction | Laramide giant porphyry (Resolution) | | Proterozoic hydrothermal | | Early Laramide small porphyry (Silver King) | | Laramide epithermal (Magma) | | Early Laramide skarn (Silver King) | | Entropy | |
|---|---|---|---|---|---|---|---|---|---|---|---|---|---|
| | | A* | B* | A* | B* | A* | B* | A* | B* | A* | B* | A* | B* |
| RE15JP026 | Proterozoic hydrothermal | 0.07 | 0.13 | 0.90 | 0.78 | 0.00 | 0.03 | 0.02 | 0.05 | 0.00 | 0.02 | 0.53 | 1.12 |
| RE15JP120 | Laramide epithermal | 0.00 | 0.14 | 0.00 | 0.13 | 0.50 | 0.21 | 0.50 | 0.52 | 0.00 | 0.00 | 1.00 | 1.74 |
| RE15JP073 | Proterozoic hydrothermal | 0.00 | 0.07 | 1.00 | 0.90 | 0.00 | 0.01 | 0.00 | 0.02 | 0.00 | 0.00 | 0.00 | 0.58 |
| RE15JP091 | Laramide giant porphyry | 0.89 | 0.58 | 0.00 | 0.03 | 0.06 | 0.19 | 0.06 | 0.20 | 0.00 | 0.00 | 0.61 | 1.51 |
| RE15JP091B | Laramide giant porphyry | 0.38 | 0.37 | 0.33 | 0.28 | 0.21 | 0.19 | 0.08 | 0.15 | 0.00 | 0.00 | 1.83 | 1.94 |
| RE15JP070 | Proterozoic hydrothermal | 0.00 | 0.16 | 1.00 | 0.79 | 0.00 | 0.01 | 0.00 | 0.03 | 0.00 | 0.01 | 0.00 | 0.98 |
| RE15JP090 | Proterozoic hydrothermal | 0.35 | 0.37 | 0.65 | 0.55 | 0.00 | 0.02 | 0.00 | 0.04 | 0.00 | 0.03 | 0.93 | 1.44 |
| RE15JP088 | Laramide giant porphyry | 0.10 | 0.57 | 0.90 | 0.10 | 0.00 | 0.20 | 0.00 | 0.13 | 0.00 | 0.00 | 0.00 | 1.65 |
| RE15JP051 | Proterozoic hydrothermal | 0.03 | 0.09 | 0.97 | 0.83 | 0.00 | 0.02 | 0.00 | 0.05 | 0.00 | 0.01 | 0.19 | 0.90 |
| RE15JP049 | Proterozoic hydrothermal | 0.00 | 0.08 | 1.00 | 0.88 | 0.00 | 0.01 | 0.00 | 0.02 | 0.00 | 0.01 | 0.00 | 0.68 |
| RE16JP022 | Laramide giant porphyry | 0.84 | 0.55 | 0.00 | 0.02 | 0.00 | 0.08 | 0.16 | 0.34 | 0.00 | 0.01 | 0.63 | 1.48 |
| RE16JP081 | Laramide giant porphyry | 0.95 | 0.62 | 0.00 | 0.06 | 0.00 | 0.04 | 0.05 | 0.28 | 0.00 | 0.00 | 0.29 | 1.37 |
| RE16JP082 | Proterozoic hydrothermal | 0.00 | 0.27 | 0.95 | 0.47 | 0.05 | 0.17 | 0.00 | 0.08 | 0.00 | 0.01 | 0.92 | 1.82 |
| RE16JP082B | Laramide giant porphyry | 0.03 | 0.42 | 0.90 | 0.04 | 0.03 | 0.23 | 0.03 | 0.31 | 0.00 | 0.00 | 1.59 | 1.71 |
| RE16JP083 | Laramide giant porphyry | 0.32 | 0.37 | 0.43 | 0.20 | 0.00 | 0.08 | 0.25 | 0.34 | 0.00 | 0.00 | 1.51 | 1.85 |
| RE15JP055 | Laramide giant porphyry | 0.52 | 0.52 | 0.00 | 0.02 | 0.00 | 0.06 | 0.48 | 0.41 | 0.00 | 0.00 | 1.00 | 1.37 |
| RE16JP157 | Laramide giant porphyry | 0.65 | 0.41 | 0.00 | 0.01 | 0.18 | 0.28 | 0.16 | 0.29 | 0.00 | 0.00 | 1.28 | 1.66 |
| RE16JP203 | Laramide epithermal | 0.00 | 0.27 | 0.00 | 0.02 | 0.00 | 0.04 | 1.00 | 0.67 | 0.00 | 0.00 | 0.00 | 1.18 |
| RE16JP237 | Laramide epithermal | 0.37 | 0.38 | 0.00 | 0.04 | 0.11 | 0.13 | 0.53 | 0.44 | 0.00 | 0.01 | 1.36 | 1.67 |
| RE15JP205 | Proterozoic hydrothermal | 0.40 | 0.34 | 0.60 | 0.48 | 0.00 | 0.02 | 0.00 | 0.11 | 0.00 | 0.05 | 0.97 | 1.69 |
| RE15JP152 | Laramide epithermal | 0.00 | 0.21 | 0.19 | 0.13 | 0.00 | 0.22 | 0.81 | 0.43 | 0.00 | 0.01 | 0.70 | 1.93 |
| RE15JP150 | Laramide giant porphyry | 0.95 | 0.64 | 0.00 | 0.02 | 0.03 | 0.17 | 0.03 | 0.16 | 0.00 | 0.00 | 0.34 | 1.41 |
| RE15JP139 | Laramide giant porphyry | 0.70 | 0.45 | 0.00 | 0.13 | 0.00 | 0.03 | 0.30 | 0.39 | 0.00 | 0.00 | 0.89 | 1.58 |
| RE16JP034 | Proterozoic hydrothermal | 0.38 | 0.23 | 0.50 | 0.46 | 0.00 | 0.12 | 0.13 | 0.19 | 0.00 | 0.00 | 1.41 | 1.83 |
| RE15JP191 | Laramide giant porphyry | 0.70 | 0.45 | 0.00 | 0.10 | 0.00 | 0.16 | 0.30 | 0.29 | 0.00 | 0.01 | 0.88 | 1.85 |

| Sample ID | Random Forests majority prediction | Laramide giant porphyry (Resolution) | | Proterozoic hydrothermal | | Early Laramide small porphyry (Silver King) | | Laramide epithermal (Magma) | | Early Laramide skarn (Silver King) | | Entropy | |
|---|---|---|---|---|---|---|---|---|---|---|---|---|---|
| | | A* | B* | A* | B* | A* | B* | A* | B* | A* | B* | A* | B* |
| RE15JP106 | Laramide giant porphyry | 0.52 | 0.52 | 0.00 | 0.01 | 0.00 | 0.03 | 0.48 | 0.44 | 0.00 | 0.00 | 1.00 | 1.25 |
| RE15JP107 | Laramide giant porphyry | 0.74 | 0.51 | 0.02 | 0.07 | 0.04 | 0.15 | 0.20 | 0.27 | 0.00 | 0.00 | 1.10 | 1.68 |
| RE16JP020 | Laramide giant porphyry | 0.50 | 0.47 | 0.11 | 0.12 | 0.06 | 0.13 | 0.33 | 0.27 | 0.00 | 0.01 | 1.61 | 1.82 |
| RE16JP028 | Laramide giant porphyry | 0.92 | 0.48 | 0.00 | 0.04 | 0.08 | 0.27 | 0.00 | 0.20 | 0.00 | 0.00 | 0.39 | 1.67 |
| RE16JP019 | Laramide giant porphyry | 0.84 | 0.45 | 0.12 | 0.16 | 0.00 | 0.14 | 0.04 | 0.25 | 0.00 | 0.00 | 0.76 | 1.87 |
| RE16JP036 | Proterozoic hydrothermal | 0.00 | 0.03 | 1.00 | 0.93 | 0.00 | 0.00 | 0.00 | 0.04 | 0.00 | 0.00 | 0.00 | 0.46 |
| RE16JP014 | Early Laramide small porphyry | 0.37 | 0.37 | 0.00 | 0.03 | 0.37 | 0.34 | 0.26 | 0.25 | 0.00 | 0.00 | 1.57 | 1.73 |
| RE16JP188 | Early Laramide small porphyry | 0.33 | 0.39 | 0.10 | 0.10 | 0.57 | 0.42 | 0.00 | 0.08 | 0.00 | 0.00 | 1.31 | 1.70 |
| RE16JP192 | Laramide giant porphyry | 0.56 | 0.39 | 0.00 | 0.02 | 0.22 | 0.26 | 0.22 | 0.27 | 0.00 | 0.06 | 1.44 | 1.91 |
| RE16JP193 | Proterozoic hydrothermal | 0.10 | 0.26 | 0.71 | 0.38 | 0.19 | 0.30 | 0.00 | 0.06 | 0.00 | 0.01 | 1.13 | 1.84 |
| RE16JP194 | Early Laramide small porphyry | 0.25 | 0.37 | 0.00 | 0.03 | 0.75 | 0.42 | 0.00 | 0.18 | 0.00 | 0.00 | 0.81 | 1.66 |
| RE16JP195 | Early Laramide small porphyry | 0.05 | 0.30 | 0.00 | 0.04 | 0.95 | 0.48 | 0.00 | 0.18 | 0.00 | 0.00 | 0.30 | 1.67 |
| RE16JP030 | Early Laramide small porphyry | 0.36 | 0.35 | 0.21 | 0.20 | 0.43 | 0.35 | 0.00 | 0.09 | 0.00 | 0.00 | 1.53 | 1.87 |
| RE16JP035 | Laramide epithermal | 0.22 | 0.36 | 0.16 | 0.15 | 0.00 | 0.05 | 0.62 | 0.44 | 0.00 | 0.00 | 1.33 | 1.70 |
| RE16JP031 | Laramide giant porphyry | 0.97 | 0.51 | 0.00 | 0.01 | 0.00 | 0.26 | 0.03 | 0.22 | 0.00 | 0.00 | 0.20 | 1.57 |

Abbreviations; A* = Proportion of individual analyses predicted to belong to class. B* = Average probability of class membership among indiviual spot analyses

Table 8.5 Results of Random Forests classification of unknown chlorite from the Superior district.

| Sample ID | Random Forests majority prediction | Laramide giant porphyry (Resolution) | | Proterozoic hydrothermal | | Early Laramide small porphyry (Silver King) | | Laramide epithermal (Magma) | | Entropy | |
|---|---|---|---|---|---|---|---|---|---|---|---|
| | | A* | B* | A* | B* | A* | B* | A* | B* | A* | B* |
| RE16JP006 | Proterozoic hydrothermal | 0.00 | 0.06 | 1.00 | 0.70 | 0.00 | 0.02 | 0.00 | 0.21 | 0.00 | 1.20 |
| RE16JP005 | Proterozoic hydrothermal | 0.00 | 0.20 | 1.00 | 0.67 | 0.00 | 0.05 | 0.00 | 0.07 | 0.00 | 1.36 |
| RE15JP032 | Proterozoic hydrothermal | 0.00 | 0.06 | 1.00 | 0.91 | 0.00 | 0.02 | 0.00 | 0.01 | 0.00 | 0.55 |
| RE15JP026 | Laramide giant porphyry | 0.50 | 0.39 | 0.00 | 0.14 | 0.33 | 0.28 | 0.17 | 0.19 | 1.46 | 1.89 |
| RE15JP120 | Proterozoic hydrothermal | 0.38 | 0.36 | 0.43 | 0.21 | 0.00 | 0.12 | 0.19 | 0.31 | 1.51 | 1.89 |
| RE15JP176 | Proterozoic hydrothermal | 0.05 | 0.11 | 0.90 | 0.79 | 0.05 | 0.08 | 0.00 | 0.02 | 0.55 | 1.03 |
| RE15JP011 | Laramide giant porphyry | 1.00 | 0.53 | 0.00 | 0.09 | 0.00 | 0.03 | 0.00 | 0.35 | 0.00 | 1.49 |
| RE15JP091B | Laramide epithermal | 0.00 | 0.13 | 0.09 | 0.18 | 0.73 | 0.38 | 0.18 | 0.30 | 1.10 | 1.88 |
| RE15JP091 | Laramide epithermal | 0.10 | 0.16 | 0.00 | 0.17 | 0.60 | 0.34 | 0.30 | 0.33 | 1.30 | 1.92 |
| RE16JP060 | Proterozoic hydrothermal | 0.18 | 0.31 | 0.82 | 0.49 | 0.00 | 0.04 | 0.00 | 0.16 | 0.68 | 1.63 |
| RE15JP088 | Laramide giant porphyry | 0.81 | 0.49 | 0.00 | 0.12 | 0.19 | 0.38 | 0.00 | 0.01 | 0.71 | 1.46 |
| RE15JP051 | Proterozoic hydrothermal | 0.00 | 0.21 | 0.50 | 0.21 | 0.50 | 0.30 | 0.00 | 0.28 | 1.00 | 1.98 |
| RE15JP085 | Proterozoic hydrothermal | 0.00 | 0.10 | 0.83 | 0.64 | 0.08 | 0.13 | 0.08 | 0.14 | 0.82 | 1.52 |
| RE15JP049 | Proterozoic hydrothermal | 0.00 | 0.16 | 0.76 | 0.58 | 0.24 | 0.17 | 0.00 | 0.09 | 0.80 | 1.62 |
| RE15JP111 | Laramide giant porphyry | 0.65 | 0.38 | 0.06 | 0.22 | 0.00 | 0.06 | 0.29 | 0.34 | 1.17 | 1.78 |
| RE16JP081 | Early Laramide small porphyry | 0.00 | 0.19 | 0.14 | 0.23 | 0.29 | 0.24 | 0.57 | 0.34 | 1.38 | 1.96 |
| RE16JP082 | Laramide epithermal | 0.10 | 0.27 | 0.00 | 0.08 | 0.90 | 0.53 | 0.00 | 0.12 | 0.45 | 1.65 |
| RE16JP043 | Laramide epithermal | 0.07 | 0.30 | 0.07 | 0.16 | 0.86 | 0.38 | 0.00 | 0.15 | 0.74 | 1.90 |
| RE16JP157 | Laramide giant porphyry | 0.59 | 0.38 | 0.00 | 0.00 | 0.05 | 0.27 | 0.36 | 0.35 | 1.18 | 1.58 |
| RE15JP058 | Laramide giant porphyry | 0.80 | 0.60 | 0.00 | 0.00 | 0.04 | 0.25 | 0.16 | 0.15 | 0.87 | 1.35 |
| RE16JP237 | Laramide epithermal | 0.47 | 0.52 | 0.00 | 0.00 | 0.53 | 0.46 | 0.00 | 0.02 | 1.00 | 1.13 |
| RE16JP058 | Early Laramide small porphyry | 0.00 | 0.13 | 0.00 | 0.07 | 0.19 | 0.33 | 0.81 | 0.46 | 0.71 | 1.69 |
| RE15JP196 | Proterozoic hydrothermal | 0.00 | 0.24 | 1.00 | 0.52 | 0.00 | 0.06 | 0.00 | 0.18 | 0.00 | 1.67 |
| RE15JP156 | Laramide giant porphyry | 0.55 | 0.38 | 0.45 | 0.36 | 0.00 | 0.09 | 0.00 | 0.16 | 0.99 | 1.80 |
| RE15JP152 | Proterozoic hydrothermal | 0.10 | 0.29 | 0.90 | 0.54 | 0.00 | 0.08 | 0.00 | 0.09 | 0.47 | 1.59 |
| RE15JP135 | Laramide giant porphyry | 1.00 | 0.59 | 0.00 | 0.08 | 0.00 | 0.12 | 0.00 | 0.21 | 0.00 | 1.59 |

| Sample ID | Random Forests majority prediction | Laramide giant porphyry (Resolution) | | Proterozoic hydrothermal | | Early Laramide small porphyry (Silver King) | | Laramide epithermal (Magma) | | Entropy | |
|---|---|---|---|---|---|---|---|---|---|---|---|
| | | A* | B* | A* | B* | A* | B* | A* | B* | A* | B* |
| RE15JP200 | Proterozoic hydrothermal | 0.00 | 0.30 | 0.50 | 0.30 | 0.00 | 0.06 | 0.50 | 0.35 | 1.00 | 1.80 |
| RE15JP139 | Proterozoic hydrothermal | 0.00 | 0.07 | 1.00 | 0.86 | 0.00 | 0.03 | 0.00 | 0.03 | 0.00 | 0.78 |
| RE15JP141 | Proterozoic hydrothermal | 0.00 | 0.22 | 1.00 | 0.54 | 0.00 | 0.05 | 0.00 | 0.20 | 0.00 | 1.63 |
| RE15JP191 | Laramide giant porphyry | 1.00 | 0.74 | 0.00 | 0.06 | 0.00 | 0.10 | 0.00 | 0.09 | 0.00 | 1.22 |
| RE15JP106 | Laramide giant porphyry | 0.92 | 0.63 | 0.00 | 0.08 | 0.00 | 0.15 | 0.08 | 0.15 | 0.41 | 1.53 |
| RE16JP020 | Laramide giant porphyry | 0.63 | 0.35 | 0.00 | 0.22 | 0.38 | 0.31 | 0.00 | 0.12 | 0.95 | 1.90 |
| RE16JP028 | Laramide giant porphyry | 0.86 | 0.40 | 0.14 | 0.21 | 0.00 | 0.24 | 0.00 | 0.15 | 0.59 | 1.90 |
| RE16JP014 | Laramide giant porphyry | 0.89 | 0.45 | 0.00 | 0.14 | 0.00 | 0.13 | 0.11 | 0.28 | 0.50 | 1.81 |
| RE16JP192 | Proterozoic hydrothermal | 0.11 | 0.22 | 0.89 | 0.61 | 0.00 | 0.09 | 0.00 | 0.08 | 0.50 | 1.50 |
| RE16JP193 | Laramide giant porphyry | 1.00 | 0.44 | 0.00 | 0.21 | 0.00 | 0.11 | 0.00 | 0.24 | 0.00 | 1.84 |
| RE16JP194 | Proterozoic hydrothermal | 0.21 | 0.29 | 0.79 | 0.41 | 0.00 | 0.10 | 0.00 | 0.20 | 0.74 | 1.84 |
| RE16JP195 | Laramide giant porphyry | 0.50 | 0.41 | 0.00 | 0.06 | 0.50 | 0.37 | 0.00 | 0.16 | 1.00 | 1.73 |
| RE16JP035 | Early Laramide small porphyry | 0.35 | 0.36 | 0.29 | 0.20 | 0.00 | 0.19 | 0.35 | 0.25 | 1.58 | 1.95 |
| RE16JP031 | Early Laramide small porphyry | 0.22 | 0.36 | 0.00 | 0.05 | 0.00 | 0.13 | 0.78 | 0.46 | 0.76 | 1.65 |

Abbreviations; A* = Proportion of individual analyses predicted to belong to class. B* = Average probability of class membership among indiviual spot analyses.

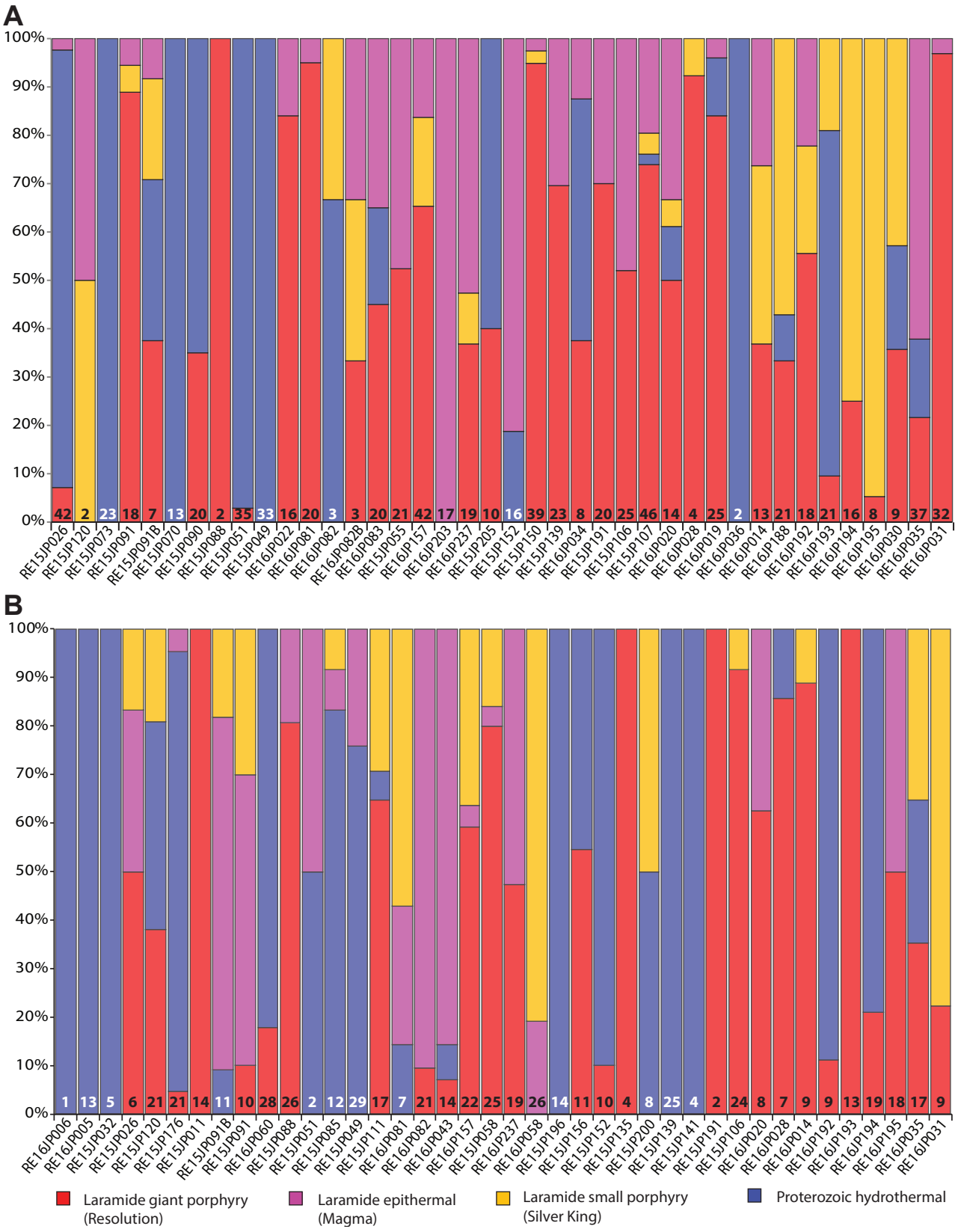


Figure 8.6 Stacked column for (A) epidote and, (B) chlorite, showing the total number of analyses for each sample and the proportion of those analyses grouped into each class, organised spatially from south to north along the range front. There is a crude zonation (especially in epidote) from Proterozoic hydrothermal alteration in the south, Resolution/Magma in the middle section and Silver King style epidote in the northern part. All data listed in Table 8.4 and Table 8.5.

between A* and B*, as well as entropy (degree of randomness) can lend insight into decision making in the random forests algorithm. Generally, entropy in the proportional classification (entropy A*; Table 8.4) has a negative relationship with the number of analyses per sample, suggesting that the classification of epidote from samples with <10 analyses is prone to more disorder, and therefore uncertainty in the classification, than those with more analyses. In the case of the latter, average probability can be useful in assessing the degree of possible misclassification (Table 8.4).

Generally, the classification results in Figure 8.6 show that Proterozoic hydrothermal epidote is most abundant in the southern part of the district, an area with the greatest exposure of age-permissive host rocks (Apache Basalt). In contrast, early Laramide small porphyry-class epidotes account for larger proportions of analyses in the north of the district (Figure 8.6 A), Laramide giant porphyry and Laramide epithermal epidotes are most abundant in the central part of the study area (Figure 8.6 A). However, some epidote classifications of Laramide giant porphyry have been identified around Silver King, and vice versa, indicating either a degree of chemical overlap between the two groups and/or that the two hydrothermal systems genuinely overlapped spatially. The classification of early Laramide small porphyry epidotes in the south of the district is restricted to very small proportions of samples, (e.g., RE15JP150, RE16JP237, RE15JP091; Figure 8.6 A). In cases where they appear to represent large proportions of samples, those samples have very few valid analyses (e.g., RE15JP120, RE16JP082, RE16JP082B; Figure 8.6 A). The occurrences of small porphyry are spatially related to faults and commonly coexist with Magma-like epidote, implying a compositional, rather than spatial overlap. The apparent error in the class membership likely arises from the significance of Pb and Sr to the discriminant projections that control the classification of Resolution and Silver King epidote types (DP1, and DP3, Table 8.2). No unknown samples were classified as Laramide skarns based on the unmineralised training data sample, despite there being some samples containing skarn mineralogy (e.g., RE15JP191, RE16JP019). Instead these samples were classified dominantly as Resolution-type epidote, suggesting that they share more similarities with propylitic epidote from a mineralised source than skarn epidote from a weakly or unmineralised source. Similarly, the northernmost sample, although mixed, appears to have a dominantly Resolution or Magma–type signature (Table 8.4).

#### 8.4.2.2 Chlorite

Nine of the samples (23%) yielded chlorite analyses that were all classified to a single class (Table 8.5; Figure 8.6 B). In general, the degree of mixing that was noted among epidote types is also apparent for the different chlorite types. Generally, Proterozoic hydrothermal classifications account for a larger proportion of the chlorite analyses than was noted for epidote. The Proterozoic chlorite provides a widely distributed background against which the Laramide classes appear more confined to mappable cells.

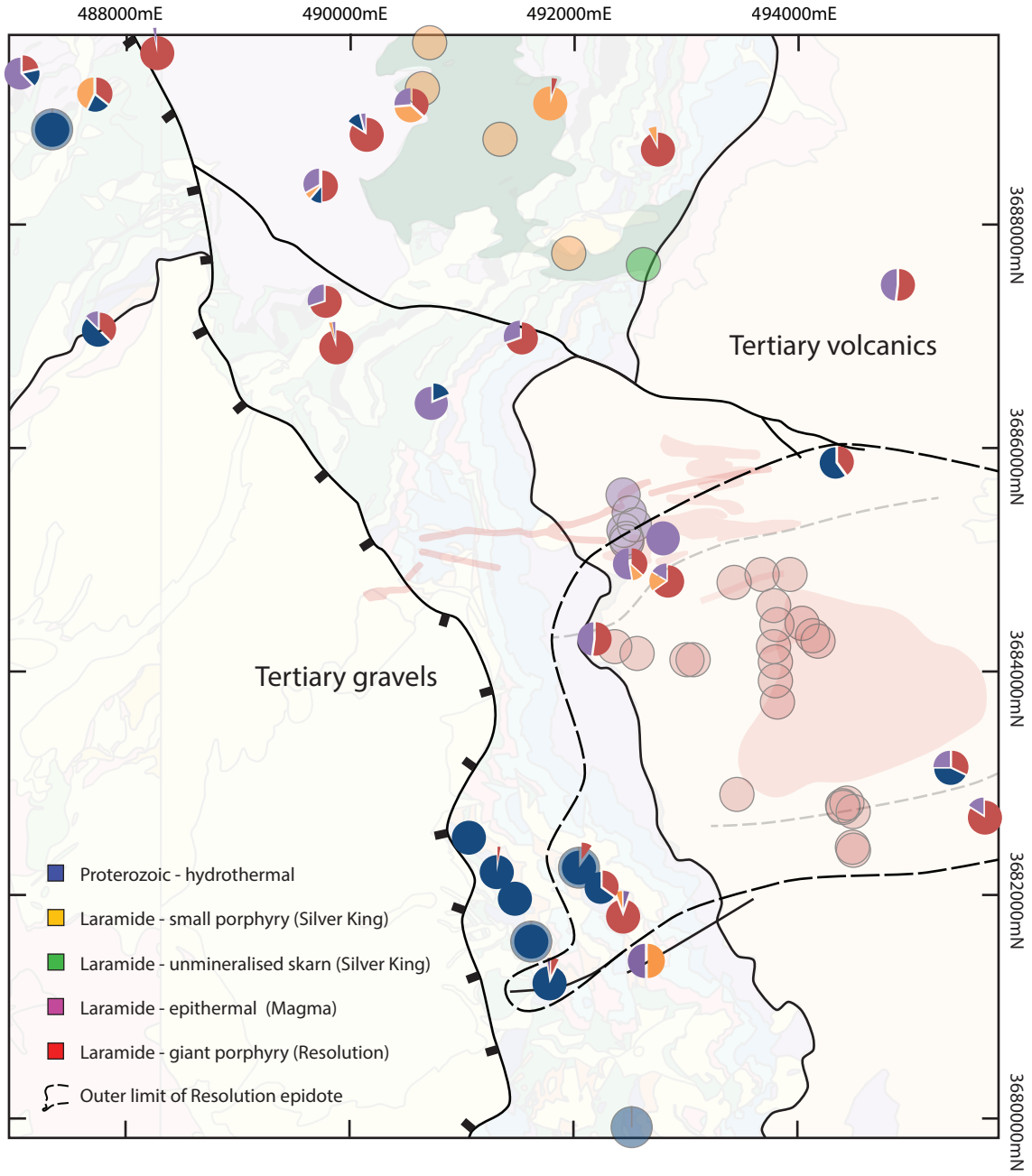


Figure 8.7 Map showing the proportional classifaction of unknown epidote from the Superior district, expressed as pie charts for each sample. Larger, faded circles represent analyses used in the training data. All data listed in Table 8.4.

### 8.4.3 Spatial distribution of classified data

#### 8.4.3.1 Epidote

The southern part of the range front is dominated by Proterozoic hydrothermal epidote (Figure 8.7). However, several samples in this area contain Resolution epidotes. The propylitic alteration halo to the Resolution porphyry copper deposit is therefore considered to crop out at surface in the range front in the vicinity of the Belmont fault zone (Figure 8.7). Based on its distribution, at its greatest extent, the epidote footprint of Resolution extends to at least 4 km in the southern part of the district from the centre of the ore shell. Furthermore, the intensity of Laramide epidote in this distal environment

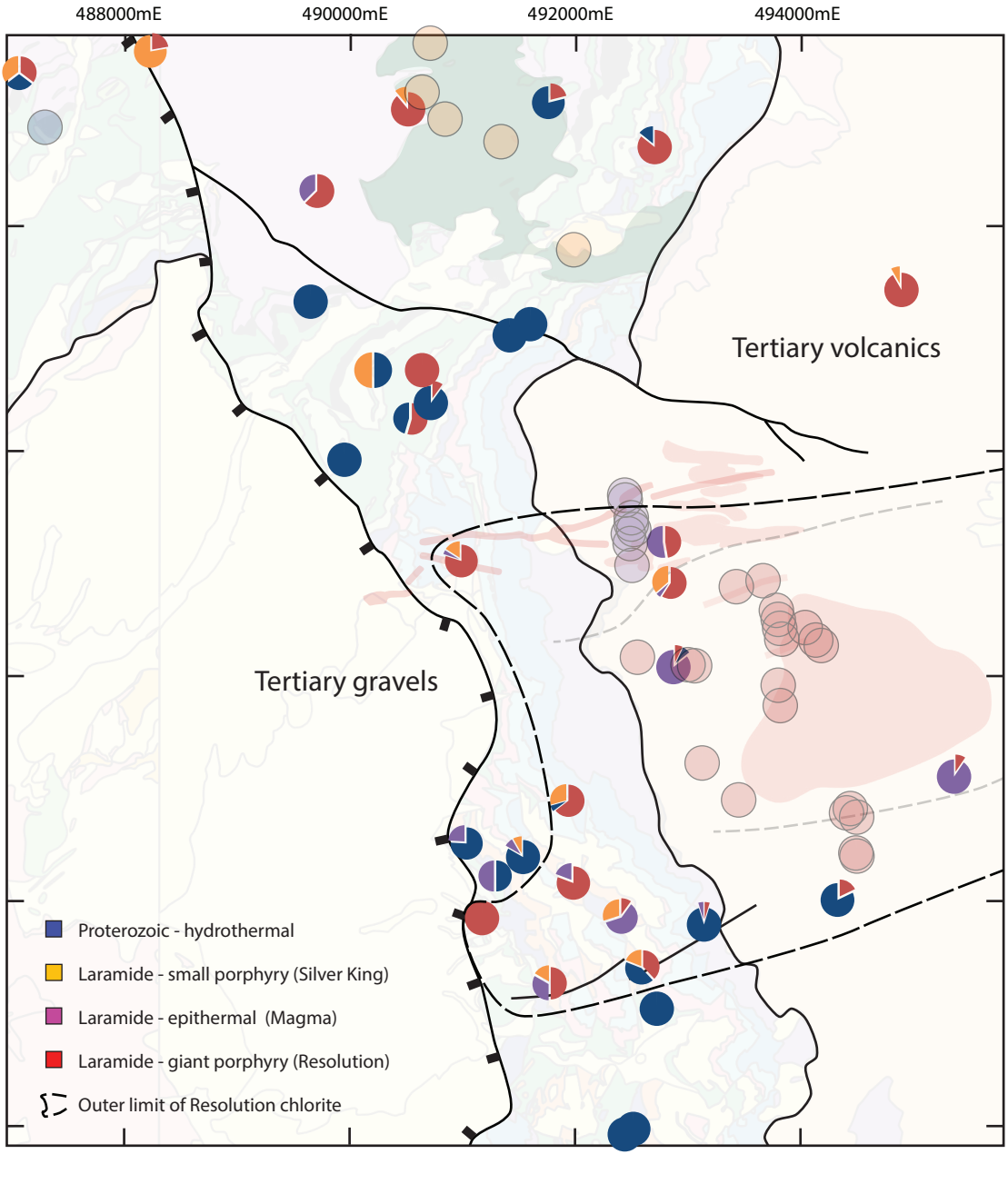


Figure 8.8 Map showing the proportional classifaction of unknown chlorite from the Superior district, expressed as pie charts for each sample. Larger, faded circles represent analyses used in the training data. All data listed in Table 8.5.

decreases markedly at distances between 3 and 4 km from Resolution, as demonstrated by the relative proportion of Resolution-like epidote in the distal samples (Figure 8.7).

Although the Laramide epithermal class is mostly hosted by Proterozoic dolerite, only one of the unknown dolerite-hosted epidote samples was classified as entirely epithermal. This result highlights the limited host rock control on epidote chemistry. Samples classified as epithermal are generally from around Magma or other faults intersected by drilling (Figure 8.7).

Samples close to the quartz diorite stock in the north of the district generally have mixed epidote classifications. These samples are mostly dominated by Resolution-type rather than Silver King-type epidote (Figure 8.7). It may be that the differences between the two epidote types may reflect proximity

to the causative heat source (i.e., Resolution epidote samples collected distal to a large heat source, and Silver King epidote samples collected proximal to a smaller heat source; Figure 8.7). Between the Magma Vein and the Conley Springs Fault, there are four samples that show a combination of dominantly Resolution- and Magma-style epidote, with only limited Proterozoic and negligible Silver King-type components (Figure 8.7), suggesting an abundance of Laramide porphyry-style epidote in this area (Figure 8.7). Additionally, four samples with mixed but dominantly Laramide epidote compositions occur in the northwest of the district (Figure 8.7).

#### 8.4.3.2 Chlorite

Seven of the 12 chlorite-bearing samples in the southern range front have compositions similar to Resolution-style chlorite. This is interpreted to indicate that Resolution-related chlorite alteration crops out at surface, extending the Resolution geochemical footprint to at least 4.2 km from the deposit centre (Figure 8.8). More of the chlorite samples in the southern range front have a Resolution-style compositions than the analysed epidote samples (Figure 8.7 and 8.8).

Chlorite samples classified as epithermal are generally located proximal to known vein arrays and major faults (Figure 8.8), as was the case for epithermal epidote. Porphyry-related chlorite is not as obviously structurally controlled as epidote (Figure 8.8).

Some of the chlorite from around Silver King is classified as Resolution-related (Figure 8.8). A similar result was noted in the epidote classification results (Figure 8.7). Laramide-style chlorite alteration has been detected between the Magma vein and the Conley Springs Fault, notably with a much larger Proterozoic component. Laramide chlorite was also detected in the NW corner of the district (Figure 8.8).

### 8.4.4 Epidote mapping

Laser-ablation ICP-MS mapping was undertaken to validate intra-sample variability predicted by the Random Forests classification results from Figure 8.6. Figure 8.10 shows selected laser mapping results from sample RE15JP026 (Figure 8.9). Additional laser mapping results for other samples can be found in Appendix 3C. Laser mapping of grains in Sample RE15JP026 shows at least three major epidote growth stages. Firstly, a K-feldspar inclusion rich, but generally trace element poor core, dominated by low- and moderate concentrations of Mn and Ti respectively (domain pЄ1; Figure 8.10). This early stage is overgrown by a more Mn rich and Ti poor rim, accompanied by low levels of B, As, Bi, U and Y (domain pЄ2; Figure 8.10). A very fine rim of high La accompanies the final phase of this second growth stage, and may represent and short episode of LREE stability (domain pЄ2b; Figure 8.10). The third domain is strongly enriched in Pb and Sr and shows a very strong relative enrichment around the edges of crystals in the lower right of the image (domain KT; Figure 8.10). Later still, Zn and Cu appear to exploit cracks and fractures throughout the mapped area, suggesting that some metals may have been

introduced late in the growth history of the composite epidote grain. There is a possibility that sulfide-rich residue from polishing equipment accumulated against higher relief surfaces and could explain the Cu and Zn-rich cracks.

The relative timing and attribution of epidote growth zones in Figure 8.10 with known epidote-forming events within the Superior district can be constrained by comparison of elemental associations observed within the growth zones with those identified by discriminant projection analysis of geochronologically and spatially constrained training data (Figure 8.4). Laramide epidote is characterised by strong enrichments of Pb and Sr (Table 8.2; Figure 8.4), such as can be seen in the KT domain (Figure 8.10), suggesting that this phase of epidote growth is Laramide in age. It is probably related to Resolution, given its location. Training data for Proterozoic epidote is characterised by enrichments in predominantly U, B and HREE, which correlate with the pЄ2 domain (Figure 8.10), implying this growth zone has a Proterozoic timing. However, geochronological constrains and the construction of a training dataset for Proterozoic epidote was only possible where sufficient U was encountered during spot analysis, which is confined to only the second stage of Proterozoic epidote growth (domain pЄ2b; Figure 8.10 pЄ2b; Figure 8.10), therefore biasing the Proterozoic epidote training data toward trace element-rich pЄ2 compositions. It probably does not account for the more volumetrically abundant, trace element poor pЄ1-type epidote. Lanthanum, also appears to be a significant trace element in the Proterozoic epidote grains, but due to its confinement to late-stage rims and less chance of incorporation during spot analysis, it was not part of the suite of elements that characterise the Proterozoic epidote training data (Table 8.2). Further complications arise due to the overlap in Ti, and to some degree La, enrichments in Silver King type epidote (DP3; Table 8.2; Figure 8.4). The possible overlap between pЄ1-type Proterozoic epidote with Silver King could explain some of the intra-sample heterogeneity and misclassification observed in Figure 8.6, especially in the south of the district.

Overall, epidote laser mapping validates the Laramide overprinting of Proterozoic epidotes implied in Figure 8.6. However, there are potential sources of misclassification, particularly of due to the potential similarity between Silver King and pЄ1-type Proterozoic epidote around Resolution. There is also the possibility of mixed compositions from spots that have sampled multiple types of epidote.

### 8.4.5 Changes in trace element concentrations with distance

#### 8.4.5.1 Epidote

Epidote and chlorite mineral chemistry has been shown to vary systematically with increasing distance from the known or estimated deposit centre in several porphyry deposits (Cooke et al., 2014, 2015, 2017; Baker et al., 2015, 2017; Wilkinson et al., 2015, 2017). For the Superior district, Figure 8.11 shows the compositional range of selected trace elements from individual samples classified as Resolution-related by the Random Forests algorithm plotted in order of increasing distance to the centre of Resolution.

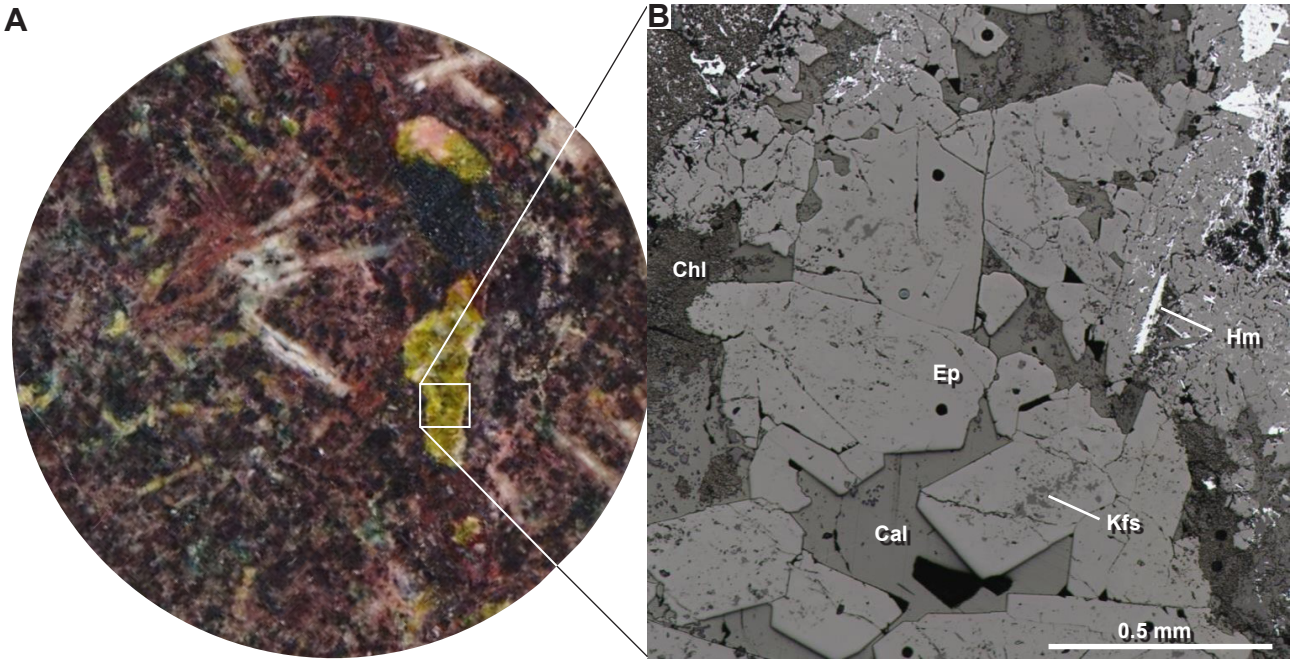


Figure 8.9 A. RGB scan and B. Reflected light image of epidote - calcite - chlorite amygdale from basalt-hosted RE15JP026 from the Superior range front. Abbreviations; Ep = epidote; Chl = chlorite; Cal = calcite; Kfs = K-feldspar; Hm = hematite.

Although there are some crude trends visible in the Sb data, and to a lesser degree for the Pb, Zn and Sr concentrations in epidote, systematic geochemical gradients from sample to sample are not obvious from Figure 8.11. This is probably due to a number of factors, the most important probably being a non-homogeneous thermal aureole and/or discrete structurally and stratigraphically controlled flow paths. When sample distances are grouped using Jenks natural breaks (Figure 8.12, Figure 8.13) and when results are averaged over each distance interval, the concentration of many trace elements can be seen to change significantly with distance from the centre of the mineralising system. These trends are more obvious in chlorite data than for epidote (Figure 8.14, Figure 8.15, Figure 8.16). In each case, the number of bins was chosen to show the maximum variability for epidote and chlorite. Uranium concentrations in epidote tend to decrease with distance from Resolution, whereas La, As, Sb, Pb, Sr and to a lesser extent Zn and Mn in epidote define an enrichment halo approximately 2 km from the deposit (Figure 8.14). Copper, Cr and B in epidote generally show well developed trends that increase with distance (Figure 8.14). In most cases, elements tend to become more similar in composition to Proterozoic background with increasing distance from Resolution (Figure 8.14). However, distinctly higher concentrations of Pb, Sr and to a lesser degree Zn, are noted for Resolution-related epidote compared to the background Proterozoic epidote. The Pb data define the greatest spatial extent of the Resolution epidote geochemical footprint (Figure 8.14).

#### 8.4.5.2 Chlorite

Chlorite-bearing samples have been subdivided into groups based on distance from the deposit, in the

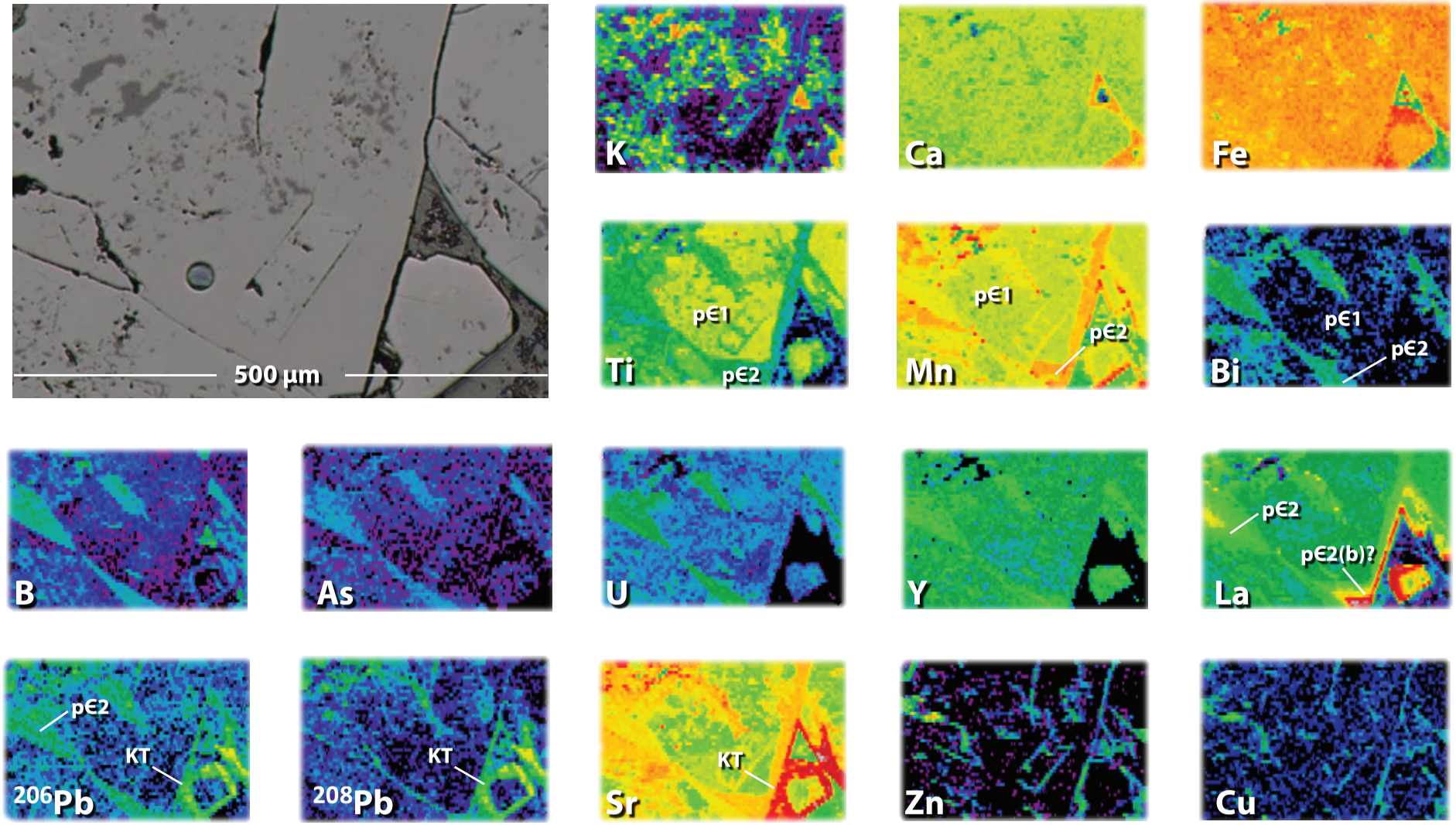


Figure 8.10 LA-ICP-MS mapping results for amygdale-hosted epidote in RE15JP026 from the Superior range front (same sample as in Figure 8.9). Note the early Ti- and Mn-rich phase (pЄ1), followed by a trace element poor phase of epidote crystallisation (pЄ2). The Laramide (KT) epidote is rich in Pb and Sr and overgrows the previous epidote crystals.

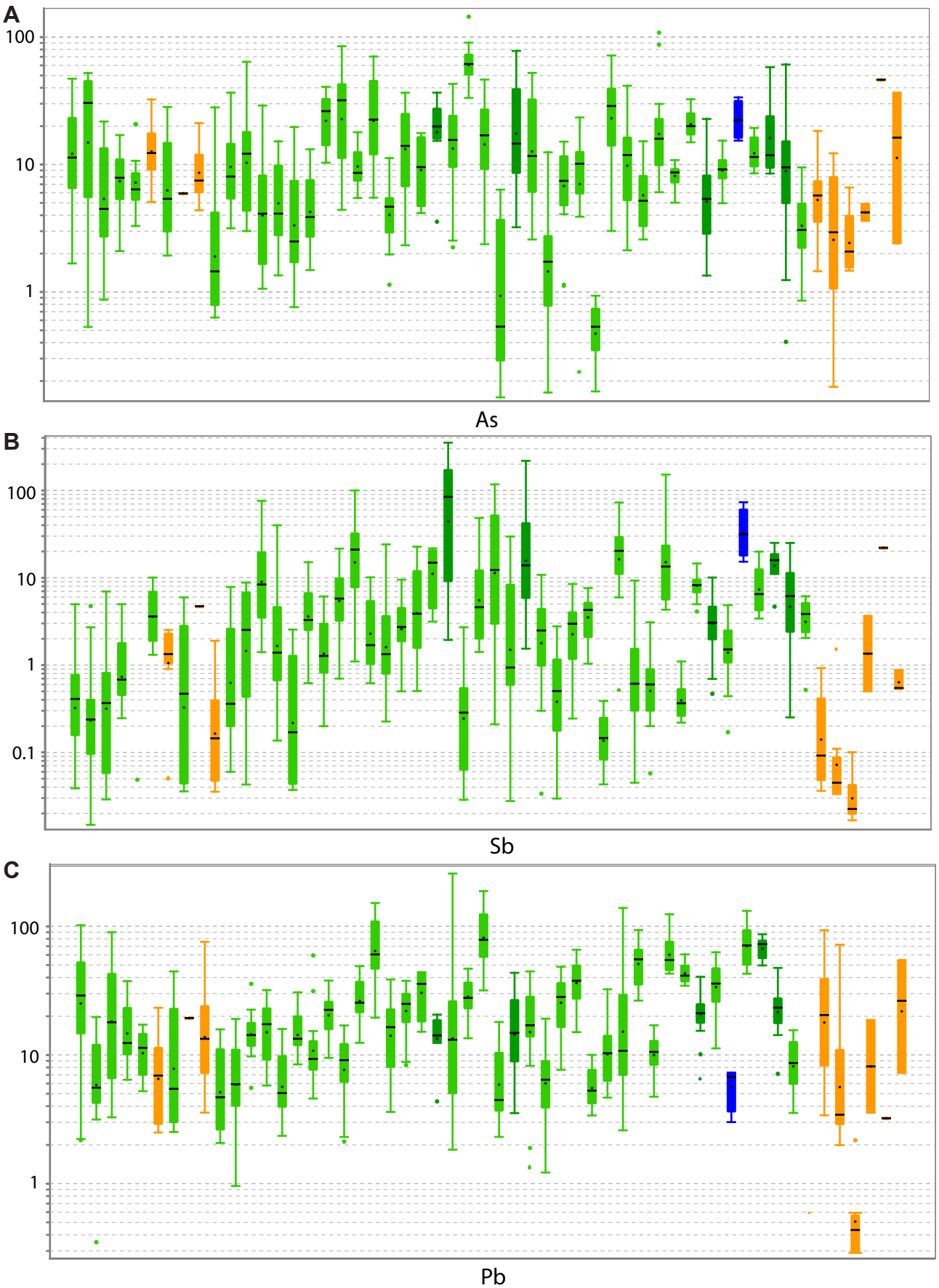


Figure 8.11 Ranges of concentrations for selected trace elements in epidote for individual samples predicted as Resolution-related (including training data). Samples are arranged by increasing distance from the centre of the Resolution deposit (left to right) and coloured by host rock composition (Kvs - light green; dolerite - dark green; basalt - orange and limestone - blue). A. Arsenic, B. Antimony, C. Lead, D. Zinc, E. Manganese, F. Strontium. All data listed in Appendix 3A.

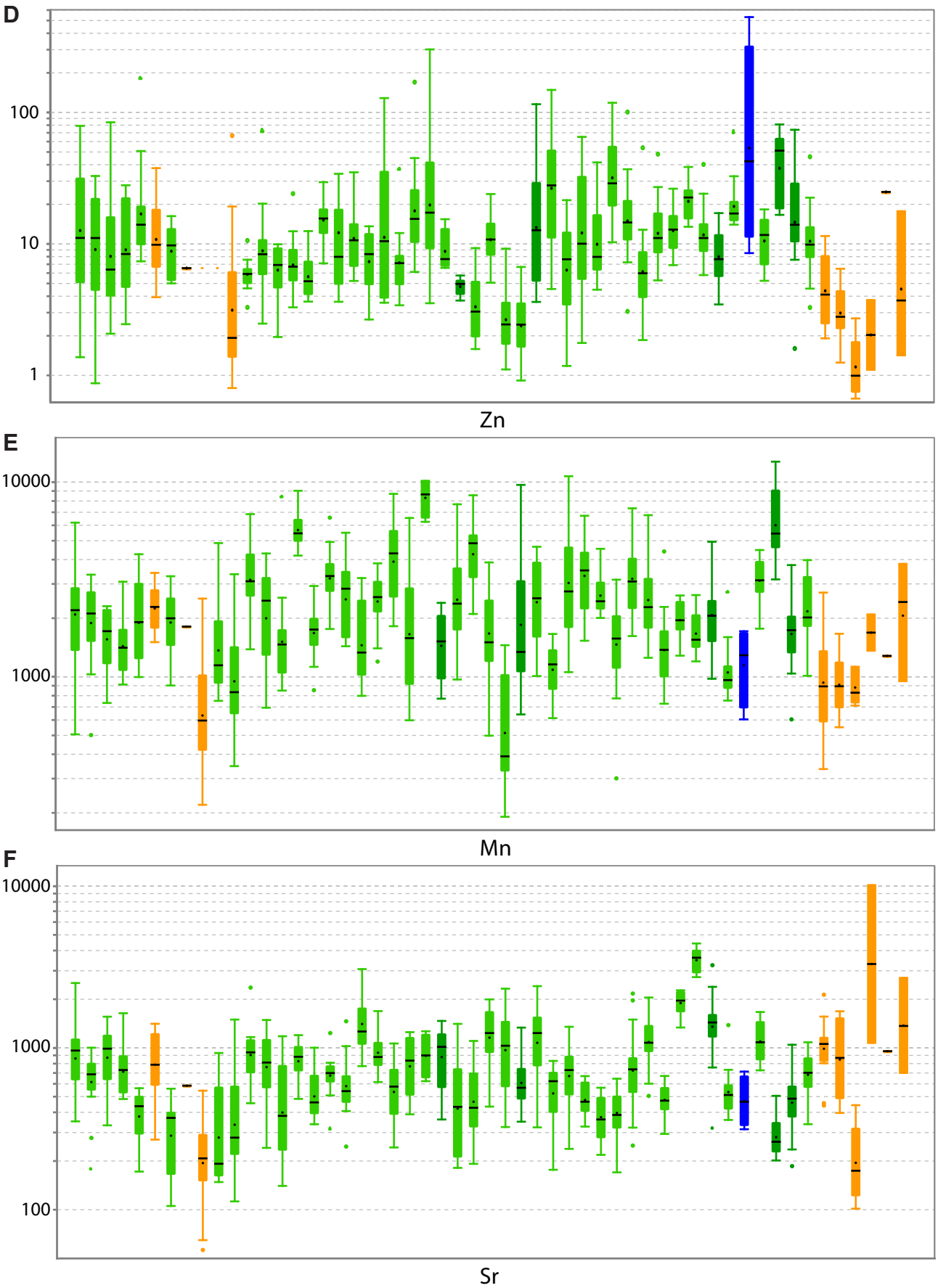


Figure 8.11 (cont.)

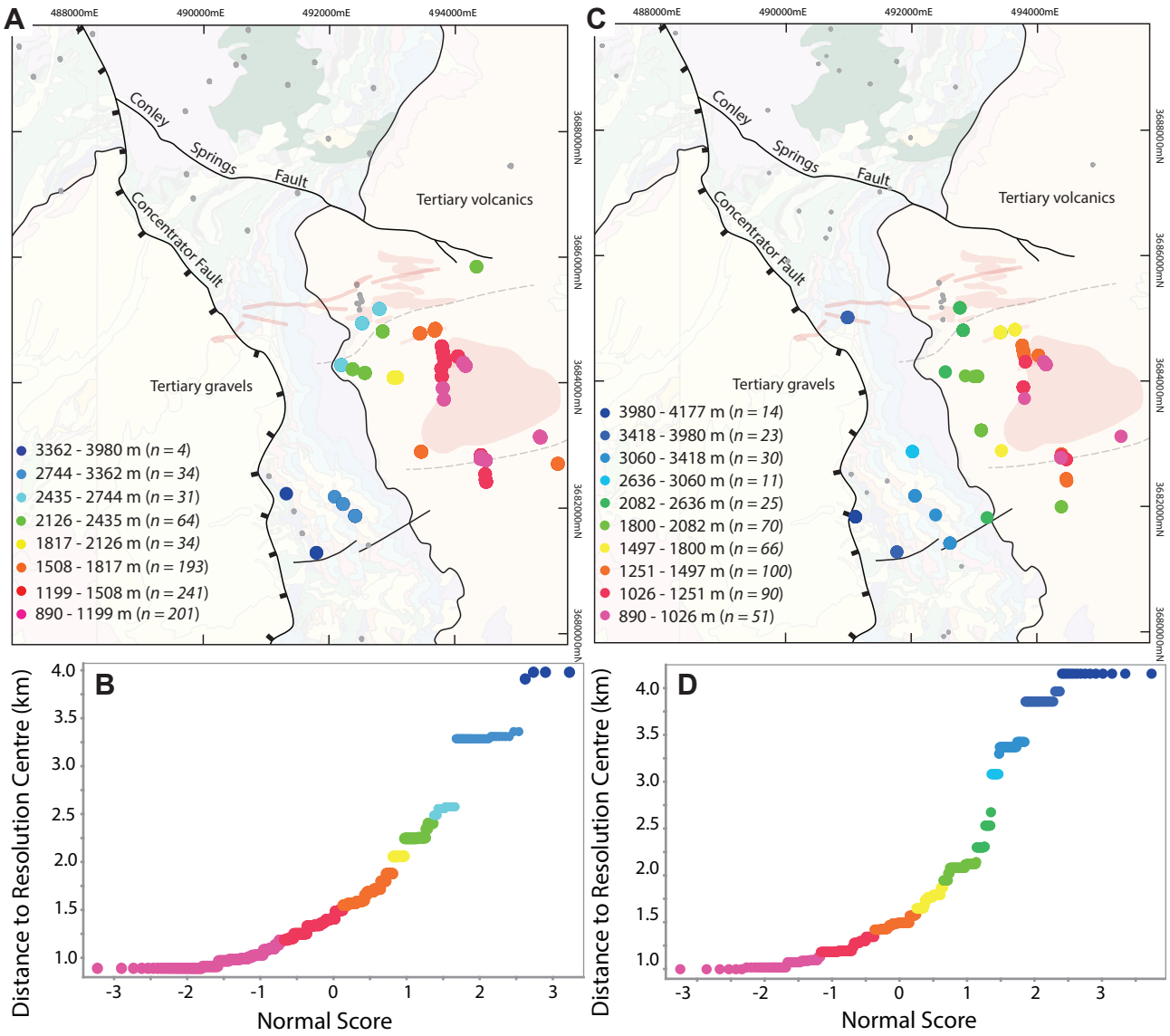


Figure 8.12 A. Map and B. probability plot of natural breaks in distance of Resolution classified epidote analyses from the centre of the Resolution deposit. C. Map and D. probability plot of natural breaks in distance of Resolution classified chlorite analyses from the centre of the Resolution deposit. Groups used for plotting changes in epidote and chlorite chemistry with increasing distance in later figures. All data provided in Appendices 3A and 3B.

same fashion as for epidote, using natural breaks in the data and shown with the overall compositional range of Proterozoic background samples (Figure 8.13). Major element compositions of chlorite show change systematically with distance from Resolution, up to a distance 2 – 2.6 km (Figure 8.15). Aluminium and Mg systematically decrease, whereas Fe and Si increase (Figure 8.15). Similar patterns of proximal Mg and more distal Fe concentration in chlorite were reported from Southwest Tintic (Norman et al., 1991), Batu Hijau (Wilkinson et al., 2015) and the Collahuasi district (Baker et al., 2015).

Trace element compositions of chlorite vary systematically with distance from Resolution, up to around 2 km (Figure 8.16). Elements that substitute into chlorite at high temperatures, such as Ti, V and Cr show some systematic decreases with distance, but the variations in their abundances are less obvious than for the major elements (Figure 8.16, Figure 8.15). Zinc, Mn and Pb are comparatively depleted proximally with only weak increases with distance (Figure 8.16). Elements such as Sr, B, Co, Cu and as Zr define

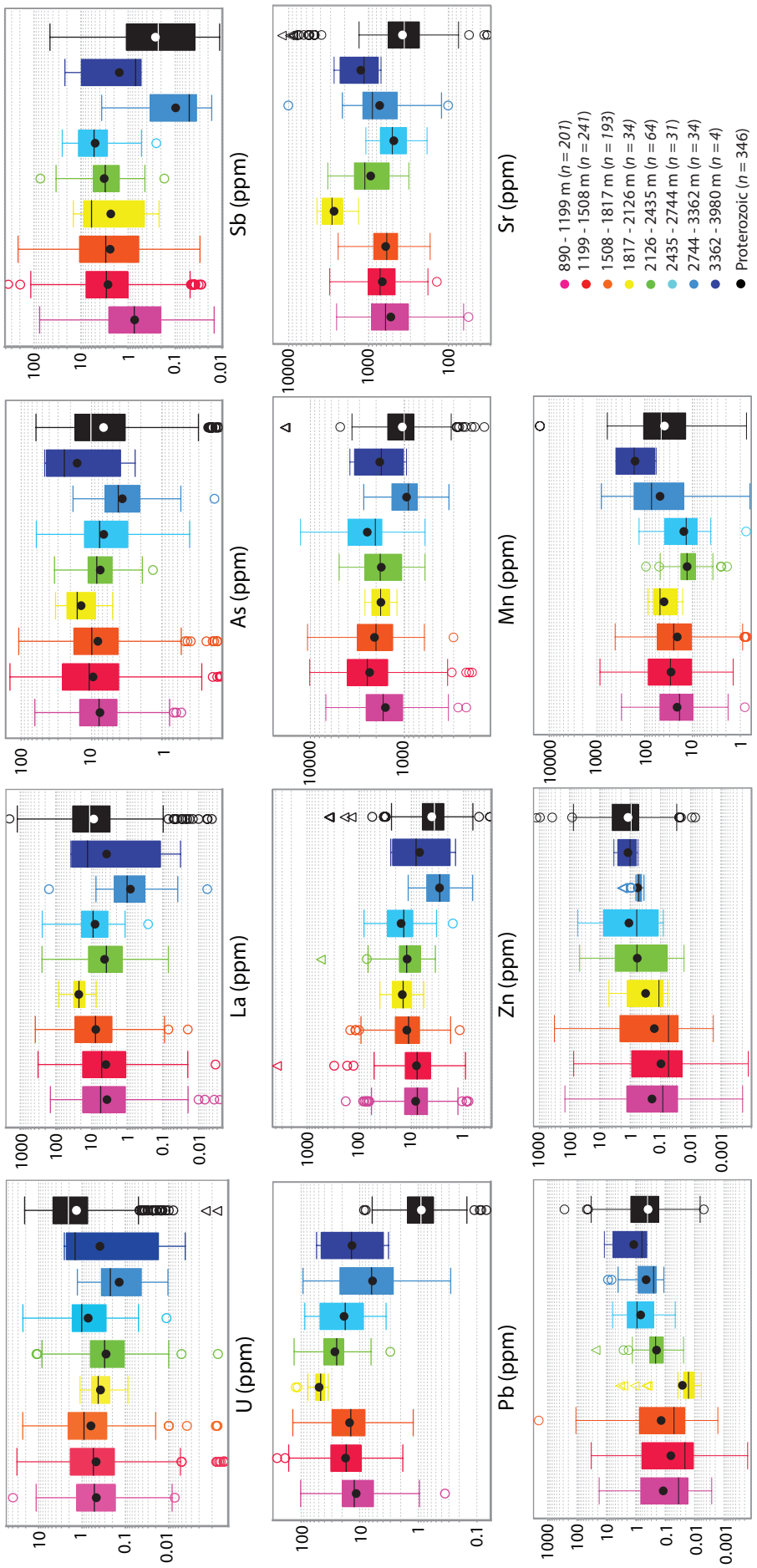


Figure 8.13 Tukey plots showing the ranges of concentrations for selected trace elements in epidote classified as Resolution-style grouped, using natural breaks as per Figure 8.12 A-B, by distance from the centre of the Resolution deposit (left to right). Also show are the compositional ranges for Proterozoic hydrothermal epidote, which can be considered background. All data listed in Appendix 3A.

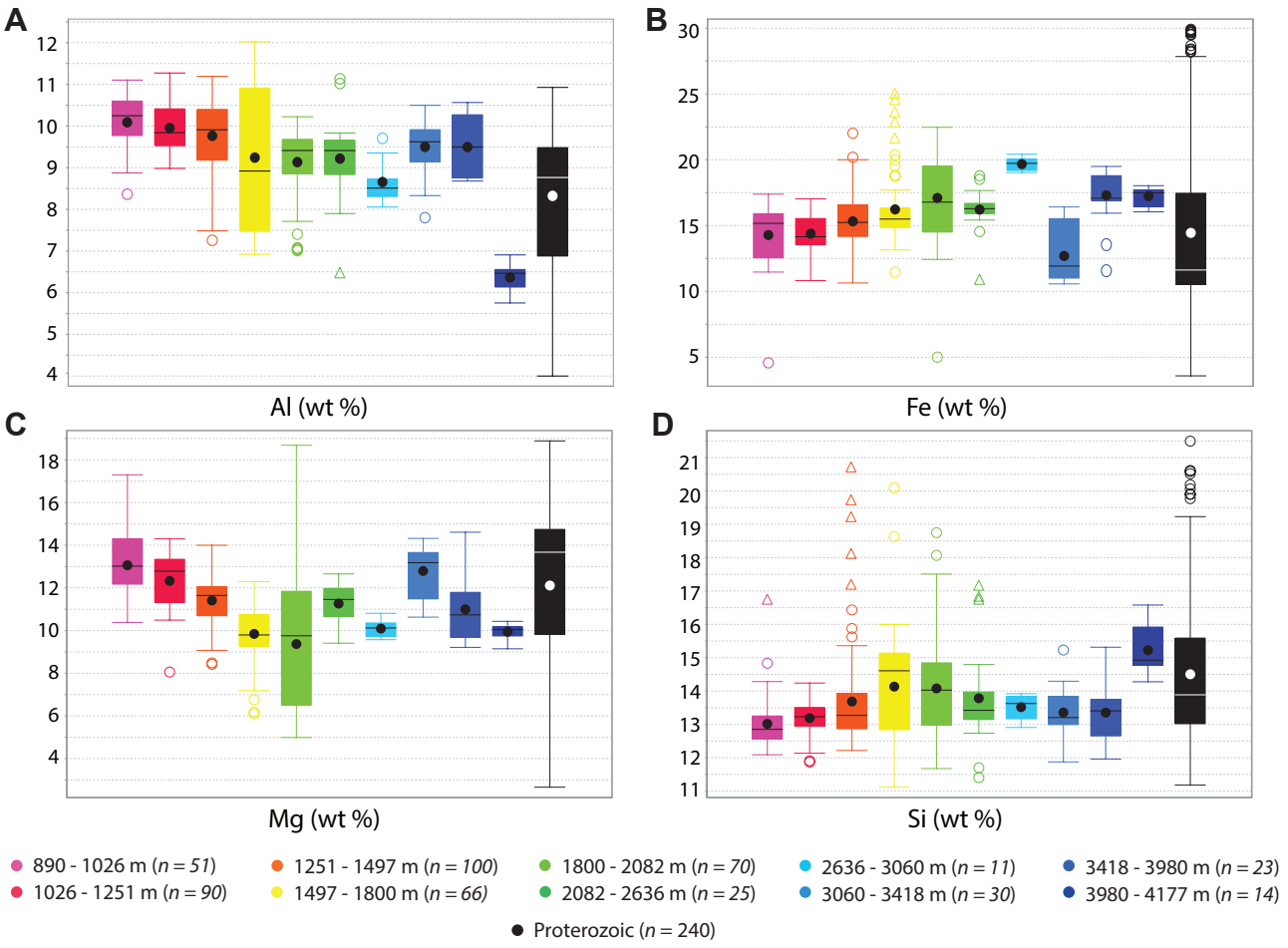


Figure 8.14 Tukey plots showing ranges of concentrations for major elements in chlorite classified as Resolution-style, grouped by distance from the centre of the Resolution deposit (left to right). Also shown are compositional ranges for Proterozoic hydrothermal chlorite, which can be considered background. All data listed in Appendix 3B.

enrichment patterns, with distance from Resolution out to around 2 km (Figure 8.16). Similarly to epidote, most of the elements in chlorite tend to homogenise towards background Proterozoic values (e.g., Ti, V, Cr, Pb, Sr, B, Zr, Co, Cu; Figure 8.16). A few trace elements have compositions that are clearly distinct from Proterozoic background (e.g., Zn, Mn, Li; Figure 8.16), providing criteria for the distinction between Laramide and Proterozoic chlorite.

### 8.4.6 Chlorite proximitor calculations

Wilkinson et al. (2015) showed that the abundances of pairs of trace elements in chlorite that vary inversely with distance from a known hydrothermal centre can define a proximitor ratio calibrated by distance from a known deposit. Several of these proximitor ratios were defined for Batu Hijau by Wilkinson et al. (2015) and were originally applied to the Resolution blind test sample suite by Cooke et al. (2015). This work is continued here in an attempt to extend the outer limit of proximitor ratio application (~2 - 2.5 km; Wilkinson et al., 2015; 1.4 km, Cooke et al., 2015).

Trace elements in chlorite in the Superior district that show enrichments or depletions with distance are evident in Figure 8.15 and Figure 8.16. Of the trace elements in chlorite that are elevated proximal

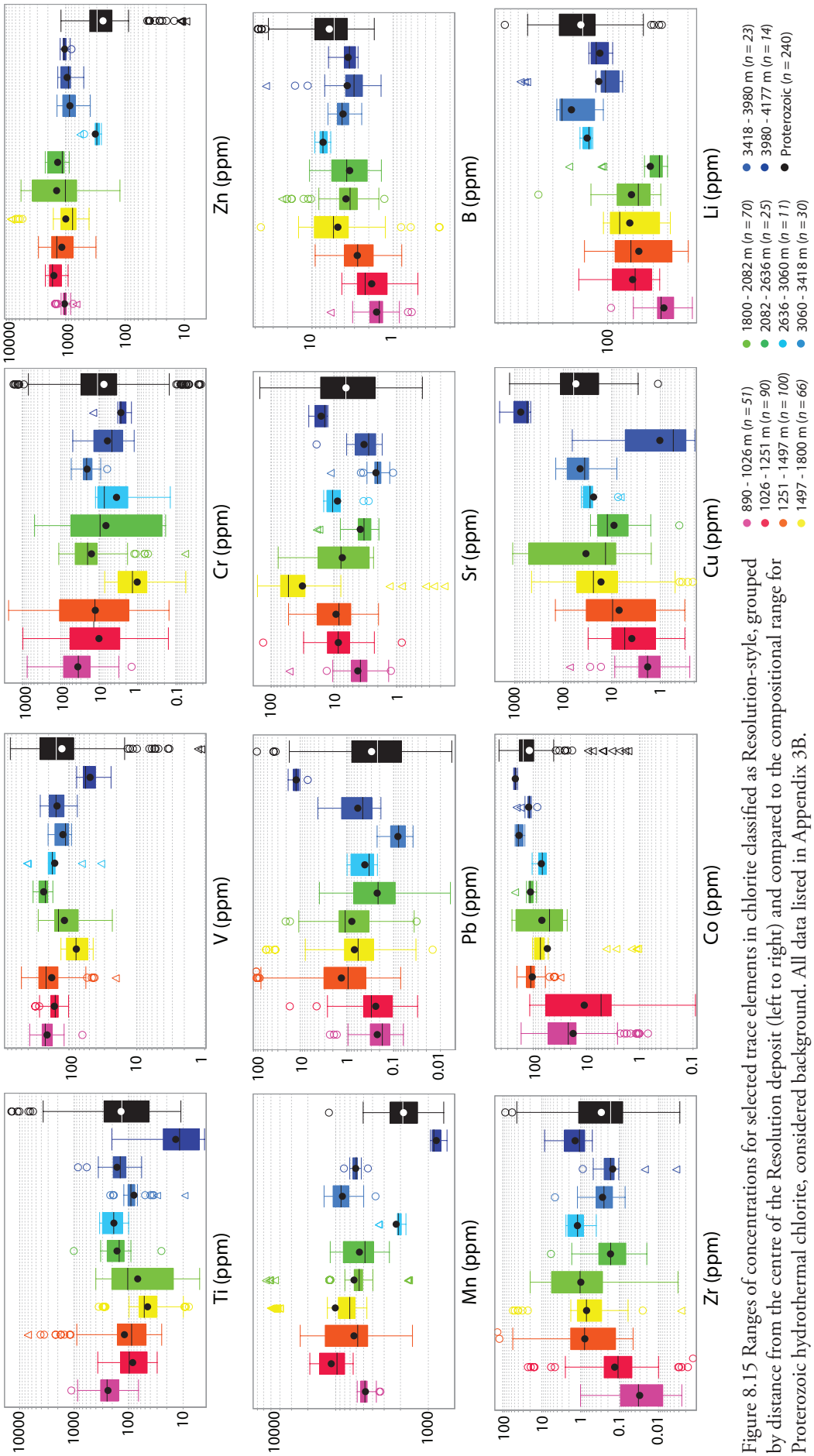


Figure 8.15 Ranges of concentrations for selected trace elements in chlorite classified as Resolution-style, grouped by distance from the centre of the Resolution deposit (left to right) and compared to the compositional range for Proterozoic hydrothermal chlorite, considered background. All data listed in Appendix 3B.

Table 8.6 Results of proximitor calculations for chlorite in the Superior district, using equations from Wilkinson et al. (2015)

| Proximitor ratio | Maximum distance (m) | Slope | | Intercept | | $R^2$ | |
|---|---|---|---|---|---|---|---|
| | | All spots | Sample average | All spots | Sample average | All spots | Sample average |
| Ti/Sr | 1600 | -0.0018 | -0.0017 | 3.29 | 3.12 | 0.26 | 0.31 |
| V/Co | 2100 | -0.0018 | -0.0011 | 3.03 | 2.19 | 0.37 | 0.34 |
| Mg/Fe | 1500 | -0.00027 | -0.00026 | 0.238 | 0.228 | 0.33 | 0.29 |
| Mg/Si | 1700 | -0.00022 | -0.00026 | 0.213 | 0.269 | 0.43 | 0.72 |
| Mg/ Sr | 1700 | -0.0012 | -0.00070 | 5.64 | 5.00 | 0.35 | 0.11 |
| Mg/Zr | 1800 | -0.0021 | -0.0017 | 8.35 | 7.99 | 0.28 | 0.39 |
| Mg/B | 2000 | -0.00086 | -0.00055 | 5.78 | 5.39 | 0.36 | 0.32 |
| Mg/Cu | 2000 | -0.0013 | -0.00063 | 6.04 | 5.24 | 0.20 | 0.09 |

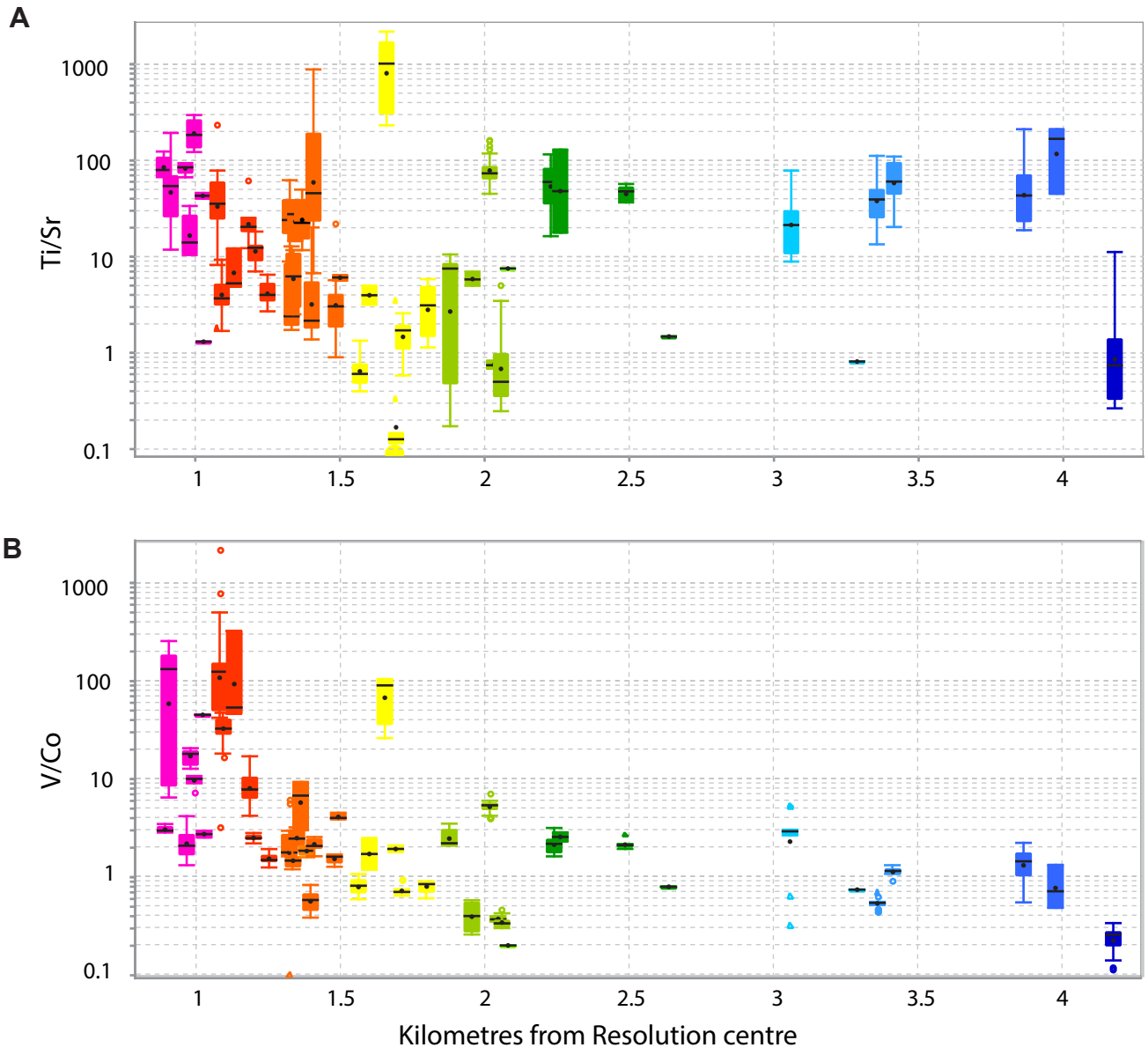


Figure 8.16 Ranges of values for previously published chlorite proximitor ratios in all Resolution-style classified chlorite spot analyses for a particular samples plotted by distance from the centre of the Resolution deposit (left to right). Data listed in Appendix 3B.

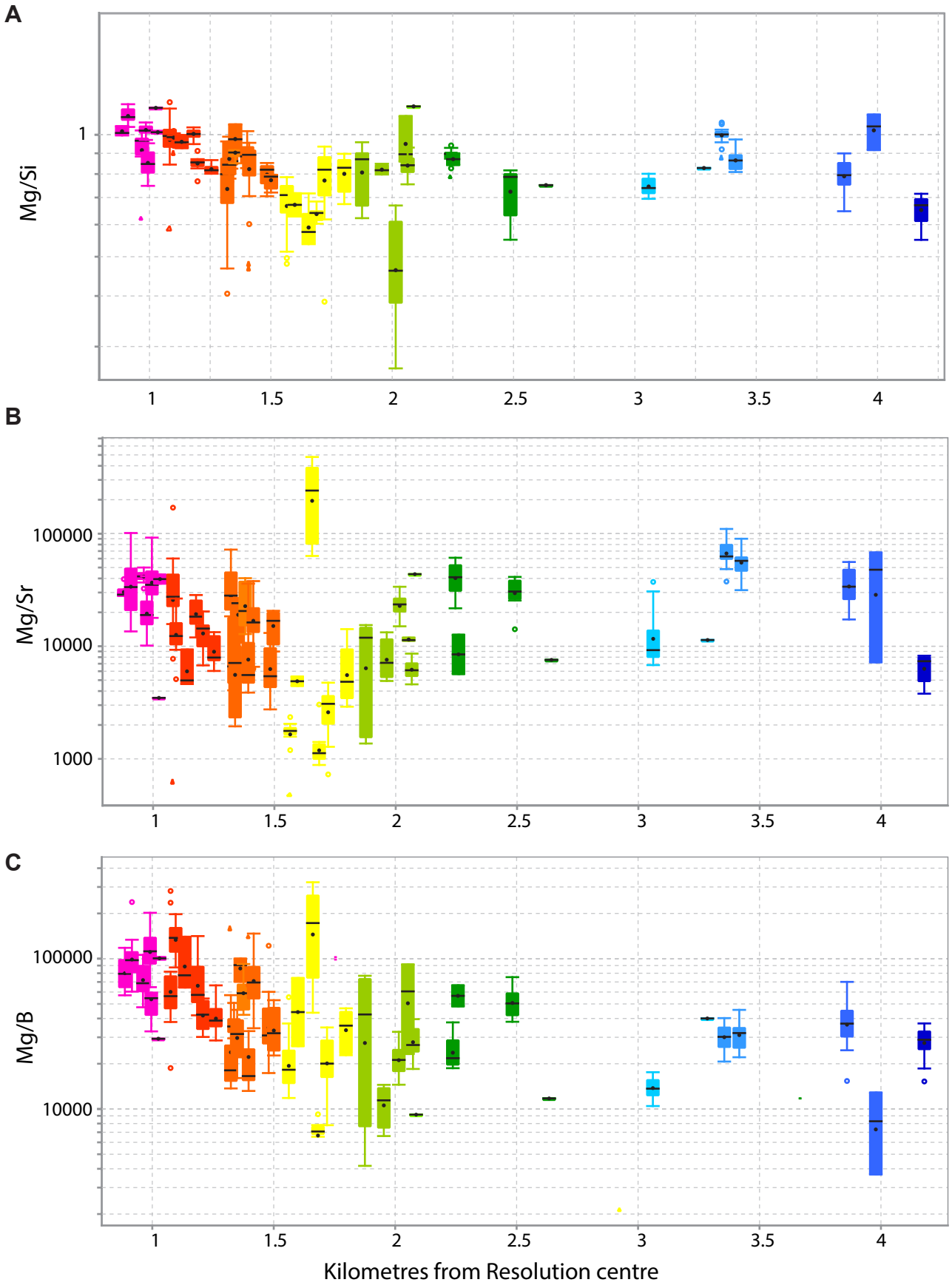


Figure 8.17 Ranges of values for selected chlorite proximitor ratios in all Resolution-style classified chlorite spot analyses for a particular samples plotted by distance from the centre of the Resolution deposit (left to right). Data listed in Appendix 3B.

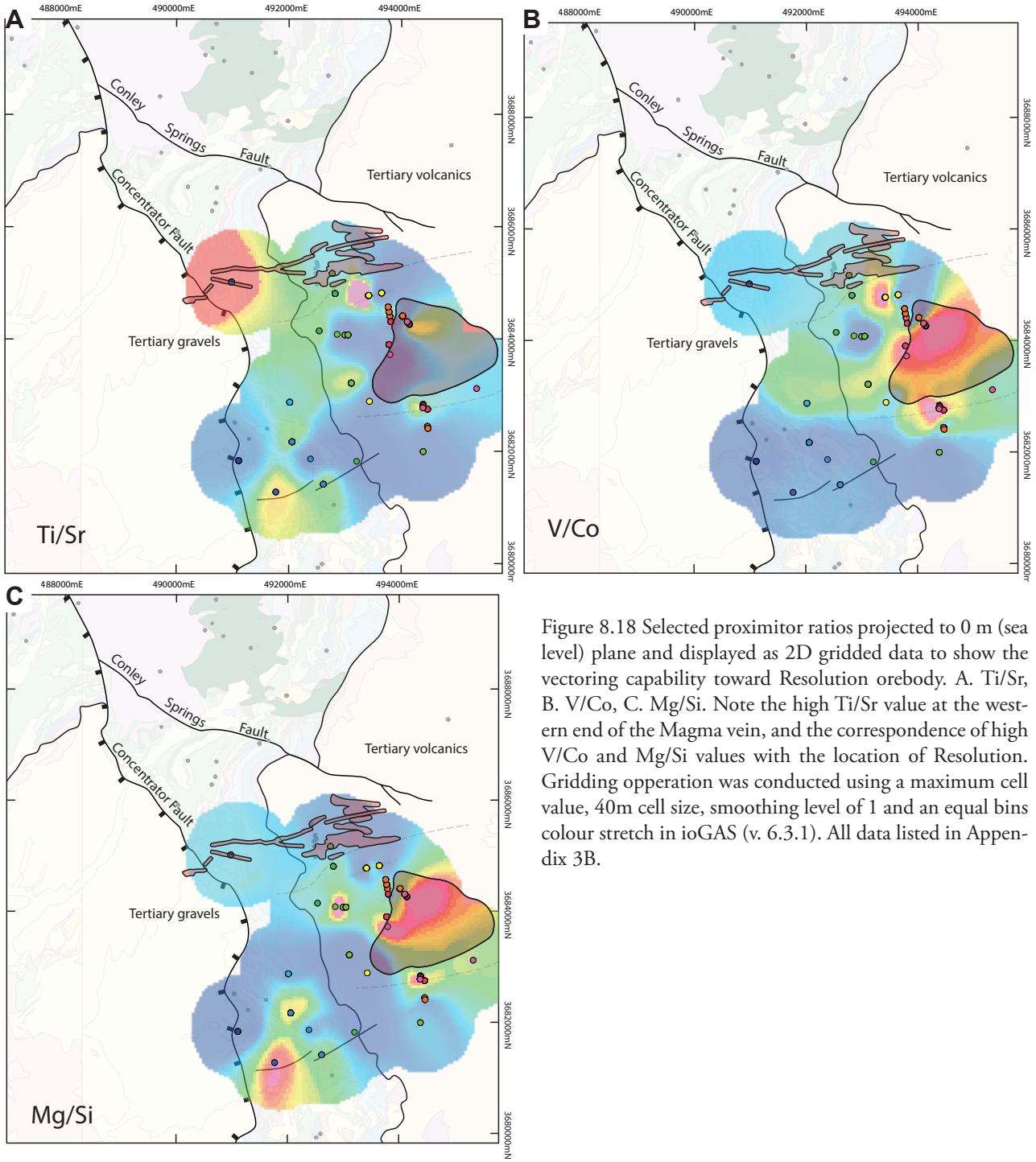


Figure 8.18 Selected proximitor ratios projected to 0 m (sea level) plane and displayed as 2D gridded data to show the vectoring capability toward Resolution orebody. A. Ti/Sr, B. V/Co, C. Mg/Si. Note the high Ti/Sr value at the western end of the Magma vein, and the correspondence of high V/Co and Mg/Si values with the location of Resolution. Gridding opperation was conducted using a maximum cell value, 40m cell size, smoothing level of 1 and an equal bins colour stretch in ioGAS (v. 6.3.1). All data listed in Appendix 3B.

to the deposit, Mg shows the greatest magnitude of compositional change and is therefore used as the main numerator in this instance. Selected proximitor ratios developed by Wilkinson et al. (2015) are also shown for comparison (Table 8.6, Figure 8.16). Conventional ratios such as Ti/Sr and V/Co show broadly consistent spatial relationships, but are interrupted by one or two anomalously high results (Figure 8.16). Ratios such as Mg/Fe, Mg/Si, Mg/Sr and Mg/Zr all show well developed trends with distance, but are limited to distances of 2 km or less (Table 8.6, Figure 8.17). Ratios of Mg/B and Mg/Cu show consistent trends with distance out to around 2 km but there is significant variability within samples (Table 8.6, Figure 8.17). $R^2$ values tend to be poor when all the data are plotted, but improve

somewhat when sample averages (median) values are plotted (Table 8.6, Figure 8.17). Although V/Co has lower $R^2$ values when plotted with respect to distance, it maps the general position of the Resolution ore shell much better than the Mg-based ratios when plotted spatially (Figure 8.18), which along with Ti/Sr also provide significant false positive anomalies in the range front (Figure 8.18).

## 8.5 Discussion

The application of mineral chemistry analyses around Resolution was intended to chemically distinguish multiple generations of epidote-bearing alteration including Proterozoic 'background' compositions, and to determine whether the limits of the mineral chemistry footprint could be defined. The principal factors affecting the outcome of this approach include differences in fluid composition responsible for the different generations of epidote and chlorite distal alteration (or lack thereof), spatial distinction of samples with respect mineralisation and protolith compositions, and the degree of chemical and spatial overlap between Proterozoic and Laramide hydrothermal systems within the district.

### 8.5.1 Possible protolith effects on epidote and chlorite compositions

Due to the restricted spatial distribution of igneous rocks within the Superior district, there is some possibility that a degree of host-rock bias was built in to the training data used in the multivariate analysis. Unfortunately, this is an unavoidable aspect of the local geology, since propylitic alteration from each hydrothermal system was largely contained within one major host rock (e.g., Resolution – Kvs, Magma – dolerite sills, Silver King – quartz diorite stock). There is some evidence that protolith compositions may have affected the dolerite-hosted Magma epithermal training data, as the Magma-related epidote and chlorite are characterised by elevated Ni, Cr, V and Co (Table 8.2, Figure 8.4) and Ni, Cr, Co (Table 8.3, Figure 8.5), respectively. However, similar compositions of epithermal epidote and chlorite were also identified in the Apache Basalt, Pinal Schist and dolerite (Figure 8.8), suggesting the host rock was of little consequence in these final chlorite classifications. The classification of epithermal chlorite shows more correlation with the spatial locations of major structures and epithermal vein arrays than it does with a single rock type (Figure 8.7 and Figure 8.8), supporting the hypothesis that host rock did not significantly influence the classification.

### 8.5.2 Chemical overlap between hydrothermal systems

The mapped distributions of Laramide epidote and chlorite in the Superior district suggest that there may be considerable spatial overlap of hydrothermal alteration domains of different ages across the district, (Figures 8.6 and 8.7). The recognition of overlapping alteration systems in exploration is important. If unrecognised, they can serve to confuse a footprint and vectoring studies. There is also the possibility of structural disruption of the western part of the district by the Concentrator Fault (Figure 3.2). The combination of overlapping alteration domains and structural dismemberment may have obscured the

full extent of the geochemical footprint of each Laramide hydrothermal system. There are, however, clear chemical distinctions between the Laramide and Proterozoic alteration assemblages (e.g., high and low Pb and Sr in epidote; high and low Zn and Mn in chlorite; Figure 8.4 and Figure 8.5).

Chemical overlap between the Laramide hydrothermal systems made multivariate classification of Laramide propylitic alteration complicated in the Superior district. In particular, there appears to have been some misclassification of Silver King and Resolution affinities for epidote and chlorite, probably based on proximity to Laramide hydrothermal centres (Figure 8.6, Figure 8.7, Figure 8.8). For epidote, exclusion of the early, high temperature pЄ1-type epidote compositions from the Proterozoic training data and possible compositional overlaps of pЄ1-type epidote with Silver King-type epidote could have contributed to some misclassification. The apparent chemical overlap between Silver King and Resolution could also be a complicated combination of distance from heat source and the relative sizes of the thermal aureoles. Silver King is centred on a relatively small, less productive intrusive complex and could have a more spatially restricted trace element substitution pattern in epidote, making some distal elements in epidote appear more proximal than at Resolution, where the mineralisation (and propylitic alteration) is some distance from its much larger causative heat source. This is supported by the higher Ti concentration in chlorite at Silver King, which is typical of high temperature chlorite (DP2, Figure 8.5, Table 8.3; Walshe, 1986; Wilkinson et al., 2015).

### 8.5.3 Spatial variability and mixed distal compositions

Changes in trace element concentrations in epidote with distance from Resolution are not particularly well developed (Figure 8.13). Instead, distinct changes in epidote trace element chemistry occur at certain distances, caused by the overprinting of Proterozoic epidote by the Resolution hydrothermal fluid (Figure 8.13). Elements such as Zn and Sb are distinctly enriched only out to a distance of about 2.6 km, whereas Pb in epidote is elevated out to nearly 4 km, overprinting the signature of the Proterozoic epidote, which is Pb-depleted (Figure 8.14). The variability in overprinting distance results in the most distal epidote grains related to Resolution being composite in nature and having chemical characteristics due both to Proterozoic and Laramide alteration (Figure 8.10). This created complexity in multivariate classification of epidote (e.g., Figure 8.6), but also suggests different outer limits of mobility of individual elements. The same is true for chlorite (Figure 8.16). Spatial trends are somewhat better developed in chlorite probably because many of the substitutions, especially major elements, are temperature -dependant (Walshe, 1986). Some elements show a halo < 2 km, with low magnitude variation and low concentrations nearer the centre (e.g., Co, Li; Figure 8.16), while some elements show variability up to 4.2 km (e.g., Cu; Figure 8.16).

Plotting elements that are inversely correlated with distance from a known hydrothermal centre can allow for the construction of proximitor equations (Wilkinson et al., 2015). In the Superior district, the most suitable numerators are the major elements Mg and Al, which can be combined with other

major elements (e.g., Fe, Si) or a suite of trace elements (e.g., Sr, B, Cu, Zr). In contrast, Wilkinson et al. (2015) and Cooke et al. (2015) both found Ti/Sr and V/Co (among others) to be the most effective at delineating the thermal aureole around Batu Hijau and Resolution, respectively. A key difference between studies at Batu Hijau and Resolution is the strong structural control on fluid flow and sampling geometry and Resolution. The lack of significant structural disruption at Batu Hijau implies a relatively homogenous thermal aureole and mineral chemistry footprint, compared with the strong NE-striking fault control at Resolution, especially outside the graben (e.g., epithermal veins; Figure 3.2). In the current study, stepping out from previous sampling within the Resolution graben to the outer limits of the propylitic halo was restricted to drill hole sampling between the graben-bounding faults and alteration in surface exposures. This lack of a continuous sampling transect results in somewhat clustered sample points, in terms of distance from the centre of Resolution (Figures 8.6 and 8.7), which then combined with fluid flow localised by the NE-striking faults affected the size and style of the mineral chemistry footprint. Aside from the permeability architecture, other possible reasons for the variable spatial distribution of trace element mineral chemistry data in the Superior district include the distance from causative heat source and/or orientation of sample transects relative to thermal gradient, although the relative contributions of these aspects are impossible to quantify.

The $R^2$ values for Resolution proximitor ratios plotted with distance are poor (Table 8.6). Gridded ratio data provide an alternate method of visualisation (Figure 8.18). Some chlorite proximitor ratios (Figure 8.16 and Figure 8.17) show a zone of anomalously high values around 1600 m, the approximate location of the North Boundary Fault, suggesting this was a disruption to the chemical and thermal gradient Resolution gradient, providing evidence that structural architecture was a major factor controlling heat distribution, and therefore trace element substitutions in chlorite around Resolution.

Broadly, the trace elements that do show systematic variability with distance are similar to those identified by Cooke et al. (2014), Wilkinson et al. (2015) and Wilkinson et al. (2017), (e.g., La, Pb, Zn, Mn and Cu in epidote; Al, Fe, Mg, Si, Ti, V and Cr in high temperature chlorite and Zn, Mn, Sr, Co and Cu in low temperature chlorite), suggesting these elements behave consistently throughout many diverse porphyry districts worldwide. The effective distance of these gradients, especially in chlorite (~ 2 km) is consistent with Wilkinson et al. (2015), but means that chlorite vectoring results from this study do not improve on those reported by Cooke et al. (2015).

### 8.5.4 Geochemical footprint of Resolution

Overall, the mineral chemistry analyses have defined a geochemical footprint of at least 4 km (epidote) and 4.2 km (chlorite) from the centre of the Resolution ore body (Figure 8.7 and Figure 8.8). This is significant both for exploration implications and from a mineral chemistry case-study viewpoint. Previous mineral chemistry studies around porphyry deposits have not positively identified geochemical background (e.g., Wilkinson et al., 2015; Baker et al., 2015; Pacey, 2016) and therefore it could be argued

simply mapping the occurrence of propylitic alteration minerals is sufficient to identify the footprint of a mineralised system. However, overlap of district alteration in the Superior district highlights the problems with this approach. Fortunately, Resolution epidote and chlorite have demonstrably different chemistry from Proterozoic epidote and chlorite and mineral chemistry analyses have allowed the definition of the western extent of the Resolution footprint. Although the western-most extent of this footprint was truncated by the Concentrator Fault (Figure 8.8), the narrowing and restricted nature of the footprint in the range front suggests it probably does not extent much farther across the fault. The footprint is localised along the eastern projection of the South Boundary fault (Belmont), suggesting that this was a major fluid escape structure during Laramide mineralisation (Figure 8.8). Although the overall footprint of the Resolution hydrothermal system as defined by the multivariate classification generally extends to around 4 km (Figure 8.7; Figure 8.8), most of the elements that show systematic change with distance do so only up to around 2 km (Figure 8.13, Figure 8.14, Figure 8.15).

### 8.5.5 Exploration targets

Between Magma and the Conley Springs Fault, a large number of mineral chemistry analyses have been classified as Resolution-affiliated (Figure 8.8 Figure 8.7). These samples are located over five kilometres from Resolution. Given the mineral chemistry footprint of Resolution in the southern range front is around 4 km (Figure 8.7, Figure 8.8), this is likely to be another porphyry-related propylitic alteration zone bounded to the north by two samples that where classified wholly as Proterozoic, indicating distinction from the Silver King system. It therefore appears that this anomalous area may relate to an fourth, as yet unknown Laramide hydrothermal system, possibly related to the Magma vein.

Several samples in the far NW part of the study area, on the west side of the Concentrator Fault, were also classified as Laramide, based on multivariate analysis. This area may be part of another discrete Laramide propylitic alteration cell, or perhaps more likely, may be a dislocated part of the aforementioned zone between Magma and Conley Springs, disrupted by late dextral strike-slip movement along the Concentrator Fault (Section 3.4.2.8). Precise restoration of this phase of movement along the Concentrator Fault is problematic due to the lack of well constrained piece points exposed in the hangingwall and unknown degree of block rotation. Despite this, approximate reconstruction using the contact between the dolerite sill and base of the Mescal Limestone would create a single contiguous alteration domain, centred around the western projection of the Magma vein (Figure 8.19). There also remains the possibility that the anomalism around Magma may be related to distal alteration from other hydrothermal systems (Figure 8.19).

## 8.6 Conclusions

- Geochronology and spatial relationships allowed the definition of five epidote and four chlorite types from the Superior district (Figure 8.1). These are Proterozoic hydrothermal,

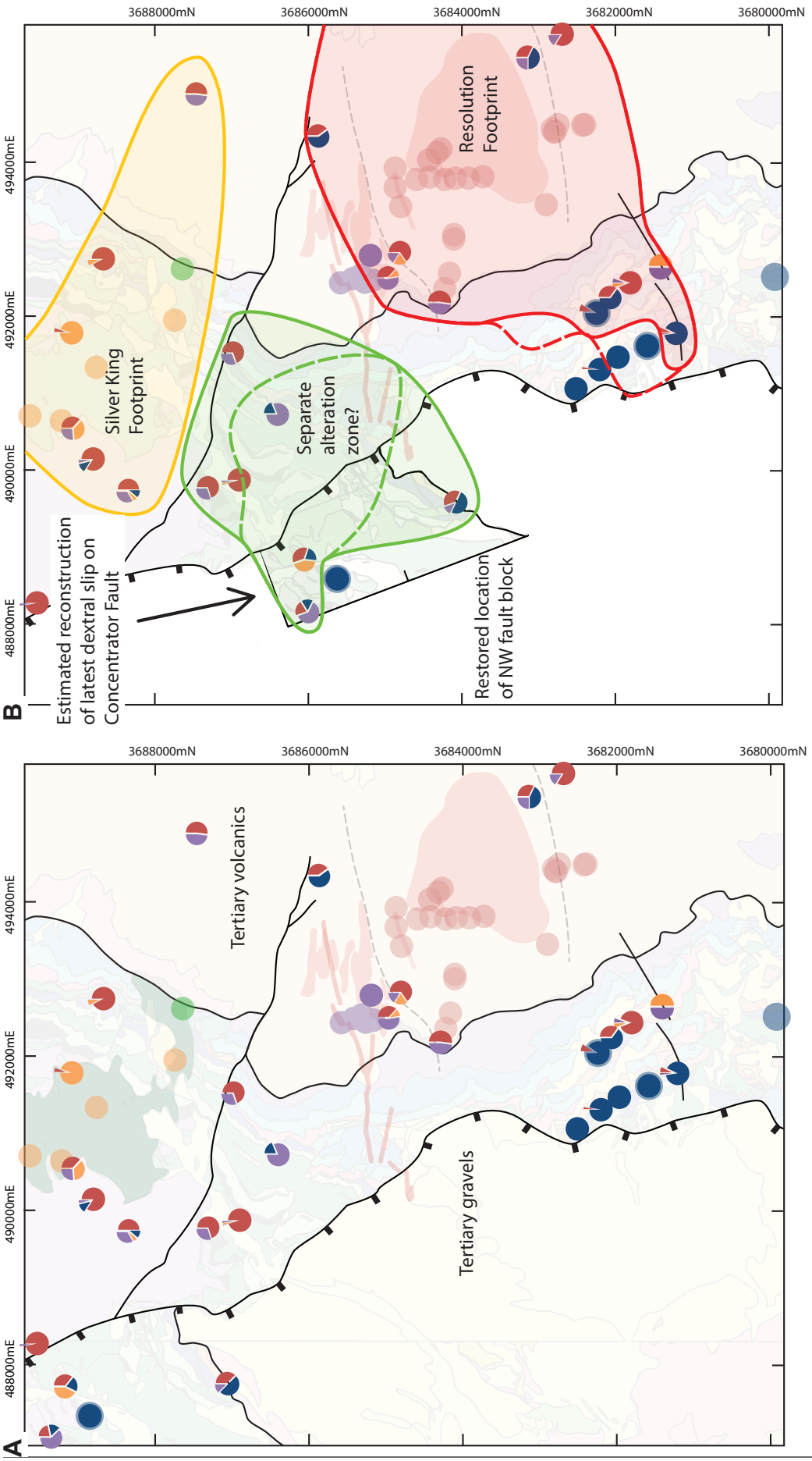


Figure 8.19 Geochemical footprints in epidote of hydrothermal systems of the Superior district in (A) Current structural configuration, and (B) Restored configuration. showing a possible scenario for the reconstruction of strike-slip movement along the Concentrator Fault and a contiguous new alteration domain at the western end of the Magma vein. Dashed lines show the chlorite footprint where it differs from epidote. All data listed in Table 8.4 and Table 8.5. Legend as per Figure 8.7 and Figure 8.8.

early Laramide unmineralised skarn (Silver King skarn; epidote only), early Laramide small porphyry (Silver King propylitic), Laramide epithermal (Magma) and Laramide giant porphyry (Resolution)

- Discriminant projection analysis identified distinct element associations between the Laramide and Proterozoic epidote and chlorite types. Generally, Laramide epidote is significantly enriched in Pb Sr, Sb, Zn and Mn (Table 8.2, Figure 8.4). Proterozoic epidote is enriched in U, B and HREE (Table 8.2, Figure 8.4). Proterozoic chlorite is significantly depleted in Zn and Mn relative to Laramide chlorite (Table 8.3, Figure 8.5). Chemical distinction between the different generations of Laramide epidote and chlorite is less clear than that between Laramide and Proterozoic alteration minerals (Table 8.2, Table 8.3, Figure 8.5 Figure 8.4)

- Silver King skarn epidote is characterised by elevated U, LREE and Sn, compared to Silver King propylitic epidote which is characterised by elevated Sr concentrations (Table 8.2, Figure 8.4). Silver King propylitic chlorite has higher concentrations of Al, Ti and V than other types of Laramide chlorite (Table 8.3, Figure 8.5)

- Magma epidotes have high Ni, Cr and V compared to other Laramide epidote types (Table 8.2, Figure 8.4), while chlorite from Magma also contains higher Ni Cr and Co (Table 8.3, Figure 8.5)

- Some samples were classified as containing multiple generations of epidote and chlorite. Evidence for this was validated by laser mapping of epidote which revealed overprinting of B-, Bi-, U- and Y-rich epidote (interpreted to be of Proterozoic origin) by Pb- and Sr-rich epidote (interpreted to be of Laramide origin; Figure 8.10). Laser mapping of epidote also identified an early, Ti-rich and trace element poor period of Proterozoic epidote growth (p€1; Figure 8.10) and a late rim of LREE epidote (p€2b; Figure 8.10)

- Based on mineral chemistry, the Resolution geochemical footprint extends to between 4 km (epidote) and 4.2 km (chlorite) in a southwesterly direction from the centre of the deposit (Figures 8.6 and 8.7)

- The vectoring capacity of chlorite breaks down at around 2 km from the centre of Resolution, within the graben, (Figure 8.16). The most effective proximitor ratio is Mg/Si with a sample average $R^2$ value of 0.72 (Table 8.6, Figure 8.17)

- Consistent mineral chemistry anomalism is present between Magma and the Conley Spring

Fault and in the far NW of the district and may be part of an as yet unknown hydrothermal system, dislocated by dextral strike slip along the Concentrator fault, highlighting further exploration potential in the district

- The Ti-enriched (p€1), U-, B-, HREE-enriched epidote (p€2) and Zn- and Mn-depleted chlorite characteristic of the 1,183 ± 23 Ma Proterozoic altered basalt (Figure 6.10 E) define new mineral chemistry background compositions for future exploration of the region.

# Chapter 9: Isotope Geochemistry

## 9.1 Introduction

This chapter presents new stable (C, O and S) and radiogenic (Pb) isotope data from hydrothermal minerals from the Superior district (Figure 9.1). The datasets are used to assess the usefulness of each technique in vectoring toward mineralised centres. They also have implications for possible genetic relationships and permit broad inferences to be made about likely hydrothermal fluid sources.

## 9.2 Carbon and oxygen isotopes

### 9.2.1 Introduction

Carbonate minerals, particularly calcite, are common on the peripheries of porphyry deposits hosted in volcanic and calcareous sedimentary terranes, occurring both as part of the hydrothermal alteration assemblage and in epithermal veins. Carbon and oxygen isotopic data from carbonate minerals can be used to evaluate the fluid sources and evolution (e.g., Pass et al., 2014) or to map areas of hydrothermal fluid flow and vector towards mineralisation in magmatic-hydrothermal systems (Djouka-Fonkwe et al., 2012). Carbon-oxygen isotopes have demonstrated their utility in studies of numerous types of hydrothermal ore deposits, including VHMS (e.g., Green et al., 1983) and Carlin-type systems (Vaughan et al., 2016). Systematic variations in the isotopic ratios of carbon and oxygen can reflect temperature gradients, degrees of fluid-rock interaction and/or fluid mixing (Hoefs, 2015). In this study, C-O isotopes are used primarily to test their vectoring potential regarding isotopic variations associated with the epithermal veins of the range front, and to establish likely fluid source(s). Basalt-hosted Proterozoic amygdaloidal calcite was also analysed in order to assess isotopic differences between calcite related to Proterozoic hydrothermal activity and distal Laramide-related epithermal signals.

Whole-rock geochemical analyses were also acquired from each sample analysed isotopically to act as a comparator dataset. This facilitates considerations as to whether bulk trace element geochemical analyses are sufficient in determining geochemical gradients and the location of fluid source(s).

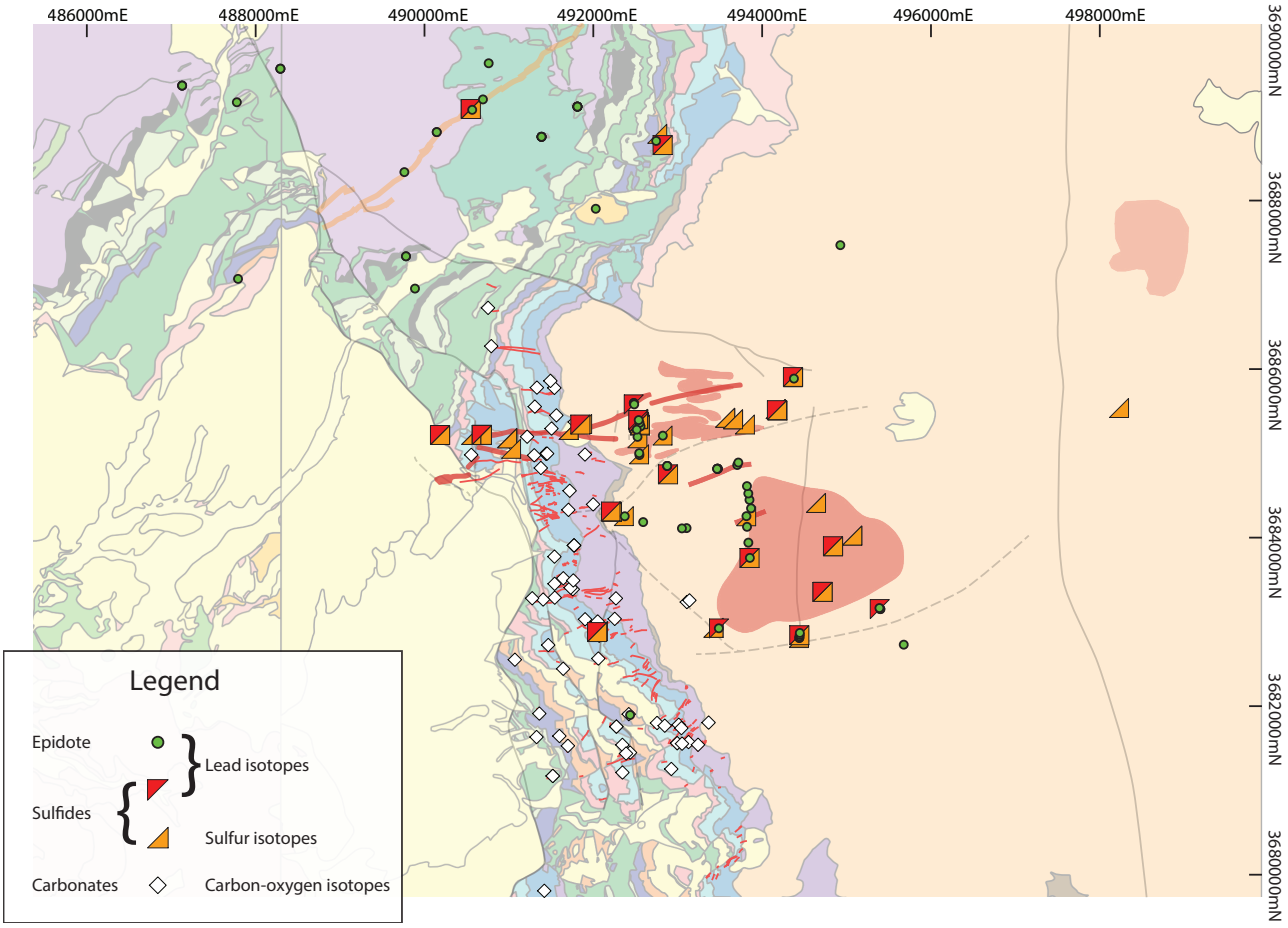


Figure 9.1 Map showing the types and locations of samples taken from the Superior district that were subjected to isotopic analysis during the current study.

### 9.2.2 Previous work

A detailed C-O isotopic study was conducted in the Superior district by Friehauf and Pareja (1998) to test for district scale isotopic halos developed in the Paleozoic limestone around the C-bed manto ore body of the Magma mine. Their study concluded that there was a significant difference in $\delta^{18}O$ values for the hydrothermal carbonates compared to the host-rock carbonate (10 to 18‰ and 20 to 28‰, respectively). In contrast, the $\delta^{13}C$ compositions were indistinguishable (Figure 9.2, Table 9.1). They also noted that alteration-related isotopic halos extend only ~1 m or less from the main contact between the orebody and host limestones, and that samples of host-rock within millimetres of sulfide-carbonate veinlets are isotopically indistinguishable from background sedimentary carbonate. The $\delta^{13}C$ composition of the unaltered carbonate host rocks varied systematically up stratigraphy and masked any larger scale gradient caused by discrete hydrothermal overgrowths (Figure 9.2). Friehauf and Pareja (1998) also established that weathered samples were isotopically indistinguishable from fresh samples, providing encouragement for surface sampling conducted during the current study.

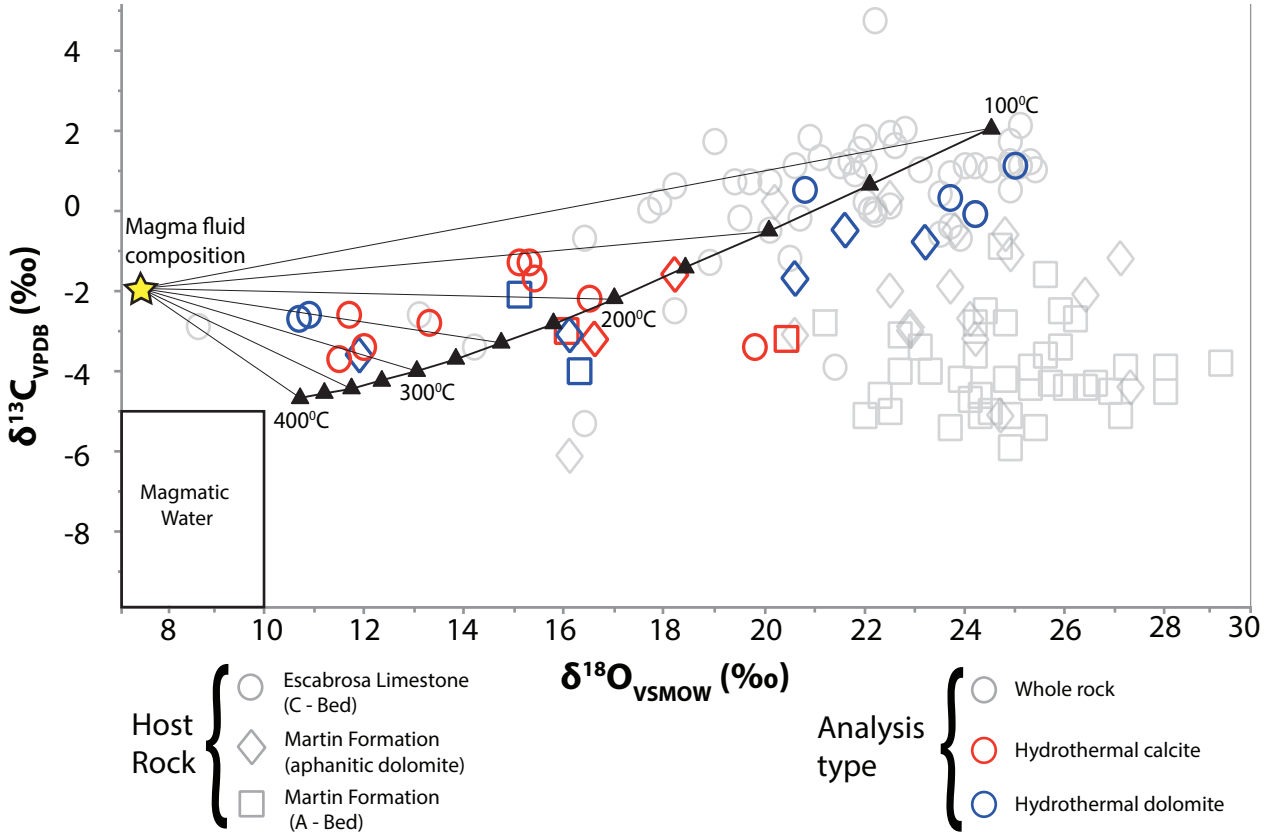


Figure 9.2 Data from Friehauf and Pareja (1998) showing background isotopic values for some of the Paleozoic carbonate rocks in the Superior district and hydrothermal carbonates. $H_2CO_3$ cooling curve modeled using calculations of O'Neil et al., (1969) using an inital fluid composition of 7.5 ‰ $\delta^{18}O$ and -2 ‰ $\delta^{13}C$.

### 9.2.3 Methods

#### 9.2.3.1 Sample selection

Sampling for the current study focussed on manganiferous epithermal veins exposed along the range front (Figure 9.3). The Magma, Cross Canyon and Belmont areas were preferentially targeted, as their vein systems are best exposed. Infill samples between the main vein systems were also collected in order to check for isotopic gradients between the major vein arrays. The sample suite was augmented by three drillhole samples that contained manganiferous epithermal veins, allowing the sample suite to be extended eastwards under cover towards Resolution (Figure 9.3).

Amygdaloidal basalt samples were chosen based on the detection of Proterozoic epidote in the sample, either by U-Pb dating (Chapter 6) or multivariate trace element classification. Samples of the host stratigraphy were also collected for analysis, allowing comparison with the extensive sample suite of Friehauf and Pareja (1998).

Four distinct paragenetic stages of carbonate were identified, within the Laramide carbonate veins. Main-stage calcite is finely intergrown with black manganese oxides (dominantly cryptomelane), identified in the field with HCl. One sample of main stage calcite occurred as bladed calcite (Figure 4.17 A). Main-

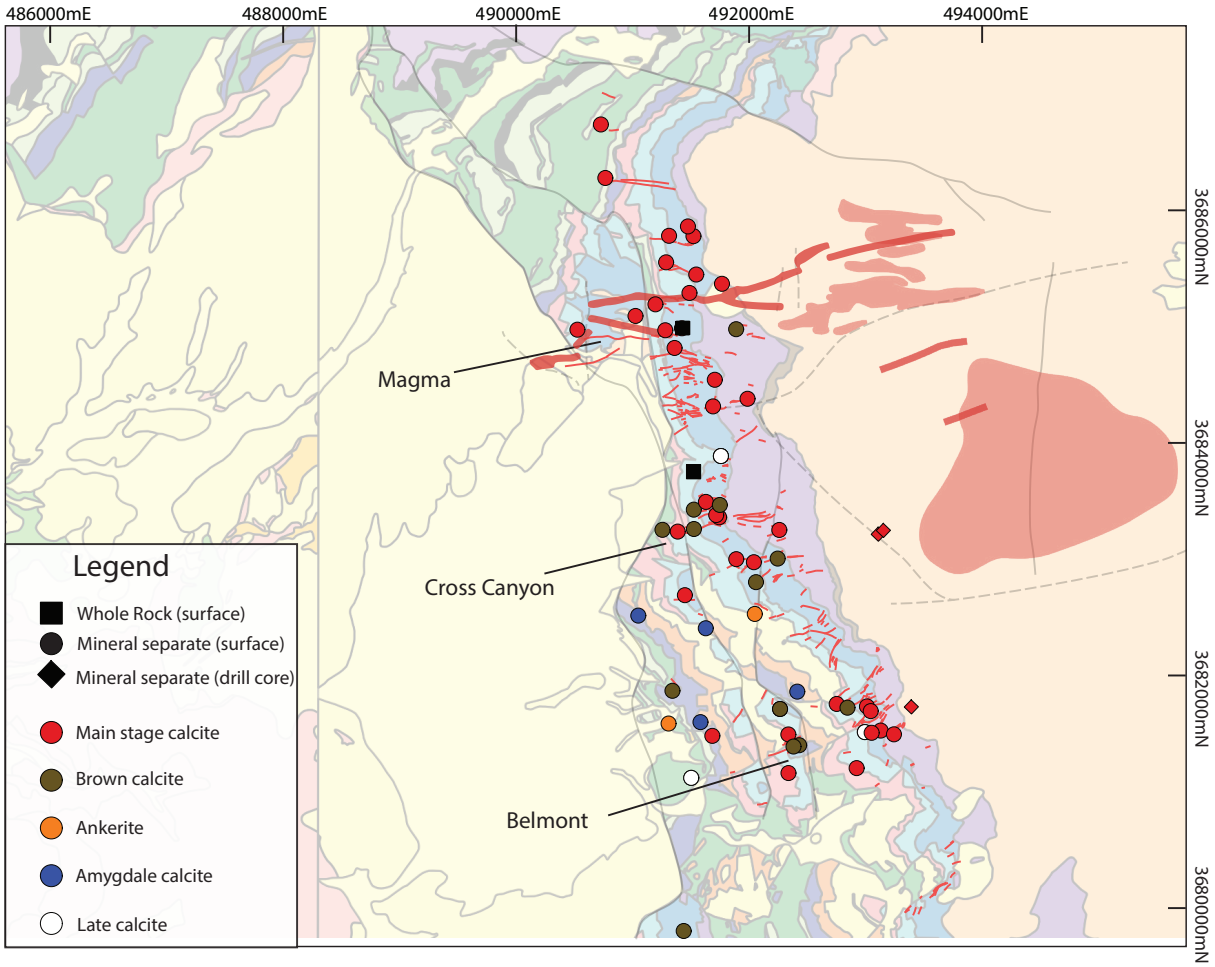


Figure 9.3 Map showing the dominant mineralogy and locations of C-O isotope samples from the Superior district collected during the current study. Geology and mineralisation as per Figure 3.2

stage calcite is cross-cut in many samples by a phase of distinctive brown calcite that varies texturally from ~1 cm thick bedding-parallel bands, to clots or massive vein infill infills, or rims around clasts in vein breccias. Main-stage and brown calcite are cut by a stage of white calcite that occurs as vein infills, breccia cement or stringers. This sequence was observed in many hand specimens (Figure 4.16 B, D). Some samples contained ankerite as the dominant vein fill. Ankerite veins were always cross cut by white calcite veins, suggesting it may be equivalent in timing with the brown calcite observed in other samples.

#### 9.2.3.2 Whole-rock analyses

Samples selected for isotopic analyses were also submitted for whole-rock major and trace element analyses. This was conducted as per methods outlined in Chapter 5.

#### 9.2.3.3 Isotopic analyses

Carbon and oxygen isotope compositions were determined for 70 paragenetically constrained minerals from 64 samples from the Superior district (Appendix 4A; Table 9.1). The sample suite included 50 main stage calcite, 14 brown calcite and three ankerite samples. Host rock samples include one dolomite

and two calcite matrix samples taken from each of the main carbonate units in the Superior district. Approximately 10 mg of powder was prepared by hand drilling directly from in-situ coarse grain carbonate minerals using a Dremel Multipro 225 T2 flex-shaft drill. The drill bit was thoroughly cleaned using a quartz blank between samples. Powders were transferred on clean weighing paper into a vial and weighed to check that the minimum sample size requirement had been met. Samples were analysed by Dr Christian Dietz at the Central Science Laboratory, University of Tasmania, Australia, for isotopic analysis. Analyses were performed on sub-samples weighing between 0.05 to 0.51 mg. The subsamples were digested with 200 microlitres of 103% $H_3PO_4$ at 70 °C on Isoprime MultiFlow with a reaction time of 18 hours. The generated $CO_2$ was extracted, cleaned on a gas chromatography column and analysed for $^{13}C/^{12}C$ and $^{18}O/^{16}O$ ratios on an Isoprime 100 continuous-flow mass spectrometer. Values were normalised to the Vienna Pee Dee Belemnite (VPDB) and Vienna Mean Standard Ocean Water (VSMOW) scale, respectively. Normalisation and drift correction was based on the measurement of international reference standards NBS18 and NBS19, and two in-house reference standards (ANU M1 and ANU PRM2). Precision of the measurements, determined by repetitive analysis (n = 7) of Takaka marble2 were 0.05‰ and 0.10‰ for $\delta^{13}C$ and $\delta^{18}O$, respectively.

### 9.2.4 Results

The $\delta^{13}C$ and $\delta^{18}O$ values from epithermal veins of the Superior district range from -9.5 to 2.4 ‰ and 10.5 to 23.7 ‰ respectively (Table 9.1). Proterozoic amygdale-hosted calcite has low $\delta^{18}O$ and high $\delta^{13}C$ values, averaging 13.9 and 0.1 ‰ respectively (Table 9.1). The range in $\delta^{18}O$ values of hydrothermal carbonate are 10.5 to 23 ‰ for main stage calcite, 12.5 to 22.0 ‰ for brown calcite, and 16 to 19 ‰ for late stage calcite (Table 9.1). The large spread of data define a weakly negative correlation (Figure 9.4) that cannot be explained by a simple cooling curve (e.g., Pass et al., 2014) as can be done with data from Friehauf and Pareja (1998; Figure 9.2). For samples with early and late carbonate were analysed, $\delta^{18}O$ are generally lower in later phases, whereas $\delta^{13}C$ are generally higher (Figure 9.4). Bladed calcite has low $\delta^{13}C$ values compared to the rest of the data although the $\delta^{18}O$ values are comparable (Figure 9.4). Isotopic compositions of limestones and dolomites analysed during this study are consistent with the results of Friehauf and Pareja (1998; Table 9.1; Figure 9.4), although there are insufficient whole-rock analyses from this study to fully corroborate the Palaeozoic stratigraphic variation in isotope concentrations. Most of the hydrothermal carbonates have considerably lower $\delta^{18}O$ values than the carbonate wallrocks, consistent with the findings of Friehauf and Pareja (1998). The vein carbonates from this study have a larger spread in $\delta^{13}C$ values, but a generally tighter $\delta^{18}O$ range compared to previous results (Figure 9.2; Figure 9.4).

Friehauf and Pareja (1998) demonstrated a systematic change in both $\delta^{13}C$ and $\delta^{18}O$ isotopic compositions of limestones and dolomites up stratigraphy. Although not highlighted explicitly by Friehauf and Pareja (1998), hydrothermal dolomite $\delta^{13}C$ values mimic the stratigraphic increase in $\delta^{13}C$

Table 9.1 Summary of carbon and oxygen isotopic analysis of carbonates from the Superior district. All data listed in Appendix 4A.

| Dataset | Material | Rock type | Mineral | | $\delta^{13}C_{VPDB}$ (‰) | | | | $\delta^{18}O_{VSMOW}$ (‰) | | | |
|---|---|---|---|---|---|---|---|---|---|---|---|---|
| | | | | *n* | Min | Max | Avg. | Std Dev. | Min | Max | Avg. | Std Dev. |
| Freihauf and Pareja, 1998 | Whole rock | C bed hangingwall | Calcite | 9 | -5.3 | 4.7 | 0.0 | 2.8 | 14.2 | 24.5 | 20.4 | 3.5 |
| | | C bed | Dolomite | 46 | -3.9 | 2.1 | 0.4 | 1.3 | 8.7 | 25.4 | 21.5 | 3.2 |
| | | Aphanitic dolomite | Dolomite | 12 | -6.1 | 0.3 | -2.3 | 1.7 | 16.1 | 27.3 | 23.5 | 2.6 |
| | | A bed | Dolomite | 39 | -5.9 | -0.9 | -4.0 | 1.1 | 21.2 | 29.1 | 24.9 | 1.7 |
| | Veins | C bed hangingwall | Calcite | 5 | -3.4 | -1.3 | -2.2 | 0.8 | 13.3 | 19.8 | 16.0 | 2.2 |
| | | C bed | Calcite | 4 | -3.7 | -1.7 | -2.9 | 0.8 | 11.5 | 15.4 | 12.7 | 1.6 |
| | | | Dolomite | 6 | -2.7 | 1.1 | -0.6 | 1.5 | 10.7 | 25.0 | 19.2 | 6.1 |
| | | Aphanitic dolomite | Calcite | 2 | -3.6 | 1.6 | -1.0 | 0.8 | 16.6 | 18.2 | 17.4 | 0.8 |
| | | | Dolomite | 5 | -3.6 | -0.5 | -1.9 | 1.2 | 11.9 | 23.2 | 18.7 | 4.1 |
| | | A bed | Dolomite | 2 | -4.0 | -2.1 | -3.1 | 1.0 | 15.1 | 16.3 | 15.7 | 0.6 |
| This study | Whole rock | All | Calcite and dolomite | 3 | -1.8 | 1.3 | 0.0 | 1.3 | 16.3 | 24.6 | 19.2 | 3.8 |
| | Vein | Undifferentiated | Main stage calcite | 43 | -9.5 | 0.8 | -4.2 | 2.8 | 10.5 | 23.7 | 18.2 | 2.7 |
| | | | Brown calcite | 14 | -6.7 | 0.6 | -2.9 | 2.5 | 12.9 | 22.0 | 17.5 | 2.7 |
| | | | Ankerite | 3 | -3.3 | 0.8 | -1.7 | 1.7 | 15.3 | 20.4 | 18.6 | 2.3 |
| | | | Late calcite | 3 | -0.5 | 2.4 | 0.5 | 1.3 | 16.0 | 18.9 | 17.4 | 1.2 |
| | Proterozoic Amygdale | Apache Basalt | Calcite | 4 | -1.6 | 1.5 | 0.1 | 1.4 | 11.7 | 15.6 | 13.9 | 3.6 |

Abbreviations: Min = minimum; Max = maximum; Avg = average; Std Dev = Standard deviation

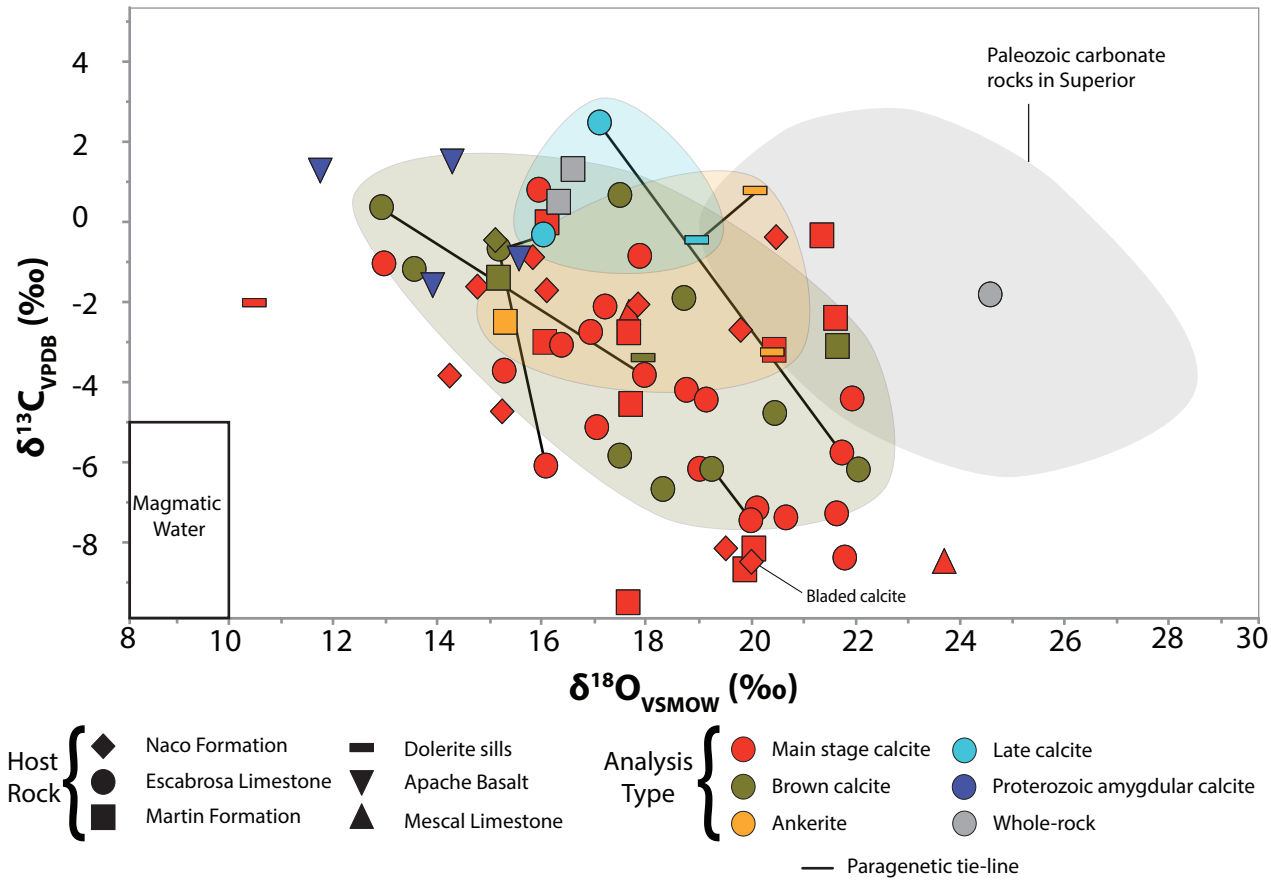


Figure 9.4 Results of $\delta^{18}O$ and $\delta^{13}C$ analysis, plotted with fields of Paleozoic carbonate rocks from the Superior district (Friehauf and Pareja, 1998) and magmatic water.

compositions (Table 9.1; Figure 9.2). In contrast, vein calcite seems less affected by host rock (Table 9.1; Figure 9.2). Hydrothermal calcite tends to have lower average $\delta^{18}O$ values than dolomite from the same host rock (Aphanitic dolomite and C bed; Table 9.1), suggesting that either these two phases were not in equilibrium, or that there was a difference in the isotopic fractionation behaviour between these two minerals. Garlick (1966) and Savin and Less (1988) showed that dolomite tends to preferentially concentrate $^{18}O$, and that hydrothermal dolomite is affected by the $\delta^{18}O$ and $\delta^{13}C$ compositions of its host rock.

### 9.2.4.1 Isotopic zonation

There are spatial variations in main stage calcite $\delta^{18}O_{calcite}$ and $\delta^{13}C_{calcite}$ values. The eastern end of the vein arrays are dominated by lower $\delta^{18}O_{calcite}$ values (Figure 9.5 A), with an inverse gradient defined by $\delta^{13}C$ values (Figure 9.5 B). Interestingly, the depleted $\delta^{18}O_{calcite}$ values are found in drillhole samples immediately west of the Resolution ore body. In both the $\delta^{13}C_{calcite}$ and $\delta^{18}O_{calcite}$ data sets, there appear to be sharp lateral isotopic gradients away from the central part of the vein arrays (Figure 9.5), indicating that isotopic anomalism may be tightly restricted to 10s of meters around the larger veins within any one array.

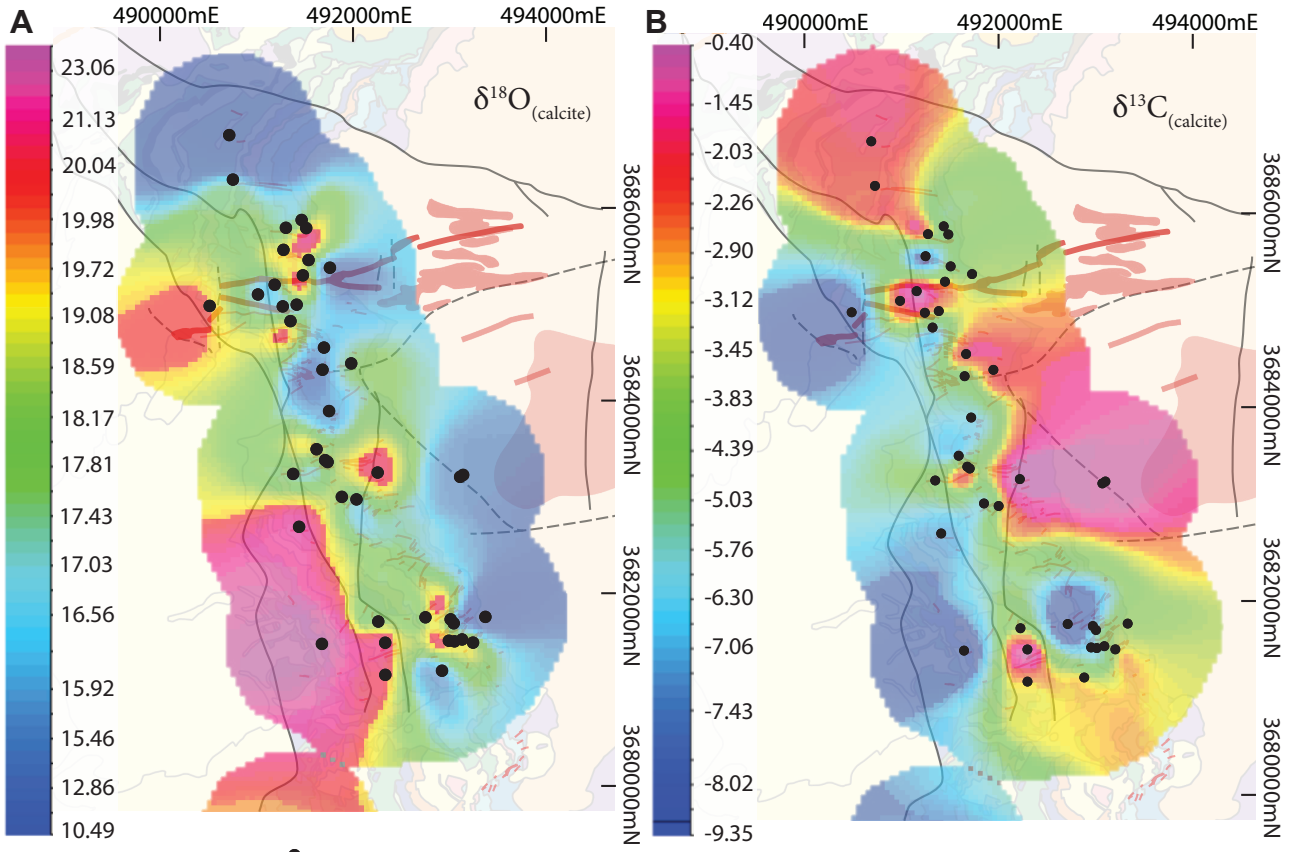


Figure 9.5 Map showing gridded (A) $\delta^{18}O$ (B) $\delta^{13}C$ isotopic data for main stage calcite from the Superior district. Geology and mineralisation as per Figure 3.2

### 9.2.4.2 Trace element zonation

Whole-rock trace element anomalism appears to be structurally controlled around the epithermal veins (Figure 9.6, Figure 9.7). Silver and gold concentrations in whole rock are both elevated around the western surface exposures of the Magma vein. Copper, Mo, Sn and Bi are variable, but do show positive anomalism close to Resolution, particularly in drill hole samples under Apache Leap (Figure 9.6). These anomalous concentrations transition into broad but subtle geochemical anomalies in the central east of the range front and at the eastern end of the major veins (Figure 9.6). Common to many pathfinder elements is the spatially restricted but strikingly high amplitude anomaly in the south of the range front (Figure 9.6). This anomaly is defined by different samples for different elements but defines a spatially coherent whole-rock anomaly in the proximal (Ag, Au, Cu, Mo, Sn and Bi; Figure 9.6) and distal (As, Sb, Pb, Zn and Mn; Figure 9.7). A segmented pattern of whole-rock geochemical anomalism along the range front is continued in the more distal pathfinder suite of elements (Figure 9.7). Most trace elements show a relatively coherent anomaly towards the western end of Magma in the north of the range front, at the eastern end of veins in the centre of the range front, and an isolated central hot spot in the south of the range front (Figure 9.7). Elevated Zn and Mn in the south of the range front does coalesce with anomalies in the vicinity of Belmont, suggesting they may be related (Figure 9.7).

There is some correspondence of trace element anomalism and $\delta^{18}O_{calcite}$ depletion. Elevated Au, Cu, Mo

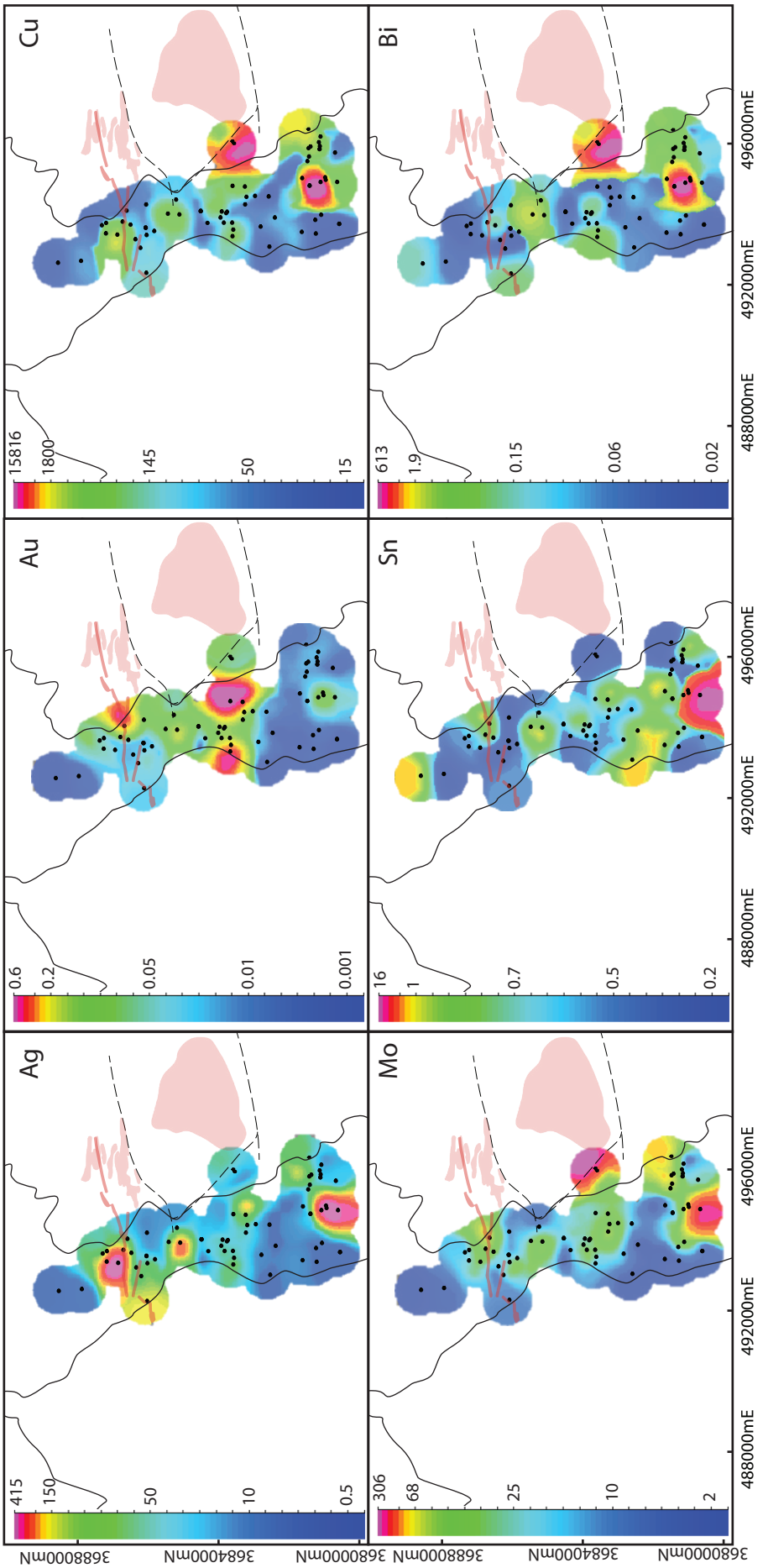


Figure 9.6 Map showing gridded whole-rock proximal trace element data for vein samples also submitted for isotopic analysis. Geology and mineralisation as per Figure 3.2. All data listed in Appendix 1C

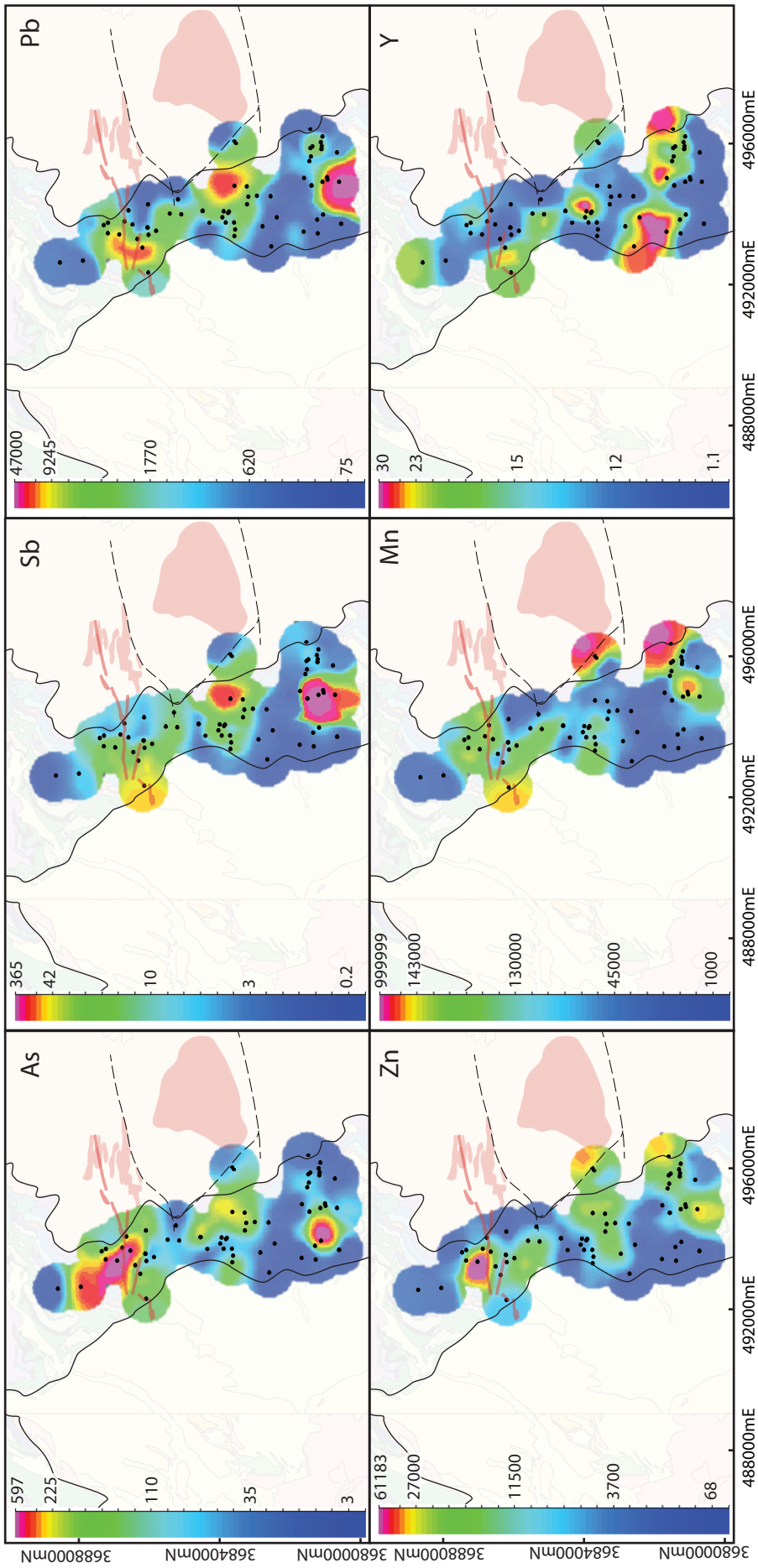


Figure 9.7 Map showing gridded whole-rock proximal trace element data for vein samples also submitted for isotopic analysis. Geology and mineralisation as per Figure 3.2 All data listed in Appendix 1C.

and Bi from drillhole samples broadly coincide with the domain of low $\delta^{18}O$ in the centre of the range front closest to Resolution (Figure 9.5 A, Figure 9.6). Arsenic, Sb, Pb Zn and Mn are also anomalous in this area of the central range front, but further to the west (Figure 9.7). There are also notable differences between the isotopic zonation patterns and whole-rock trace element data. Silver, copper and to some extent bismuth, all show slightly higher concentrations towards the western end of the Magma vein at the northern end of the range front. Lower $\delta^{18}O$ depletion in hydrothermal carbonate rocks was detected at the eastern end of the Magma vein. The strong whole-rock geochemical anomaly in the south of the range front does not correspond with a $\delta^{18}O_{calcite}$ depletion zone.

### 9.2.5 Discussion

#### 9.2.5.1 Carbon-oxygen isotopic compositions and trends

$\delta^{13}C_{calcite}$ from the Superior district shows a broad spread of values. This is interpreted to be the product of water-rock interaction with country rocks that contain a wide range of $\delta^{13}C$ values. The Dripping Springs Quartzite has been reported to contain Proterozoic kerogens (Desborough et al., 1984) which could impart very low $\delta^{13}C$ values (Hoefs 2015). In contrast, the Mescal Limestone contains evidence of evaporitic horizons, which would impart much higher $\delta^{13}C$ values. Interaction with dolerite sills would probably impart lower, igneous $\delta^{13}C$ values, if the dolerite was not leached of magmatic carbon during Proterozoic metasomatism. Unfortunately, insufficient samples of the Apache Group stratigraphy were collected during this study to fully interrogate this hypothesis. The range of $\delta^{18}O_{calcite}$ from epithermal veins of the Superior district is larger and the values are significantly higher than would be expected for a magmatic-hydrothermal fluid (Figure 9.8). The range $\delta^{18}O_{calcite}$ values is transitional between magmatic fluid and the field defined by Paleozoic rocks in the Superior district and is therefore interpreted as a combination of cooling of a magmatic-hydrothermal fluid and fluid-rock interaction.

Due to the spread in both $\delta^{13}C$ and $\delta^{18}O$ data from epithermal veins in the Superior district collected during the current study, it was not possible to model the initial isotopic fluid composition. As a result, little can be said regarding the likelihood or extent of fluid mixing in the formation of the early-stage carbonates analysed in the current study. Despite this, the decrease in $\delta^{18}O_{calcite}$ and increase in $\delta^{13}C$ with time (Figure 9.4) may hint at the possible influence of meteoric fluids in the formation of late-stage calcite. Alternative sources of this late-stage isotopic signature could be sea water or metamorphic fluids - both of which are considered unlikely here.

Bladed calcite is present in the epithermal veins around Belmont, in the Superior district. Bladed calcite forms in low sulfidation epithermal systems as a result of boiling (Simmons and Christenson, 1994; Simmons et al., 2005). Consequently, the presence of bladed calcite in the range front veins is indicative that these processes may have taken place. However, the lack of a major offset in isotopic values between samples with boiling textures and of those without suggests that either boiling was not a widespread

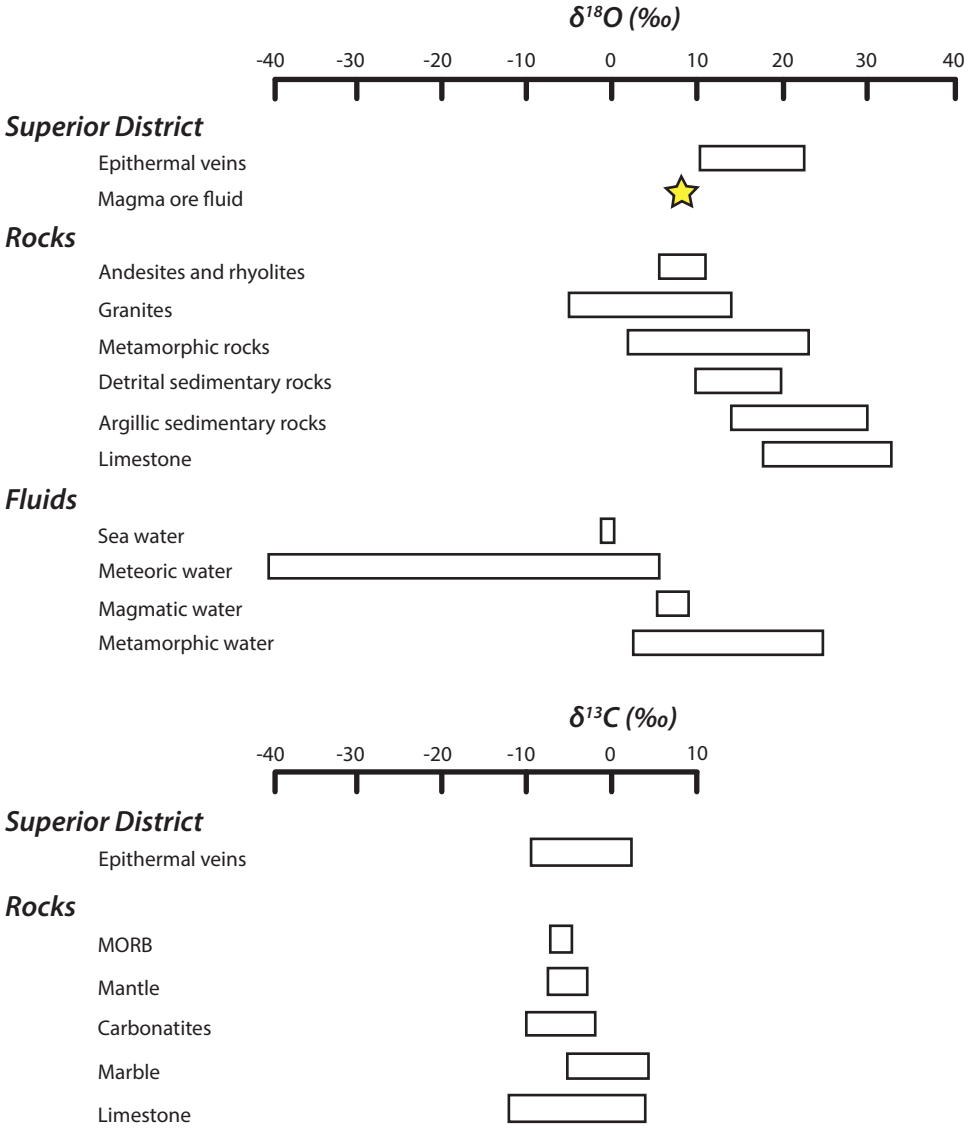


Figure 9.8 Major reservoirs of oxygen and carbon isotopes. Arrows denote direction of isotopic shift over successive paragenetic stages for the data from the Superior district. Reservoirs from Hoefs (2015).

phenomenon.

#### 9.2.5.2 Spatial relationships

A well-developed NE-SW along-strike gradient is apparent in both $\delta^{18}O_{calcite}$ and $\delta^{13}C_{calcite}$ isotopic data when plotted spatially (Figure 9.5). However, since the $\delta^{13}C_{calcite}$ values are likely to have been compromised by interaction with diverse country rocks, only $\delta^{18}O_{calcite}$ is of value in defining spatial relationships and fluid sources. The relatively low $\delta^{18}O_{calcite}$ values toward the eastern end of individual vein arrays compared to the west, imply that the fluids are depleted in $^{18}O$ and/or are hotter nearer Resolution fluids (Figure 9.5 A). The general spatial correspondence of low $\delta^{18}O_{calcite}$ values and major structures, especially the North Boundary fault and the Magma Vein, provide additional support for fluid flow from Resolution along these structures (Figure 9.5 A). The domain of relative $\delta^{18}O$ depletion

can be used to map the isotopic footprint of Resolution out to approximately 2.5 km from the centre of the deposit (Figure 9.5 A).

One calcite sample in the north of the district recorded a relatively low $\delta^{18}O_{calcite}$ value (Figure 9.5 A). It was collected in the general vicinity of a conventional whole-rock and mineral chemistry anomaly highlighted from Chapter 8 (Figure 8.19).

#### 9.2.5.3 Whole-rock trace element data

Relationships between the C-O isotopic data and vein whole-rock geochemistry data is complex. The coherent zonation patterns defined by the isotopic data (Figure 9.5 A) is not mimicked by the whole-rock trace element data from the same samples (Figure 9.6, Figure 9.7). The trace element data highlight three geochemical anomalies along the range front. The western end of the Magma vein contains relatively high Ag, Cu, Bi, As, Sb, Pb, Mn and Y, whereas Au, Mo and Sn, are enriched in the eastern exposures (Figure 9.6, Figure 9.7). Gold, Cu, Mo, Bi, As, Sb, Pb, Zn and Mn show some degree of anomalism at the vein exposures in the central portion of the range front (Figure 9.6). This area of geochemical anomalism corresponds with the broad zone of lower $\delta^{18}O_{calcite}$ isotopic values and may be mapping geochemical dispersion along ENE-striking epithermal veins directly from Resolution, or via the West Boundary Fault. Lastly, there is a conspicuous whole-rock geochemical anomaly defined in the central-south portion of the range front (Figure 9.6, Figure 9.7). For some elements, such as Zn and Mn, this appears to be part of a larger anomaly to the east around Belmont, suggesting it could represent an outflow zone along this structure. In turn, this indicates that fluid transport along these structures was not uniformly lateral, but in places could have a strongly vertical component.

The somewhat incoherent nature of many of the whole-rock geochemical anomalies associated with the range front veins could be due to the tight nature of geochemical halos around epithermal veins in carbonate host rocks with a high fluid-buffering capacity, combined with inability to always sample to the central portion of the vein. It could also relate to the distance from Resolution being far enough away that typical whole-rock anomalism begins to become discontinuous. Overall however, the vein geochemistry and the relative depletion in $\delta^{18}O$ tend to highlight the same major structures (Figure 9.5 A, Figure 9.6, Figure 9.7).

## 9.3 Sulfur isotopes

### 9.3.1 Introduction

Sulfur isotopic analyses can be used to understand the geochemical evolution in ore deposits, in terms of sulfur sources, transport and precipitation mechanisms (Ohmoto, 1972; Ohmoto and Rye, 1979; Ohmoto, 1986; Ohmoto and Goldhaber, 1997; Seal, 2006). Variable $\delta^{34}S$ signatures of sulfide and sulfate minerals within ore deposits are typically the result of a) temperature-dependant fractionation

between fluid and mineral, b) variations in redox state of the hydrothermal fluid, and c) varied sources of sulfur (Rye, 1992; Rye et al., 1993). Sulfur isotopes can also be used to map fluid flow in hydrothermal systems from higher temperature, oxidised mineralised centres outwards (e.g., Cadia, Wilson et al., 2007; Didipio, Wolfe and Cooke, 2011). Porphyry deposits associated with I-type granites generally report a narrow range of $\delta^{34}S$ values around 0 ‰ with $\delta^{34}S$ sulfide approximating that of the local igneous rocks and country rocks; implying that magmatic sulfur is the primary sulfur source (Ohmoto and Goldhaber, 1997). Based on sulfur isotope studies of deposits throughout the western U.S. and South America, porphyry deposits typically have $\delta^{34}S$ sulfide values around 0 ± 5 ‰ (Field and Gustafson, 1979; Ohmoto and Rye, 1979; Ohmoto, 1986; Ohmoto and Goldhaber, 1997). Oxidised fluids in porphyry and high sulfidation epithermal deposits precipitate sulfides depleted in $^{34}S$, so that sulfide isotopic values range between -10 and 0 ‰ (Rye, 1992; Rye et al., 1993; Wilson et al., 2007; Cooke et al., 2011).

### 9.3.2 Previous sulfur isotope studies in the Superior district

Previous sulfur isotope studies of porphyry deposits in the Western U.S. provide a comparative framework to the current study (e.g., Field and Gustafson, 1979; Ohmoto and Rye, 1979; Figure 9.10). At Superior, Friehauf (2008) analysed twelve sulfide samples from 'C-Bed', one of the largest of the Palaeozoic limestone-hosted mantos at the Magma Mine. He analysed eight pyrite, three chalcopyrite, one bornite and one sphalerite sample, with $\delta^{34}S$ values ranging from -4.8 ‰ to +10.1 ‰. Friehauf (2008) demonstrated systematic differences between the inner, sulfide-rich part of the manto, and the outer hematite-stable gangue. He concluded that in the absence of biogenetically reduced isotopically light sulfur, the presence of high $\delta^{34}S$ evaporates observed in the wall rocks and a probable magmatic source, the shift from negative to positive $\delta^{34}S$ values observed in the manto was the result of Raleigh distillation of sulfur from a single magmatic source ($\delta^{34}S$ = ~0 ‰), combined with redox-buffering conditions for the conversion of early hematite to pyrite (Friehauf, 2008).

### 9.3.3 Methods

In this study, sulfur isotope compositions were analysed for 69 paragenetically constrained mineral samples from the Superior district (Figure 9.1). The sample suite included 41 pyrite, 9 chalcopyrite, 6 sphalerite, 4 enargite, 3 chalcocite, 2 galena and 1 bornite and 3 composite pyrite-chalcopyrite samples. Samples were selected in order to determine the variability of $\delta^{34}S$ over time, across several rock units and alteration stages, and also spatially. Approximately 10 mg of powder was prepared from each sample by hand drilling coarse grained sulfides using a Dremel Multipro 225 T2 Flex-shaft drill. The drill bit was cleaned between samples using a chalk block. Powders were transferred on clean weighing paper into a vial and weighed. Samples were submitted to Christine Cook at the Central Science Laboratory, University of Tasmania, Australia, for sulfur isotopic analyses. Analyses were performed on sub-samples,

weighing <1 mg, by conventional isotope ratio mass spectrometry methods using an Isoprime100 mass spectrometer coupled to an Elementar vario PYRO cube elemental analyser. Seven international standards (IAEA-S-1, -2 and -3, IAEA-SO-6 and -7, and NBS127) were also analysed within each analytical session and the results are reported with reference to the Canyon Diablo Troilite (0.0‰ $\delta^{34}S$) international standard. There is an estimated analytical uncertainty of ± 0.1 ‰.

### 9.3.4 Results

The results of sulfur isotopic analyses of samples from Resolution, Magma and Silver King are summarised in Table 9.2. Samples are grouped by deposit and alteration or mineralisation stage. At Resolution this is based on the paragenesis presented by Hehnke et al. (2012), whereas at Magma, the, sulfide mineral assemblages have been broadly grouped into early (generally pyrite-rich) and late stages (generally Cu sulfide-rich) based on paragenetic work conducted by Gustafson (1961) and validated via hand specimen observations in the current study. Samples from Silver King were grouped by alteration types observed in hand specimen during the current study (Section 4.6.3). The $\delta^{34}S$ values for sulfide minerals from the Superior district lie between -9.64 ‰ and +4.41 ‰, relative to the Canyon Diablo Troilite (CDT; Table 9.2, Figure 9.9).

Sulfur isotope values for sulfides from Resolution range from 1.5 ‰ to -9.6 ‰. Pyrite from Resolution shows a wide range of values from -7.2 to 1.5 to ‰, whereas chalcopyrite shows a more restricted, moderately negative range from -3.3 to -2.97 to ‰ (Table 9.2, Figure 9.9). One biotite-altered pyrite-chalcopyrite bearing sample from a deep drillhole approximately 5 km east of Resolution was also analysed, returning a $\delta^{34}S$ value of -5.9 ‰ (RE16JP058; Table 9.2). Higher sulfidation state minerals such as chalcocite, enargite and bornite show a broader, more negative range of $\delta^{34}S$ values, between -6 and -2.8 ‰ (Table 9.2). Sphalerite from Resolution returns the most negative sulfur isotope value in this dataset (-9.64 ‰; Table 9.2)

Sulfur isotope results have been subdivided by deposit and alteration facies (Table 9.2; Figure 9.9). At Resolution, early potassic stage sulfides (n = 2) have $\delta^{34}S$ values that range from -3 to -0.7 ‰. Phyllic stage sulfides (n = 12) have a wider range, from -3.6 to 0.2 ‰, with three strongly negative outlier samples reporting values between -9.64 and -6 ‰ (Table 9.2; Figure 9.9) . Only one sample from each of the argillic and intermediate argillic assemblages were analysed – they yielded $\delta^{34}S$ values of 3 ‰ and -2 ‰, respectively. Sulfides from the advanced argillic assemblage (n = 4) have a narrower, more negative range from -5.2 to -3.6 ‰. A pronounced shift toward more positive values is evident in propylitic altered samples (n = 5) and skarns (n = 1). $\delta^{34}S$ values in propylitic-altered rocks range from -3.6 to 0.5 ‰, with three of the five samples returning values >0 ‰. Pyrite from the skarn has a $\delta^{34}S$ value of -0.5 ‰. At Magma, high sulfidation mineralisation from the veins and mantos (n = 10) have $\delta^{34}S$ values ranging from -6.6 to -2.7 ‰, whereas the samples of intermediate sulfidation mineralisation (n = 25) return a range of $\delta^{34}S$ values between -5.36 and 2.2 ‰ (Table 9.2). Propylitic (n = 1) and skarn samples

Table 9.2 Results of sulfur isotopic analysis of sulfides from the Superior district.

| Sample ID | UTM mE | UTM mN | RL (m) | Deposit | Mineral | Alteration assemblage or mineralisation stage | $\delta^{34}S_{(CDT)}$ |
|---|---|---|---|---|---|---|---|
| RE16JP058 | 498256 | 3685518 | -21 | Resolution East? | Pyrite-chalcopyrite | Potassic | -5.9 |
| RE16JP242 | 494730 | 3683330 | -1030 | Resolution | Chalcopyrite | Potassic | -2.9 |
| RE16JP242 | 494730 | 3683330 | -1030 | Resolution | Pyrite | Potassic | -0.7 |
| RE16JP243 | 494854 | 3683874 | -469 | Resolution | Chalcopyrite | Phyllic | -3.3 |
| RE16JP243 | 494854 | 3683874 | -469 | Resolution | Pyrite | Phyllic | -1.9 |
| RE16JP052 | 493861 | 3683734 | -35 | Resolution | Pyrite | Phyllic | -1.7 |
| RE16JP094 | 494449 | 3682785 | -127 | Resolution | Pyrite | Phyllic | 0.1 |
| RE16JP092 | 494449 | 3682781 | -162 | Resolution | Pyrite | Phyllic | -3.5 |
| RE15JP187 | 493431 | 3682903 | 303 | Resolution | Sphalerite | Phyllic | -9.6 |
| RE15JP187 | 493431 | 3682903 | 303 | Resolution | Pyrite | Phyllic | -3.1 |
| RE15JP098 | 494193 | 3685488 | -520 | Resolution | Pyrite | Phyllic | -6.0 |
| RE15JP094 | 494172 | 3685505 | -682 | Resolution | Pyrite | Phyllic | -7.1 |
| RE15JP056 | 492224 | 3684283 | -76 | Resolution | Chalcopyrite | Phyllic | -3.3 |
| RE15JP114 | 492056 | 3682864 | 371 | Resolution | Pyrite | Phyllic | -2.3 |
| RE15JP117 | 492048 | 3682852 | 204 | Resolution | Pyrite | Phyllic | -1.6 |
| RE16JP244 | 495082 | 3684000 | -524 | Resolution | Pyrite | Advanced argillic (early) | -3.5 |
| RE16JP187 | 494651 | 3684388 | -194 | Resolution | Pyrite | Advanced argillic (early) | -4.2 |
| RE16JP244 | 495082 | 3684000 | -524 | Resolution | Chalcocite | Advanced argillic (late) | -3.6 |
| RE16JP187 | 494651 | 3684388 | -194 | Resolution | Enargite | Advanced argillic (late) | -5.2 |
| RE16JP098 | 494453 | 3682815 | 139 | Resolution | Pyrite | Propylitic | 0.5 |
| RE16JP047 | 493820 | 3684230 | 0 | Resolution | Pyrite | Propylitic | -2.3 |
| RE15JP093 | 494171 | 3685506 | -696 | Resolution | Pyrite | Propylitic | 0.1 |
| RE15JP055 | 492213 | 3684286 | -83 | Resolution | Pyrite | Propylitic | -3.6 |
| RE16JP041 | 492206 | 3684289 | -87 | Resolution | Pyrite | Propylitic | 0.2 |
| RE15JP052 | 492364 | 3684232 | 4 | Resolution | Pyrite | Argillic | -3.9 |
| RE15JP105 | 494187 | 3685492 | -562 | Resolution | Pyrite | Intermediate argillic | 1.5 |
| RE15JP095 | 494187 | 3685493 | -569 | Resolution | Pyrite | Skarn | -0.5 |
| RE16JP222 | 490179 | 3685197 | -388 | Magma | Pyrite | High sulfidation vein (early) | -3.6 |
| RE16JP223 | 490676 | 3685198 | -419 | Magma | Pyrite | High sulfidiation vein (early) | -5.0 |
| RE16JP222 | 490179 | 3685197 | -388 | Magma | Enargite | High sulfidiation vein (late) | -6 |
| RE16JP223 | 490676 | 3685198 | -419 | Magma | Bornite | High sulfidiation vein (late) | -4.2 |
| RE16JP223 | 490676 | 3685198 | -419 | Magma | Chalcocite | High sulfidiation vein (late) | -4.3 |
| RE16JP225 | 490549 | 3685197 | -325 | Magma | Enargite | High sulfidiation vein (late) | -2.7 |
| RE16JP228 | 491708 | 3685257 | -326 | Magma | Enargite | High sulfidiation vein (late) | -2.8 |
| RE15JP059 | 491023 | 3685033 | -316 | Magma | Pyrite | Intermediate sulfidation vein (early) | -1.2 |
| RE15JP208 | 494377 | 3685888 | -363 | Magma | Pyrite | Intermediate sulfidation vein (early) | 0.7 |
| RE16JP088 | 490979 | 3685163 | 15 | Magma | Pyrite | Intermediate sulfidation vein (early) | -5.3 |
| RE16JP089 | 490976 | 3685156 | 12 | Magma | Pyrite | Intermediate sulfidation vein (early) | -2.5 |
| RE16JP102 | 492556 | 3685311 | -21 | Magma | Pyrite | Intermediate sulfidation vein (early) | -1.2 |
| RE16JP105 | 492547 | 3685342 | -34 | Magma | Pyrite | Intermediate sulfidation vein (early) | -1.8 |
| RE16JP109 | 492534 | 3685386 | -54 | Magma | Chalcopyrite | Intermediate sulfidation vein (early) | 2.2 |
| RE16JP205 | 492526 | 3685158 | 6 | Magma | Pyrite | Intermediate sulfidation vein (early) | -2.8 |

| Sample ID | UTM mE | UTM mN | RL (m) | Deposit | Mineral | Alteration assemblage or mineralisation stage | $\delta^{34}S_{(CDT)}$ |
|---|---|---|---|---|---|---|---|
| RE16JP225 | 490549 | 3685197 | -325 | Magma | Pyrite | Intermediate sulfidation vein (early) | -1.9 |
| RE16JP227 | 491848 | 3685321 | -144 | Magma | Pyrite | Intermediate sulfidation vein (early) | -1.8 |
| RE16JP228 | 491708 | 3685257 | -326 | Magma | Pyrite | Intermediate sulfidation vein (early) | -2.4 |
| RE16JP233 | 493571 | 3685401 | -196 | Magma | Pyrite | Intermediate sulfidation vein (early) | -4.1 |
| RE16JP235 | 493805 | 3685322 | -127 | Magma | Pyrite | Intermediate sulfidation vein (early) | -0.8 |
| RE16JP238 | 492825 | 3685190 | -36 | Magma | Pyrite | Intermediate sulfidation vein (early) | -0.0 |
| RE16JP233 | 493571 | 3685401 | -196 | Magma | Sphalerite | Intermediate sulfidation vein (early) | -1.9 |
| RE16JP234 | 493664 | 3685384 | -136 | Magma | Sphalerite | Intermediate sulfidation vein (early) | -1.7 |
| RE16JP234 | 493664 | 3685384 | -136 | Magma | Sphalerite | Intermediate sulfidation vein (early) | -0.2 |
| RE16JP102 | 492556 | 3685311 | -21 | Magma | Chalcopyrite | Intermediate sulfidation vein (late) | -3.6 |
| RE16JP106 | 492545 | 3685349 | -37 | Magma | Chalcopyrite | Intermediate sulfidation vein (late) | -3.4 |
| RE16JP106 | 492545 | 3685349 | -37 | Magma | Galena | Intermediate sulfidation vein (late) | -3.8 |
| RE16JP109 | 492534 | 3685386 | -54 | Magma | Galena | Intermediate sulfidation vein (late) | 2.1 |
| RE16JP109 | 492534 | 3685386 | -54 | Magma | Sphalerite | Intermediate sulfidation vein (late) | 1.0 |
| RE16JP109 | 492534 | 3685386 | -54 | Magma | Sphalerite | Intermediate sulfidation vein (late) | -1.3 |
| RE16JP231 | 491868 | 3685328 | -134 | Magma | Chalcopyrite | Intermediate sulfidation vein (late) | -3.4 |
| RE15JP207 | 494378 | 3685886 | -356 | Magma | Pyrite | Manto (early) | -4.1 |
| RE15JP207 | 494378 | 3685886 | -356 | Magma | Chalcopyrite | Manto (late) | -6.2 |
| RE15JP207 | 494378 | 3685886 | -356 | Magma | Chalcocite | Manto (late) | -3.6 |
| RE16JP103 | 492554 | 3685319 | -24 | Magma | Pyrite-chalcopyrite | Skarn (Mescal) | 0.5 |
| RE16JP110 | 492534 | 3685389 | -55 | Magma | Pyrite | Skarn (Mescal) | 4.4 |
| RE16JP154 | 492891 | 3684729 | -17 | 2nd South vein | Pyrite | Propylitic | -0.1 |
| RE16JP202 | 492546 | 3684967 | 23 | North Boundary | Pyrite | Intermediate sulfidation vein (early) | -1.6 |
| RE16JP015 | 490545 | 3689075 | 1183 | Silver King | Pyrite | Quartz-pyrite cemented breccia | 1.3 |
| RE16JP066 | 492016 | 3687601 | 1137 | Silver King | Chalcopyrite | Phyllic | -3.2 |
| RE16JP027 | 492045 | 3681192 | 991 | Silver King | Pyrite-chalcopyrite | Potassic | -1.0 |
| RE16JP026 | 492827 | 3688646 | 1288 | Silver King | Pyrite | Potassic | 0.9 |

(n = 2) have elevated $\delta^{34}S$ values, with the propylitic-altered sample returning a $\delta^{34}S$ value of -0.14 ‰, and the skarn samples returning values of 4.4 ‰ and 0.6 ‰ (Table 9.2). At Silver King, potassic stage sulfide $\delta^{34}S$ values (n = 2) are -1.02 to 0.94 ‰. The pyrite from the phyllic-altered sample has $\delta^{34}S$ value of -3.2 ‰ (Table 9.2). Pyrite from a hydrothermal breccia at the western edge of the quartz diorite has the highest $\delta^{34}S$ value of 1.3 ‰.

Overall, the range of $\delta^{34}S$ values from the Superior district is comparable to previous results from the Western U.S porphyry copper province (Figure 9.10). Resolution and Magma display similar ranges in $\delta^{34}S$ values and are most comparable isotopically to the Globe-Miami and Ajo deposits (Figure 9.10).

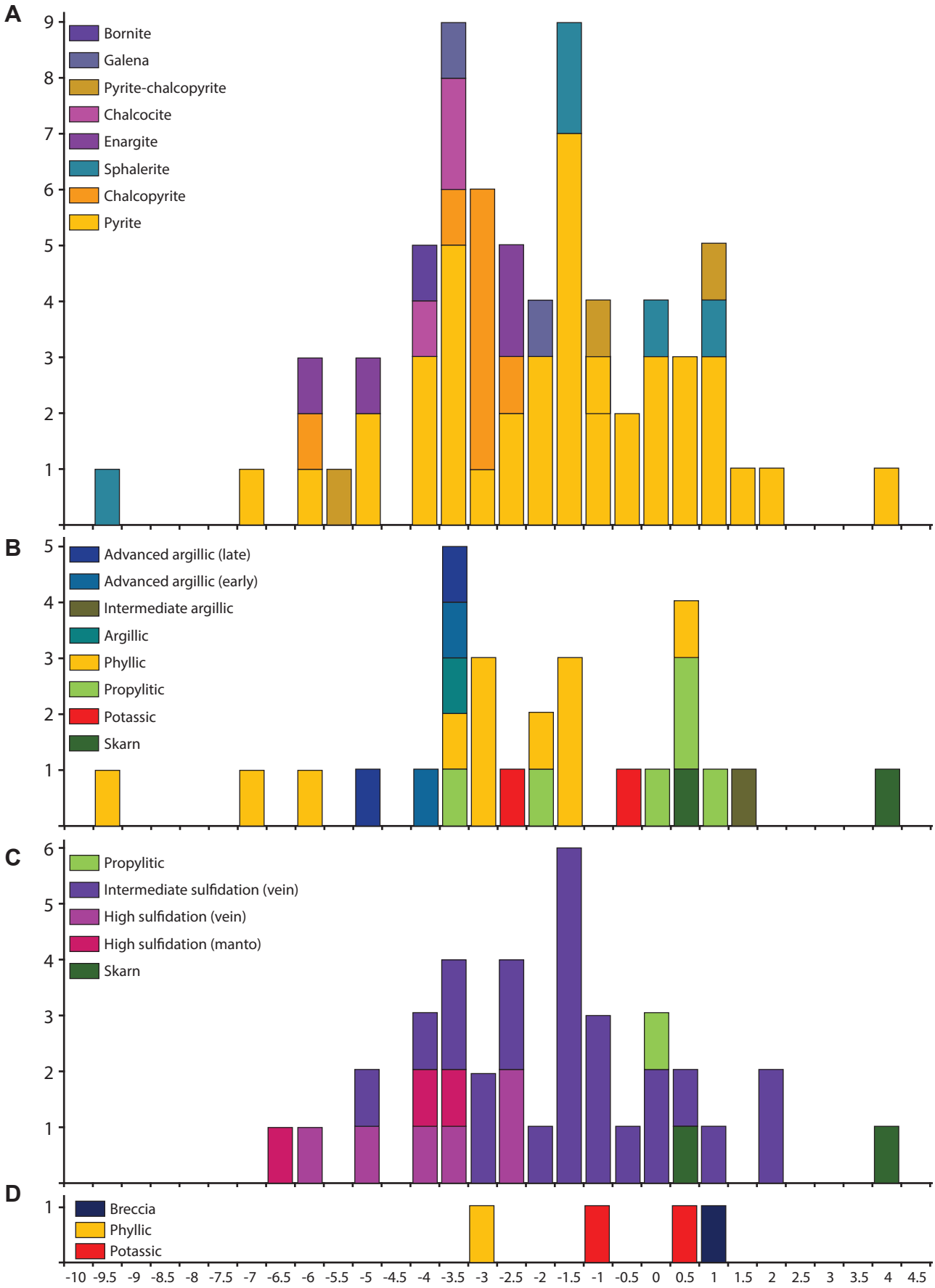


Figure 9.9 Sulfur isotope histograms for; A. All samples from the Superior district, B. Alteration stages from Resolution, C. Alteration and mineralisation types from Magma and, D. Silver King. All data listed in Table 9.2.

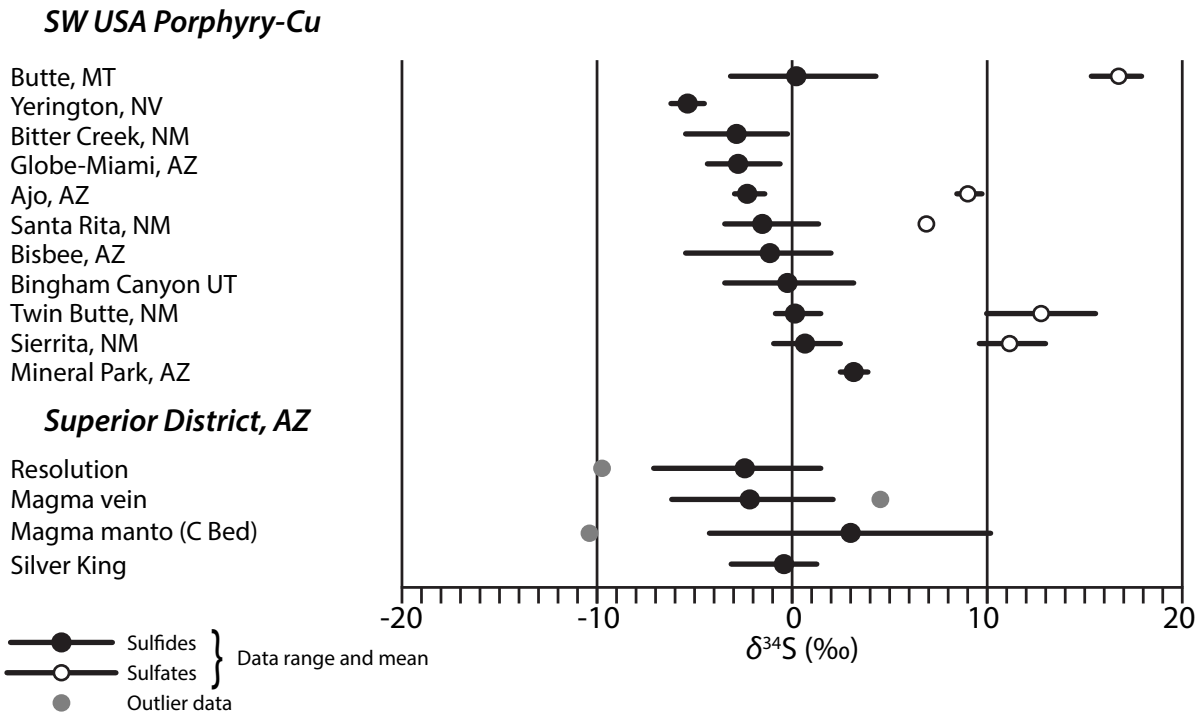


Figure 9.10 Sulfur isotope results from other porphyry Cu deposits from the Southwestern USA. Data for SW USA porphyries compiled by Cooke et al. (2014) and references therein. Magma (C bed manto) from Friehauf (2008).

Sulfur isotope data from Silver King has a more restricted and overall slightly less negative range of $\delta^{34}S$ values, and is perhaps most isotopically similar to the carbonate-hosted Bingham Canyon deposit in Utah (Figure 9.10).

### 9.3.4.1 Sulfur isotopic zonation patterns

Spatial zonation in $\delta^{34}S$ values across the Superior district has been illustrated using only the results from pyrite analyses. Some samples contain analyses from multiple sulfide minerals but the spatial coverage of these additional sulfide minerals is limited. Samples from the Mescal Limestone were also excluded on the basis of their anomalously enriched $\delta^{34}S$ values, which may imply some incorporation of seawater sulfate from evaporites within the Mescal Limestone during the formation of sulfides (Table 9.2). The spatial zonation patterns defined by $\delta^{34}S_{pyrite}$ values is striking when projected to surface and plotted in plan view (Figure 9.11 A). Samples from the centre of Resolution and Resolution East define a broad zone of lower $\delta^{34}S$ values. This zone is bounded to the north and south by a halo of slightly elevated $\delta^{34}S$ values (Figure 9.11 A). There is also an area of $\delta^{34}S_{pyrite}$ depletion to the west of the broader Resolution low which correlates spatially with the location of the West Boundary Fault. Samples from Silver King have elevated $\delta^{34}S_{pyrite}$ values. Samples near Magma deposit tend to define a strong eastward transition from low to high $\delta^{34}S_{pyrite}$ values (Figure 9.11 A). This trend is also apparent when projected along the Magma long section (Figure 9.11 B).

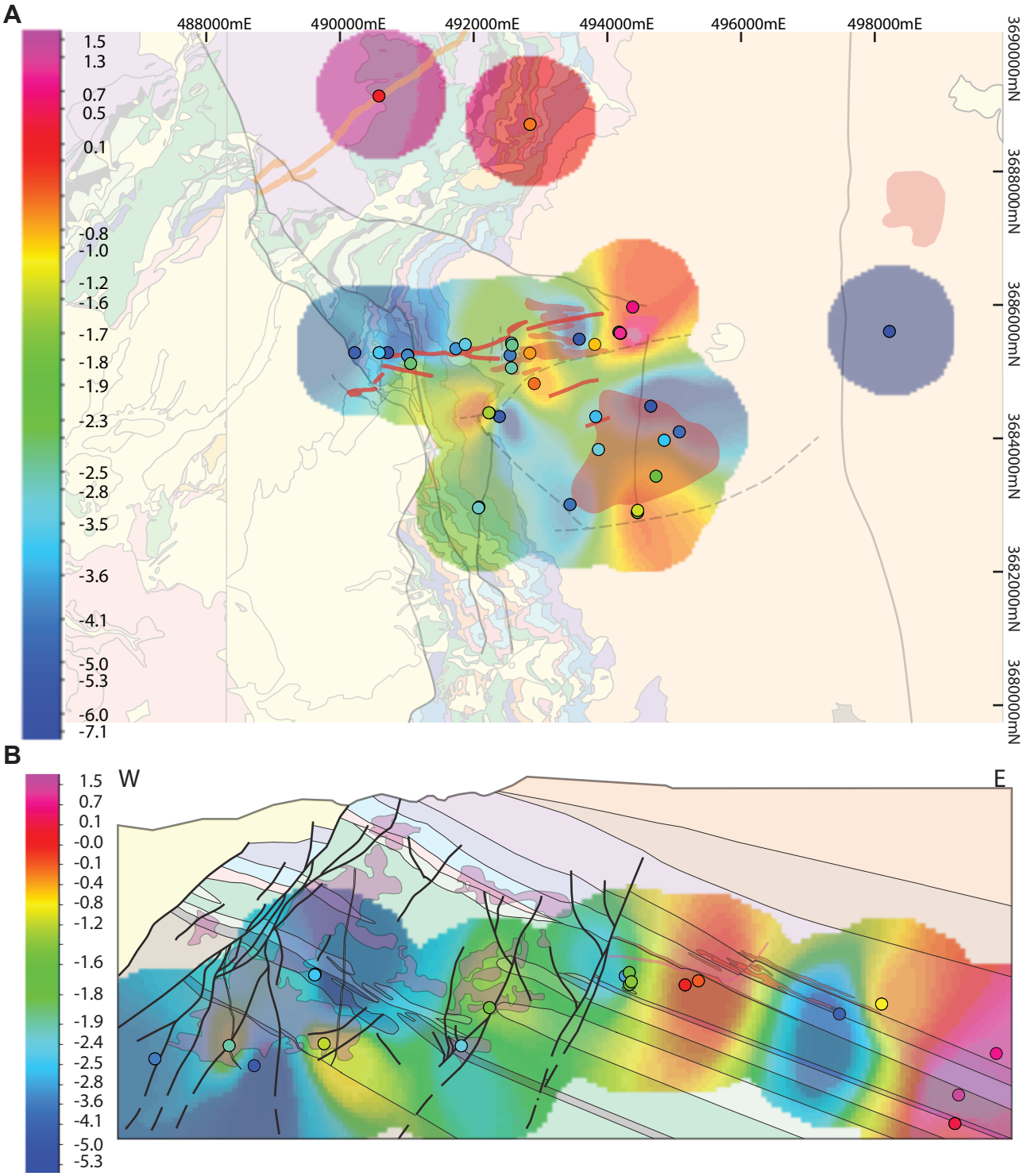


Figure 9.11 Gridded sulfur isotope results from pyrite for (A) the Superior district (plan view) and (B) the Magma vein system (samples projected onto long section). Geology and mineralisation as per Figure 3.2 and Figure 4.8. All data listed in Table 9.2

### 9.3.5 Discussion

The $\delta^{34}S$ sulfide values obtained from the Superior district in this study range between -9.6 ‰ and 4.4 ‰, averaging -2.3 ‰. This range of $\delta^{34}S$ values overlaps with the range of values observed in most porphyry systems in the western U.S. (Figure 9.10; Field and Gustafson, 1979; Ohmoto and Rye, 1979; Ohmoto and Goldhaber, 1997; Wilson et al., 2007). The near zero $\delta^{34}S$ values suggest a dominantly

magmatic sulfur source (Ohmoto and Rye 1979, Field and Fifarek, 1985). The broad range of $\delta^{34}S$ values and general excursion toward more negative values in the Superior district suggest hydrothermal fluids have evolved under oxidising (sulfate present) conditions (Ohmoto and Rye, 1979; Rye, 1993), although sulfide-sulfate pairs were not available to constrain $\delta^{34}S$ in sulfates or calculate the bulk isotopic composition of the fluid.

Spatial zonation of $\delta^{34}S$ values within the Superior district is remarkable in that it appears to map out the locations of ore zones and major structures (Figure 9.11 A). Resolution and Resolution East are highlighted by a zone of pronounced $\delta^{34}S$ depletion, surrounded by a halo of slightly less depleted samples (Figure 9.11 A). Interrupting this zonation is a small northwest-trending elliptical zone of depletion that approximates the location of the West Boundary fault, suggesting it may have been an important hydrothermal fluid pathway (Figure 9.11 A).

Isotopic zonation patterns at Resolution suggest that the central portion of the system was oxidised. Sulfur isotope values become more negative with decreasing relative age and proximity to the surface (potassic average: -1.8 ‰, phyllic: -3.7 ‰, argillic: -4.0 ‰, early advanced argillic: -3.9 ‰, late advanced argillic: -4.5 ‰; Table 9.2, Figure 9.9), consistent with increasing oxidation and decreasing temperature. In the absence of biogenetically reduced light sulfur, more negative $\delta^{34}S$ values could also be interpreted as reflecting the increasing influence of more magmatic sulfur. In comparison, the more lateral outflow zones dominated by propylitic and intermediate argillic alteration tend to show a shift towards more positive $\delta^{34}S$ values. This pattern can be explained by a combination of cooling and fluid-rock interaction, where magmatic hydrothermal fluids cool and interact with reduced country rocks (Wilson et al., 2007). The single potassic sample from Resolution East has a strongly negative $\delta^{34}S$ value of -5.9 ‰ implying an oxidised fluid source nearby. This could relate to a separate, undiscovered porphyry system, or may be a deep structurally dislocated of the deep potassic alteration domain at Resolution.

At Silver King, the potassic stage has higher $\delta^{34}S$ values than at Resolution, perhaps implying that the hydrothermal fluid at Silver King was less oxidised. The $\delta^{34}S$ value from the breccia is similar to sulfides from potassic altered rocks at Silver King.

In the Magma vein, the overall eastward trend towards higher $\delta^{34}S$ values in pyrite (Figure 9.11 A-B) approximates the distribution of higher sulfidation state mineralisation (Figure 4.8). This in turn suggests higher oxidation states and limited or no interaction with sedimentary sulfur. This could imply an oxidised fluid source (possibly another porphyry) at the western end of the Magma vein. The sulfide samples from the western end are hosted in the Proterozoic stratigraphy, whereas those in the east are hosted in the Paleozoic stratigraphy (Figure 9.11 B) and so it is also possible that water-rock interaction is causing a shift to higher $\delta^{34}S$ values higher up the stratigraphy. However, it is important to consider that the present day orientation of the Magma Vein and its wall rocks are the result of the post-mineralisation westward tilting (Maher, 2008) and therefore the samples analysed in the current study are not a true

horizontal transect through the vein.

Magmatic sulfur is the dominant sulfur source in the Superior district. The anomalously high $\delta^{34}S$ sulfide values associated with pyrite from skarns at Resolution and Magma potentially indicate local incorporation of $^{34}S$ from evaporitic wall rocks (Proterozoic Mescal Limestone). An alternative hypothesis was proposed by Friehauf (2008), who argued that early deposition of hematite provided an oxidant to convert $H_2S$ to $SO_4$ resulting in the sulfidation of hematite and preferential incorporation of isotopically light sulfur into sulfides in the ore zone and isotopically heavy sulfur into sulfides in the distal gangue. Friehauf did not consider the evaporitic wall rocks as he only studied the non-evaporitic Paleozoic carbonates. Sulfur isotope fractionation driven by wall-rock buffering may explain the shift toward more positive values in some of the Magma vein samples from this study (-6.3 to 4.4 ‰; Table 9.2) compared to the narrow range for vein samples (-4.8 to -4.6 ‰; n = 3) reported by Friehauf (2008).

## 9.4 Lead isotopes

### 9.4.1 Introduction

Lead isotope compositions of sulfide minerals can be used to inform metal sources, fluid pathways and spatial zonation patterns in hydrothermal systems (Heyl et al., 1966; Stacey et al., 1968; Gulson, 1986; Sanford, 1992; Bouse et al., 1999). Comparison of the Pb isotope composition of sulfides against those of potential host- or country-rock reservoirs, through which a hydrothermal fluid has migrated or may have been sourced, can provide information on the plumbing system and degrees of fluid-rock interaction (Macfarlane et al., 1990; Sanford, 1992; Tosdal et al., 1999). Lead isotopic exchange between hydrothermal fluids and their wall rocks is especially relevant when dealing with emplacement of young hydrothermal systems into older country rocks (e.g., Bouse et al., 1999; Pettke et al., 2010).

Investigation of Pb isotopic composition of epidote from the Superior district was conducted for two reasons. Firstly, as a result of method development outlined in Chapter 5, Pb isotope data for epidote was already available for comparison in this study. As epidote can occur beyond the pyrite halo in the distal alteration halo to porphyry deposits, epidote Pb isotope analyses offer the opportunity to extend the footprint of Pb isotopic footprint of porphyry deposits.

This section presents new Pb isotope data from sulfides and epidote for Resolution, Magma and the Silver King area. These results inform discussions of genetic relationships between the deposits, and allows the use of Pb isotope data in vectoring towards mineralised centres to be assessed from the Superior district.

### 9.4.2 Sulfides

#### 9.4.2.1 Previous work

The tectono-isotopic framework of the south western United States is relatively well-constrained, based

on work by Bennet and DePaolo (1987), Wooden et al. (1988), Wooden and Miller (1990) and Wooden and Dewitt (1991). They demonstrated the differing magmatic and isotopic histories of the various basement terranes of the southwest US, including lower μ and higher κ values for south east Arizona. Bouse et al. (1999) and Pettke et al. (2010) provided a wide-ranging Pb isotope study across the western US porphyry Cu province, and a detailed Pb isotope study of the Bingham Canyon deposit, respectively. They demonstrated that the Pb isotopic compositions of sulfides (Bouse et al., 1999) and fluid inclusions (Pettke et al., 2010) from the aforementioned ore deposits are generally much less radiogenic than should be the case for ore deposits of this age. They also showed at the $^{204}$Pb-based isotopic composition of Laramide plutons broadly reflected the isotopic compositions of the different basement terranes into which the plutons were emplaced. Additionally, the isotopic ratios in plutons decreased becoming more 'retarded' with time (Bouse et al., 1999). Together these phenomena are interpreted to reflect the increasing involvement of a low-μ reservoir over time, and that this reservoir is the lower crust. Bouse et al. (1999) also demonstrated a temporal and spatial shift in Pb isotopic compositions at the deposit to district scale, with younger and/or distal sulfides generally having more radiogenic values. This implies significant fluid-rock interaction and scavenging of Pb from the country rocks in the waning stages of magmatic activity and/or on the peripheries of porphyry deposits in the region. The results of Bouse et al. (1999) used in the future sections to help interpret new results from the Superior district. This framework is used to help answer the questions of genetic relationships between deposits and vectoring towards mineralisation in the Superior district.

#### 9.4.2.2 Methods

***Pyrite etching***

Polished 25 mm round mounts were etched using sodium hypochlorite (NaOCl) in order to identify growth zones and compositional heterogeneity of the pyrite grains prior to LA-ICP-MS analyses. NaOCl was applied to the surface of samples which were then left to stand for two minutes before being dipped in water to remove the solution and air dried. Etched samples were reviewed by reflected light microscopy. Laser spot targets were chosen to span the range of domains revealed by the chemical etching technique.

***Laser ablation ICPMS***

Pyrite and galena were chosen for Pb isotope characterisation as both are common in the distal parts of porphyry systems, and so in the Superior district. A total of 22 paragenetically constrained samples were prepared as polished 25 mm diameter round mounts for lead isotope analysis by laser ablation inductively coupled plasma mass spectrometry (LA-ICP-MS) at CODES, University of Tasmania, Australia, following the methods of Meffre et al. (2008; Table 9.3). For each sample, 5-10 spot analyses were made for each type of sulfide present in the sample. Lead isotopes were measured along with

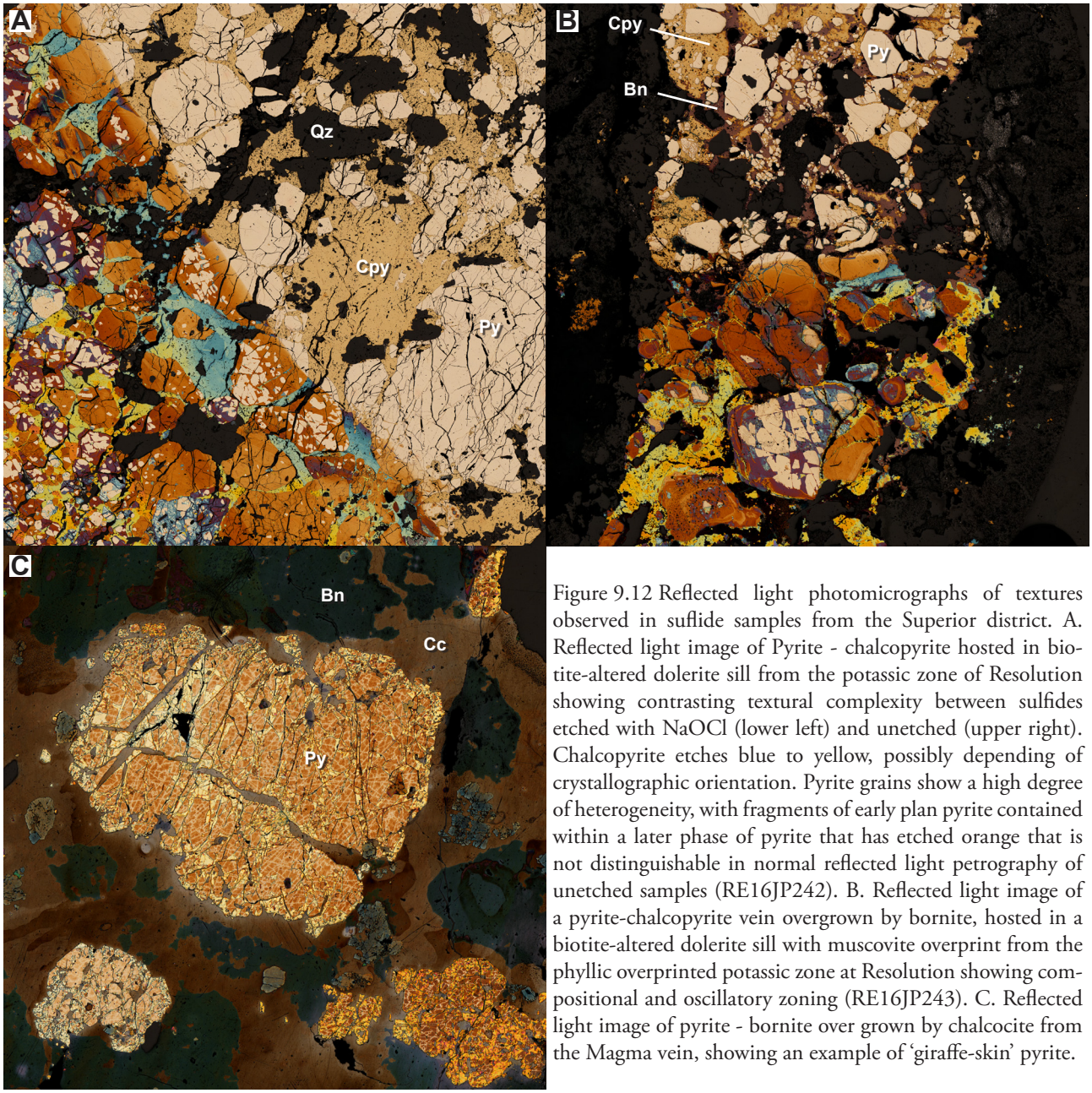


Figure 9.12 Reflected light photomicrographs of textures observed in suflide samples from the Superior district. A. Reflected light image of Pyrite - chalcopyrite hosted in biotite-altered dolerite sill from the potassic zone of Resolution showing contrasting textural complexity between sulfides etched with NaOCl (lower left) and unetched (upper right). Chalcopyrite etches blue to yellow, possibly depending of crystallographic orientation. Pyrite grains show a high degree of heterogeneity, with fragments of early plan pyrite contained within a later phase of pyrite that has etched orange that is not distinguishable in normal reflected light petrography of unetched samples (RE16JP242). B. Reflected light image of a pyrite-chalcopyrite vein overgrown by bornite, hosted in a biotite-altered dolerite sill with muscovite overprint from the phyllic overprinted potassic zone at Resolution showing compositional and oscillatory zoning (RE16JP243). C. Reflected light image of pyrite - bornite over grown by chalcocite from the Magma vein, showing an example of 'giraffe-skin' pyrite.

selected trace elements (As, Au, Cu, Fe, Hg, U and Th) using an Agilent 7700 quadrupole ICP-MS equipped with a 193 nm Excimer laser and the Resonetics S155 laser ablation system. Instrument parameters are those outlined by Meffre et al. (2008) and Woodhead et al. (2009). The instrument drift and mass bias correction factors were calculated using the NIST610 standard, which was analysed twice at the beginning and end of the run and once every 30 min throughout the run. Each analysis began with a 12 s blank gas measurement followed by a further 50 s of analysis while the laser was switched on. Pyrite was sampled with a 110 μm spot diameter where possible, depending on grain size, using the laser at 10 Hz and fluence of approximately 3.5 J $cm^{-2}$. The counting time on all elements was 0.01 s, except for Au and $^{204}Pb$ which were counted for 0.1 s to improve analytical precision and to lower detection limits. Data reduction for trace elements was performed using methods outlined

in Danyushevsky et al. (2011). Integration intervals were selected based on Fe time-resolved spectra, which were used to confirm pyrite was being analysed for the duration of the analysis. Uncertainties on laser ablation analyses are summarised in Table 9.3, but are generally in the acceptable range of ± 0.027 for $^{206}$Pb ratios. The uncertainties for $^{204}$Pb ratios are somewhat higher, around ± 0.21, due to the low isotopic abundance of $^{204}$Pb.

Epidote sample preparation followed the procedure outlined in sections 6.5 (epidote geochronology) and 8.3 (epidote mineral chemistry). Samples used in the method development from Chapter 6 have geochronological and trace element data. Other samples routinely analysed by the trace element method have analyses of $^{206}$Pb and $^{207}$Pb.

#### 9.4.2.3 Results

***Etching***

Pyrite samples from the Superior district contain a variety of pyrite textures, ranging from veins to disseminations at the hand specimen scale. Pyrite grains range from and euhedral to anhedral in shape. Etching in sodium hypochlorite has revealed significant intra-grain heterogeneity. Within massively textured, locally fractured pyrite (Figure 9.12 A), at least two major subtypes can be distinguished. The first type is an early-formed massive, fragmented pyrite that typically does not change colour after etching. This is overgrown by distinct grains of pyrite that etch to a variable orange colour (Figure 9.12 A -B). The orange-coloured pyrite is always the younger paragenetic stage in composite grains. It varies in colour from orange to purple after etching, and oscillatory zoning can be seen in some samples (Figure 9.12 C). The apparent paragenetic progression from early plain pyrite to later orange-purple etched pyrite was consistent across the district, including samples from Copper King, Magma and Resolution. In one sample a third type of pyrite was observed that typically etches brown and is criss-crossed by a lighter brown-yellow pyrite, reminiscent of giraffe skin (RE16JP222; Figure 9.12 C)

***Pb isotope ratios***

In total, 308 LA-ICP-MS spot analyses of Pb isotopic compositions of sulfide grains were collected from 24 Superior district samples. Fifty five analyses were discarded due to very low Pb concentrations, including all analyses from the phyllic altered samples from Silver King and the advanced argillic samples from Resolution. Weighted averages were generated from individual spot analyses (Table 9.3). The full dataset of individual spot analyses is provided in Appendix 4B. No significant difference was found in Pb isotope concentrations between the different types of etched pyrite (Appendix 4B).

A summary of weighted average results from the geochronology and trace element analyses of epidote are provided in Table 9.4 and Figure 9.15. The full results from individual spot analyses for each epidote sample can be found in Appendix 4B. As samples analysed by the trace element method do not have

Table 9.3 Summary table of results for Pb isotopic analysis of sulfide samples from the Superior district. Sample locations as per Table 9.2.

| Sample ID | Deposit | Mineral | Stage | $^{207}Pb/^{206}Pb$ | Error (1σ) | $^{208}Pb/^{206}Pb$ | Error (1σ) | $^{206}Pb/^{204}Pb$ | Error (1σ) | $^{207}Pb/^{204}Pb$ | Error (1σ) | $^{208}Pb/^{204}Pb$ | Error (1σ) | $^{206}Pb/^{238}U$ | $^{208}Pb/^{232}Th$ |
|---|---|---|---|---|---|---|---|---|---|---|---|---|---|---|---|
| RE16JP242 | Resolution | Pyrite | Potassic | 0.774 | 0.01 | 1.848 | 0.03 | 20.16 | 1.0 | 15.25 | 0.4 | 37.38 | 0.9 | 3200 | 21550 |
| RE16JP052 | Resolution | Pyrite | Phyllic | 0.867 | 0.01 | 2.123 | 0.04 | 19.78 | 0.4 | 17.02 | 0.4 | 41.64 | 1.0 | 14740 | 13014 |
| RE16JP243 | Resolution | Pyrite | Phyllic | 0.868 | 0.004 | 2.137 | 0.01 | 17.75 | 0.2 | 15.53 | 0.1 | 37.92 | 0.4 | 26783 | 140657 |
| RE15JP105 | Resolution | Pyrite | Int Arg | 0.868 | 0.004 | 2.127 | 0.01 | 17.75 | 0.1 | 15.39 | 0.1 | 37.64 | 0.3 | 72777 | 108626 |
| RE15JP055 | Resolution | Pyrite | Propylitic | 0.870 | 0.004 | 2.133 | 0.02 | 17.84 | 0.1 | 15.53 | 0.1 | 38.13 | 0.6 | 84808 | 295319 |
| RE16JP082 | Resolution | Pyrite | Propylitic | 0.875 | 0.004 | 2.137 | 0.004 | 17.78 | 0.1 | 15.55 | 0.1 | 37.94 | 0.2 | 52 | 31 |
| RE16JP098 | Resolution | Pyrite | Propylitic | 0.876 | 0.003 | 2.141 | 0.01 | 17.71 | 0.1 | 15.52 | 0.1 | 37.96 | 0.2 | 55212 | 1964636 |
| RE15JP180 | Resolution | Galena | Propylitic | 0.877 | 0.004 | 2.134 | 0.01 | 17.72 | 0.1 | 15.54 | 0.1 | 37.74 | 0.2 | 79656 | 477385 |
| RE15JP207 | Magma | Pyrite | HS manto | 0.877 | 0.003 | 2.144 | 0.01 | 17.72 | 0.04 | 15.56 | 0.03 | 38.05 | 0.1 | 8612 | 1265331 |
| RE16JP222 | Magma | Pyrite | HS vein (e) | 0.877 | 0.001 | 2.158 | 0.01 | 17.70 | 0.05 | 15.52 | 0.03 | 38.21 | 0.1 | 9287 | 8125 |
| RE16JP223 | Magma | Pyrite | HS vein (e) | 0.878 | 0.001 | 2.145 | 0.002 | 17.69 | 0.03 | 15.52 | 0.03 | 37.94 | 0.1 | 6316 | 3314 |
| RE16JP223 | Magma | Bornite | HS vein (l) | 0.878 | 0.002 | 2.148 | 0.004 | 17.56 | 0.1 | 15.39 | 0.1 | 37.67 | 0.2 | 903 | 186 |
| RE16JP223 | Magma | Chalcocite | HS vein (l) | 0.879 | 0.004 | 2.139 | 0.01 | 17.65 | 0.3 | 15.53 | 0.4 | 37.85 | 0.5 | 9385 | 135309 |
| RE16JP108 | Magma | Pyrite | IS vein (e) | 0.880 | 0.01 | 2.137 | 0.01 | 17.79 | 0.2 | 15.68 | 0.2 | 38.02 | 0.4 | 3693 | 156930 |
| RE16JP227 | Magma | Pyrite | IS vein (e) | 0.880 | 0.004 | 2.146 | 0.01 | 17.75 | 0.2 | 15.63 | 0.1 | 38.12 | 0.4 | 20850 | 222678 |
| RE16JP106 | Magma | Galena | IS vein (l) | 0.880 | 0.001 | 2.151 | 0.003 | 17.61 | 0.02 | 15.51 | 0.02 | 37.88 | 0.1 | | |
| RE16JP106 | Magma | Pyrite | IS vein (l) | 0.880 | 0.02 | 2.158 | 0.06 | 17.51 | 0.2 | 15.41 | 0.2 | 37.68 | 0.6 | | |
| RE15JP117 | Magma | Pyrite | Propylitic | 0.880 | 0.00 | 2.147 | 0.01 | 17.55 | 0.1 | 15.45 | 0.1 | 37.64 | 0.1 | 41170 | 60079 |
| RE16JP064b | Magma | Pyrite | Propylitic | 0.881 | 0.01 | 2.138 | 0.02 | 17.38 | 0.1 | 15.33 | 0.1 | 37.15 | 0.4 | 4449 | 65909 |
| RE16JP154 | Magma | Pyrite | Propylitic | 0.882 | 0.01 | 2.148 | 0.02 | 17.51 | 0.3 | 15.43 | 0.3 | 37.57 | 0.7 | 759 | 21950 |
| RE16JP026 | Silver King | Pyrite | Potassic | 0.883 | 0.002 | 2.153 | 0.004 | 17.62 | 0.1 | 15.57 | 0.1 | 37.95 | 0.2 | 16584 | 672073 |
| RE16JP015 | Silver King | Pyrite | Breccia | 0.884 | 0.001 | 2.162 | 0.01 | 17.61 | 0.1 | 15.55 | 0.1 | 38.06 | 0.3 | 7784 | 88163 |

$^{204}Pb$ data, they cannot be plotted on $^{204}Pb$ data-based diagrams (Figure 9.15 A-B). Instead, they are plotted on the $^{207}Pb/^{206}Pb$ vs. $^{208}Pb$ and $^{206}Pb$ diagram (Figure 9.15 C). Comparison of the two analytical methods is provided in section 6.5.5.

The $Pb_{sulfide}$ isotopic composition varies considerably across the district ($^{206}Pb/^{204}Pb$; 17.380 to 20.162, $^{207}Pb/^{206}Pb$; 0.774 – 0.884; Table 9.3). This large range is due to a few highly radiogenic analyses and some analytical uncertainty with 20 of the 22 sample) averages (>90 %) contained within a $^{206}Pb/^{204}Pb$ range of 17.380 – 17.838, and 21 of the 22 sample averages within a $^{207}Pb/^{206}Pb$ range of 0.867 – 0.884 (Table 9.3). The $Pb_{sulfide}$ isotopic results are relatively non-radiogenic, plotting well to the left of the expected isochron for a hydrothermal fluid of Laramide age (Figure 9.13), but typical of the 'retarded' Pb isotope signature of the western US (Bouse et al., 1999; Pettke et al., 2010). The Resolution data plot lie both above and below the average crustal growth curve of Stacey and Kramers (1975), showing no preference for lower $^{207}Pb/^{204}Pb$, as might be expected from samples from this crustal province (Figure 9.13 A Wooden and Dewit, 1991; Bouse et al., 1999). In contrast, $^{208}Pb/^{204}Pb$ and $^{208}Pb/^{206}Pb$ ratios are strongly offset towards higher values, reflecting the higher, Th/U character typical of SE Arizona (Figure 9.13 B-C; Bouse et al., 1999). Only one sample from Magma plots above the average crustal growth curve (Figure 9.14 D-F). Overall, the bulk $Pb_{sulfide}$ isotopic signature at Resolution is somewhat less radiogenic than that at Magma (Figure 9.13 and Figure 9.14 respectively).

The epidote Pb isotopic data define similar patterns to $Pb_{sulfide}$ isotope data ($Pb_{sulfides}$; Figure 9.13 and Figure 9.14). The epidote samples cluster around 500 Ma on the low-μ adjusted SE Arizona growth curve (Figure 9.15). Similar to the $Pb_{sulfides}$ data, there are a small number of highly radiogenic samples (Table 9.4 and Figure 9.15). The $^{206}Pb/^{238}U$ data for these radiogenic samples are consistent with the rest of the $Pb_{epidote}$ isotope data, suggesting their radiogenic nature is not due to contamination by mobile radiogenic Pb. Unlike the $Pb_{sulfides}$ data, there is one highly non-radiogenic sample distinct from the main ~500 Ma cluster (Table 9.4; Figure 9.15).

The $Pb_{epidote}$ isotope data show significant variability with regard to $^{208}Pb/^{204}Pb$ compared to $^{207}Pb/^{204}Pb$ (Figure 9.15 A-B). The steep gradient of the sample array through the middle section of the growth curve suggests that the sources of thorogenic and uranogenic Pb are somewhat decoupled. The spread in data between the different rock-types implies that there is limited host rock control on $^{208}Pb/^{204}Pb$ and $^{207}Pb/^{204}Pb$ compositions (Figure 9.15 B).

The epidote trace element dataset has Pb isotopic compositional ranges for $^{206}Pb/^{204}Pb$ from 16.53 to 20.62, $^{207}Pb/^{204}Pb$ from 15.36 to 15.78, $^{208}Pb/^{204}Pb$ from 36.08 to 39.87 and $^{207}Pb/^{206}Pb$ from 1.93 to 2.21 (Table 9.4). Trace element $Pb_{epidote}$ isotopic data cluster around the 500 Ma position on the SE Arizona growth curve, although there is considerable scatter (Figure 9.15 C). These data also show greater variability in both $^{207}Pb/^{206}Pb$ and $^{208}Pb/^{206}Pb$ compared to the $^{204}Pb_{epidote}$ data (Table 9.4; Figure 9.15). Basalt-hosted samples show a systematic offset towards lower $^{208}Pb/^{206}Pb$ values, whereas skarn-

Table 9.4 Summary table of results for Pb isotopic analysis of epidote samples from the Superior district. All sample locations provided in Appendix 3A.

| Sample ID | Rock Type | Method | $^{207}Pb/^{206}Pb$ | Error (1σ) | $^{208}Pb/^{206}Pb$ | Error (1σ) | $^{206}Pb/^{204}Pb$ | Error (1σ) | $^{207}Pb/^{204}Pb$ | Error (1σ) | $^{208}Pb/^{204}Pb$ | Error (1σ) | $^{206}Pb/^{238}U$ | $^{208}Pb/^{232}Th$ |
|---|---|---|---|---|---|---|---|---|---|---|---|---|---|---|
| RE15JP106 | Dolerite | Geochronology | 0.867 | 0.001 | 2.120 | 0.003 | 17.87 | 0.04 | 15.50 | 0.03 | 37.94 | 0.1 | 28.60 | 104.9 |
| RE15JP150 | Dolerite | Geochronology | 0.895 | 0.002 | 2.115 | 0.004 | 17.38 | 0.09 | 15.53 | 0.07 | 36.74 | 0.2 | 8.404 | 10.11 |
| RE15JP181 | Kvs | Geochronology | 0.876 | 0.001 | 2.136 | 0.002 | 17.70 | 0.05 | 15.51 | 0.03 | 37.79 | 0.1 | 8.973 | 114.2 |
| RE15JP191 | Schist | Geochronology | 0.831 | 0.002 | 2.052 | 0.003 | 18.92 | 0.07 | 15.67 | 0.03 | 38.76 | 0.1 | 10.45 | 139.7 |
| RE16JP019 | Schist | Geochronology | 0.863 | 0.001 | 2.097 | 0.001 | 17.97 | 0.06 | 15.50 | 0.03 | 37.66 | 0.1 | 58.88 | 7511 |
| RE16JP031 | Andesite dike | Geochronology | 0.762 | 0.003 | 1.928 | 0.007 | 20.62 | 0.13 | 15.78 | 0.01 | 39.87 | 0.1 | 39.69 | 2274 |
| RE16JP035 | Schist | Geochronology | 0.930 | 0.003 | 2.182 | 0.005 | 16.53 | 0.08 | 15.36 | 0.03 | 36.08 | 0.1 | 37.84 | 1901 |
| RE16JP062 | Dolerite | Geochronology | 0.877 | 0.000 | 2.139 | 0.001 | 17.64 | 0.01 | 15.47 | 0.01 | 37.70 | 0.02 | 54.69 | 282.3 |
| RE16JP081 | Basalt | Geochronology | 0.879 | 0.001 | 2.091 | 0.006 | 17.61 | 0.04 | 15.48 | 0.03 | 36.89 | 0.1 | 23.56 | 8047 |
| RE16JP150 | Kvs | Geochronology | 0.872 | 0.001 | 2.128 | 0.001 | 17.74 | 0.02 | 15.47 | 0.02 | 37.78 | 0.1 | 7.835 | 564.0 |
| RE16JP157 | Dolerite | Geochronology | 0.878 | 0.0004 | 2.138 | 0.001 | 17.65 | 0.02 | 15.50 | 0.01 | 37.71 | 0.03 | 38.40 | 2342 |
| RE16JP194 | Quartz diorite | Geochronology | 0.883 | 0.0004 | 2.131 | 0.001 | 17.56 | 0.02 | 15.50 | 0.02 | 37.41 | 0.04 | 110.6 | 923.3 |
| RE16JP200 | Quartz diorite | Geochronology | 0.882 | 0.0005 | 2.184 | 0.001 | 17.52 | 0.01 | 15.47 | 0.01 | 38.28 | 0.02 | 250.7 | 500.4 |
| RE15JP053 | Kvs | Trace element | 0.85 | 0.02 | 2.14 | 0.02 | N/A | N/A | N/A | N/A | N/A | N/A | 5.463 | 22.77 |
| RE15JP091 | Basalt | Trace element | 0.88 | 0.01 | 2.07 | 0.02 | N/A | N/A | N/A | N/A | N/A | N/A | 20.20 | 5131 |
| RE15JP205 | Skarn | Trace element | 0.79 | 0.02 | 2.09 | 0.02 | N/A | N/A | N/A | N/A | N/A | N/A | 0.2436 | 0.2431 |
| RE15JP216 | Dolerite | Trace element | 0.85 | 0.02 | 1.95 | 0.05 | N/A | N/A | N/A | N/A | N/A | N/A | 115.0 | 5069 |
| RE16JP007 | Kvs | Trace element | 0.84 | 0.04 | 2.06 | 0.06 | N/A | N/A | N/A | N/A | N/A | N/A | 266.4 | 1089 |
| RE16JP012 | Quartz diorite | Trace element | 0.84 | 0.03 | 2.06 | 0.05 | N/A | N/A | N/A | N/A | N/A | N/A | 308.9 | 1726 |
| RE16JP014 | Schist | Trace element | 0.86 | 0.01 | 2.10 | 0.02 | N/A | N/A | N/A | N/A | N/A | N/A | 27.48 | 105.7 |
| RE16JP020 | Schist | Trace element | 0.82 | 0.01 | 2.09 | 0.03 | N/A | N/A | N/A | N/A | N/A | N/A | 10.60 | 61.11 |
| RE16JP022 | Dolerite | Trace element | 0.90 | 0.01 | 2.17 | 0.02 | N/A | N/A | N/A | N/A | N/A | N/A | 197.8 | 7405 |
| RE16JP028 | Basalt | Trace element | 0.83 | 0.01 | 2.00 | 0.02 | N/A | N/A | N/A | N/A | N/A | N/A | 170.8 | 1072 |
| RE16JP030 | Basalt | Trace element | 0.88 | 0.02 | 2.05 | 0.02 | N/A | N/A | N/A | N/A | N/A | N/A | 3.145 | 27.70 |
| RE16JP039 | Kvs | Trace element | 0.90 | 0.01 | 2.17 | 0.01 | N/A | N/A | N/A | N/A | N/A | N/A | 91.22 | 1547 |
| RE16JP040 | Kvs | Trace element | 0.90 | 0.01 | 2.19 | 0.02 | N/A | N/A | N/A | N/A | N/A | N/A | 49.94 | 29.72 |
| RE16JP045 | Kvs | Trace element | 0.88 | 0.01 | 2.14 | 0.03 | N/A | N/A | N/A | N/A | N/A | N/A | 6.859 | 479.2 |

| Sample ID | Rock Type | Method | $^{207}Pb/^{206}Pb$ | Error (1σ) | $^{208}Pb/^{206}Pb$ | Error (1σ) | $^{206}Pb/^{204}Pb$ | Error (1σ) | $^{207}Pb/^{204}Pb$ | Error (1σ) | $^{208}Pb/^{204}Pb$ | Error (1σ) | $^{206}Pb/^{238}U$ | $^{208}Pb/^{232}Th$ |
|---|---|---|---|---|---|---|---|---|---|---|---|---|---|---|
| RE15JP106 | Dolerite | Geochronology | 0.867 | 0.001 | 2.120 | 0.003 | 17.87 | 0.04 | 15.50 | 0.03 | 37.94 | 0.1 | 28.60 | 104.9 |
| RE15JP150 | Dolerite | Geochronology | 0.895 | 0.002 | 2.115 | 0.004 | 17.38 | 0.09 | 15.53 | 0.07 | 36.74 | 0.2 | 8.404 | 10.11 |
| RE15JP181 | Kvs | Geochronology | 0.876 | 0.001 | 2.136 | 0.002 | 17.70 | 0.05 | 15.51 | 0.03 | 37.79 | 0.1 | 8.973 | 114.2 |
| RE15JP191 | Schist | Geochronology | 0.831 | 0.002 | 2.052 | 0.003 | 18.92 | 0.07 | 15.67 | 0.03 | 38.76 | 0.1 | 10.45 | 139.7 |
| RE16JP019 | Schist | Geochronology | 0.863 | 0.001 | 2.097 | 0.001 | 17.97 | 0.06 | 15.50 | 0.03 | 37.66 | 0.1 | 58.88 | 75106 |
| RE16JP031 | Andesite dike | Geochronology | 0.762 | 0.003 | 1.928 | 0.007 | 20.62 | 0.13 | 15.78 | 0.01 | 39.87 | 0.1 | 39.69 | 2274 |
| RE16JP035 | Schist | Geochronology | 0.930 | 0.003 | 2.182 | 0.005 | 16.53 | 0.08 | 15.36 | 0.03 | 36.08 | 0.1 | 37.84 | 190099 |
| RE16JP062 | Dolerite | Geochronology | 0.877 | 0.000 | 2.139 | 0.001 | 17.64 | 0.01 | 15.47 | 0.01 | 37.70 | 0.02 | 54.69 | 282.3 |
| RE16JP081 | Basalt | Geochronology | 0.879 | 0.001 | 2.091 | 0.006 | 17.61 | 0.04 | 15.48 | 0.03 | 36.89 | 0.1 | 23.56 | 804668 |
| RE16JP150 | Kvs | Geochronology | 0.872 | 0.001 | 2.128 | 0.001 | 17.74 | 0.02 | 15.47 | 0.02 | 37.78 | 0.1 | 7.835 | 564.0 |
| RE16JP157 | Dolerite | Geochronology | 0.878 | 0.0004 | 2.138 | 0.001 | 17.65 | 0.02 | 15.50 | 0.01 | 37.71 | 0.03 | 38.40 | 2342 |
| RE16JP194 | Quartz diorite | Geochronology | 0.883 | 0.0004 | 2.131 | 0.001 | 17.56 | 0.02 | 15.50 | 0.02 | 37.41 | 0.04 | 110.6 | 923.3 |
| RE16JP200 | Quartz diorite | Geochronology | 0.882 | 0.0005 | 2.184 | 0.001 | 17.52 | 0.01 | 15.47 | 0.01 | 38.28 | 0.02 | 250.7 | 500.4 |
| RE15JP053 | Kvs | Trace element | 0.85 | 0.02 | 2.14 | 0.02 | N/A | N/A | N/A | N/A | N/A | N/A | 5.463 | 22.77 |
| RE15JP091 | Basalt | Trace element | 0.88 | 0.01 | 2.07 | 0.02 | N/A | N/A | N/A | N/A | N/A | N/A | 20.20 | 5131 |
| RE15JP205 | Skarn | Trace element | 0.79 | 0.02 | 2.09 | 0.02 | N/A | N/A | N/A | N/A | N/A | N/A | 0.2436 | 0.2431 |
| RE15JP216 | Dolerite | Trace element | 0.85 | 0.02 | 1.95 | 0.05 | N/A | N/A | N/A | N/A | N/A | N/A | 114.96 | 5069 |
| RE16JP007 | Kvs | Trace element | 0.84 | 0.04 | 2.06 | 0.06 | N/A | N/A | N/A | N/A | N/A | N/A | 266.40 | 1089 |
| RE16JP012 | Quartz diorite | Trace element | 0.84 | 0.03 | 2.06 | 0.05 | N/A | N/A | N/A | N/A | N/A | N/A | 308.94 | 1726 |
| RE16JP014 | Schist | Trace element | 0.86 | 0.01 | 2.10 | 0.02 | N/A | N/A | N/A | N/A | N/A | N/A | 27.48 | 105.7 |
| RE16JP020 | Schist | Trace element | 0.82 | 0.01 | 2.09 | 0.03 | N/A | N/A | N/A | N/A | N/A | N/A | 10.60 | 61.11 |
| RE16JP022 | Dolerite | Trace element | 0.90 | 0.01 | 2.17 | 0.02 | N/A | N/A | N/A | N/A | N/A | N/A | 197.8 | 7405 |
| RE16JP028 | Basalt | Trace element | 0.83 | 0.01 | 2.00 | 0.02 | N/A | N/A | N/A | N/A | N/A | N/A | 170.8 | 10718 |
| RE16JP030 | Basalt | Trace element | 0.88 | 0.02 | 2.05 | 0.02 | N/A | N/A | N/A | N/A | N/A | N/A | 3.145 | 27.70 |
| RE16JP039 | Kvs | Trace element | 0.90 | 0.01 | 2.17 | 0.01 | N/A | N/A | N/A | N/A | N/A | N/A | 91.22 | 1547 |
| RE16JP040 | Kvs | Trace element | 0.90 | 0.01 | 2.19 | 0.02 | N/A | N/A | N/A | N/A | N/A | N/A | 49.94 | 29.72 |
| RE16JP045 | Kvs | Trace element | 0.88 | 0.01 | 2.14 | 0.03 | N/A | N/A | N/A | N/A | N/A | N/A | 6.859 | 479.2 |
| RE16JP046 | Kvs | Trace element | 0.88 | 0.02 | 2.14 | 0.02 | N/A | N/A | N/A | N/A | N/A | N/A | 13.81 | 201.6 |
| RE16JP047 | Kvs | Trace element | 0.88 | 0.01 | 2.11 | 0.02 | N/A | N/A | N/A | N/A | N/A | N/A | 15.76 | 197.8 |

| Sample ID | Rock Type | Method | $^{207}Pb/^{206}Pb$ | Error (1σ) | $^{208}Pb/^{206}Pb$ | Error (1σ) | $^{206}Pb/^{204}Pb$ | Error (1σ) | $^{207}Pb/^{204}Pb$ | Error (1σ) | $^{208}Pb/^{204}Pb$ | Error (1σ) | $^{206}Pb/^{238}U$ | $^{208}Pb/^{232}Th$ |
|---|---|---|---|---|---|---|---|---|---|---|---|---|---|---|
| RE16JP048 | Kvs | Trace element | 0.85 | 0.01 | 2.11 | 0.02 | N/A | N/A | N/A | N/A | N/A | N/A | 7.109 | 965.6 |
| RE16JP050 | Kvs | Trace element | 0.86 | 0.01 | 2.10 | 0.02 | N/A | N/A | N/A | N/A | N/A | N/A | 61.30 | 536.4 |
| RE16JP052 | Kvs | Trace element | 0.88 | 0.01 | 2.13 | 0.03 | N/A | N/A | N/A | N/A | N/A | N/A | 107.9 | 4459 |
| RE16JP053 | Kvs | Trace element | 0.89 | 0.02 | 2.14 | 0.04 | N/A | N/A | N/A | N/A | N/A | N/A | 89.20 | 3825 |
| RE16JP054 | Kvs | Trace element | 0.88 | 0.01 | 2.15 | 0.02 | N/A | N/A | N/A | N/A | N/A | N/A | 8.575 | 853.1 |
| RE16JP056 | Kvs | Trace element | 0.88 | 0.01 | 2.15 | 0.02 | N/A | N/A | N/A | N/A | N/A | N/A | 13.79 | 1956 |
| RE16JP057 | Kvs | Trace element | 0.89 | 0.07 | 2.16 | 0.10 | N/A | N/A | N/A | N/A | N/A | N/A | 1094 | 64913 |
| RE16JP063 | Dolerite | Trace element | 0.85 | 0.01 | 2.11 | 0.02 | N/A | N/A | N/A | N/A | N/A | N/A | 74.36 | 1668 |
| RE16JP067 | Quartz diorite | Trace element | 0.89 | 0.01 | 2.16 | 0.02 | N/A | N/A | N/A | N/A | N/A | N/A | 39.08 | 556.0 |
| RE16JP077 | Quartz diorite | Trace element | 0.85 | 0.01 | 2.10 | 0.02 | N/A | N/A | N/A | N/A | N/A | N/A | 84.11 | 781.9 |
| RE16JP083 | Basalt | Trace element | 0.85 | 0.01 | 2.06 | 0.03 | N/A | N/A | N/A | N/A | N/A | N/A | 4.628 | 171.9 |
| RE16JP091 | Kvs | Trace element | 0.88 | 0.01 | 2.12 | 0.02 | N/A | N/A | N/A | N/A | N/A | N/A | 15.03 | 229.4 |
| RE16JP095 | Kvs | Trace element | 0.90 | 0.01 | 2.15 | 0.02 | N/A | N/A | N/A | N/A | N/A | N/A | 31.57 | 1419 |
| RE16JP097 | Kvs | Trace element | 0.88 | 0.02 | 2.14 | 0.03 | N/A | N/A | N/A | N/A | N/A | N/A | 4.599 | 75.93 |
| RE16JP100 | Kvs | Trace element | 0.85 | 0.04 | 2.08 | 0.05 | N/A | N/A | N/A | N/A | N/A | N/A | 5.560 | 160.4 |
| RE16JP101 | Dolerite | Trace element | 0.88 | 0.01 | 2.15 | 0.01 | N/A | N/A | N/A | N/A | N/A | N/A | 15.35 | 1778 |
| RE16JP104 | Dolerite | Trace element | 0.89 | 0.05 | 2.15 | 0.07 | N/A | N/A | N/A | N/A | N/A | N/A | 195.0 | 10300 |
| RE16JP107 | Dolerite | Trace element | 0.88 | 0.01 | 2.17 | 0.02 | N/A | N/A | N/A | N/A | N/A | N/A | 51.47 | 5293 |
| RE16JP145 | Kvs | Trace element | 0.87 | 0.01 | 2.11 | 0.02 | N/A | N/A | N/A | N/A | N/A | N/A | 1.818 | 1392 |
| RE16JP147 | Kvs | Trace element | 0.88 | 0.07 | 2.15 | 0.10 | N/A | N/A | N/A | N/A | N/A | N/A | 272.1 | 9254 |
| RE16JP149 | Kvs | Trace element | 0.89 | 0.01 | 2.16 | 0.01 | N/A | N/A | N/A | N/A | N/A | N/A | 161.0 | 892.8 |
| RE16JP153 | Kvs | Trace element | 0.87 | 0.02 | 2.07 | 0.03 | N/A | N/A | N/A | N/A | N/A | N/A | 0.5021 | 2.734 |
| RE16JP188 | Breccia | Trace element | 0.87 | 0.01 | 2.13 | 0.02 | N/A | N/A | N/A | N/A | N/A | N/A | 91.89 | 1088 |
| RE16JP192 | Schist | Trace element | 0.86 | 0.01 | 2.14 | 0.01 | N/A | N/A | N/A | N/A | N/A | N/A | 493.7 | 5649 |
| RE16JP193 | Dolerite | Trace element | 0.85 | 0.02 | 2.02 | 0.03 | N/A | N/A | N/A | N/A | N/A | N/A | 74.90 | 1301 |
| RE16JP194 | Dolerite | Trace element | 0.88 | 0.01 | 2.15 | 0.02 | N/A | N/A | N/A | N/A | N/A | N/A | 111.2 | 6482 |
| RE16JP195 | Dolerite | Trace element | 0.88 | 0.01 | 2.12 | 0.02 | N/A | N/A | N/A | N/A | N/A | N/A | 114.3 | 1195 |
| RE16JP196 | Quartz diorite | Trace element | 0.90 | 0.01 | 2.21 | 0.02 | N/A | N/A | N/A | N/A | N/A | N/A | 47.58 | 217.1 |
| RE16JP197 | Quartz diorite | Trace element | 0.86 | 0.01 | 2.19 | 0.02 | N/A | N/A | N/A | N/A | N/A | N/A | 8.230 | 73.87 |

| Sample ID | Rock Type | Method | $^{207}Pb/^{206}Pb$ | Error (1σ) | $^{208}Pb/^{206}Pb$ | Error (1σ) | $^{206}Pb/^{204}Pb$ | Error (1σ) | $^{207}Pb/^{204}Pb$ | Error (1σ) | $^{208}Pb/^{204}Pb$ | Error (1σ) | $^{206}Pb/^{238}U$ | $^{208}Pb/^{232}Th$ |
|---|---|---|---|---|---|---|---|---|---|---|---|---|---|---|
| RE16JP199 | Quartz diorite | Trace element | 0.87 | 0.01 | 2.12 | 0.02 | N/A | N/A | N/A | N/A | N/A | N/A | 9.506 | 1195 |
| RE16JP201 | Kvs | Trace element | 0.87 | 0.01 | 2.08 | 0.03 | N/A | N/A | N/A | N/A | N/A | N/A | 4.450 | 103.5 |
| RE16JP203 | Dolerite | Trace element | 0.90 | 0.01 | 2.16 | 0.02 | N/A | N/A | N/A | N/A | N/A | N/A | 24.19 | 2830 |
| RE16JP206 | Dolerite | Trace element | 0.87 | 0.01 | 2.11 | 0.02 | N/A | N/A | N/A | N/A | N/A | N/A | 42.63 | 531.5 |
| RE16JP207 | Dolerite | Trace element | 0.88 | 0.03 | 2.13 | 0.04 | N/A | N/A | N/A | N/A | N/A | N/A | 11.43 | 633.9 |
| RE16JP237 | Dolerite | Trace element | 0.88 | 0.09 | 2.14 | 0.14 | N/A | N/A | N/A | N/A | N/A | N/A | 20.03 | 53892 |
| RE16JPOR1 | Skarn | Trace element | 0.83 | 0.03 | 2.05 | 0.04 | N/A | N/A | N/A | N/A | N/A | N/A | 8.920 | 6860 |

hosted samples tend to plot at both lower $^{207}Pb/^{206}Pb$ and $^{208}Pb/^{206}Pb$ values compared to the rest of the trace element $Pb_{epidote}$ isotopic data cluster, implying some protolith control on $^{206}Pb_{epidote}$ compositions (Figure 9.15). Schist-hosted samples are more radiogenic on average (Figure 9.15 C), probably due to mobile radiogenic Pb contamination. The average $Pb_{epidote}$ isotopic compositions from dolerite sills, Kvs and quartz diorite are similar (Figure 9.15 C). Apache Basalt samples typically tend to have lower $^{206}Pb/^{238}U$ values. $^{206}Pb/^{238}U$ in the same host rock change dramatically (e.g., RE16JP081, RE16JP083; Table 9.4,) suggesting the presence of complicated and heterogeneous Pb sources. Individual epidote spot analyses have yielded both low and high $^{206}Pb/^{238}U$ (Appendix 4B).

***Temporal isotopic change***

Separating samples paragenetically highlights changes in $Pb_{sulfides}$ isotopic composition with time (Figure 9.13 and Figure 9.14). The temporal change at Resolution is limited, possibly showing a subtle shift towards more radiogenic values with time for both $^{206}Pb/^{204}Pb$ and $^{208}Pb/^{204}Pb$, though the associated errors caused by the low abundances of Pb, make this assertion equivocal (Figure 9.13 A-B). There is a minor increase in $^{207}Pb/^{206}Pb$ and $^{208}Pb/^{206}Pb$ that can be seen at Resolution, with phyllic, propylitic and to a lesser extent intermediate argillic samples all plotting at higher values compared to the potassic-altered sample. One propylitic sample has lower, more radiogenic $^{207}Pb/^{206}Pb$ and $^{208}Pb/^{206}Pb$ values (Figure 9.13 C).

Two sulfide samples with high $^{206}Pb/^{204}Pb$ values were analysed from Magma and Silver King – bornite from an intermediate sulfidation vein sample and pyrite from a potassic-altered sample, respectively (Table 9.3). The remaining data cluster around the 500 Ma isochron on the Arizona growth curve (Figure 9.14). High sulfidation-state mineral assemblages from at the western end of the Magma vein have $^{206}Pb/^{204}Pb$ ratios of around 17.85. Intermediate sulfidation and propylitic assemblages from the same area have $^{206}Pb/^{204}Pb$ values around 17.50, a trend also reflected in the $^{207}Pb/^{204}Pb$ and $^{208}Pb/^{204}Pb$ ratios (Figure 9.14 A-B). The observed trend is somewhat different on the $^{207}Pb/^{206}Pb$ vs $^{208}Pb/^{206}Pb$ diagram (Figure 9.14 C). While the general progression is still toward less radiogenic $^{207}Pb/^{204}Pb$ and $^{208}Pb/^{204}Pb$ isotopic compositions at Magma, four high sulfidation phases (from two samples) from the western end of the vein cluster around 350-400 Ma on the growth curve (Figure 9.14 C), possibly indicating a different source of Pb for these samples that are interpreted to be early in the overall paragenetic history of Magma (e.g., Gustafson, 1961). This $Pb_{sulfide}$ isotopic signature could reflect distinct magmatic source, less contaminated with lower crustal Pb than the remaining $Pb_{sulfide}$ samples, or that it contains a larger component of wallrock-derived mobile $^{206}Pb$. Since the remaining $Pb_{sulfide}$ samples from Magma are unlikely to be derived from a different magmatic source, it is interpreted that the different $Pb_{sulfide}$ isotopic signature observed in some high sulfidation samples reflects the incorporation of mobile Pb from the Proterozoic wall-rocks. In contrast, the low $^{207}Pb/^{206}Pb$ vs $^{208}Pb/^{206}Pb$ observed in the potassic sample from Silver King, that is associated with a distinct early Laramide igneous complex, is probably

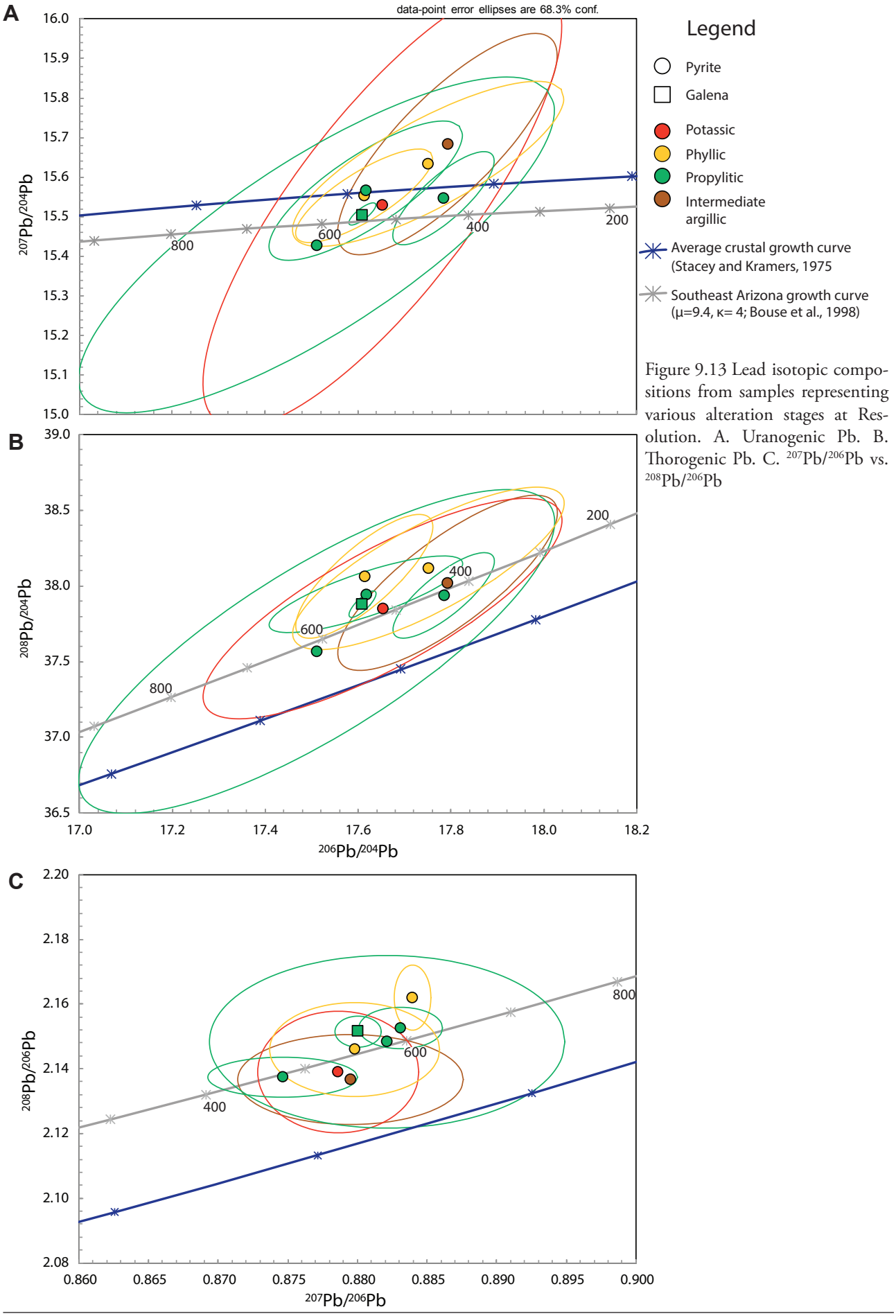


Figure 9.13 Lead isotopic compositions from samples representing various alteration stages at Resolution. A. Uranogenic Pb. B. Thorogenic Pb. C. $^{207}Pb/^{206}Pb$ vs. $^{208}Pb/^{206}Pb$

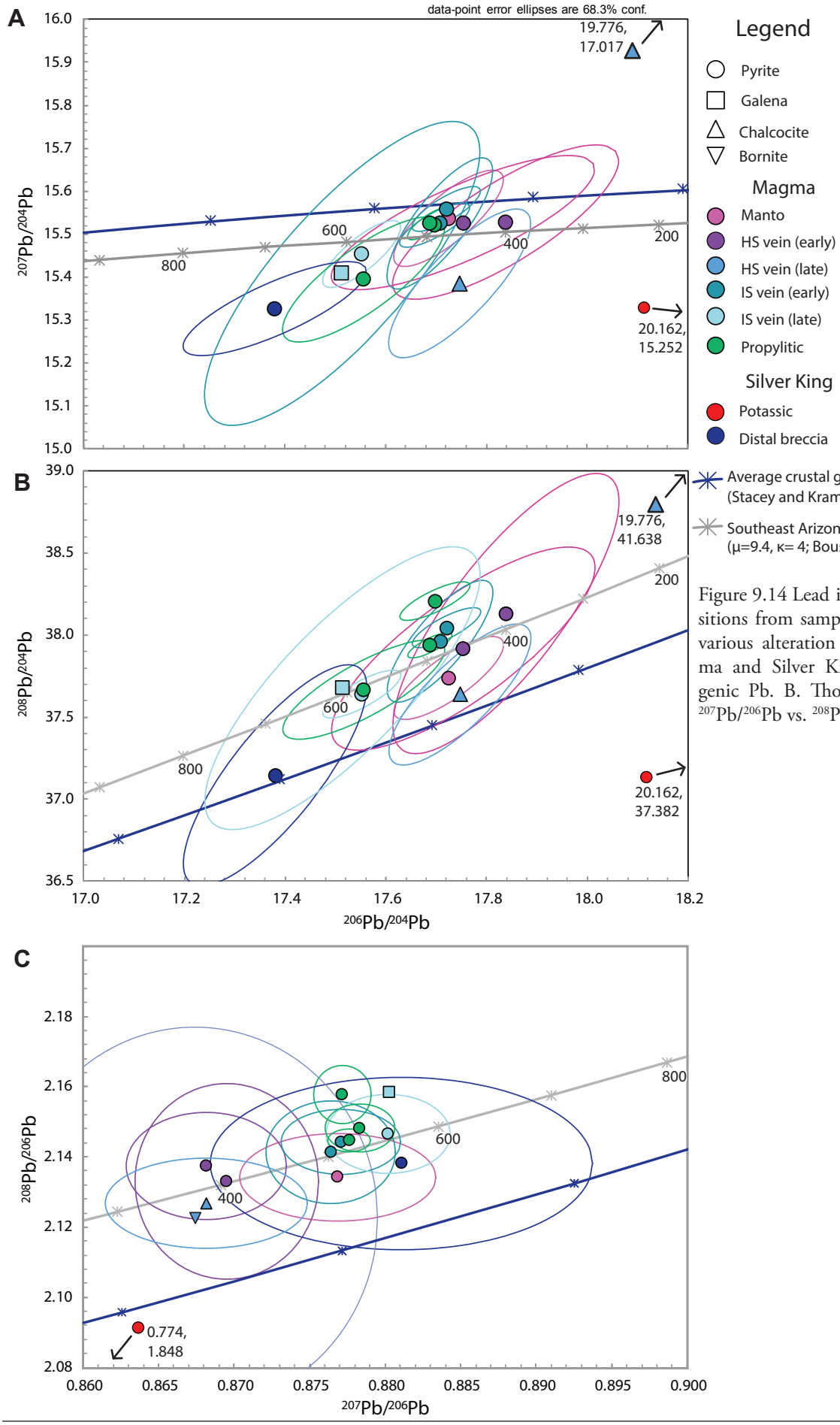


Figure 9.14 Lead isotopic compositions from samples representing various alteration stages at Magma and Silver King. A. Uranogenic Pb. B. Thorogenic Pb. C. $^{207}Pb/^{206}Pb$ vs. $^{208}Pb/^{206}Pb$ plot.

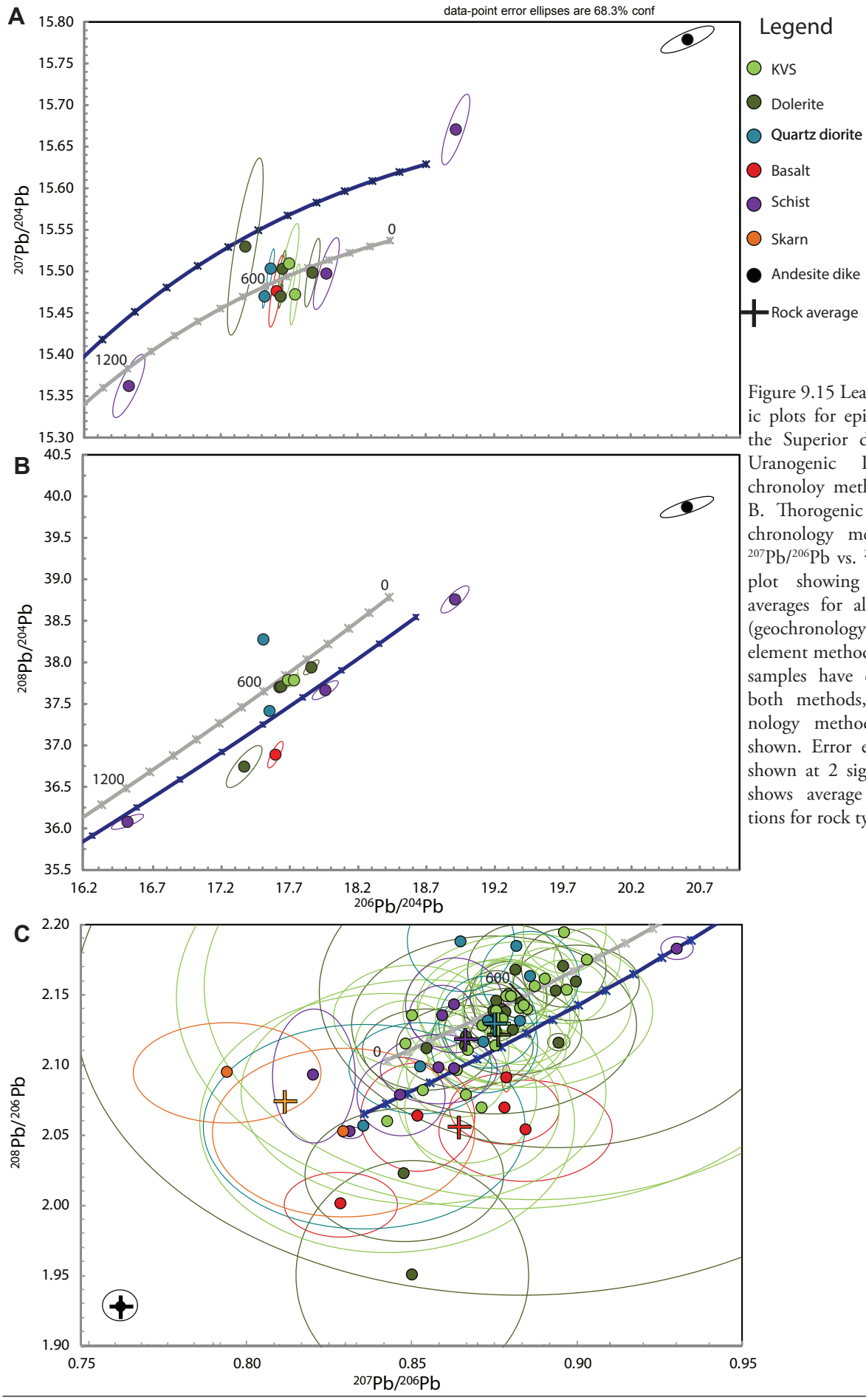


Figure 9.15 Lead isotopic plots for epidote from the Superior district. A. Uranogenic Pb (geochronoloy method only). B. Thorogenic Pb (geochronology method). C $^{207}Pb/^{206}Pb$ vs. $^{208}Pb/^{206}Pb$ plot showing weighted averages for all samples, (geochronology and trace element methods). Where samples have data from both methods, geochronology method data is shown. Error ellipses are shown at 2 sigma. Cross shows average compositions for rock types.

the result of a less lower crustally contaminated magmatic source, as well as mobile Pb from Proterozoic wallrocks.

***Comparison between deposits***

Pb isotope data from galena tend to have low analytical uncertainties. They are used here to compare Pb isotope compositions between deposits in the district (Table 9.3). Galena from a propylitic-altered rock from Resolution, and an intermediate sulfidation vein at Magma have been plotted together with data from Bouse et al. (1999; Figure 9.16). Unfortunately, no data for galena from Silver King was available at the time of this study. The results show that the three samples, despite their low uncertainties, overlap and so no distinctions can be made between the samples. This permits a common source of Pb.

Plotting all the $Pb_{sulfide}$ data from Resolution and Magma shows they have similar $^{206}Pb/^{204}Pb$ and $^{208}Pb/^{204}Pb$ values, but Resolution have higher $^{207}Pb/^{204}Pb$ values (Figure 9.17 A-B). Resolution also shows higher (less radiogenic) $^{207}Pb/^{206}Pb$ values (Figure 9.17 C), suggesting that although galena from both deposits appears similar, there may be an observable distinction in overall Pb source when all the data are plotted.

***District scale spatial zonation***

Spatial representation of Pb isotope compositions can be difficult to interpret due to the need for two ratios to be plotted simultaneously on a growth curve. To overcome this, Pb isotope ratios can be combined to produce a single number that approximates the position of the sample along the growth curve, or the degree to which it is radiogenic (Figure 9.18 A). For the current study, the $^{207}Pb/^{206}Pb$ and $^{208}Pb/^{206}Pb$ ratios have been combined using the expression: $((^{207}Pb/^{206}Pb)*3.5) + (^{208}Pb/^{206}Pb)$ to produce an arbitrary number that represents how radiogenic each sample is (Figure 9.18 A). Higher values equate to less radiogenic and potentially more magmatic dominated Pb (Figure 9.18 A). When plotted spatially, there is a well-developed $Pb_{sulfide}$ isotopic pattern across the Superior district (Figure 9.18 B). Broadly, Resolution demonstrates a general outward transition from lower $Pb_{sulfide}$ (more radiogenic) values that approximate the down-dip projection of the Anxiety fault, to a halo of higher (less radiogenic) $Pb_{sulfide}$ isotope values (Figure 9.18 B). This gradient is also visible at Magma, where the samples from the western end of the vein have low, more radiogenic values increasing in an easterly direction, away from the Concentrator Fault. The transition at Magma extends only as far as 492500 mE, where values begin to decrease again (Figure 9.18 B).

Another way to spatially visualise Pb isotopic compositional changes is to plot the data as a function of distance from Resolution. Since the distance to the hypothetical centre of Resolution is known, isotopic ratios of samples from this deposit can be plotted in this way (Figure 9.19). As there is a large spread of data and high uncertainty associated with some analyses, an uncertainty threshold of 50% was applied to the data, reducing the maximum uncertainty from >2 to <0.02. Although this removes 50% of the data,

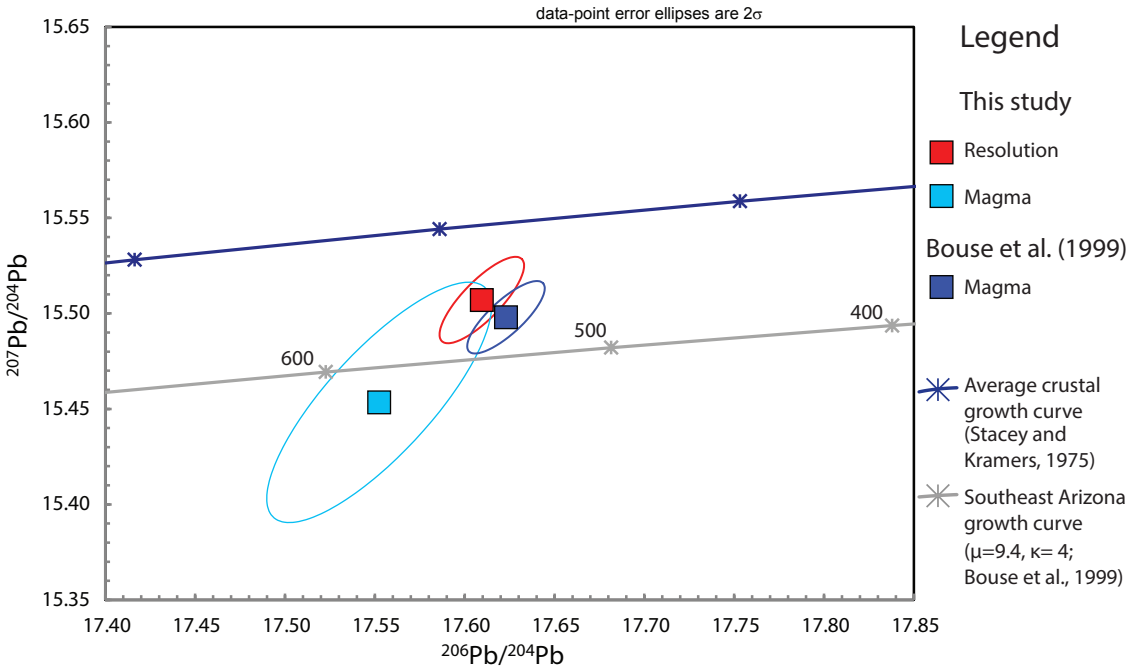


Figure 9.16 Comparative uranogenic Pb plot showing the Pb isotopic compositions of galena from Resolution and Magma, including data from Bouse et al. (1999).

it means only the most precise analyses are displayed. The closest samples to Resolution have low values and are surrounded by a halo of higher radiogenic $Pb_{sulfide}$ values between 750 - 1000 m (Figure 9.19). One propylitic sample is offset downwards from this main trend of high values. Beyond the shoulder of high, less radiogenic samples, values return to levels similar to the centre of the system at around 1,250 m, before becoming highly variable from 2 km onwards. The large range in Pb isotopic signatures distal to Resolution hint at a complex plumbing network outboard from the deposit (Figure 9.19). Given the strong structural control on distal fluid flow around Resolution, especially with regard to the graben-bounding faults, the notion of compartmentalised flow paths is plausible. However, a more detailed understanding of the deep plumbing system under and adjacent to Resolution is required to fully resolve whether this occurs.

Similarly to $Pb_{sulfides}$ data, $Pb_{epidote}$ data can be calculated as a single variable that approximates the degree to which the sample is radiogenic, in order to enable spatial visualisation (Figure 9.18 B, Figure 9.19 and Figure 9.20). $Pb_{epidote}$ isotopic composition demonstrates a well-defined halo of radiogenic values immediately surrounding the Resolution ore body up to a distance of approximately 2 km (Figure 9.20 A). The proximal $Pb_{epidote}$ isotopic low in the SE of the graben is controlled primarily by basalt samples with low $^{206}Pb/^{238}U$ values, indicative of at least some in situ radiogenic component. The variability in epidote $^{206}Pb/^{238}U$ values highlight the location of major underground structural features (Figure 9.20 B). This could imply that the Laramide epidotes spatially associated with these structures are U-enriched compared to other samples, possibly at least in part derived from leaching of the local Proterozoic rocks.

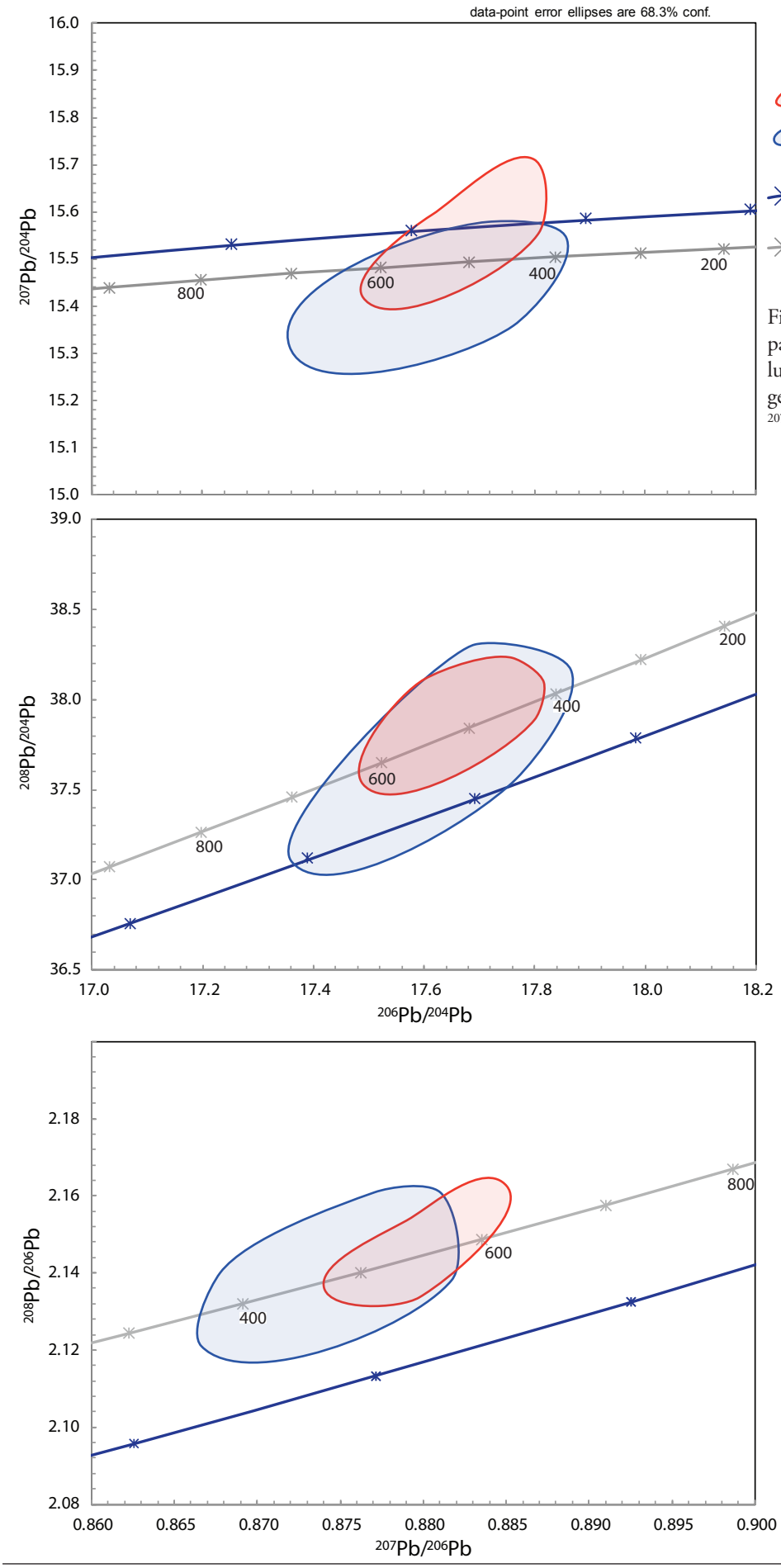


Figure 9.17 $Pb_{sulfide}$ isotopic comparison of samples from Resolution and Magma. A. Uranogenic Pb. B. Thorogenic Pb. C. $^{207}Pb/^{206}Pb$ vs. $^{208}Pb/^{206}Pb$ plot.

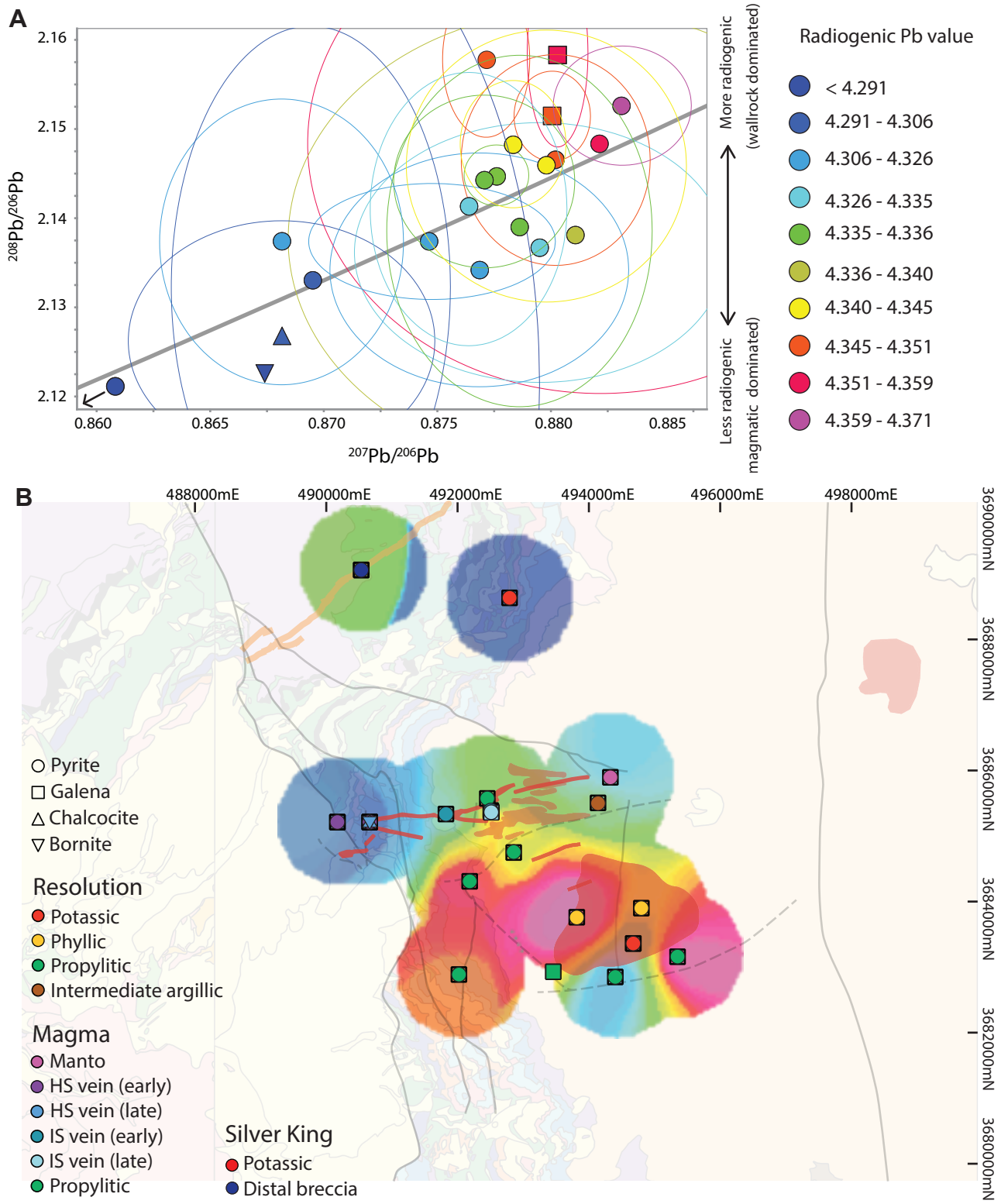


Figure 9.18 A. $^{207}Pb/^{206}Pb$ vs. $^{208}Pb/^{206}Pb$ plot showing the radiogenic $Pb_{sulfides}$ value for all samples from the Superior district on the SE Arizona growth curve Error ellipses are shown at 2 sigma. Inverted colour scale to emphasise magmatic Pb. B. Gridded radiogenic $Pb_{sulfides}$ value for sample averages from the Superior district.

A key difference between the two data sets is the epidote sample with a $^{206}Pb/^{204}Pb$ value of 16.527 (Table 9.4; Figure 9.15 A-B). The position of this particularly non-radiogenic sample on the growth curve suggests it may not related to the same hydrothermal event as Resolution or Magma. It may be

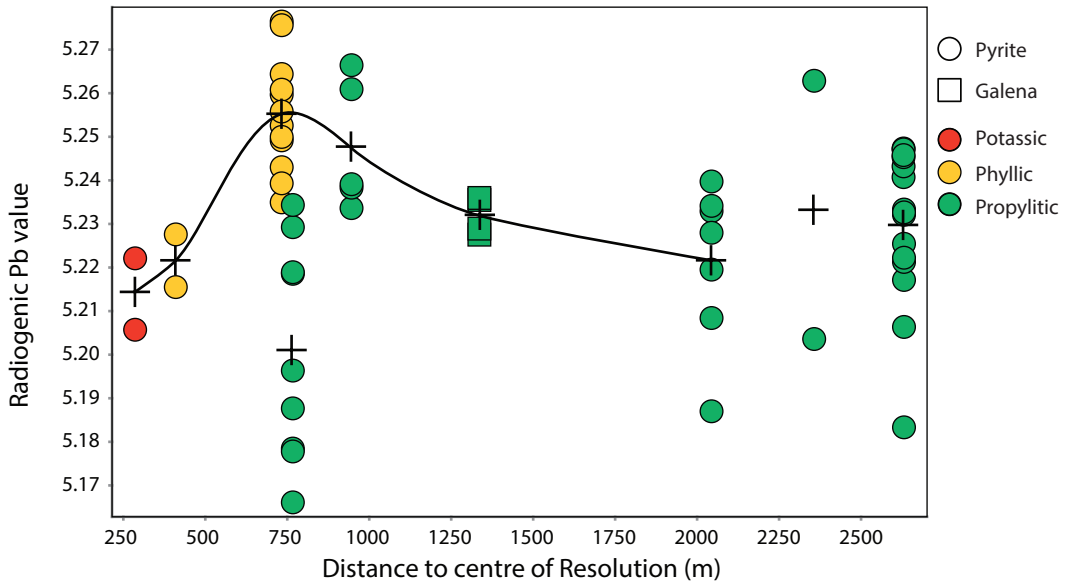


Figure 9.19 Plot of combined Pb of individual pyrite spot analyses and sample medians (crosses) plotted as a function of distance to the centre of the Resolution deposit. A threshold of >0.006 $^{207}Pb/^{206}Pb$ uncertainty (50% of all data) was applied.

that this samples represents a magmatic Pb source that was more strongly contaminated by the lower crust (e.g., Bouse et al., 1999) or was derived from a more strongly metasomatised SCLM source than the other $Pb_{epidote}$ and $Pb_{sulfide}$ samples from the Superior district.

Another key difference between $Pb_{sulfides}$ and $Pb_{epidote}$ relates to Proterozoic basalts in the SE corner of the graben, where $Pb_{sulfides}$ suggest a Laramide magmatic signature (Table 9.4; Figure 9.18 B). However, $Pb_{epidote}$ in this area are significantly more radiogenic, with low $^{206}Pb/^{238}U$, indicative of a Proterozoic U source for some of the Pb in these epidotes. It may be that there is Proterozoic epidote and Laramide pyrite in this sample.

The stronger $Pb_{epidote}$ anomaly at Silver King compared to Resolution may relate to the distance from source rock and/or the lesser degree to which the pluton it was contaminated in the lower crust. Alteration and mineralisation from the broader Silver King system is hosted within or adjacent to its progenitor intrusion. The progenitor intrusion at Resolution has not been intersected in drilling. Therefore, the ore fluids at Resolution have travelled an unknown distance through radiogenic upper crustal Proterozoic country rocks after exsolution, thereby imparting a slightly subdued Pb isotopic signal. Despite its subdued nature, the Resolution Pb isotopic halo is considerably larger than that observed around the apex of the quartz diorite stock at Silver King.

#### 9.4.2.4 Summary

Overall the retarded Pb isotopic signature of sulfides and epidote observed in the Superior district is consistent with that observed throughout the western US (e.g., Bouse et al., 1999). The low Pb abundances in some samples resulted in large uncertainties for $^{204}Pb$ and the rejection of some analyses. At the district scale, less radiogenic $Pb_{sulfide}$ isotopic values envelope Resolution, whereas peripheral alteration types and

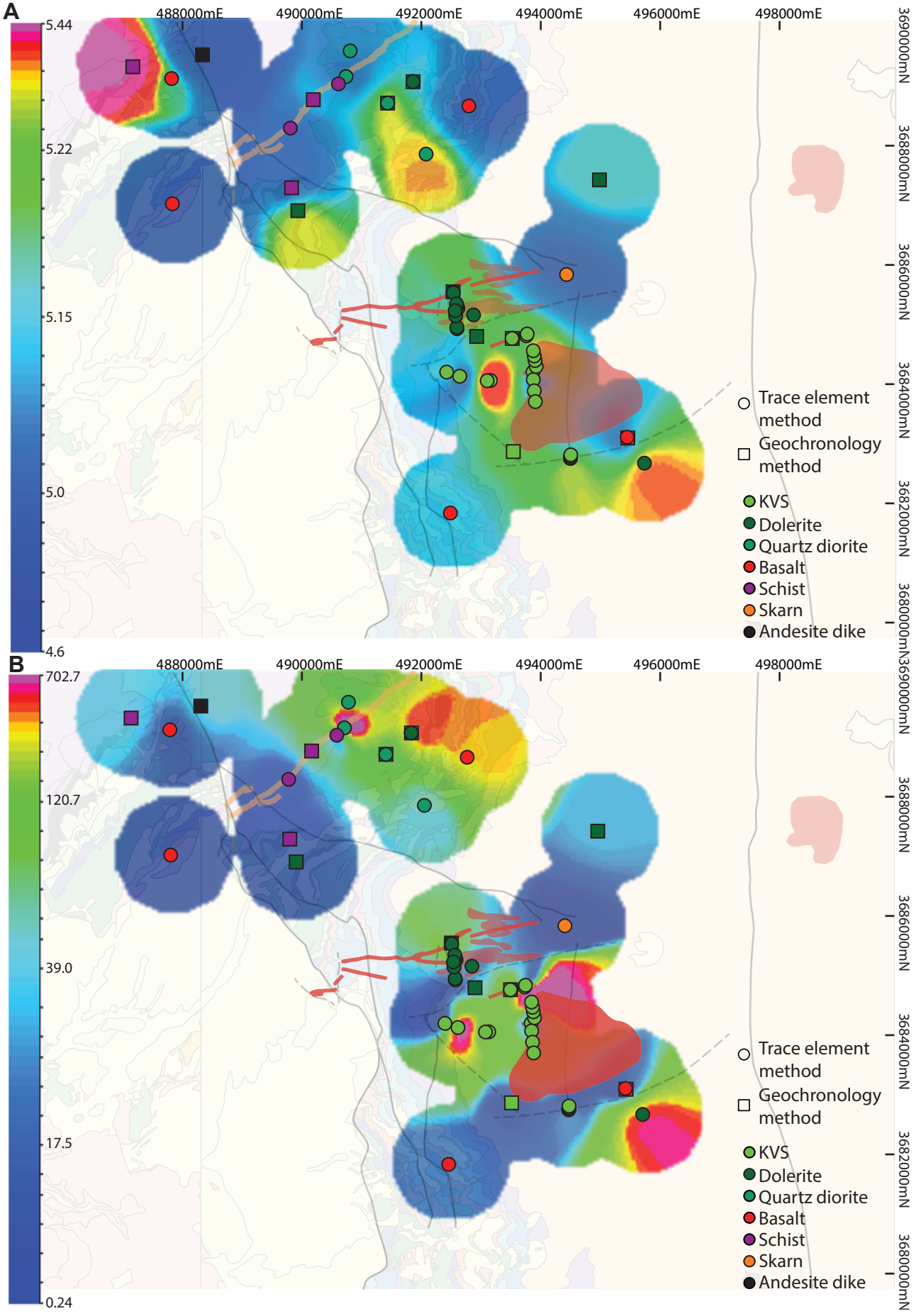


Figure 9.20 Gridded Pb isotope results for the Superior district. A. Radiogenic Pb value. B. $^{206}Pb/^{238}U$

smaller deposits tend to have more radiogenic Pb (Figure 9.18 B). Previous studies have interpreted this Pb isotopic pattern as reflecting increased recycling of lower crustal Pb by Laramide magmatism over time and more radiogenic Pb reflecting isotopic mixing with some scavenging of upper crustal Pb from Proterozoic country rocks (Bouse et al., 1999 and references therein). Alternatively, the generally non-radiogenic nature of Pb isotopes in the district could relate to the influence of metasomatised SCLM (Pettke et al., 2010), although the two hypotheses are impossible to evaluate here.

Magma has somewhat more radiogenic $^{206}Pb_{sulfide}$ isotopic compositions than Resolution (Table 9.3; Figure 9.13 and Figure 9.14), implying that either Magma is sourced from an isotopically distinct fluid or, is derived from the distal Resolution ore fluid that was contaminated by upper crustal mobile Pb during fluid-rock interaction. A direct comparison of Pb isotopic composition of galena is permissive of either scenario.

The general similarity in $^{204}Pb$ compositions between $Pb_{sulfide}$ and $Pb_{epidote}$ is consistent with epidote and sulfides being deposited from the same hydrothermal fluid. As with $Pb_{sulfides}$, the clustering around the 500 Ma position on growth curve (Figure 9.13 and Figure 9.14) could to relate to either the Laramide recycling of lower crustal Pb (e.g., Bouse et al., 1999), or input from a metasomatised SCLM Pb source (e.g., Pettke et al., 2010).

Resolution is characterised by a large, but amplitude non-radiogenic Pb anomaly based on both the $Pb_{epidote}$ and $Pb_{sulfide}$ data (Figure 9.18 B and Figure 9.20). Magma is more radiogenic towards the western end of the vein - although it is not possible to discriminant upper crustal mobile Pb as a result of interaction with Proterozoic country rocks (i.e. distal to Resolution) from a distinct fluid source with less lower crustal Pb.

There appears to be only limited host rock control on radiogenic Pb in epidote from the Superior district. In the Superior district, lower $^{206}Pb/^{238}U$ in epidote correlates spatially with the location of the North and South Boundary Faults, and to a lesser extent the Concentrator and Conley Springs Faults, (Figure 9.20 B). This suggests that the Laramide epidotes spatially associated with these structures are U-enriched compared to other samples, possibly at least in part derived from leaching of the local Proterozoic rocks.

## 9.5 Conclusions

### 9.5.1 Carbon and oxygen isotopes

- $\delta^{13}C$ and $\delta^{18}O$ from main stage calcite from epithermal veins in the Superior district range from -9.5 to 2.4 ‰ and 10.5 to 23.7 ‰ respectively (Table 9.1; Figure 9.4)
- The large spread in $\delta^{13}C$ values most likely relates to isotopic exchange with a wide variety of carbon sources in the host stratigraphy (Table 9.1; Figure 9.4; (Desborough et al., 1984)

- $\delta^{18}O_{calcite}$ isotopic composition lies between magmatic values and those of the Paleozoic sediments from the Superior district and are interpreted to reflect a distal cooling trend (Figure 9.4)

- Paragenetically, hydrothermal carbonate shows a decrease in $\delta^{18}O_{calcite}$ values over time from 18.2 ‰ to 17.4 ‰ and is interpreted to be reflect fluid mixing between the magmatic-hydrothermal fluid and meteoric water partially equilibrated with carbonate wall rocks (Figure 9.4)

- Spatially, the $\delta^{18}O_{calcite}$ data define a $\delta^{18}O$ depletion halo at the eastern extent of some epithermal veins (Figure 9.5 A), consistent with Resolution being their fluid source. Whole-rock trace element anomalism in the centre and south of the Superior range front also support an easterly fluid source, consistent with Resolution (Figure 9.7 and 9.8)

### 9.5.2 Sulfur isotopes

- $\delta^{34}S$ of sulfides in the Superior district range from -9.64 ‰ and +4.41 ‰ (Table 9.2; Figure 9.9 and 9.10), suggesting they evolved under oxidising conditions, and that magmatic sulfur was the dominant sulfur source (Ohmoto and Rye 1979, Field and Fifarek, 1985)

- Some $\delta^{34}S$-enriched sulfur isotope compositions are observed in skarn samples from both Magma and Resolution, suggesting some evaporate-sourced sulfur was locally fixed in skarn-related sulfides, most notably in the Mescal Limestone (Figure 9.9)

- Fractionation of $^{34}S$ is dominated by increasing oxidation state and decreasing temperature in the central part of Resolution, where the $\delta^{34}S$ values become progressively more negative with later paragenetic stages and increasing proximity to the paleosurface (Ohmoto and Rye, 1979; Rye, 1993; Figure 9.11). Outwards from the centre of Resolution, fluid-rock interaction strongly influenced fractionation of $^{34}S$, where fluids migrated laterally through cooler, more reduced country rocks $\delta^{34}S$ trends towards more positive values

- Spatially, the depletion in $\delta^{34}S$ approximates the locations of ore zones and major structures at Resolution, and highlights the potential for a high temperature oxidised fluid source to the west of the Magma vein and at Resolution East (Figure 9.11)

### 9.5.3 Pb isotopes

- $Pb_{sulfide}$ isotopic compositions from the Superior district range between $^{206}Pb/^{204}Pb$: 17.380 to 20.162; $^{207}Pb/^{204}Pb$: 15.25 to 17.02; $^{208}Pb/^{204}Pb$: 37.15 to 41.64; $^{207}Pb/^{206}Pb$: 0.774 to

0.884; Table 9.3)

- $Pb_{sulfide}$ isotopic compositions did not vary between pyrite growth zones revealed by etching, implying a common hydrothermal origin across growth zones

- $Pb_{epidote}$ isotopic compositions varied as follows $^{206}Pb/^{204}Pb$: 16.53 to 20.62; $^{207}Pb/^{204}Pb$: 15.36 to 15.78; $^{208}Pb/^{204}Pb$: 36.08 to 39.87; and $^{207}Pb/^{206}Pb$: 1.93 to 2.21 (Table 9.4)

- $Pb_{sulfide}$ and $Pb_{epidote}$ isotopic compositions are particularly non-radiogenic, in keeping with the retarded Pb isotopic signature in the rest of the SW US porphyry province. This is interpreted to represent the increasing involvement of either low-μ lower crustal material (Bouse et al., 1999 and references therein) or metasomatised SCLM (Pettke et al., 2010) during productive melt generation.

- $Pb_{sulfide}$ isotopic compositions of early alteration-mineralisation stages are characterised by a component of upper crustal Proterozoic wall-rock derived Pb during the initial, stages of mineralisation, becoming increasingly less radiogenic as the igneous source contributed more magmatic and/or lower crustal Pb to the system (Figure 9.13, 9.14 and 9.16)

- $Pb_{sulfide}$ and $Pb_{epidote}$ isotope values become more radiogenic with increasing distance from Resolution due to scavenging of upper crustal Proterozoic wall rock derived Pb.

- On average, $Pb_{sulfide}$ from Magma is characterised by somewhat more radiogenic $^{206}Pb_{sulfide}$ than Resolution (Figure 9.17). This could be interpreted as a distinct magmatic Pb source, or isotopic mixing of the Resolution ore fluid and upper crustal mobile radiogenic Pb from the Paleoproterozoic basement

- Spatially, there is a halo of less radiogenic, magmatic $Pb_{sulfides}$ 750 to 1000 m from the centre of the Resolution ore shell. This footprint of less radiogenic $Pb_{epidote}$ extends out to approximately 2 km

- One schist-hosted epidote sample in the NW of the district has an anomalously non-radiogenic $Pb_{epidote}$ ($^{206}Pb/^{204}Pb$: 16.53; $^{207}Pb/^{204}Pb$: 15.36; $^{208}Pb/^{204}Pb$: 36.08; $^{207}Pb/^{206}Pb$: 0.93; Table 9.4) in the NW of the district may indicate the presence of a separate hydrothermal system with a distinct fluid source (Figure 9.20 A)

- Lower $^{206}Pb/^{238}U$ in some epidotes close to the inferred location of long-lived N-, and NE-striking structures suggest the incorporation of Proterozoic U-derived Pb into Laramide propylitic epidote

# Chapter 10: Conclusions

## 10.1 Context

The southwestern US porphyry-Cu province has a protracted geologic history, beginning with the deposition and subsequent deformation of the Pinal Schist, ca. 1,650 Ma, with multiple deformation and magmatic events since that time. The Superior district is a well-endowed part of the SW US province with evidence for a range of Laramide mineralisation styles (Figure 4.1). The rocks and ore deposits of the Superior district, in particular the giant Resolution deposit, have been well studied (e.g., Troutman, 2001; Ballantyne et al., 2003; Manske and Paul, 2002; Harrison, 2007; Zulliger, 2007; Schwarz, 2010; McCarrel, 2012; Hehnke et al., 2012), but have rarely been considered in a broad district or regional scale context in academic studies. The Superior district is located at the edge of the basin and range province provides a relatively continuous section through Paleoproterozoic – Tertiary rocks (Figure 3.2, Figure 3.3). The exposure of rocks deposited over such a broad time interval provides an excellent opportunity to study events preserved in the basement rocks and their influences on Laramide mineralising processes. Determining the relationships and far field geochemical footprints of the multiple centres of Laramide aged mineralisation in the Superior district, in particular Resolution, require district scale assessment of the spatial and temporal aspects of these mineralised centres as well as evaluation of potentially overlapping hydrothermal footprints.

## 10.2 Proterozoic evolution of the Superior district

### 10.2.1 Paleoproterozoic basement and Mesoproterozoic sedimentation

The Paleoproterozoic basement to the Superior district comprises the heterogeneous Pinal Schist, which was deposited above a NW dipping subduction zone before the accretion of the Cochise block to the SE and subsequent welding to the North American continent during the Mazatzal Orogeny around 1,650 Ma (Eisele and Isachson, 2001; Whitmeyer and Karlstrom, 2007; Meijer, 2014). The Mazatzal Orogeny produced the major NE and conjugate NNW-striking structural architecture that dominates the basement rocks in the region. Following a significant depositional hiatus, the Apache Group was deposited in an evaporitic, periodically emergent basin (Shride, 1967; Wrucke, 1989), that

later accumulated Grenvillian syn-orogenic Troy Quartzite in a foreland position (Mulder et al., 2017). The basin architecture was controlled by transtensional movement along NE and NNW-striking faults (Timmons et al., 2005; Figure 3.20).

### 10.2.2 Mesoproterozoic dolerite sills

The region was intruded by voluminous dolerite sills between approximately 1,110 and 1,075 Ma, broadly coeval with mafic-ultramafic magmatism recorded in the Midcontinent rift (Bright et al., 2014 and references therein). Whole-rock geochemistry from Proterozoic mafic sills and flows in the Superior district, show that the Mesoproterozoic dolerite sills are not directly related to the Apache Basalt (Figure 5.8). The dolerite sills were derived from a shallower, more enriched mantle source compared to the basalts. The enriched nature of this source region implies it evolved under the distal influence of the Mesoproterozoic Midcontinent rift plume. There are four discrete compositional groups recognised within the dolerite sills, as determined from immobile trace element geochemistry (Figure 5.4 - 5.7). The compositional groups have distinct high and low Ti sources and have undergone significantly different amounts of crustal contamination and fractional crystallisation histories, which has resulted in different metal budgets. The most strongly crustally contaminated dolerite type is strongly enriched in PGEs (20 ppb Pt + Pd) suggesting that assimilation of crustal silicate material may have suppressed early sulfur saturation and preserved PGEs in the melt. Although no magmatic sulfides have been identified in this sample suite to date, there remains the possibility that late stage sulfur saturation and sulfide immiscibility did occur locally if the melt interacted with sufficient crustal sulfur during emplacement. In comparison to selected mafic suites from the Midcontinent rift, the dolerite sills from the Superior district are most geochemically similar to the relatively shallow sourced, unmineralised Logan, Nipigon and Pigeon River suites, rather than the more deeply sourced and mineralised ultramafic intrusions.

## 10.3 Proterozoic metasomatism

The intrusion of dolerite sills into the Apache Group is interpreted to have driven the migration of large volumes of residual evaporitic brines through E-striking faults and permeable horizons in the stratigraphy at the southern edge of the basin, resulting in a variety of Proterozoic alteration assemblages (Figure 7.1). During the initial prograde phase, brines leached significant quantities of K, U, Th and LILEs, most likely from the upper Dripping Springs siltstone member and base metals and Fe from the Apache Basalt (Figure 7.22). The Apache Basalt was pervasively orthoclase - chlorite-altered close to major fluid pathways. Orthoclase - chlorite alteration was then overprinted by epidote - chlorite - calcite alteration in more distal locations (Figure 7.18). High temperature magnetite skarns and chrysotile veins were formed in the Mescal Limestone, close to dolerite sills. During the retrograde phase, thermal collapse allowed ingress of fluids into the dolerite sills, resulting in widespread actinolite - biotite - chlorite - albite alteration and veining (Figure 7.22).

Hydrothermal geochronology of apatite from amygdales in the Apache Basalt has shown that epidote - chlorite - calcite alteration was broadly coeval with the intrusion of the dolerite sills between 1,247 ± 52 and 1,153 ± 45 Ma (Figure 6.9). This age, and the weakly uraniniferous nature of the Proterozoic hydrothermal system in the Superior district, suggests a genetic relationship to the mineral occurrences described from the Sierra Ancha region in east Central Arizona (Figure 2.15; Figure 6.9), where there is also strong empirical evidence for the involvement of dolerite sills (Wrucke et al., 1986 and references therein). Reductants such as the Pioneer Shale may have provided chemical traps for metals elsewhere in the basin, although the limited endowment of the Sierra Ancha deposits suggests the Proterozoic system was short lived and fluids were poorly focussed.

In the Superior district, epidotes from altered Proterozoic basalts and veins in the Paleoproterozoic Pinal Schist have U/Pb ratios that permit radiometric dating. Collectively, the Proterozoic epidotes define an age of 1183 ± 23 Ma (Figure 6.10). LA-ICP-MS geochronology applied to epidote was conducted alongside LA-ICP-MS apatites geochronology from the same samples indicate that, (1) epidote can be dated using LA-ICP-MS with the same precision as for apatite (~5 %; Figures 6.8 and 6.10) and, (2) the Mesoproterozoic hydrothermal activity produced widespread epidote alteration in the Proterozoic rocks of the Superior district.

## 10.4 Phanerozoic evolution of the Superior district

### 10.4.1 Regional Paleozoic to Mesozoic geologic evolution

The Paleozoic rocks of the Superior district indicate inter-tidal sedimentation during the Cambrian followed by periodic but significant marine transgressions in the Devonian, Mississippian and Pennsylvanian, while the region occupied a passive margin setting on the western edge of Laurentia (Beus, 1989; Middleton, 1989; Figure 2.5). Initiation of subduction and development of a continental margin occurred between the Triassic and Jurassic (Dickinson et al., 1989; Tosdal et al., 1989; Dickinson and Lawton 2001; Figure 2.7). During the earliest stages of uplift along the coast, Cu-U deposits formed in karst environments in the Paleozoic rocks inboard of the continental margin (Wenrich, 1985; Wenrich and Titley, 2008; Figure 2.16). Once subduction was established, small porphyry Cu and IOCG deposits formed along the magmatic arc (Barton et al., 2011; Dilles et al., 2000; Table 2.3; Figure 2.16), but no rocks or mineralisation of this age is known from the Superior district.

### 10.4.2 Laramide evolution of the Superior district

In the Superior district, a Cretaceous quartzose sandstone (Kqs) with a detrital zircon age of 96.8 ± 2.2 Ma, was deposited above the Paleozoic unconformity and may be equivalent to the fluvio-deltaic Fort Crittenden Formation deposited at the margin of the Jurassic border rift system (Zulliger, 2007; Table 3.2). This was followed by the deposition of the 74.1 ± 2.1 Ma andesitic, and 67.8 ± 2.3 to 66.4 ±1.1

Ma rhyodacitic facies of the Cretaceous volcaniclastic sequence, which signalled the onset of magmatism in the district (Hehnke et al., 2012; Table 3.2). The Cretaceous package of rocks, collectively named the Kvs, are preserved only in the Resolution graben and do not crop out at surface in the Superior district (Manske and Paul, 2002; Figure 3.2). The andesitic and rhyodacitic facies of the Kvs are temporally and geochemically similar to the 74.8 ± 0.33 Ma quartz diorite stock and the 66.9 ± 2.9 to 61.3 ± 1.4 Ma Schultze Granite respectively, implying they are cogenetic volcanic equivalents (Table 3.2). Structural mapping conducted during this study indicates Laramide compression and uplift were at least partially accommodated along the ancestral Concentrator Fault (Figure 3.25), that may have origins in the Paleo- or Mesoproterozoic (Figure 3.20; Timmons et al., 2005).

In the north of the district the 74.8 ± 0.33 Ma quartz diorite is intruded by a 73.6 ± 1.6 Ma dacite plug (Hehnke et al., 2012; Table 3.2), which contains breccia-hosted, polymetallic mineralisation and associated intense illite - muscovite alteration at the historic Silver King workings (Figure 4.11). Ar-Ar geochronology conducted during this study indicate that the muscovite alteration of the dacite intrusion and aplite dike, known locally as the Grandfather Lead, occurred at 74.31 ± 0.11 and 75.70 ± 0.12 Ma respectively, coeval with the emplacement of the igneous complex (weighted plateau ages; Table 6.2, Figure 6.5). Field mapping conducted during this study and by O'Neal (2015), indicates the muscovite alteration of the dacite is part of a larger zoned alteration domain typical of a porphyry Cu deposit (Figure 4.11).

Between Silver King and the Resolution deposit is the Magma high-intermediate sulfidation vein system and carbonate replacement deposits (Hammer and Peterson, 1967; Paul and Knight, 1995; Figure 3.2). The veins are hosted in NE-striking faults that predate vein formation and that have been variably intruded by dacite porphyry dikes with a single, low precision, U-$Pb_{zircon}$ age of 69.1 ± 4.0 Ma (Seedorff et al., 2005; Table 3.2). Paragenetically, the deposit transitions from skarns, confined to the eastern end of the mine, to pyrite followed by sulfides with increasing Cu:S ratio in veins and as replacement bodies (Gustafson, 1961; Friehauf, 1998). There is a spatial zonation in the main ore body from enargite to bornite to chalcopyrite to sphalerite-galena with increasing proximity to the surface. Alteration at Magma ranges from strong pervasive muscovite or sheeted quartz - epidote - calcite veins. Alteration is spatially restricted, forming only within < 1 m from mineralisation. Ar-Ar dating of muscovite from Magma conducted during this study indicates cooling ages ranging from 68.22 ± 0.11 to 67.39 ± 0.29 Ma (Table 6.2; Figure 6.5).

Resolution is the most significant deposit in the Superior district. It is a stockwork and breccia-hosted porphyry Cu-Mo deposit emplaced primarily in dolerite sills and Cretaceous volcaniclastic rocks within the blind Resolution graben (Mankse and Paul, 2002; Figure 6.5). Early- to syn-mineralisation dikes intrude the sequence and have ages ranging from 69.3 ± 1.1 to 66.0 ± 0.6 Ma (Hehnke et al., 2012; Table 3.2). Alteration assemblages at Resolution are consistent with other porphyry deposits globally

(e.g., Seedorff et al., 2005; Sillitoe, 2010; Cooke et al., 2014). Quartz - molybdenite mineralisation at Resolution commenced at 65.1 ± 0.3 Ma, while secondary biotite and muscovite range in age from 63.5 ± 0.38 to 62.1 ± 0.34 Ma, and from 63.3 ± 0.46 to 61.9 ± 0.34 Ma respectively. Since the $U\text{-}Pb_{zircon}$ ages from the porphyry dikes at Magma and Resolution overlap, there remains the possibility that Ar-Ar ages from Resolution reflect younger cooling ages than those at Magma due to the prolonged magmatism at Resolution. The paragenetic relationships of quartz-molybdenite veins to hydrothermal biotite presented by Schwarz (2010) and Hehnke et al. (2012), require the $Re\text{-}Os_{molybdenite}$ crystallisation ages of 65.4 Ma to predate and therefore provide an upper limit on, the formation hydrothermal biotite at Resolution. The ages therefore imply that cooling of muscovite alteration at Magma and the first crystallisation of molybdenite at Resolution are separated by a minimum time period of 1.7 m.y. (Figure 6.5), which may imply the two deposits formed from different fluid pulses from the Schultze Granite.

At Superior East, located approximately 5 km NE of Resolution, rhyodacite porphyry dikes intruded the Pinal Schist around 63.8 ± 1.2 ($U\text{-}Pb_{zircon}$; Table 3.2; Hehnke et al., 2012), with $Re\text{-}Os_{molybdenite}$ and $Ar\text{-}Ar_{muscovite}$ ages of 63.5 ± 0.3 and 62.4 ± 0.11 Ma, respectively, suggesting quartz - molybdenite vein formation at Superior East may have overlapped with those at Resolution (Table 3.2; Hehnke et al., 2012).

Following the emplacement of porphyry - epithermal mineralisation in the district, much of the overlying volcanic material was eroded and the deposits were partially exposed, as demonstrated by the presence of mineralised clasts and native copper within the overlying Tertiary Whitetail Conglomerate (Figure 3.18). Tertiary conglomerates are common across the southwest, where they occur within half grabens formed by the onset of Basin and Range style extensional tectonics, which has been attributed to the cessation of the Laramide Orogeny and delamination of the subducted Farrellon slab (e.g., Humphries, 2009). Slab delamination lead to asthenospheric upwelling, melting of the crust and voluminous silicic volcanism (Figure 2.13; Humphreys, 2009). In the Superior district, this is demonstrated primarily by the Apache Leap Tuff ignimbrite and other associated volcanic rocks (Figure 3.1, Peterson, 1969). Continued extensional stress caused significant normal faulting on the Concentrator and associated NNW striking faults that displaces the pre-Tertiary stratigraphy an unknown distance in the hangingwall (Figure 3.2). The transition to a transform tectonic margin may have been responsible for late-stage dextral slip on the Concentrator Fault, as demonstrated by horizontal grooves and slicken fibres identified during structural mapping conducted during the current study (Figure 3.24 and Figure 3.25).

## 10.5 Far-field geochemical footprint of Resolution

Calcite from ENE-striking epithermal veins define a 2.3 km $\delta^{18}O$ depletion halo around Resolution, and support a fluid source to the east (Figure 9.5 A). The $\delta^{13}C$ values were compromised by interaction with a wide variety of carbon sources in the host stratigraphy and do not define a clear zonation pattern around Resolution (Figure 9.5 B). Paragenetically late-stage calcite phases were precipitated from

meteoric-derived fluids that had partially equilibrated with Paleozoic carbonate rocks, implying a degree of fluid mixing as the hydrothermal system waned (Figure 9.4).

Sulfur isotopic composition of sulfide minerals from the Superior district highlight discrete mineralised domains, interpreted as regions affected by increasingly oxidised magmatic fluid. The NE corner of the Resolution ore shell, 'Resolution East', the West Boundary Fault, and the western limit of the Magma vein are all characterised by more negative sulfur isotopic compositions (Figure 9.11). The sulfur isotopic halo around Resolution extends as far as the West Boundary Fault, or 2.4 km to the west of the deposit. Pb isotopic concentrations of pyrite define a footprints of 750 m to 1,000 m around Resolution. The lead isotope footprint defined by pyrite analyses is characterised by a ring or shoulder where samples become slightly less radiogenic, compared to the centre of the deposit and more distal alteration zones (Figure 9.18, Figure 9.19). Pb isotope analysis of epidote extends the Pb isotopic footprint around Resolution to 1.5 km from the centre of the deposit (Figure 9.19). Plotting the raw U/Pb values in epidote can be helpful in identifying structures that hosted Proterozoic fluids that were reactivated to focus Laramide mineralisation (Figure 9.20).

The concurrent collection of trace element and corresponding geochronological data has allowed the use of supervised machine learning techniques to help identify the geochemical signature of epidote associated with Proterozoic metasomatism from distal Laramide aged propylitic alteration. The Proterozoic alteration suite was characterised by epidote enriched in U, B, Co, and HREE (Figure 8.4) and chlorite depleted in Zn and Mn (Figure 8.5). Laramide propylitic alteration produced epidote enriched in Pb and Sr and chlorite enriched in Zn and Mn (Figure 8.4, and Figure 8.5). There was generally poor distinction in the mineral chemistry between the various Laramide deposits of the Superior district, but epidote was generally more distinctive than chlorite (Figure 8.6, Figure 8.7 and Figure 8.8). Epidote from Silver King tended to have higher Sr concentrations, while epidotes from around the Magma vein were more enriched in Ni, Cr and V, compared to Resolution (Figure 8.4, and Figure 8.5). Once classified, the Resolution-related epidote and chlorite mineral chemistry signatures define a 3.98 km and 4.17 km geochemical halo around the deposit that extends to surface exposures in the range front (Figure 8.7 and Figure 8.8). These footprints could extend further west but are truncated by the Concentrator Fault (Figure 8.4, and Figure 8.5). Elemental dispersion patterns observed in epidote and chlorite related to Resolution (Figure 8.13, Figure 8.14 and Figure 8.15) are similar to those reported by previous workers (e.g., Cooke et al., 2014; Wilkinson et al., 2015). However, elements that are commonly elevated in epidote proximal to mineralisation, such as Cu, Bi and Sn (Cooke et al., 2014) did not show strong trends with distance from Resolution (Figure 8.13). Additionally, elements that can define a geochemical shoulder in epidote such as As, Sb, Zn, and Mn (Cooke et al., 2014) show subtle variation away from Resolution (Figure 8.13). Trends with distance are better developed in chlorite. Major elements Al and Mg in chlorite show strong decrease spatially away from the mineralisation, inversely correlated with Fe and Si (Figure 8.14). Proximal trace elements in chlorite, such as Ti, V and Cr tend to show less well developed trends than

major elements (Figure 8.15). The best compositional trends defined by chlorite around Resolution were Sr, B, Zr and Cu, all strongly partitioning into chlorite with greater distance up to 2 km away from the deposit (Figure 8.15). The chlorite proximitor equation of Wilkinson et al. (2015) appears to be effective to a distance of < 2 km and therefore is only applicable within the Resolution graben. Statistically, the best chlorite proximitor ratio was Mg/Si ($R^2$ = 0.72; Table 8.6, Figure 8.18), although it did not predict the location of the Resolution ore body as effectively as the raw V/Co value (Figure 8.18).

Anomalous Resolution-style mineral chemistry and $\delta^{18}O$ results have highlighted areas in the NW of the district, which are not associated with known mineralisation (Figure 8.7, Figure 8.8 and Figure 9.5). If a phase of dextral strike slip movement along the Concentrator Fault occurred, this anomaly could be restored along strike from the Magma vein, perhaps suggesting discovery potential in the hangingwall of the Concentrator Fault, and providing credence to the notion that Magma may have an undiscovered porphyry source to the west of current exposure (e.g., Maher 2008).

## 10.6 Directions for further research

### 10.6.1 Detailed examination of Proterozoic fluid chemistry

Many details regarding the Proterozoic hydrothermal system that affected the Apache Group stratigraphy remain unclear. Basin wide mapping of alteration within the Apache Group would help to constrain the extent and wider architecture of the hydrothermal system. Was this hydrothermal system only active on the southern margins of the Apache basin? Was the fluid focused along other structures in different parts of the basin? Is this style of alteration confined to the Apache group stratigraphy? Alteration mapping in other Mesoproterozoic basins such as the Unkar and Pahrump could help with understanding connectivity and architecture between these depocentres. Could this system be the cause of copper veins reported from the Proterozoic rocks by Noble (1914) in the Grand Canyon? Hydrothermal geochronology of altered rocks from different parts of the Apache basin, and other Mesoproterozoic basins, could help constrain the extent and duration of the Proterozoic hydrothermal system. The array of available alteration minerals could allow the quantification of the temperature, salinity and fluid source using fluid inclusion studies in quartz and apatite, and Sr isotope studies on epidote and actinolite.

Ultimately, what remains to be seen is whether or not the Proterozoic hydrothermal system had the longevity and architecture to efficiently focus brines into suitable traps for metal precipitation. If so, what was the extent of this Proterozoic metal contribution to pre-enrich structures that later focussed high grade porphyry copper deposits such as Resolution?

### 10.6.2 Geochronology of the Magma Vein

The discovery of older than expected Ar-Ar ages from the Magma vein has prompted the need for further geochronologic studies from that deposit. Sulfide phases with sufficient Re could be used for Re-Os

geochronology, which would provide a much more precise date on mineralisation than Ar-Ar ages from altered wallrock. Skarn mineralisation, described from the eastern end of the mine by Freihauf (1998) may also be a candidate for dating.

### 10.6.3 Epidote geochronology

The most important aspect for improving epidote as a more robust geochronometer is the development of a well characterised epidote U-Pb dating standard. Given the need for coarse, inclusion free crystals with a high U-Pb ratio, and corroboratory geochronology, this material will most likely come from a high temperature skarn with high resolution U-$Pb_{zircon}$ dating of the causative intrusion. In the future, epidote geochronology will allow widespread hydrothermal geochronology of alteration where multiple generations of epidote alteration are suspected and/or more conventional minerals are absent, such as in the American southwest.

### 10.6.4 Mineral chemistry

This study has identified a Proterozoic 'background' composition for epidote and chlorite. However, the identification of Laramide metamorphic epidote and chlorite would be highly significant in understanding the Laramide chemical background values in these minerals. This would allow a two-stage filtering process for explorers in the SW US.

Comparative study of actinolite associated with Proterozoic alteration of the dolerite sills and actinolite associated with the inner propylitic zone of porphyry Cu deposits in the southwestern US would add to the application of mineral chemistry to exploration in this part of the world, where the two alteration assemblages are indistinct and may overlap close to a Laramide porphyry deposit.

## 10.7 Applications to Exploration

Research findings applicable to exploration in the Superior district and the wider region include;

- Some of the Mesoproterozoic dolerite sills are enriched in PGEs and may be and exploration target if they interacted with a local reduced sulfur source
- Proterozoic hydrothermal activity strongly leached base metals from Apache Group rocks and may have formed sediment-hosted base-metal mineralisation at an appropriate chemical trap site elsewhere in the basin - probably at major structural intersections with Proterozoic reductants such as the Pioneer Shale
- The currently available evidence leaves the door open for an undiscovered porphyry-type mineralisation, originally related to the Magma vein that may have been structurally dislocated by dextral movement along the Concentrator Fault

- Epidote U-Pb geochronology and trace element mineral chemistry can be used to effectively delineate areas of Laramide alteration prospective for giant porphyry Cu deposits from the widespread Proterozoic propylitic altered rocks of the Superior district. This approach has potential applications for mineral exploration globally

# References


Ague, J.J. and Van Haren, J.L., 1996, Assessing metasomatic mass and volume changes using the bootstrap, with application to deep crustal hydrothermal alteration of marble: Economic Geology, v. 91, p. 1169-1182.

Aleinikoff, J.N, Reed, J.C, Wooden, J.L., 1993, Lead isotopic evidence for the origin of Paleo- and Mesoproterozoic rocks of the Colorado Province, U.S.A: Precambrian Research, v. 63 p. 97-122.

Allaby, M. 1999, A dictionary of earth sciences. Oxford University Press, Oxford.

Allen, C.M. and Campbell, I.H., 2012, Identification and elimination of a matrix-induced systematic error in LA–ICP–MS 206Pb/238U dating of zircon: Chemical Geology, v. 332, p. 157-165.

ALS Fees Schedule: https://www.alsglobal.com/myals/downloads

Amato, J.M., Boullion, A.O., Serna, A.M., Sanders, A.E., Farmer, G.L., Gehrels, G.E., and Wooden, J.L., 2008, Evolution of the Mazatzal province and the timing of the Mazatzal orogeny: Insights from U-Pb geochronology and geochemistry of igneous and metasedimentary rocks in southern New Mexico: Bulletin of the Geological Society of America, v. 120, p. 328–346.

Amato, J.M., Lawton, T.M., Mauel, D.J., Leggett, W.J., González-León, C.M., Farmer, G.L., Wooden, J.L; 2009, Testing the Mojave-Sonora megashear hypothesis: Evidence from Paleoproterozoic igneous rocks and deformed Mesozoic strata in Sonora, Mexico: Geology, v. 37, p. 75–78.

Anderson, C., and Creasey, S.C., 1958, Geology and Ore Deposits of the Jerome Area, Yavapai County, Arizona: Geoloical Survey Professional Paper 308.

Anderson, T.H., and Silver, L.T., 1979, The role of the Mojave-Sonora megashear in the tectonic evolution of northern Mexico, in Anderson, T.H., and Roldan-Quintana, J., eds., Geology of northern Sonora: Hermosillo, Universidad Nacional Autonoma de Mexico, Instituto de Geologica, p. 59–68.

Anderson, T. H., Nourse, J. A., McKee, J. W., and Steiner, M. B., eds., 2005, The Mojave-Sonora megashear hypothesis: Development, assessment, and alternatives: Geological Society of America Special Paper 393, 712 p.

Anderson, P., 1986, The Proterozoic Tectonic Evolution of Arizona: unpublished PhD thesis, Uni-

versity of Arizona, Tucson, 416 p.

Anthony, E., 1986, Geochemical evidence for crustal melting as the origin of the igneous suite at Sierrita porphyry copper deposit, southestern Arizona. Unpublished Ph.D. thesis, University of Arizona, Tucson, 85 p.

Arndt, N.T., Lesher, C.M., Czamanske, G.K., 2005, Mantle derived magmas and magmatic Ni–Cu–PGE deposits. Economic Geology 100th Anniversary Volume, p. 5–24.

Arnold, A.H., 2008, Geologic Implications of a Geochemical Study of Three Two-Mica Granites in Southern Arizona. Unpublished MSc. thesis, University of Arizona, Tucson 155 p.

Arth, J. G., 1976. Behaviour of trace elements during magmatic processes—a summary of theoretical models and their applications. Journal of Research of the U.S. Geological Survey, v. 4, p. 41-47.

Axen, G., 2008, A brief overview of Cenozoic extensional tectonism in western North America: in J.E. Spencer, J.E., Titley, S.R., eds., Circum-Pacific Tectonics, Geologic Evolution, and Ore Deposits, Digest, vol. 22, Arizona Geological Society, Tucson (2008), pp. 397-407

Babcock, R.C., Jr., Ballantyne, G.H., and Phillips, C.H., 1995, Summary of the geology of the Bingham district, Utah, in Pierce, F.W., and Bolm, J.G., eds., Porphyry copper deposits of the American Cordillera: Tucson, The Arizona Geological Society Digest, v. 20, p. 316–335.

Baker, J., Peate, D., Waight, T., Meyzen C., 2004, Pb isotopic analysis of standards and samples using a 207Pb–204Pb double spike and thallium to correct for mass bias with a double-focusing MC-ICP-MS: Chemical Geology, v. 211, p. 275–303.

Baker, M.J., Wilkinson, J.J., Wilkinson, C.C., Cooke, D.R., and Inglis, S., 2015. Chlorite trace element chemistry as an explorationtool: a case study from the Collahuasi mining district, northern Chile, In: World-Class Ore Deposits: Discovery to Recovery; Society of Economic Geology 2015 Conference, Hobart, Tasmania, September 27-30, 2015.

Baker, M.J., Cooke, D.R., Hollings, P.N., and Piquer, J., 2017. Identification of hydrothermal alteration related to mineralisation using epidote mineral chemistry, In: Proceedings; 15th Biennial Society for Geology Applied to Mineral Deposits (SGA) Conference, Quebec City, August 20-23, 2017, 1069– 1071.

Bailey, E.H. and Stevens, R.E., 1960, Selective staining of K-feldspar and plagioclase on rock slabs and thin sections: American Mineralogist: Journal of Earth and Planetary Materials, v. 45, p.1020-1025.

Bailey, R.C., 1990, Trapping of aqueous fluids in the deep crust. Geophysical Research Letters, v. 17, p. 1129-1132.

Ballantyne, G. H., 1981, Chemical and mineralogical variations in propylitic zones surrounding porphyry copper deposits: Unpublished PhD. thesis, University of Utah, 208 p.

Ballantyne, G.H., Marsh, T.M., Hehnke, C., Andrews, D.S., Eichenlaub, A.B., and Krahulec, K.A., 2003, The Resolution copper deposit, a deep, high-grade porphyry copper deposit in the Superior district, Arizona: Marcofest Conference, 3-5 April 2003, Golden, Colorado, 2003, 12 p.

Bar, M., Kolodny, Y. and Bentor, Y.K., 1974, Dating faults by fission track dating of epidotes? an attempt: Earth and Planetary Science Letters, v. 22, p. 157-162.

Barker, S. L., Dipple, G.M., Hickey, K.A., Lepore, W.A., and Vaughan, J.R., 2013, Applying stable isotopes to mineral exploration: Teaching an old dog new tricks: Economic Geology, v. 108, p. 1–9.

Barth, A.P., Wooden, J.L., Coleman, D.S., 2001, SHRIMP-RG U-Pb zircon geochronology of Mesoproterozoic metamorphism and plutonism in the southwesternmost United States: Journal of Geology, v. 109 p. 319–327

Barth, A.P., Wooden, J.L., Coleman, D.S., and Fanning, C.M., 2000, Geochronology of the Proterozoic basement of southwesternmost North America, and the origin and evolution of the Mojave crustal province: Tectonics, v. 19, p. 616–629.

Barton, M.D, 1996, Granitic magmatism and metallogeny of southwestern North America: Earth and Environmental Science Transactions of the Royal Society of Edinburgh, v. 87, p. 261-280.

Barton, M.D., 2014, Iron oxide(–Cu–Au–REE–P–Ag–U–Co) systems: in Scott, S.D., ed., Treatise on Geochemistry (2nd edition, volume 13): Amsterdam, Elsevier, p. 515–541.

Barton, M.D., Battles, D. A., Bebout, G. E., Capo, R. C., Christensen, J. N., Davis, S. R., Hanson, R. B., Michelsen, C. J., and Trim, H. E., 1988, Mesozoic contact metamorphism in the western United States, in Ernst, W. G., ed., Metamorphism and crustal evolution of the western United States (Rubey Volume VII): Englewood Cliffs, Prentice Hall, p. 110-178.

Barton, M.D., and Brooks Hanson, R. 1989, Magmatism and the development of low-pressure metamorphic belts: Implications from the western United States and thermal modeling: Geological Society of America Bulletin, v. 101 p.1051–1065

Barton, M.D., Brown, J. G., Haxel, G. B., Hayes, T. S., Jensen, E. P., Johnson, D. A., Kamilli, R. J., Long, K. R., Maher, D. J., and Seedorff, E., 2005, Centre for Mineral Resources: U. S. Geological Survey-University of Arizona, Department of Geosciences Porphyry Copper Deposit Life Cycles Field Conference, Southeastern Arizona, May 21-22, 2002: U. S. Geological Survey Scientific Investigations Report 2005-5020, 50 p

Barton, M.D., Girardi, J.D., Kreiner, D.C., Seedorff, E., Zurcher, L., Dilles, J.H., Haxel, G.B., and Johnson, D. A, 2011, Jurassic igneous-related metallogeny of southwestern North America: Great Basin Evolution and Metallogeny, p. 373–396.

Barton, M.D., and Johnson, D.A., 1996, Evaporitic-source model for igneous-related Fe oxide-(REE-Cu-Au-U) mineralization: Geology, v. 24, no. 3, p. 259–262.

Barton, M.D.and Johnson, D.A., 2000, Alternative Brine Sources for Fe-Oxide (-Cu-Au) Systems: Implications for Hydrothermal Alteration and Metals: in Porter, T.M. (eds), Hydrothermal Iron Oxide Copper-Gold & Related Deposits: A Global Perspective, Australian Mineral Foundation, Adelaide, p. 43-60.

Barton, M.D., Johnson, D.A., and Zurcher, L., 2000, Phanerozoic Iron-Oxide (-REE-Cu-Au-U) systems in southwestern North America and their origins, in Roberts, M.. and Fairclough, M.. eds., Fe-oxide-Cu-Au deposits: A discussion of critical issues ans current developments, EGRU Contribution 58: James Cook University, Townsville, p. 5–11.

Barton, M. D., Seedorff, E., Maher, D. J.,Stavast, W. J. A., Kamilli, R. J., Hayes, T. S., Long, K. R., and Haxel, G. B., 2007, Laramide porphyry copper systems and superimposed Tertiary extension: A life cycle approach to the Globe-Superior-Ray area, Arizona: Ores and orogenesis: Circum-Pacific tectonics, geologic evolution, and ore deposits: Arizona Geological Society, Symposium, Tucson, September 2007, Field Trip 4 Guidebook, 61 p.

Barton, M.D., Staude, J-M.G., Zürcher, L., and Megaw, P.K.M., 1995, Porphyry copper and other intrusion-related mineralization in Mexico, in Peirce, F.W., and Bolm, J.G., eds., Porphyry copper deposits of the American Cordillera: Arizona Geological Society Digest, v. 20, p.487–524.

Bassett, K.N., and Busby, C.J., 2005, Tectonic setting of the Glance Conglomerate along the Sawmill Canyon fault zone, southern Arizona: A sequence analysis of an intra-arc strike-slip basin, in Anderson, T.H., Nourse, J.A., McKee, J.W., and Steiner, M.B., eds., The Mojave-Sonora megashear hypothesis: Development, assessment, and alternatives: Geological Society of America Special Paper 393, p. 377–400.

Bateman, A.M., 1923, An Arizona Asbestos Deposit: Economic Geology, v. 18, p. 663-683.

Baumgartner, L.P. and Olsen, S.N., 1995, A least-squares approach to mass transport calculations using the isocon method: Economic Geology, v. 90, p. 1261-1270.

Baumgartner R., Fontbote L., and Vennemann T., 2008, Mineral Zoning and Geochemistry of Epithermal Polymetallic Zn-Pb-Ag-Cu-Bi Mineralization at Cerro de Pasco, Peru: Economic Geology v. 103, p. 493-537.

Beeunas, M.A. and Knauth, L.P., 1985, Preserved stable isotopic signature of subaerial diagenesis in the 1.2-by Mescal Limestone, central Arizona: implications for the timing and development of a terrestrial plant cover: Geological Society of America Bulletin, v. 96, p. 737-745.

Bendezu, R., and Fontboté, L., 2009, Cordilleran Epithermal Cu-Zn-Pb-(Au-Ag) Mineralization in the Colquijirca District, Central Peru: Deposit-Scale Mineralogical Patterns: Economic Geology, v. 104. p. 905-944.

Bennett, V., and DePaolo, D., 1987, Proterozoic crustal history of the western United States as determined by neodymium isotopic mapping: Geological Society of America Bulletin, v. 99, p. 1130.

Berthold, M.R. and Hand, D.J. eds., 2007, Intelligent data analysis: an introduction. Springer. 515 p.

Best, F.C., 2012, The petrogenesis and Ni-Cu-PGE potential of the Dido Batholith, north Queensland, Australia, unpublished PhD thesis, University of Tasmania, Hobart. 291 p.

Beus, S.S., 1989, Devonian and Mississippian Geology of Arizona, in Jenney, J.P and Reynolds, S.J. (eds.), Geologic evolution of Arizona, Arizona Geological Society Digest 17, p. 287-311.

Blake, W.P., 1883, The Silver King Mine of Arizona, Tuttle Moorehouse and Taylor, New Haven, 48 p.

Blakey, R.C., and Knepp, R., 1989, Pennsylvanian and Permian geology of Arizona: in Jenney, J.P. and Reynolds, S.J., eds., Geologic evolution of Arizona, Arizona Geological Society Digest 17, p. 313-347.

Boston, K.R., Rubatto, D., Hermann, J., Engi, M. and Amelin, Y., 2017, Geochronology of accessory allanite and monazite in the Barrovian metamorphic sequence of the Central Alps, Switzerland: Lithos, v. 286, p. 502-518.

Bouse, R.M., Ruiz J., Titley, S.R., Tosdal, R.M. and Wooden, J.L., 1998, Lead isotope compositions of Late Cretaceous and early Tertiary igneous rocks and sulfide minerals in Arizona; implications for the sources of plutons and metals in porphyry copper deposits: Economic Geology, v. 94, p. 211–244

Bowring, S.A., and Karlstrom, K.E., 1990. Growth, stabilization, and reactivation of Proterozoic lithosphere in the southwestern United States: Geology, v. 18, p. 1203–1206.

Breiman, L., 2001, Random forests: Machine learning, v. 45, p. 5-32.

Bright, R.M., Amato, J.M., Denyszyn, S.W., and Ernst, R.E., 2014. U-Pb geochronology of 1.1 Ga diabase in the southwestern United States: Testing models for the origin of a post-Grenville large igneous province: Lithosphere, v. 6, p. 135–156.

Bryant, D.G., and Metz, H.E., 1966, Geology and ore deposits of the Warren mining district, in Titley, S.R., and Hicks, C.L., eds., Geology of the porphyry copper deposits, southwestern North America: Tucson, University of Arizona Press, p. 189–203.

Buick, I.S., Frei, R. and Cartwright, I., 1999, The timing of high temperature retrogression in the Reynolds Range, central Australia: constraints from garnet and epidote Pb-Pb dating: Contributions to Mineralogy and Petrology, v. 135, p. 244-254.

Busby, C.J., Bassett, K.N., Steiner, M.B., and Riggs, N.R., 2005, The Mojave-Sonora Megashear Hypothesis: Development, Assessment, and Alternatives: Geological Society of America Special Paper 393, p. 359-376.

Burchard, E.F., 1931, Iron ore on Canyon Creek, Fort Apache Indian Reservation, Arizona: U.S. Geological Survey Bulletin 821-C, p. 51-78.

Camprubí, A., Ferrari, L., Cosca, M.A., Cardellach, E. and Canals, A., 2003, Ages of epithermal deposits in Mexico: regional significance and links with the evolution of Tertiary volcanism. Economic Geology, v. 98, p. 1029-1037.

Cannell, J., Cooke, D.R., Walshe, J.L., and Stein, H., 2005, Geology, mineralization, alteration, and structural evolution of the El Teniente porphyry Cu-Mo deposit: Economic Geology, v. 100, p. 979–1003.

Centeno-García, E., Guerrero-Suastegui, M., and Talavera-Mendoza, O., 2008, The Guerrero composite terrane of western México: Collision and subsequent rifting in a supra-subduction zone, *in* Draut, A., Clift, P. D., and Scholl, D. W., eds., Formation and applications of the sedimentary record in arc collision zones: Geological Society of America Special Paper 436, p. 279-308.

Chamberlain, K.R., Bowring, S.A., 2000, Apatite–Feldspar U–Pb thermochronometer: A reliable, mid-range (450 °C), diffusion-controlled system: Chemical Geology, v. 172, p. 173-200.

Chawla, N.V., Bowyer, K.W., Hall, L.O. and Kegelmeyer, W.P., 2002, SMOTE: synthetic minority over-sampling technique: Journal of artificial intelligence research, v. 16, p. 321-357.

Chew, D.M., Sylvester, P.J. and Tubrett, M.N., 2011, U–Pb and Th–Pb dating of apatite by LA-ICPMS: Chemical Geology, v. 280, p. 200-216.

Chiaradia, M., Banks, D., Cliff, R., Marschik, R. and De Haller, A., 2006, Origin of fluids in iron oxide–copper–gold deposits: constraints from $^{37}Cl$, $^{87}Sr/^{86}Sr_i$ and Cl/Br: Mineralium Deposita, v. 41, p. 565-573.

Chiaradia, M., Schaltegger, U., Spikings, R., Wotzlaw, J.F. and Ovtcharova, M., 2013, How accurately can we date the duration of magmatic-hydrothermal events in porphyry systems?—an invited paper: Economic Geology, v. 108, p. 565-584.

Clark,W.B., and Lydon, P.A., 1962, Mines and Mineral Resources of Calaveras County, California; County Rept 2: California Division of Mines and Geology, 27 p.

Cook, S.S., 1994, The geologic history of supergene enrichment in the porphyry copper deposits of southwestern North America: Unpublished PhD thesis, University of Arizona, Tucson. 163 p.

Cooke, D.R., 2001, Epidote trace element geochemistry and geochronology. CODES-DMR-SPIRT Odovician Project Final Report, 19 p.

Cooke, D.R., Agnew, P., Hollings, P., Baker, M. B., Chang, Z., Wilkinson, J., White, N. C., Zhang, L., Thompson, J., Gemmell, B., Fox, N., Chen, H. and Wilkinson, C, 2017, Porphyry Indicator Minerals (PIMS) and Porphyry Vectoring and Fertility Tools (PVFTS) – Indicators of Mineralization Styles and Recorders of Hypogene Geochemical Dispersion Halos. p. 457-470, Proceedings of Exploration 17: Sixth Decennial International Conference on Mineral Exploration.

Cooke, D.R., Baker, M., Hollings, P., Sweet, G., Chang, Z., Danyushevsky, L., Gilbert, S., Zhou, T., White, N., Gemmell, J.B., and Inglis, S., 2014a, New advances in detecting the distal geochemical footprints of porphyry systems— epidote mineral chemistry as a tool for vectoring and fertility assessments, in Kelley, K.D., and Golden, H.C., eds., Building Exploration Capability for the 21st Century: Colorado, p. 127–152.

Cooke, D.R., Bull, S.W., Donovan, S., and Rogers, J.R., 1998, K-metasomatism and base metal depletion in volcanic rocks from the McArthur basin, Northern Territory—implications for base metal mineralization: Economic Geology, v. 93, p. 1237–1263.

Cooke, D.R., Bull, S.W., Large, R.R. and McGoldrick, P.J., 2000, The importance of oxidized brines for the formation of Australian Proterozoic stratiform sediment-hosted Pb-Zn (Sedex) deposits: Economic Geology, v. 95, p. 1-18.

Cooke, D.R., Hollings, P., and Walshe, J., 2005, Giant Porphyry Deposits: Characteristics, Distribution, and Tectonic Controls: Economic Geology 100th anniversary volume, p.801-818.

Cooke D.R, Hollings P., Wilkinson J.J., and Tosdal R.M., 2014b, Geochemistry of Porphyry Deposits, in, Holland H.D., and Turekian, K.K., (eds.) Treatise on Geochemistry, Elsevier, Oxford, pp. 357-381

Cooke, D.R., Wilkinson, J.J., Baker, M., Agnew, P., Wilkinson, C.C., Martin, H., Chang, Z., Chen, H., Gemmell, J.B., Inglis, S., Danyushevsky, L., Gilbert, S., and Hollings, P., 2015, Using mineral chemistry to detect the location of concealed porphyry deposits – an example from Resolution, Arizona, In: Proceedings; International Applied Geochemistry Symposium, Tucson, Arizona.

Condie, K.C., 1981, Geochemical and isotopic constraints on the origin and source of Archaean granites. Special Publication, Geological Society of Australia, 7, 469-479.

Condie, K.C., 1982, Plate-tectonics model for Proterozoic continental accretion in the southwestern United States: Geology, v. 10, p. 37–42.

Condie, K. C., 1986, Geochemistry and tectonic setting of Early Proterozoic supracrustal rocks in the southwestern United States: Geology, v. 94, p. 845-864.

Condie, K.C., 1992, Proterozoic terranes and continental accretion in southwestern North America, in Condie, K.C., ed., Proterozoic Crustal Evolution: Developments in Precambrian Geology, Amsterdam, Netherlands, Elsevier, p. 447–480.

Condie, K.C., and De Melas, J.P., 1985, The Pinal Schist: An early Proterozoic quartz wacke association in southeastern Arizona: Precambrian Research, v. 27, p. 337–356.

Conway, C. M., and Karlstrom, K. E., 1986, Early Proterozoic geology of Arizona, Eos Trans. AGU, v. 67, p. 681–682,

Copeland, P., and Condie, K.C., 1986, Geochemistry and tectonic setting of Lower Proterozoic supracrustal rocks of the Pinal Schist, southeastern Arizona: Geological Society of America Bulletin, v. 97, p. 1512–1520

Cox, R., Martin, M.W., Comstock, J.C., Dickerson, L.S., Ekstrom, I.L., and Sammons, J.H., 2002, Sedimentology, stratigraphy, and geochronology of the Proterozoic Mazatzal Group, central Arizona: Geological Society of America Bulletin, v. 114, no. 12, p. 1535–1549.

Corbett, G.J., and Leach, T.M., 1998, Southwest Pacific Rim gold–copper systems: structure, alteration and mineralization. Society of Economic Geologists Special Publication v. 6, p. 1–240.

Cracknell, M.J. and Reading, A.M., 2014, Geological mapping using remote sensing data: A comparison of five machine learning algorithms, their response to variations in the spatial distribution of training data and the use of explicit spatial information: Computers & Geosciences, v. 63, p. 22-33.

Cracknell, M.J., Reading, A.M. and McNeill, A.W., 2014, Mapping geology and volcanic-hosted massive sulfide alteration in the Hellyer–Mt Charter region, Tasmania, using Random Forests™ and Self-Organising Maps: Australian Journal of Earth Sciences, v. 61, p. 287-304.

Crawford, A.J., Meffre, S., Squire, R.J., Barron, L.M., Fallon, T.J., 2007, Middle and Late Ordovician magmatic evolution of the Macquarie arc, Lachlan orogen, New South Wales: Australian Journal of Earth Science, v. 54, p. 181–215

Creasey, S.C., 1980, Chronology of intrusion and deposition of porphyry copper ores, Globe-Miami district, Arizona: Economic Geology, v. 75, p. 830-844.

Creasey, S.C., 1984, The Schultze Granite, the Tea Cup Granodiorite, and the Granite Basin Porphyry: A geochemical comparison of mineralized and unmineralized stocks in southern Arizona: U.S. Geological Survey Professional Paper 1303, p. 41

Cundari, R.M., Carl, C.F.J., Hollings, P. and Smyk, M.C. 2013, New and Compiled Whole-Rock Geochemical and Isotope Data of Midcontinent Rift-Related Rocks, Thunder Bay Area; Ontario Geological Survey, Miscellaneous Release—Data 308.

Dann, J.C., 1997, Pseudostratigraphy and origin of the Early Proterozoic Payson ophiolite, central Arizona: Geological Society of America Bulletin, v. 109, p. 347–365.

Darling, J.R., Storey, C.D. and Engi, M., 2012, Allanite U–Th–Pb geochronology by laser ablation

ICPMS: Chemical Geology, v. 292, p. 103-115.

Davis, G.H., 1979, Laramide folding and faulting in southeastern Arizona: American Journal of Science, v. 279, p. 543-569.

Davies, J.F. and Whitehead, R.E., 2006, Alkali-alumina and MgO-alumina molar ratios of altered and unaltered rhyolites: Exploration and Mining Geology, v. 15, p. 75-88.

Danyushevsky, L., Robinson, P., Gilbert, S., Norman, M., Large, R., McGoldrick, P. and Shelley, M., 2011, Routine quantitative multi-element analysis of sulphide minerals by laser ablation ICP-MS: Standard development and consideration of matrix effects: Geochemistry, Exploration, Environment, Analysis, v. 11, p. 51-60.

DePaolo, D.J., 1981, Neodymium isotopes in the Colorado Front Range and crust-mantle evolution in the Proterozoic: Science, v. 291, p. 193–196.

Desborough, G.A., Poole, F.G., Daws, T.A., and Scarborough, Robert, 1984, Hydocarbon source rock evaluation of the Middle Proterozoic Apache Group, Gila County, Arizona, in Woodward, Jane, Meissner, F. F., and Clayton, J.L., eds., Hydrocarbon source rocks of the greater Rocky Mountain region: Rocky Mountain Association of Geologists, p. 51-55.

Dickinson, W. R., 1981, Plate tectonic evolution of the southern Cordillera, in Dickinson, W. R., and Payne, W. D., eds., Relations of tectonics to ore deposits in the southern Cordillera: Arizona Geological Society Digest, v. 14 p. 113-135.

Dickinson, W.R., 1989, Tectonic setting of Arizona through geologic time, *in* Penny, J.P., and Reynolds, S.J., eds., Geologic Evolution of Arizona: Arizona Geological Society Digest, v. 17, p. 1–16.

Dickinson, W.R., 2002, The Basin and Range Province as a Composite Extensional Domain: International Geology Review, v. 44, no. 1, p. 1–38.

Dickinson, W.R., Fiorillo, A.R., Hall, D.L., Monreal, R., Potochnik, A.R., and Swift, P.N., 1989, Cretaceous stratigraphy of southeastern Arizona, in Jenney, J.P., and Reynolds, S.J., eds., Geologic evolution of Arizona: Arizona Geological Society Digest, v. 17, p. 447–461.

Dickinson, W.R., and Lawton, T.F., 2001, Carboniferous to Cretaceous assembly and fragmentation of Mexico: Geological Society of America bulletin v. 113, p. 1142-1160.

Dilles, J.H., 1987, Petrology of the Yerington Batholith, Nevada; evidence for evolution of porphyry copper ore fluids: Economic Geology, v. 82, p. 1750–1789.

Dilles, J.H., and Einaudi, M.T., 1992, Wall-rock alteration and hydrothermal flow paths about the Ann-Mason porphyry copper deposit, Nevada—a 6-km vertical reconstruction: Economic Geology, v. 87, p. 1963–2001.

Dilles, J.H., Einaudi, M.T., Proffett, J.M., and Barton, M.D., 2000, Overview of the Yerington porphyry copper district: Magmatic to non-magmatic sources of hydrothermal fluids, their flow paths, alteration affects on rocks, and Cu-Mo-Fe-Au ores, in Dilles, J.H., Barton, M.D., Johnson, D.A., Proffett, J.M., and Einaudi, M.T., eds, Contrasting Styles of Intrusion Associated Hydrothermal Systems: Society of Economic Geologists Guide Book Series, v. 32, p. 55–66.

Dilles, J.H., Famer, G.L., and Field, C.W., 1995, Sodium-calcium alteration by non-magmatic

saline fluids in porphyry copper deposits - Results from Yerington, Nevada: in Thompson, J.F.P., ed., magmas, Fluids, and Ore Deposits, Mineralogical Association of Canada Short Course, v. 23, p. 309–338.

Dilles, J.H. and Proffett, J.M., 1995, Metallogenesis of the Yerington batholith, Nevada. Arizona Geological Society Digest, v. 20, p 306-315.

Dilles, J.H., and Stephens, A., 2011, Age and geology of the Jurassic Lights Creek Copper district, California: An Fe-oxide copper gold association, in Steininger, R. C., and Pennell, W. M., eds., Great Basin evolution and metallogeny: Geological Society of Nevada, Symposium, Reno/Sparks, May 2010, Proceedings, v. 2, p. 1007-1018.

Djouka-Fonkwé, M.L., Kyser, K., Clark, A.H., Urqueta, E., Oates, C.J. and Ihlenfeld, C., 2012, Recognizing propylitic alteration associated with porphyry Cu-Mo deposits in lower greenschist facies metamorphic terrain of the Collahuasi district, northern chile—implications of petrographic and carbon isotope relationships: Economic Geology, v. 107, p. 1457-1478.

Donadini, F., L.J. Pesonen, K. Korhonen, A. Deutsch and S.S. Harlan, 2011, Paleomagnetism and paleointensity of the 1.1 Ga old diabase sheets from Central Arizona: Geophysica, v. 47, p. 3–30.

Donadini F. Pesonen L.J. Korhonen K. Deutsch A. Harlan S. Heaman L., 2012, Symmetric and asymmetric reversals in the 1.1 Ga central Arizona diabases: The debate continues, in Helsinki, Mertanen S. Pesonen L.J. Sangchan P., eds., Supercontinent Symposium 2012, Programme and Abstracts, p. 35–36.

Drake, M.J. and Holloway, J.R., 1981, Partitioning of Ni between olivine and silicate melt: the "Henry's Law problem" reexamined: Geochimica et Cosmochimica Acta, v. 45, p. 431-437.

Drewes, H., 1973, Large-scale thrust faulting in southeastern Arizona, in Geological Society of America Abstracts with Programs:, v. 5, p. 35.

Drewes, H., 1976, The Cordilleran thrust belt (Laramide orogeny) between Nevada and Chihuahua, in 25th International Geological Congress, Sydney, Australia:, p. 118–119.

Drewes, H.D., 1981, Geologic Map and Sections of the Bowie Mountain South Quadrangle, Cochise County, Arizona: U.S. Geological Survey Miscellaneous Investigations Map I-1363, scale 1:24,000.

Dubois, R. L., and Brummett, R. W., 1968, Geology of the Eagle Mountain Mine area, in Ridge, J.D., ed., Ore Deposits of the United States 1933-1967: American Institute of Mining and Metallurgical Engineering, p. 1592–1606.

Duebendorfer, E.M., Chamberlain, K.R. and Jones, C.S., 2001, Paleoproterozoic tectonic history of the Cerbat Mountains, northwestern Arizona: Implications for crustal assembly in the southwestern United States: Geological Society of America Bulletin, v. 113, p. 575-590.

Duebendorfer, E.M., Chamberlain, K.R., and Fry, B., 2006, Mojave-Yavapai boundary zone, southwestern United States: A rifting model for the formation of an isotopically mixed crustal boundary zone: Geology, v. 34, p. 681–684.

Dumitru, T.A., Gans, P.B., Foster, D. A., and Miller, E.L., 1991, Refrigeration of the western Cordilleran lithosphere during Laramide shallow-angle subduction: Geology, v. 19, p.

1145–1148.

Duncan, R.J. and Maas, R., 2014, Assessing the origin of old apparent ages derived by Pb stepwise leaching of vein-hosted epidote from Mount Isa, northwest Queensland, Australia: Contributions to Mineralogy and Petrology, v. 168, p. 1085.

Dutkiewicz, A., Rasmussen, B. and Buick, R., 1998, Oil preserved in fluid inclusions in Archaean sandstones.Nature, v. 395, p. 885-888.

Echavarri-Perez, A. and Rangin, C., 1978, El Yacimiento cuprifero del Arco, B. C., su ambiente geologico y sus caracteristicas de alteracion y mineralizacion. Boletin del Departamento de Geologia Universidad Sonora, v. 1 p. 1-18.

Einaudi, M.T., 1977, Petrogenesis of the copper bearing skarn at the Mason Valley mine, Yerington district, Nevada: Economic Geology, v. 72. p. 769–795.

Einaudi, M.T., 1982, Description of skarns associated with porphyry copper plutons in southwestern North America, in Titley, S.. ed., Advances in geology of the porphyry copper deposits, southwestern North America: University of Arizona Press, Tucson, p. 139–183.

Einaudi, M.T., 2000, Skarns of the Yerington District, Neveda: a trip log and commentary, In: Dilles, J.H., Barton, M.D., Johnson, D.A., Profett, J.M., Einaudi, M.T. (eds.), Guidebook Series 32, Contrasting Styles of Intrusion-Associated Hydrothermal Systems, p. 101–126.

Eisele, J., and Isachsen, C.E., 2001, Crustal growth in southern Arizona: U-Pb geochronologic and Sm-Nd isotopic evidence for addition of Paleoproterozoic Cochise block to the Mazatzal Province: American Journal of Science, v. 301, p. 773–797.

Ernst, R.E., Wingate, M.T.D., Buchan, K.L., and Li, Z.X., 2008, Global record of 1600–700 Ma large igneous provinces (LIPs): Implications for the reconstruction of the proposed Nuna (Columbia) and Rodinia supercontinents: Precambrian Research, v. 160, p. 159–178.

Escolme, A.J., 2017, Geology, geochemistry and geometallurgy of the Productora Cu-Au-Mo deposit, Chile, unpublished PhD thesis, University of Tasmania, Hobart. 313 p.

Fackler-Adams, B.N., Busby, C.J., and Mattinson, J.M., 1997, Jurassic magmatism and sedimentation in the Palen Mountains, southeastern California: Implications for regional tectonic controls on the Mesozoic arc: Geological Society of America Bulletin, v. 109, p. 1464–1484.

Farmer, G.L., Bowring, S.A., Matzel, J., Espinosa Maldonado, G., Fedo, C., and Wooden, J., 2005, Paleoproterozoic Mojave province in northwestern Mexico?: Isotopic and U-Pb zircon geochronologic studies of Precambrian and Cambrian crystalline and sedimentary rocks, Caborca, Sonora, in Anderson, T.H., et al., eds., The Mojave-Sonora megashear hypothesis: Development, assessment, and alternatives: Geological Society of America Special Paper 393, p. 183–198.

Favorito, D. A., and Seedorff, E., 2017, Characterization and reconstruction of Laramide shortening and superimposed Cenozoic extension, Romero Wash-Tecolote Ranch area, southeastern Arizona: Geosphere, v. 13, no. 2, p. 577-607 Ferguson, C. A., 2005, Field guide to the overlooks of Fish Creek Canyon, Superstition Mountains, Pinal County, Arizona: Arizona Geological Survey Open-File Report 05-01, 16 p.

Ferguson, C. A., and Trapp, R. A., 2001, Stratigraphic nomenclature of the Miocene Superstition volcanic field, central Arizona: Arizona Geological Survey Open-File Report 01-06, 103 p.

Field, C.W. and Fifarek, R.H., 1985, Light stable isotope systematics in epithermal environments. In: B.R. Berger and P.M. Bethke (Eds), Geology and Geochemistry of Epithermal Systems: Reviews in Economic Geology, v. 2, p. 99-128.

Field, C.W. and Gustafson, L.B., 1976, Sulfur isotopes in the porphyry copper deposit at El Salvador, Chile: Economic Geology, v. 71, p. 1533-1548.

Fisher, R.A., 1936, The use of multiple measurements in taxonomic problems: Annals of eugenics, v. 7, p. 179-188.

Force, E.R., 1998, Laramide alteration of Proterozoic diabase; a likely contributor of copper to porphyry systems in the Dripping Spring Mountains area, southeastern Arizona: Economic Geology, v. 93, p. 171-183.

Fornash, K. F., Patchett, P. J., Gehrels, G. E., and Spencer, J. E., 2013, Evolution of granitoids in the Catalina metamorphic core complex, southeastern Arizona: U-Pb, Nd, and Hf isotopic constraints: Contributions to Mineralogy and Petrology, v. 165, no. 6, p. 1295-1310.

Fouts, J.A., 1974, Petrology and chemistry of some diabase sills in central Arizona: Unpublished-PhD thesis, University of Arizona, Tucson, 158 p.

Frei, R., and Kamber, B.S., 1995, Single mineral Pb-Pb dating: Earth Planetary Science Letters v. 129, p. 261-268.

Friehauf, K. C., 1998, Geology and geochemistry of porphyry-related, carbonate-hosted massive replacement Cu-Au deposits--A case study of the Superior district, Arizona: Unpublished Ph.D. thesis, Stanford University, 221 p.

Friehauf, K.C., and Pareja, G.A., 1998, Can oxygen isotope halos be produced around high-temperature dolostonehosted ore deposits?; evidence from the Superior District, Arizona: Economic Geology, v. 93, p. 639–650.

Friehauf, K. C., 2008, Iron-sulfur redox and its effect on sulfur-isotope fractionation in carbonate-hosted Cu-Au replacement ores, Superior, Arizona, USA, in Spencer, J.E. and Titley, S.R. eds, Ores and Orogenesis: Circum-Pacific Tectonics, Geologic Evolution, and Ore Deposits Arizona Geological Society Digest 22 p. 583

Galbraith, F. W., III, 1935, Geology of the Silver King area, Superior, Arizona: Unpublished Ph. D. dissertation, University of Arizona, Tucson, 153 p. + plates

Garlick, G.D., 1966, Oxygen isotope fractionation in igneous rocks: Earth and Planetary Science Letters, v. 1, p. 361-368.

Garwin, S., 2000, The setting, geometry and timing of intrusion-related hydrothermal systems in the vicinity of the Batu Hijau porphyry copper-gold deposit, Sumbawa, Indonesia: Unpublished PhD thesis, University of Western Australia, Perth, 320 p.

Garwin, S., 2002, The geological setting of intrusion-related hydrothermal systems near the Batu Hijau porphyry copper-gold deposit, Sumbawa, Indonesia: Society of Economic Geologists Special Publication 9, p. 333–366.

Gilmour, P., and Still, A.R., 1968. The geology of the Iron King mine, in Ridge, J.D., ed., Ore

Deposits of the United States, 1933-1967: New York, American Institute of Mining, Metalurgical and Petroluem Engineers, v 2, p. 1238-1257

Goldfarb, R.J., Baker, T., Dube, B., Groves, D., Hart, C., Gosslein, P., 2005, Distribution, character and genesis of gold deposits in metamorphic terranes. Economic Geology One Hundredth Anniversary Volume. editor / J.W. Hedenquist ; J.F.H. Thompson ; R.J. Goldfarb ; J.P. Richards. Colorado USA : Society of Economic Geologists, 2005. pp. 407-450

González-León, C., Lawton, T.F., 1995, Stratigraphy, depositional environments, and origin of the Cabullona basin, northeastern Sonora, Geological Society of America Special Papers 301, p. 121-142

González-León, C.M., Solari, L., Solé, J., Ducea, M.N., Lawton, T.F., Bernal, J.P., Becuar, E.G., Gray, F., Martínez, M.L., and Santacruz, R.L., 2011, Stratigraphy, geochronology, and geochemistry of the Laramide magmatic arc in north-central Sonora, Mexico: Geosphere, v. 7, no. 6, p. 1392–1418.

Granger, H. C., and Raup, R.B., 1969, Geology of uranium deposits in the Dripping Spring Quartzite, Gila County, Arizona: U.S. Geological Survey Professional Paper 595, 108 p.

Grant, J.A., 1986, The isocon diagram; a simple solution to Gresens' equation for metasomatic alteration: Economic geology, v. 81, p. 1976-1982.

Grant, J.A., 2005, Isocon analysis: A brief review of the method and applications: Physics and Chemistry of the Earth, v. 30, p. 997-1004.

Gray G.G. Lawton T.F. Murphy J.J., 2008, Looking for the Mojave-Sonora megashear in northeastern Mexico, *in* Moore G., ed., Geological Society of America Field Guide 14, 2008, p. 1–26.

Green, T.H. and Pearson, N.J., 1987a. An experimental study of Nb and Ta partitioning between Ti-rich minerals and silicate liquids at high pressure and temperature. Geochim. Cosmochim. Acta, v. 51, p. 55-62.

Green, G.R., Ohmoto, H., Date, J., and Takahashi, T., 1983. Whole-rock oxygen isotope distribution in the Fukazawa-Kosaka area, Hokuroku District, Japan, and its potential application to mineral exploration. Economic Geology Monograph 5, p. 395-411.

Gregory, C.J., Rubatto, D., Allen, C.M., Williams, I.S., Hermann, J. and Ireland, T., 2007, Allanite micro-geochronology: a LA-ICP-MS and SHRIMP U–Th–Pb study: Chemical Geology, v. 245, p. 162-182.

Gregory, C.J., McFarlane, C.R.M., Hermann, J., Rubatto, D., 2009, Tracing the evolution of calc-alkaline magmas: In situ Sm-Nd isotope studies of accessory minerals in the Bergell Igneous Complex, Italy: Chemical Geology, v. 260, p. 73–86.

Guilbert, J. M., and Lowell, J. D., 1974, Variations in zoning patterns in porphyry ore deposits: Canadian Institute of Mining and Metallurgy Bulletin, v. 67, no. 742, p. 99-109.

Guillong, M. and Günther, D., 2002, Effect of particle size distribution on ICP-induced elemental fractionation in laser ablation-inductively coupled plasma-mass spectrometry: Journal of Analytical Atomic Spectrometry, v. 17, p. 831-837.

Gulson, B.L., 1986, Lead isotopes in mineral exploration; Elsevier Science: Amsterdam. 245 p.

Gustafson, L. B., 1961, Paragenesis and hypogene zoning at the Magma mine, Superior, Arizona: Unpublished Ph.D. thesis, Harvard University, 93 p.

Gustafson, L., and Hunt, J., 1975, The porphyry copper deposit at El Salvador, Chile: Economic Geology, v. 70, p. 857–912.

Halley, S., Dilles, J.H., and Tosdal, R.M., 2015, Footprints—Hydrothermal alteration and geochemical dispersion around porphyry copper deposits: Society of Economic Geologists (SEG) Newsletter, v. 100, p. 1–17.

Halley, S., Wood, D., Stoltze, A., Godfroid, J., Goswell, H., and Jack D., 2016, Using Multi-element geochemistry to map multiple components of a mineral system: case study from a sediment-hosted Cu-Ni camp, NW Province, Zambia: Society of Economic Geologists (SEG) Newsletter, v. 104, p. 1–21.

Hammer, D.F, 1973, Geologic investigation of the Magma Mine, Pinal County, Arizona. Unpublished private report to Magma Copper Co.

Hammer, D.F, 2011, The Silver King Mine, Pioneer mining district, Pinal County, Arizona. Unpublished private report to Resolution Copper. 28 p.

Hammer, D.F., and Peterson, D. W., 1968, Geology of the Magma mine area, Arizona, in Ridge, J. D., ed., Ore deposits of the United States, 1933-1967 (Graton-Sales Volume): New York, American Institute of Mining, Metallurgical, and Petroleum Engineers, v. 2, p. 1282-1310.

Hammond J.G., 1983, Late Precambrian diabase intrusions in the southern Death Valley region, California: their petrology, geochemistry, and tectonic significance. Unpublished PhD thesis, University of Southern California, Los Angeles, p 281

Hammond, J.G., 1986, Geochemistry and petrogenesis of Proterozoic diabase in the southern Death Valley region of California: Contributions to Mineralogy and Petrology, v. 93, p. 312-321.

Hammond, J.G., 1990, Middle Proterozoic diabase intrusions in the southwestern U.S.A. as indicators of limited extensional tectonism, in Gower, C.F., Rivers, T., and Ryan, B., ed., Mid-Proterozoic Laurentia-Baltica: Geological Association of Canada Special Paper 38, p. 517–531.

Hammond, J. G. and Wooden, J. L., 1990, Isotopic constraints on the petrogenesis of Proterozoic diabase in Southwestern USA. In A. J. Parker, P. D. Rickwood, and D. H. Tucker (Eds.), Mafic dykes and emplacement mechanisms (pp. 145–156). Rotterdam: Balkema.

Hanson, R.E., Crowley, J.L., Bowring, S.A., Ramezani, J., Gose, W.A., Dalziel, I.W.D., Pancake, J.A., Seidel, E.K., Blenkinsop, T.G., and Mukwakwami, J., 2004, Coeval large-scale magmatism in the Kalahari and Laurentian cratons during Rodinia assembly: Science, v. 304, p. 1126–1129,

Harrer, C.M., 1964, Reconnaissance of iron resources in Arizona: U.S. Bureau of Mines Information Circular 8236, 204 p.

Harrison, R., 2007, The evolution of hydrothermal alteration-mineralisation events in the Resolution porphyry Cu-Mo deposit, Superior, Arizona: Unpublished MSc thesis, University of Bristol, England, 43 p.

Harshman, E., N., 1939, Geology pf the Belmont-Queen Creek are, Superior, Arizona. Unpublished PhD thesis, University of Arizona, 232 p.

Haxel, Gordon, Tosdal, R. M., May, D. J., and Wright,J. E.,1984, Latest Cretaceous and early Tertiary orogenesis in south-central Arizona; thrust faulting, regional metamorphism, and granitic plutonism: Geological Society of America Bulletin, v. 95, p. 631-653.

Haxel, G., Anderson, T., Briskey, J., Tosdal, R., Wright, J., and May, D., 2008, Late Jurassic igneous rocks in south-central Arizona and north-central Sonora, in Spencer, J. and Titley, S. eds., Ores and orogenesis: Circum-Pacific tectonics, geological evolution, and ore deposits: Arizona Geological Society Digest, v. 22, Tucson.

Hedenquist, J.W. and Houghton, B.F., 1987, Epithermal Gold Mineralization and its Volcanic Environments: Earth Resources Foundation, The University of Sydney, 422 pp.

Heidrick, T., and Titley, S.R., 1982, Fracture and dike patterns in Laramide plutons and their structural and tectonic implications, in Titley, S., ed., Advances in Geology of the Porphyry Copper Deposits, Southwestern North America: The University of Arizona press, p. 73–91.

Helsley, C.E., and Spall, H., 1972, Paleomagnetism of 1140 to 1150 million-year diabase sills from Gila County, Arizona: Journal of Geophysical Research, v. 77, p. 2115-2128.

Hedenquist, J.W., and Richards, J.P., 1998, The influence of geochemical techniques on the devel-opment of genetic models for porphyry copper deposits: Reviews in Economic Geology, v. 10, p. 235–256.

Hemley, J.J., Montoya, J.W., Marinenko, J.W., and Luce, R.W., 1980, Equilibria in the system $Al_2O_3$-$SiO_2$-$H_2O$ and some general implications for alteration-mineralization processes: Economic Geology, v. 75, p. 210–228.

Hendricks, J.D., 1972, Younger Precambrian Basaltic Rocks of the Grand Canyon, Arizona (M.S. thesis). Northern Arizona University, Flagstaff, p. 122.

Hehnke, C., Ballantyne, G., Martin, H., Hart, W., Schwartz, A., and Stein, H. 2012, Geology and Exploration Progress at the Resolution Porphyry Cu-Mo Deposit: Society of Economic Geologists, Special Publication 16, p. 147-156.

Henley, R.W., and Ellis, A.J., 1983, Geothermal systems, ancient and modern: Earth Science Reviews, v. 19, p. 1–50.

Henry, C. D., 2008, Ash-flow tuffs and paleovalleys in northeastern Nevada: Implications for Eocene paleogeography and extension in the Sevier hinterland, northern Great Basin: Geosphere, v. 4, p.

Hereford, R., 1977, Deposition of the Tapeats Sandstone (Cambrian) in central Arizona: Geological Society of America Bulletin, v. 88, p. 199-211.

Helsley, C. E., and Spall, H., 1972, Paleomagnetism of 1,140 to 1,150 million year diabase sills from Gila County, Arizona, Journal of Geophysical Research, v. 77, pp. 2115-2128.

Heyl, A.V., Delevaux, M.H., Zartman, R.E. and Brock, M.R., 1966, Isotopic study of galenas from the upper Mississippi Valley, the Illinois-Kentucky, and some Appalachian Valley mineral districts: Economic Geology, v. 61, p. 933-961.

Heyl, G.R., 1948, Foothill copper-zinc belt of the Sierra Nevada, California, in Jenkins, O.P., eds.,

Copper in California: California Division of Mines Bulletin 144, p. 11–30.

Hildebrand, R.S., 2015, Dismeberment and northward migration of the Cordilleran orogen: Baja-BC resolved: GSA Today, v. 25, p. 4–11.

Hill, B.M., and Bickford, M.E., 2001, Paleoproterozoic rocks of central Colorado: Accreted arcs or extended older crust?: Geology, v. 29, p. 1015–1018.

Hoefs, J., 2015, Stable isotope geochemistry, 7th ed.: Springer-Verlag, Berlin, Germany, 285 p.

Holland, M. E., Karlstrom, K. E., Doe, M. F., Gehrels, G. E., Pecha, M., Shufeldt, O. P., Belousova, E. 2015, An imbricate midcrustal suture zone: The mojave-yavapai province boundary in grand canyon, Arizona: Bulletin of the Geological Society of America, v. 127 p. 9-10.

Holliday, J.R., and Cooke, D.R., 2007, Advances in geological models and exploration methods for copper ± gold porphyry deposits: Proceedings of the Fifth Decennial International Conference on Mineral Exploration: Toronto, Canada, Decennial Mineral Exploration Conferences, p. 791–809.

Hollings, P., Cooke, D.R., and Clark, A. 2005, Regional geochemistry of Tertiary igneous rocks in central Chile: Implications for the geodynamic environment of giant porphyry copper and epithermal gold mineralization. Economic Geology, v. 100, p. 887–904.

Hollings, P., Hart, T.,Richardson, A. and MacDonald, C.A., 2007, Geochemistry of the Mesoproterozoic Intrusive Rocks of the Nipigon Embayment, Northwestern Ontario: Evaluating the Earliest Phases of Rift Development: Canadian Journal of Earth Sciences, v. 44, p. 1087-1110.

Hollings, P., Smyk, M., Heaman, L. H. and Halls, H., 2010, The geochemistry, geochronology and paleomagnetism of dikes and sills associated with the Mesoproterozoic Midcontinent Rift near Thunder Bay, Ontario, Canada: Precambrian Research, v. 183, p. 553–571.

Howard, K.A., 1991, Intrusion of horizontal dikes: Tectonic significance of Middle Proterozoic diabase sheets widespread in the upper crust of the southwestern United States: Journal of Geophysical Research, v. 96, p. 12,461– 12,478

Huang, Q., Kamenetsky, V.S., McPhie, J., Ehrig, K., Meffre, S., Maas, R., Thompson, J., Kamenetsky, M., Chambefort, I., Apukhtina, O. and Hu, Y., 2015, Neoproterozoic (ca. 820–830 Ma) mafic dykes at Olympic Dam, South Australia: links with the Gairdner large igneous province: Precambrian Research, v. 271, p. 160-172.

Humphreys, E. D., 2009, Relation of flat subduction to magmatism and deformation in the western United States, *in* Kay, S. M., Ramos, V. A., and Dickinson, W. R., eds., Backbone of the Americas: Shallow subduction, plateau uplift, and ridge and terrane collision: Geological Society of America Memoir 204, p. 85-98.

Hutchinson, D.R., White, R.S., Cannon, W.F. and Schulz, K.J., 1990, Keweenaw hotspot: geophysical evidence for a 1.1 Ga mantle plume beneath the Midcontinent Rift system. Journal of Geophysical Research, v. 95, p. 10869-10884.

Ilg, B.R., Karlstrom, K.E., Hawkins, D.P., and Williams, M.L., 1996, Tectonic evolution of Paleoproterozoic rocks in the Grand Canyon: Insights into middlecrustal processes: Geological Society of America Bulletin, v. 108, p. 1149–1166

Iriondo, A., and Atkinson, W., 2000, Orogenic gold mineralization along the proposed trace of the Mojave-Sonora megashear: Evidence for the Laramide Orogeny in NW Sonora: Geological Society of America Abstracts with Programs, v. 32, no. 7, p. 393

Irving, A.J., Frey, F.A., 1978, Distribution of trace elements between garnet megacrysts and host volcanic liquids of kimberlitic to rhyolitic composition: Geochimica et Cosmochimica Acta, v. 42, p. 771-787

Izaguirre, A., Camprubí, A., and Iriondo, A., 2015, Mesozoic orogenic gold deposits in Mexico: Ore Geology Reviews, v. 81, p. 1172 - 1183.

Jackson, M.J., Powell, T.G., Summons, R.E., and Sweet, I.P., 1986, Hydrocarbon shows and petroleum source rocks in sediments as old as 1.7x 109 years: Nature, v. 322, p. 727-729.

Janoušek, V., Farrow, C.M. and Erban, V., 2006, Interpretation of whole-rock geochemical data in igneous geochemistry: introducing Geochemical Data Toolkit (GCDkit): Journal of Petrology, v. 47, p. 1255-1259.

John, D.A., Ayuso, R.A., Barton, M.D., Blakely, R.J., Bodnar, R.J., Dilles, J.H., Floyd, G., Graybeal, F.T., Mars, J.C., McPhee, D.K., Seal, R.R., Taylor, R.D., and Vikre, P.G., 2010, Porphyry copper deposit model, Chapter B of Mineral deposit models for resource assessment: US Geological Survey Scientific Investigations Report 2010-5070-B, 169 p.

Johnson, D.A. and Barton, M.D., 2000, Time-space development of an external brine-dominated, igneous-driven hydrothermal system; Humboldt mafic complex, western Nevada, Part I: in Dilles, J.H., Barton, M.D., Johnson, D.A., Proffett, J.M., Einaudi, M.T., eds., Contrasting styles of intrusion-associated hydrothermal systems: Guidebook Series, Society of Economic Geologists, v. 32, p. 127–143.

Kamenetsky, V.S., Lygin, A.V., Foster, J.G., Meffre, S., Maas, R., Kamenetsky, M.B., Goemann, K. and Beresford, S.W., 2016, A story of olivine from the McIvor Hill complex (Tasmania, Australia): Clues to the origin of the Avebury metasomatic Ni sulfide deposit: American Mineralogist, v. 101, p. 1321-1331.

Karlstrom, K.E., and Conway, C.M., 1986, Symposium report: Early Proterozoic geology of Arizona: Geology, v. 14, no. 7, p. 625-626.

Karlstrom, K.E., and Bowring, S.A., 1988, Early Proterozoic assembly of tectonostratigraphic terranes in southwestern North America: The Journal of Geology, v. 96, p. 561–576,

Karlstrom, K.E., Amato, J.M., Williams, M.L., Heizler, M., Shaw, C.A., Read, A.S., and Bauer, P., 2004, Proterozoic tectonic evolution of the New Mexico region: A synthesis, in Mack, G.H., and Giles, K.A., eds., The Geology of New Mexico: A Geologic History: Socorro, New Mexico, New Mexico Geological Society, p. 1–34.

Keays, R.R., and Lightfoot, P.C., 2015, Geochemical stratigraphy of the Keweenawan Midcontinent Rift volcanic rocks with regional implications for the genesis of associated Ni, Cu, Co, and platinum group element sulfide mineralization. Economic Geolology, v. 110, p. 1235–1267

Keep, M., 1996, The Pinal Schist, southeast Arizona, USA: Contraction of a Paleoproterozoic rift basin: Journal of the Geological Society of London, v. 153, p. 979–993,

Keith, S. B., 1983, Results of mapping project near Ray, Pinal County, Arizona: Arizona Bureau of

Mines Open File Report 83-14, 11 plates, map scale 1:12,000, 74 p.

Kemp,W. R., 1982, Petrochemical affiliations of volcanogenic massive sulfide deposits of the foothill copper-zinc belt, Sierra Nevada, California: Unpublished PhD Thesis, University of Nevada, Reno, 458 pp.

Kehayov, R., 2015, Resolution Breccia Study. Unpublished report to Resolution Copper Minng RTX report, 41 p.

Kinross Gold, 2015, Annual report; http://www.annualreports.com/HostedData/AnnualReportArchive/K/TSX_K_2015.pdf

Koppers, A., 2002, ArArCALC—Software for $^{40}Ar/^{39}Ar$ age calculations: Computers and Geoscience, v. 28, 605–619, (Available at http://earthref.org/tools/ararcalc.htm.)

Koppers, A., H. Staudigel, J. R. Wijbrans, and M. Pringle, 2003, Short-lived and discontinuous intraplate volcanism in the South Pacific: Hot spots or extensional volcanism?: Geochemistry, Geophysics and Geosystems, v. 4.

Koski, R.A., and Cook, D.S., 1982, Geology of the Christmas porphyry copper Deposit, in Titley, S.R. ed., Advances in Geology of the Porphyry Copper Deposits, Southwestern North America: University of Arizona Press, Tucson, p. 353–374.

Kozlovsky, Ye.A., 1984, The world's deepest well. Scientific American v. 251, p. 98-104.

Krantz, R. W., 1989, Laramide structures of Arizona, *in* Jenney, J. P., and Reynolds, S. J., eds., Geologic evolution of Arizona: Arizona Geological Society Digest 17, p. 463-483.

Kuhn, S.; Cracknell, M.J.; Reading, A.M., 2018, Lithologic mapping using Random Forests applied to geophysical and remote-sensing data: A demonstration study from the Eastern Goldfields of Australia: Geophysics, v. 83, p. 183–193.

Kuiper, K. F., Deino, A., Hilgen, F. J., Krijgsman, W., Renne, P. R., Wijbrans, J. R., 2008, Synchronizing Rock Clocks of Earth History, Science v. 320, p. 500.

Lang, J., Thompson, J.F., Mortensen, J., Baker, T., Coulsen, I., Duncan, R., Maloof, T., James, J., Friedman, R., and Lepitre, M., 2001, Regional and system-scale controls on the formation of copper and/or gold magmatic-hydrothermal mineralization, Special Publication 2. (J. R. Lang, Ed.): Mineral Deposit Research Unit, University of British Columbia, Vancouver, 115 p.

Lang, J.R., and Titley, S.R., 1998, Isotopic and geochemical characteristics of laramide magmatic systems in Arizona and implications for the genesis of porphyry copper deposits: Economic Geology, v. 93, p. 138–170.

Lasky, S., 1936, Geology and ore deposits of the Bayard area, Central mining district, New Mexico: U.S Geological Survey Bulletin, v. 870, p. 144.

Large, R.R., Gemmell, J.B., Paulick, H., and Huston, D.L., 2001, The alteration box plot: A simple approach to understanding the relationship between alteration mineralogy and lithogeo-chemistry associated with volcanic-hosted massive sulfide deposits: Economic Geology, v. 96, p. 957–971.

Lavery, N.G., 1985. The use of Flourine as a pathfinder for volcanic-hosted massive sulfide ore deposits: Journal of Geochemical Exploration, v 23, p 35-60.

Lazowski, A.K., DeCelles, P.G., Gehrels, G.E., 2013. Detrital zircon geochronology of Cordilleran retroarc foreland basin strata, western North America, Tectonics, v 32, p 1027-1048.

Lechler, P.J., and Desilets, M.O., 1987, A review of the use of loss on ignition as a measurement of total volatiles in whole-rock analysis: Chemical Geology, v. 63, p. 341–344.

Le Maitre, R.W., 1989, A classification of igneous rocks and glossary of terms: recommendations of the International Union of Geological Sciences Subcommission on the Systematics of Igne¬ous Rocks: Blackwell Scientific Publications, Oxford, United Kingdom, 253 p.

Lehman, T.M., 1991. Sedimentation and tectonism in the Laramide Tornillo Basin of West Texas. Sedimentary Geology, v. 75, p. 9 – 28.

Leveille, R.A., and Stegen, R.J., 2012, The Southwestern North America Porphyry Copper Province: Society of Economic Geology Special Publication 16, p. 361–401.

Lindberg, P. A., 1989, Precambrian ore deposits of Arizona, *in* Jenney, J. P., and Reynolds, S. J., eds., Geologic evolution of Arizona, Arizona Geological Society Digest 17, p. 187-210.

Lipske, J. L., and Dilles, J. H., 2000, Advanced argillic and sericitic alteration in the subvolcanic environment of the Yerington porphyry copper system, Buckskin Range, Nevada: Society of Economic Geologists Guidebook Series, v. 32, p. 91-99.

Lister, G.S., Davis, G.A., 1989, The origin of metamorphic core complexes and detachment faults formed during Tertiary continental extension in the northern Colorado River region, USA: Journal of Structural Geology v. 11, p. 65– 94.

Livicarri, R.F., 1991. Role of crustal thickening and extensional collapse in the tectonic evolution of the Sevier-Laramide orogeny, western United States: Geology, v. 19, p. 1104-1107.

Loader M.L., 2015, Mineral Indicators of Porphyry Cu Fertility. Unpublished PhD thesis, Imperial College London, UK. 436 p.

Longerich, H.P., Jackson, S.E. and Günther, D., 1996, Inter-laboratory note. Laser ablation inductively coupled plasma mass spectrometric transient signal data acquisition and analyte concentration calculation: Journal of Analytical Atomic Spectrometry, v. 11, p. 899-904.

Lowell, J.D., and Guilbert, J.M., 1970, Lateral and vertical alteration-mineralization zoning in porphyry ore deposits: Economic Geology, v. 65 , p. 373–408.

Loucks, R.R., 2014, Distinctive composition of copper-ore-forming arcmagmas: Australian Journal of Earth Sciences, v. 61, p. 5-16.

Ludwig, K.R., 2003, Isoplot 4.15: A Geochronological Toolkit for Microsoft Excel, Berkeley Geochronological Centre Special Publication 4, Berkeley, California, p.74.

Ludwig, K.R., and Simmons, K.R., 1992, U-Pb dating of uranium deposits in collapse breccia pipes of the Grand Canyon region: Economic Geology, v. 87, p. 1747-1765.

Macdonald, K.C., Fox. P.J., Perram, L.J., Eisen, M. F., Haymon, R. M., Miller, S. P., Carbotte, S. M., Cormier, M.-H. and Shor A. N., 1988, A new view of the mid-ocean ridge from the behaviour of ridge-axis discontinuities: Nature, v. 335, p. 217–225.

Mach, C., 2008, Tectonic controls, timing and geochemistry of supergene enrichment of the Tyrone porphyry copper deposit, Grant County, New Mexico: Unpublished PhD thesis,

University of Nevada, Reno, 268 p.

Macfarlane, A.W., Marcet, P., LeHuray, A.P. and Petersen, U., 1990, Lead isotope provinces of the Central Andes inferred from ores and crustal rocks: Economic Geology, v. 85, p. 857-1880.

Magnani, M.B., Miller, K.C., Levander, A., and Karlstrom, K., 2004, The Yavapai-Mazatzal boundary: A long lived assembly structure in the lithosphere of southwestern North America: Geological Society of America Bulletin, v. 116, p. 1137–1142, doi: 10.1130/B25414.1.

Maher, D.J., 2008, Reconstruction of Middle Tertiary Extension and Laramide Porphyry Copper Systems, East-Central Arizona. Unpublished Ph.D. Thesis, University of Arizona, Tucson, 328 p.

Manske, S.L., and Paul, A.H., 2002, Geology of a major new porphyry copper centre in the Superior (Pioneer) district, Arizona: Economic Geology, v. 97, p. 197–220.

Mao, M., Rukhlov, A.S., Rowins, S.M., Spence, J. and Coogan, L.A., 2016, Apatite trace element compositions: A robust new tool for mineral exploration: Economic Geology, v. 111, p. 1187-1222.

Marsh, T.M., Einaudi, M.T., and McWilliams, M., 1997, $^{40}Ar/^{39}Ar$ geochronology of the Cu-Au and Au-Ag mineralization in the Potrerillos District, Chile: Economic Geology, v. 92, p. 784– 806.

Mattinen, P.R., and Bennett, G.H., 1986, The Green Mountain massive sulphide deposit, Besshi-style mineralization within the California Foothills copper-zinc belt: Journal of Geochemical Exploration, v. 25, p. 185–200.

Marillo-Sialer, E., Woodhead, J., Hergt, J., Greig, A., Guillong, M., Gleadow, A., Evans, N. and Paton, C., 2014, The zircon 'matrix effect': evidence for an ablation rate control on the accuracy of U–Pb age determinations by LA-ICP-MS: Journal of Analytical Atomic Spectrometry, v. 29, p. 981-989.

Masterman G.J., 2003, Structural and geochemical evolution of the Rosario Cu-Mo porphyry deposit and related Cu-Ag veins, Collahuasi district, Northern Chile: Unpublished PhD thesis, University of Tasmania, Hobart, Australia: 253 p.

Maynard, S.R., 2005, Laccoliths of the Ortiz porphyry belt, Santa Fe County, New Mexico. New Mexico Geology, v. 27, p. 3-21.

Mayo, D.P., Anderson, J.L., Wooden, J.L., 1998, Isotopic constraints on the petrogenesis of Jurassic plutons, southeastern California: International Geology Review, v. 40, p. 257–278.

McCarrel, M.J., 2012, Characterization and Correlation of Skarn Mineralization and Protoliths, Resolution Porphyry Copper Deposit, Superior District, Arizona: unpublished MSc thesis, University of Arizona, Tucson, 51 p.

McConnell, R. L., 1972, The Apache Group (Proterozoic) of central Arizona, with special reference to the paleoecology of the Mescal Formation: Unpublished PhD thesis, University of California, Santa Barbara. 170 p.

McConnell, R.L., 1975, Biostratigraphy and depositional environment of algal stromatolites from the Mescal Limestone (Proterozoic) of central Arizona: Precambrian Research, v. 2, p. 317–328.

McDonough W.F., and Sun S-S., 1995, The composition of the Earth: Chemical Geology, v. 120 p. 223-253.

McFarlane, C.R., 2016, Allanite U-Pb geochronology by 193 nm LA ICP-MS using NIST610 glass for external calibration: Chemical Geology, v. 438, p. 91-102.

McIntosh, W. C., and Ferguson, C. A., 1998, Sanidine, single crystal, laser-fusion $^{40}Ar/^{39}Ar$ geochronology database for the Superstition volcanic field, central Arizona: Arizona Geological Survey Open-File Report 98-27, 74 p.

Meffre, S., Large, R.R., Scott, R., Woodhead, J., Chang, Z., Gilbert, S.E., Danyushevsky, L.V., Maslennikov. V. and Hergt, J.M., 2008, Age and pyrite Pb-isotopic composition of the giant Sukhoi Log sediment-hosted gold deposit, Russia: Geochimica et Cosmochimica Acta, v. 72, p. 2377-2391.

Meijer, A., 2014, The Pinal Schist of southern Arizona: A Paleoproterozoic forearc complex with evidence of spreading ridge-trench interaction at ca. 1.65 Ga and a Proterozoic arc obduction event: Geological Society of America Bulletin, v. 126, no. 9/10, p. 1145–1163.

Middleton, L.T., 1989, Cambrian and Ordovician depositional systems in Arizona, in Jenney, J.P., and Reynolds, S.J., eds., Geologic Evolution of Arizona: Arizona Geological Society Digest, v. 17, p. 239–258.

Miller, C.F., and Bradfish, L.J, 1980, An inner cordilleran belt of muscovite bearing putons: Geology, v 8, p. 412-416

Min, K., Mundil, R., Renne, P. R., and Ludwig, K. R., 2000, A test for systematic errors in $^{40}Ar/^{39}Ar$ geochronology through comparison with U/Pb analysis of a 1.1-Ga rhyolite: Geochimica et Cosmochimica Acta, v. 64, p. 73–98.

Mulder, J. A., Karlstrom, K. E., Fletcher, K., Heizler, M. T., Timmons, J. M., Crossey, L. J., Pecha, M. 2017, The syn-orogenic sedimentary record of the Grenville Orogeny in southwest Laurentia: Precambrian Research, v. 294, p. 33-52.

Mukherjee, P.K., and Gupta, P.K., 2008, Arbitrary scaling in ISOCON method of geochemical mass balance: An evaluation of the graphical approach: Geochemical Journal, v. 42, p. 247-253.

Mysen, B.O., 1979, Trace element partitioning between garnet peridotite minerals and water-rich vapor: experimental data from 5 to 30 kbar: American Mineralogist, v. 64, p. 274-287.

Nabelek, P.I., 1980, Nickel partitioning between olivine and liquid in natural basalts: Henry's Law behaviour: Earth Planetary Science Letters, v. 48, p. 293-302.

Naeser, C.W., Engels, J.C. and Dodge, F.C.W., 1970, Fission track annealing and age determination of epidote minerals: Journal of Geophysical Research, v. 75, p. 1579-1584.

Nehru, C.E., and Prinz, M., 1970, Petrologic study of the Sierra Ancha sill complex, Arizona: Geological Society of America Bulletin, v. 81, p. 1733-1766.

Neuerberg, G.J., and Granger, H. C., 1960, A geochemical test of diabase as an ore source for the uranium deposits of the Dripping Spring district, Arizona: Neues Jahrbuch fur Mineralogie, v. 94, p. 759-797.

Newberry, R.J., Einaudi, M.T., and Eastman, H.S., 1991, Zoning and genesis of the Darwin

Pb-Zn-Ag skarn deposit, California: A reinterpretation based on new data: Economic Geology, v. 86, p. 960–982.

Nickerson, P. A., and Seedorff, E., 2016, Dismembered porphyry systems near Wickenburg, Arizona: District-scale reconstruction with an arc-scale context: Economic Geology, v. 111, no. 2, p. 447-466.

Nicholson, S.W., and Shirley, S.B., 1990, Midcontinent Rift volcanism in the Lake Superior region: Sr, Nd, and Pb isotopic evidence for a mantle plume origin, Journal of Geophysical Research, v. 95, 10851-10868.

Noble, L.F., 1914, The Shinumo quadrangle, Grand Canyon district, Arizona: U.S .. Geological Survey Bulletin 549, 100 p.

Norman, D.K., Parry, W.T. and Bowman, J.R., 1991, Petrology and geochemistry of propylitic alteration at Southwest Tintic, Utah. Economic Geology, v. 86, pp.13-28.

Nutt, C.J., and Hofstra, A.H., 2007, Bald Mountain Gold Mining District, Nevada: A Jurassic Reduced Intrusion-Related Gold System: Economic Geology, v. 102, p. 1129–1155.

Nutt, C.J., 1981, A model of uranium mineralization in the Dripping Spring Quartzite, Gila County, Arizona: U.S. Geological Survey Open-file Report 81-524, 49 p.

Nutt, C.J, 1984. Strata-bound uranium deposits in the Dripping Spring Quartzite, in Ferguson, J., eds, Proterozoic unconformity and stratabound uranium deposits, a technical document issued by the international atomic energy agency, Vienna, pp. 95-111.

Ohmoto, H., 1972, Systematics of sulfur and carbon isotopes in hydrothermal ore deposits: Economic Geology, v. 67, p. 551-578.

Ohmoto, H., 1986, Stable isotope geochemistry of ore deposits: Reviews in Mineralogy and Geochemistry, v, 16, p. 491-559.

Ohmoto, H., and Goldhaber, M.B., 1997, Sulfur and carbon isotopes, in Barnes H.L., ed., Geochemistry of hydrothermal ore deposits, 3rd ed.: New York, Wiley, p. 517–612.

Ohmoto, H., and Rye, R.O., 1979, Isotopes of sulfur and carbon, in Barnes, H.L., ed., Geochemis¬try of hydrothermal ore deposits, 2nd ed.: New York, Wiley, p. 509–567.

Olson, S.F., 1984, The stratigraphic and structural setting of the Potrerillos porphyry copper dis¬trict, northern Chile: Revista Geológica de Chile, v. 16, p. 3–29.

O'Neal, 2015: O'Neal, S. P., 2015, Characterization of two centres of porphyry-style Cu-(Mo) alteration in the western Superior mining district, Arizona: Unpublished P. S. M. thesis, University of Arizona, 106 p.

O'Neil, J.R., Clayton, R.N. and Mayeda, T.K., 1969, Oxygen isotope fractionation in divalent metal carbonates. The Journal of Chemical Physics, v. 51, p. 5547-5558.

Pacey, A., 2017, The characteristics, geochemistry and origin of propylitic alteration in the Northparkes porphyry Cu-Au system; unpublished Ph.D .thesis, Imperial College London, 631 p.

Pareja, G. A., 1998, The gold-rich jasperoids of the Superior district, Arizona: Controls on their location, and their relationship to porphyry-related carbonate-hosted massive sulfide

bodies: Unpublished PhD. thesis, Stanford University, Stanford, California, 213 p.

Pass H.E., 2010, Breccia-hosted chemical and mineralogical zonation patterns of the northest zone, Mt. Polley Cu–Ag–Au alkali porphyry deposit, British Columbia, Canada. Unpublished PhD. thesis University of Tasmania, Hobart, Australia. 219 p.

Pass, H.E., Cooke, D.R., Davidson, G., Maas, R., Dipple, G., Rees, C., Ferreira, L., Taylor, C. , and Deyell, C.L., 2014, Isotope geochemistry of the Northeast zone, Mount Polley alkalic Cu-Au- Ag porphyry deposit, British Columbia: A case for carbonate assimilation: Economic Geology, v. 109, p. 859–890.

Paul, A. H., and Knight, M. J., 1995, Replacement ores in the Magma mine, Superior, Arizona, in Pierce, F. W., and Bolm, J. G., eds., Porphyry copper deposits of the American Cordillera: Arizona Geological Society Digest 20, p. 366-372.

Paul, A.H., and Manske, S.L., 1999, Discovery of the Magma Porphyry system, Superior, Arizona [abs.]: Geological Society of America Abstracts with Programs, v. 31, no. 6, p. A-85.

Paul, A. H., and Manske, S. L., 2005, History of exploration at the Magma mine, Superior, Arizona, in Rhoden, H. N., Steininger, R. C., and Vikre, P. G., eds., Window to the World: Geological Society of Nevada Symposium, Reno, Nevada, May 2005, Proceedings, v. 1, p. 629–638.

Pearce, J.A., 1980, Geochemical evidence for the genesis and eruptive setting of lavas from Tethyan ophiolites: In Proceedings of the International Ophiolite Symposium, p. 261-272

Pearce, J.A., 1996, A user's guide to basalt discriminantion diagrams. Trace element geochemistry of volcanic rocks; applications for massive sulphide exploration: Geological Association of Canada, Short Course Notes, v. 12, p. 79-113.

Pearce, J.A., 2008, Geochemical fingerprinting of oceanic basalts with applications to ophiolite classification and the search for Archean oceanic crust, Lithos, v. 100, p. 14–48,

Pearce, J.A., 2014, Immobile element fingerprinting of ophiolites. Elements, v. 10, p. 101-108.

Petrus, J.A. and Kamber, B.S., 2012, VizualAge: A novel approach to laser ablation ICP-MS U-Pb geochronology data reduction: Geostandards and Geoanalytical Research, v. 36, p. 247-270.

Peterson, D. W., 1969, Geologic map of the Superior quadrangle, Pinal County, Arizona: U. S. Geological Survey Geologic Quadrangle Map GQ-818, scale 1: 24,000.

Peterson, J.A., 1994, Maps Showing Platinum-group-element Occurrences in the Conterminous United States, US Geological Survey Map notes to accompany map MI-2270

Pettke, T., Oberli, F. and Heinrich, C.A., 2010, The magma and metal source of giant porphyry-type ore deposits, based on lead isotope microanalysis of individual fluid inclusions: Earth and Planetary Science Letters, v. 296, p. 267-277.

Phillips, D., Matchan, E.L., Honda, M. and Kuiper, K.F., 2017, Astronomical calibration of $^{40}Ar/^{39}Ar$ reference minerals using high-precision, multi-collector (ARGUSVI) mass spectrometry. Geochimica et Cosmochimica Acta, v. 196, p. 351-369.

Piechocka, A.M., Sheppard, S., Fitzsimons, I.C., Johnson, S.P., Rasmussen, B. and Jourdan, F., 2018, Neoproterozoic $^{40}Ar/^{39}Ar$ mica ages mark the termination of a billion years of in-

traplate reworking in the Capricorn Orogen, Western Australia. Precambrian Research, v. 310, p. 391-406.

Puckett, J.C., 1970, Petrographic study of a quartz diorite stock near Superior, Pinal county, Arizona: Unpublished M.Sc. thesis, University of Arizona, Tucson, 47 p.

Quintanar-Ruiz, F. J., 2008, La Herradura ore deposit: An orogenic gold deposit in northwestern Mexico: Unpublished M. S. thesis, University of Arizona, Tucson, 97 p.

Ransome, F.L., 1903, Geology of the Globe copper district, Arizona: U.S. Geological Survey Professional Paper 12, 168 p.

Ransome, F. L., 1904, Description of the Globe quadrangle (Ariz.): U.S. Geol. Survey Geol. Atlas, Folio 111, 17 p

Ransome, F.L., 1914, Copper deposits near Superior, Arizona: U.S. Geological Survey Bulletin 540, p. 139–158.

Ransome, F. L., 1915, The Tertiary orogeny of the North American Cordillera and its problems, in Problems of American geology: New Haven, Yale University Press, 505 p.

Ransome, F. L. 1916. Some Paleozoic sections in Arizona and their correlation. U.S. Geological Survey Professional Paper 98. p. 133-166.

Rao, C.R., 1948, The utilization of multiple measurements in problems of biological classification: Journal of the Royal Statistical Society. v. 10, p. 159-203.

R Core Team, 2018. R: A language and environment for statistical computing. R Foundation for Statistical Computing, Vienna, Austria. URL https://www.R-project.org/.

Reches, Z., 1978, Development of monoclines: Part I. Structure of the Palisades Creek branch of the East Kaibab monocline, Grand Canyon, Arizona, in Matthews, V., III, ed., Laramide folding associated with basement block faulting in the western United States: Geological Society of America Memoir 151, p. 235-271.

Rehrig, W.A., and Heidrick, T.L., 1972, Regional fracturing in laramide stocks of Arizona and its relationship to porphyry copper mineralization: Economic Geology, v. 67, p. 198–213.

Reyes, A.G., 1990, Petrology of Philippine geothermal systems and the application of alteration mineralogy to their assessment: Journal of Volcanology and Geothermal Research, v. 43, p. 279-309.

Richards, J.P., 2003, Tectono-magmatic precursors for porphyry Cu-(Mo-Au) deposit formation: Economic Geology, v. 96, p. 1515–1533.

Richard, S.M., and Spencer, J.E., 1998, Compilation geologic map of the Ray-Superior area, central Arizona, scale 1:24,000: Arizona Geological Survey Open-File Report 98–13, 47 p.

Rollinson, H., 1993, Using geochemical data: Evaluation, presentation, interpretation: Longman, Harlow, United Kingdom, 352 p.

Runyon, S. E., Barton, M. D., Dilles, J. H., Ohlin, H. N., Seedorff, E., Carpenter, K., and Johnson, D. A., 2015a, Iron oxide-rich mineralization and related alteration in the Yerington district, Lyon County, Nevada, in Pennell, W. M., and Garside, L. J., eds., New concepts and discoveries: Geological Society of Nevada, Symposium, Reno/Sparks, May 2015,

Proceedings, v. 1, p. 251-283.

Rye, R.O., 1993, The evolution of magmatic fluids in the epithermal environment: the stable isotope perspective: Economic Geology, v. 88, p. 733–753.

Sanford, R.F., 1992, Lead isotopic compositions and paleohydrology of caldera-related epithermal veins, Lake City, Colorado. Geological Society of America Bulletin, v. 104, p. 1236-1245.

Savin, S.M. and Lee, M.L., 1988, Isotopic studies of phyllosilicates: Reviews in Mineralogy and Geochemistry, v. 19 p. 189-223.

Schoene, B., Crowley, J.L., Condon, D.J., Schmitz, M.D. and Bowring, S.A., 2006, Reassessing the uranium decay constants for geochronology using ID-TIMS U–Pb data: Geochimica et Cosmochimica Acta, v. 70, p. 426-445.

Schmidt, M.W., Dardon, A., Chazot, G., Vannucci, R., 2004, The dependence of Nb and Ta rutile-melt partitioning on melt composition and Nb/Ta fractionation during subduction processes: Earth and Planetary Science Letters, v. 226, p. 415–432.

Schmitz, M.D. and Schoene, B., 2007, Derivation of isotope ratios, errors, and error correlations for U-Pb geochronology using $^{205}$Pb-$^{235}$U-($^{233}$U)-spiked isotope dilution thermal ionization mass spectrometric data: Geochemistry, Geophysics, Geosystems,v. 8. Q08006, doi:10.1029/2006GC001492.

Schofield, R. E., 1976, The petrology and geochemistry of the Cienega Falls diabase sill, Salt River Canyon area, Gila County, Arizona, Unpublished Ph.D. thesis, University of Arizona, 82 p.

Schott, T.G., 1994, Mineralization, lithology, and alteration in the Mesozoic rocks, Superior mine, Superior, Arizona: Unpublished M.Sc. thesis, New Mexico Institute of Mining and Technology, Socorro, 197 p.

Schwarz, A., 2007, Geology of the Resolution porphyry Cu-Mo system [abs.]: Ores and orogenesis: A symposium honoring the career of William R. Dickinson: Arizona Geological Society, Tucson, September 2007, Program with Abstracts, p. 83-84.

Schwarz, A., 2010, early diabase-hosted alteration-mineralization in the Resolution Cu-Mo deposit, Pinal county, Arizona: The foundation of a giant porphyry system, Unpublished M.Sc thesis, Queens University, 153 p.

Seager, W.R, 2004, Laramide (Late Cretaceous-Eocene) tectonics of southwestern New Mexico, in Mack, G. H. ed., The geology of New Mexico: a geologic history: New Mexico Geological Society Special Publication 11, p 183-202

Seal, R.R., 2006, Sulfur isotope geochemistry of sulfide minerals: Reviews in mineralogy and geochemistry, v. 61, p. 633-677.

Seedorff, E., 1991, Royston district, western Nevada: A Mesozoic porphyry copper system that was tilted and dismembered by Tertiary normal faults, in Raines, G.L., Lisle, R.E., Schafer, R.W., and Wilkinson, W.H., eds., Geology and ore deposits of the Great Basin: Geological Society of Nevada, Symposium, Reno/Sparks, April 1990, Proceedings, v. 1, p. 359-391.

Seedorff, E., Barton, M.D., Stavast, W.J. a, and Maher, D.J., 2008, Root zones of porphyry systems: Extending the porphyry model to depth: Economic Geology, v. 103, p. 939–956.

Seedorff, E., Dilles, J.H., Proffett, J.M., Einaudi, M.T., Zurcher, L., Stavast, W.J.A., Johnson, D.A.,

and Barton, M.D., 2005, Porphyry Deposits: Characteristics and Origin of Hypogene Features: Economic Geology 100th Anniversay Volume, p. 251–298.

Seedorff, E., Barton, M.D., Gehrels, G.E., Johnson, D.A., Maher, D.J., Stavast, W.J.A., and Flesch, E., 2005b, Implications of new U-Pb dates from porphyry copper-related plutons in the Superior-Globe-Ray-Christmas area, Arizona [abs.]: Geological Society of America Abstracts with Programs, v. 37, p. 164.

Sell, J.D., 1995, Discovery of a deep (3500 feet) unexposed porphyry copper deposit at Superior East, Pinal County, Arizona, in Pierce, F.W., and Bolm, J.G., eds., Porphyry copper deposits of the American Cordillera: Arizona Geological Society Digest, v. 20, p. 373–395.

Selverstone, J., Hodgins, M., Aleinikoff, J.N., and Fanning, M.C., 2000, Mesoproterozoic reactivation of a Paleoproterozoic transcurrent boundary in the northern Colorado Front Range: Implications for 1.7- and 1.4-Ga tectonism: Rocky Mountain Geology, v. 35, no. 2, p. 139–162.

Shervais, J. W., 1982. Ti-V plots and the petrogenesis of modern and ophiolitic lavas. Earth and planetary science letters, v. 59, p. 101-18.

Short, M.N.**,** and Ettlinger, I. A., 1926, Ore deposition and enrichment at the Magma mine, Superior, Arizona: American Institute of Mining Engineers Transactions, v. 74, p. 174-222.

Short, M.N., Ettlinger, I.A., Galbraith, F.W., Harshman, E.N., Wardwell, H.R., and Kuhn, T.H., 1942, Geologic map of the Superior mining area, Arizona (1:12000): Arizona Bureau of Mines, Geological Series 16, Bulletin 150.

Short, M.N., Galbraith, F. W., Harshman, E. N., Kuhn, T. H., and Wilson, E. D., 1943, Geology and ore deposits of the Superior mining area, Arizona: Arizona Bureau of Mines and Geology Series no. 16, Bulletin 151, 159 p.

Short M.N., and Wilson, E.D., 1938, Magma mine area, Superior: Arizona Bureau of Mines Bulletin, v. 145, pp. 90-98

Showalter, 1982, A structural study of folds and tear faults in the Roadside Hills area, Tucson Mountains, Pima County, Arizona: Unpublished PhD thesis, University of Arizona, Tucson, 82 p.

Shride, A.F., 1967, Younger Precambrian Geology in Southern Arizona: U.S. Geological Survey Professional Paper 566, 89 p.

Sillitoe, R.H., 1985, Ore-related breccias in volcanoplutonic arcs: Economic Geology, v. 80, p. 1467–1514.

Sillitoe, R.H., 1997, Characteristics and controls of the largest porphyry copper-gold and epither¬mal gold deposits in the circum-Pacific region: Australian Journal of Earth Sciences, v. 44, p. 373–388.

Sillitoe, R., 2005, Supergene oxidized and enriched porphyry copper and related deposits: Economic Geology 100th Anniversay Volume, p. 723 - 768.

Sillitoe, R.H., 2010, Porphyry copper systems: Economic Geology, v. 105, p. 3–41.

Sillitoe, R.H., 2013, Geology and potential of the Superior East porphyry copper prospect and environs, Arizona. Unpublished report to Rio Tinto Exploration, 11 p.

Sillitoe, R.H., Creaser, R.A., Kern, R.R., and Lenters, M.H., 2014, Squaw peak, Arizona: Paleoproterozoic precursor to the laramide porphyry copper province: Economic Geology, v. 109, p. 1171–1177.

Sillitoe, R.H., and Gappe, I.M., Jr., 1984, Philippine porphyry copper deposits: Geologic setting and characteristics: Bangkok, Thailand, United Nations ESCAP, CCOP Technical Publication 14, 89 p.

Silver, L. T., 1978, Precambrian formations and Precambrian history in Cochise County, southeastern Arizona, in Callender, J. F., Wilt, J. C., and Clemons, R. E., eds., Land of Cochise: New Mexico Geological Society 29th Field Conference Guidebook, p. 157-163.

Silver, L. T., and Anderson, T. H., 1974, Possible left-lateral early to middle Mesozoic disruption of the southwestern North American craton margin: Geological Society of America Abstracts with Programs, v. 6, p. 955-956.

Simmons, S.F. and Christenson, B.W., 1994, Origins of calcite in a boiling geothermal system: American Journal of Science, v. 294, p. 361-400.

Simmons, S.F., White, N.C. and John, D.A., 2005, Geological characteristics of epithermal precious and base metal deposits. Economic Geology 100th Anniversary Volume, p. 485-522.

Simmons, S.F., Brown, K.L., and Browne, P.R.L., 2006, Precious metals in hydrothermal systems of the Taupo Volcanic Zone, in Christie, A.B., and Brathwaite, R.L., eds., Geology and Exploration of New Zealand Mineral Deposits: AusIMM Monograph 25, p. 203–211.

Simon, A.C., Pettke, T., Candela, P.A., Piccoli, P.M. and Heinrich, A.H., 2004, Magnetite solubility and iron transport in magmatic-hydrothermal environments. Geochimica et Cosmochimica Acta, v. 68, p. 4905–4914.

Smith, D., 1969, Mineralogy and petrology of an olivine diabase sill complex and associated unusually potassic granophyres, Sierra Ancha, central Arizona: Unpublished PhD. thesis, California Institute of Technology, Pasadena. 314 p.

Smith, D., 1970, Mineralogy and petrology of the diabasic rocks in a differentiated olivine diabase sill complex, Sierra Ancha, Arizona: Contributions to Mineralogy and Petrology, v. 27, p. 95-113.

Smith, D., and Silver, L.T., 1975, Potassic granophyre associated with Precambrian Diabase, Sierra Ancha, central Arizona: Geological Society of America Bulletin, v. 86, p. 503–513.

Smye, A.J., Roberts, N.M., Condon, D.J., Horstwood, M.S. and Parrish, R.R., 2014, Characterising the U–Th–Pb systematics of allanite by ID and LA-ICPMS: Implications for geochronology. Geochimica et Cosmochimica Acta, v. 135, p. 1-28.

Spencer J.E., and Welty J.W., 1989, Mid-Tertiary ore deposits of Arizona, in Jenny. J.P and Reynolds, S.J., eds, Geologic evolution of Arizona: Tucson, Arizona Geological Society Digest 17, p. 585-607.

Spencer, J.E. and Reynolds, S.J., 1989, Middle Tertiary tectonics of Arizona and adjacent areas, in Jenny J.P., and Reynolds, S.J eds., Geologic Evolution of Arizona: Arizona Geological Survey Digest 17, p. 539-573

Stacey, J.S., Zartman, R.E. and Nkomo, I.T., 1968, A lead isotope study of galenas and selected

feldspars from mining districts in Utah: Economic Geology, v. 63, p. 796-814.

Stacey, J.S., Kramers, J.D., 1975, Approximation of terrestrial lead isotope evolution by a two-stage model: Earth and Planetary Science Letters, v. 26, p. 207–221.

Staude, J.M.G., and Barton, M.D., 2001, Jurassic to Holocene tectonics, magmatism, and metallogeny of Northwestern Mexico: Bulletin of the Geological Society of America, v. 113, no. 10, p. 1357–1374.

Stavast, W.J.A., 2006, Three-dimensional evolution of magmatic hydrothermal systems, Schultze Granite and Ruby Star Granodiorite, Arizona: Unpublished Ph.D. thesis, University of Arizona, Tucson, 414 p.

Steiger, R. H., and Jäger, E., 1977, Subcommission on geochronology: Convention on the use of decay constant in geo- and cosmochronology, Earth Planetary Science Letters, v. 36, p. 359–362.

Stevens, G., 1997, Melting, carbonic fluids and water recycling in the deep crust: an example from the Limpopo Belt, South Africa: Journal of Metamorphic Geology, v. 15, p. 141-154.

Stewart, J.H., 1982. Regional relations of Proterozoic Z and Lower Cambrian rocks in the Western United States and northern Mexico. In: Cooper, J.D., Troxel, B.W., and Wright, L.A. (eds.), Geology of Selected Areas in the San Bernardino Mountains, western Mojave Desert, and southern Great Basin, California. Geological Society of America Codilleran Section Volume and Guidebook: Death Valley Publishing, Company, Shoshone, California, p. 171-180.

Stewart, J.H., Poole, F.G., Ketner, K.B., Madrid, R.J., Roldán-Quintana, J., and Amaya-Martínez, R., 1990, Tectonics and stratigraphy of the Paleozoic and Triassic southern margin of North America, Sonora, México, in Gehrels, G.E., and Spencer, J.E., eds., Geologic Excursions through the Sonoran Desert Region, Arizona and Sonora: Arizona Geological Survey Special Paper 7, p. 183–202.

Stewart, L.A. 1955, Chrysotile asbestos deposits of Arizona. US Department of the Interior, Information Circular 7706, 124 p.

Stone, P., Light, T., E, Grauch, V.J.S., Yeend, W. E., and Schreiner, R. A., 1985, Mineral resources of the Palen-McCoyWilderness Study Area, Riverside County, California: U.S. Geological Survey Bulletin 1710-A, 15 p.

Storey, L.O., 1978, Geology and Mineralization of the Lights Creek Stock, Plumas County, California: Arizona Geological Society Digest, v. 11, p. 49–58.

Skotnicki, S.J. and Knauth, L.P., 2007, The middle Proterozoic Mescal paleokarst, central Arizona, USA: karst development, silicification, and cave deposits: Journal of Sedimentary Research, v. 77, p. 1046-1062.

Swift, P.N., and Force, E., 2001, Subduction-margin assemblages in the Proterozoic Pinal and Cochise blocks, southeastern Arizona: American Journal of Science, v. 301, p. 755–772,

Taylor, J. R., 1997, An Introduction to Error Analysis: The Study of Uncertainties in Physical Measurements, 327 pp., University Science Books, Mill Valley, California.

Thompson, J., Meffre, S., Maas, R., Kamenetsky, V., Kamenetsky, M., Goemann, K., Ehrig, K. and

Danyushevsky, L., 2016, Matrix effects in Pb/U measurements during LA-ICP-MS analysis of the mineral apatite: Journal of Analytical Atomic Spectrometry, v. 31, p. 1206-1215.

Thomson, B., Aftalion, M., McIntyre, R.M., and Rice, C., 1995, Geochronology and tectonic setting of silicic dike swarms and related silver mineralization at Candelaria, western Nevada: Economic Geology, v. 90, p. 2182–2196.

Timmons, J.M., Karlstrom, K.E., Dehler, C.M., Geissman, J.W., and Heizler, M.T., 2001, Proterozoic multistage (ca. 1.1 and 0.8 Ga) extension recorded in the Grand Canyon Supergroup and establishment of northwest- and north-trending tectonic grains in the southwestern United States: Geological Society of America Bulletin, v. 113, p. 163–181.

Timmons, J.M., Karlstrom, K.E., Heizler, M.T., Bowring, S.A., Gehrels, G.E., and Crossey, L.J., 2005, Tectonic inferences from the ca. 1255–1100 Unkar Group and Nankoweap Formation, Grand Canyon: Intracratonic deformation and basin formation during protracted Grenville-age orogenesis: Geological Society of America Bulletin, v. 117, p. 1573–1595,

Titley, S.R., 1982, Geologic Setting of Porphyry Copper Deposits, Southwestern Arizona, in Titley, S. ed., Advances in Geology of the Porphyry Copper Deposits, Southwestern North America: University of Arizona Press, Arizona, p. 37–56.

Titley, S.R., 1987, The crustal heritage of silver and gold ratios in Arizona ores: Geological Society of America Bulletin, v. 99, p. 814–826.

Titley, S.R., 1991, Correspondence of ores of silver and gold with basement terranes in the American southwest: Mineralium Deposita, v. 71, p. 66–71.

Titley, S.R., 2001, Crustal affinities of metallogenesis in the American Southwest: Economic Geology, v. 96, p. 1323–1342.

Titley, S.R., and Marozas, D., 1995, Processes and products of supergene copper enrichment, in Pierce, F. and Bolm, J. eds., Porphyry Copper Deposits of the American Cordillera: Arizona Geological Society Digest 20: Tucson, p. 156–168.

Titley, S.R., and Zürcher, L., 2008, Regeional Geology & Deposit styles of the trans boder region, southwestern North America, in Spencer, J.E. and Titley, S.R. eds., Ores and orogenesis: Circum-Pacific tectonics, geological evolution, and ore de- posits: Arizona Geological Society Digest, 22: Arizona Geological Society, Tucson, p. 275–294.

Tosdal, R.M., Haxel, G.B., and Wright, J.E., 1989, Jurassic Geology of the Sonoran Desert Region, Southern Arizona, Southeastern California and Northernmost Sonora: Construction of a Continental-Margin Magmatic Arc, in Jenney, J.. and Reynolds, S. (eds.), Geologic Evolution of Arizona, Arizona Geological Society Digest v. 17, Tucson.

Tosdal R.M., Wooden J.L., Bouse R., 1999, Pb isotopes, ore deposits, and metallogenic terranes. In: Lambert, D.D., Ruiz, J., eds., Application of radiogenic isotopes to ore deposit research and exploration: Reviews in Economic Geology, v. 12, p. 1–28

Troutman, S. M., 2001, Advanced argillic alteration in the deeply buried Magma Porphyry Cu-Mo prospect, Superior, Arizona: Unpublished MSc. thesis, Stanford University, 115 p.

Valencia, V.A., Barra, F., Weber, B., Ruiz, J., Gehrels, G., Chesley, J., and Lopez-Martinez, M., 2006, Re–Os and U–Pb geochronology of the El Arco porphyry copper deposit, Baja California Mexico: Implications for the Jurassic tectonic setting: Journal of South Ameri-

can Earth Sciences, v. 22, no. 1-2, p. 39–51.

Valencia-Moreno, M., Ochoa-Landín, L., Noguez-Alcántara, B., Ruiz, J., and Pérez-Segura, E., 2007, Geological and metallogenetic characteristics of the porphyry copper deposits of México and their situation in the world context, in Alaniz-Álvarez, S. A., and Nieto-Samaniego, Á. F., eds., Geology of México: Celebrating the Centenary of the Geological Society of México: Geological Society of America Special Paper 422, p. 433-458.

Vaughan, J.R., Hickey, K.A., and Barker, S.L.L., 2016, Isotopic, chemical, and textural evidence for pervasive calcite dissolution and precipitation accompanying hydrothermal fluid flow in low-temperature, carbonate-hosted gold systems: Economic Geology, v. 111, p. 1127–1157.

von Blackenburg, F., 1992, Combined high-precision chronometry and geochemical tracing using accessory minerals: applied to the Central-Alpine Bergell intrusion (central Europe): Chemical Geology, v. 100, p. 19-40.

Walshe, J.L., 1986, A six-component chlorite solid solution model and the conditions of chlorite formation in hydrothermal and geothermal systems: Economic Geology, v. 81, p. 681-703.

Ward, P.L., 1991, On plate tectonics and the geologic evolution of southwestern North America: Journal of Geophysical Research, v. 96, p. 12479.

Wardwell, H.R., 1941, Geology pf the Potts Canyon mining area near Superior, Arizona. Unpublished MSc thesis, University of Arizona, Tucson, 140 p.

Wiedenbeck, M., et al., 1995. Three natural zircon standards for U–Th–Pb, Lu–Hf, trace element and REE analyses: Geostandards Newsletter, v. 19, p. 1–23

Wenrich, K.J., and Titley, S.R., 2008, Uranium exploration for northern Arizona (USA) breccia pipes in the 21st century and consideration of genetic models, in Spencer, J.E., and Titley, S.R., eds., Ores and orogenesis: Circum-Pacific tectonics, geologic evolution, and ore deposits: Arizona Geological Society Digest 22, p. 295-309.

Wenzel, F., and Sandmeier, K.J., 1992, Geophysical evidence for fluids in the crust beneath the Black-Forest, SW Germany Earth-Science Reviews, v. 32, p. 61-75.

White, N.C., and Hedenquist, J.W., 1990, Epithermal environments and styles of mineralization: Variations and their causes, and guidelines for exploration: Journal of Geochemical Exploration, v. 36, p. 445–474.

Williams, N.C., and Davidson, G.J., 2004, Possible submarine advanced argillic alteration at the Basin Lake prospect, western Tasmania, Australia: Economic Geology, v. 99, p. 987–1002.

Williams, P.J., Barton, M.D., Johnson, D.A., Fontboté, L., de Haller, A., Mark, G., Oliver, N.H.S., and Marschik, R., 2005, Iron oxide copper-gold deposits: Geology, Space-time distribution, and possible modes of origin: Economic Geology, 100th Anniverary Volume, p. 371–405

Wilson, E.D., 1928, Asbestos deposits of Arizona: Arizona Bureau of Mines Bulletin, v. 126, p. 100.

Wilson, A.J., 2003, The geology, genesis and exploration context of the Cadia gold-copper porphyry deposits, NSW, Australia: Unpublished PhD thesis, University of Tasmania, Hobart, 335 p.

Wilson, A.J., Cooke, D.R., Stein, H.J., Fanning, C.M., Holliday, J.R., and Tedder, I.J., 2007, U-Pb and Re-Os geochronologic evidence for two alkalic porphyry ore-forming events in the Cadia district, New South Wales, Australia: Economic Geology, v. 102, p. 3–26.

Winant, A.R.**,** 2010, Sericiticand advanced argillic mineral assemblages and their relationship to copper mineralization,Resolution porphyry Cu-(Mo) deposit, Superior district, Pinal County, Arizona: Unpublished M.S. thesis, Tucson, University of Arizona, 79 p.

Whitmeyer, S.J., and Karlstrom, K.E., 2007, Tectonic model for the Proterozoic growth of North America: Geosphere, v. 3, p. 220–259,

Wilkinson, J.J., Chang, Z., Cooke, D.R., Baker, M.J., Wilkinson, C.C., Inglis, S., Chen, H., Gemmell, J.B., 2015a, The chlorite proximitor: a new tool for detecting porphyry ore deposits: Journal of Geochemical Exploration, v. 152, p. 10–26.

Wilkinson, C.C., Harman, E.M., and Wilkinson, J.J., 2015b, Epidote chemistry in contrasting hydrothermal and metamorphic environments, In: World-Class Ore Deposits: Discovery to Recovery; Society of Economic Geology 2015 Conference, Hobart, Tasmania, September 27-30, 2015

Wilkinson J.J., Cooke D.R., Baker M.J, Chang, Z., Wilkinson C.C., Chen H., Fox N., Hollings P., White, N.C., Gemmell J.B., Loader M.A., Pacey, A., Sievwright, R.H., Hart, L.A., and Brugge E.R., 2017a, Porphyry indicator minerals and their mineral chemistry as vectoring and fertility tools: in McClenaghan, M.B. and Layton-Matthews, D., (eds.) Application of indicator mineral methods to bedrock and sediments; Geological Survey of Canada, Open File 8345, 90 p

Wilkinson, J.J., Baker, M.J., Cooke, D.R., Wilkinson, C.C., and Inglis, S., 2017b, Exploration targeting in porphyry Cu systems using propylitic mineral chemistry: a case study of the El Teniente deposit, Chile, In: Proceedings; 14th Biennial Society of Geology Applied to Mineral Deposits (SGA) conference, Quebec City, August 20–23, 2017

Wilson, A.J., Cooke, D.R., Harper, B.J. and Deyell, C.L., 2007, Sulfur isotopic zonation in the Cadia district, southeastern Australia: exploration significance and implications for the genesis of alkalic porphyry gold–copper deposits: Mineralium Deposita, v. 42, p. 465-487.

Wooden, J.L., and DeWitt, E., 1991, Pb isotopic evidence for a major Early crustal boundary in western Arizona, in Karlstrom, K.E., ed., Proterozoic geology and ore deposits of Arizona: Arizona Geological Digest v. 19, p. 27–50.

Wooden J.L., and Aleinikoff, J.N., 1987, Pb isotopic evidence for Early Proterozoic crustal evolution in the southwestern U.S., Geological Society of America, Abstracts with Programs, v. 19, p. 198

Wooden, J.L., and Miller, D.M., 1990, Chronologic and isotopic framework for Early Proterozoic crustal evolution in the eastern Mojave Desert Region, SE California: Journal of Geophysical Research, v. 95, p. 20,133-20,146.

Wooden, J., Nutman, A.P., Miller, D.M., Howard, K.., Bryant, B., DeWitt, E., and Mueller, P., 1994, SHRIMP U-Pb zircon evidence for Late Archean and Early Proterozoic crustal evolution in the Mojave and Arizona crustal provinces, in Geological Society of America Abstracts with Programs, v. 26, no. 6, p. 69

Woodhead, J., Hergt, J., Meffre, S., Large, R.R., Danyushevsky, L. and Gilbert, S., 2009, In situ

Pb-isotope analysis of pyrite by laser ablation (multi-collector and quadrupole) ICPMS: Chemical Geology, v. 262, p. 344-354.

Wright, J.E. and Haxel, G., 1982, A garnet-two-mica granite, Coyote Mountains, southern Arizona: Geologic setting, uranium-lead isotopic systematics of zircon, and nature of the granite source region. Geological Society of America Bulletin, v. 93, p. 1176-1188.

Wrucke, C.T., 1989, The Middle Proterozoic Apache Group, Troy Quartzite, and associated diabase of Arizona, in Jenney, J.P., and Reynolds, S.J., eds., Geologic Evolution of Arizona: Arizona Geological Society Digest, v. 17, p. 239–258.

Wrucke, C.T., Otton, J.K., and Desborough, G.A., 1986, Summary and origin of the mineral commodities in the Middle Proterozoic Apache Group in central Arizona, in Beatty, Barbara, and Wilkinson, P.A.K., eds., Frontiers in geology and ore deposits of Arizona and the Southwest: Arizona Geological Society Digest 16, p. 12-17.

Wrucke, C.T., and Shride, A.F., 1972, Correlation of Precambrian diabase in Arizona and southern California: Geological Society of America Abstracts with Programs, v. 4, p. 265–266.

York, D., 1969, Least squares fitting of a straight line with correlated errors, Earth and Planetary Science Letters, v. 5, p. 320–324,

Zulliger, G., 2007, Mid-Late Cretaceous Stratigraphy and Volcanic – Intrusive Transition at the Resolution porphyry Cu-Mo deposit, SW Arizona. Age and timing constraints based on U/Pb, Re/Os and Ar/Ar dating. Internal report to Resolution Copper Mining, 41 p.